DRAFT
HYDROFOIL DESIGN CRITERIA AND SPECIFICATIONS

Volume IIA
Hydrofoil Ship Hydrodynamic
Specifications and Criteria
(Technical Substantiation)

Contract N00600-76-C-0246, Task 010

Grumman Aerospace Corporation
Bethpage, New York 11714

VOLUME IIA

TECHNICAL SUBSTANTIATION

SECTION CHARACTERISTICS

This volume was published in 1980 and 1981. The masters are in a file cabinet in the Naval Ship Systems Office. The art work masters would need careful checking because the glue is now quite old.

Because the 80/81 volume is quite large and to save time, the 1984 Substantiation, which had quite a different subject matter, was made Volume IIB. To accomodate this arrangement the following pages, for whichthere are no masters, were inserted in Volume IIA.

VOLUME IIA

TECHNICAL SUBSTANTIATION

SECTION CHARACTERISTICS

NOTE: See VOLUME IIB for three-dimensional characteristics.

CONTENTS

CONTENTS

CONTENTS (Contd)

ILLUSTRATIONS

ILLUSTRATIONS (Contd)

ILLUSTRATIONS (Contd)

ILLUSTRATIONS (Contd)

ILLUSTRATIONS **(Contd)**

ILLUSTRATIONS (Contd)

ILLUSTRATIONS (Contd)

ILLUSTRATIONS (Contd)

TABLES

TABLES (Contd)

1. Scope. This volume is intended to substantiate the equations specified in Volume II of the Design Criteria and Specification for U.S. Navy Hydrofoil Ships, Hydrodynamics and Performance Prediction Criteria. The nature of that substantiation is a display of the confidence level associated with each equation by comparison of classic versions of the equations with each other and with whatever appropriate experimental measurements are available. Those comparisons reveal qualitative differences between the substantiation for aerodynamic (infinite depth) performance predictions and that for predicting the effect of the free surface upon the aerodynamic performance. Promoting the hydrodynamic predictive state of the art then becomes an important second objective for this volume.

1.1 Purpose. Free surface lift, lift distribution, and drag effects present enormous theoretical complexities for the general case and Reynolds Number effects, model loads, cavitation, ventilation, and prototype depth control and environmental conditions all obscure measurements of those effects. The hydrofoil craft industry also lacks the test.and operational flight experience with numbers of craft ofmanytypes and the laboratory resources available to the aircraft industry. For all these reasons the hydrofoil industry must maximize the benefit to be obtained from every prototype and model test and this volume, in time, can serve that purpose..

Hydrodynamic theory currently is well in advance of experiment in the sense that it includes effects which cannot be measured by experiment.

In this volume such portions of the theory are **explicitely** neglected to reduce the predictions to a level which is testable and significant to the prototype. One result of this process is that the predictions are comprehensible and convenient to the design **hydro-**dynamicist who is generally limited to consideration of only the most significant effects.

Hydrodynamic measurements are compared with each other and with theory in order to select prediction equations and associated confidence levels and to display areas of experimental difficulties. Time **contraints** became significant at this point and, in certain cases for important characteristics, continuing and severe experimental difficulties are illustrated only by a single example. All predictions subject to experimental verification **are** consideredin sufficient detail to establish a significant format for the comparison of prediction and measurement.

In summary, this volume provides a context into which future theoretical developments and experimental measurements can be set for direct comparison with the existing state of the art. Those comparisons can guide resources to areas promising Yhe greatest rate of return in terms of improved confidence level for significant craft characteristics and they will guide modifications to the equations and uncertainty ranges of Volume II.

2. Applicable Documents. The following companion Design Criteria and Specification for U.S. Navy Hydrofoil Ships form a part of this specification:

Volume	I	General Information Manual
Volume	IA	General Information Manual - Technical Substantiation
Volume	II	Hydrodynamic and Performance Prediction Criteria
Volume	III	Hydrofoil Ship Control and Dynamics Specifications and Criteria
Volume	IIIA	Hydrofoil Ship Control and Dynamics Specifications and Criteria - Technical Substantiation
Volume	IV	Structural Design Criteria
Volume	IVA	Structural Design Criteria - Technical Substantiation
Volume	V	Propulsion System Design Criteria
Volume	VA	Propulsion System Design Criteria - Technical Substantiation

The following documents are referred to frequently throughout this volume:

USAF Stability and Control DATCOM, McDonnel Douglas Corporation, Douglas Aircraft Division for Flight Control Division, Air Force Flight Dynamics Laboratory, Wright-Patterson Air Force Base, Ohio Jan. 1974. revision. (Referred to as "DATCOM" throughout this volume).

Engineering Sciences Data Unit, 251-259 Regent Street, London WIR7AD, 4 Sept. 1974 revision. (Referred to as "ESDU" throughout this volume).

All other references are listed at the end of each sub-section.

3. Requirements.

3.1 Hull Hydrostatics. To be supplied.

3.2 Hull Hydrodynamics. To be supplied.

3.3 Section Characteristics.

3.3.1 Section Lift.

3.3.1.1 Reynolds Number and Mach Number Effects. Viscous effects reduce the thick airfoil potential section lift curve slope by an increment which is still generally empirical. The DATCOM Method 1 for section lift curve slope is a tabulation of the RN= 9×10^6 slopes of Reference 1. The DATCOM Method 2 is essentially the ESDU procedure which is of interest because it relates the practical lift curve slope to its potential value in the form of a rational accountability for the viscous effect and because it indicates that the section lift curve slope increases throughout the Reynolds Number range. However, the magnitude of this slope increase for Reynolds Numbers of 9×10^6 to 25×10^6 is of the order of the precision of the measurement and no significant validation of the DATCOM Method 2 is available.

References 2 and 3 provide a measure of similar 64-Series sections over the Reynolds Number range from $.7 \times 10^6$ to 25×10^6 and those results are compared with the DATCOM Method 2 on Figure 3.3.1.1-1. This particular set of data clearly displays transition point movement in the drag data (see Section 3.3.9) but there is no evidence of that movement in the lift curves.

Figure 3.3.1.1-2 compares all of the Reference 2 data with the DATCOM Method 2 with inconclusive results and, in fact, current data precision precludes a test of this method for high Reynolds Numbers in model or prototype scale for the 6-Series section. The 20" trailing edge angle prediction of Figure 3.3.1.1-2 represents a 9% 16-Series section which could provide a more significant test of the prediction.

Practically all of the smooth surface data of references 2 and 3 is included in a ±5% band defined by

$$\frac{c_{\ell_\alpha RN}}{c_{\ell_\alpha}} = .874 + .042 RN \times 10^{-6} \pm .05 \qquad RN < 3 \times 10^6$$

$$= 1 \pm .05 \qquad RN \geqslant 3 \times 10^6 \qquad \text{3.3.1.1-1}$$

Similarly, practically all of the standard leading edge roughness data of those references lies within the band defined by:

$$\frac{c_{\ell_\alpha RN}}{c_{\ell_\alpha}} = .79 + .07\, RN \times 10^{-6} \pm .05 \qquad RN < 3 \times 10^6$$

$$= 1 \pm .05 \qquad RN \geqslant 3 \times 10^6 \qquad \text{3.3.1.1-2}$$

Equations 3.3.1.1 - 1 & 2 can be employed to summarize References 2 and 3 as on Figure 3.3.1.1-3. Figure 3.3.1.1-3 indicates that the lift curve slope effect of leading edge roughness shown on Figure 3.3.1.1-1 is characteristic; i.e. when the roughness produces any effect at all, it is not the effect of a natural movement of the transition point to the leading edge.

Figure 3.3.1.1-3 indicates that Equation 3.3.1.1-1 will be valid for all hydrofoil model and prototype applications with the possible exception of prototype sections of large trailing edge angle, e.g. 16-Series sections, where the ESDU prediction would make Equation 3.3.1.1-1 low by some 10% ± 5% at a Reynolds Number of 100 x 10^6.

Mach Number effects are of interest to the hydrodynamicist only when making reference to aerodynamic data, and the 16-Series section characteristics of Reference 4 present a notable example. Lift curve slopes measured at significant Mach Number can be corrected to zero Mach Number by means of the classic parameter $\sqrt{1-M^2}$:

$$c_{\ell_\alpha} = c_{\ell_{\alpha M}} \sqrt{1-M^2} \qquad 3.3.1.1\text{-}3$$

This correction exceeds the 5% precision associated with lift curve slope measurements for Mach Numbers greater than .3. It should be noted that the section characteristics of Reference 1 were measured at Mach Numbers less than about .17.

There is no evidence in References 1 or 2 of a Reynolds Number effect upon the section zero lift angle for Reynolds Numbers of 3 x 10^6 or more. Figure 18 of Reference 3 indicates that for Reynolds Numbers less than 3 x 10^6 the zero lift angle effect is genrally negligible and of random character among the sections. Isolated exceptions in Reference 3, notably the NACA 4415 section, present negative zero lift angle shifts of 1/2 degree or more which are indicative of an abnormal laminar flow extent. Reference 5 presents a similar -8/10 degree zero lift angle shift for the 16-309 section at a Reynolds Number of 1.9 x 106.

The DATCOM text notes in Section 4.1.1.1 that the effect of compressibility on the zero lift angle is negligible up to the critical Mach Number. Figure 3.3.1.1-4, which was compiled from Reference 4, indicates that the zero lift angle for the 16-Series is practically independent of Mach Number to a critical Mach Number.

Thus, for a nominal measurement precision of ±1/3 degree, the section zero lift angle can be said to be independent of Reynolds Number, Mach number, and fixed transition and that zero lift angle shifts of -1/2 degree or more are indicative of an abnormal laminar flow extent.

Note: Because the transition strip employed for Reference 5 produced normal section lift and drag characteristics while that of References l-3 did not, the descriptions of the two transition strips are given in Section 6.1.1.1.

REFERENCES

1. Abbott, I. H. and von Doenhoff, A. E.: Theory of Wing Sections. Dover, 1959.

2. **Loftin,** Jr. L. K. and Bursnall, W. J.: The Effects Of Variations In Reynolds Number Between 3.0×10^6 and 25.0×10^6 Upon The Aerodynamic Characteristics Of A Number Of NACA 6-Series Airfoil Sections. NACA Report 964, 1950.

3. **Loftin,** Jr. L. K. and Smith, H. A.: Aerodynamic Characteristics Of 15 NACA Airfoil Sections At Seven Reynolds Numbers From 0.7×10^6 to 9.0×10^6. NACA Technical Note 1945, Oct. 1945.

4. Lindsey, W. F.: Stevenson, D. B.: and Daley, B. N.: Aerodynamic Characteristics of 24 NACA 16-Series Airfoils At Mach Numbers Between 0.3 and 0.8. NACA Technical Note 1546, Sept. 1948.

5. Teeling, P.: Low Speed Wind Tunnel Tests Of A NACA 16-309 Airfoil With Trailing-Edge Flap, DeHavilland Aircraft Of Canada Limited Report No. ECS 76-3, October 1976.

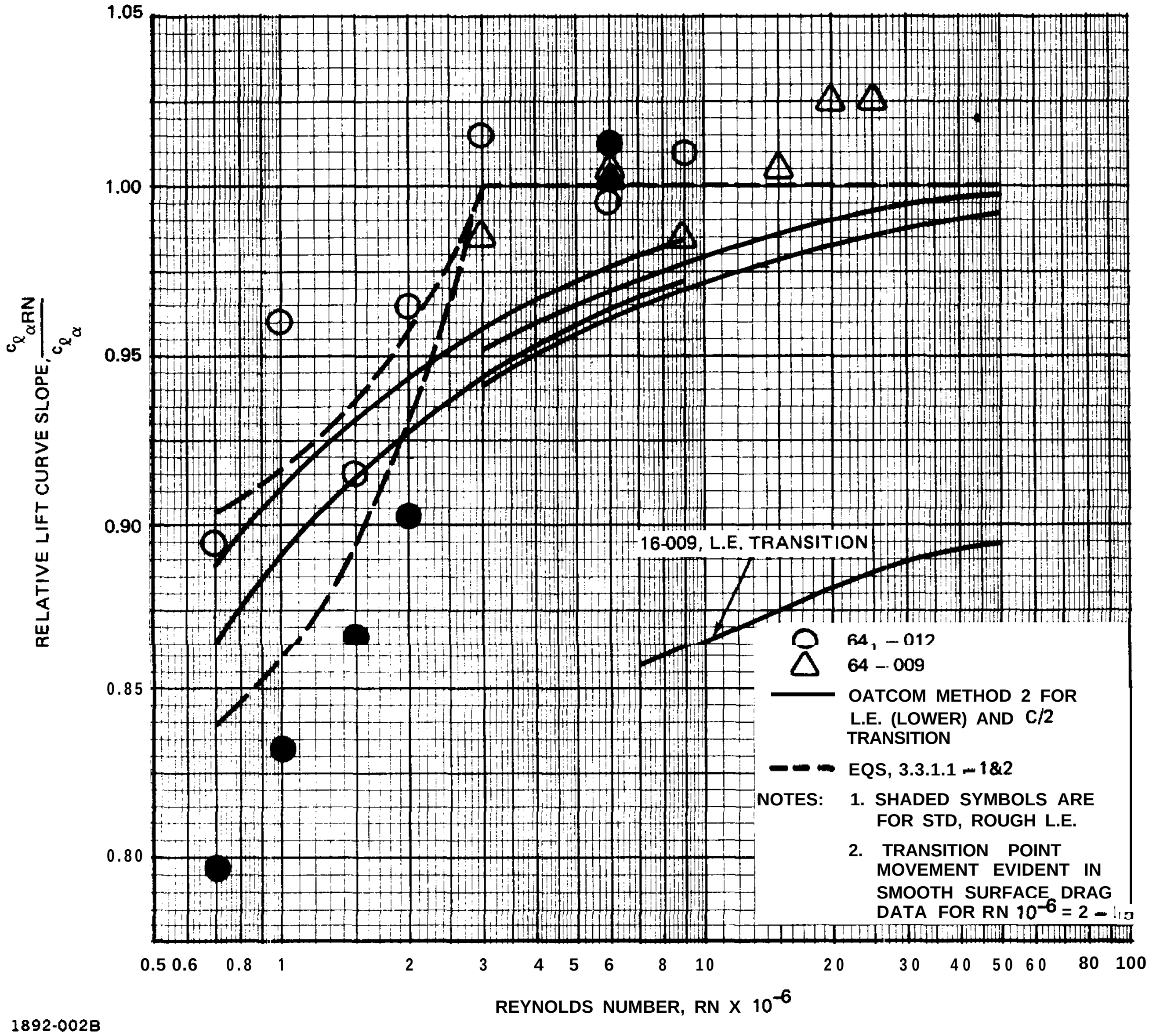

1892-002B

Fig. 3.3.1.1-1 Lift Curve Slope Reynolds Number Effect, Symmetric **64-Series** Section

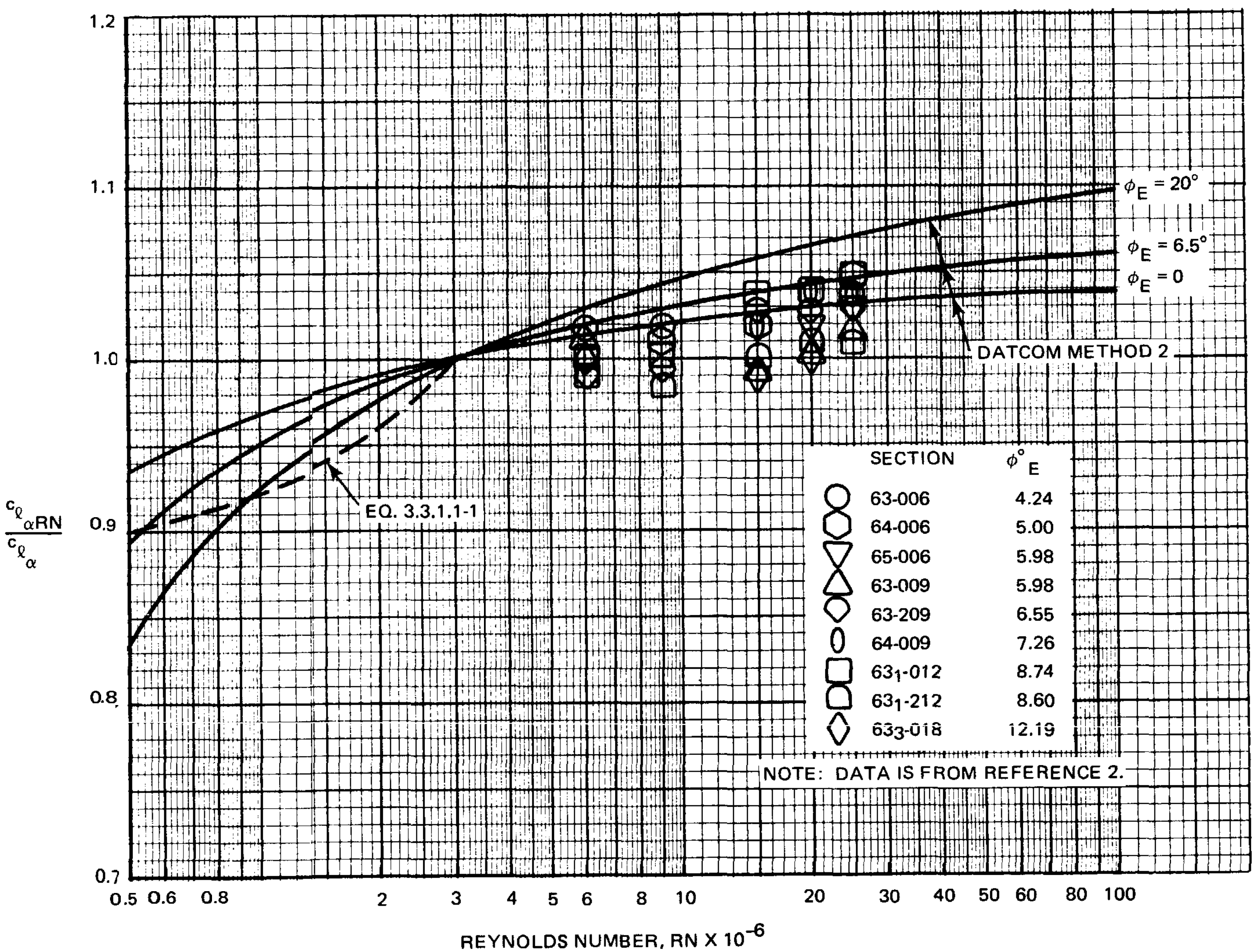

1892-003B

Fig. 3.3.1.1-2 Section Lift Curve Slope at High Reynolds Number

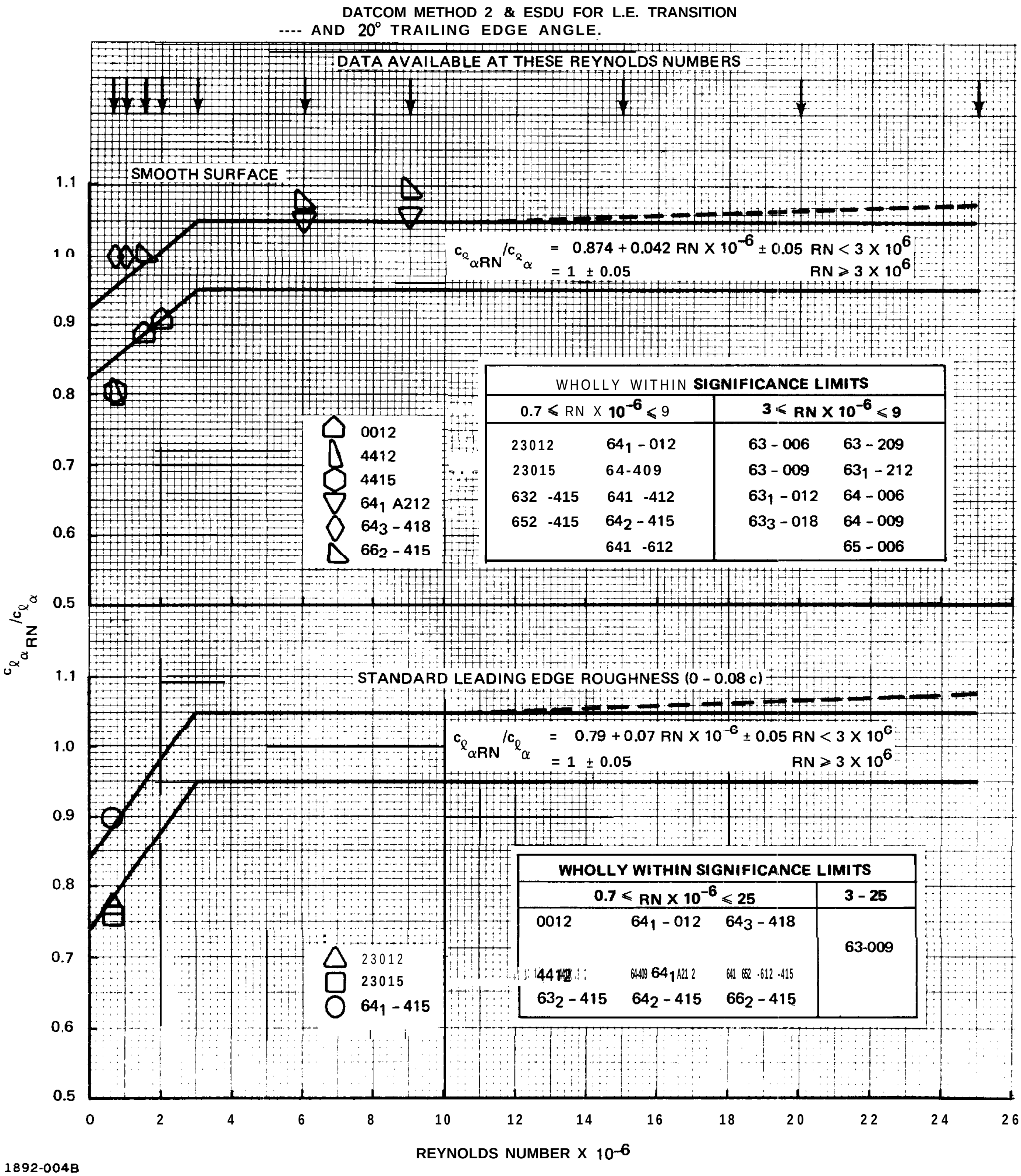

Fig. 3.3.1.1-3 Section Lift Curve Slope vs Reynolds Number
Adapted From References 2 and 3

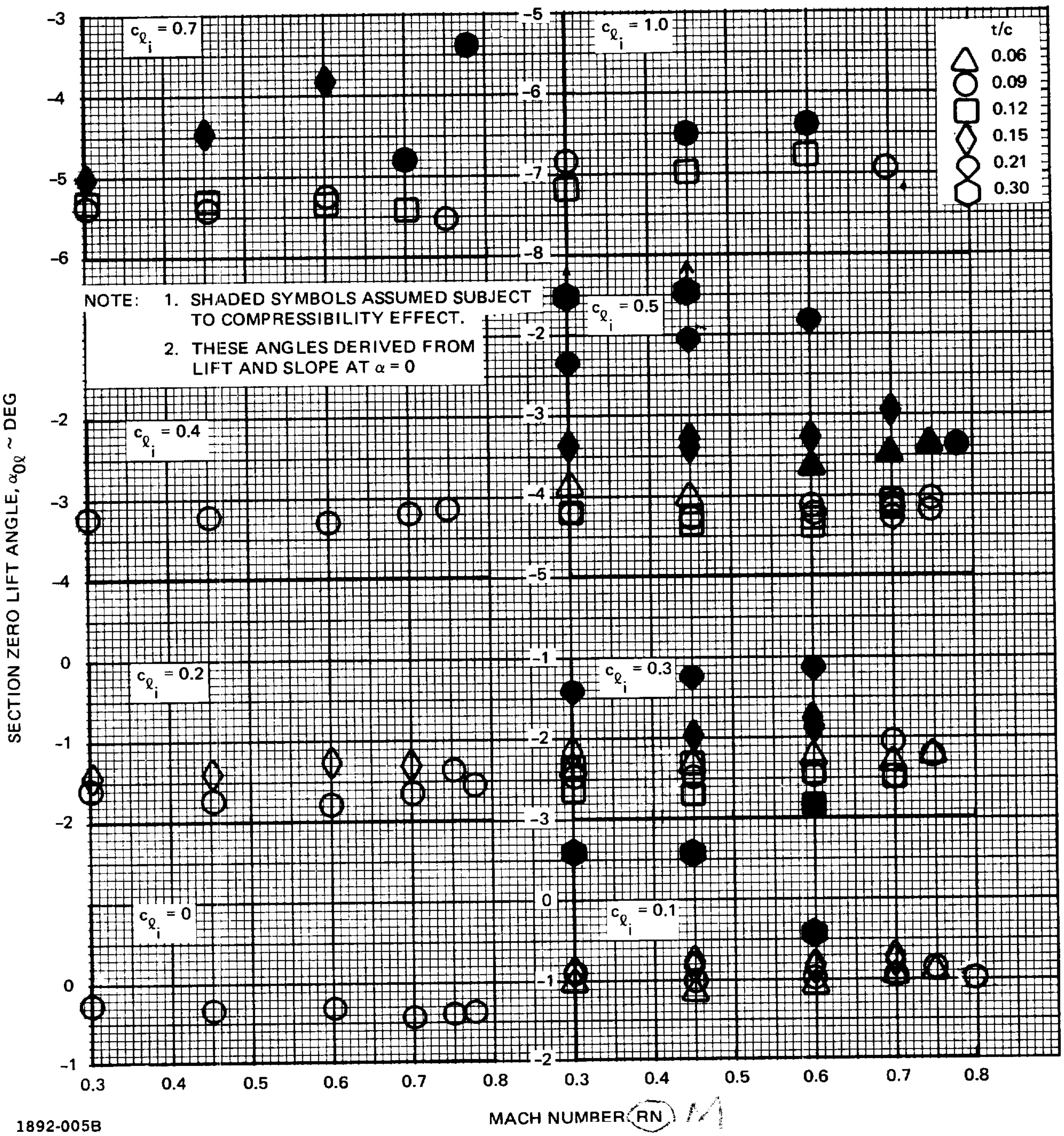

Fig. 3.3.1.14 16-Series Section Zero Lift Angle

3.3.1.2 Section Lift Curve Slope.

POTENTIAL LIFT CURVE SLOPE

Classic thin airfoil potential theory presents a section lift curve slope of 2π. Thick airfoil potential theory (e.g. references 1 and 2) adds an incremental lift curve slope which is a function of the thickness and of its distribution. The incremental lift curve slope cannot be expressed rationally in any useful analytic expression but is approximated in the DATCOM by:

$$\kappa_{pot} \equiv c_{\ell_{\alpha pot}}/2\pi = 1 + .748 \frac{t}{c} (1 + .215\, \phi_E) \qquad 3.3.1.2\text{-}1$$

For the trailing edge angles of Table 6.1.2.2-11, Equation 3.3.1.2-1 becomes:

$$\begin{aligned} \kappa_{pot} &= 1 + .748 \frac{t}{c} \left(1 + .215 \frac{\phi_E}{t/c} \frac{t}{c}\right) \\ &= 1 + .748 \frac{t}{c} + .161 \frac{\phi_E}{t/c} \left(\frac{t}{c}\right)^2 \end{aligned} \qquad 3.3.1.2\text{-}2$$

For a 20% 16-series section the quadratic term contributes only 2.4% to the lift curve slope and equation 3.3.1.2-2 is usually expressed as a linear function of the thickness ratio:

$$\kappa_{pot} = 1 + c_{\kappa_{pot}} \frac{t}{c} \qquad 3.3.1.2\text{-}3$$

where: $c_{Kpot} = 4/3\sqrt{3} = .770$ Abbott & von Doenhoff, Reference 2

$= .822$ Hoerner, Fig. H-21, Reference 3

$= .75 - .8$ ESDU, WINGS .01.01.05

The Abbott & von Doenhoff value is employed here as representative.

VISCOUS EFFECT — GENERAL SECTION

The viscous reduction in the potential lift curve slope is an empirical function of the section thickness and thickness distribution and its analytical form is therefore dependent upon the experimental sample considered. Abbott & von Doenhoff present the most satisfactory single source for such a data sample and the DATCOM Method 1 presents, in DATCOM Table 4.1.1-A and -B, the 9×10^6 Reynolds Number lift curve slopes of Reference 2.

ESDU WINGS .01.01.05 employs the trailing edge angle as defined by the ordinates at the 90% and 99% chord stations as a thickness distribution parameter against which to correlate an unspecified sample of measured lift curve slopes. The result is presented as a function of Reynolds Number and transition point position. DATCOM Method 2 employs the ESDU result for the leading edge transition but with a 5% increase in the predicted lift curve slope.

The ESDU and DATCOM predictions are compared with the measured lift curve slopes of DATCOM Tables 4.1.1-A and 4.1.1-B on Figures 3.3.1.2 1-5. The comparisons as a function of the ESDU trailing edge angle definition are presented only for those sections for which that angle is evaluated in DATCOM Table 4.1.1.2-A. Also shown on Figures 3.3.1.2 l-5 are the lift curve slope F'S thickness ratio trend lines of Figure 57 of Reference 2 which are for a Reynolds Number of 6 x 10^6.

Because the ESDU trailing edge angle definition presents some difficulty with regard to the 99% chord station, the experimental viscous effects are also plotted against the nominal aft 5% chord trailing edge angle on Figures 3.3.1.2 1-5. The potential lift curve slopes employed for these plots were those of Equation 3.3.1.2-3 with the .77 slope of Abbott & von Doenhoff. All of the Abbott & von Doenhoff R = 9 x 10^6 slopes except those for interpolated sections are included on Figures 3.3.1.2 l-5 and in Table 3.3.1.2-I for the 5% chord trailing edge angle. The table presents the 5% chord trailing edge angle' $c_{\ell_\alpha}/c_{\ell_{\alpha pot}}$ ratios referencedto the potential lift curve slopes of Equations 3.3.1.2-1 and 3.3.1.2-3.

By any definition, the trailing edge angle only serves as a parameter against which to measure the complex effects of the thickness distribution upon the viscous reduction of the potential lift. Table 3.3.1.2-11 presents a statistical comparison of the utility of the two trailing edge angle definitions for this purpose and indicates that the 5% chord trailing edge angle and potential lift curve slope of Equation 3.3.1.2-3 correlates this particular data sample as effectively as the ESDU trailing edge angle with Equation 3.3.1.2-1.

The quadratic correlations of Table 3.3.1.2-11 are unnecessarily complex for the precision offered by the data and that for the 5% chord trailing edge angle is compared with two simpler correlations in Table 3.3.1.2-111.

Table 3.3.1.2-III presents a statistical comparison of the 5% chord trailing edge angle quadratic correlation of Table 3.3.1.2-11 with a linear correlation having unit value at zero thickness. For one common slope for the entire data sample the linear correlation is as good as the quadratic correlation except for the 4 and 5 digit sample which is in significant error. The individual slopes of the table are means for the sub-classes of the sample by section series and indicate that the 4 and 5 digit and 63-Series sections are similar and distinct from the remainder of the sample. Dividing the sample into two sub-classes of distinct slope provides a correlation which is practically equivalent to the quadratic correlation and to the best linear correlation, that for distinct slopes for each section, provided by the data sample.

The 2-Class correlation of Table 3.3.1.2-111 can be summarized in terms of a nominal standard deviation by:

$$c_{\ell_\alpha}/c_{\ell_{\alpha pot}} \pm 1\sigma = 1 - .00715\, \phi^{\circ}_{5\%} \pm 1.8\% \text{ for } (x/c)_{t/c_{max}} \leqslant 35\%$$

$$= 1 - .01059\, \phi^{\circ}_{5\%} \pm 4.5\% \text{ for } (x/c)_{t/c_{max}} > 35\% \qquad 3.3.1.2\text{-}4$$

where there is no loss of significance if the standard deviation is interpreted as a $c_{\ell_\alpha}/c_{\ell_{\alpha pot}}$ increment rather than a percentage. Equation 3.3.1.2-4 is compared with the sample on Figures 3.3.1.2 1-5.

It will be recognized that the data sample provides poor viscous effect definition for those sections of aft maximum thickness location. Those samples could be interpreted as presenting a viscous effect at zero thickness and even as presenting a viscous effect of zero slope with trailing edge angle. The effect of the elimination of the after body cusp is even more poorly defined and the interpretation of that effect depends upon the trailing edge angle slope assigned to the cusped sections. Finally, the classification of Equation 3.3.1.2-4 by maximum thickness location is only an observation, lacking rational foundation.

Table 3.3.1.2-IV compares the 2-Class correlation of Table 3.3.1.2-111 with the DATCOM Method 2 slope prediction, which is essentially the ESDU procedure, as the precision for that prediction is defined in Table 4.1.1.2-A of the DATCOM. The significance of the DATCOM mean error is diluted by the 1.05 empirical factor of DATCOM Equation 4.1.1.2-a but comparison of the standard deviations and their relationship to the mean errors indicates that Equations 3.3.1.2-3 and 4 offer the DATCOM confidence level with less complexity.

ESDU WINGS 01.01.05 specifies a nominal accuracy of ±5% for the section lift curve slope prediction which is the accuracy associated with Reynolds Number effect in Section 3.3.1.1 and which might be compared with standard deviations of 5.8% to 10.4% obtained by comparing three individual measurements of forty-three experimental, threedimensional, hydrodynamic lift curve slopes.

VISCOUS EFFECT – 16-SERIES SECTION

The 16-Series section presents a particular problem because the data of Reference 4 was measured at Mach Numbers of .3 to .8 and Reynolds Numbers of .85 - 2 x 10^6 compared, for example, with Reference 2 which presents no data for Mach Numbers higher than .17 or for Reynolds Numbers less than 3 x 10^6. There is much distortion in the curves of Reference 4 and the distinction between the Reynolds Number and Mach Number effects is not obvious. The lift curve slopes considered here were measured on Figures 4-9 of Reference 4 and are interpretations of interpretations of the basic data; they are therefore displayed in Table 3.3.1.2-V for reference.

Only the range of Reynolds Number is given in Reference 4 and the relationship between Reynolds Number and Mach Number assumed here for that data is:

$$RN \times 10^{-6} = 2.667\ M \qquad 3.3.1.2\text{-}5$$

Then from Equations 3.3.1.1-1, 3.3.1.1-3, and 3.3.1.2-3 the lift curve slopes of Table 3.3.1.2-V were expressed as $c_{\ell_\alpha}/c_{\ell_{\alpha pot}}$ ratios for a Reynolds Number of 3 x 10^6 and zero Mach Number by the Equation:

$$\frac{c_{\ell_\alpha}}{c_{\ell_{\alpha pot}}} = \frac{c_{\ell_{\alpha meas}}^{\circ}}{c_{\ell_{\alpha RN}}/c_{\ell_\alpha}} \times \frac{c_{\ell_\alpha}}{c_{\ell_{\alpha M}}} \Bigg/ \frac{2\pi}{57.3}\,\kappa_{pot} \qquad 3.3.1.2\text{-}6$$

where: $\dfrac{c_{\ell_{\alpha RN}}}{c_{\ell_\alpha}} = .874 + .042\ RN \times 10^{-6}$ from Eq. 3.3.1.1-1

$= .874 + .042 \times 2.667\ M$ from Eq. 3.3.1.2-5

$\dfrac{c_{\ell_\alpha}}{c_{\ell_{\alpha M}}} = \sqrt{1-M^2}$ from Eq. 3.3.1.1-3

$\kappa_{pot} = 1 + .77\dfrac{t}{c}$ from Eq. 3.3.1.2-3

Equation 3.3.1.2-6 may be written:

$$\frac{c_{\ell_\alpha}}{c_{\ell_{\alpha pot}}} = 81.43\ \frac{\sqrt{1-M^2}}{(M+7.8)(1+.77\frac{t}{c})} \qquad 3.3.1.2\text{-}7$$

and the results of this reduction of the data of Table 3.3.1.2-V are presented in Table 3.3.1.2-VI and on Figure 3.3.1.2-6. No systematic dependencies other than trailing edge angle could be derived from the tabulated data and for trailing edge angle it is only evident, on Figure 3.3.1.2-6, that the data is better correlated by the JO715 coefficient of Equation 3.3.1.2-4 than by the .01059 coefficient. For the .00715 coefficient, prediction errors for Table 3.3.1.2-W are tabulated in Table 3.3.1.2-VII. Taking the .3 and .45 Mach Number results as representative of the section, that is discounting all data measured at Mach Numbers of .6 or more, the 16-Series section lift curve slope becomes:

$$\frac{c_{\ell_\alpha}}{c_{\ell_{\alpha pot}}} \pm 1\sigma = 1 - .00715\,\phi_{5\%}^{\circ} \pm 7\% \qquad 3.3.1.2\text{-}8$$

$$\approx 1 - .00715\phi_{5\%}^{\circ} \pm .07$$

which is compared with the data on Figure 3.3.1.2-6.

The **16-Series** section was developed to delay compressibility effect. Reference 5 has historical interest with regard to the development of the section and contains an early observation of the favorable drag effect of aft maximum thickness locations. Reference 4 only expands the **thickness** – camber matrix of Reference 5. Roth test programs were intended to display the onset and effect of compressibility for practical application, primarily to aircraft propellers. The test conditions produced significant Reynolds Number and Mach Number effects uncharacteristic of hydrodynamic applications.

The tests of Reference 6 were conducted for hydrodynamic application. The test Mach Numbers were **.11** and **.23** and certain of the tests were **run** with and without transition strip to aid interpretation of these and other model tests in terms of prototype characteristics.

The unflapped lift measurements of Reference 6 are shown in Tables **3.3.1.2-VIII** and -1X. with a summary in Table 3.3.1.2-X. The distinct segments of the lift curves measured by **DeHavilland** define scale effects to be anticipated in future model measurements; the increased lift curve slope for the lower end of the lift curve for the smooth section for both Reynolds Numbers is indicative of an abnormal laminar flow extent on the chord. The effectiveness of the **DeHavilland** transition strip should be noted. The two measured slopes of Table 3.3.1.2-X which are appropriate as hydrodynamic prototype models are shown on Figure 3.3.1.2-6 where they are in adequate agreement with Equation 3.3.1.2-8.

SUMMARY

Equations 3.3.1.2-4 & 8 may be summarized as:

$$\frac{c_{\ell_\alpha}}{c_{\ell_{\alpha pot}}} = 1 - \overset{\circ}{m}_\phi \, \overset{\circ}{\phi}_{5\%} \pm 1\sigma \qquad 3.3.1.2\text{-}9$$

where: $\overset{\circ}{m}_\phi$ = **.00715** for 4 & 5 digit sections
for **16-Series** sections
for 63-Series sections and
generally for sections of $(x/c)_{t/c_{max}} \leqslant 35\%$

= **.01059** for sections of $(x/c)_{t/c_{max}} > 35\%$
except l&Series sections

σ = **.018** for 4 & 5 digit sections and
generally for sections of $(x/c)_{t/c_{max}} \leqslant 35\%$

= **.045** for sections of $(x/c)_{t/c_{max}} > 35\%$
except **16-Series** section

= **.070** for **16-Series** section

From Equation 3.3.1.2-3, Equation 3.3.1.2-9 may be written:

$$\kappa = \left(1 + c_{\kappa_{pot}} \frac{t}{c}\right)\left(1 - \overset{\circ}{m}_{\phi}\, \overset{\circ}{c}_{\phi} \frac{t}{c}\right) \qquad 3.3.1.2\text{-}10$$

$$= 1 + \left(c_{\kappa_{pot}} - \overset{\circ}{m}_{\phi}\, \overset{\circ}{c}_{\phi}\right) \frac{t}{c} - c_{\kappa_{pot}}\, \overset{\circ}{m}_{\phi}\, \overset{\circ}{c}_{\phi} \left(\frac{t}{c}\right)^2$$

$$= 1 + c_{1_\kappa} \frac{t}{c} + c_{2_\kappa} \left(\frac{t}{c}\right)^2$$

where the .77 $c_{\kappa_{pot}}$ of Reference 2 is employed here.

Values of c_ϕ for the sections of Reference 2 are tabulated in Section 6.1.2. Values for the coefficients of Equation 3.3.1.2-10 for the same sections are tabulated in Table 3.3.1.2-XI and the quadratics are presented graphically on Figure 3.3.1.2-7. The same curves are presented as a function of trailing edge angle on Figure 3.3.1.2-8.

The mominal precision associated with the prediction of the lift curve slope is that of the precision of measurement of Section 3.3.1.1, ±5%.

HANDE

The HANDE viscous section lift curve slope is:

$$\kappa = 1 - 1.563 \left(\frac{t}{c}\right)^{1.35} \qquad 3.3.1.2\text{-}11$$

which is virtually identical with the 65A Series curve of Figure 3.3.1.2-7.

LIMITATIONS

Inadequate support for the following conclusions which are expressed or implied in Equation 3.3.1.2-10 should be noted:

1. **16-Series** viscous effect generally,
2. Section classification by maximum thickness chord station for viscous effect,
3. Identification of 6 x A – Series viscous effect with that of the parent section,
4. Identification of potential lift curve slope only with the maximum thickness ratio.

REFERENCES

1. Pope, Alan: Basic Wing and Airfoil Theory. McGraw-Hill, 1951.
2. Abbott, I. H. and von Doenhoff, A. E.: Theory of Wing Sections. Dover, 1959.
3. Hoemer, S. F.: Fluid-Dynamic Lift. Published by the Author, 1970.
4. Lindsey, W. F.; Stevenson, D. B.; and Daley, B. N.: Aerodynamic Characteristics of 24 NACA 16-Series Airfoils At Mach Numbers Between 0.3 and 0.8. NACA Technical Note 1546, Sept. 1948.
5. Stack, John: Tests Of Airfoils Designed To Delay The Compressibility Burble. NACA Report 763, 1943.
6. Teeling, P.: Low Speed Wind Tunnel Tests Of A NACA 16-309 Airfoil With Trailing Edge Flap; DeHavilland Aircraft of Canada Limited Report ECS 76-3, October 1976.

TABLE 3.3.1.2-I EXPERIMENTAL $c_{\ell_\alpha}/c_{\ell_{\alpha pot}}$ RATIOS, R = 9 X 10^6 (SHEET 1 OF 3)

NOTES;	1	2	3	4	5	6
		ESDU T.E. ANGLE		NOMINAL 5% T.E. ANGLE		
SECTION	MEAS c_{ℓ_α} /DEG	ϕ_E DEG	$c_{\ell_\alpha}/c_{\ell_{\alpha pot}}$	$\phi_{5\%}$ DEG	$c_{\ell_\alpha}/c_{\ell_{\alpha pot}}$	$c_{\ell_\alpha}/c_{\ell_{\alpha pot}}$
4 & 5 DIGIT SECTIONS						
0006	0.108	7.50	0.9415	7.74	0.9414	0.9414
0009	0.109	11.30	0.9289	11.61	0.9288	0.9296
1408	0.109	10.03	0.9359	10.32	0.9359	0.9364
1410	0.108	12.48	0.9134	12.90	0.9133	0.9145
1412	0.108			15.48	0.8995	0.9016
2412	0.105	15.06	0.8746	15.48	0.8745	0.8766
2415	0.106	18.55	0.8631	19.35	0.8268	0.8666
2418	0.103	22.25	0.8197	23.22	0.8194	0.8250
2421	0.103			27.09	0.7812	0.8086
2424	0.098			30.96	0.7432	0.7543
4412	0.105	15.13	0.8746	15.48	0.8745	0.8766
4415	0.105	18.80	0.8549	19.35	0.8547	0.8584
4418	0.105			23.22	0.8353	0.8410
4421	0.103			27.09	0.8007	0.8086
4424	0.100			30.96	0.7597	0.7697
23012	0.107	15.06	0.8913	15.48	0.8912	0.8933
23015	0.107	18.68	0.8712	19.35	0.8710	0.8748
23018	0.107			23.22	0.8512	0.8570
23021	0.103	28.18	0.8003	27.09	0.8007	0.8086
23024	0.097			30.96	0.7369	0.7466
63-SERIES SECTIONS						
63-006	0.112	4.24	0.9769	2.94	0.9771	0.9763
63-009	0.111	5.98	0.9471	4.41	0.9474	0.9467
63-206	0.112	4.55	0.9768	2.94	0.9771	0.9763
63-209	0.110	6.55	0.9384	4.41	0.9389	0.9381
63-210	0.113	7.30	0.9570	4.90	0.9576	0.9568
63_1-012	0.116	8.74	0.9681	5.88	0.9690	0.9684
63_1-212	0.114	8.60	0.9515	5.88	0.9523	0.9517
63_1-412	0.117	8.70	0.9765	5.88	0.9773	0.9767
63_2-015	0.117			7.35	0.9567	0.9565
63_2-215	0.116			7.35	0.9485	0.9483
63_2-415	0.118	10.38	0.9638	7.35	0.9649	0.9647
$63_2$615	0.117			7.35	0.9567	0.9565
63_3-018	0.118	12.19	0.9433	8.82	0.9447	0.9451
63_3-218	0.118			8.82	0.9447	0.9451
63_3-418	0.118			8.82	0.9447	0.9451
63_3-618	0.118			8.82	0.9447	0.9451
63_4-021	0.118			10.29	0.9252	0.9263
63_4-221	0.118			10.29	0.9252	0.9263
63_4-421	0.120			10.29	0.9409	0.9420

1892-006B(1)

TABLE 3.3.1.2-I EXPERIMENTAL $c_{\ell_\alpha}/c_{\ell_{\alpha pot}}$ RATIOS, $R = 9 \times 10^6$ (SHEET 2 OF 3)

NOTES;	1	2	3	4	5	6
		ESDU T.E. ANGLE		NOMINAL 5% T.E. ANGLE		
SECTION	MEAS c_{ℓ_α} /DEG	ϕ_E DEG	$c_{\ell_\alpha}/c_{\ell_{\alpha pot}}$	$\phi_{5\%}$ DEG	$c_{\ell_\alpha}/c_{\ell_{\alpha pot}}$	$c_{\ell_\alpha}/c_{\ell_{\alpha pot}}$
64-SERIES SECTIONS						
64-006	0.109	5.00	0.9506	3.42	0.9508	0.9501
64-009	0.110	7.26	0.9383	5.13	0.9387	0.9381
64-108	0.110			4.56	0.9456	0.9449
64-110	0.110			5.70	0.9320	0.9314
64-206	0.110	5.13	0.9593	3.42	0.9595	0.9589
64-208	0.113	6.62	0.9710	4.56	0.9714	0.9707
64-209	0.107			5.13	0.9131	0.9126
64-210	0.110	8.08	0.9314	5.70	0.9320	0.9314
64_1-012	0.111	9.35	0.9262	6.84	0.9269	0.9267
64_1-112	0.113			6.84	0.9436	0.9433
64_1-212	0.113	9.54	0.9429	6.84	0.9436	0.9433
64_1-412	0.112	9.52	0.9345	6.84	0.9353	0.9350
64_2-015	0.112			8.55	0.9154	0.9156
64_2-215	0.112			8.55	0.9154	0.9156
64_2-415	0.115	11.58	0.9388	8.55	0.9399	0.9402
64_3-018	0.111			10.26	0.8881	0.8891
64_3-218	0.115			10.26	0.9201	0.9211
64_3-418	0.116	13.50	0.9268	10.26	0.9281	0.9291
64_3-618	0.116			10.26	0.9281	0.9291
64_4-021	0.110			11.97	0.8617	0.8635
64_4-221	0.117			11.97	0.9165	0.9185
64_4-421	0.120			11.97	0.9400	0.9420
65-SERIES SECTIONS						
65-006	0.105	5.98	0.9155	4.2	0.9158	0.9153
65-009	0.107	8.86	0.9123	6.3	0.9129	0.9126
65-206	0.105	6.11	0.9155	4.2	0.9158	0.9153
65-209	0.106	8.94	0.9038	6.3	0.9044	0.9040
65-210	0.108	9.78	0.9140	7.0	0.9147	0.9145
65-410	0.112			7.0	0.9486	0.9484
65_1-012	0.110	11.39	0.9173	8.4	0.9181	0.9183
65_1-212	0.108	11.44	0.9006	8.4	0.9014	0.9016
65_1-212 a = 0.6	0.108	11.38	0.9271	8.4	0.9014	0.9016
65_1-412	0.111			8.4	0.9265	0.9267
65_2-015	0.111			10.5	0.9065	0.9075
65_2-215	0.112			10.5	0.9147	0.9156
65_2-415	0.111	13.70	0.9055	10.5	0.9065	0.9075
65_2-415 a = 0.5	0.111			10.5	0.9065	0.9075
65_3-018	0.100			12.6	0.7993	0.8009
65_3-218	0.100			12.6	0.7993	0.8009
65_3-418	0.110	15.82	0.8779	12.6	0.8792	0.8810

1892-006B(2)

TABLE 3.3.1.2-I EXPERIMENTAL $c_{\ell_\alpha}/c_{\ell_{\alpha pot}}$ RATIOS, R = 9 X 10^6 [SHEET 3 OF 3)

NOTES;	1	2	3	4	5	6
		ESDU T.E. ANGLE		NOMINAL 5% T.E. ANGLE		
SECTION	MEAS c_{ℓ_α} /DEG	ϕ_E DEG	$c_{\ell_\alpha}/c_{\ell_{\alpha pot}}$	$\phi_{5\%}$ DEG	$c_{\ell_\alpha}/c_{\ell_{\alpha pot}}$	$c_{\ell_\alpha}/c_{\ell_{\alpha pot}}$
65_3-418 a = 0.5	0.115			12.6	0.9191	0.9211
65_3-618	0.113			12.6	0.9032	0.9051
65_3-618 a = 0.5	0.104			12.6	0.8312	0.8330
65_4-021	0.112			14.7	0.8762	0.8792
65_4-221	0.115			14.7	0.8996	0.9028
65_4-421	0.116	18.19	0.9059	14.7	0.9075	0.9106
65_4-421 a = 0.5	0.116			14.7	0.9075	0.9106
66-SERIES SECTIONS						
66-006	0.100	7.82	0.8717	5.70	0.8720	0.8717
66-009	0.103	11.43	0.8777	8.55	0.8783	0.8784
66-206	0.108	7.94	0.9414	5.70	0.9417	0.9414
66-209	0.107	11.48	0.9118	8.55	0.9124	0.9126
66-210	0.110	12.72	0.9302	9.50	0.9310	0.9314
66_1-012	0.106			11.40	0.8839	0.8849
66_1-212	0.102			11.40	0.8506	0.8515
66_2-015	0.105			14.25	0.8563	0.8584
66_2-215	0.106			14.25	0.8645	0.8666
66_2-415	0.106	17.86	0.8633	14.25	0.8645	0.8666
63A SERIES SECTIONS						
63A010	0.105	11.42	0.8883	11.50	0.8882	0.8891
63A210	0.103	11.55	0.8713	11.50	0.8713	0.8722
64A SERIES SECTIONS						
64A010	0.110	11.82	0.9305	11.90	0.9304	0.9314
64A210	0.105	11.93	0.8881	11.90	0.8882	0.8891
64A410	0.100	11.89	0.8459	11.90	0.8459	0.8468
64A212	0.100	14.06	0.8332	14.28	0.8332	0.8348
64_2A215	0.095	17.43	0.7739	17.85	0.7737	0.7767

NOTES:

1. THESE ARE THE MEASURED SLOPES OF REFERENCE 2 AS PRESENTED IN DATCOM TABLE 4.1.1-A & B.
2. CALCULATED FROM 90% & 99% CHORD ORDINATES OF DATCOM TABLE 4.1.1.2-A, SEE SECTION 6.1.1.2.
3. MEASURED c_{ℓ_α} ÷ POTENTIAL c_{ℓ_α} OF EQUATION 3.3.1.2-1.
4. CALCULATED FROM NOMINAL $\phi^\circ_{5\%}$/t/c% RATIOS OF TABLE 6.1.1.2-I.
5. MEASURED c_{ℓ_α} ÷ POTENTIAL c_{ℓ_α} OF EQUATION 3.3.1.2-1 FOR NOMINAL 5% CHORD TRAILING EDGE ANGLE?
6. MEASURED c_{ℓ_α} ÷ POTENTIAL c_{ℓ_α} OF EQUATION 3.3.1.2-3 WITH 0.770 CONSTANT.

1892-006B(3)

TABLE 3.3.1.2-II TRAILING EDGE ANGLE DEFINITION -STATISTICAL COMPARISON

T.E. ANGLE		ESDU			5% CHORD					
$c_{\ell_\alpha}/c_{\ell_{\alpha_{pot}}}$		$0.9931 - 0.0081088\,\phi^\circ_E + 2.5263 \times 10^{-5}\,\phi^{\circ 2}_E$		$0.98141 - 0.0076371\,\phi^\circ_{5\%} + 3.2371 \times 10^{-5}\,\phi^{\circ 2}_{6\%}$						
K pot		$1 + 0.748\, t/c\,(1 + 0.215\,\phi)$							$1 + 0.77\, t/c$	
SECTION	SAMPLE SIZE N	MEAN ERROR M, %	STD DEVIATION σ, %	MEAN ERROR M, %	STD DEVIATION σ, %	SAMPLE SIZE N	MEAN ERROR M, %	STD DEVIATION σ, %	MEAN ERROR M, %	STD DEVIATION σ, %
4- & 5-DIGIT	12	0.50	1.14	1.69	1.26	20	0.87	2.43	1.44	2.08
63-SERIES	10	2.24	2.07	1.96	1.65	19	2.36	1.30	2.35	1.33
63A SERIES	2	-3.39	1.33	-2.06	1.39	2	-2.06	1.39	-1.97	1.39
M-SERIES	10	1.07	1.62	0.72	1.29	22	0.40	2.02	0.43	2.05
64A SERIES	5	-5.07	5.49	-3.77	5.47	5	-3.77	5.47	-3.58	5.36
65-SERIES	11	-0.48	2.69	-1.51	2.09	24	-1.32	4.03	-1.19	4.05
66-SERIES	6	-1.19	3.81	-2.04	3.54	10	-2.39	2.89	-2.29	2.90
ALL	56	-0.10	3.22	-0.08	2.99	102	-0.07	3.30	0.09	3.27

T.E. ANGLE DEFINITION EFFECT

EFFECT OF SAMPLE

K pot PREDICTION EFFECT

NOTES:

1. $$E = 1 - \frac{\text{PREDICTED } c_{\ell_\alpha}/c_{\ell_{\alpha_{pot}}}}{\text{MEASURED } c_{\ell_\alpha}/c_{\ell_{\alpha_{pot}}}} = 1 - \frac{\text{PREDICTED } c_{\ell_\alpha}}{\text{MEASURED } c_{\ell_\alpha}}$$

2. $c_{\ell_\alpha}/c_{\ell_{\alpha_{pot}}}$ EQUATIONS ARE QUADRATIC REGRESSION ANALYSES ON 56 MEMBER SAMPLE

1892-007B

TABLE 3.3.1.2-III VISCOUS EFFECT STATISTICAL ANALYSIS, 5% CHORD T. E. ANGLE, $K_{pot} = 1 + 0.77\ t/c$

$c_{\ell_\alpha}/c_{\ell_{\alpha_{pot}}}$		QUADRATIC FIT		$1 - C\phi^{\circ}_{5\%}$								
CLASSIFICATION		REF TABLE 3.3.1.2-II		COMMON SLOPE			2 CLASSES			INDIVIDUAL C		
SECTION	SAMPLE SIZE N	MEAN ERROR M, %	STD DEVIATION σ, %	SLOPE C	MEAN ERROR M, %	STD DEVIATION σ, %	SLOPE C	MEAN ERROR M, %	STD DEVIATION σ, %	SLOPE C	MEAN ERROR M, %	STD DEVIATION σ, %
4- & 5-DIGIT	20	1.44	2.08		5.08	1.96		-0.10	1.66	0.007080	-0.27	1.69
63-SERIES	19	2.35	1.33		1.82	1.69	0.007147	0.23	1.33	0.007216	0.28	1.33
63A SERIES	2	-1.97	1.39		-1.45	1.38		-4.23	1.41	0.010380	0	1.36
	39							-0.15	1.74			
64-SERIES	22	0.43	2.05	0.009269	0	2.32		1.08	2.54	0.009871	0.50	2.42
64A SERIES	5	-3.58	5.36		-2.41	4.68		-0.29	4.28	0.010408	-0.58	4.33
65-SERIES	24	-1.19	4.05		-0.98	4.27	0.010589	0.53	4.43	0.010864	0.84	4.47
66-SERIES	10	-2.29	2.90		-2.03	3.16		-0.48	3.39	0.011623	0.73	3.61
	61							0.49	3.61			
ALL	102	0.09	3.27		0.76	3.79		0.23	3.01		0.35	2.96

NOTES:

1. SLOPES; C, ARE MEAN FOR EACH CLASS EXCEPT THAT 63A SERIES WAS OMITTED FROM 2-CLASS CLASSIFICATION; I.E.. THERE WERE 39 SAMPLES FOR MEAN SLOPE, 41 FOR ERROR.
2. E = 1 -PREDICTED/MEASURED.

1892-008B

TABLE 3.3.1.2-IV STATISTICAL COMPARISON WITH DATCOM METHOD 2

SECTION	2-CLASS CORRELATION OF TABLE 3.3.1.2-III			DATCOM METHOD 2 DATCOM TABLE 4.1.1.2-A		
	SAMPLE SIZE N	MEAN ERROR M, %	STD DEVIATION σ, %	SAMPLE SIZE N	MEAN ERROR M, %	STD DEVIATION σ, %
4- & 5-DIGIT	20	-0.10	1.66	29	0.60	2.05
63-SERIES	19	0.23	1.33	18	0.44	2.62
63A SERIES	2	-4.23	1.41	4	-3.17	2.32
	41	-0.15	1.74			
64-SERIES	22	1.08	2.54	15	0.30	2.40
64A SERIES	5	-0.29	4.28	15	-1.96	4.59
65-SERIES	24	0.53	4.43	24	0.03	3.96
65A SERIES	0	–	–	1	-0.90	–
66-SERIES	10	-0.48	3.39	15	-0.94	4.30
	61	0.49	3.61			
ALL	102	0.23	3.01	121	-0.22	3.38

NOTE: DATCOM SIGNS FOR ERRORS ARE REVERSED TO AGREE WITH DEFINITION OF TABLE 3.X1.2-111

1892-0098

TABLE 3.3.1.2-V REFERENCE 4 LIFT CURVE SLOPES (SHEET 1 OF 2)

MACH NUMBER, M		0.3			0.45			0.6			0.7			0.75			0.775 (EXCEPT AS NOTED)		
SECTION	REF.4 FIG. NO.	$c_{\ell_\alpha}^{\circ}$	$c_{\ell_{\alpha=0}}$ (1)	LIN c_ℓ RANGE	$c_{\ell_\alpha}^{\circ}$	$c_{\ell_{\alpha=0}}$	LIN c_ℓ RANGE	$c_{\ell_\alpha}^{\circ}$	$c_{\ell_{\alpha=0}}$	LIN c_ℓ RANGE	$c_{\ell_a}^{\circ}$	$c_{\ell_{\alpha=0}}$	LIN c_ℓ RANGE	$c_{\ell_\alpha}^{\circ}$	$c_{\ell_{\alpha=0}}$	LIN c_ℓ RANGE	$c_{\ell_\alpha}^{\circ}$	$c_{\ell_{\alpha=0}}$	LIN c_ℓ RANGE
16-009	4	0.087	0.025	<-0.2 >0.6	0.085	0.030	c-O.2 0.6+	0.0855	0.030	-0.165 >0.65	0.995	0.45	<-0.17 >0.41	0.114	0.045	<-0.2 >0.48	0.114	0.045	c-O.22 >0.48
16-106	7	0.100	1.05	<-0.11 0.515	0.099	0.115	<-0.12 0.31	0.111	0.115	<-0.13 0.78	0.126	0.120	<-0.17 >0.73	0.1385	0.125	<-0.18 >0.4 4.05	(M=0.8) 0.1625	(M=0.8) 0.150	(M=0.8) <-0.2 >0.45
16-109	4	0.096	0.090	c-O.1 0.755	0.089	0.095	c-O.1 0.765	0.0946	0.100	<-0.1 0.745	0.123	0.120	-0.02 0.38	0.150	0.130	-0.05 0.475	0.129	0.140	<-0.145 >0.38
	7	0.095	0.090	<-0.1 0.655	0.0935	0.100	<-0.1 0.675	0.100	0.100	c-O.1 0.67	0.126	0.120	-0.03 0.36	0.150	0.125	-0.09 0.51	(M=0.8) 0.1265	(M=0.8) 0.130	(M=0.8) <-0.16 >0.35
16-115	6	0.0905	0.075	-0.145 0.26	0.0945	0.075	-0.125 0.25	0.1005	0.060	6.13 0.28	0.1075	0.075	-0.15 0.33						
	7	0.0925	0.060	-0.14 0.255	0.0935	0.060	-0.13 0.25	0.100	0.065	-0.135 0.28	0.106	0.080	-0.16 0.31						
16-130	7	0.065	-0.030 (-0.035)	-0.015 0.13	0.0565	-0.030	-0.15 0.085	0.102	0.025 (0.045)	-0.175 0.02									
16-209	4	0.097	0.150	0.045 0.685	0.092	0.160	0.035 0.73	0.097	0.175	<-0.025 0.765	0.1195	0.200	0.055 0.49	0.144	0.200	0.12 >0.74	0.131	0.205	<0.17 >0.7
16-215	6	0.0875	0.125	-0.08 0.35	0.0925	0.130	0 0.33	0.1045	0.135	0.07 0.325	0.1075	0.140	0 0.39						
16-306	6	0.112	0.265	<-0.2 0.465	0.113	0.275	<-0.03 0.49	0.130	0.295	<-0.2 0.9	0.1525	0.350	<-0.29 >0.925	0.161	0.360	-0.2 >0.73			
16-309	4	0.0975	0.240	<-0.15 0.56	0.097	0.240	-0.1 0.61	0.109	0.265	-0.155 0.6	0.1275	0.320	<-0.23 0.39	0.155	0.365	-0.185 >0.67	0.1135	0.305	<0.08 >0.52
	a	0.100	0.235	<-0.175 0.54	0.0995	0.250	0.15 0.56	0.110	0.270	<-0.2 0.95	0.1525	0.315	0.25 >0.9	0.160	0.360	-0.25 >0.67			
16312	5	0.080	0.215	[illegible] 0.76	0.085	0.230	<-0.1 0.9	0.092	0.265	<-0.1 >0.95	DISTORTED								
	8	0.091	0.215	0.13 0.47	0.0975	0.230	0.22 0.49	0.110	0.270	0.18 0.52	0.1115	0.260	0.2 >0.7						
16-315	6	0.0875	0.190	0 0.48	0.100	0.200	0.14 0.45	0.1075	0.210	0.14 0.53	DISTORTED								
	6	0.086	0.190	-0.02 0.46	0.1005	0.200	0.15 0.45	0.108	0.200	0.155 0.53	DISTORTED								
16-321	a	0.080	0.115	6.07 0.425	0.080	0.100	-0.06 0.39	0.0825	0.095	-0.1 0.4									
16-409	4	0.100	0.325	<-0.1 0.595	0.1045	0.335	<-0.1 0.62	0.1125	0.370	<-0.11 0.7	0.1355	0.435	<-0.13 0.76	0.156	0.450 (0.4901	<-0.21 0.34	0.120	(0.350)	0.05 >0.33
16-506	9	0.107	0.415	<-0.05 0.63	0.1105	0.445	<-0.05 0.66	0.130	0.475	<-0.08 0.73	0.159	0.555	C0.16 >0.83	0.175	0.590	co.2 0.68			

1892-010B(1)

TABLE 3.3.1.2-V REFERENCE 4 LIFT CURVE SLOPES (SHEET 2 OF 2)

MACH NUMBER, M		0.3			0.45			0.6			0.7			0.75			0.775 (EXCEPT AS NOTED)		
SECTION	REF. 4 FIG. NO.	$c_{\ell_\alpha}^\circ$	$c_{\ell_{\alpha=0}}$ (1)	LIN c_ℓ RANGE	$c_{\ell_\alpha}^\circ$	$c_{\ell_{\alpha=0}}$	LIN c_ℓ RANGE	$c_{\ell_\alpha}^\circ$	$c_{\ell_{\alpha=0}}$	LIN c_ℓ RANGE	$c_{\ell_a}^\circ$	$c_{\ell_{\alpha=0}}$	LIN c_ℓ RANGE	$c_{\ell_\alpha}^\circ$	$c_{\ell_{\alpha=0}}$	LIN c_ℓ RANGE	$c_{\ell_\alpha}^\circ$	$c_{\ell_{\alpha=0}}$	LIN c_ℓ RANGE
16-509	4	0.100	0.415	<-0.18 0.61	0.1025	0.440	c-O.18 0.645	0.113	0.480	-0.14 0.745	0.132	0.550	0 >0.78	0.1375	0.560	<-0.03 0.63	0.1585	0.535 (0.560)	<0.2 0.53
	9	0.100	0.415	<-0.175 0.61	0.1045	0.445	<-0.175 0.645	0.1175	0.485	-0.14 0.71	0.129	0.555	-0.03 >0.78	0.1335	0.560	<-0.25 0.63			
16-512	5	0.087	0.365	<0 0.68	0.090	0.385	<0 0.6	0.0985	0.425	<0 0.66	0.1083	0.440	<-0.02 0.8						
	9	0.087	0.365	0.08 0.68	0.090	0.390	<0 0.6	0.098	0.430	0.125 0.675	0.108	0.445	c-O.02 0.8	DISTORTED					
16-515	6	0.092	0.310	0.225 0.64	0.099	0.330	0.29 0.58	0.100	0.330	0.31 0.7	0.1075	0.315	co.035 >0.7						
	9	0.091	0.305	0.245 0.64	0.095	0.325	0.28 0.625	0.0985	0.325	0.325 0.72	0.105	0.315	0.285 >0.72	DISTORTED					
16-521	9	0.0855	0.200	0.025 0.56	0.088	0.180	0.1 0.47	0.091	0.165	0.135 0.535	DISTORTED								
16-530	9	0.0665	-0.095	<-0.11 0.33	0.065	-0.12 (-0.15)	6.07 0.28	DISTORTED											
16-709	4	0.1025	0.550	<-0.06 0.785	0.108	0.585	<-0.055 0.75	0.1225	0.645	0.13 0.755	0.156	0.745	0.14 0.745	0.1075	0.590 (0.595)	<0.125 0.58	0.135	0.455 (0.480)	-0.03 0.41
16-712	5	0.093	0.495	0.025 0.80	0.1015	0.54	0.04 0.8	0.1125	0.600	0.09 >1.05	0.105	0.57	<0.13 >0.76						
16-715	6	0.0885	0.445	0.05 0.82	0.1025	0.46	0.375 0.675	0.123	0.470	0.41 0.89	DISTORTED								
16-(1.0)0.9	4	0.1135	0.775	<0.09 0.795	0.1235	0.800	<0.085 0.72	0.1425	0.910	0.245 0.91	0.111	0.770	0.24 0.84						
16-(1.0)12	5	0.100	0.715	0.2 1.0	0.108	0.755	0.21 1.04	0.120	0.815	0.3 >1.1									

NOTE: WHERE THE LIFT CURVE IS NOT LINEAR AT $\alpha = 0$, THE $c_{\ell_{\alpha=0}}$ IS SHOWN WITHOUT PARENTHESIS AND THE LINEAR EXTENSION OF THE LIFT CURVE TO $\alpha = 0$ IS INDICATED WITH PARENTHESIS.

1892-010B(2)

TABLE 3.3.1.2-W REFERENCE 4 $c_{\ell_\alpha}/c_{\ell_{\alpha\,pot}}$ RATIOS

SECTION	$\phi°_{5\%}$	REF. 4 FIG. NO.	MACH NUMBER, M						
			0.3	0.45	0.6	0.7	0.75	0.775	0.8
16 – 009	22.26	4	0.7803	0.7007	0.6201	0.6366	0.6716	0.6398	
16 – 106	14.84	7	0.9167	0.8341	0.8228	0.8240	0.8340		0.8824
16 – 109	22.26	4	0.8610	0.7336	0.6854	0.7870	0.8837	0.7240	
		7	0.8520	0.7707	0.7253	0.8062	0.8837		0.6827
16 – 115	37.09	6	0.7780	0.7467	0.6987	0.6593			
		7	0.7952	0.7388	0.6952	0.6624			
16 – 130	74.19	7	0.5064	0.4046	0.6426				
16 – 209	22.26	4	0.8699	0.7584	0.7035	0.7646	0.8483	0.7352	
16 – 215	37.09	6	0.7522	0.7309	0.7265	0.6593			
16 – 306	14.84	8	1.0267	0.9520	0.9637	0.9973	0.9694		
16 – 309	22.26	4	0.8744	0.7996	0.7905	0.8158	0.9131		
		8	0.8969	0.8202	0.7978	0.9757	0.9426		
16 – 312	29.68	5	0.7023	0.6859	0.6531				
		8	0.7989	0.7867	0.7809	0.6983			
16 – 315	37.09	6	0.7522	0.7902	0.7474				
		8	0.7565	0.7941	0.7508				
16 – 321	51.93	8	0.6604	0.6070	0.5508				
16 – 409	22.26	4	0.8969	0.8614	0.8159	0.8669	0.9190	0.6735	
16 – 506	14.84	9	0.9808	0.9310	0.9637	1.0398	1.0537		
16 – 509	22.26	4	0.8969	0.8449	0.8195	0.8445	0.8100	0.8896	
		9	0.8969	0.8614	0.8522	0.8254	0.7865		
16 – 512	29.68	5	0.7638	0.7262	0.6993	0.6783			
		9	0.7638	0.7262	0.6957	0.6764			
16 – 515	37.09	6	0.7909	0.7823	0.6952	0.6593			
		9	0.7823	0.7507	0.6848	0.6440			
16 – 521	51.93	9	0.7058	0.6677	0.6075				
16 – 530	74.19	9	0.5181	0.4654					
16 – 709	22.26	4	0.9193	0.8903	0.8884	0.9981	0.6333	0.7577	
16 – 712	29.68	5	0.8164	0.8190	0.7987	0.6576			
16 – 715	37.09	6	0.7608	0.8099	0.8551				
16 – (1.0) 09	22.26	4	1.0179	1.0180	1.0335	0.7102			
16 – (1.0) 12	29.68	5	0.8779	0.8714	0.8519				

NOTE: CORRECTED TO M = 0 AND RN = 3×10^6 AND NORMALIZED BY $2\pi\,(1 + 0.77\ t/c)$

1892-0118

TABLE 3.3.1.2-VII REFERENCE 4 LIFT CURVE SLOPE PREDICTION ERROR

SECTION	REF 4 FIG. NO.	MACH NUMBER, M						
		0.3	0.46	0.6	0.7	0.75	0.776	0.6
16-009	4	-13.32	-15.99	-15.31	0.91	13.32	13.52	
16-106	7	- 2.55	-3.58	7.62	18.61	25.96		36.90
16-109	4	-2.70	-10.78	-4.33	19.85	34.27	23.57	
	7	-3.78	-5.44	1.41	21.75	34.27		24.16
16-115	6	.69	4.90	10.57	16.40			
	7	2.84	3.88	10.13	16.78			
16-130	7	2.50	-12.17	37.86				
16-209	4	-1.64	-7.16	-1.64	17.50	31.53	24.74	
16-215	6	-2.71	2.84	14.00	16.40			
16-306	8	8.44	9.25	21.12	32.76	36.31		
16-309	4	-1.12	-1.64	9.55	22.67	36.39		
	8	1.41	0.91	10.37	35.35	38.38		
16-312	5	-17.96	-11.02	-2.57				
	8	-3.70	3.21	14.21	15.37			
16-315	6	-2.71	10.13	16.40				
	8	-2.13	10.57	16.78				
16-409	[illegible]	[illegible]	[illegible]	[illegible]	27.24	36.80	17.84	
16-506	Q	4.16	7.20	21.12	35.51	41.40		
16-509	4	1.41	3.81	12.75	25.31	28.30	37.80	
	9	1.41	5.66	16.09	23.57	26.15		
16-512	5	-8.47	-4.85	4.20	12.87			
	9	-8.47	-4.85	3.71	12.62			
16-515	6	2.31	9.22	10.13	16.40			
	9	1.24	5.40	8.76	14.41			
16-521	9	6.34	9.00	12.00				
16-530	9	4.69	2.50					
16-709	4	3.81	8.71	19.52	36.80	8.29	26.97	
16-712	5	-1.47	7.03	16.12	-10.13			
16-715	6	-1.55	12.32	26.93				
16-(1.0)09	4	13.14	20.17	30.81	11.18			
16-(1.0)12	5	5.63	12.62	21.36				

NOTES:

1. PREDICTION IS $\dfrac{c_{\ell_\alpha}}{c_{\ell_{\alpha pot}}} = 1 - 0.00715\,\phi^{\circ}$ 5%

2. ERROR, % = $100\left(1 - \dfrac{\text{PRED } c_{\ell_\alpha}}{\text{MEAS } c_{\ell_\alpha}}\right)$

3. MEAN ERROR FOR TABLE, N = 139
   $M = 10.70\%$
   $\sigma = 13.44\%$

4. MACH NUMBER EFFECT IS
   M = -0.40% AT M = 0.3 TO
   M ≈ 30.53% AT M = 0.8

5. MEAN ERROR FOR 0.3 AND 0.45 MACH NUMBER:
   N = 64
   $M = 1.01\%$
   $\sigma = 7.31\%$

1892-012B

TABLE 3.3.1.2-VIII REFERENCE 6 MEASURED LIFT CURVES WITHOUT TRANSITION STRIP. UNFLAPPED

RN $\times 10^{-6}$	c_ℓ	α DEG	CURVE FIT c_ℓ	ERROR Δc_ℓ	LIFT CURVE
1.9	-0.114	-4.06	-0.114	0	$c_\ell = 0.2885 + 0.09853\ \alpha^\circ$
	-0.012	-3.04	-0.013	-0.001	$\alpha_{0L} = -2.91^\circ$
	0.087	-2.02	0.088	0.001	$r^2 = 0.9999$, $M=0$, $\delta = 0.001$
	0.167	-0.98	0.167	0	$c_\ell = 0.2650 + 0.10000\ \alpha^\circ$
	0.266	0.1	0.266	0	$\alpha_{0L} = -2.65^\circ$
	0.369	1.04	0.369	0	$r^2 = 1.0000$, $M=0$, $\delta = 0$
	0.414	1.55			
	0.439	2.06			TRANSITION REGION
	0.466	2.57			
	0.500	3.06	0.498	-0.002	
	0.593	4.07	0.595	0.002	$c_\ell = 0.2049 + 0.09587\ \alpha^\circ$
	0.691	5.08	0.692	0.001	$\alpha_{0L} = -2.14^\circ$
	0.792	6.11	0.791	-0.001	$r^2 = 0.9998$ $M=0$, $\delta=0.002$
4.05	-0.144	-4.06	-0.144	0	$c_\ell = 0.2798 + 0.10441\ \alpha^\circ$
	-0.39	-3.05	-0.039	0	$\alpha_{0L} = -2.68^\circ$
	0.69	-2.02	0.69	0	$r^2 = 1.0000$, $M=0$, $\delta = 0$
	0.171	-1.01			
	0.259	0.01			TRANSITION REGION
	0.346	1.02			
	0.381	1.54			
	0.417	2.07	0.414	-0.003	
	0.463	2.58	0.464	0.001	
	0.511	3.08	0.513	0.002	$c_\ell = 0.2095 + 0.09869\ \alpha^\circ$
	0.612	4.09	0.613	0.001	$\alpha_{0L} = -2.12^\circ$
	0.713	5.09	0.712	-0.001	$r^2 = 0.9998$, $M=0$, $\delta = 0.002$
	0.814	6.12	0.814	0	

r^2 = COEFFICIENT OF DETERMINATION

M = MEANERROR

σ = STANDARD DEVIATION FOR ERROR

1892-013B

TABLE 3.3.1.24X REFERENCE 6 MEASURED LIFT CURVES WITH TRANSITION STRIP, UNFLAPPED

RN $\times 10^{-6}$	c_ℓ	α DEG	CURVE FIT c_ℓ	ERROR Δc_ℓ	LIFT CURVE
1.9	-0.186	-4.06	-1.88	-0.002	
	-0.089	-3.03	-0.088	0.001	
	0.006	-2.01	0.010	0.004	
	0.106	-0.98	0.110	0.004	
	0.205	0	0.205	0	
	0.306	1.03	0.305	-0.001	$c_\ell = 0.2051 + 0.09682\,\alpha°$
	0.354	1.53	0.353	-0.001	$\alpha_{0L} = -2.12°$
	0.407	2.06	0.404	0.003	$r^2 = 0.9999$
	0.455	2.55	0.452	-0.003	$M = 0,\ \sigma = 0.004$
	0.509	3.09	0.504	-0.005	
	0.603	4.07	0.599	-0.004	
	0.696	5.10	0.699	0.003	
	0.791	6.12	0.798	0.007	
4.05	-0.196	-4.08	-0.198	-0.002	
	-0.094	-3.03	-0.093	0.001	
	0.005	-2.02	0.007	0.002	
	0.105	-1.01	0.108	0.003	
	0.209	0.01	0.210	0.001	$c_\ell = 0.2666 + 0.09963\,\alpha°$
	0.311	1.03	0.311	0	$\alpha_{0L} = -2.09°$
	0.362	1.52	0.360	-0.002	$r^2 = 1.0000$
	0.418	2.08	0.416	-0.002	$M = 0,\ \sigma = 0.002$
	0.465	2.55	0.463	-0.002	
	0.517	3.07	0.514	-0.003	
	0.614	4.08	0.615	0.001	
	0.716	5.09	0.716	0	
	0.816	6.13	0.819	0.003	

r^2 = COEFFICIENT OF DETERMINATION

M = MEAN ERROR

δ = STANDARD DEVIATION FOR ERROR

1892-014B

TABLE 3.3.1.2-X REFERENCE 6 MEASURED LIFT CURVE SLOPES

TRANSITION STRIP	c_ℓ RANGE FROM	c_ℓ RANGE TO	$c_{\ell_{\alpha_M}}^{\circ}$ FOR RN X 10^{-6} = 1.9	$c_{\ell_{\alpha_M}}^{\circ}$ FOR RN X 10^{-6} = 4.06	$\sqrt{1-M^2}$ FOR RN X 10^{-6} = 1.9	$\sqrt{1-M^2}$ FOR RN X 10^{-6} = 4.05	$c_{\ell_\alpha}^{\circ}$ FOR RN X 10^{-6} = 1.9	$c_{\ell_\alpha}^{\circ}$ FOR RN X 10^{-6} = 4.05	MEASURED $\frac{c_{\ell_{\alpha 1.9}}}{c_{\ell_{\alpha 4.05}}}$	SECT 3.3.1.1 $\frac{c_{\ell_{\alpha 1.9}}}{c_{\ell_{\alpha 4.05}}}$	$\frac{c_{\ell_{\alpha 4.05}}}{2\pi(1 + 0.77\ t/c)}$	Eq. 3.3.1.2-h
OFF	-0.114	0.087	0.09853	0.10441	0.9939	0.9732	0.09793	0.10161	0.9638	0.9538	0.8666	0.8409
	0.167	0.369	0.10000				0.09939		0.9782			
	≥ 0.500		0.09587	0.09869			0.09529	0.09605	0.9921		0.8192	
ON	ALL		0.09682	0.09963			0.09621	0.09696	0.9923	0.9230	0.8270	

1892-015B

TABLE 3.3.1.2-XI QUADRATIC COEFFICIENTS -SECTION LIFT CURVE SLOPE

SECTION	m°_ϕ	c°_ϕ	$m^\circ_\phi c^\circ_\phi$	c_{1_K}	c_{2_K}
4- & 5-DIGIT	0.00715	129	0.922	-0.152	-0.710
63-SERIES	0.00715	49	0.350	0.420	-0.270
63A SERIES	0.00715	115	0.822	-0,052	-0.633
64-SERIES	0.01059	57	0.604	0.166	-0.465
64A SERIES	0.01059	119	1.260	-0.490	-0.970
65-SERIES	0.01059	70	0.741	0.029	-0.571
65A SERIES	0.01059	133	1,408	-0.638	-1.084
66-SERIES	0.01059	95	1.006	-0.236	-0.775
16-SERIES	0.00715	247	1.766	-0.996	-1.360

m°_ϕ IS FROM EQUATION 3.3.1.2-g

c°_ϕ IS FROM TABLE 6.1.1.2-I

$c_{1_K} = 0.77 - m^\circ_\phi c^\circ_\phi$

$c_{2_K} = -0.77\, m^\circ_\phi \cdot c^\circ_\phi$

1892-016B

$K = 1 + c_{1_K} \frac{t}{c} + c_{2_K} \left(\frac{t}{c}\right)^2$

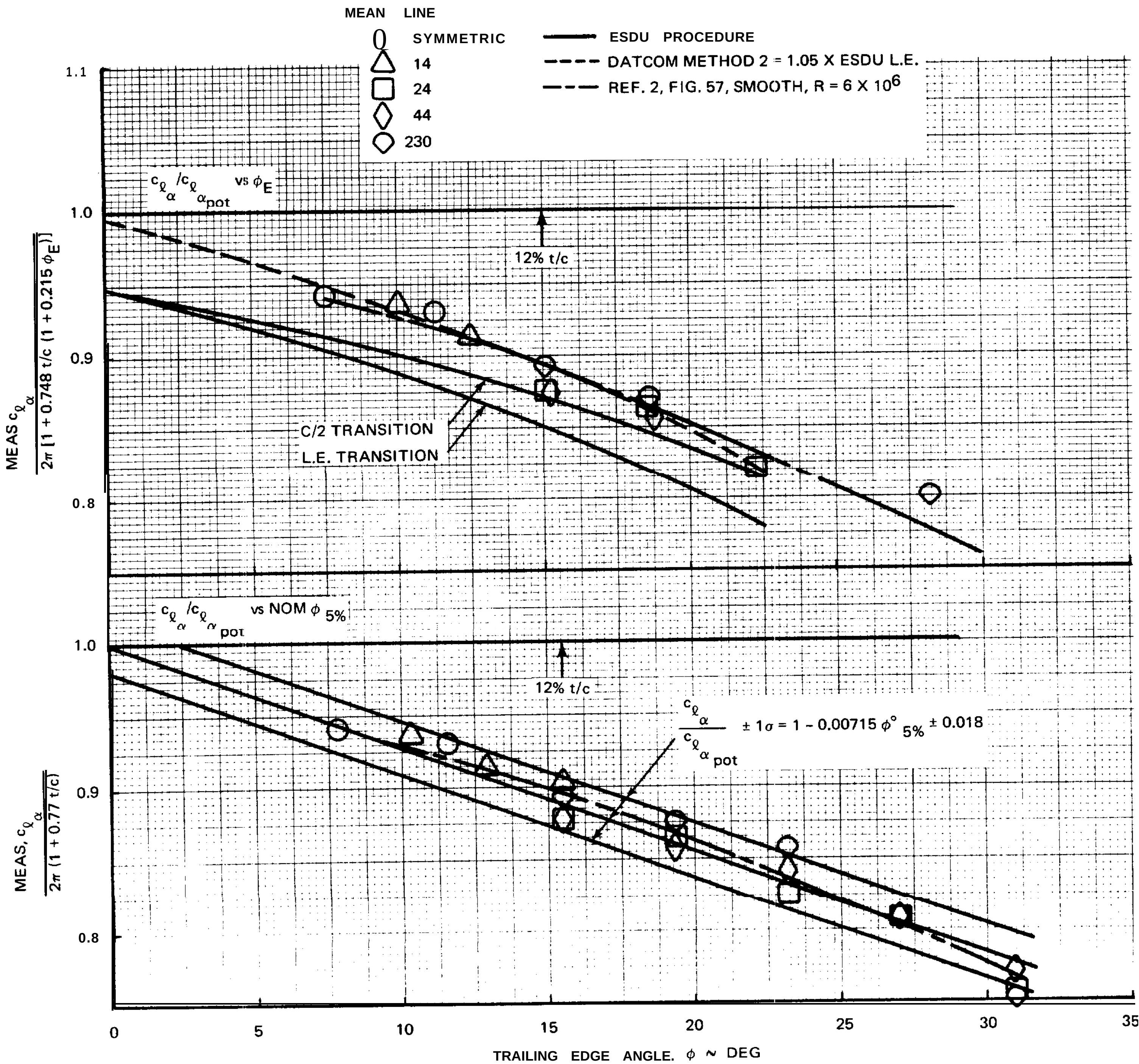

1892-017B

Fig. 3.3.1.2-1 $c_{\ell_\alpha}/c_{\ell_{\alpha_{pot}}}$ vs Trailing Edge Angle, Reynolds Number = 9×10^6, 4 & 5 Digit Sections

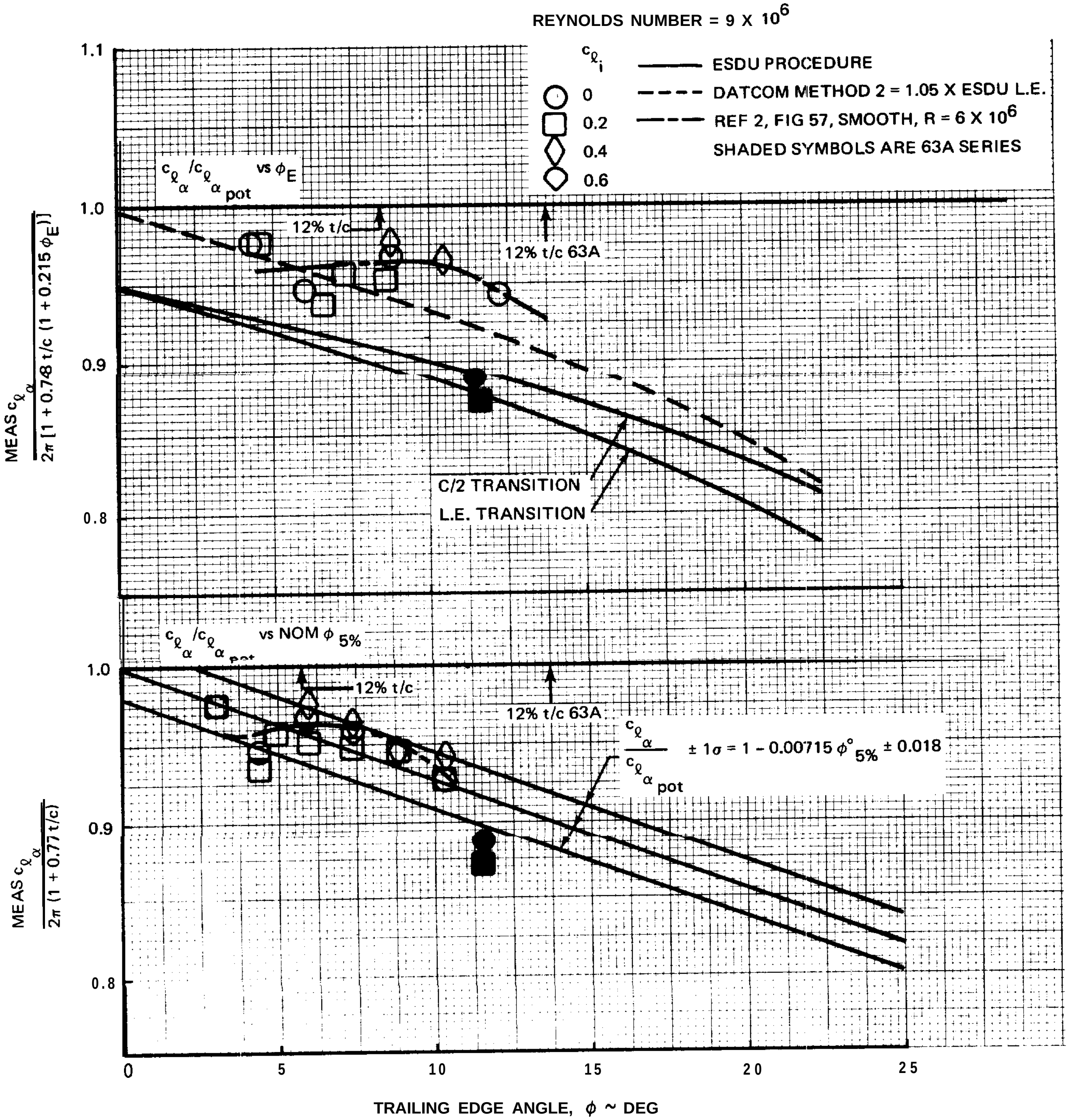

1892-018B

Fig. 3.3.1.2-2 $c_{\ell_\alpha}/c_{\ell_{\alpha\,pot}}$ vs Trailing Edge Angle, **63-Series** Sections

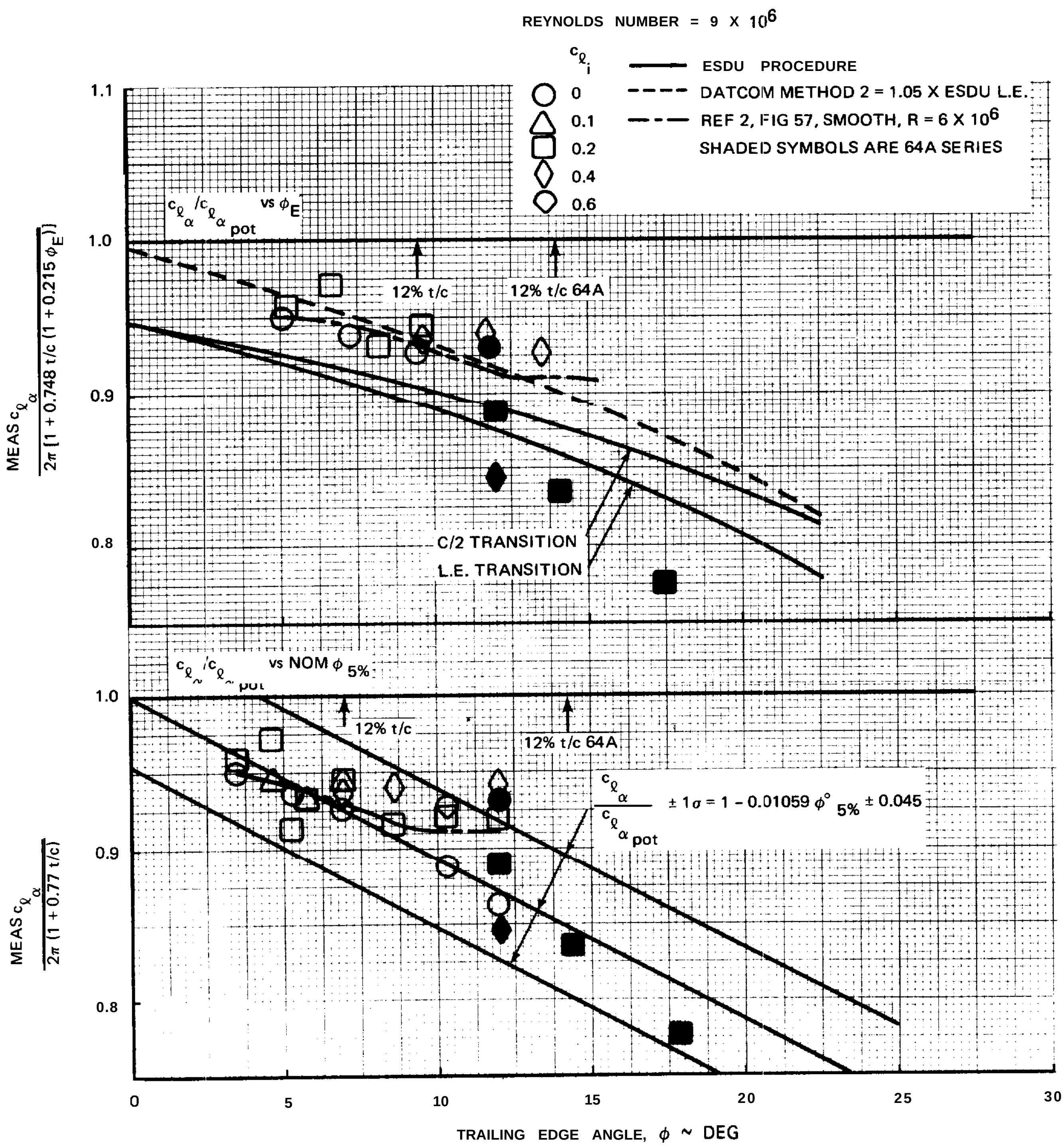

1892-019B

Fig. 3.3.1.2-3 $c_{\ell_\alpha}/c_{\ell_{\alpha\,pot}}$ vs Trailing **Edge** Angle, **64-Series** Sections

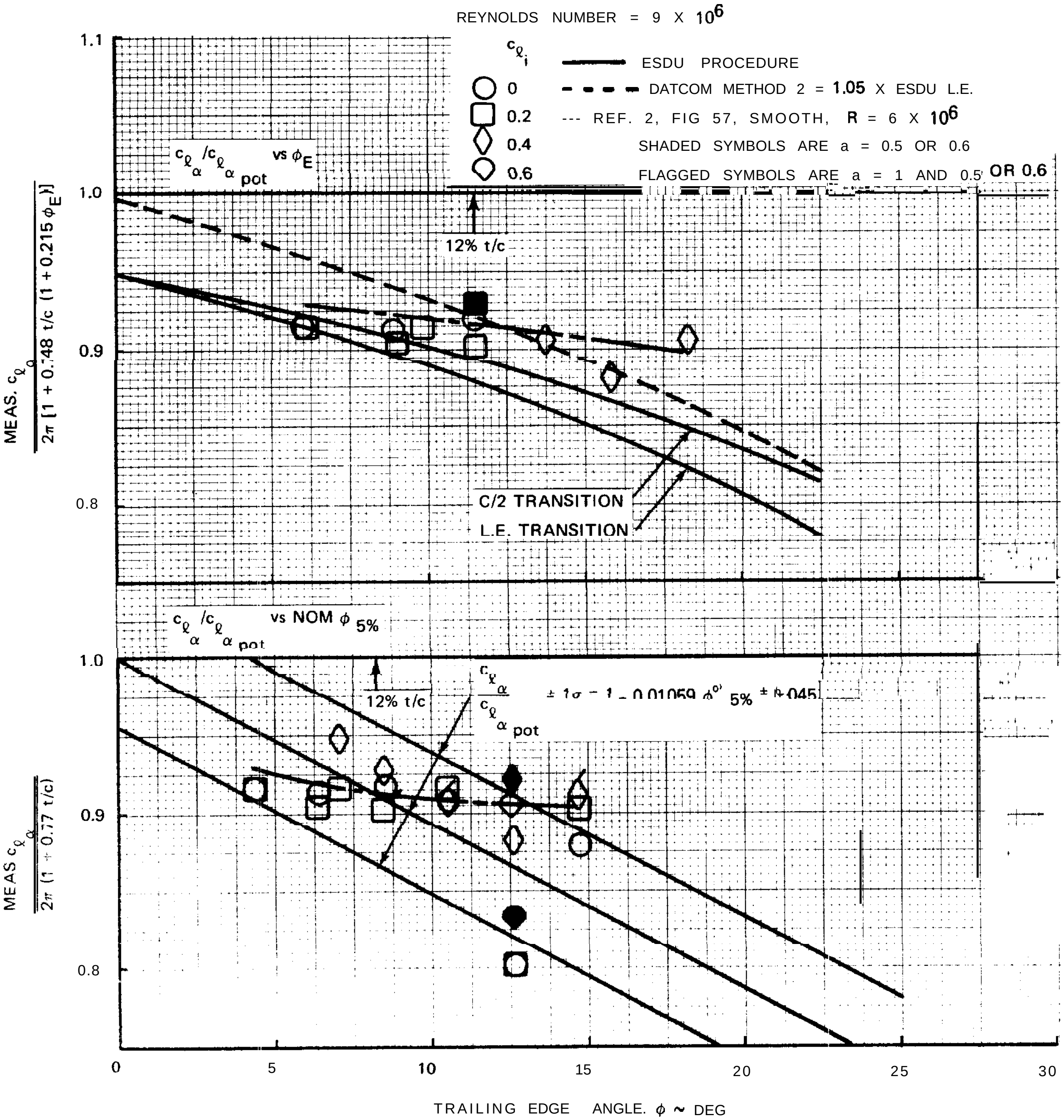

1892-020B

Fig. 3.3.1.2-4 $c_{\ell_\alpha}/c_{\ell_{\alpha\,pot}}$ vs Trailing Edge Angle, 66-Series Sections

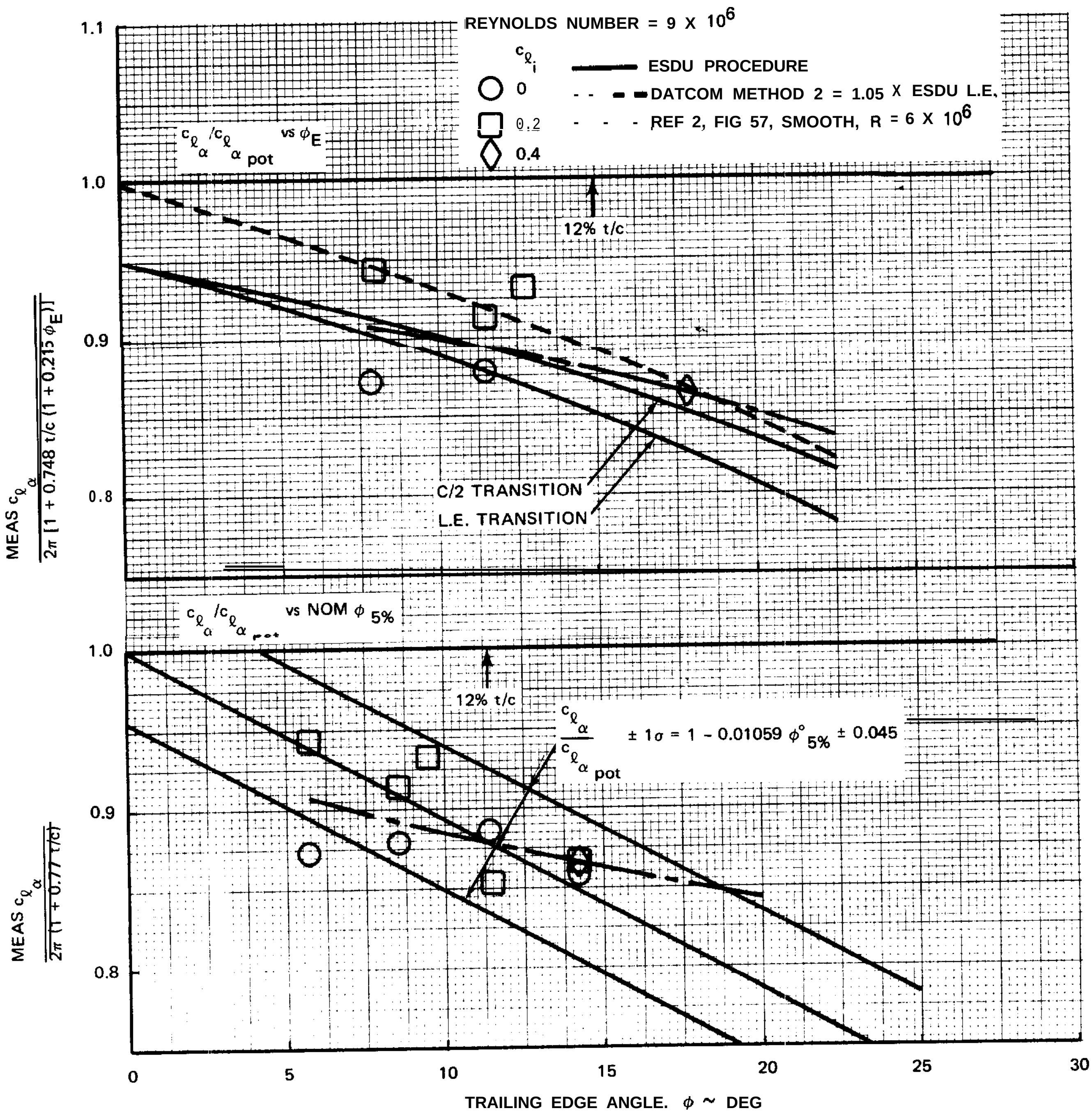

1892-021B

Fig. 3.3.1.2-5 $c_{\ell_\alpha}/c_{\ell_{\alpha\,pot}}$ vs Trailing Edge Angle, 66-Series Sections

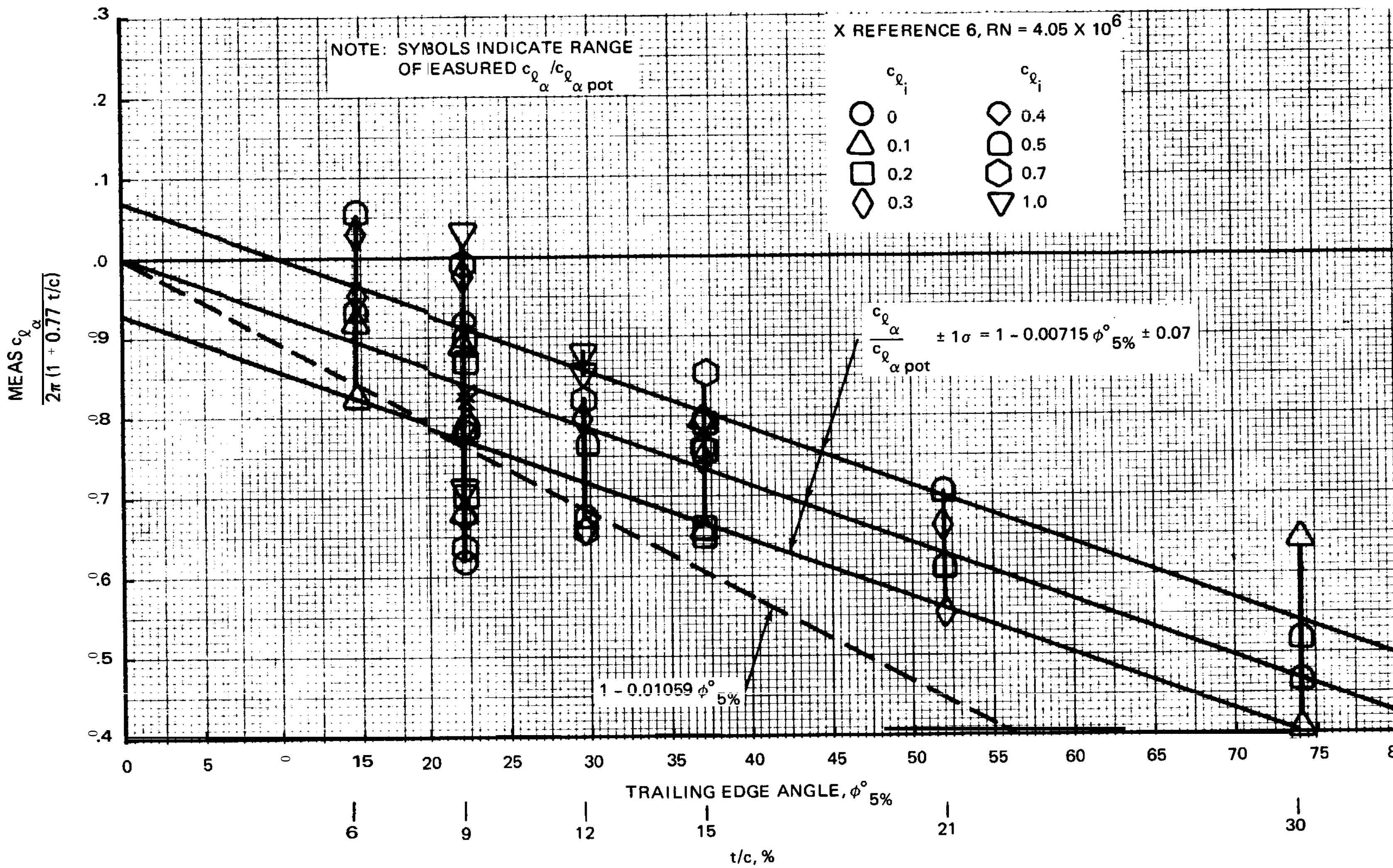

1892-022B

Fig. 3.3.1.2-6 $c_{\ell_\alpha}/c_{\ell_{\alpha\,pot}}$ vs Trailing Edge Angle, 16-Series Sections

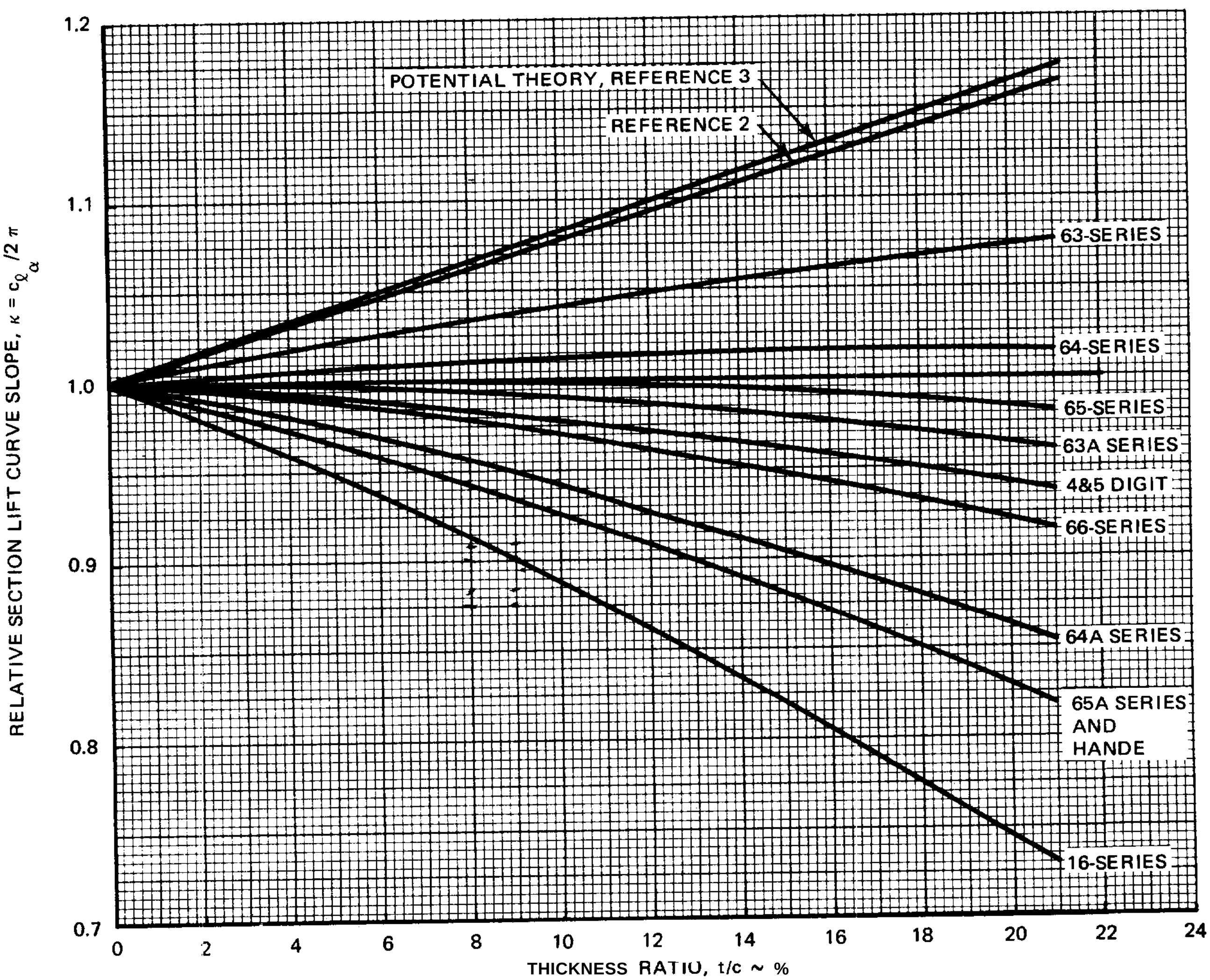

1892-023B

Fig. 3.3.1.2-T Relative Section Lift Curve Slope, κ

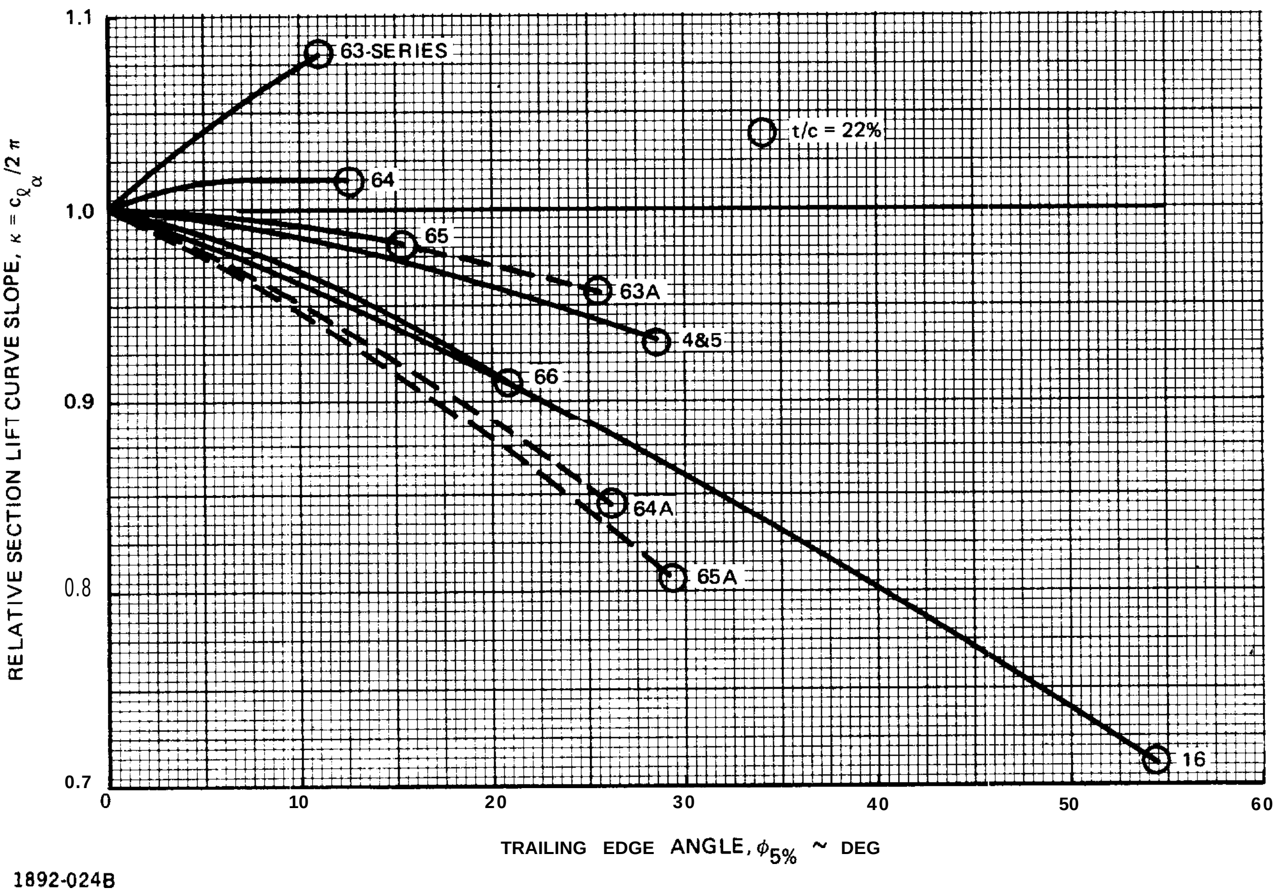

Fig. 3.3.1.2-8 Relative Section Lift Curve Slope, κ vs Trailing Edge Angle

3.3.1.3 Section Zero Lift Angle. Thin airfoil potential theory presents the design lift coefficient, c_{ℓ_i}, at the ideal angle of attack, α_i, producing a zero lift angle defined by:

$$\alpha_{0\ell_{pot}} = \alpha_i - c_{\ell_i}/2\pi \qquad 3.3.1.3\text{-}1$$

No general expression for the potential effect of section thickness is available. Experimental section characteristics indicate that, while not the thin airfoil theory value, the zero lift angle is practically invariant with thickness, Reynolds Number, and (below some critical value) Mach Number. The zero lift angle therefore provides a convenient intercept for the definition of the linear portion of the section lift curve.

A critical Reynolds Number, characteristic of the section and associated with zero lift angle shifts of -1/2 degree or more has been noted in Section 3.3.1.1. It is illustrated by comparison of Tables 3.3.1.2-VIII and -IX and by the 4415 section of Figure 18 (a) of Reference 4.

The DATCOM applies the emperical factors of Reference 1 to the thin airfoil potential zero lift angles for the 4 & 5 Digit and 6-Series sections and those factors are compared with the 9 x 10^6 Reynolds Number data of DATCOM Table 4.1.1-A and -B and with the 6 x 10^6 Reynolds Number trend lines of Figure 56 of Reference 1 on Figures 3.3.1.3-1 to -6. The distinctive κ_0 factors employed on the figures for the 6A Series sections and for the a < 1.0 mean line were arbitrarily selected to reduce the mean errors and standard deviations for these sections to magnitudes comparable with those of the parent section.

The 16-Series section zero lift angles of Figure 3.3.1.1-4 are plotted against their potential value on Figure 3.3.1.3-7. The measured zero lift angles of Reference 2 correlate well with the 4 Digit section factor but Reference 3 seems to present convincing evidence that the Reference 2 angles are subject to Reynolds Number effect throughout. The measured angles of Figure 3.3.1.3-7 for high c_{ℓ_i} might indicate emergence from that Reynolds Number effect but are more likely to indicate the onset of compressibility effect. On the basis of the Reference 3 evidence the 16-Series section is here classified with the 6-Series sections.

The measured and predicted zero lift angles for the data or Reference '1 are compared statistically in Table 3.3.1.3-I. The 6A and a < 1.0 samples are scarcely of significant size but their accuracies and precisions were both generally improved by employing the .93 and 1.15 factors rather than the .74 factor of the parent section. The predictive improvement is particularly significant to the effective design lift coefficient, considered in the next sub-section.

2

SUMMARY

The statistical analysis of Table 3.3.1.3-I may be summarized by:

$$\alpha_{0\ell} = \kappa_0\, \alpha_{0\ell_{pot}} \pm \sigma \qquad 3.3.1.3\text{-}2$$

$$= \kappa_0 \left(\alpha_i - c_{\ell_i}/2\pi\right) \pm \sigma$$

$$= -\kappa_0\, c_{\ell_i}/2\pi \pm \sigma \text{ for a = 1.0 mean line}$$

where: κ_0 = .74 for 16- and 6-Series sections on a = 1.0 mean line

= .93 for 4 Digit sections and 6A Series sections on a = 1.0 mean line

= 1.08 for 5 Digit sections

= 1.15 for 6-Series sections on a < 1.0 mean line

σ = 1/3 deg.

LIMITATIONS

1. The multiplicity of coefficients for Equation 3.3.1.3-2 is indicative of the lack of a rational relationship between the zero lift angle and the thickness and camber distributions.

2. Some generality not substantiated by the data samples is inferred by Equation 3.3.1.3-2. Characteristics of one intermediate example each, 64 and 230, of the 4 and 5 Digit families of mean lines have been extended over the families. The "a" family of mean lines is ill-defined.

3. Reference 1 includes only one example of the a = .8 mean line which is sometimes employed physically or effectively for the a = 1.0 mean line. For the 65, 3-418, a = .8 section κ_0 is .989. Note, however, that this mean line does not have a zero ideal angle of attack.

HANDE

The HANDE zero lift angle equation is an empirical curve fit, quadratic in c_{ℓ_i}, to an unspecified data sample. The form of the equation does not permit comparison with Equation 3.3.1.3-2 in general form. The HANDE equation may be written:

$$\alpha_{0\ell_H} = \alpha_i - 1.007\, \frac{c_{\ell_i}}{2\pi} + 1.151 \left(\frac{c_{\ell_i}}{2\pi}\right)^2 \qquad 3.3.1.3\text{-}3$$

For small cambers the result is a larger negative angle than that of Equation 3.3.1.3-2 by the factor $1/\kappa_0$, typically 1/2 degree more negative. The HANDE equation, then, tends to predict the effect of an abnormal extent of laminar flow on the chord which may have existed in the data sample employed.

Typical comparisons of Equations 3.3.1.3-2 and -3 are shown on Figure 3.3.1.3-7 and the HANDE equation is compared with the data sample of Table 3.3.1.3-I in Table 3.3.1.3-R..

REFERENCES

1. Abbott, I. H. and von **Doenhoff,** A. E.: Theory of Wing Sections. Dover, 1959.
2. Lindsey, W. F.; Stevenson, D. B. and Daley, B. N.: Aerodynamic Characteristics Of 24 NACA 16-Series Airfoils At Mach Numbers Between 0.3 and 0.8. NACA Technical Note 1546, September 1948.
3. Teeling, P: Low Speed Wind Tunnel Tests Of A NACA 16-309 Airfoil With Trailing Edge Flap. **DeHavilland** Aircraft of Canada Limited Report No. ECS 76-3, October 1976.
4. **Loftin,** Laurence K. and Smith, Hamilton A.: Aerodynamic Characteristics of 15 NACA Airfoil Sections At Seven Reynolds Numbers From 0.7 x 10^6 to 9.0 x 10^6. NACA Technical Note 1945, October 1949.

TABLE 3.3.1.3-I ZERO LIFT ANGLE STATISTICAL ANALYSIS

SECTION	MEAN LINE	COEFF κ_0	NUMBER IN SAMPLE N	(1) MEAN $\Delta\alpha_{o\ell}$ DEG	$\Delta\alpha_{o\ell}$ STD DEVIATION σ, DEG
16-SERIES	a= 1.0	0.74	NOTE 2		
63-SERIES			16	-0.01	0.35
64-SERIES			16	0.02	0.26
65-SERIES			16	0.06	0.20
66-SERIES			6	-0.01	0.31
4-DIGIT	64	0.93	13	0.07	0.54
5 DIGIT	230	1.06	5	0.06	0.23
STANDARD SECTIONS			74	0.03	0.33
6XA SERIES					
63A SERIES	a = 1.0	0.93	1	0.20	–
64A SERIES			4	0	0.35
6XA SERIES			5	0.04	0.32
6-SERIES, a < 1.0					
63 SERIES	a = 0.3	1.15	1	0.03	–
65 SERIES	a = 0.5(5), 0.6, 0.8		7	0.08	0.22
66 SERIES	a = 0.6		1	0.90	–
6X-SERIES, a ≠ 1.0			9	0.17	0.33
TOTAL EXPERIENCE					
ALL SECTIONS			88	0.04	0.33

NOTES: 1. $\Delta\alpha_{o\ell}$ = MEASURED $\alpha_{o\ell}$ – PREDICTED $\alpha_{o\ell}$

2. INFERRED FROM REFERENCE 2 WITH GUIDANCE FROM REFERENCE 3.

1892-025B

TABLE 3.3.1.3-II HANDE ZERO LIFT ANGLE STATISTICAL ANALYSIS

SECTION	MEAN LINE	NUMBER IN SAMPLE N	(1) MEAN $\Delta\alpha_{o\ell}$ DEG	$\Delta\alpha_{o\ell}$ STD DEVIATION σ, DEG
16-SERIES	a = 1.0	NOTE 2		
63-SERIES		16	0.60	0.45
64-SERIES		16	0.50	0.32
65-SERIES		16	0.63	0.29
66-SERIES		8	0.48	0.36
4-DIGIT	64	13	0.06	0.56
5 DIGIT	230	5	-0.19	0.25
STANDARD SECTIONS'		74	0.43	0.46
6XA SERIES				
63A SERIES	a= 1.0	1	0.27	
64A SERIES		4	0.06	0.33
6XA SERIES		5	0.10	0.30
6-SERIES, a < 1 .0				
63 SERIES	a = 0.3	1	-0.53	
65 SERIES	a = 0.5(5), 0.6, 0.8	7	-0.56	0.34
66 SERIES	a = 0.6	1	0.06	
6X-SERIES, a $\neq$ 1.0		9	-0.49	0.36
TOTAL EXPERIENCE				
ALL SECTIONS		88	0.31	0.52

NOTES: 1. $\Delta\alpha_{o\ell}$ = MEASURED $\alpha_{o\ell}$ - PREDICTED $\alpha_{o\ell}$

2. SEE FIGURE 3.3.1.3-7 FOR TYPICAL COMPARISONS OF EQUATIONS 3.3.1.3-2 AND -3.

1892-026B

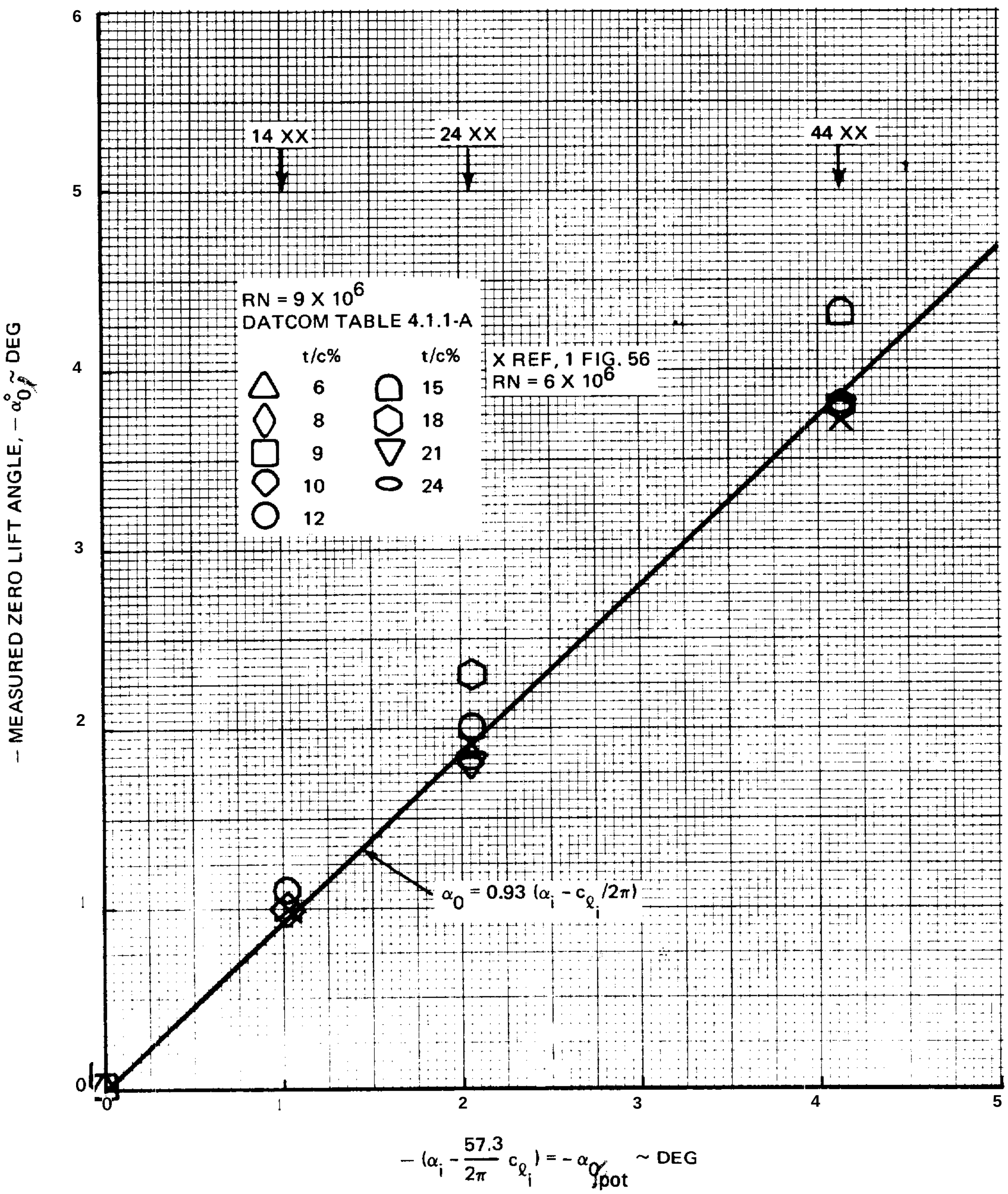

1892-027B

Fig. 3.3.1.31 Zero Lift Angle, 4 Digit Sections

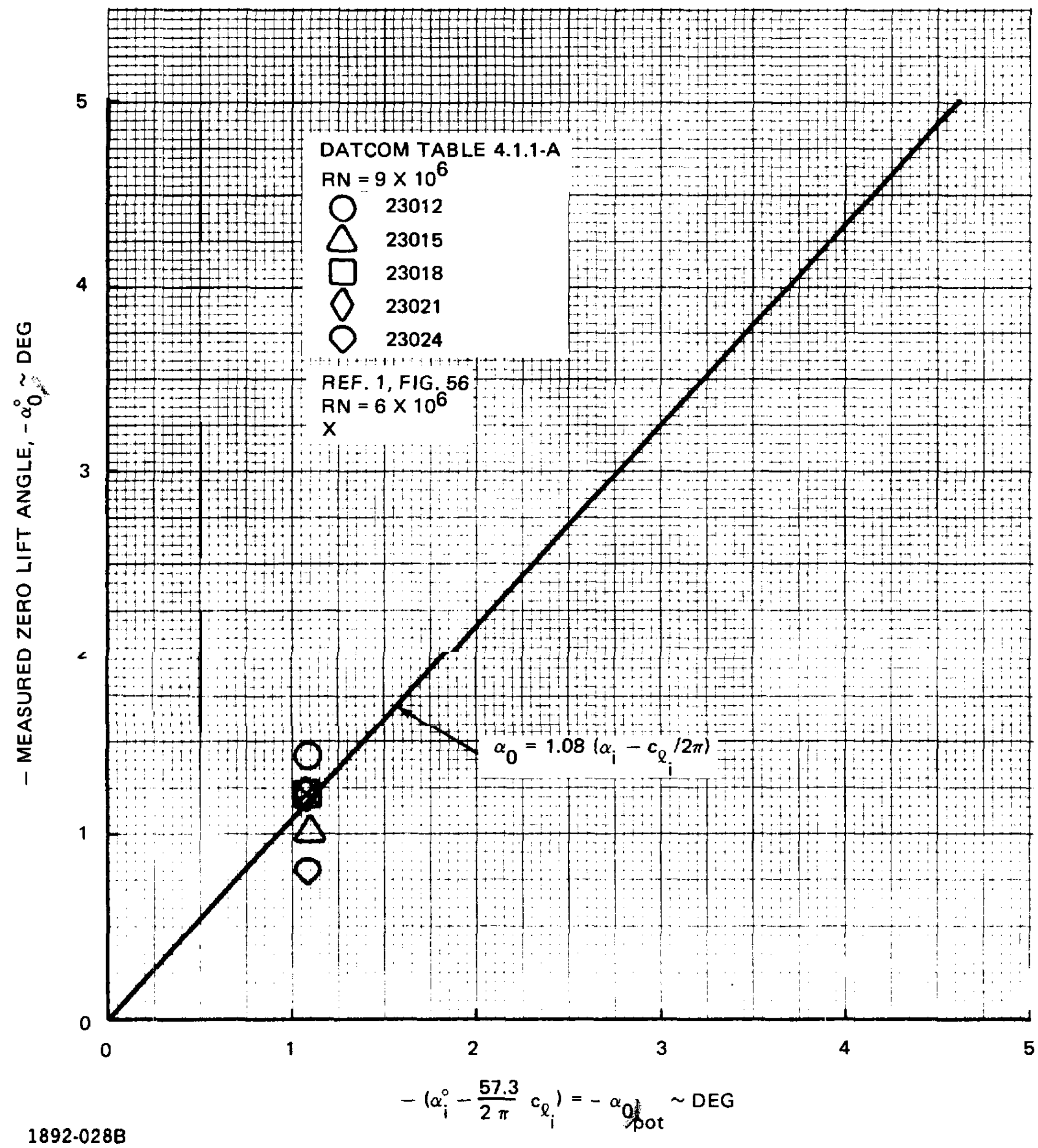

1892-028B

Fig. 3.3.1.3-2 Zero Lift Angle, 5 Digit Sections

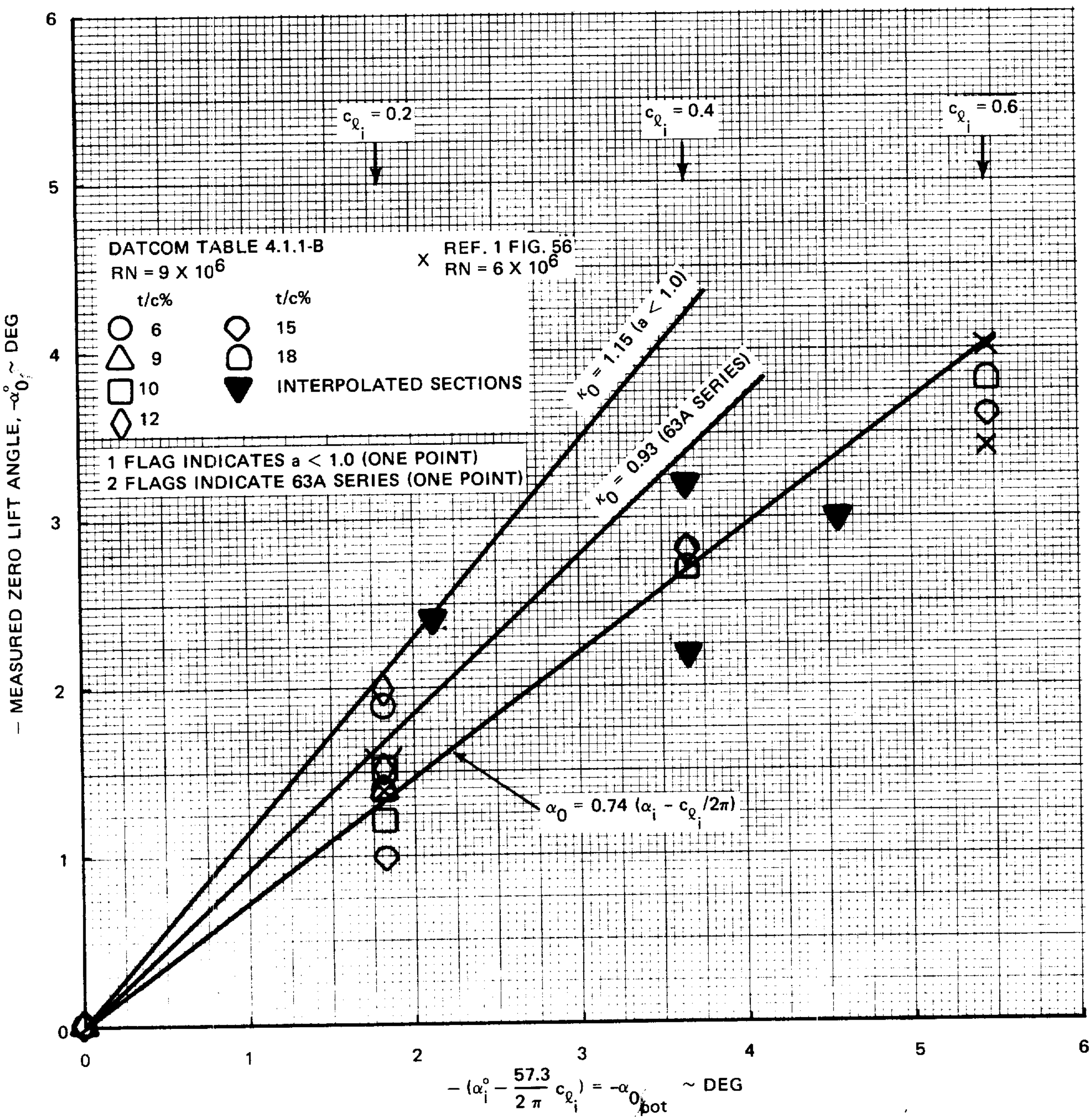

1892-029B

Fig. 3.3.1.3-3 Zero Lift Angle, 63-Series Sections

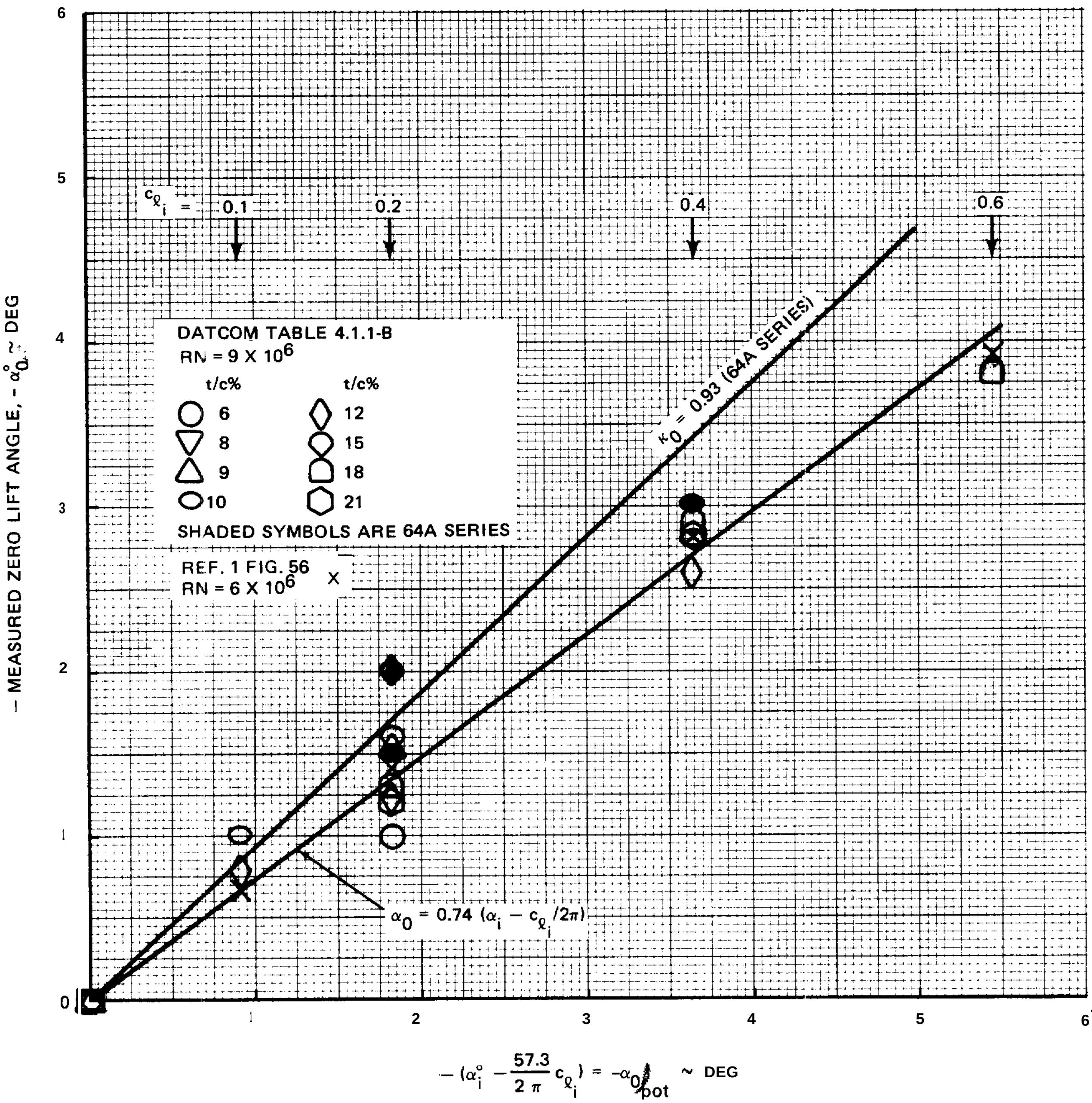

1892-030B

Fig. 3.3.1.3-4 Zero Lift Angle, 64Series Sections

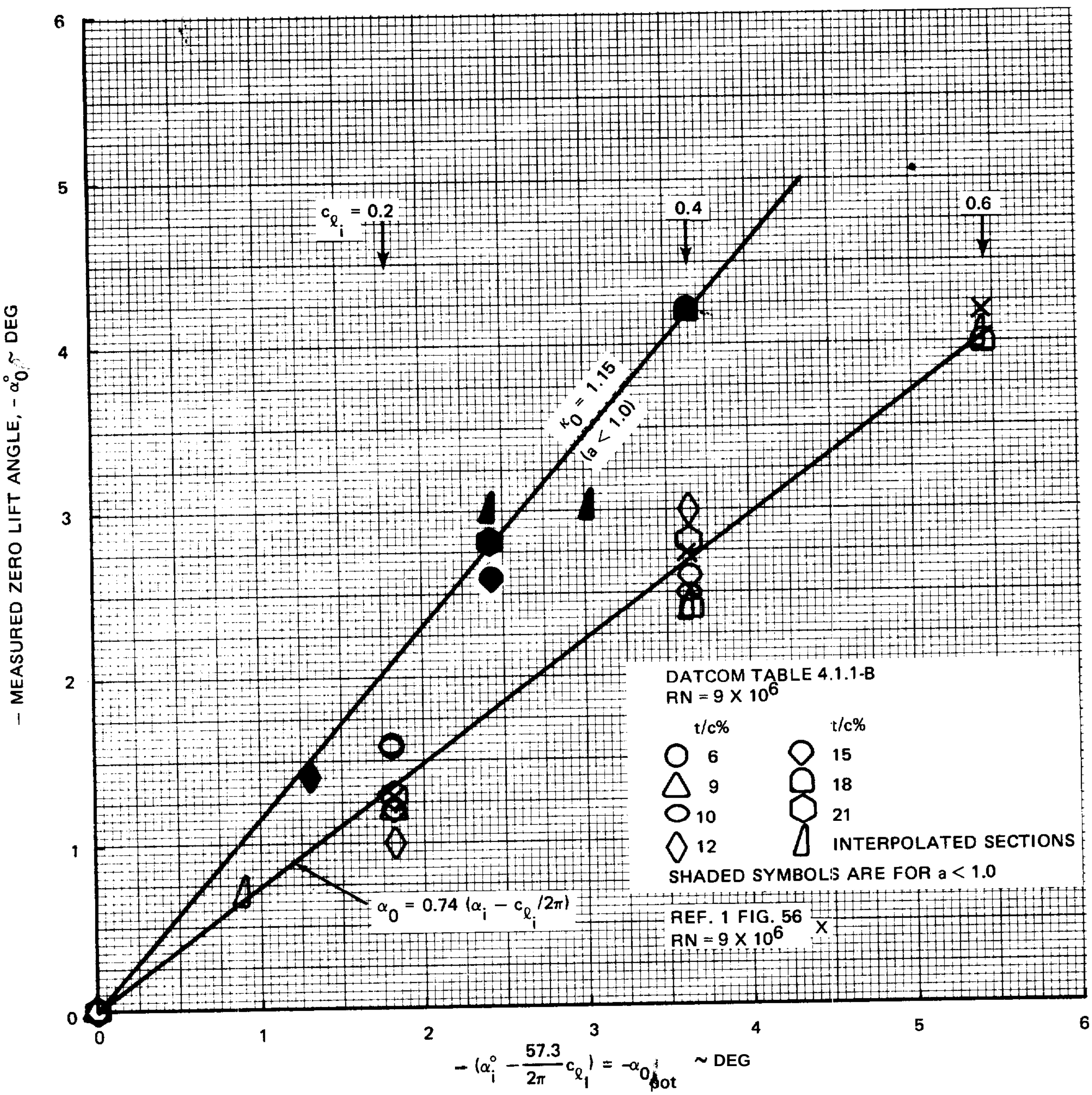

1892-031B

Fig. 3.3.1.3-5 Zero Lift Angle, 65-Series Sections

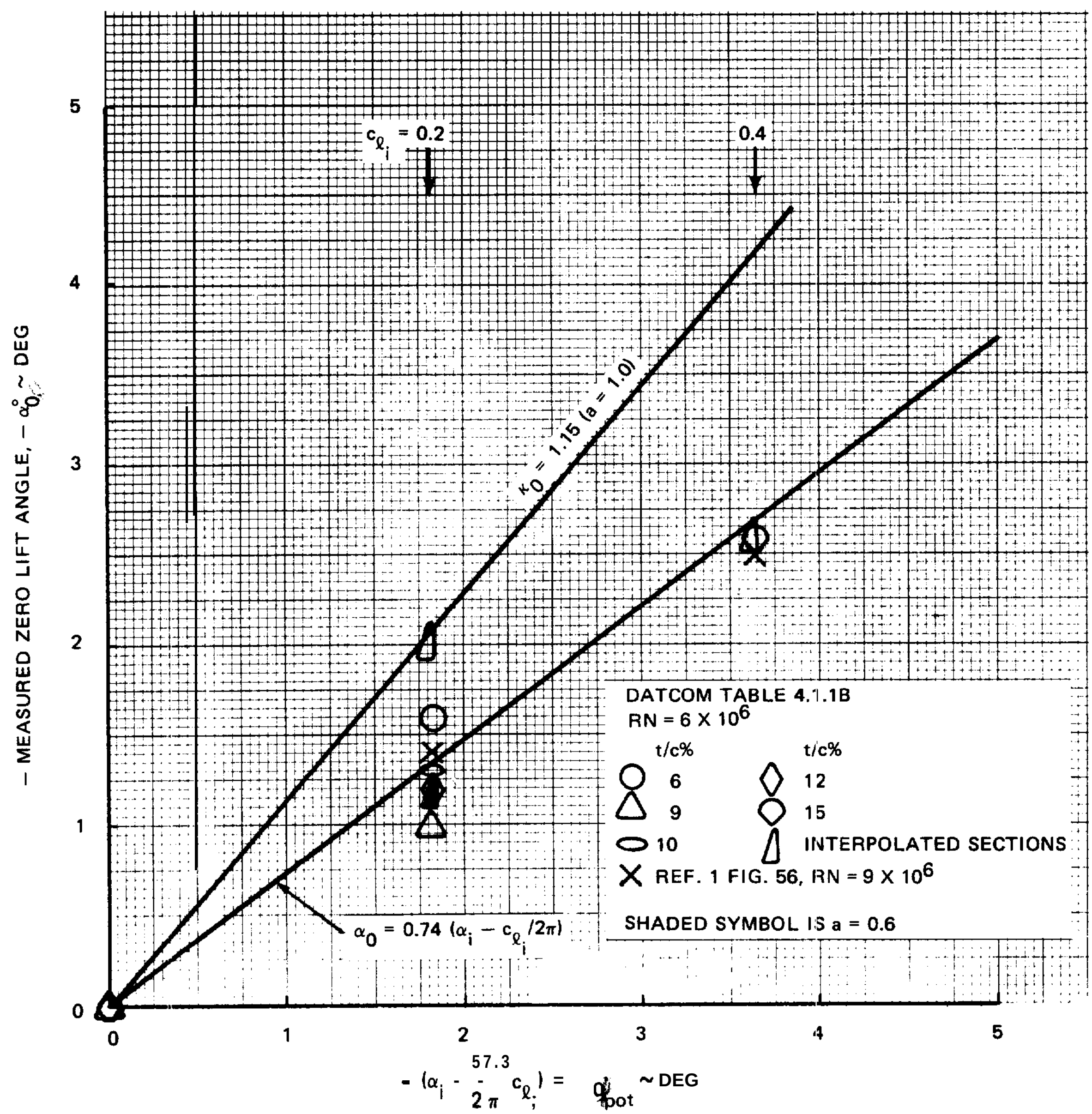

1892-032B

Fig. 3.3.1.3-6 Zero Lift Angle, 66-Series Sections

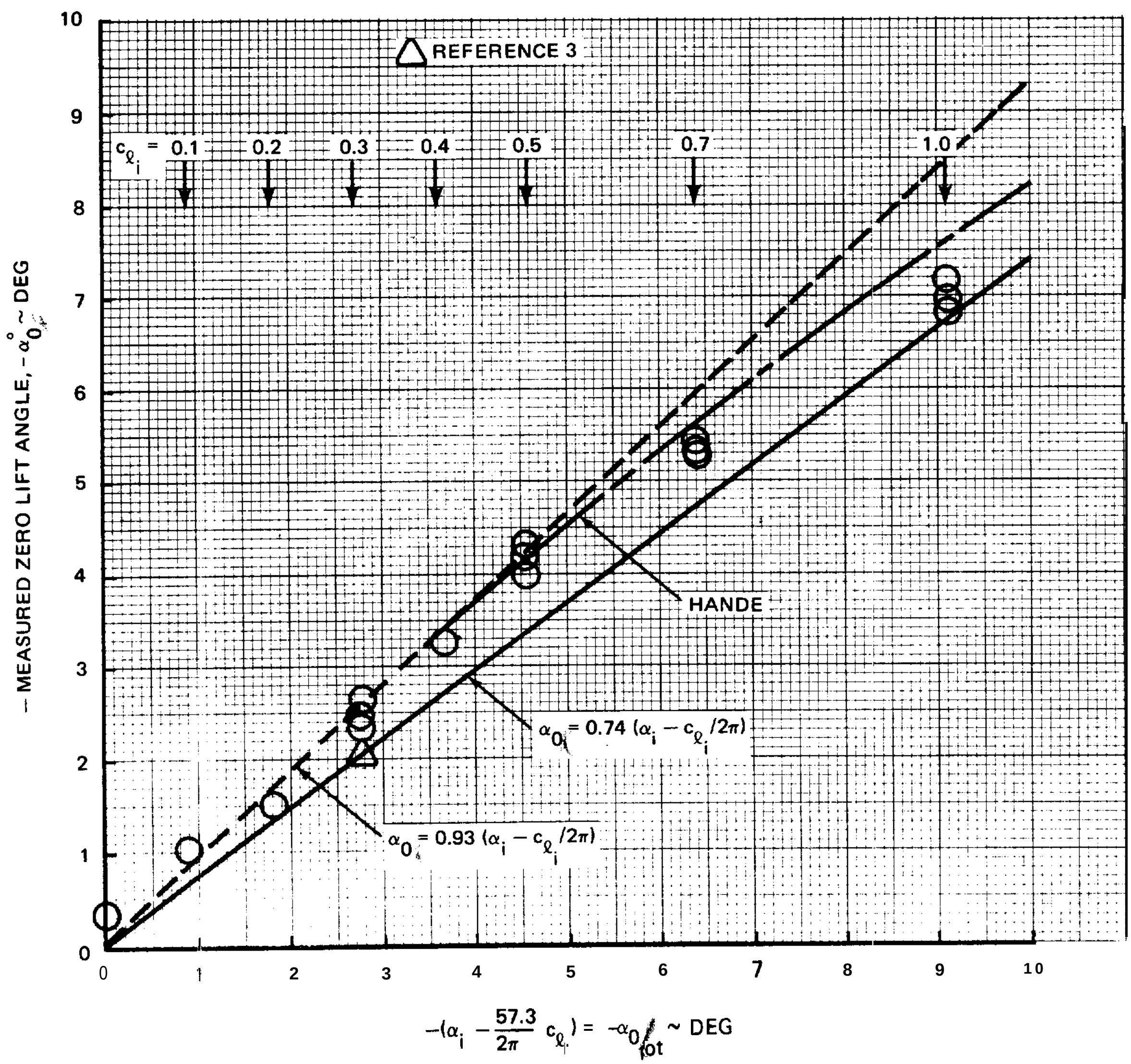

1892-033B

Fig. 3.3.1.3-7 Zero Lift Angle, 16-Series Sections, From Fig. 3.3.1.1-4

3.3.1.4 Effective Design Lift Coefficient. The intercept for the slope-intercept form of the section lift curve could be defined at the zero lift angle or at the ideal angle of attack. The zero lift angle provides the more convenient reference because it is virtually invariant with Reynolds Number and because it is an axis intercept. The empirical definition for the effective design lift coefficient then suffers, however, because it becomes a derived characteristic. The predictive accuracy and precision for the lift curve slope and zero lift angle therefore influence the interpretation of experimental cavitation characteristics because the effective design lift coefficient establishes the proportion of basic and additional type lift on the section.

The effective design lift coefficient is defined by the viscous section lift curve slope and zero lift angle:

$$c_{\ell_{i_{eff}}} = c_{\ell_\alpha}\left(\alpha_i - \alpha_{0\ell}\right) \qquad 3.3.1.4\text{-}1$$

$$= 2\pi\kappa\left(\alpha_i - \alpha_{0\ell}\right)$$

Then from Equation 3.3.1.3-2:

$$c_{\ell_{i_{eff}}} = 2\pi\kappa\left[\alpha_i - \kappa_0\left(\alpha_i - \frac{c_{\ell_i}}{2\pi}\right)\right] \qquad 3.3.1.4\text{-}2$$

$$= 2\pi\kappa\left[\left(1-\kappa_0\right)\alpha_i + \frac{c_{\ell_i}}{2\pi}\kappa_0\right]$$

$$\left(\frac{c_{\ell_{i_{eff}}}}{c_{\ell_i}}\right) = \left[2\pi\frac{\alpha_i}{c_{\ell_i}} \quad + \kappa_0\right] \kappa$$

$$= \kappa_0\kappa \qquad \text{for } a = 1.0 \text{ mean line}$$

where: κ is from Equation 3.3.1.2-10

κ_0 is from Equation 3.3.1.3-2

The data sample employed to test Equation 3.3.1.4-2 was the same as that employed in Sections 3.3.1.2 and .3, DATCOM Tables 4.1.1-A and -B which contain zero lift angles and lift curve slopes reported in Reference 3. The effective design lift coefficients were calculated from those angles and slopes for comparison with Equation 3.3.1.4-2 on Figures 3.3.1.4-1 through -5.

The 16-Series comparison of Figure 3.3.1.4-6 presents a special problem. The effective design lift coefficients are taken from Table 3.3.1.2-V but Section 3.3.1.3 concludes that the zero lift angle for this data has been displaced throughout by an abnormal extent of laminar flow. The measured and predicted effective design lift coefficients are therefore similarly displaced on Figure 3.3.1.4-6. It should be noted that the discrepancy between Equation 3.3.1.4-2 and the correlation of Reference 1 for the data of Figure 3.3.1.46 reflects application rather than interpretation. The data as measured :is generally applicable for aircraft propellers but all Reynolds Number and Mach Number effects must be removed for marine application. For the present there is only the **DeHavilland** data available to guide the marine application.

Approximating the variance of $c_{\ell_{i_{eff}}}/c_{\ell_i}$ **by:**

$$\mathrm{Var.}\left(\frac{c_{\ell_{i_{eff}}}}{c_{\ell_i}}\right) = \left[\frac{\partial\left(c_{\ell_{i_{eff}}}/c_{\ell_i}\right)}{\partial \kappa}\right]^2 \sigma_\kappa^2 + \left[\frac{\partial\left(c_{\ell_{i_{eff}}}/c_{\ell_i}\right)}{\partial \kappa_0}\right]^2 \sigma_{\kappa_0}^{\;2} \qquad 3.3.1.4\text{-}3$$

that variance becomes:

$$\mathrm{Var.}\left(\frac{c_{\ell_{i_{eff}}}}{c_{\ell_i}}\right) = \left[2\pi\frac{\alpha_i}{c_{\ell_i}}\left(1-\kappa_0\right)+\kappa_0\right]^2 \sigma_\kappa^{\;2} + \left(1-2\pi\frac{\alpha_i}{c_{\ell_i}}\right)^2 \kappa^2\sigma_{\kappa_0}^{\;2} \qquad 3.3.1.4\text{-}4$$

where the standard deviation for κ_0 is related to the nominal **1/3** degree zero lift angle standard **deviation,** $\sigma_{\alpha_{0\ell}}$, by:

$$\sigma_{\kappa_0} = \frac{2\pi}{c_{\ell_i}}\;\frac{\sigma_{\alpha_{0\ell}}}{2\pi\frac{\alpha_i}{c_{\ell_i}}-1} \qquad 3.3.1.4\text{-}5$$

and Equation 3.3.1.4-3 may be written:

$$\mathrm{Var.}\left(\frac{c_{\ell_{i_{eff}}}}{c_{\ell_i}}\right) = \left[2\pi\frac{\alpha_i}{c_{\ell_i}}\left(1-\kappa_0\right)+\kappa_0\right]^2 \sigma_\kappa^2 + \left(\frac{2\pi}{c_{\ell_i}}\right)^2 \kappa^2\sigma_{\alpha_{0\ell}}^{\;2} \qquad 3.3.1.4\text{-}6$$

$$=\left[\frac{2\pi}{57.3}\frac{\alpha_i^\circ}{c_{\ell_i}}\left(1-\kappa_0\right)+\kappa_0\right]^2 \sigma_\kappa^2 + \left(\frac{2\pi}{c_{\ell_i}}\right)^2 \kappa^2\left(\frac{\sigma^\circ_{\alpha_{0\ell}}}{57.3}\right)^2$$

$$=\left(\kappa_0\sigma_\kappa\right)^2 + \left(\frac{2\pi}{57.3}\kappa\frac{\sigma^\circ_{\alpha_{0\ell}}}{c_{\ell_i}}\right)^2 \qquad \text{for } a = 1.0 \text{ mean line}$$

The second term of Equation 3.3.1.4-6 is an order of magnitude larger than the first for the sections appropriate to marine application and the appearance of the section thickness ratio, in κ, and design lift coefficient divides the available sample into so many subclasses that statistical analysis is meaningless. The influence of the design lift coefficient in Equation 3.3.1.4-6 is evidenced by the increased scatter for small c_{ℓ_i}**'s** on Figures 3.3.1.4-1 through -5. For that reason the figures are repeated in absolute terms on Figures **3.3.1.4-7** through -11.

A statistical prediction error analysis based upon the same sub-classes employed in Section 3.3.1.3 is presented in Table 3.3.1.4-I. As indicated by Equation 3.3.1.4-6, any such analysis is very much a function of the data sample and two successively more restricted sub-sets of the total sample centered on the most used hydrofoil section are added to Table 3.3.1.4-I.

SUMMARY

The statistical analysis of Table 3.3.1.4-I may be summarized by:

$$c_{\ell_{i_{eff}}} = \left[2\pi \frac{\alpha_i}{c_{\ell_i}} \left(1-\kappa_0\right) + \kappa_0\right] \kappa \, c_{\ell_i} \pm \sigma \qquad 3.3.1.4\text{-}7$$

$$= \kappa_0 \, \kappa \, c_{\ell_i} \pm \sigma \quad \text{for } a = 1.0 \text{ mean line}$$

where: κ is from Equation 3.3.1.2-10

κ_0 is from Equation 3.3.1.3-2

$\sigma = 0.03$

LIMITATIONS

The limitations upon the prediction of the effective design lift coefficient are those associated with the prediction of the lift curve slope and zero lift angle, Sections 3.3.1.2 and .3.

HANDE

The HANDE lift curve slope and zero lift angle both differ in form from those of Equations 3.3.1.2-10 and 3.3.1.3-2 with HANDE generally presenting a more negative zero lift angle and a lower lift curve slope. The two effects tend to cancel at the ideal angle of attack so that the two effective design lift coefficients cannot be compared, even qualitatively, except for particular cases. Two such particular case comparisons are shown on Figure 3.3.1.4-12.

It should be noted that HANDE does not make the cavitation application of the design lift coefficient which therefore becomes only one point on the section lift curve.

REFERENCES

1. Lindsey, W. F.; Stevenson, D. B.; and Daley, B. N.: Aerodynamic Characteristics Of 24 NACA 16-Series Airfoils At Mach Numbers Between 0.3 and 0.8. NACA Technical Note 1546, September 1948.

2. Teeling, P.: Low Speed Wind Tunnel Tests Of A NACA 16-309 Airfoil With Trailing-Edge Flap, DeHavilland Aircraft of Canada Limited Report No. ECS 76-3, October 1976.

3. Abbott, I. H. and von Doenhoff, A. E.: Theory Of Wing Sections, Dover, 1959.

TABLE 3.3.1.4-I EFFECTIVE DESIGN LIFT COEFFICIENT – STATISTICAL ANALYSIS

SECTION	MEAN LINE	NUMBER IN SAMPLE N	(1) MEAN $\Delta c_{\ell_{i_{eff}}}$	$\Delta c_{\ell_{i_{eff}}}$ STD DEVIATION
16-SERIES	a = 1.0	SEE NOTE 2		
63-SERIES		16	0.003	0.042
64-SERIES		16	0.003	0.030
65-SERIES		16	–0.002	0.022
66-SERIES		8	0.004	0.039
4-DIGIT	64	13	0.004	0.020
5 DIGIT	230	5	–0.004	0.028
STANDARD SECTIONS		74	0.002	0.030
6XA SERIES				
63A SERIES	a = 1.0	1	–0.029	–
64A SERIES		4	–0.005	0.036
6XA SERIES		5	–0.010	0.033
6-SERIES, a < 1.0				
				–
65 SERIES	a = 0.5(5), 0.6, 0.8	7	4.002	0.027
66 SERIES	a ≈ 0.6	1	-0.037	–
6X-SERIES, a < 1.0 63 SERIES	a ≈ 0.3	9 1	-0.009 -0.030	0.027
TOTAL EXPERIENCE				
ALL SECTIONS		88	0	0.030
t/c = 0.06-0.12, c_{ℓ_i} = 0.2-0.6		29	0.001	0.030
t/c = 0.08-0.12, c_{ℓ_i} = 0.2-0.4		13	-0.011	0.023

NOTES: 1. $\Delta c_{\ell_{i_{eff}}}$ = MEASURED $c_{\ell_{i_{eff}}}$ - PREDICTED $c_{\ell_{i_{eff}}}$

2. NO APPROPRIATE DATA SAMPLE AVAILABLE.

1892-034B

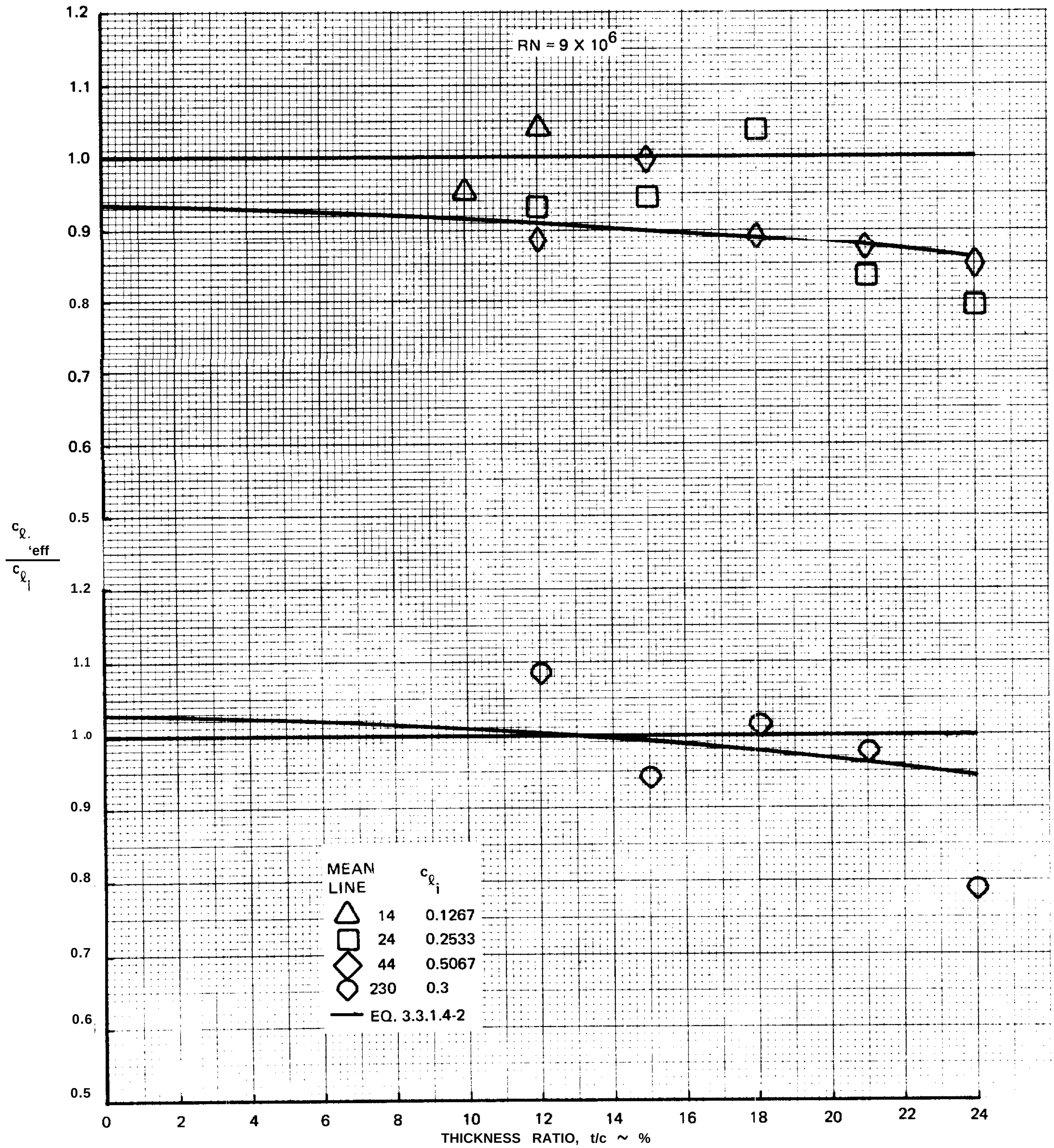

1892-035B

Fig. 3.3.1.4-1 Relative $c_{\ell_{i_{eff}}}$ vs Thickness Ratio, 4&5 Digit Sections

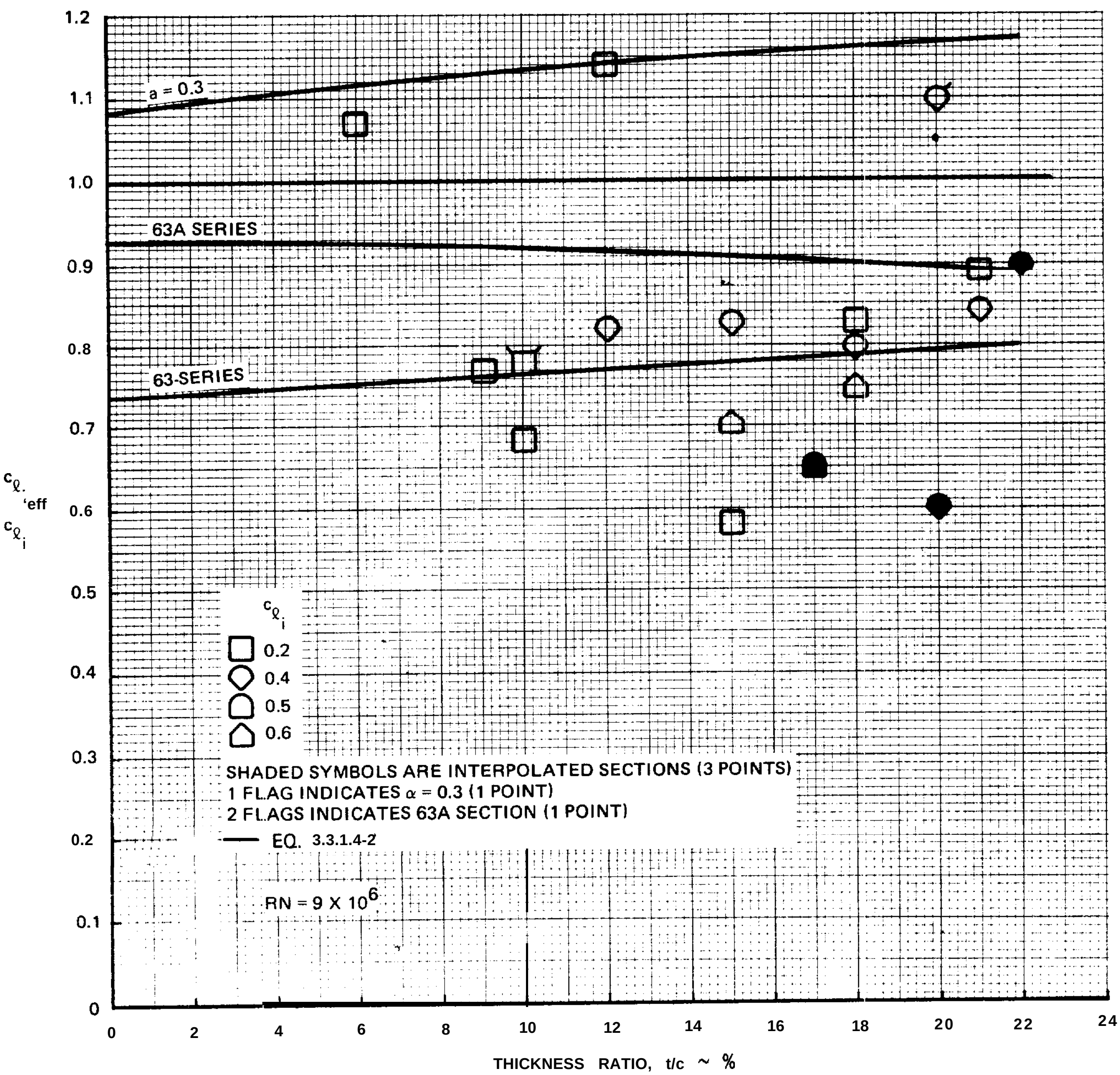

Fig. 3.3.1 A-2 Relative $c_{\ell_{eff}}$ vs Thickness Ratio, **63-Series** Sections

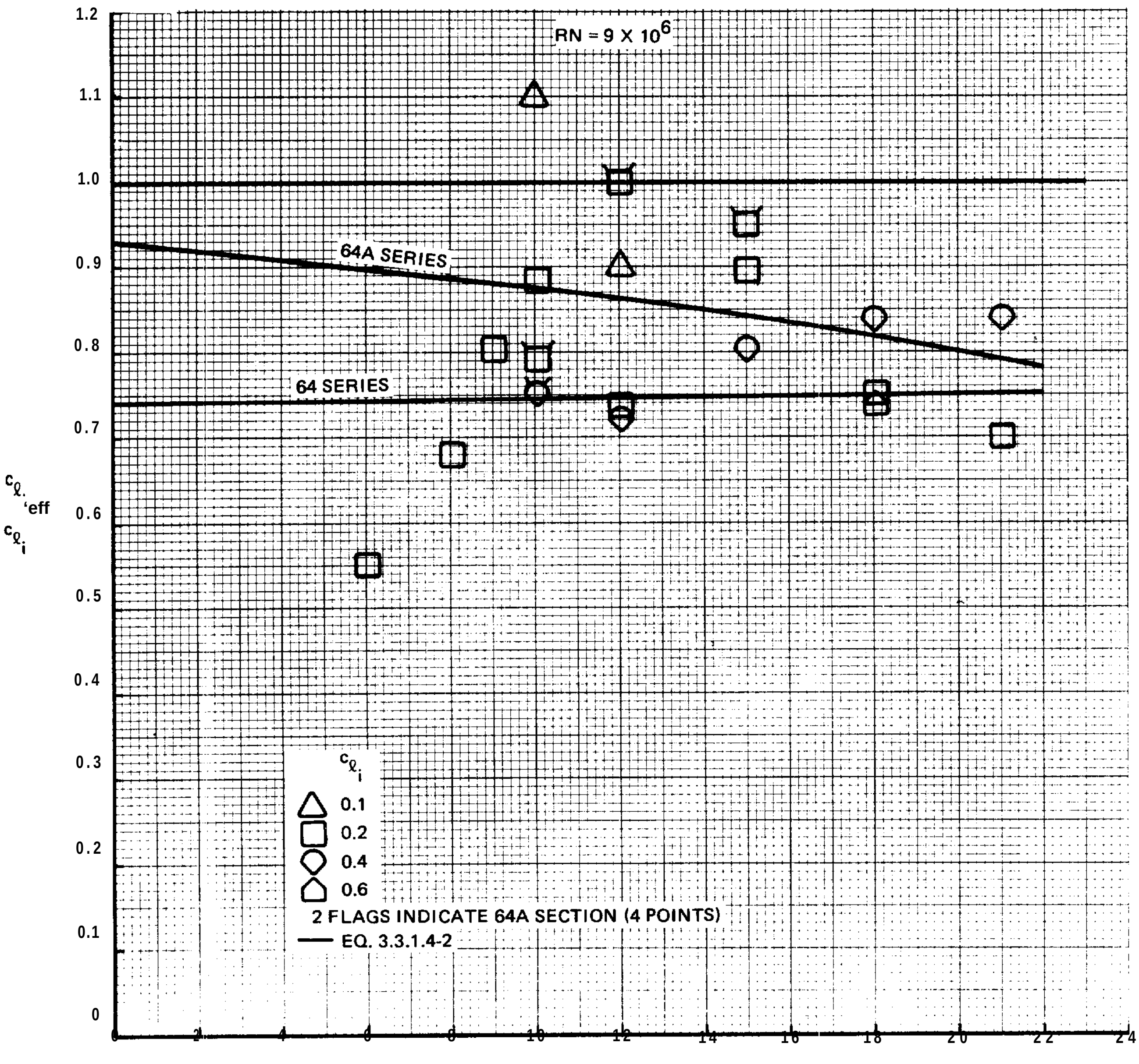

Fig. 3.3.1.4-3 Relative $c_{\ell_{i_{eff}}}$ vs Thickness Ratio, **64-Series** Sections

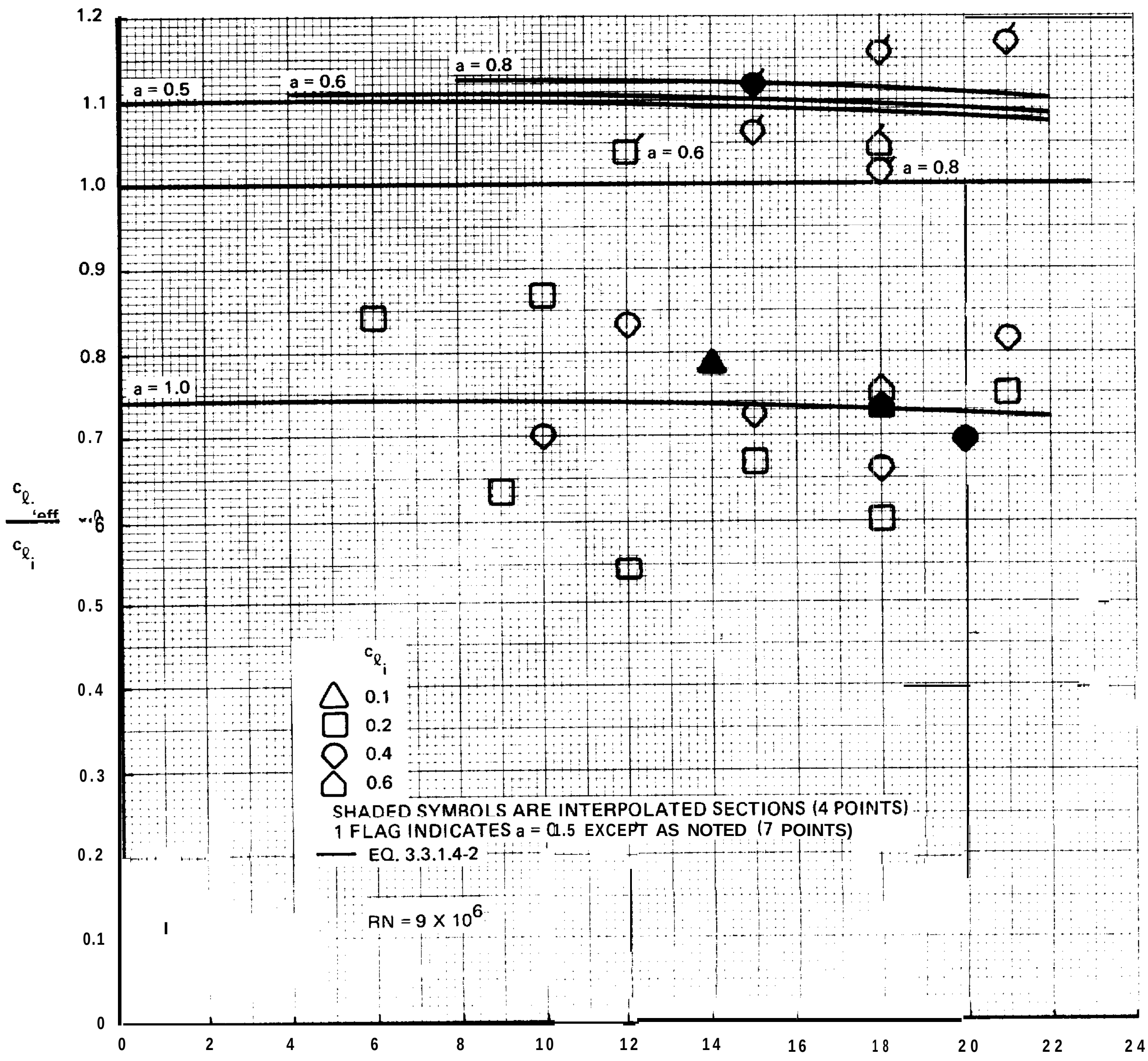

1892-038B

Fig. 3.3.1.4-4 Relative $c_{\ell_{i_{eff}}}$ vs Thickness Ratio, 65-Series Sections

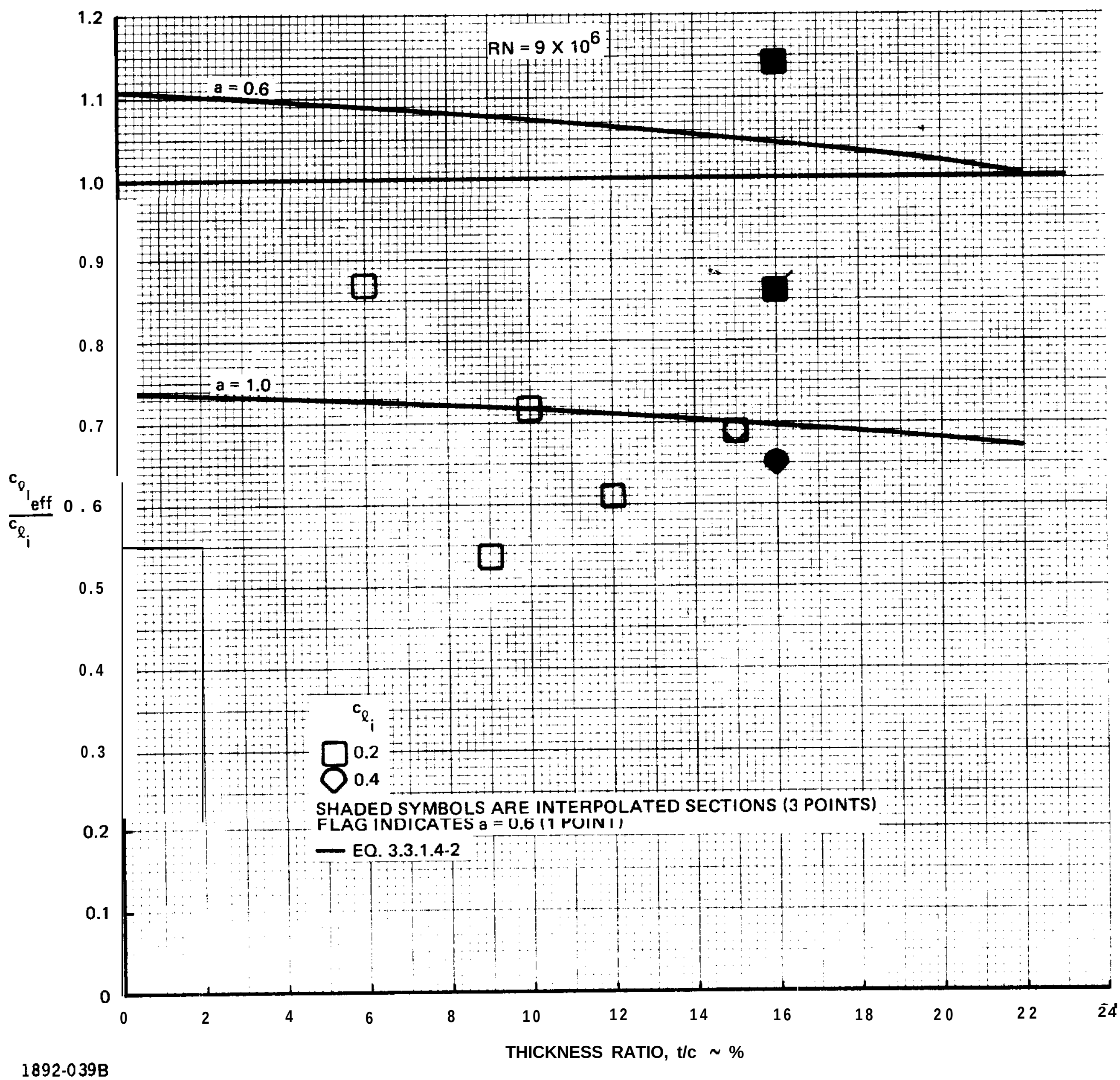

1892-039B

Fig. 3.3.1.4-5 Relative $c_{\ell_{i_{eff}}}$ vs Thickness Ratio, 66-Series Sections

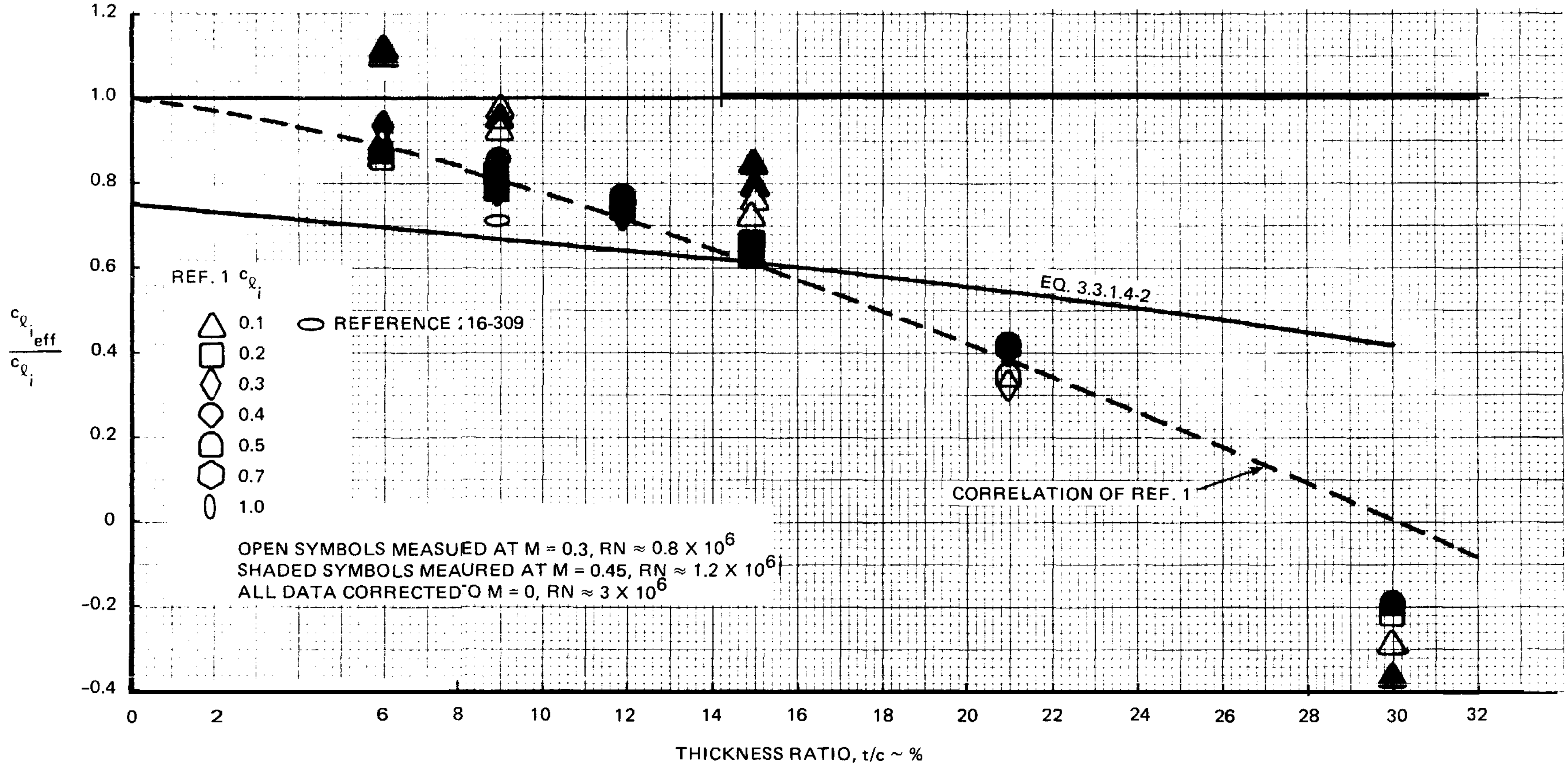

1892-040B

Fig. 3.3.1.4-6 $c_{\ell_{i_{eff}}}$ vs Thickness Ratio, 16-Series Sections

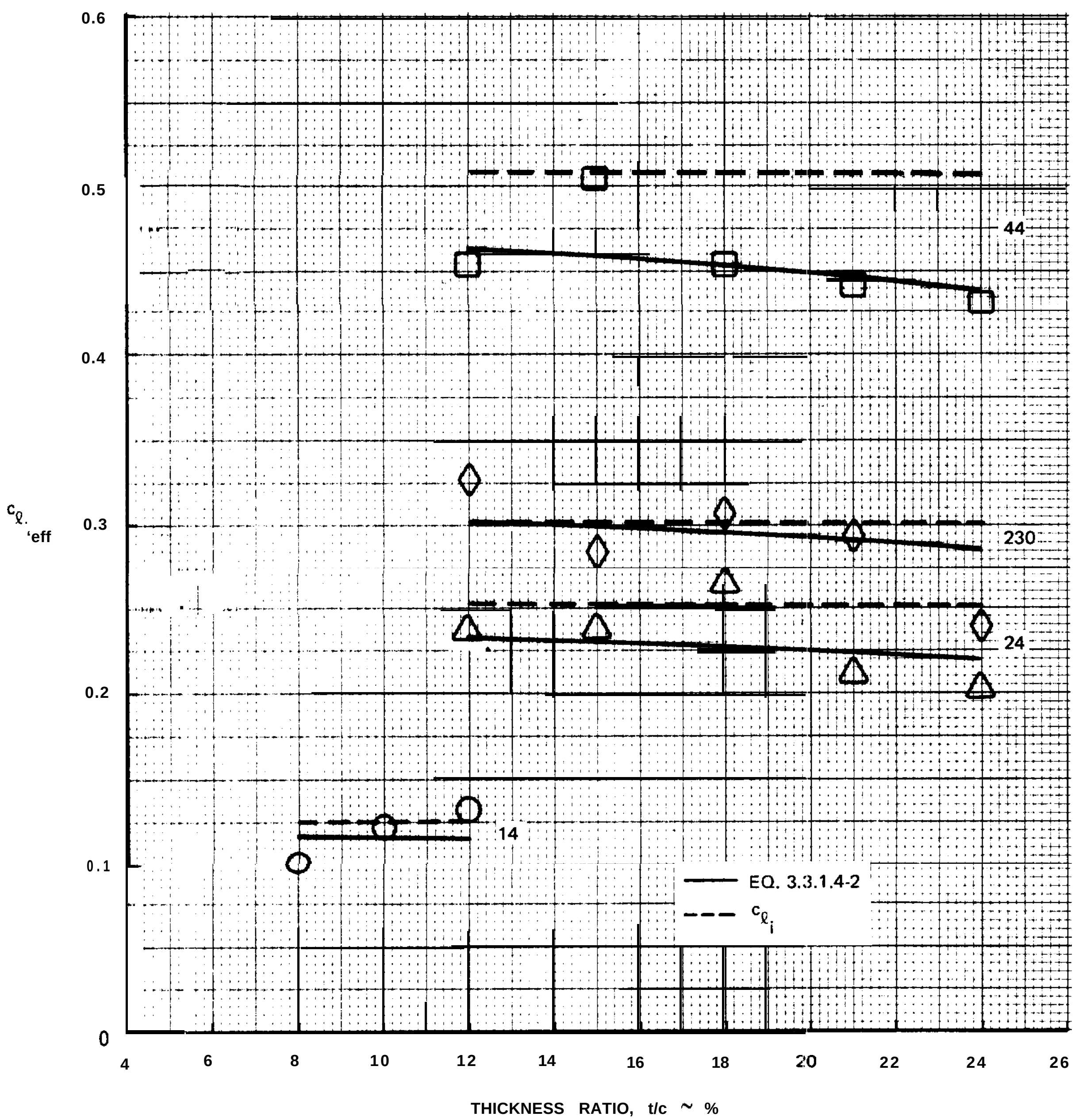

1892-041B

Fig. 3.3.1.4-7 $c_{\ell_{eff}}$ vs Thickness Ratio, 4&5 Digit Sections, RN = 9 X 10^6

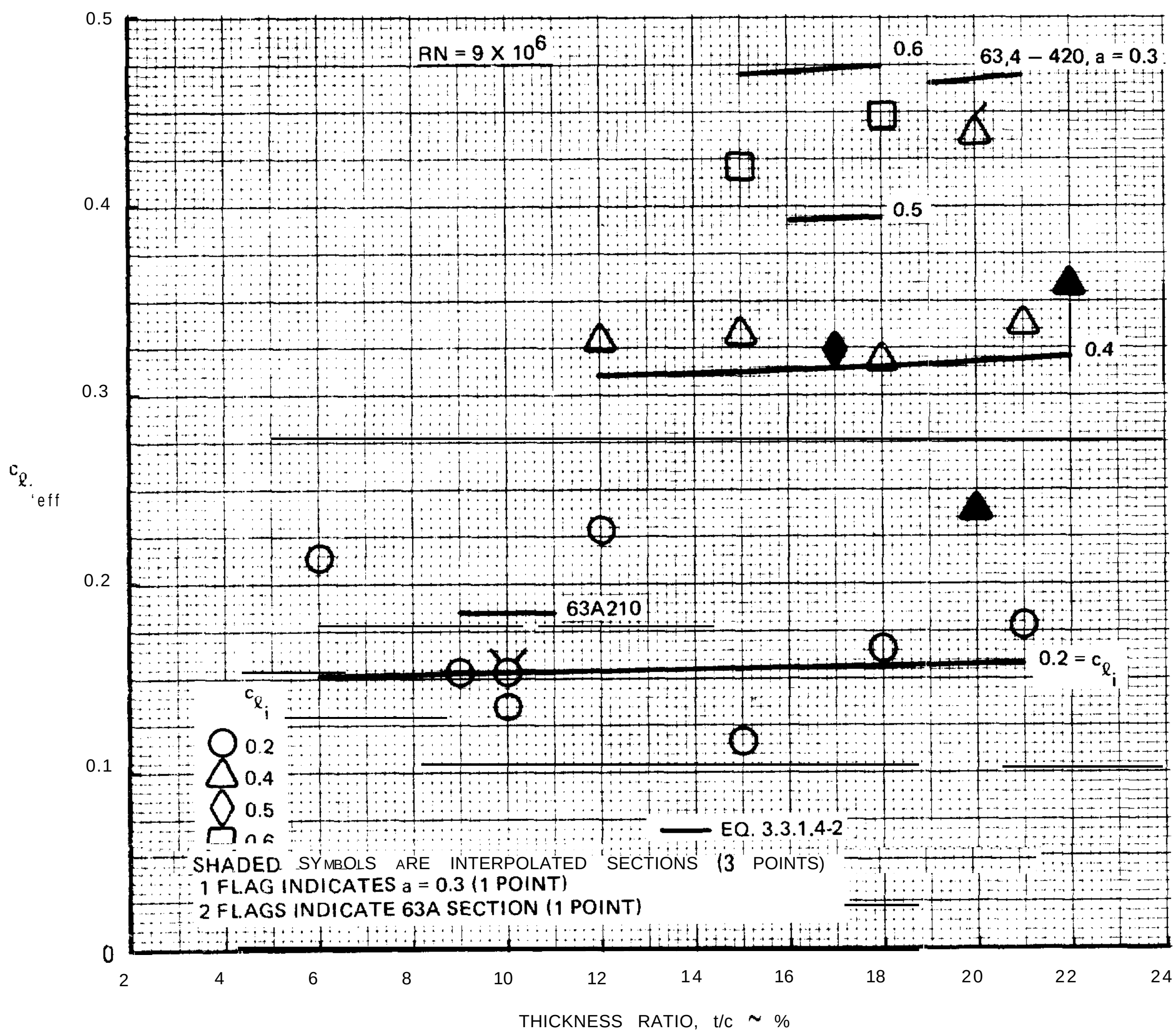

Fig. 3.3.1.4-8 $c_{\ell_{i_{eff}}}$ vs Thickness Ratio, 63-Series Sections

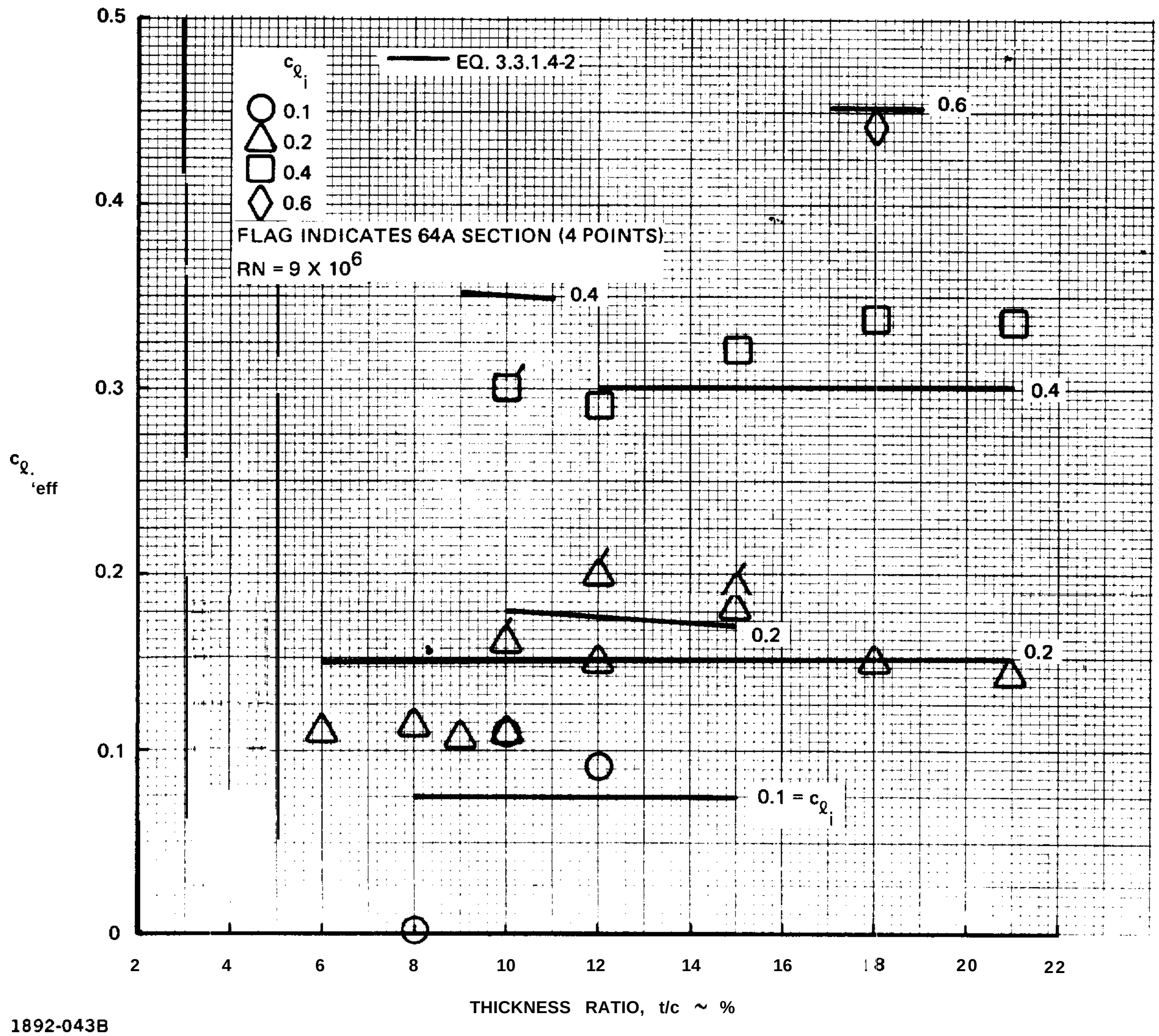

Fig. 3.3.1.4-9 $c_{\ell_{i_{eff}}}$ vs Thickness Ratio, **64-Series** Sections

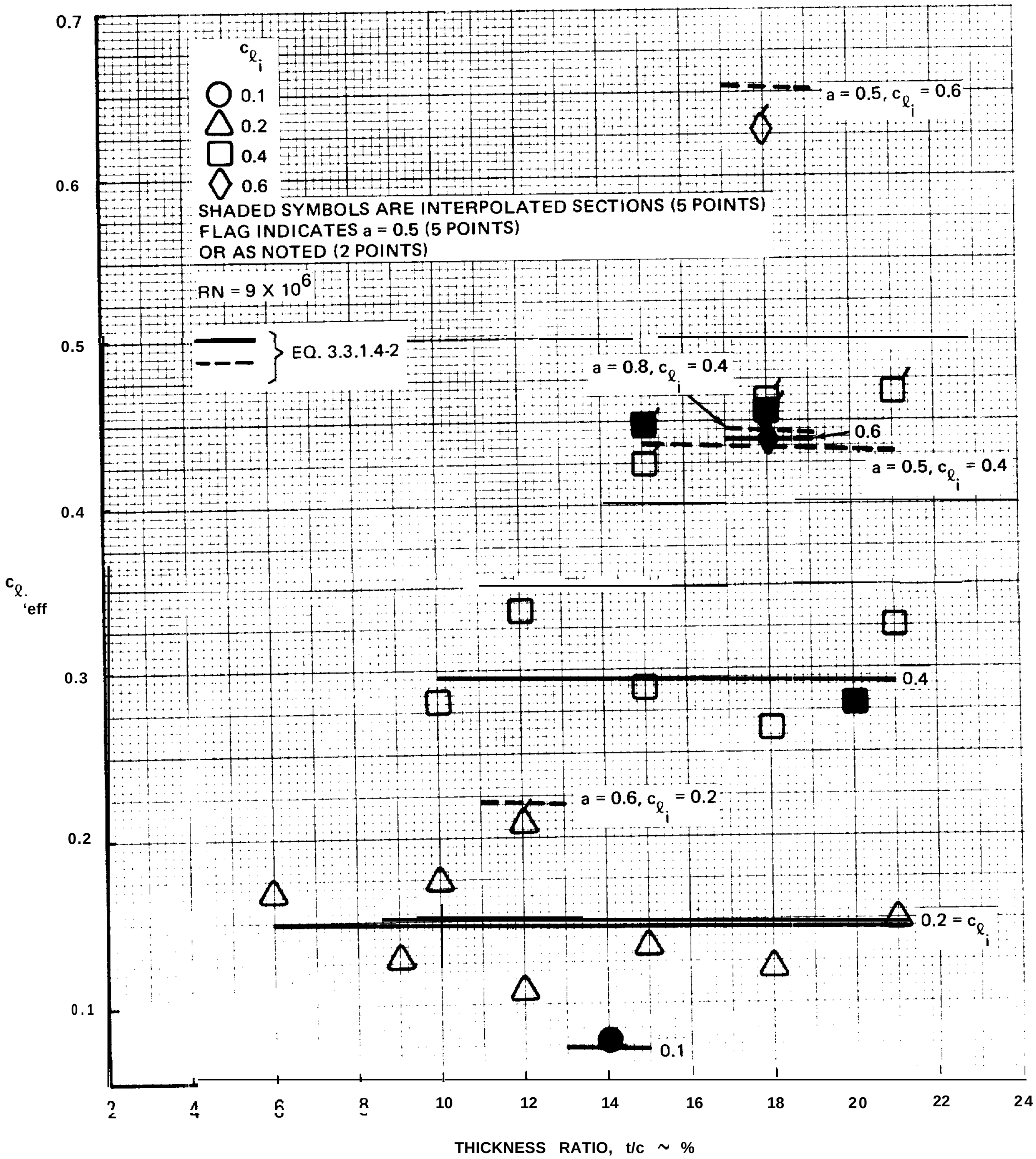

1892-044B

Fig. 3.3.1.4-10 $c_{\ell_{i_{eff}}}$ vs Thickness Ratio, 65-Series Sections

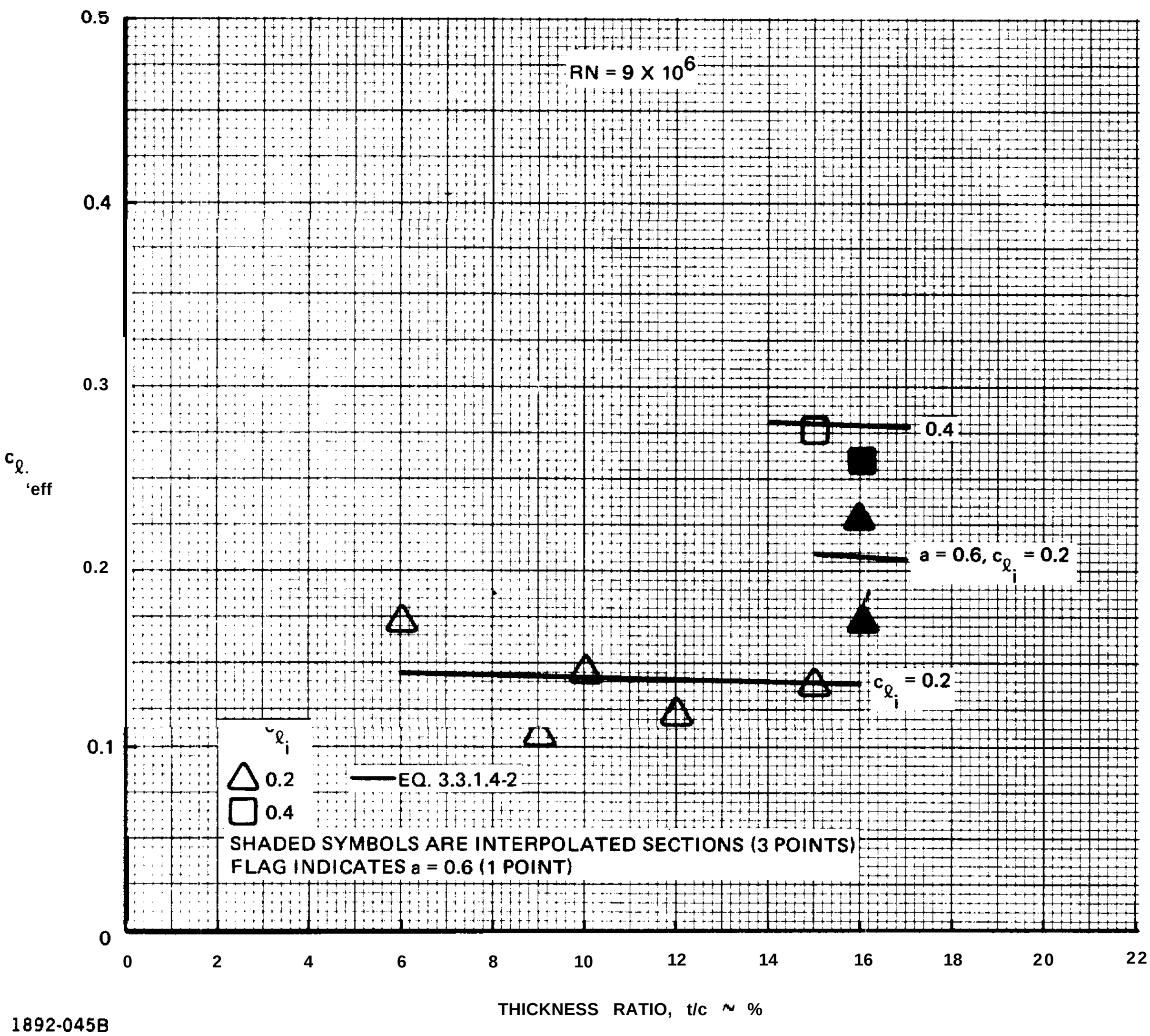

Fig. 3.3.1.4-11 $c_{\ell_{i_{eff}}}$ vs Thickness Ratio, 66-Series Sections

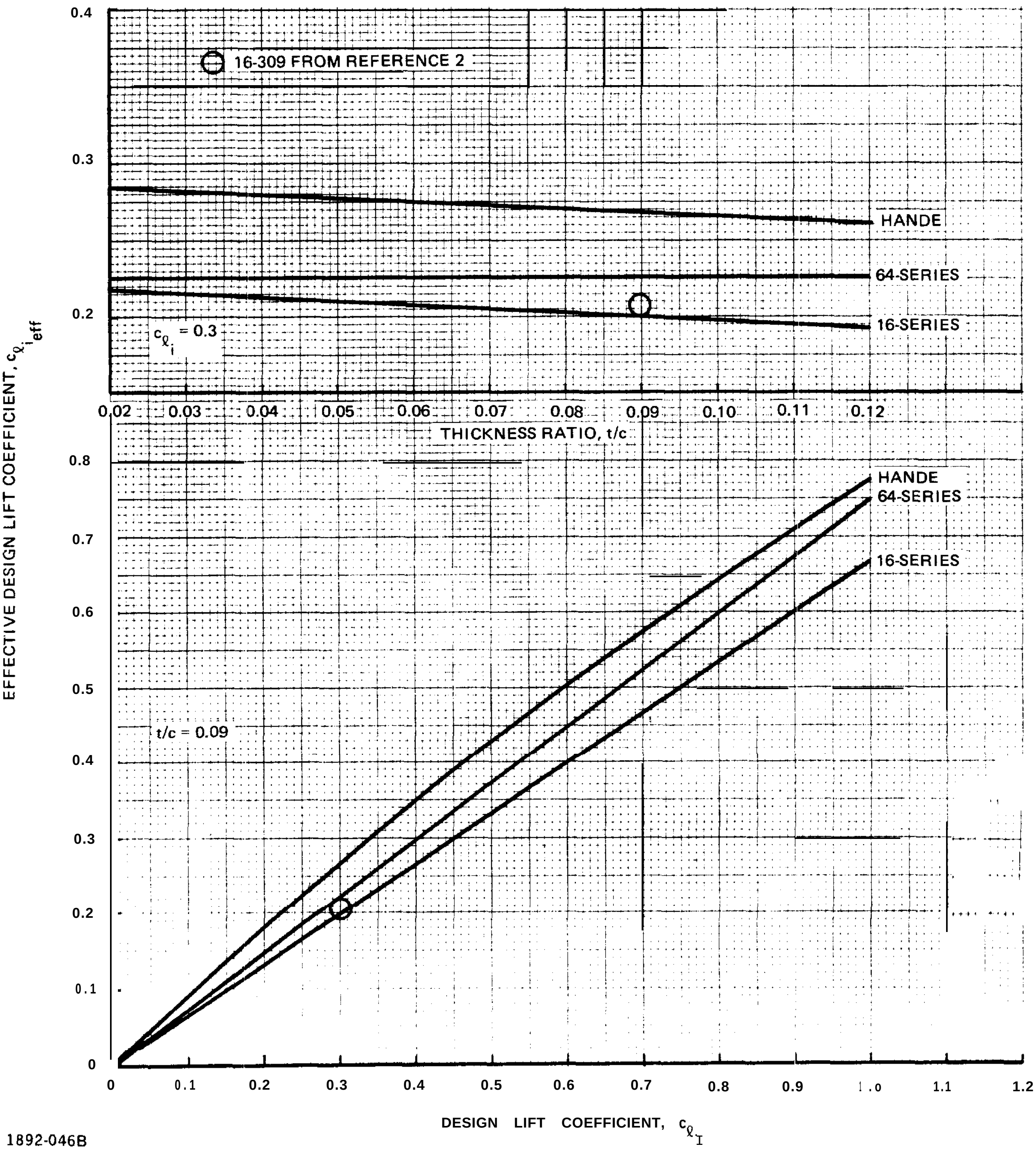

1892-046B

Fig. 3.3.1.4-12 HANDE Effective Design Lift Coefficient

3.3.1.5 Flap Effectiveness.

3.3.1.5.1 Trailing Edge Flap.

POTENTIAL FLAP EFFECTIVENESS

The flapped thin airfoil is classically considered, e.g. Reference 1, to be a cambered foil but the execution is quite laborious and Allen's expression for the results, Reference 2, is employed here to summarize those results.

Noting that Allen's θ and θ_0 are:

$$\theta = \cos^{-1}\left(1-2\,\frac{x}{c}\right)$$
$$\theta_0 = \cos^{-1}\left(1-2\,\frac{h}{c}\right) \qquad 3.3.1.5.1\text{-}1$$

deflection of the flap produces "additional" and "basic" increments of lift coefficient where the additional lift coefficient is given by Allen's Equation (A-15);

$$c_{\ell_{a_\delta}} = \frac{dc_{\ell_a}}{d\delta} = 2\left(\pi - \theta_0\right) \qquad 3.3.1.5.1\text{-}2$$

$$= 2\ \cos^{-1}\left(2\frac{h}{c}-1\right)$$

The basic lift coefficient is given by Allen's Equation (A-16):

$$c_{\ell_{b_\delta}} = \frac{dc_{\ell_b}}{d\delta} = 2\sin\theta_0 \qquad 3.3.1.5.1\text{-}3$$

$$= 4\sqrt{\frac{h}{c}\left(1-\frac{h}{c}\right)}$$

The total incremental lift due to the flap is:

$$c_{\ell_\delta} = c_{\ell_{a_\delta}} + c_{\ell_{b_\delta}} \qquad 3.3.1.5.1\text{-}4$$

$$= 2\cos^{-1}\left(2\frac{h}{c}-1\right) + 4\sqrt{\frac{h}{c}\left(1-\frac{h}{c}\right)}$$

and the flap effectiveness is:

$$\frac{d\alpha}{d\delta} = \frac{c_{\ell_\delta}}{c_{\ell_\alpha}} = \frac{c_{\ell_\delta}}{2\pi} \qquad 3.3.1.5.1\text{-}5$$

$$= \frac{1}{\pi}\cos^{-1}\left(2\frac{h}{c}-1\right) + \frac{2}{\pi}\sqrt{\frac{h}{c}\left(1-\frac{h}{c}\right)}$$

$$= \frac{T_{10}}{\pi}$$

where the identification with Theodorsen's coefficient is made by substituting $2h/c-1$ for Theodorsen's C in the definition for T_{10} in Reference 3. Equation 3.3.1.5.1-5 is presented in Table 3.3.1.5.1-I and on Figure 3.3.1.5.1-1.

DATCOM Figure 6.1.1.1-7a presents the potential thick airfoil flap effectiveness:

$$\left(\frac{d\alpha}{d\delta}\right)_{\text{thick airfoil}} = c_{\ell_\delta \text{ thick airfoil}} \Big/ c_{\ell_\alpha \text{ thick airfoil}} \qquad 3.3.1.5.1\text{-}6$$

The DATCOM theoretical c_{ℓ_δ} for zero thickness is the flap effectiveness of Equation 3.3.1.5.1-5. It is not known whether the finite thickness theoretical c_{ℓ_δ}'s of DATCOM Figure 6.1.1.1-7a are potential theory or emperical interpretations. When the 15% t/c theoretical c_{ℓ_δ} of the figure is compared with Equation 3.3.1.2-3 the result compares with Equation 3.3.1.5.1-5 as shown on Figure 3.3.1.5.1-1; i.e. DATCOM Figure 6.1.1.1-7a indicates that the potential flap effectiveness is essentially independent of thickness.

VISCOUS FLAP EFFECTIVENESS

The classic viscous flap effectiveness is that of Reference 4, more readily available as Figure 18 of Reference 5 which is presented here in Table 3.3.1.5.1-I and on Figure 3.3.1.5.1-3.

DATCOM Figure 6.1.1.1-7b gives the experimental flap effectiveness:

$$\frac{c_{\ell_\delta} \big/ c_{\ell_{\delta \text{ theory}}}}{c_{\ell_\alpha} \big/ c_{\ell_{\alpha \text{ theory}}}} = \frac{c_{\ell_\delta} / c_{\ell_\alpha}}{c_{\ell_{\delta \text{ theory}}} \big/ c_{\ell_{\alpha \text{ theory}}}} = \frac{d\alpha/d\delta}{(d\alpha/d\delta)_{\text{theory}}} \qquad 3.3.1.5.1\text{-}7$$

where only particular cases can be compared with Toll. The most extreme flap effectiveness presented in the DATCOM, $c_{\ell_\alpha}/c_{\ell_{\alpha \text{ theory}}} = .7$, is compared with that of Toll and with thin airfoil theory on Figure 3.3.1.5.1-1. The DATCOM extreme flap chord ratios are compared with Toll and with thin airfoil theory on Figure 3.3.1.5.1-2. It must be noted that the ratio presentation of Figure 3.3.1.5.1-2 exaggerates the small flap chord case where an incremental flap effectiveness might be more suitable.

Note that Tolls Figure 19 also provides a viscous c_{ℓ_α} dependency for flap effectiveness in the form of a trailing edge angle dependency.

EXPERIENCE

Measurement of flap effectiveness requires one to two orders of magnitude more effort than the measurement of pitch characteristics and model experience is limited. Toll, DATCOM, and ESDU (which is identical with DATCOM for this characteristic) present aerodynamic "practice" based upon relatively ill-defined experience and heavily dependent upon model tests for new prototypes. Such model tests are not dependable for hydrodynamic applications until Reynolds Number effects are better established and section flap effectiveness measurements are still of important significance to hydrodynamics. Three recent definitive measurements of flap effectiveness are particularly significant though one, a GALCIT 16-309 section experiment, is not yet available for review.

Figure 3.3.1.5-4 presents a summary of the GALCIT lift measurements on a flapped 64A309 section. The predicted and measured lift curve for this section were:

Predicted: $c_{\ell_{RN}} = .2584 + .1016\,(\alpha^\circ + .535\ 6")$ 3.3.1.5.1-8

Measured: $c_{\ell_{RN}} = .2368 + .1057\,(\alpha^\circ + .5515\,\delta^\circ)$

The measured lift curve slope is 4% high and the measured zero lift angle is .3° less negative than predicted; both variances are just within the nominal ranges, 5% and 1/3 degree. The measured flap effectiveness is 3% higher than predicted.

Figure 3.3.1.5-5 presents a transformation of the figure of Page 13, Section 4 of Reference 6. This figure summarizes DeHavilland's measure of the flap effectiveness for a 16-309 section but without application of the guidance Reference 6 provides for Reynolds Number effect.

The predicted and measured lift curves of Figure 3.3.1.5-5 are:

Predicted: $c_\ell = .1996 + .09862\,(a" + .535\,\delta^\circ)$ 3.3.1.5.1-9

Measured: $c_\ell = .2470 + .09049\,(\alpha^\circ + .5912\ 6")$

This result is less conclusive. The measured lift curve slope is 8.25% low and the measured zero lift angle is .7 degree more negative than predicted. Both variances are more than nominal. The zero lift angle variance is characteristic of excessive laminar flow. The reduced lift curve slope might be explained by a reduction in the extent of that laminar flow with increasing pitch angle and would tend to increase the apparent flap effectiveness. The measured flap effectiveness is 10.5% higher than predicted.

A possible distinction between flap effectiveness and section stall should be noted on Figures 3.3.1.5-4 and, particularly, -5. The 16-309 section flap was fully effective at the 15 degree deflection at a c_ℓ of .68 but the 6 degree deflection may be weakened at a c_ℓ of 1.05. Extending the pitch range of future tests should clarify this point.

ESDU Controls 01.01.02 estimates the accuracy for flap effectiveness to be ±10%.

SUMMARY

For hydrodynamic application the experience of this section can be summarized by Toll's flap effectivenesses of Figure 3.3.1.5-3 and Table 3.3.1.5-I with a nominal accuracy of ±10%.

HANDE

HANDE does not consider flap effectiveness. $C_{L_\delta}/C_{L_\alpha}$ is emperically derived directly from an unspecified three dimensional data sample and $d\alpha/d\delta$ cannot be distinguished in the result of HANDE Section 8.2.2.8.

REFERENCES

1. Pope, Alan: Basic Wing And Airfoil Theory, McGraw-Hill, 1951.
2. Allen, H. Julian: Calculation Of The Chordwise Load Distribution Over Airfoil Sections With Plain, Split, Or Serially Hinged Trailing Edge Flaps, NACA Report No. 634, 1938.
3. Theodorsen, T.: General Theory Of Aerodynamic Instability And The Mechanism Of Flutter, NACA Report No. 496, 1935. Currently found in AIAA Selected Reprints, "Aerodynamic Flutter", edited by I. E. Garrick, 1969.
4. Swanson, Robert S. and Crandall, Stewart M.: Analysis Of Available Data on the Effectiveness of Ailerons without Exposed Overhang Balance. NACA ACR No. L4E01, 1944.
5. Toll, Thomas A.: Summary of Lateral-Control Research. NACA Report 868, 1947.
6. Teeling, P.: Low Speed Wind Tunnel Tests Of A NACA 16-309 Airfoil With Trailing Edge Flap, DeHavilland Aircraft of Canada Limited Report No. ECS 76-3, October 1976.
7. Baloga, Paul: Water Tunnel Tests Of The NACA 64A-309 Foil Section Fitted With An Adjustable Flap In Fully-Wetted And Cavitating Flows, Graduate Aeronautical Laboratories California Institute of Technology Report HSWT 1131, August 1979.

TABLE 3.3.1.5-1 FLAP EFFECTIVENESS, $d\alpha/d\delta$

FLAP CHORD RATIO, c_f/c	THIN AIRFOIL POTENTIAL THEORY	δ = -10° TO 10° SEALED GAP	δ = 0 TO 20° SEALED GAP	δ = -10° TO 10° OPEN GAP
0	0	0	0	0
0.05	0.2823	0.175	0.130	0.115
0.10	0.3958	0.300	0.245	0.225
0.15	0.4805	0.395	0.345	0.325
0.20	0.5498	0.470	0.430	0.405
0.25	0.6090	0.535	0.500	0.470
0.30	0.6607	0.590	0.570	0.525
0.40	0.7478			
0.50	0.8183			
0.60	0.8760			
0.70	0.9227			
0.75	0.9423			
0.80	0.9595			
0.85	0.9741			
0.90	0.9861			
0.95	0.9952			
1.00	1			

1892-047B

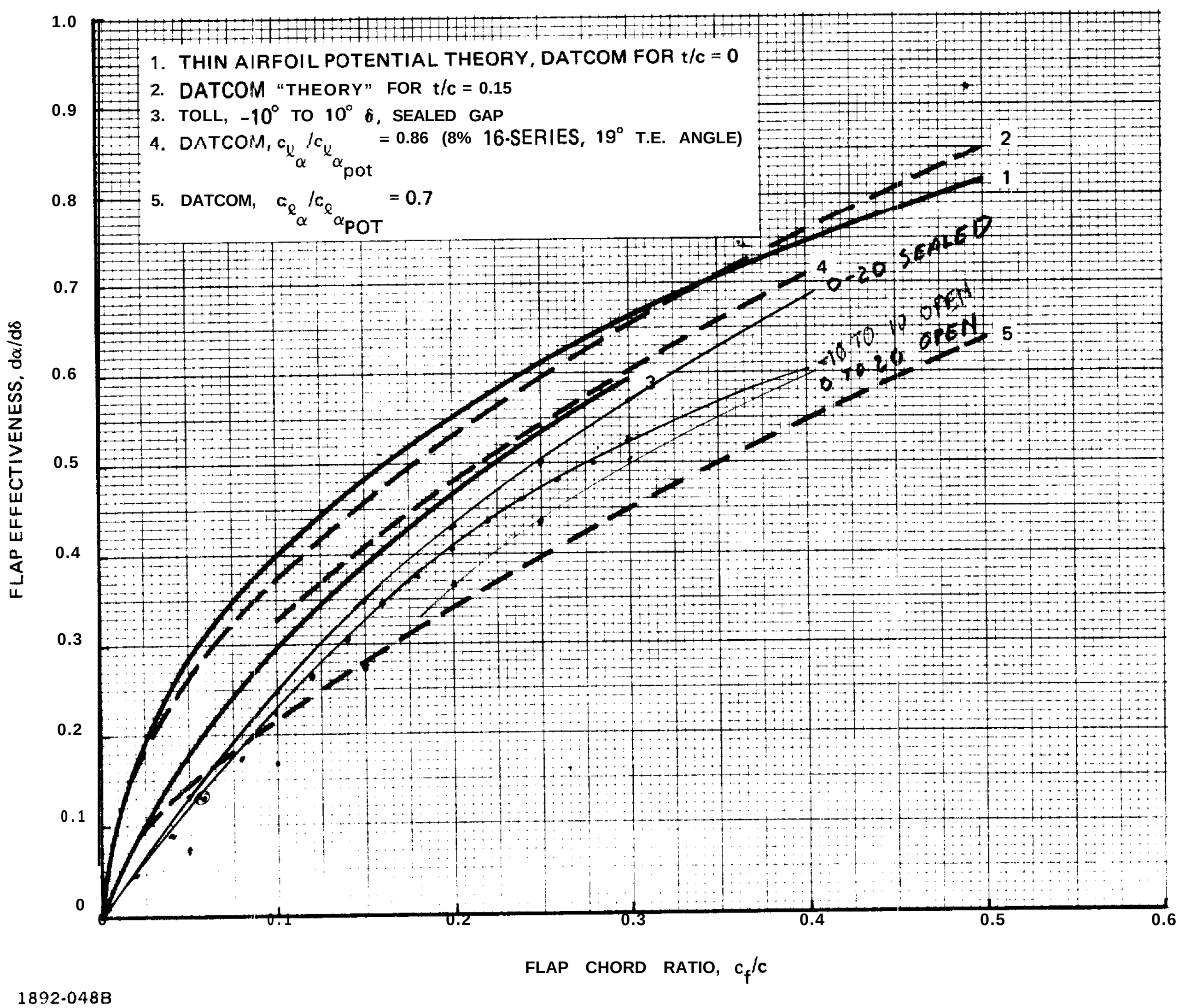

Fig. 3.3.1.5-1 DATCOM Flap Effectiveness

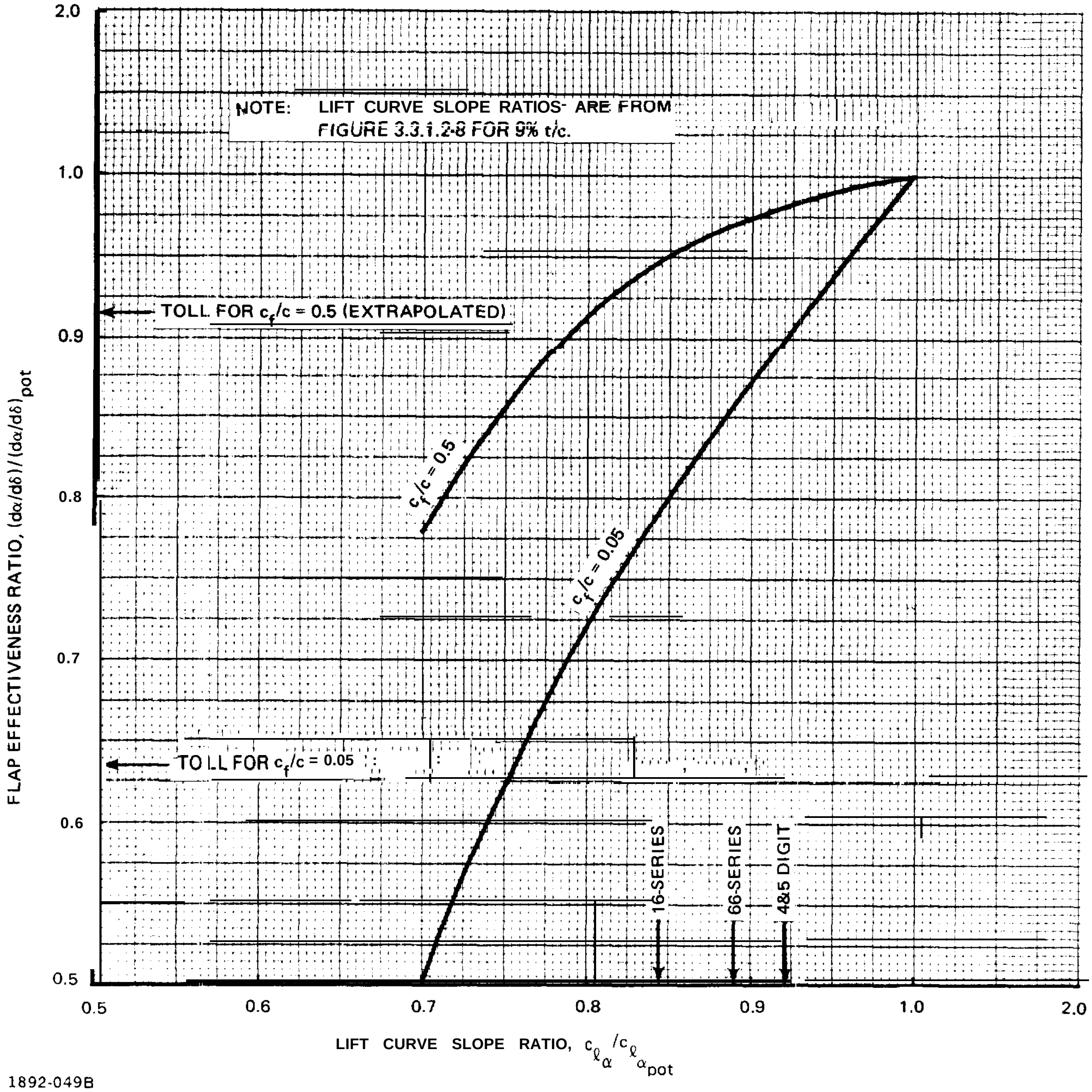

Fig. 3.3.1.5-2 DATCOM Flap Effectiveness, Extreme Flap Chord Ratio

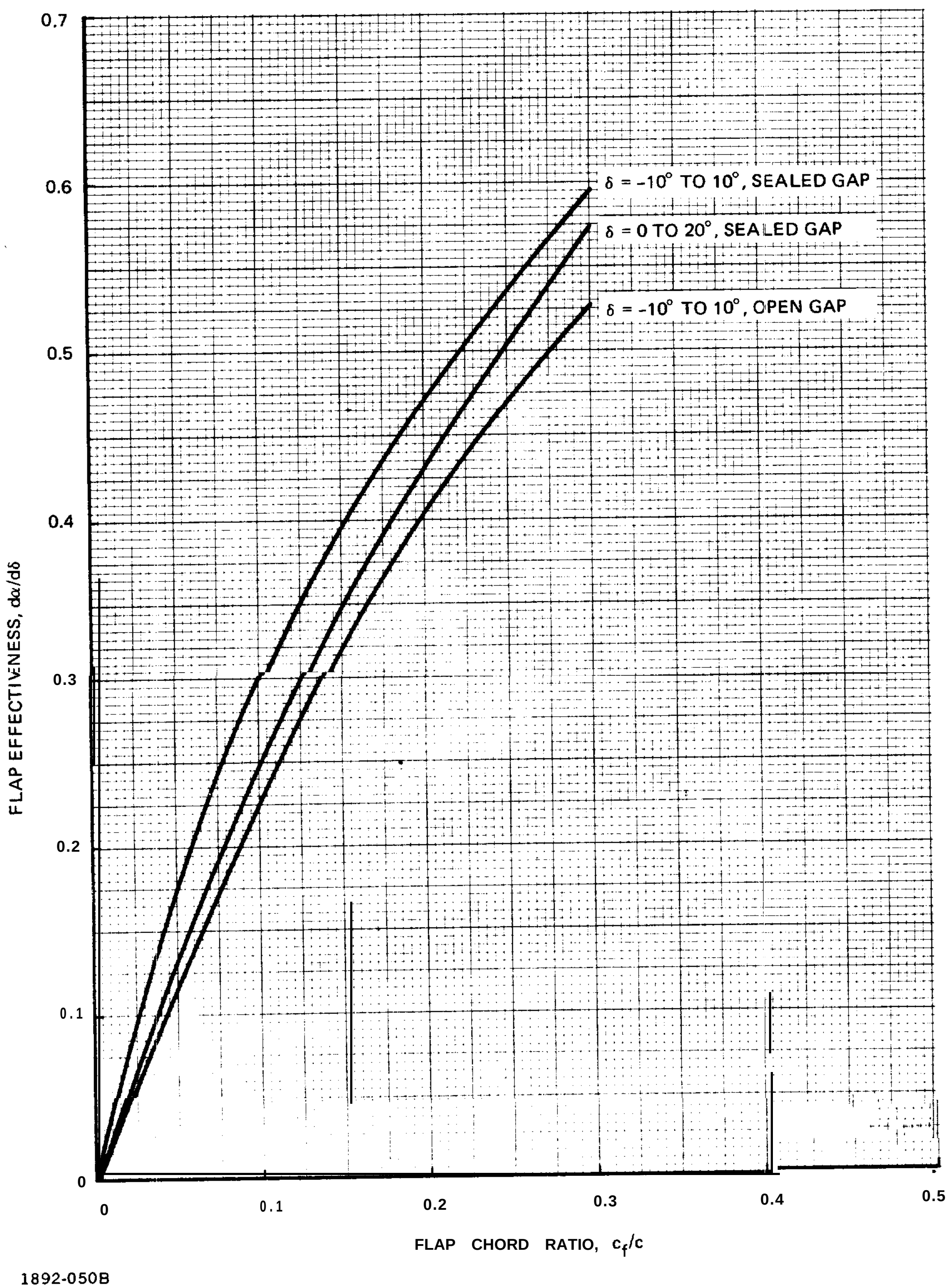

Fig. 3.3.1.5-3 Toll Flap Effectiveness

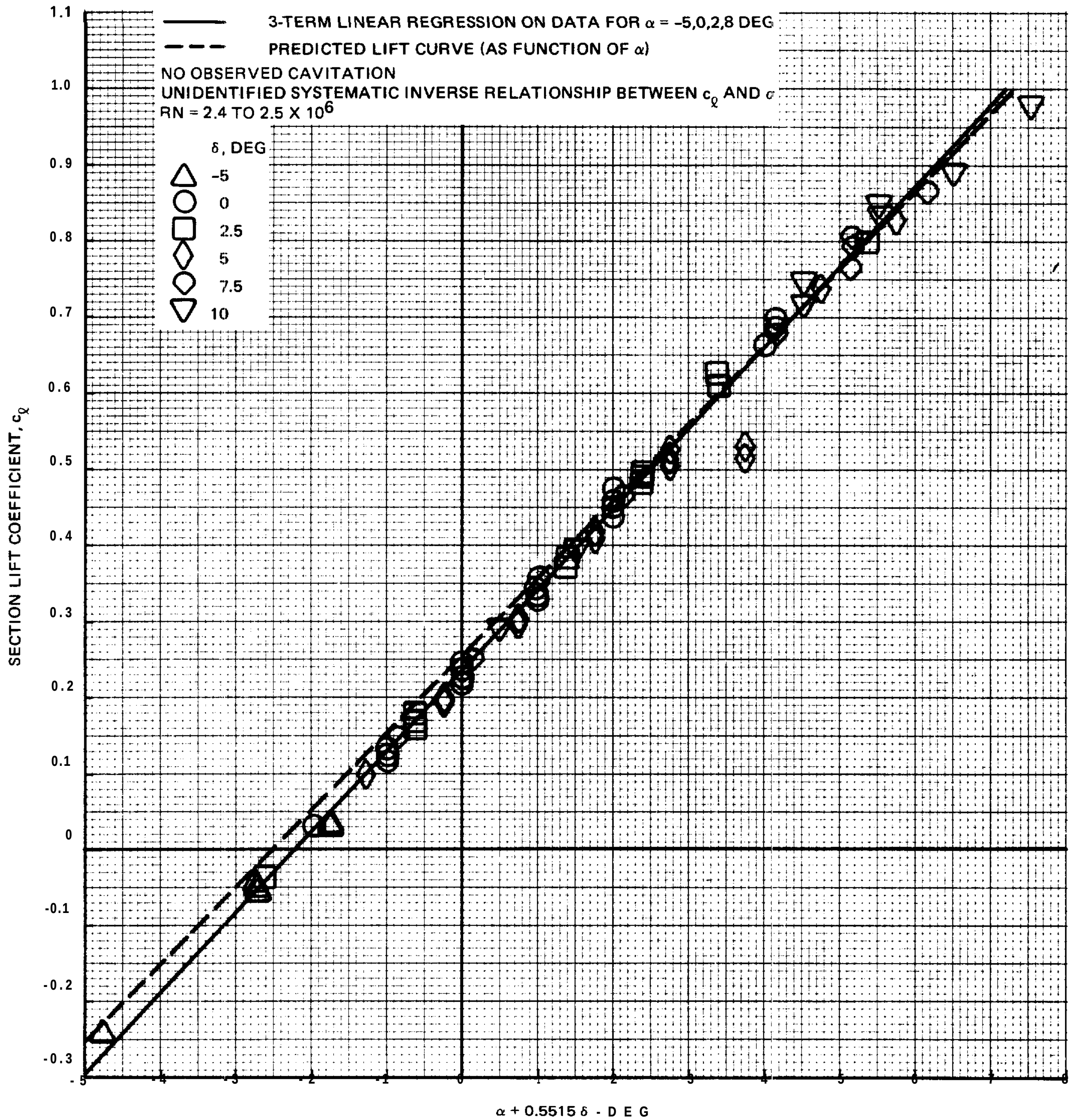

1892-051B

Fig. 3.3.1.5-4 Measured Hydrodynamic Lift Curve, Reference 7

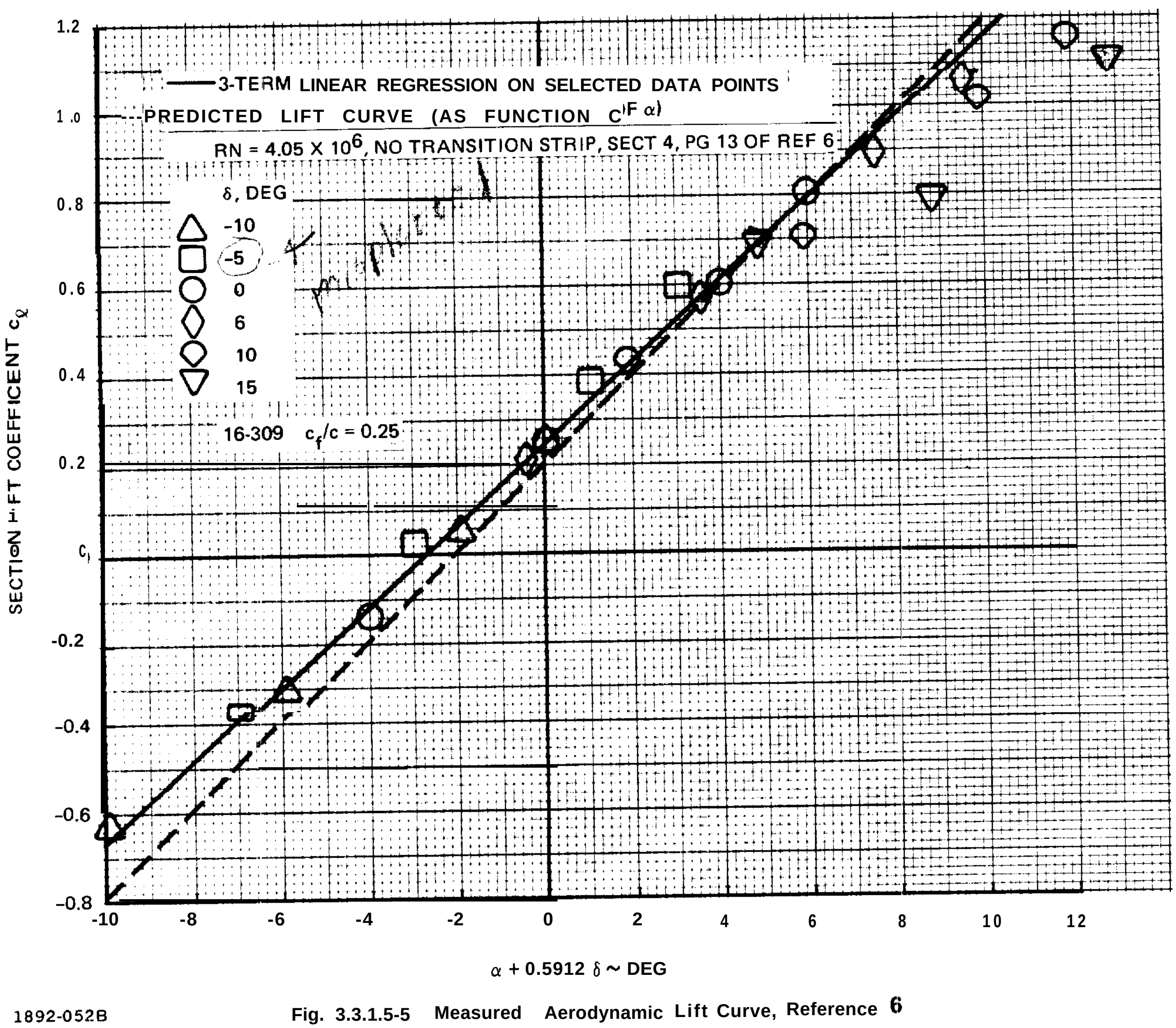

1892-052B

Fig. 3.3.1.5-5 Measured Aerodynamic Lift Curve, Reference 6

3.3.1.6 Section Lift Curve. It is convenient to express the section lift curve in the form:

$$c_\ell = c_{\ell_0} + c_{\ell_\alpha}\left(\alpha + \frac{d\alpha}{d\delta}\,\delta\right) \qquad 3.3.1.6\text{-}1$$

where: $c_{\ell_0} = c_{\ell_{i_{eff}}}$ for a = 1.0 mean line

$\alpha + \frac{d\alpha}{d\delta}\,\delta$ is a parametric angle of attack convenient to the study of experimental data.

3.3.2 Section Lift Distribution.

3.3.2.1 Additional Lift Distribution.

GENE&AL

The chordwise lift distribution for the thin flat plate airfoil is classic as given for example by Pope in Equation (7.48) and as the theoretical Pa_1 of Table 7.4 of Reference 1. That distribution is defined by:

$$\frac{c_{\ell_x}}{c_\ell} = \frac{2}{A}\sqrt{\frac{1-\frac{x}{c}}{x/c}} \qquad 3.3.2.1\text{-}1$$

which is shown on Figure 3.3.2.1-1.

Thick airfoil lift distribution is also classic, e.g. References 1 and 2, but not explicitly expressible and therefore not related to the thin airfoil lift distribution in any useful analytic manner. For the sections of Appendix I of Reference 2 the thick airfoil potential additional lift distribution is available as:

$$\frac{c_{\ell_x}}{c_\ell} = 4\frac{v}{V}\frac{\Delta v_a}{V} \qquad 3.3.2.1\text{-}2$$

and the distributions for-three very thick examples are compared with the thin airfoil distribution on Figure 3.3.2.1-1. The lift distribution in the vicinity of the flap has particular hydrodynamic interest. For typical hydrofoil thickness ratios the thickness effect on the potential additional lift distribution is small, as illustrated on Figure 3.3.2.1-2.

The viscous effect upon the additional lift distribution is largely accounted for simply by employing the viscous, rather than the potential, lift coefficient; what is not accounted for is a redistribution of lift which produces a shift in the section aerodynamic center.

AERODYNAMIC CENTER

The thick airfoil potential aerodynamic center is given by:

$$\text{a.c.} = \int_0^1 \frac{x}{c}\frac{c_{\ell_x}}{c_\ell}\, d\frac{x}{c} \approx 4\int_0^1 \frac{x}{c}\frac{v}{V}\frac{\Delta v_a}{V}\, d\frac{x}{c} \qquad 3.3.2.1\text{-}3$$

where the terms are numerically available in Reference 2 for the sections of that reference.

The potential moment distributions and aerodynamic centers for the 16-series section are shown on Figure 3.3.2.1-3 and the aerodynamic center variation with thickness ratio for the 4- and 5-digit, 16-series, and 66-series sections are shown on Figure 3.3.2.1-4.

The experimental aerodynamic centers of Reference 2 are presented here on Figures 3.3.2.1-5 thru -9. Figures 3.3.2.1-5 and -6 are taken directly from Figure 94 of Reference 2. Figures 3.3.2.1-7, -8, and -9 were taken from Appendix IV of that reference to provide more detail on Reynolds Number. The faired curves of Figures 3.3.2.1-5 thru -8 are compared on -9. No aerodynamic center measurements at Reynolds Numbers higher than those of Reference 2 can be offered here. The moment curves of Reference 2 display no drag bucket effect on the moment and no obvious systematic Reynolds Number effect is displayed in the moments of Reference 3.

Figure 3.3.2.1-10 presents the aerodynamic centers of Reference 4, derived from the slope of the $c_{m_{c/4}}$ vs. c_ℓ curves of that reference and the relationship:

$$\text{a.c.} = \frac{1}{4} - \frac{d\,c_{m_{c/4}}}{d\,c_\ell} \qquad \textbf{3.3.2.1-4}$$

The test conditions for Reference 4 were inappropriate for hydrodynamic application and the only independent measurement of the 16-series section that can be offered here is that of Page 4 of Section 7.2.4 of Reference 5 which is shown on Figure 3.3.2.1-10. It should be noted that that data, without transition strip, displays a substantial transition movement effect on the moment.

It is the difference between the potential aerodynamic centers of Figure 8.3.2.1-4 and the viscous aerodynamic centers of Figure 3.3.2.1-10, a chordwise lift redistribution, which is not accounted for by simply reducing the potential additional lift by the viscous effect on the lift curve slope.

It will be noted that Figures 3.3.2.1-4 and 3.3.2.1-10 do not define the viscous aerodynamic center shift for 63-, 64-, 65-, or 6 xA sections or for any section on an a $<$ 1.0 mean line though some of that information is available in Reference 2.

REFERENCES

1. Pope, Alan: Basic Wing and Airfoil Theory. McGraw-Hill, 1951.

2. Abbott, Ira H. and von Doenhoff, Albert E.: Theory of Wing Sections, Dover, 1959.

3. Loftin, Laurence K., Jr. and Smith, Hamilton A.: Aerodynamic Characteristics Of 15 NACA Airfoil Sections At Seven Reynolds Numbers From 0.7 x 10^6 To 9.0 x 10^6. NACA Technical Note 1945, October 1949.

4. Lindsey, W.F.; Stevenson D.B.; and Daley, B.N.: Aerodynamic Characteristics Of 24 NACA 16-Series Airfoils At Mach Numbers Between 0.3 and 0.8. NACA Technical Note 1546, September 1948.

5. Teeling, P.: Low Speed Wind Tunnel Tests Of A NACA 16-309 Airfoil With Trailing Edge Flap, DeHavilland Aircraft of Canada Limited Report No. ECS 76-3, October 1976.

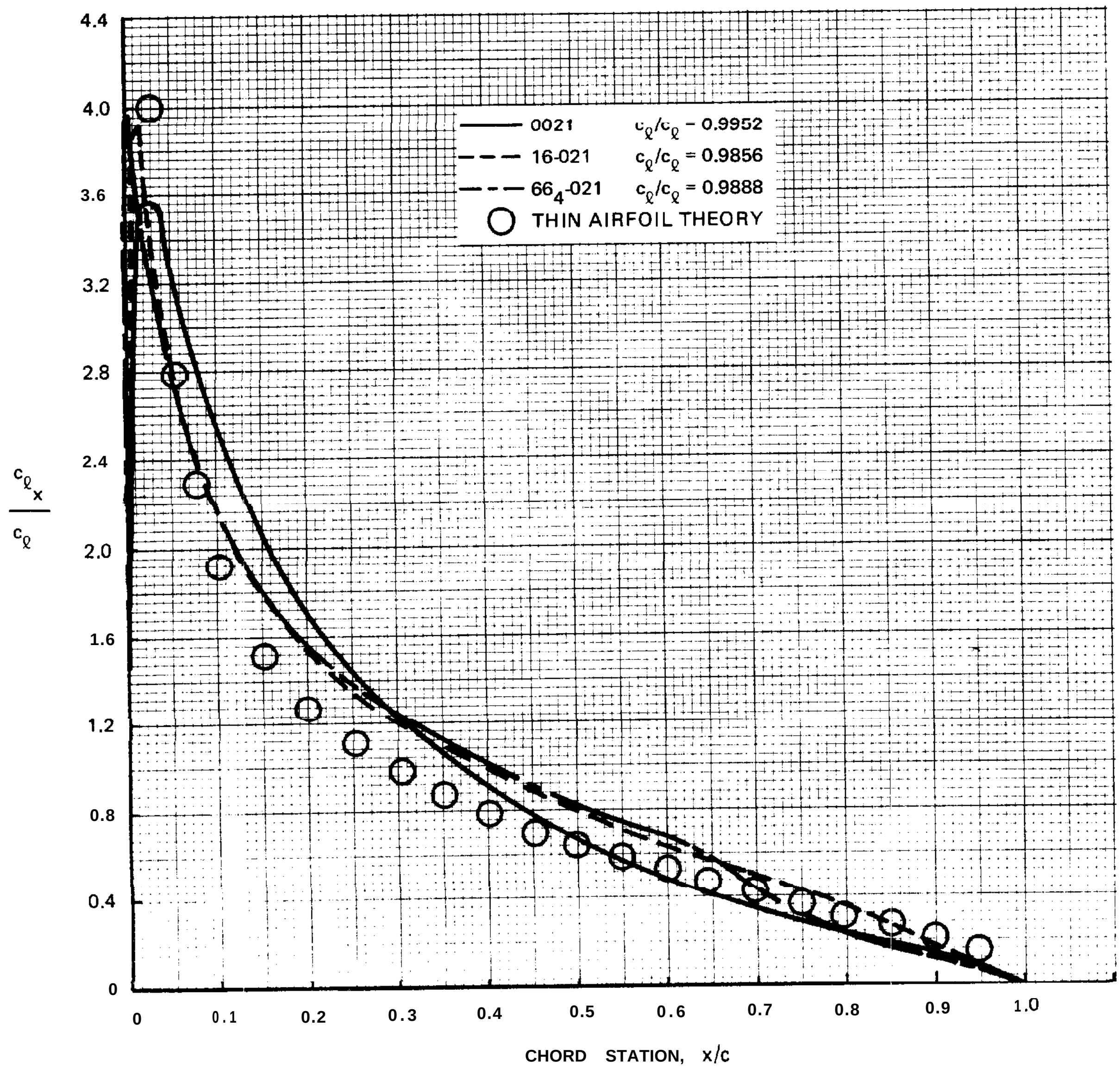

1892-061B

Fig. 3.3.2.1-1 Chordwise Lift Distributions

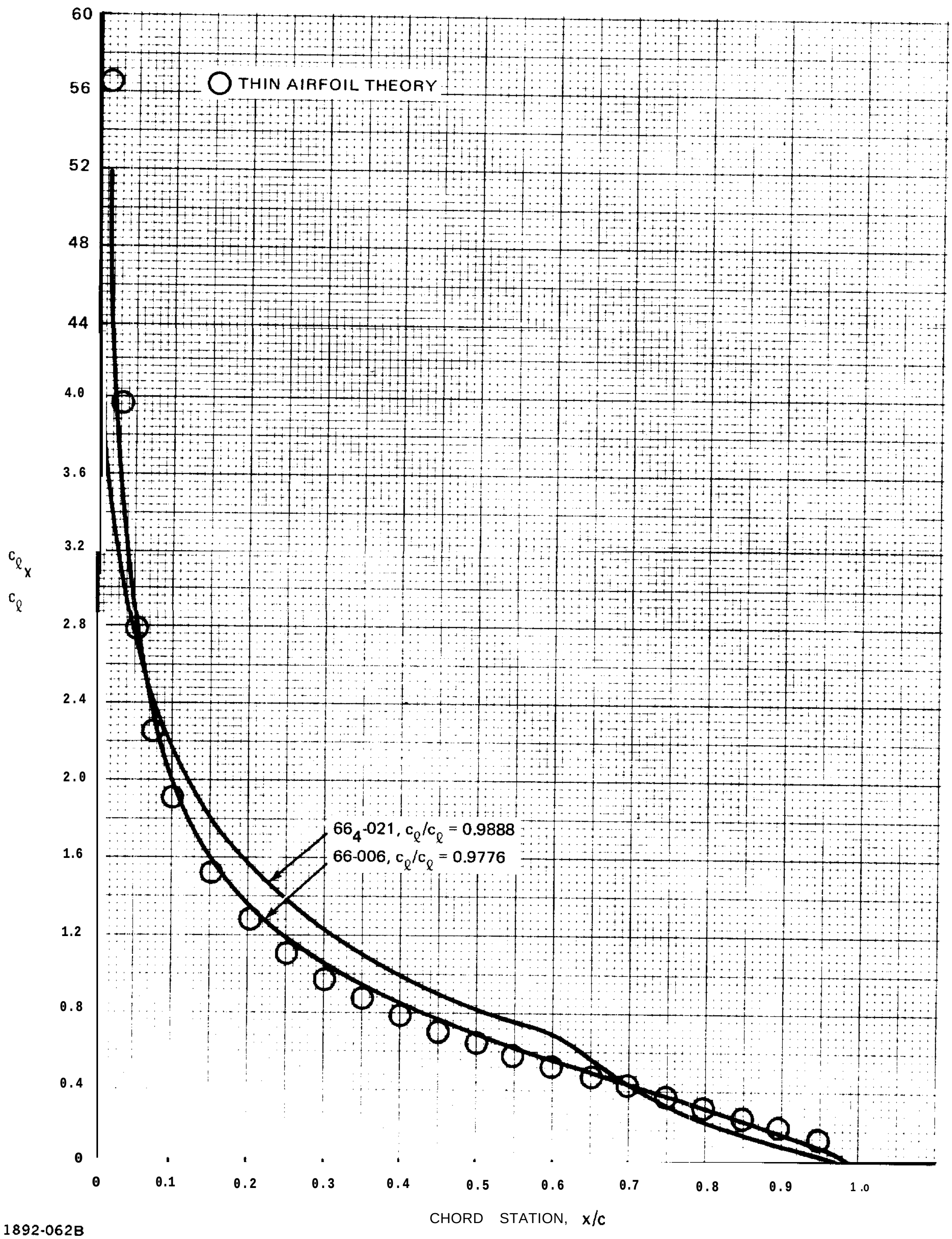

Fig. 3.3.2.1-2 Chordwise Lift Distribution, 66-Series Sections

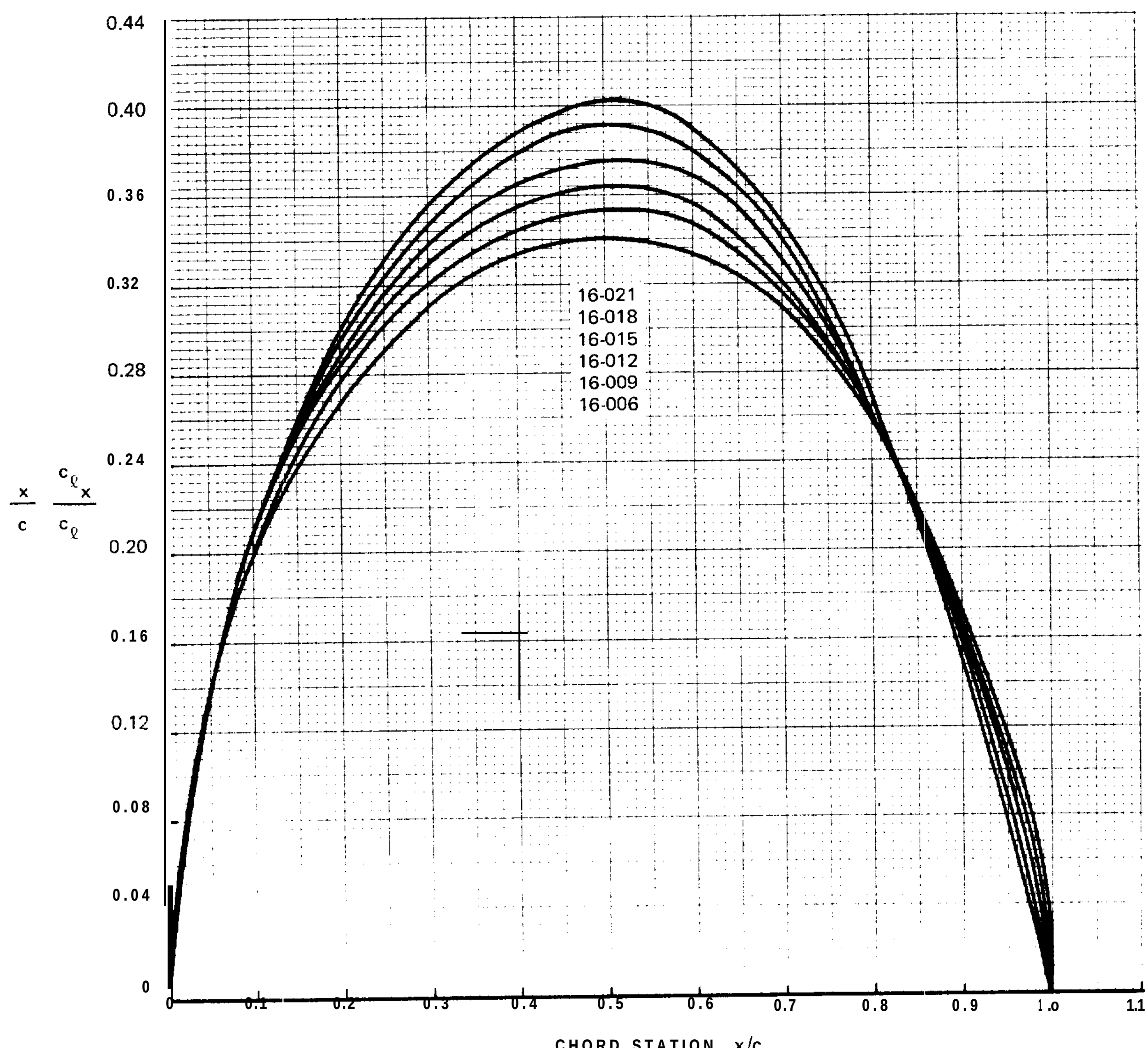

1892-063B

Fig. 3.3.2.1-3 Thick Airfoil Theory Moment Distribution, 16-Series Sections

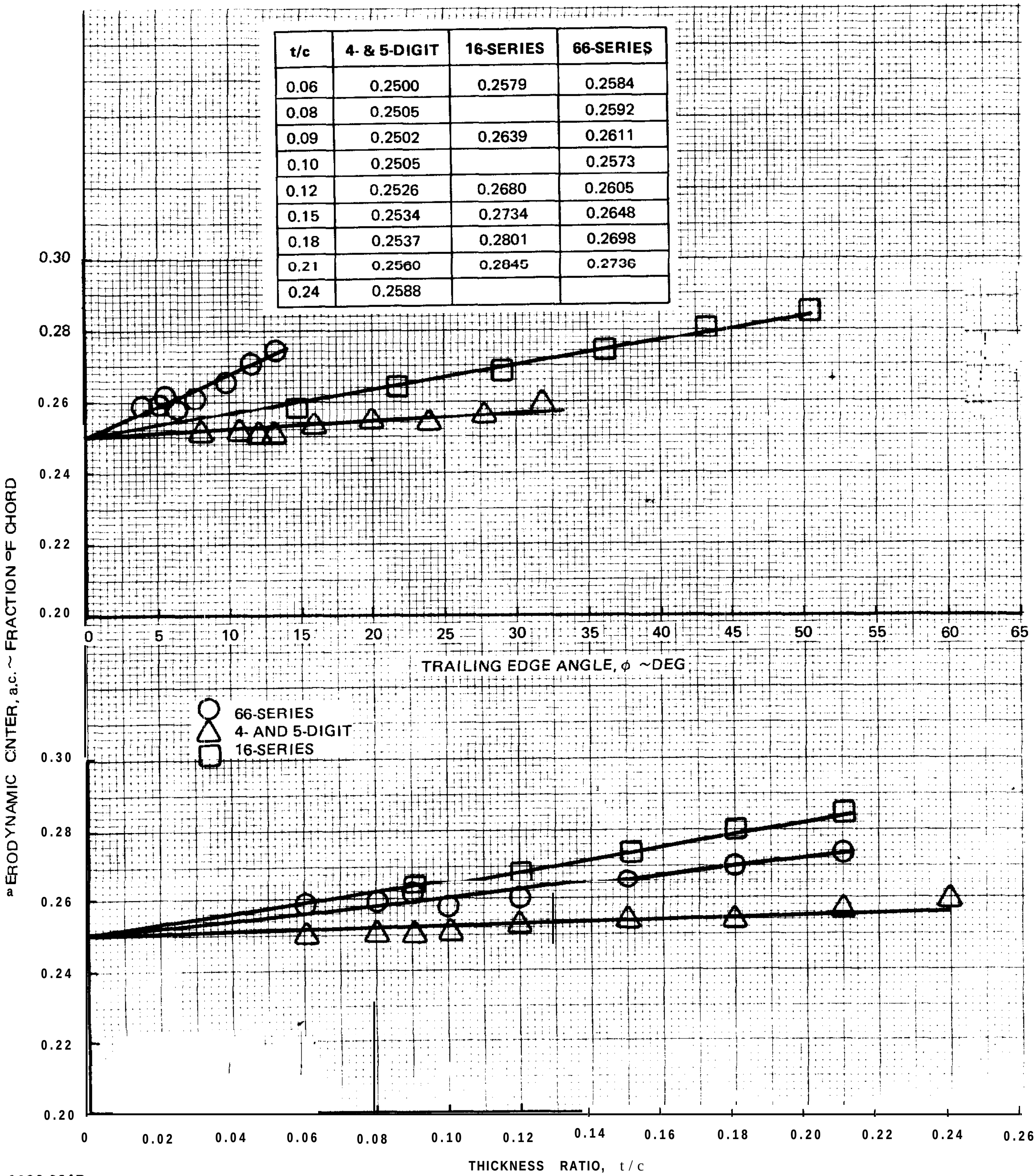

t/c	4- & 5-DIGIT	16-SERIES	66-SERIES
0.06	0.2500	0.2579	0.2584
0.08	0.2505		0.2592
0.09	0.2502	0.2639	0.2611
0.10	0.2505		0.2573
0.12	0.2526	0.2680	0.2605
0.15	0.2534	0.2734	0.2648
0.18	0.2537	0.2801	0.2698
0.21	0.2560	0.2845	0.2736
0.24	0.2588		

1892-064B

Fig. 3.3.2.1-4 Potential Aerodynamic Center

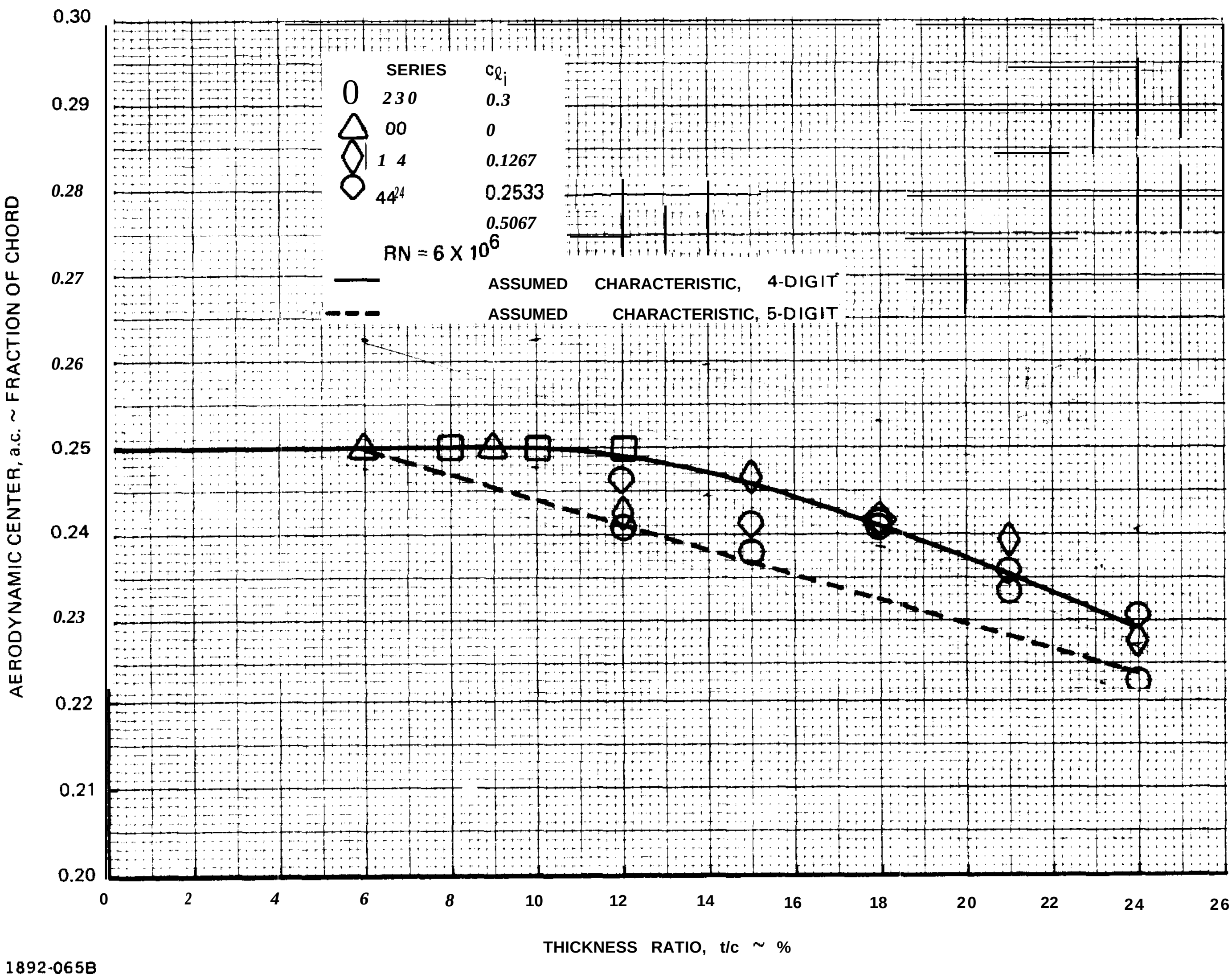

Fig. 3.3.2.1-5 Aerodynamic Center, 4-Digit and 230 Sections

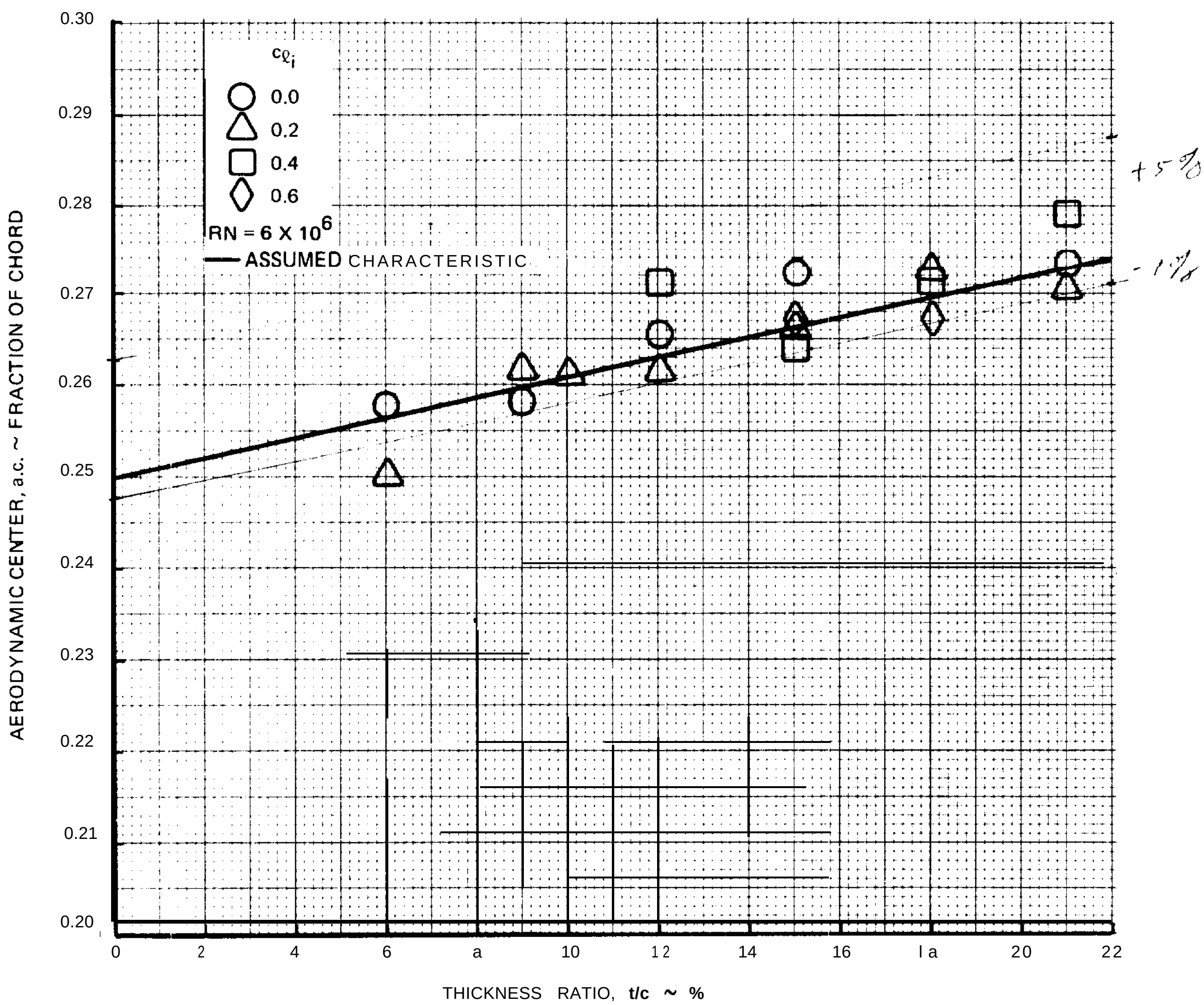

Fig. 3.3.2.1-6 Aerodynamic Center, 63-Series Section

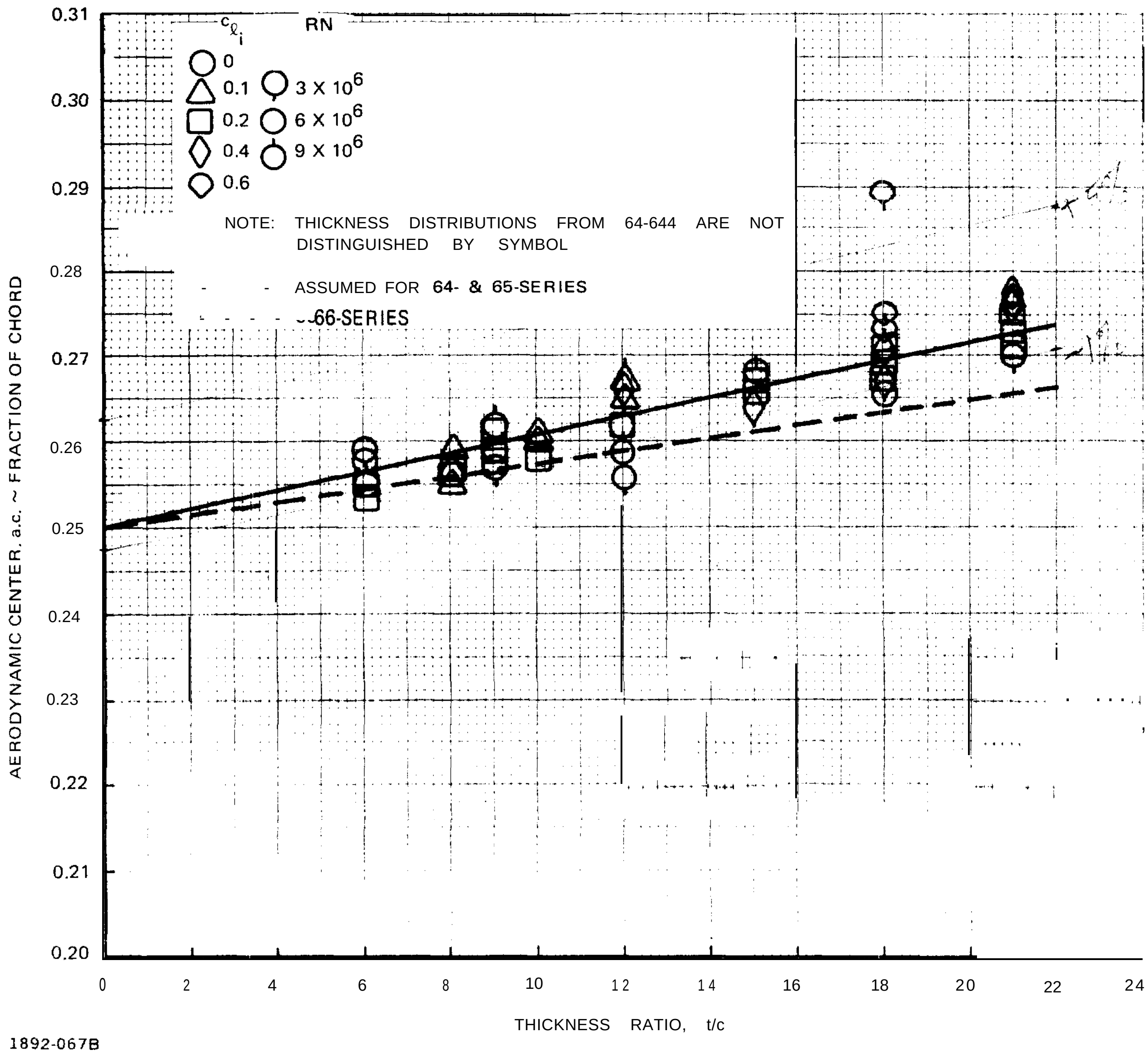

Fig. 3.3.2.1-7 Aerodynamic Center, 64-Series Sections

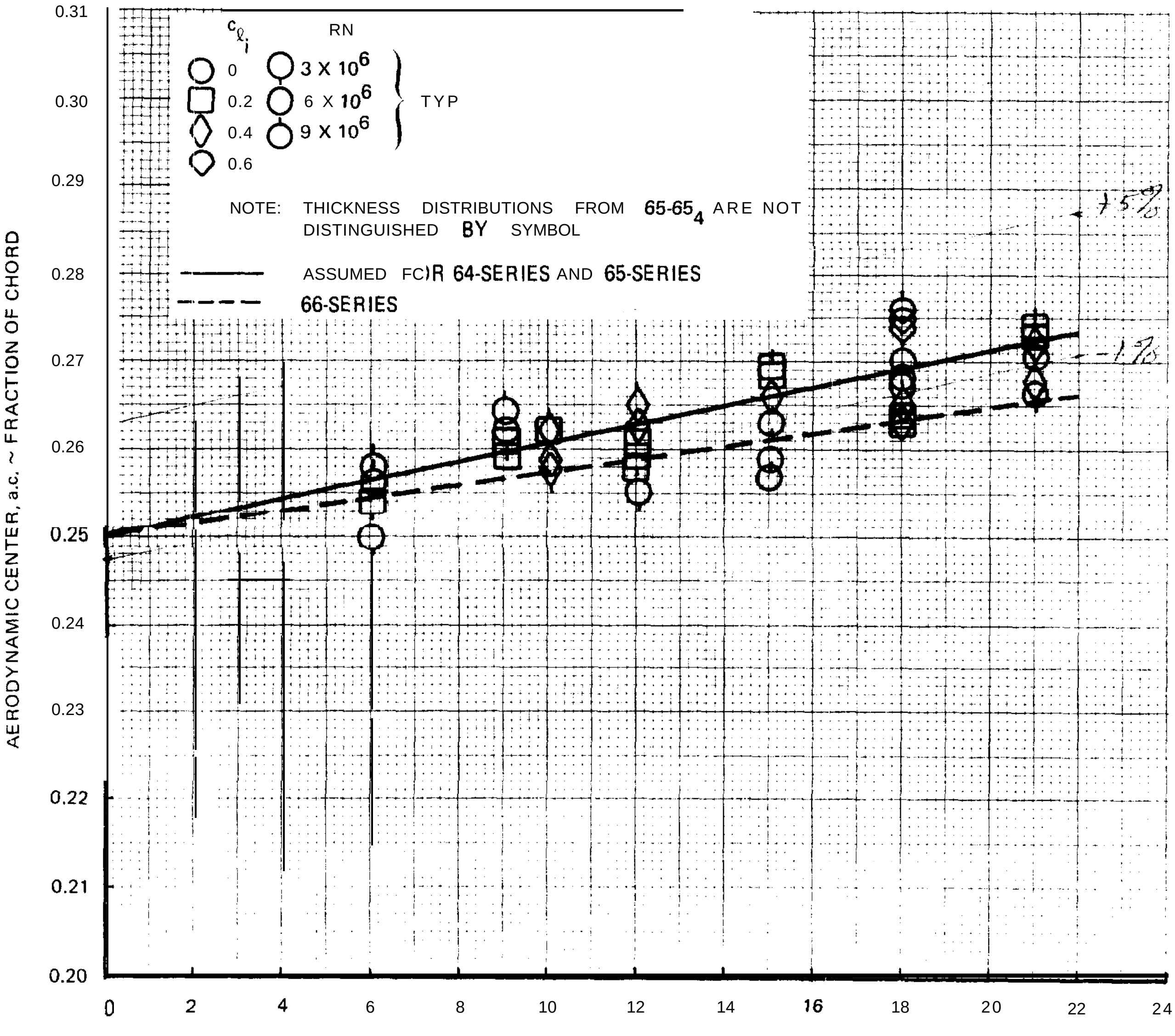

1892-068B

Fig. 3.3.2.1-8 Aerodynamic Center, 65Series Sections

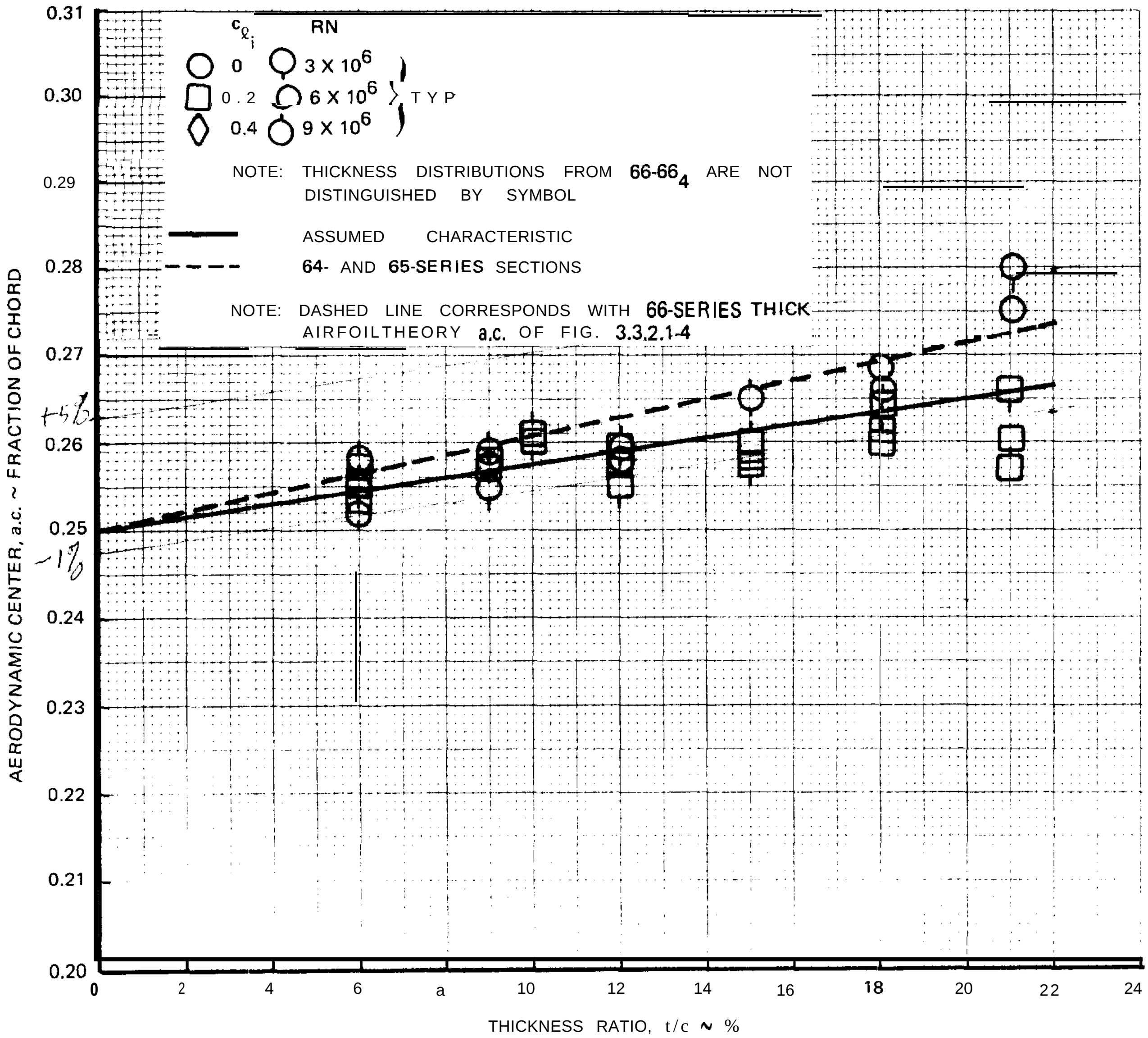

1892-069B

Fig. 3.3.2.1-9 Aerodynamic Center, 66-Series Sections

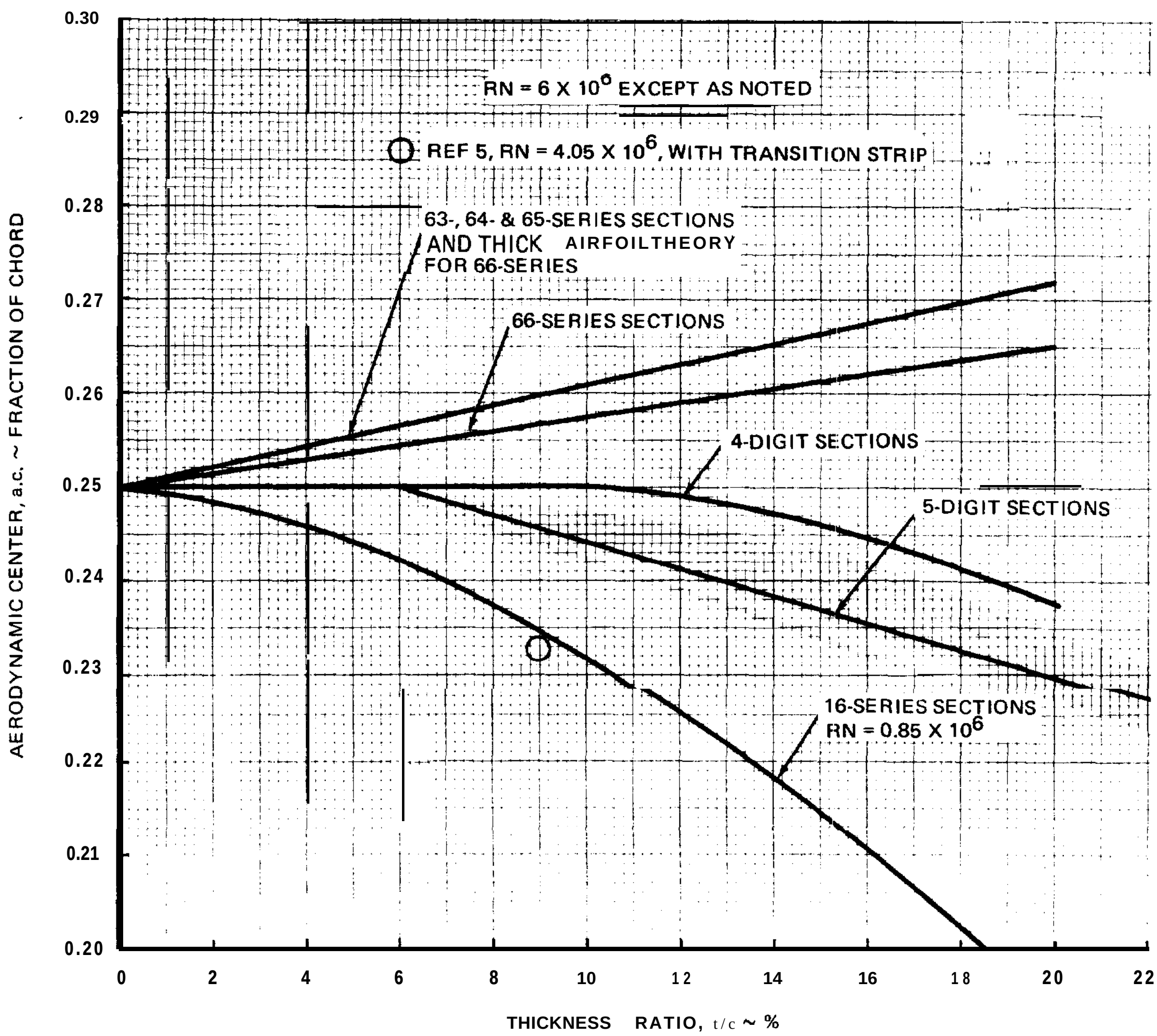

1892-070B

Fig. 3.3.2.1-10 Aerodynamic Center Summary

3.3.2.2 Viscous Effect.

PINKERTON'S FUNCTION

The classic accountability for viscous effect on the section characteristics is Pinkerton's function, discussed in References 1 and 2 for example. The source references for Pinkerton's function appear to be References 3 and/or 4, neither of which is immediately available for review. Numerous displays of the effect of the application of Pinkerton's function are available, noteably in Reference 5, but none found isolates and displays the function itself. Particular data correlations found in the literature are good but no systematic evaluation of the confidence level has been found.

Pinkerton adds a camber of specified, hypothesized shape to the section and recalculates the lift distribution by thick airfoil potential theory. As an application of thick airfoil theory the procedure is amenable only to numerical analysis and no analytic systemizations have been found in the literature with the possible exception of Pope.

The amount of camber added is proportional to angle of attack and Pinkerton's function therefore has the effect of reducing the lift curve slope and shifting the aerodynamic center. If Pinkerton's camber line is set at its zero lift angle of attack, the potential thin airfoil lift distribution on that camber line is that portion of Pinkerton's function which produces the aerodynamic center shift but neither the total nor the basic component of the Pinkerton lift distribution has been found in the literature. Pinkerton's function, then, consists of an additional component of the type of Section 3.3.2.1 and a basic component of the type of Section 3.3.2.3. The additional component is readily accounted for by employing the viscous lift curve slope of Section 3.3.1.2; i.e., no accountability is required for this component. It is the accountability for the basic component which is the subject of this section.

It should be noted that Pinkerton's function makes the viscous aerodynamic center shift from its thick airfoil position proportional to the viscous lift curve slope reduction from its thick airfoil value. Both effects are available in Reference 1 for a comprehensive test of Pinkerton's function but no such test has been found in the literature.

POPE'S P_{ac} FUNCTION

Pope presents a basic lift distribution for viscous effect in Table 7.4 of Fleference 2. The derivation for that function is not specified and it may be the basic component of Pinkerton's function.

Pope's tabulated values are shown on Figure 3.3.2.2-l. An analytic representation for this function is essential to application. The function is linear from 10% to 90% chord and Pope's first six points have been fit by a fifth order polynomial in x/c. The result presents a derivative discontinuity at 10% and 90% chord but elimination of that discontinuity produces a badly behaved function on the first and last 10% of the chord.

One requirement on this function is a zero integral over the chord and this requirement is met by making the function symmetric on the two semi-chords; thus the function need. be described only for the leading semi-chord, second, the function must present a unit integral over the chord for the moment about the mid-chord station. Pope's tabulated values violate this requirement by 3%4% which is not particuhuly significant to the section but which can have profound significance to a trailing edge flap; therefore the curve fit to Pope's tabulated values was reduced to satisfy this requirement.

The analytic form of Pope's function employed here is:

$$P_{ac} = 366.717 \frac{x}{c} - 12{,}079.49 \left(\frac{x}{c}\right)^2 + 217{,}528 \left(\frac{x}{c}\right)^3 - 1{,}933{,}922 \left(\frac{x}{c}\right)^4 + 6{,}546{,}669 \left(\frac{x}{c}\right)^5 \qquad 0 \leqslant \frac{x}{c} \leqslant .1 \qquad 3.3.2.2\text{-}1$$

$$P_{ac} = 6.84921 - 13.6984 \frac{x}{c} \qquad .1 \leqslant \frac{x}{c} \leqslant .9$$

$$P_{ac} = -P_{ac_{L.E.}} \qquad .9 \leqslant \frac{x}{c} \leqslant 1$$

Equation 3.3.2.2-l is compared with Popes tabulated values on Figure 3.3.2.2-l and in Table 3.3.2.2-I. The moment distribution for Equation 3.3.2.2-l is shown on Figure 3.3.2.2-2 and is included in Table 3.3.2.2-I.

The integral of the P_{ac} function aft of the flap hinge is required for flap analysis. This integral may be written:

$$\int_{h/c}^{1} P_{ac}\, d\frac{x}{c} = -\int_0^{1-\frac{h}{c}} P_{ac}\, d\frac{x}{c} = -\int_0^{c_f/c} P_{ac}\, d\frac{x}{c} \qquad 3.3.2.2\text{-}2$$

$$= -183.3585 \left(\frac{c_f}{c}\right)^2 \left[1 - 21.9597 \frac{c_f}{c} + 296.5884 \left(\frac{c_f}{c}\right)^2 - 2{,}109.443 \left(\frac{c_f}{c}\right)^3 + 5{,}950.7 \left(\frac{c_f}{c}\right)^4\right] \quad \text{for } \frac{c_f}{c} \leqslant .1$$

$$= 6.84921 \left[.09 - \frac{h}{c} + \left(\frac{h}{c}\right)^2\right] - .468556 \quad \text{for } .1 \leqslant \frac{h}{c} \leqslant .9$$

$$= \int_{1-\frac{h}{c}}^{1} P_{ac}\, d\frac{x}{c} \quad \text{for } \frac{h}{c} \leqslant .1$$

which is shown on Figure 3.3.2.2-3 and in Table 3.3.2.2-I.

The integral of the P_{ac} moment aft of the flap hinge line is:

$$\int_{h/c}^{1}\left(\frac{1}{2}-\frac{x}{c}\right) P_{ac}\, d\frac{x}{c} = \int_{0}^{1-\frac{h}{c}}\left(\frac{1}{2}-\frac{x}{c}\right) P_{ac}\, d\frac{x}{c} = \frac{1}{2}\int_{0}^{c_f/c} P_{ac}\, d\frac{x}{c} - \int_{0}^{c_f/c}\frac{x}{c} P_{ac}\, d\frac{x}{c} \qquad 3.3.2.2\text{-}3$$

$$= 91.67925\left(\frac{c_f}{c}\right)^2 b - 23.293\frac{c_f}{c} + 329.5279\left(\frac{c_f}{c}\right)^2 - 2{,}583.984\left(\frac{c_f}{c}\right)^3$$

$$+ 9{,}466.4\left(\frac{c_f}{c}\right)^4 - 10{,}201.2\left(\frac{c_f}{c}\right)^5\Big] \quad \text{for } \frac{c_f}{c} \leqslant .1$$

$$= 13.6984\left[.063 - \frac{1}{4}\frac{h}{c} + \frac{1}{2}\frac{h}{0c}^{2} - \frac{1}{3}\left(\frac{h}{c}\right)^3\right] + .20777 \quad \text{for } .1 \leqslant \frac{h}{c} \leqslant .9$$

$$= 1 - \int_{1-\frac{h}{c}}^{1}\left(\frac{1}{2}-\frac{x}{c}\right) P_{ac}\, d\frac{x}{c} \qquad \text{for } \frac{h}{c} \leqslant .1$$

which is shown on Figure 3.3.2.2-3 and in Table 3.3.1.2-I.

The P_{ac} characteristic of direct interest to the flap is the integral

$$\left(\frac{c}{c_f}\right)^2\int_{h/c}^{1}\left(\frac{h}{c}-\frac{x}{c}\right) P_{ac}\, d\frac{x}{c} = \left(\frac{c}{c_f}\right)^2\int_{h/c}^{1}\left(\frac{h}{c}-\frac{1}{2}+\frac{1}{2}-\frac{x}{c}\right) P_{ac}\, d\frac{x}{c} \qquad 3.3.2.2\text{-}4$$

$$= \left(\frac{c}{c_f}\right)^2\left[\left(\frac{h}{c}-\frac{1}{2}\right)\int_{h/c}^{1} P_{ac}\, d\frac{x}{c} + \int_{h/c}^{1}\left(\frac{1}{2}-\frac{x}{c}\right) P_{ac}\, d\ f\ \right]$$

which can be evaluated from integrals already evaluated.

Equation 3.3.2.2-4 is presented in large scale in Figure 3.3.2.2-4 for the last 10% of the chord. In this region where the inverse of the flap chord ratio goes to infinity it is not easy to define P_{ac} in a manner which produces a well-behaved result for Equation 3.3.2.2-4. For example, a sixth-order polynomial definition for P_{ac} produces a poorly behaved integral and a very badly behaved product of $(c/c_f)^2$ and integral. However, even a well behaved integral will produce a substantial step in the product which affects that product to flap chord ratios of 20%–25%. The significance is that an invalid representation for the boundary layer effect in this area, where boundary layer effect is most, pronounced, can have a substantial effect upon the flap moment characteristics.

The product curve of Figure 3.3.2.2-4 is badly behaved aft of the 98% chord station but that is only because the **4-place** accuracy of Table 3.3.2.2-I is not adequate for the last 2% of the chord. The first 10% of the chord is presented on an expanded scale on Figure 3.3.2.2-5 though there is no analytic difficulty in this region.

The flap moment parameter for the full chord is presented in Table 3.3.2.2-I and on Figure 3.3.2.2-6.

APPLICATION OF POPE'S FUNCTION

Pope's function provides an incremental lift distribution defined by:

$$\frac{\Delta c_{\ell_{xb}}}{c_\ell} = P_{ac} \; \Delta \text{ a.c.} \qquad 3.3.2.2\text{-}5$$

where: $\Delta \text{ a.c.} = \text{a.c.}_{pot} - \text{a.c.}$

Employing a frequently used approximation, e.g., Reference 1, the corresponding incremental velocity distribution is:

$$\frac{\Delta v_P}{V} = \frac{\Delta c_{\ell_{xb}}/c_\ell}{4\frac{v}{V}} \qquad 3.3.2.2\text{-}6$$

$$= \frac{1}{4} \; \frac{P_{ac}\,\Delta \text{ ac}}{v/V}$$

$$\approx \frac{1}{4} P_{ac}\,\Delta \text{ ac}$$

Of the standard sections, the effect of this function is most significant to the **16-Series** section where the viscous aerodynamic center shift is 4-5 times that of the **66-series** section and 15 times that of the 4 and 5 digit sections for typical hydrofoil thickness ratios. It is instructive, therefore, to consider this effect for a 16-009 section.

The potential additional lift distribution for the **16-009** section is included in Reference 1 in the form of Equation 3.3.2.1-2. Associating that lift distribution **with** the viscous lift coefficient of Equation 3.3.1.2-10 increments that lift distribution by the factor $m_\phi \; \phi_{5\%}$ of Equation 3.3.1.2-9 which has the value **.1589.** The potential aerodynamic center for this section is at 26.4% on Figure 3.3.2.1-4 and the measured aerodynamic center of Page 4 of Section 7.2.4 of Reference 6 is 23.25%. Thus the lift distribution for this section may be written:

$$\frac{c_{\ell_x}}{c_\ell} = \left(\frac{c_{\ell_x}}{c_\ell}\right)_{pot} - \frac{\Delta c_{\ell_{xa}}}{c_\ell} + \frac{\Delta c_{\ell_{xb}}}{c_\ell} \qquad 3.3.2.2\text{-}7$$

where: $\left(\frac{c_{\ell_x}}{c_\ell}\right)_{pot} = 4 \frac{v}{V} \quad \frac{\Delta v_a}{V}$ from Reference 1

$$\frac{\Delta c_{\ell_{xa}}}{c_\ell} = m_\phi \quad \phi_{5\%} \left(\frac{c_{\ell_x}}{c_\ell}\right)_{pot} = .1589 \quad \left(\frac{c_{\ell_x}}{c_\ell}\right)_{pot}$$

$$\frac{\Delta c_{\ell_{xb}}}{c_\ell} = P_{ac} \quad \mathrm{Aa.c.} \quad = P_{ac} \; (.264 - .2325) = .0315 \; P_{ac}$$

Equation 3.3.2.2-7 is shown on Figure 3.3.2.2-7 in cumulative fashion. The effect of Pope's function is highly variable over the chord length, particularly in relative terms. The significance to the trailing edge flap region should be noted. The effect throughout is quite exaggerated relative to the other standard thickness distributions.

SUMMARY

Pinkerton's function, being non-analytic, is difficult to apply. No systematic characterizations of the effects of Pinkerton's function have been found and, in particular, no test of Pinkerton's lift curve slope-aerodynamic center relationship has been found.

For all conventional sections except the Is-series, most of the viscous effect on the list distribution is accounted for simply by distributing the viscous, instead of the potential, additional lift coefficient; Pope's function is represented as accounting for the remaining viscous effect. Pope's function is analytic and easily incorporated into a design practice. It is distinct from the lift curve slope and therefore provides consistency for the lift distribution, section lift, and section moment.

As for Pinkerton's function, no tests of Pope's function can be offered. Reference 6 appears to offer an excellent source for such a test though the tabulated data, Volume III, would be required and the task would require a significant effort. A substantial additional effort would be required to incorporate Pinkerton's function into that study.

The necessity for the incorporation of Pope's function into a design procedure depends upon the section and characteristic in question. Unless the effect of the function exceeds the theoretical and experimental precision for the characteristic, the function should be neglected.

2

REFERENCES

1. Abbott, Ira H. and von Doenhoff, Albert E.: Theory of Wing Sections, Dover, 1969.
2. Pope, Alan: Basic Wing And Airfoil Theory. McGraw-Hill, 1961.
3. Pinkerton, R.M.: Calculated and Measured Pressure Distribution Over the Midspan Section of the NACA 4412 Airfoil. NACA Report 563, 1936.
4. Pinkerton, R.M.: The Variation With Reynolds Number of Pressure Distribution Over an Airfoil Section. NACA Report 613, 1937.

6. Riegels, F.W.: Aerofoil Sections. Butterworths, London. Out of print.

6. Teeling, P.: Low Speed Wind Tunnel Tests of A NACA 16-309 Airfoil With Trailing Edge Flap. DeHavilland Aircraft of Canada Report No. ECS 76-3, October 1976.

TABLE 3.3.2.2-I POPE'S P_{ac} FUNCTION

3	2	1	3	3	4	4	4	1
x/c OR h/c	POPE'S P_{ac}	P_{ac}*	(1/2 - x/c) X P_{ac}	$\int_{h/c}^{1} P_{ac}\, d\, x/c$	$\int_{h/c}^{1} (1/2 - x/c) \times P_{ac}\, d\, x/c$	$\int_{h/c}^{1} (h/c - x/c) \times P_{ac}\, d\, x/c$	$\left(\frac{c}{c_f}\right)^2 \int_{h/c}^{1} (h/c - x/c) \times P_{ac}\, d\, x/c$	c_f/c
0	0	0 1.5576	0	0	1	1	1	1
0.0125	3.2	3.0762	1.4996	-0.0220	0.9892	0.9999	1.0254	0.9875
0.025	4.5	4.3256	2.0547	-0.0694	0.9664	0.9994	1.0513	0.975
0.0375		4.8974	2.2650	-0.1274	0.9392	0.9981	1.0774	0.9625
0.05	5.5	5.2869	2.3791	-0.1912	0.9101	0.9961	1.1038	0.95
0.0625		5.5758	2.4394	-0.2592	0.8799	0.9933	1.1302	0.9375
0.075	5.9	5.6713	2.4103	-0.3297	0.8495	0.9896	1.1566	0.925
0.0875		5.5464	2.2879	-0.4000	0.8201	0.9851	1.1831	0.9125
0.1	5.7	5.4794	2.1917	-0.4686	0.7922	0.9796	1.2094	0.9
0.15	5.0	4.7945	1.6781	-0.7254	0.6958	0.9497	1.3144	0.85
0.2	4.3	4.1095	1.2329	-0.9480	0.6233	0.9077	1.4183	0.8
0.3	2.9	2.7397	0.5479	-1.2905	0.5365	0.7946	1.6216	0.7
0.4	1.4	1.3699	0.1370	-1.4959	0.5046	0.6542	1.8172	0.6
0.5	0	0	0	-1.5664	0.5000	0.5	2	0.5
0.6	-1.4	-1.3699	0.1370	-1.4959	0.4954	0.3458	2.1613	0.4
0.7	-2.9	-2.7397	0.5479	-1.2905	0.4635	0.2054	2.2822	0.3
0.8	-4.3	-4.1095	1.2329	-0.9480	0.3767	0.0923	2.3075	0.2
0.85	-5.0	-4.7945	1.6781	-0.7254	0.3042	0.0503	2.2360	0.15
0.9	-5.7	-5.4794	2.1917	-0.4686	0.2078	0.0204	2.0360	0.1
0.9125		-5.5464	2.2879	-0.4000	0.1799	0.0149	1.9461	0.0875
0.925	-5.9	-5.6713	2.4103	-0.3297	0.1505	0.0104	1.8449	0.075
0.9375		-5.5758	2.4394	-0.2592	0.1201	0.0067	1.7152	0.0625
0.95	-5.5	-5.2869	2.3791	-0.1912	0.0899	0.0039	1.5440	0.05
0.9625		-4.8974	2.2650	-0.1274	0.0608	0.0019	1.3351	0.0375
0.975	-4.5	-4.3256	2.0547	-0.0694	0.0336	0.0006	1.0160	0.025
0.9875	-3.2	-3.0762	1.4996	-0.0220	0.0108	0.0001	0.4800	0.0125
1	0	0	0	0	0	0	0	0

1892-071B *EQUATION 3.3.2.2-1

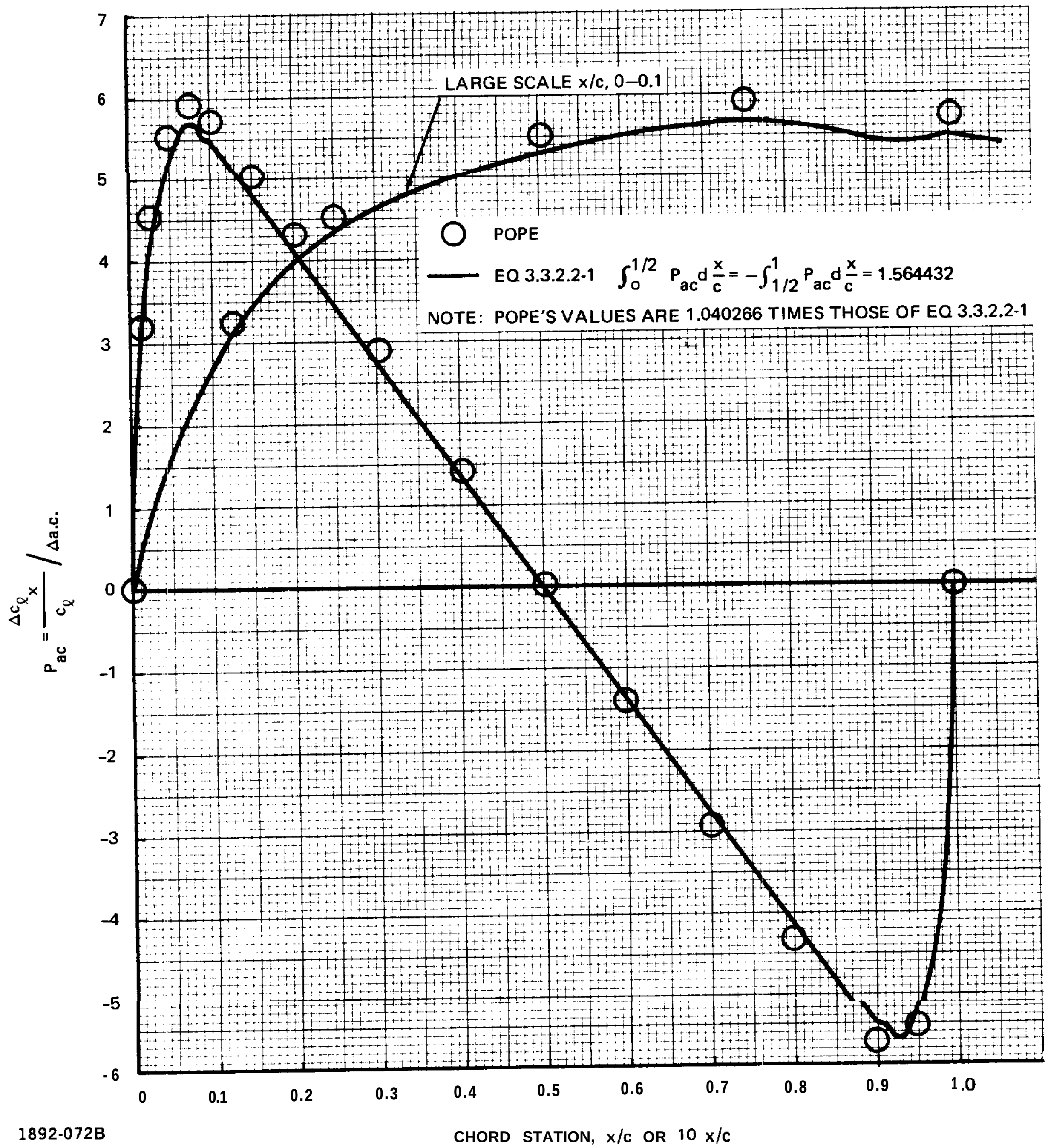

Fig. 3.3.2.2-1 Pope's P_{ac} Function

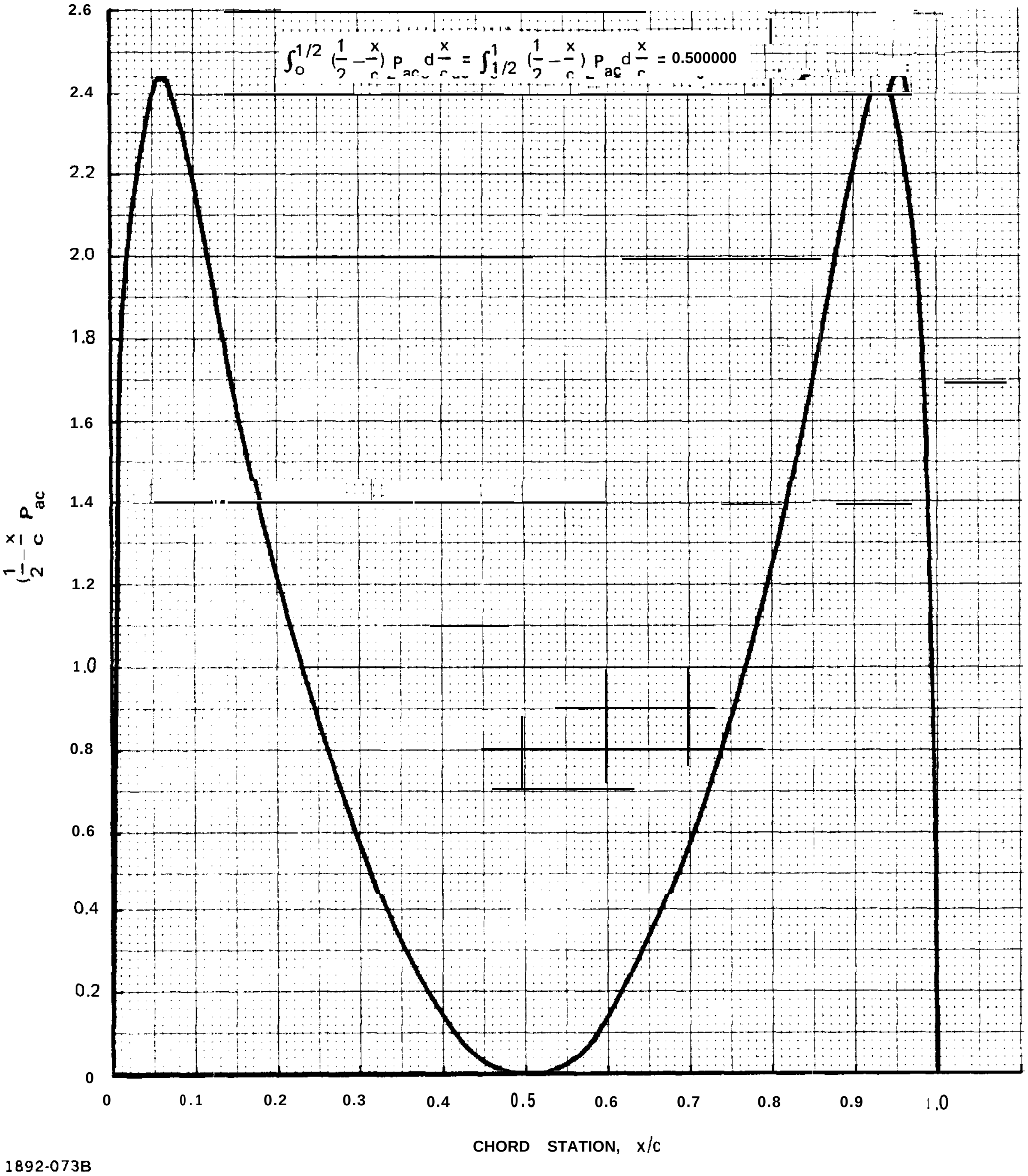

Fig. 3.3.2.2-2 Pope's Function Moment Distribution

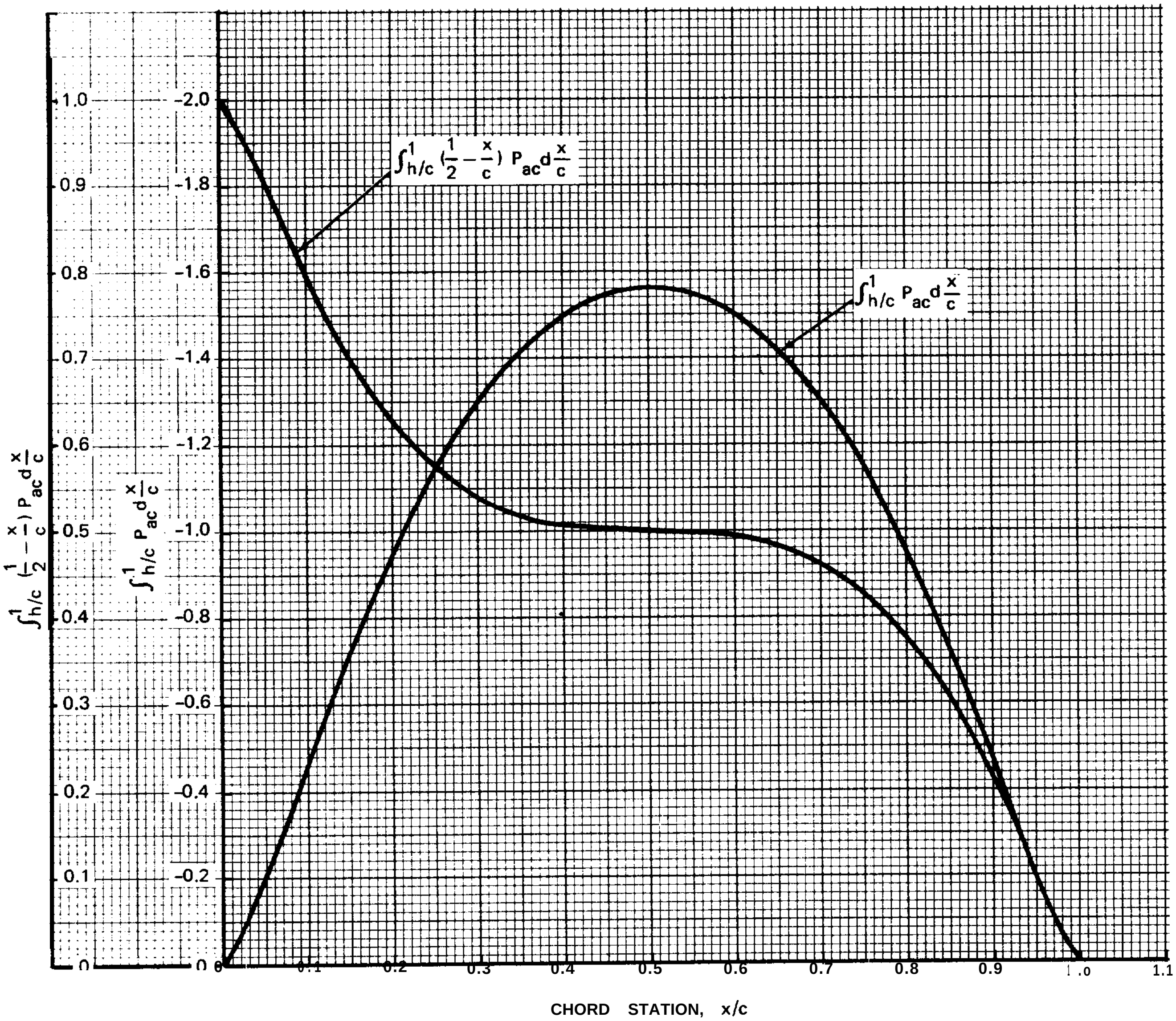

1892-074B

Fig. 3.3.2.2-3 P_{ac} Function Integrals

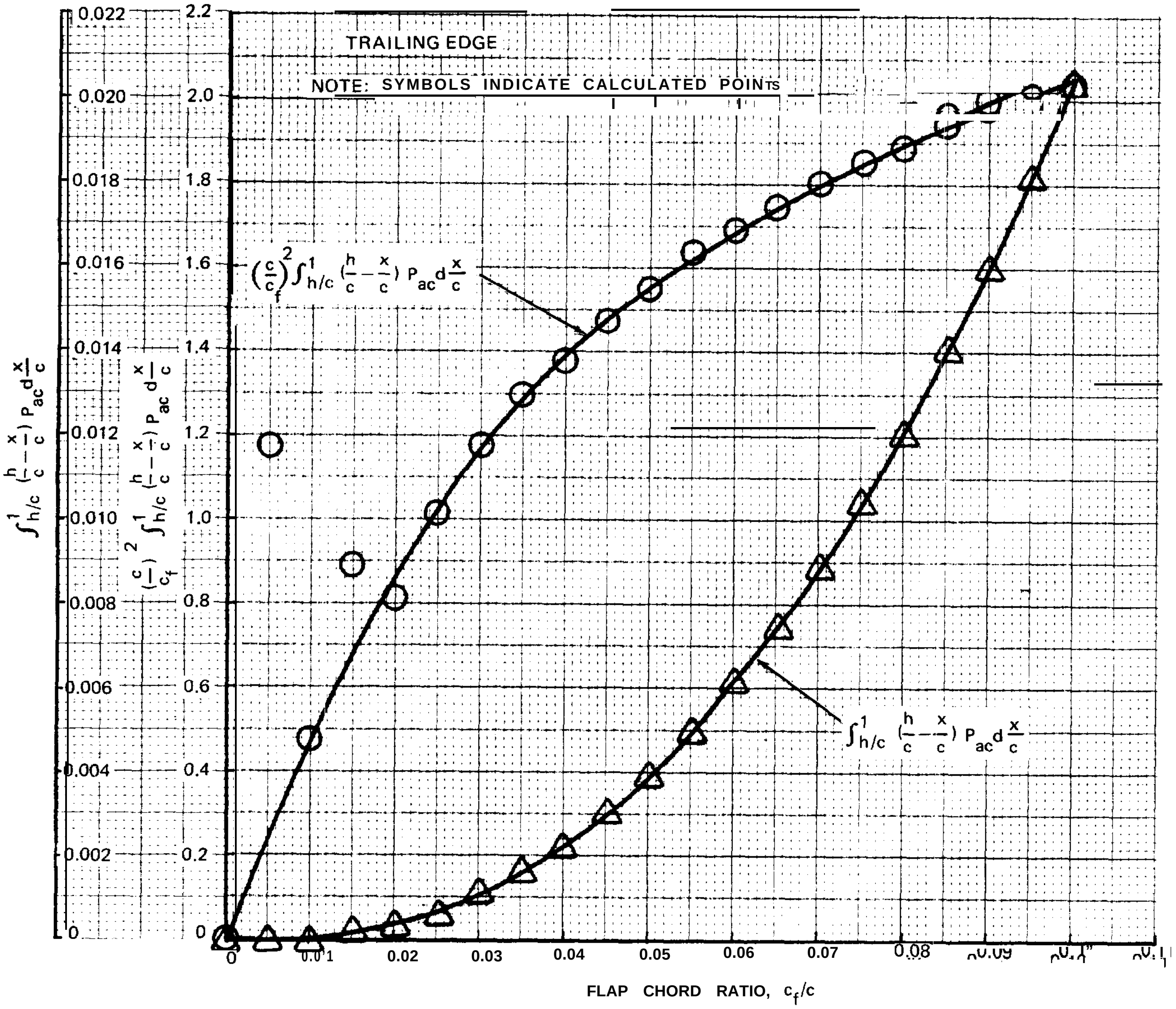

1892-075B

Fig. 3.3.2.2-4 Flap Parameter, $\left(\frac{c}{c_f}\right)^2 \int_{h/c}^{1} \left(\frac{h}{c} - \frac{x}{c}\right) P_{ac} d\frac{x}{c}$

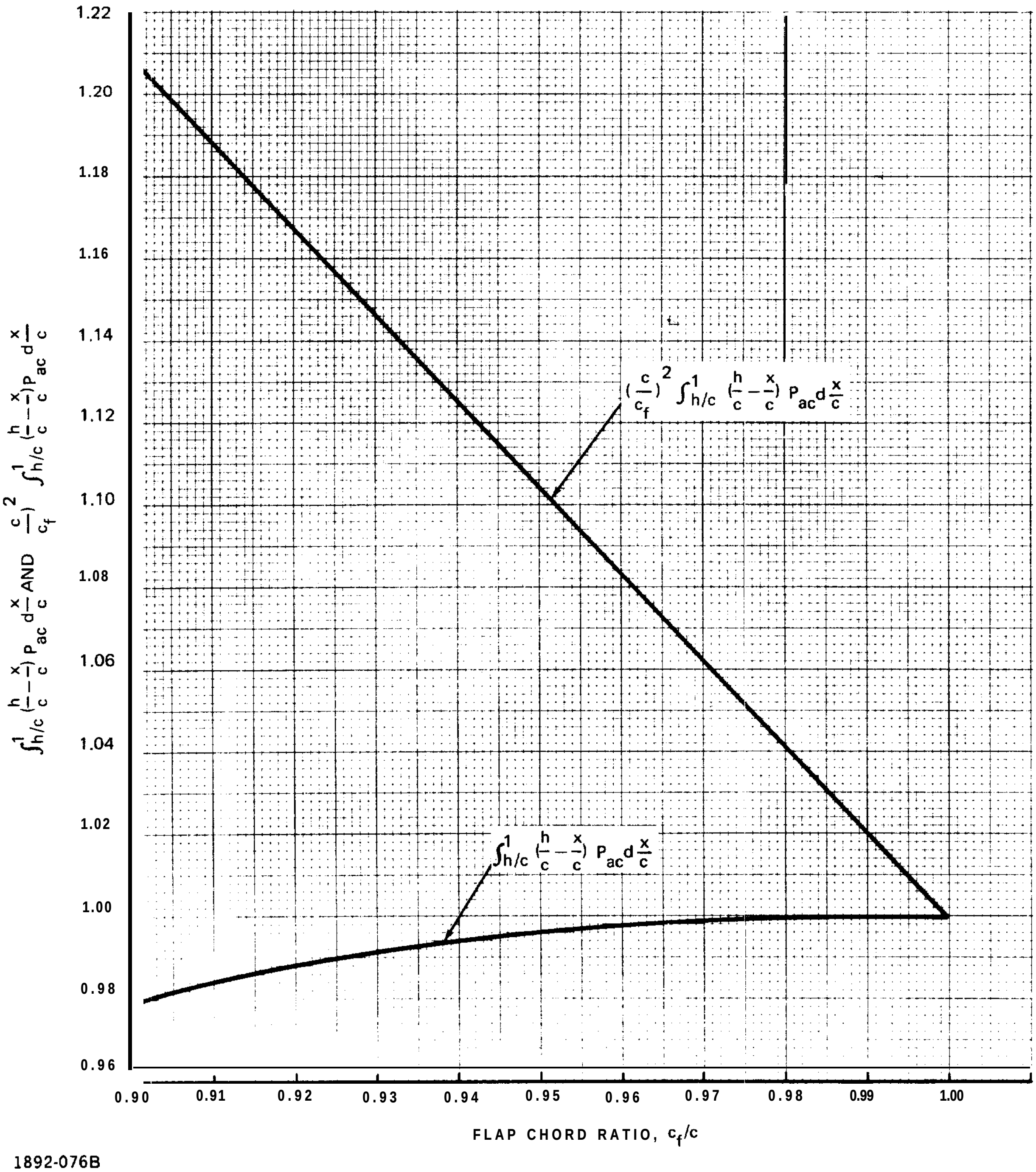

Fig. 3.3.2.2-5 Flap Parameter, $(\frac{c}{c_f})^2\int_{h/c}^{1}(\frac{h}{c}-\frac{x}{c})P_{ac}d\frac{x}{c}$

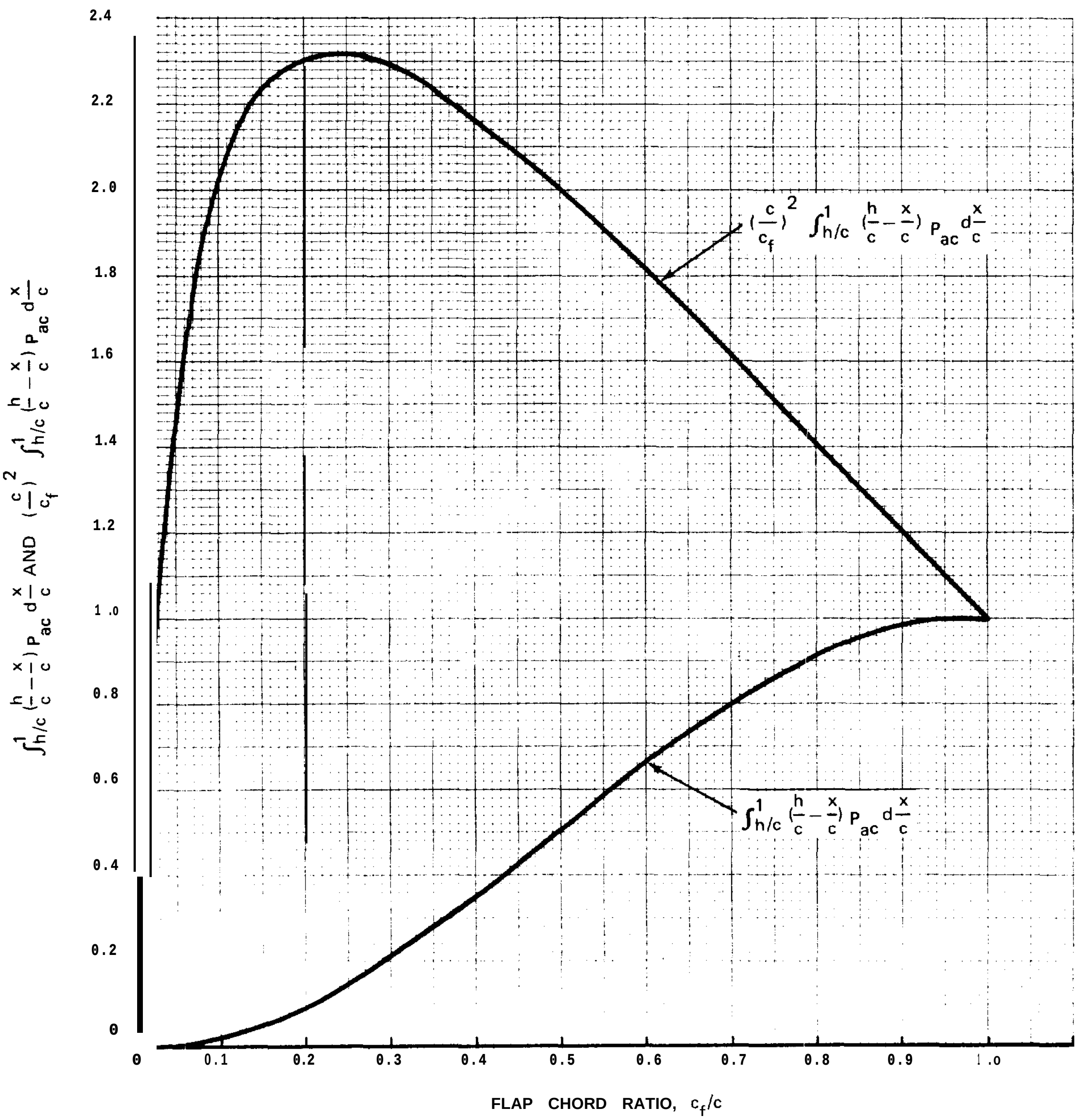

1892-077B

Fig. 3.3.2.2-6 Flap Parameter, $(\frac{c}{c_f})^2 \int_{h/c}^{1} (\frac{h}{c} - \frac{x}{c}) P_{ac} d\frac{x}{c}$

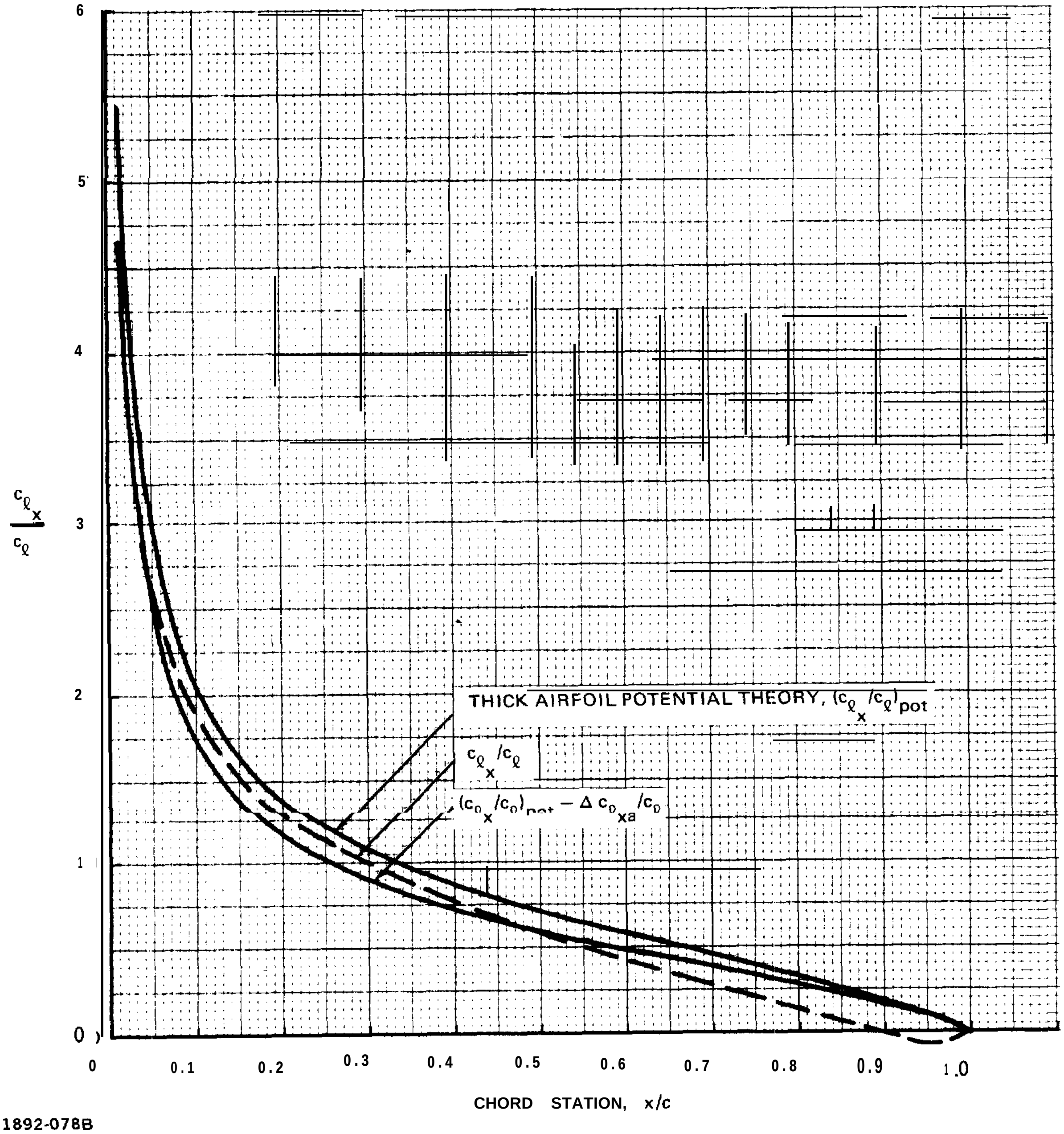

Fig. 3.3.2.2-7 Pope's Function Lift Distribution Effect. 16-009 Section

3.3.2.3 Basic Lift Distribution.

POTENTIAL LIFT DISTRIBUTION

The potential thin airfoil lift distribution for camber is classic, e.g., Pope's Chapter 7 of Reference 1. It is amenable but not convenient to analytic systemization. The PR coefficients of Appendix II of Reference 2 are the thin airfoil local lift coefficient, $c_{\ell_{xb}}$, distribution for the design angle of attack. For the "a" mean lines they are also the relative local lift coefficients, $c_{\ell_{xb}}/c_{\ell_i}$.

Thick airfoil potential theory possesses a generality which encompasses camber but only by numerical analysis. Superposition of the velocity distributions of Appendices I and II of Reference 2 produces the thick airfoil basic lift distribution for the sections included in that reference in the form:

$$c_{\ell_{xb}} = 4\frac{v}{V}\frac{\Delta v}{V} \approx 4\frac{\Delta v}{V} \qquad \text{3.3.2.3-1}$$

The integral of Equation 3.3.2.3-1 over the chord produces the thick airfoil $c_{\ell_{i\,pot}}$ and in particular for the "a" family of mean lines:

$$\frac{c_{\ell_{i\,pot}}}{c_{\ell_i}} = \int_0^1 4\frac{v}{V}\frac{\Delta v}{V}\,d\frac{x}{c} = \int_0^1 \frac{v}{V} P_R\, d\frac{x}{c} \qquad \text{3.3.2.3-2}$$

$$= \int_0^1 \frac{v}{V}\,d\frac{x}{c} \qquad \text{for } a = 1.0 \text{ mean line}$$

That is, the thickness effect for the a = 1.0 mean line can be calculated directly from the tabulated thickness velocity distributions of Appendix I of Reference 2. The result is subject to the stations employed and an approximate result is shown on Figure 3.3.2.3-1. No reference to this rather significant effect has been found in the literature.

The table on Figure 3.3.2.3-1 indicates the sensitivity of the potential c_{ℓ_i} to thickness ratio; the curves illustrate the sensitivity to the camber distribution by displaying that sensitivity over the "a" family of mean lines for certain thickness distributions.

Analytic accountability for viscous basic lift distribution must relate that distribution to the thick airfoil potential basic distribution. No such accountability can be offered here and Figure 3.3.2.3-1 is included only for reference.

VISCOUS LIFT DISTRIBUTION

The 664021 $c_{\ell_{i\ pot}}/c_{\ell_i}$ ratios of Figure 3.3.2.3-l should be compared with the 21% t/c $c_{\ell_{i\ eff}}/c_{\ell_i}$ ratios of **Figure 3.3.1.4-4;** the difference is the gross effect of viscosity upon the basic lift **distribution.** The $c_{\ell_{i\ eff}}$ might, with benefit, be related to the $c_{\ell_{i\ pot}}$ as is traditional for lift curve slope but no such approach has been found in the literature. The comparison of Figures 3.3.1.4-4 and 3.3.2.3-l does indicate a substantial distinction between the viscous effect for the a = 1.0 mean line and that for the other members of the "a" family of mean lines.

Only one measurement of the basic chordwise lift distribution can be offered here. The measurements of Figure 3.3.2.3-2 are from Sections 7.5.6 and 7.5.14 of Reference 3; the tabulated pressures were not available. The case with transition strip is one point on a lift curve considered free of scale effect in Section 3.3.1.2; the c_ℓ without transition strip is indicative of an abnormal extent of laminar flow for a prototype model.

The measured distribution of Figure 3.3.2.3-2 is compared with the thin and thick airfoil potential a = 1.0 lift distributions and with the thin airfoil potential a = .8 and 65 mean line distributions. The a = .8 potential distribution, associated with a zero ideal angle of attack, is **sometimes** employed as an approximation for the viscous a = 1.0 distribution and seems to serve the purpose well, particularly in the region which produces trailing edge flap hinge moment.

Figure 3.3.2.3-2 is repeated in terms of upper and lower surface velocity distribution on Figure 3.3.2.3-3 which emphasizes the significance of this lift distribution to the cavitation characteristics. Figure 3.3.2.3-3 seems to indicate that the 65 mean line provides the best velocity distribution approximation. Such a judgement is heavily influenced by the lower surface leading edge measurements and, in fact, the three theoretical velocity distributions are scarcely distinguishable in the data precision. A deficient thickness velocity distribution appears to be evident on Figure 3.3.2.3-3.

A single lift distribution measurement cannot substantiate an **emperical** modification to the potential theory and recourse was made to examination of the basic lift center of pressure, $c.p. = a.c. - c_{m_{ac}}/c_\ell$, which is a gross measure of the basic lift distribution but which is **implicitely** available, for all **the** sections of Appendix IV of Reference 2.

The experimental camber lift centers of pressure displayed here are derived from:

$$c.p. = a.c. - \frac{c_{m_{ac}}}{c_{\ell_{i\ eff}}} \qquad 3.3.2.3\text{-}3$$

where: a.c. and $c_{m_{ac}}$ are from Appendix IV of Reference 2 and are practically invariant with the Reynolds Numbers of that reference. The effective c_{ℓ_i}'s are the experimental values reviewed in Section 3.3.1.4.

The measured 66-series centers of pressure are compared with the thin airfoil value on Figure 3.3.2.3-4. The thick airfoil center of pressure is available from Appendix I of Reference 2 as

$$c.p. = \int_0^1 \frac{x}{c}\frac{v}{V}\, d\frac{x}{c} \qquad 3.3.2.3\text{-}4$$

which has been evaluated here only for the 66-series section for comparison on Figure 3.3.2.3-4. Viscous effect, of course, acts upon the thick airfoil value rather than the thin airfoil value. The a = .8 thin airfoil center of pressure is also shown on Figure 3.3.2.3-4.

Figures 3.3.2.3-4 and -5 present all of the measurements of the camber lift center of pressure available in Reference 2. Coverage of the 6 x A sections and of the a < 1.0 mean lines is inadequate; the "A" sections must be assumed identical with the basic sections and the a < 1.0 camber lift distributions must be assumed to be nominal. Examination of the 16-series section is limited to Figure 3.3.2.3-2; no attempt is made here to derive this characteristic from Reference 4.

Section 3.3.3.1 presents an analysis of the data of Figures 3.3.2.3-4 and -5 which indicates that the measured a = 1.0 camber lift centers of pressure correspond to the theoretical center of pressure for the a = .94 mean line.

REFERENCES

1. Pope, Alan: Basic Wing And Airfoil Theory. McGraw-Hill, 1951.
2. Abbott, Ira H. and von Doenhoff, Albert E.: Theory of Wing Sections. Dover, 1959.
3. Teeling, P.: Low Speed Wind Tunnel Tests Of A NACA 16-309 Airfoil With Trailing-Edge Flap. DeHavilland Aircraft of Canada Limited Report No. ECS 76-3, October 19'76.

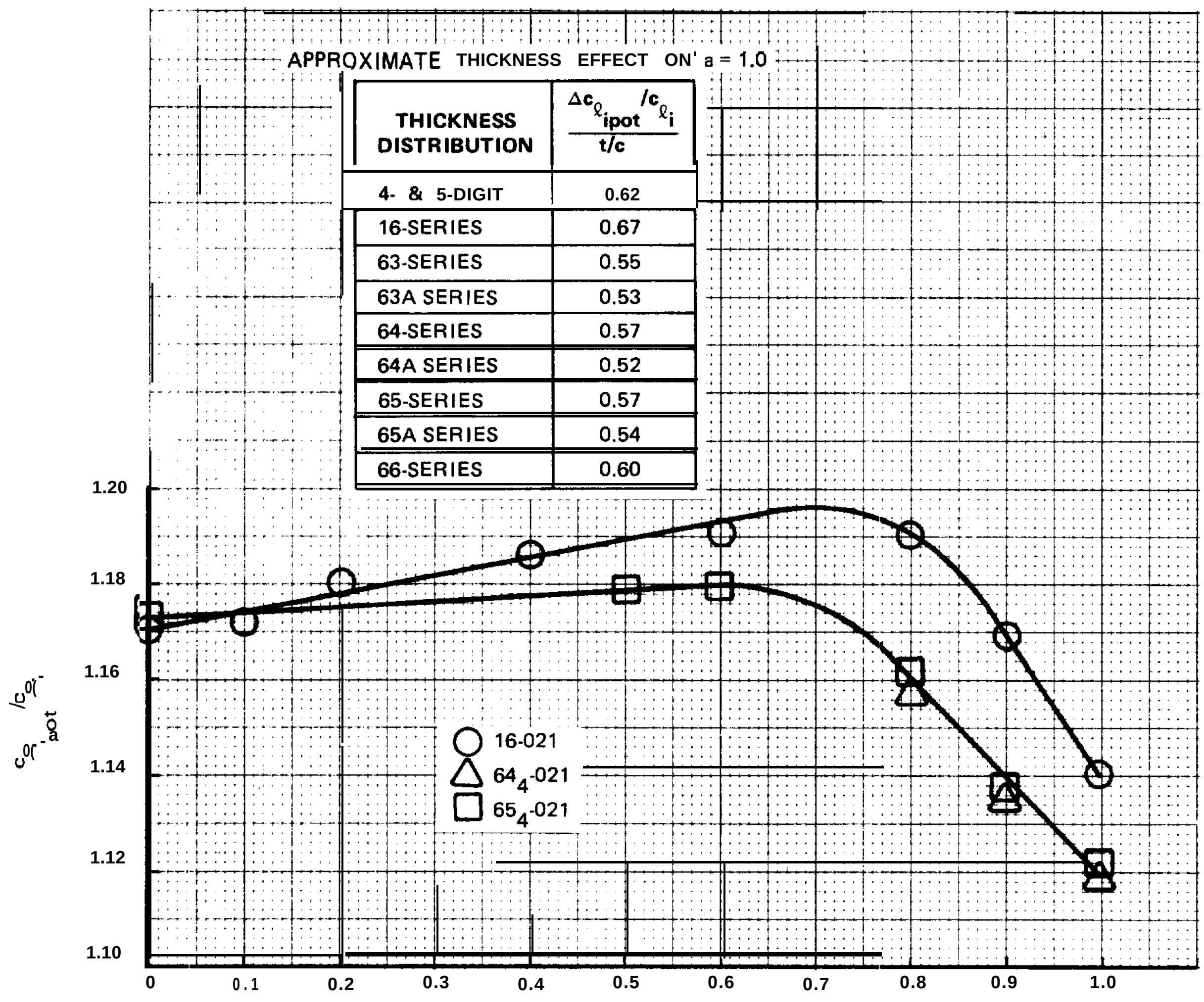

THICKNESS DISTRIBUTION	$\frac{\Delta c_{\ell_{ipot}} / c_{\ell_i}}{t/c}$
4- & 5-DIGIT	0.62
16-SERIES	0.67
63-SERIES	0.55
63A SERIES	0.53
64-SERIES	0.57
64A SERIES	0.52
65-SERIES	0.57
65A SERIES	0.54
66-SERIES	0.60

1892-079B

Fig. 3.3.2.3-l Potential Ideal Lift Coefficient

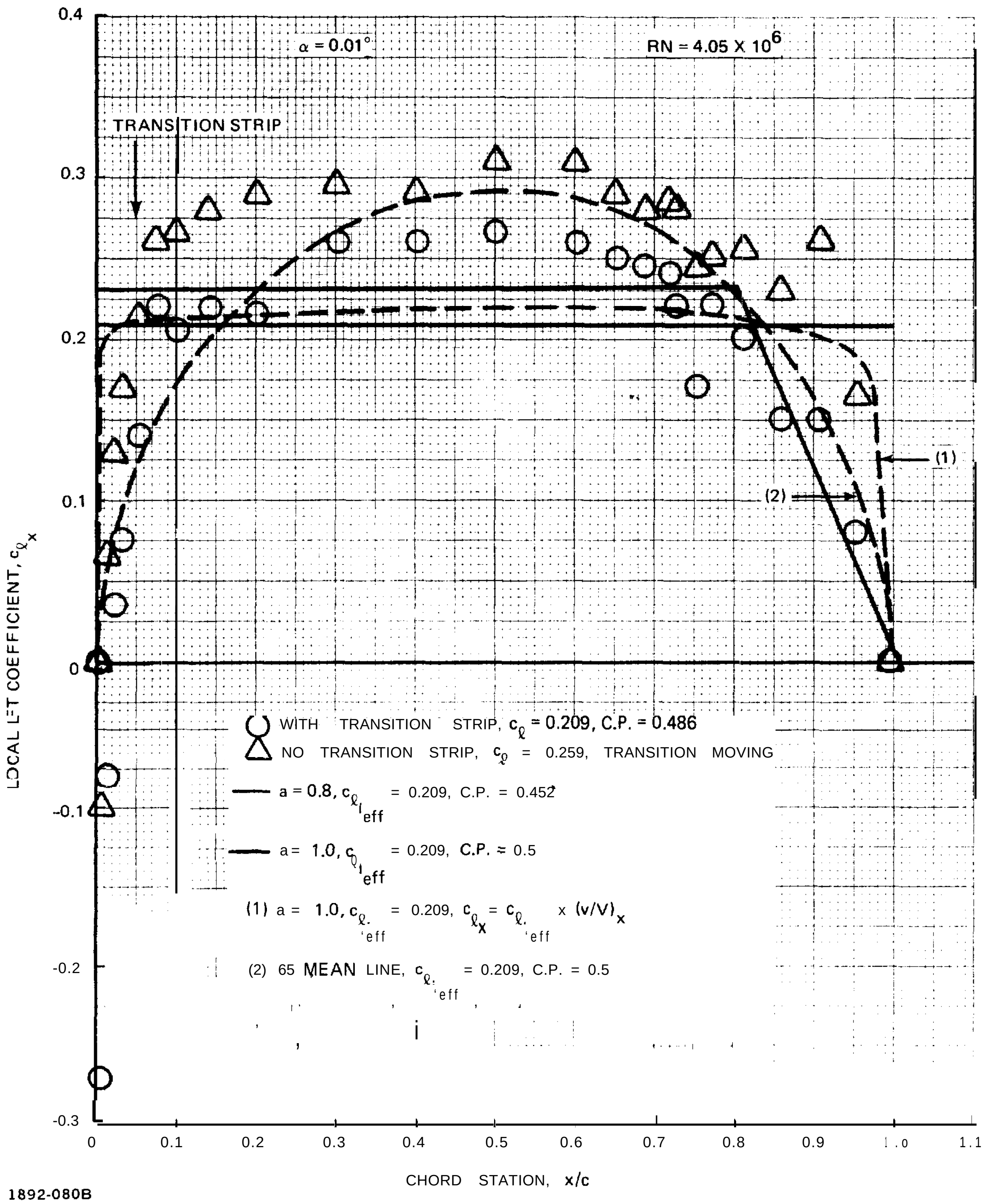

Fig. 3.3.2.3-2 Measured Camber Lift Distribution, 16-309 Section

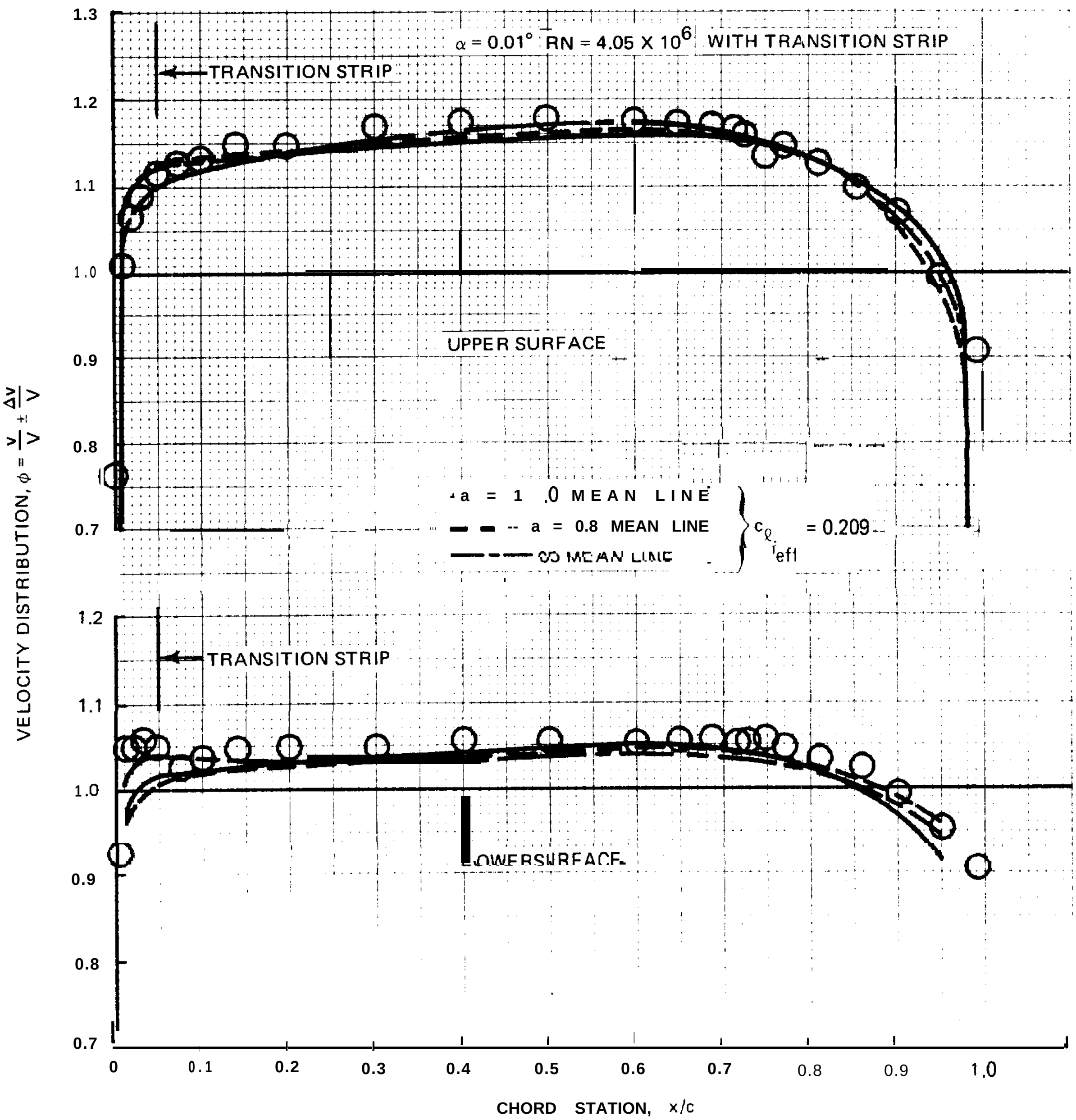

1892-081B

Fig. 3.3.2.3-3 Measured Camber Velocity Distribution, 16-309 Section

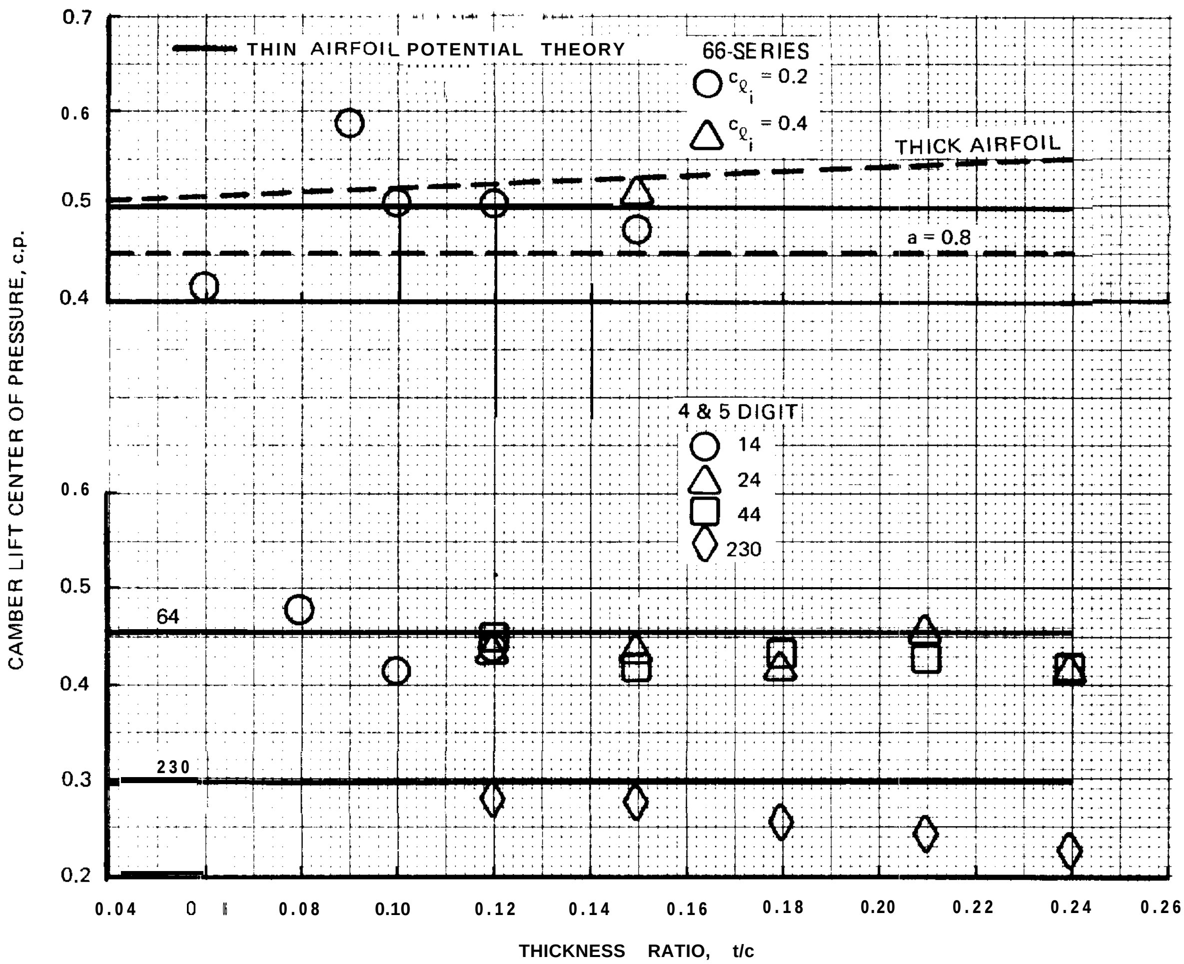

1892-082B

Fig. 3.3.2.3-4 Camber Center of Pressure, 4 & 5 Digit and 66-Series Sections

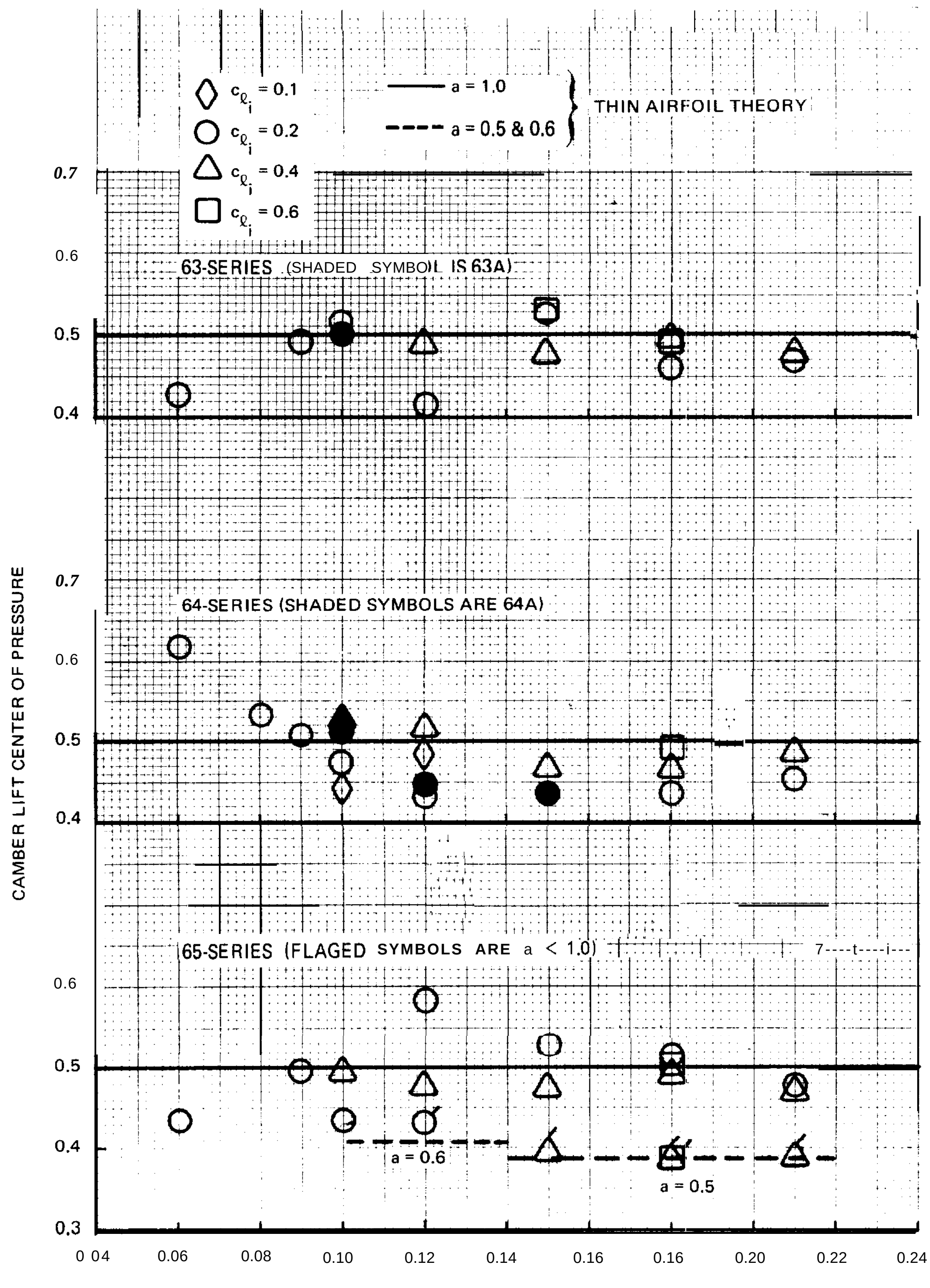

1892-083B

Fig. 3.3.2.3-5 Camber Center of Pressure, 6-Series Sections

3.3.2.4 Flap Lift Distribution.

3.3.2.4.1 Flap Basic/Total Lift Ratio. Equations 3.3.1.5.1-3 and -4 provide the thin airfoil potential theory flap lift distribution parameter, ζ:

$$\zeta = \frac{(c_{\ell_b})_\delta}{(c_\ell)_\delta} = \sqrt{\frac{h}{c}\left(1 - \frac{h}{c}\right)} \Bigg/ \left[\frac{1}{2}\cos^{-1}\left(2\frac{h}{c} - 1\right) + \sqrt{\frac{h}{c}\left(1 - \frac{h}{c}\right)}\right] \qquad 3.3.2.4\text{-}1$$

which is presented on Figure 3.3.2.4-l.

No viscous effect can be offered for this parameter. Allen offers an analytic procedure for deriving ζ from measured lift and moment data in Reference 1 but if such measurements are made in model scale no basis exists for their interpretation for **full** scale hydrofoil Reynolds Numbers.

REFERENCES

1. **Allen,** H. Julian: Calculation of the Chordwise Load Distribution Over Airfoil Sections With Plain, Split, or Serially Hinged Trailing-Edge Flaps, NACA Report No. **634, 1938.**

3.3.2.4.2 Flap Basic Lift Distribution. The thin airfoil potential flap basic lift distribution is given by Equation (A-19) of Reference 1 which may be written:

$$\frac{\left(c_{\ell_{xb}}\right)_\delta}{\left(c_{\ell_b}\right)_\delta} = \frac{1}{\pi\sqrt{\frac{h}{c}\left(1 - \frac{h}{c}\right)}} \ln \frac{\left(\sqrt{\frac{h}{c}}\sqrt{1 - \frac{x}{c}} + \sqrt{1 - \frac{h}{c}}\sqrt{\frac{x}{c}}\right)^2}{\left|\frac{h}{c} - \frac{x}{c}\right|} \qquad 3.3.2.4\text{-}2$$

which is presented numerically in Table 3.3.2.4-I and graphically on Figure 3.3.2.4-2 for flap chord ratios of 10, 20, and 30% as illustrations. No potential theory thickness effect, can be offered for this distribution.

Viscous effect redistributes the flap basic lift. In Reference 1 Allen performs this redistribution in terms of the **emperically** determined β function:

$$\beta = \left(\frac{c_{\ell_{xb}}}{c_{\ell_b}}\right)_{\text{exp}} \Bigg/ \left(\frac{c_{\ell_{xb}}}{c_{\ell_b}}\right)_{\textbf{thin airfoil theory}} \qquad 3.3.2.4\text{-}3$$

Allen does not **explicitely** define the β function but it has been numerically evaluated from Table III of Reference 1 with the result for flap angles of hydrodynamic interest shown on Figure 3.3.2.4-3.

Allen hypothesizes the limitation of the viscous effect to the flap chord. The β function is a closed curve, that is its value vanishes at the flap leading and trailing edges, end encloses zero area when plotted in absolute terms. The similarity between the β function and the Pinkerton and Pope Pa, functions will be noted and, in fact, Allen proposes employing the β function as for a full chord flap to perform the viscous redistribution of the section basic lift; thus the necessity for no viscous effect on the **forebody** of Figure 3.3.2.4-3.

For flap angles greater than **15°** Allen makes the β function dependent on. flap angle as shown on Figure 3.3.2.4-4. Only the 15" and 20" flap angles of Figure 3.3.2.4-4 have **any** possible hydrodynamic significance.

Allen's basic flap lift distributions are found in Table III of Reference 1 where the nomenclature is related to that of this note by:

$$\frac{P_{b\delta}}{c_{n_{b\delta}}} = \left(\frac{c_{\ell_{xb}}}{c_{\ell_b}}\right)_\delta = 4\left|\left(\frac{\Delta v}{V}\right)_F\right| \Big/ c_{\ell_{b\delta}} \qquad 3.3.2.4\text{-}4$$

Reference 1 is no longer readily available and Allen's chord stations differ from those of Reference 2. The distribution of Reference 1 is adequately described, however, by referencing the β function of Figure 3.3.2.4-3 to the thin airfoil theory distribution. For reference purposes the β function is tabulated in Table 3.3.2.4-11 which also includes Allen's hinge line local lift coefficients. Allen's distribution is illustrated on Figure 3.3.2.4-5 which also displays his hinge line local lift coefficient variation with flap chord ratio.

EXPERIENCE

Analysis of flap lift pressure distribution data is particularly time-consuming and the experience which can be offered here is quite limited. Reference 3 includes pressure measurements for the test conditions of Figure 3.3.2.3-2 with a 6" flap angle with transition strip and with 10" and 15" flap angles without transition strip. By subtracting the unflapped local velocities from the flapped local velocities the flap lift velocity and lift distributions can be displayed.

The lift distribution was derived from the incremental velocity distributions from the relationship:

$$c_{\ell_x} = \left(\frac{v}{V}\right)^2_{\delta_u} - \left(\frac{v}{V}\right)^2_{\delta_\ell} \qquad 3.3.2.4\text{-}5$$

$$= \left[1 + \left(\frac{\Delta v}{V}\right)_{\delta_u}\right]^2 - \left[1 - \left(\frac{\Delta v}{V}\right)_{\delta_\ell}\right]^2$$

$$= 2\left[\left(\frac{\Delta v}{V}\right)_{\delta_u} + \left(\frac{\Delta v}{V}\right)_{\delta_\ell}\right] + \left(\frac{\Delta v}{V}\right)^2_{\delta_u} - \left(\frac{\Delta v}{V}\right)^2_{\delta_\ell}$$

It must be noted that Volume III of Reference 3, which contains the tabulated data, was not -available to this study which was taken from the plotted data of Volume I. The plotted data presents unfortunate difficulties, particularly in the vicinity of the hinge.

The measured lift distributions of Figure 3.3.2.4-6 are significant to section pitching moment and flap hinge moment. The velocity distributions of Figures 3.3.2.4-7 through -9 examine the theoretical equivalence of the upper and lower surface incremental velocities and are significant to the cavitation boundaries. These measurements are encouraging for the forebody but indicate substantially lower flap lift flap hinge moment than potential theory would indicate. It is quite evident that Allen's redistribution of the flap lift cannot be tested. The data provides no foundation for a modification to the thin airfoil potential theory.

The primary hydrodynamic value of Figures 3.3.2.4-6 through -9 is in their measure of the incremental velocity at the upper surface flap hinge line and the plotted data of Volume I of Reference 3 becomes most uncertain at this point. The data indicates that Allen is optimistic at this point but provides no alternative.

SUMMARY

No alternative can be offered here to the representation of the flap lift distribution by thin airfoil potential theory with Allen's local lift coefficient at the flap hinge line.

LIMITATIONS

Allen's data sample is unspecified. Reference 1 predates the original publication of Reference 2 and Allen's data sample may not include any of the'laminar flow sections of Reference 2. Allen describes the flap hinge gaps as "small". The Reference 3 data indicates that the upper surface hinge velocity increment is 50% larger than Allen's value but that could be a 16-series section peculiarity, a peculiarity of the local model geometry, or a misinterpretation of the plotted data among the other possibilities associated with a limited view of the model test results.

REFERENCES

1. Allen, H. Julian: Calculation of the Chordwise Load Distribution Over Airfoil Sections With Plain, Split, or Serially Hinged Trailing-Edge Flaps. NACA Report No. 634, 1938.
2. Abbott, Ira H. and von Doenhoff, Albert E.: Theory of Wing Sections, Dover, 1959.
3. Teeling, P.: Low Speed Wind Tunnel Tests of A NACA 16-309 Airfoil With Trailing Edge Flap. DeHavilland Aircraft of Canada Limited Report No. ECS 76-3, October, 1976.

TABLE 3.3.2.4-I FLAP BASIC LIFT DISTRIBUTION, THIN AIRFOIL THEORY

$\frac{h}{c} = 0.9$		$\frac{h}{c} = 0.8$		$\frac{h}{c} = 0.7$	
$\frac{x}{c}$	$\frac{c_{\ell_{xb}}}{c_{\ell_b}}$	$\frac{x}{c}$	$\frac{c_{\ell_{xb}}}{c_{\ell_b}}$	$\frac{x}{c}$	$\frac{c_{\ell_{xb}}}{c_{\ell_b}}$
0	0	0	0	0	0
0.025	0.1134	0.025	0.1277	0.025	0.1462
0.05	0.1626	0.05	0.1834	0.05	0.2102
0.075	0.2020	0.075	0.2281	0.075	0.2620
0.1	0.2368	0.1	0.2678	0.1	0.3081
0.15	0.2991	0.15	0.3393	0.15	0.3921
0.2	0.3570	0.2	0.4065	0.2	0.4721
0.25	0.4135	0.25	0.4729	0.25	0.5525
0.3	0.4706	0.3	0.5409	0.3	0.6365
0.35	0.5298	0.35	0.6125	0.35	0.7272
0.4	0.5925	0.4	0.6899	0.4	0.6286
0.45	0.6603	0.45	0.7760	0.45	0.9460
0.5	0.7355	0.5	0.8742	0.5	1.0883
0.55	0.8206	0.55	0.9905	0.55	1.2718
0.6	0.9199	0.6	1.1343	0.6	1.5331
0.65	1.0399	0.65	1.3237	0.625	1.7212
0.7	1.1918	0.7	1.5998	0.65	1.9898
0.75	1.3973	0.725	1.8023	0.675	2.4570
0.8	1.7077	0.75	2.0960	0.7	
0.825	1.9427	0.775	2.6157	0.725	2.4238
0.85	2.2935	0.8	∞	0.75	1.9231
0.875	2.9376	0.825	2.5408	0.775	1.6201
0.9	∞	0.85	1.9445	0.8	1.3964
0.925	2.6985	0.875	1.5703	0.85	1.0573
0.95	1.7923	0.9	1.2807	0.9	0.7802
0.975	1.1109	0.95	0.7891	0.95	0.5084
1	0	1	0	1	0

1892-084B

TABLE 3.3.2.4-II ALLEN'S FLAP BASIC LIFT DISTRIBUTION

FLAP CHORD STATION x_f/c_f	$\beta = \frac{(c_{\ell_{xb}}/c_{\ell_b})_{ALLEN}}{(c_{\ell_{xb}}/c_{\ell_b})_{pot}}$ $\delta < 15^\circ$	$\delta = 20^\circ$	FLAP CHORD RATIO c_f/c	HINGE $\frac{c_{\ell_{xb}}}{c_{\ell_b}}$ $\delta < 15^\circ$	$\delta = 20^\circ$
0.1	1.23	0.96	0.05	8.75	5.83
0.2	1.20	1.03	0.10	6.04	4.05
0.3	1.11	1.06	0.15	4.89	3.38
0.4	1.04	1.12	0.20	4.40	3.02
0.5	0.96	1.17	0.25	4.01	2.83
0.6	0.88	1.24	0.30	3.71	2.70
0.7	0.80	1.31	0.35	3.50	2.63
0.8	0.66	1.39	0.40	3.35	2.58
0.9	0.51	1.47	0.45	3.23	2.56
0.95	0.40	1.56	0.50	3.16	2.56
			0.55	3.11	2.58
			0.60	3.06	2.62
			0.65	3.04	
			0.70	3.02	

NOTES: 1. ALLEN'S $(c_{\ell_{xb}}/c_{\ell_b})_\delta$ IS THIN AIRFOIL POTENTIAL THEORY, EQUATION 3.3.2.4-2, ON FOREBODY.

2. $x/c = \frac{h}{c} + \frac{c_f}{c}\frac{x_f}{c_f}$

1892-085B

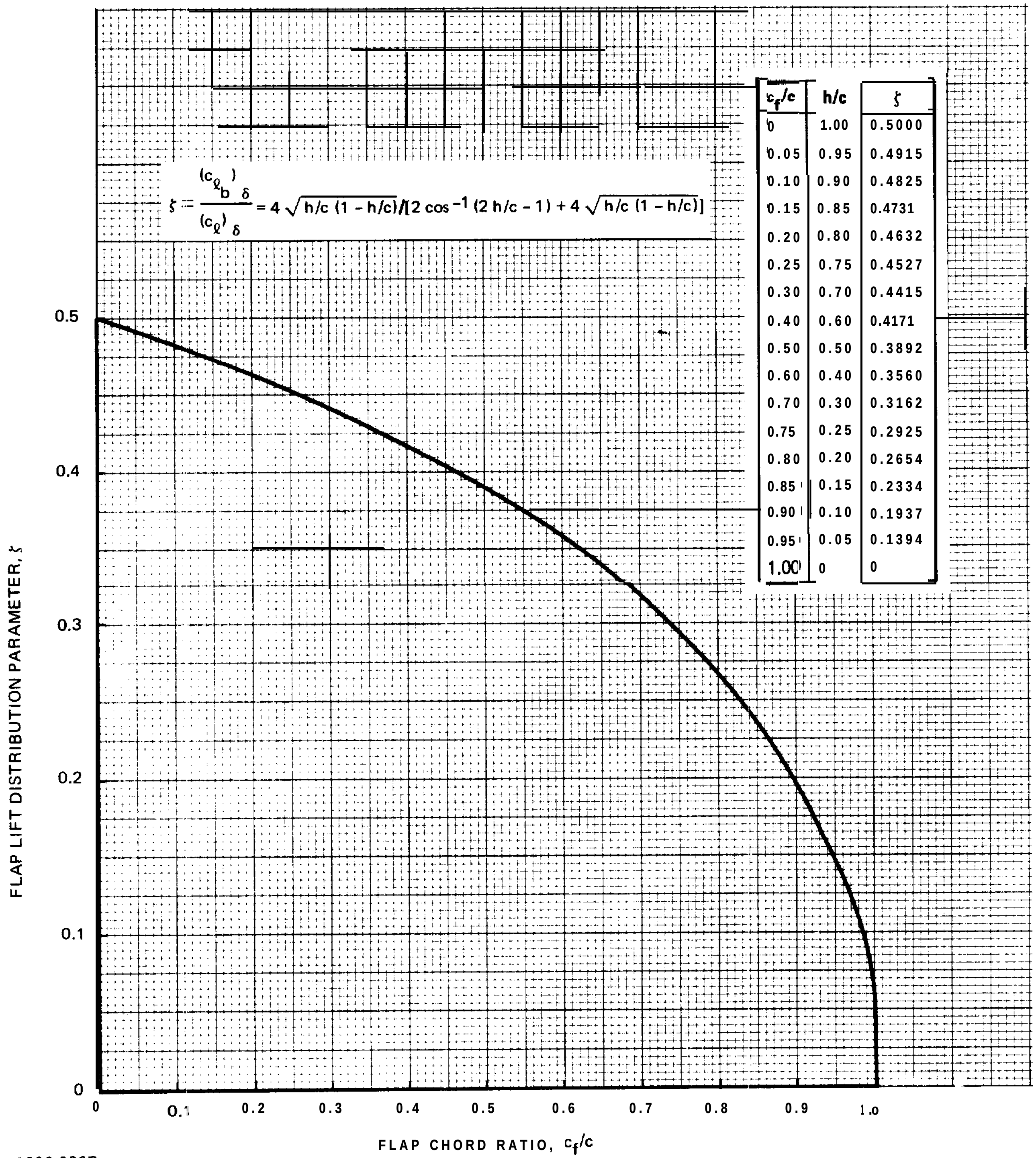

$$\zeta = \frac{(c_{\ell_b})_\delta}{(c_\ell)_\delta} = 4\sqrt{h/c\,(1 - h/c)}\Big/\left[2\cos^{-1}(2\,h/c - 1) + 4\sqrt{h/c\,(1 - h/c)}\right]$$

c_f/c	h/c	ζ
0	1.00	0.5000
0.05	0.95	0.4915
0.10	0.90	0.4825
0.15	0.85	0.4731
0.20	0.80	0.4632
0.25	0.75	0.4527
0.30	0.70	0.4415
0.40	0.60	0.4171
0.50	0.50	0.3892
0.60	0.40	0.3560
0.70	0.30	0.3162
0.75	0.25	0.2925
0.80	0.20	0.2654
0.85	0.15	0.2334
0.90	0.10	0.1937
0.95	0.05	0.1394
1.00	0	0

1892-086B

Fig. 3.3.2.4-I Flap Lift Distribution Parameter, ζ

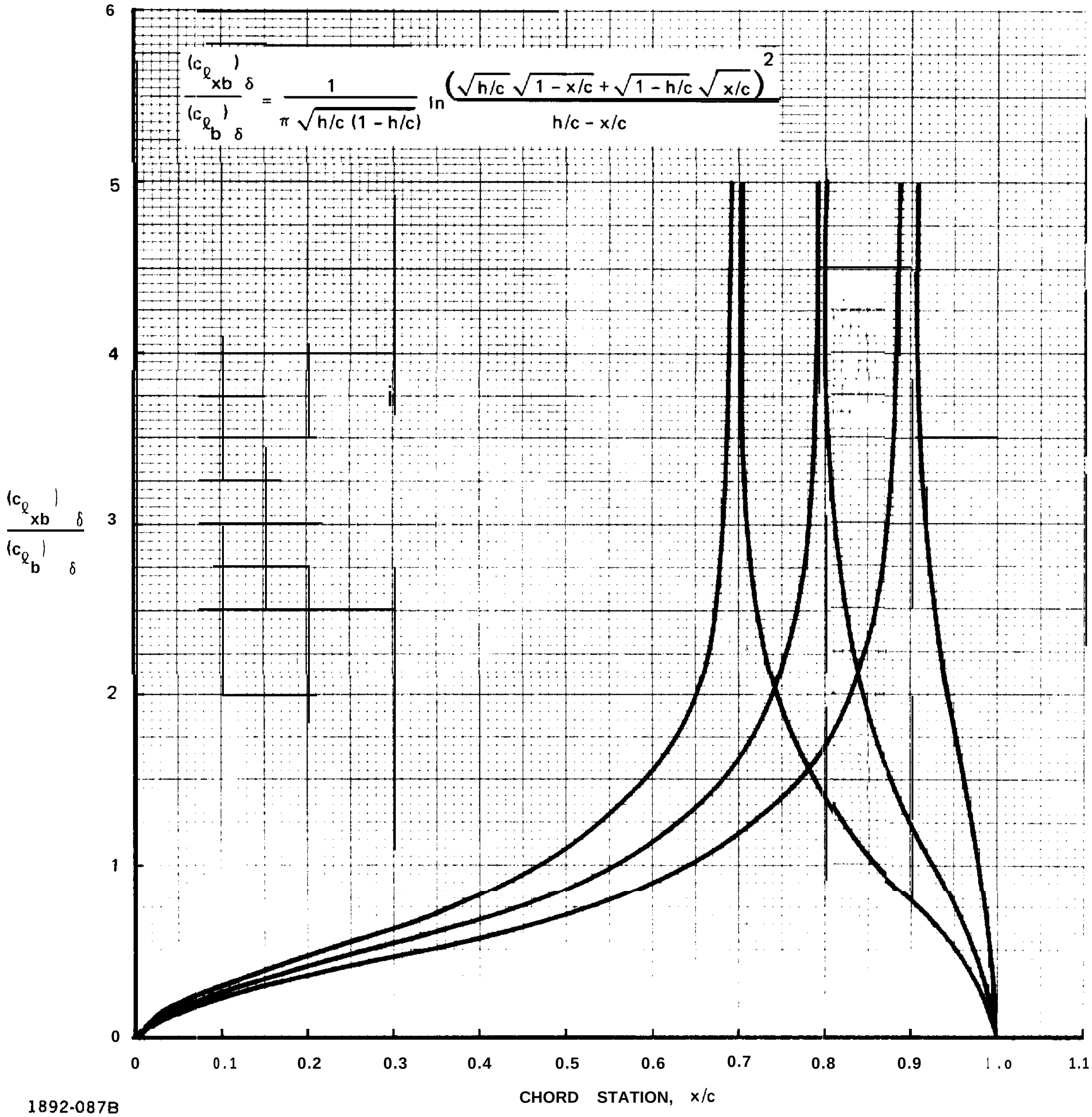

Fig. 3.3.2.4-2 Flap Basic Lift Distributions, Thin Airfoil Theory

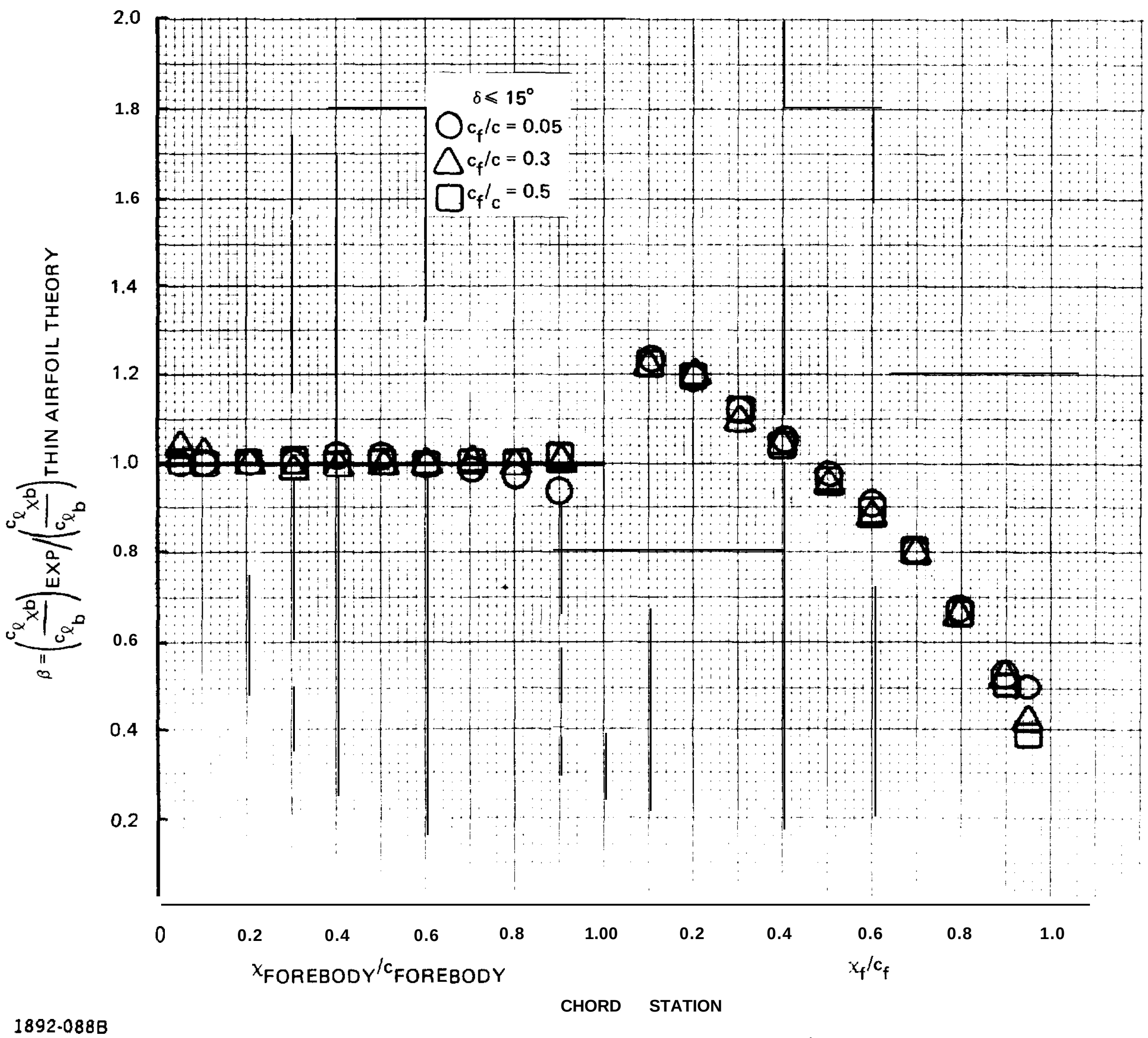

Fig. 3.3.2.4-3 Allen's Function, β

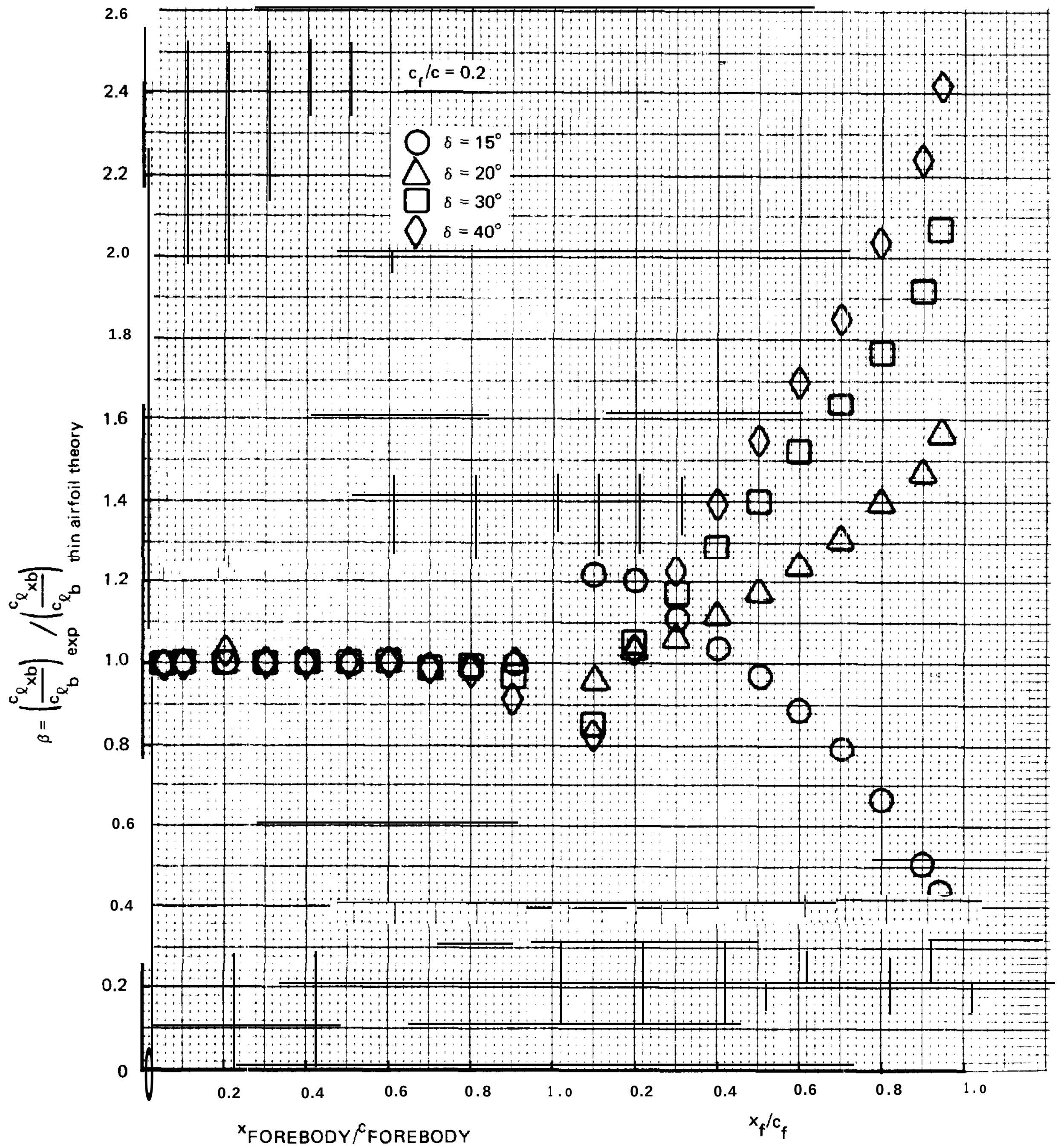

1892-089B

Fig. 3.3.2.4-4 Alien's Function, β

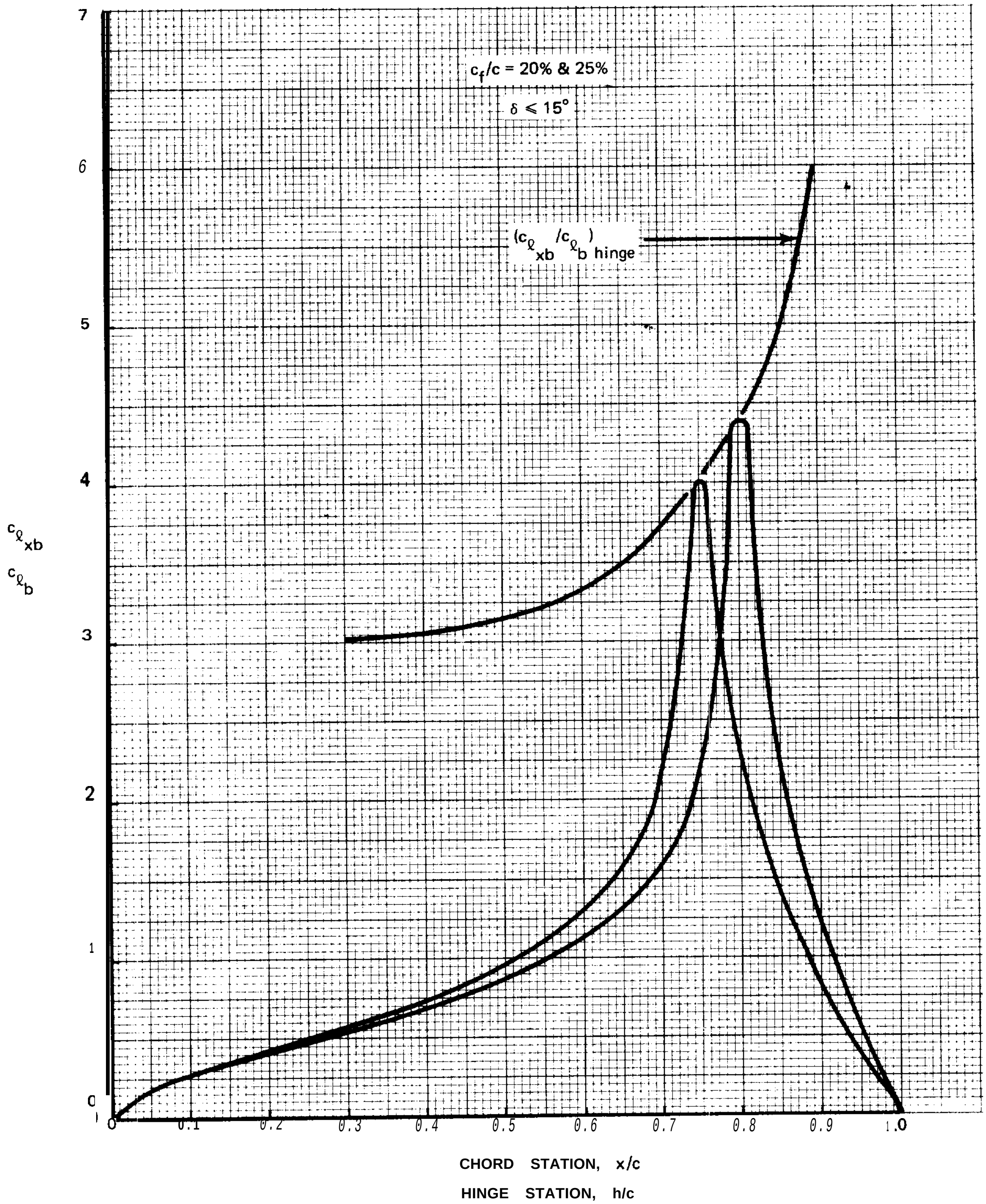

1892-090B

Fig. 3.3.2.4-5 Allen's Flap Basic Lift Distribution

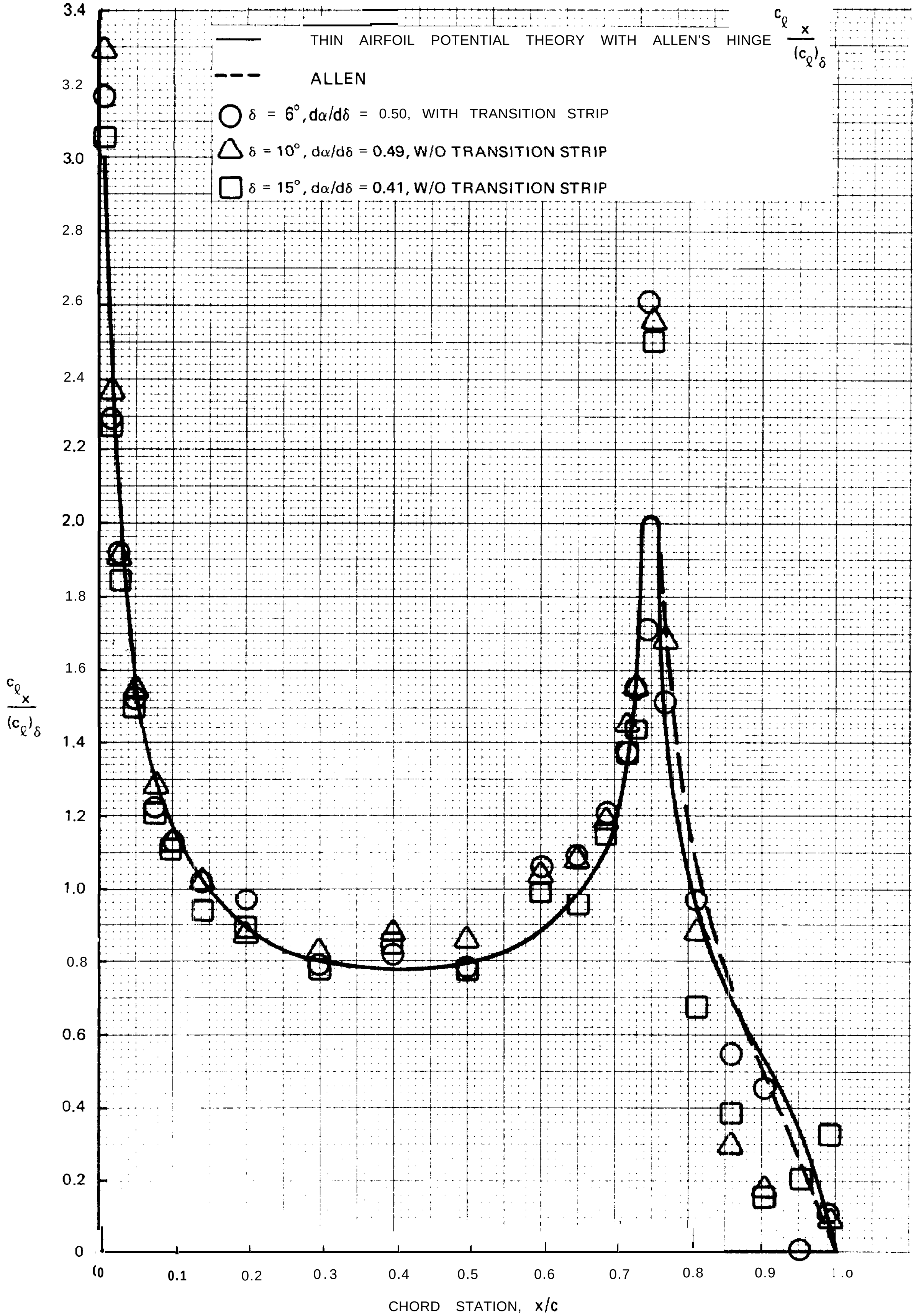

1892091B

Fig. 3.3.2.4-6 Flap Lift Distribution, 16-309 Section, 25% Chord Flap, RN = 4.05 X 10^6

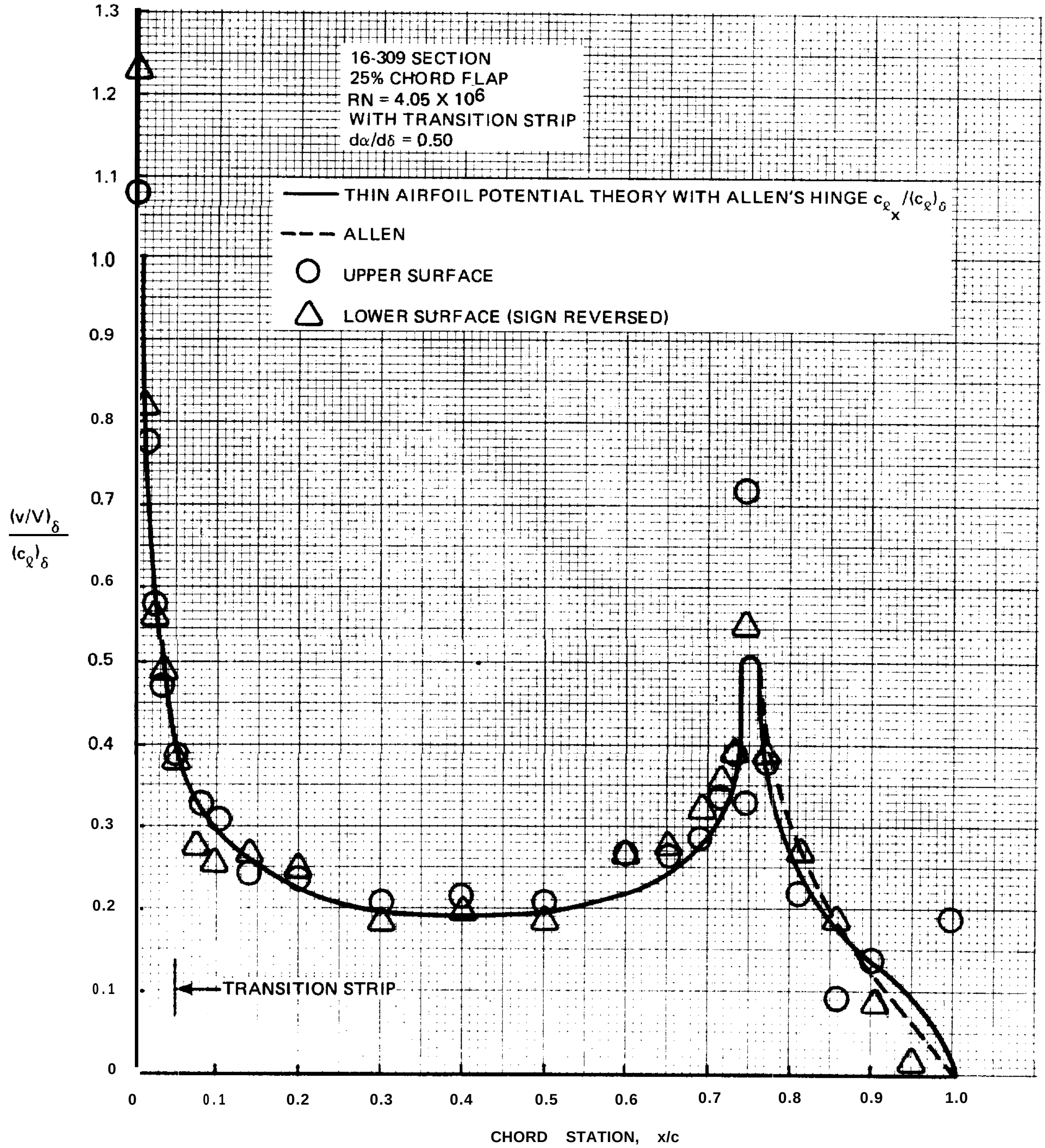

1892-092B

Fig. 3.3.2.4-7 Flap Lift Velocity Distribution, δ = 6°

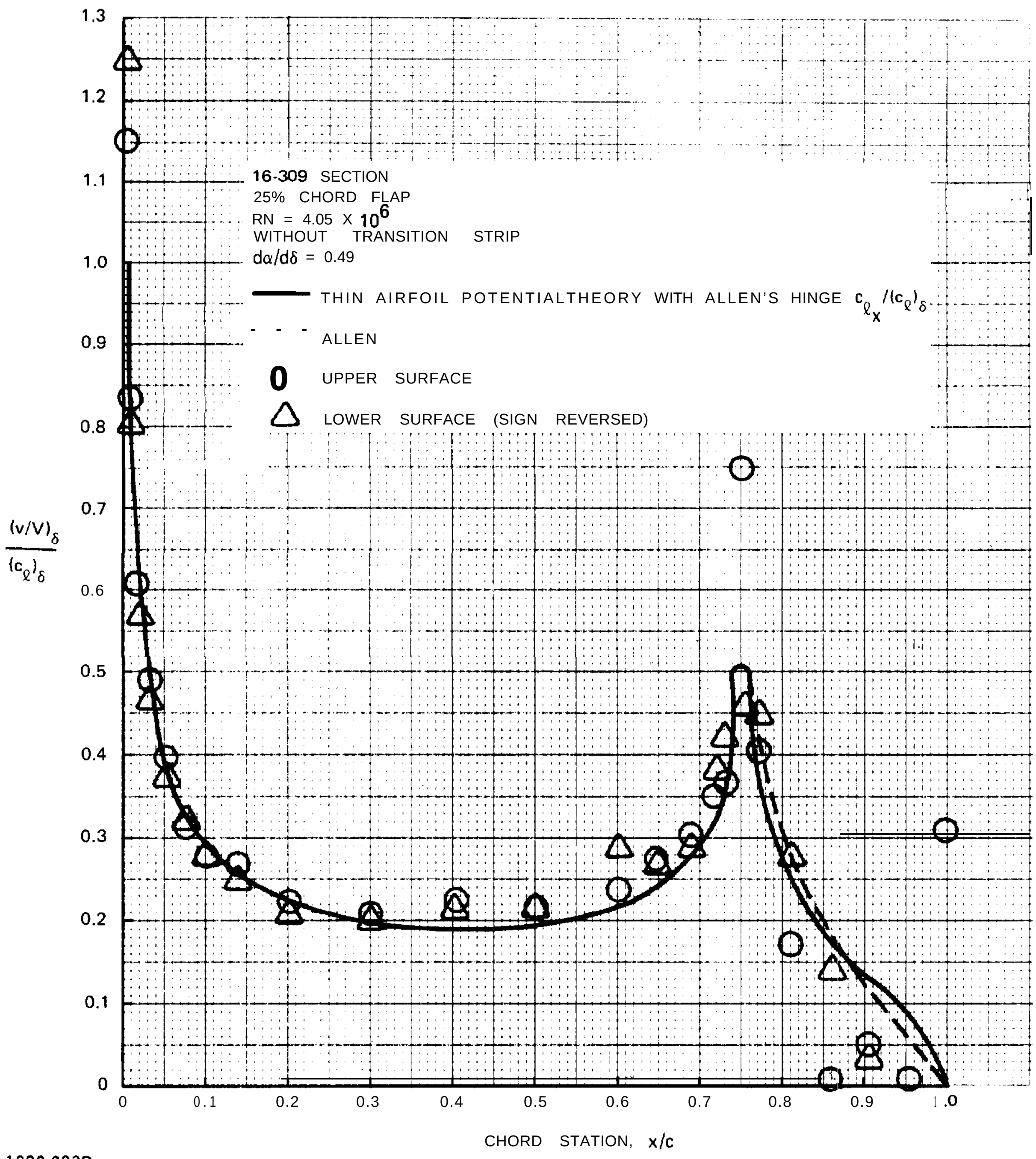

Fig. 3.3.2.4-S Flap Lift Velocity Distribution, $\delta = 10°$

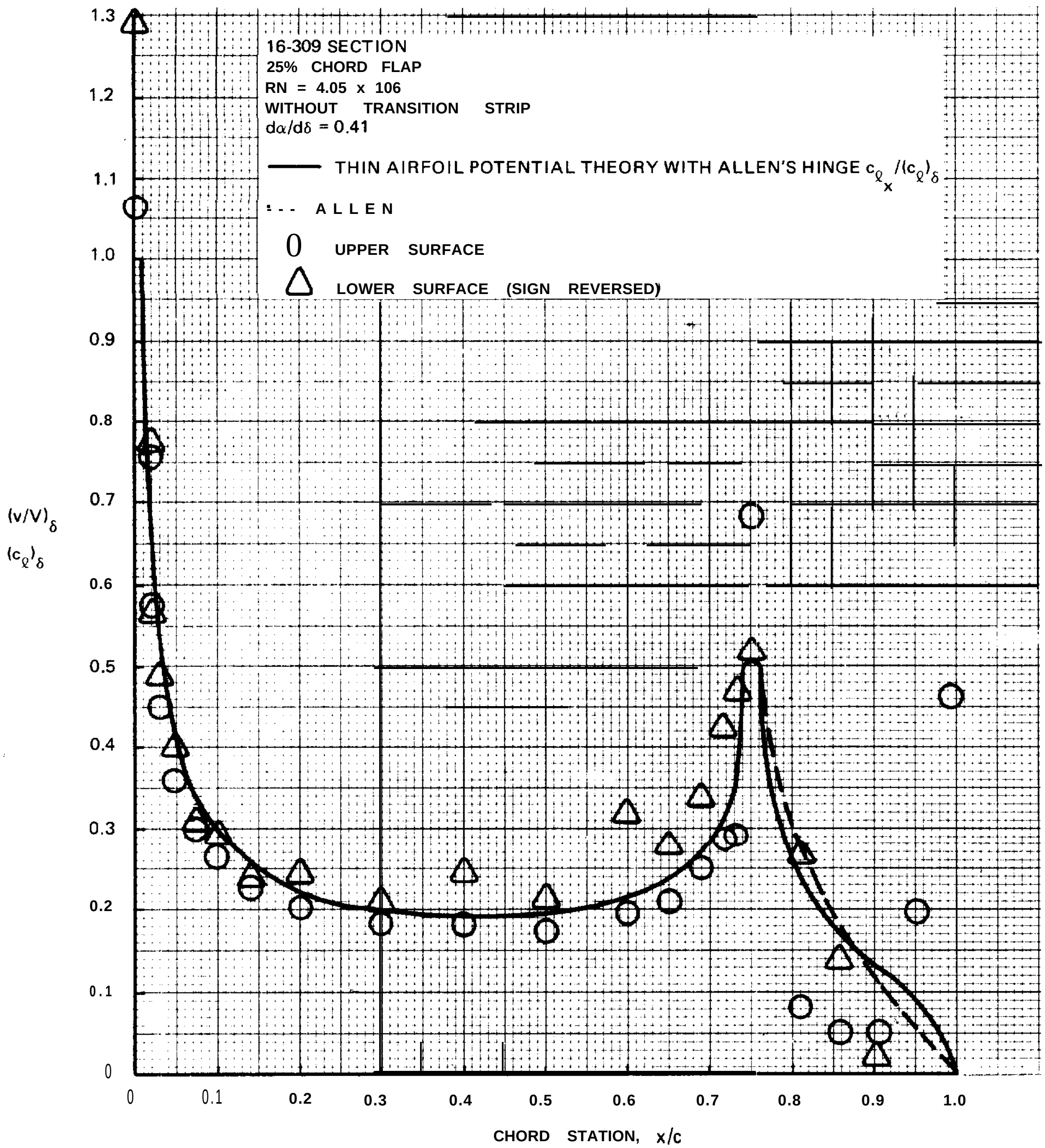

1892-094B

Fig. 3.3.2.4-9 Flap Lift Velocity Distribution, $\delta = 15^\circ$

3.3.3 Section Pitching Moment.

3.3.3.1 Section Pitching Moment. Section pitching moment has a notorious confidence level. Aircraft practice depends heavily upon model tests for this characteristic but can conduct such tests at effectively full scale Reynolds Number. Hydrodynamic full scale Reynolds Numbers are **not** available in the laboratory, where much model testing is deep in the critical Reynolds Number range. No hydrodynamic theory/model/prototype agreement is yet available for this characteristic.

Section pitching moment precision is not important to the flap lift control where the center of pressure location precision is referenced to the foil base. It is of vital importance to incidence lift control systems where the center of pressure is referenced to the foil chord for control system design. Incidence lift control loads and power requirements are heavily penalized, typically nearly doubled, by hinging the foil at one extreme of the confidence level to avoid cross-over and designing to the other extreme to insure structural integrity.

By definition the section aerodynamic center, a.c., is that chord station for which the pitching moment coefficient is constant. It follows from that definition that there is another chord station, the center of pressure **(c.p.),** for which the pitching moment vanishes:

$$\text{c.p.} = \text{a.c.} - \frac{c_{m_{ac}}}{c_\ell} \qquad 3.3.3.1\text{-}1$$

Equation 3.3.3.1-1 defines two distinct views of the section pitching moment:

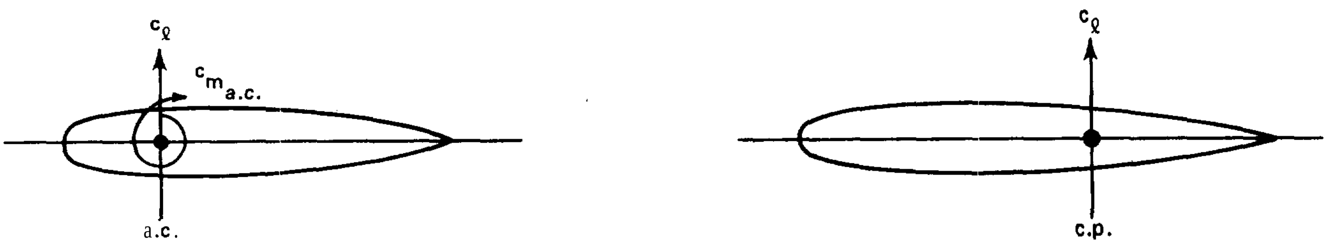

1892-096B

Of these two views the a.c. - $c_{m_{ac}}$ form is basic, being defined in terms of section characteristics; the center of pressure is a derived function of the operating conditions. The center of pressure is useful to certain particular analyses , as in Section 3.3.2.3, but is subject to misinterpretation. The a.c. - $c_{m_{ac}}$ format has more convenience generally and is the format employed here to describe the section pitching **moment.**

The aerodynamic centers for the sections of Reference 1 are summarized on Figure 3.3.2.1-10 which is included in this section of the specification volume to define the aerodynamic center for those sections.

Figures 3.3.2.1-5 through -9 display the confidence level for the curves employed, and that confidence level is presented statistically in Table 3.3.3.1-I. Initial estimates for the aerodynamic centers for sections not included in Reference 1 could be taken from a section of similar thickness distribution in Figure 3.3.2.1-10 or from a numerical analysis which produces the results of that figure. Wind tunnel confirmation of such estimates at an early design phase is essential to costly incidence lift control system projects until the confidence level is improved, more for the moment about the aerodynamic center than for the aerodynamic center.

The moment coefficient about the aerodynamic center is given by:

$$c_{m_{ac}} = - c_{\ell_{i_{eff}}} (c.p._c - a.c.) \qquad 3.3.3.1\text{-}2$$

The measured camber lift centers of pressure, $c.p._c$, for the sections of Reference 1 are shown on Figures 3.3.2.3-4 and -5 where the data scatter introduces about a 20% uncertainty into the moment arm of Equation 3.3.3.1-2. To minimize and define this uncertainty for the a = 1.0 mean line the centers of pressure of Figures 3.3.2.3-4 were rederived for themeasured $c_{m_{ac}}$'s and the predicted $c_{\ell_{i_{eff}}}$'s and aerodynamic centers of Equation 3.3.1.4-7 and Figure 3.3.2.1-10 respectively. The result, shown on Figure 3.3.3.1-1 shows those centers of pressures which must be employed with the previously established $c_{\ell_{i_{eff}}}$ and a.c. predictions, which are presumably smoothed observations, to produce the observed $c_{m_{ac}}$.

Section 3.3.2.3 notes that the thin airfoil a = 1.0 camber lift distribution is highly idealized and is frequently approximated by the a = .8 camber lift distribution. Figure 3.3.3.11-1 indicates that the a = .8 mean line center of pressure lies more than one standard deviation forward of the mean value for the measurements and would introduce a bias of about 15% into the $c_{m_{ac}}$ prediction. Therefore, on Figure 3.3.3.1-1 the a = .94 mean line lift distribution was selected to represent the a. = 1.0 mean line as specified in Section 3.3.2.3 of the Specification Volume.

In fact it is probable that the a = .8 mean line is more representative of the trailing edge lift distribution than is the a = .94 mean line but that there is also a significant reduction of lift at the leading edge (see Figure 3.3.2.3-2). Such refinements exceed the scope of this volume which is limited to attempting to provide consistent a.c., c.p., $c_{\ell_{i_{eff}}}$, and $c_{m_{ac}}$ predictions.

For the predicted $c_{\ell_{i_{eff}}}$ and a.c. and for the thin airfoil or a = .94 mean line center of pressure, as appropriate, the measured and predicted $c_{m_{ac}}$'s are compared on Figures 3.3.3.1-2 and -3 and in Table 3.3.3.1-11. The 4- and 5-digit correlations indicate a lift center of pressure forward of thin airfoil theory just as for the a = 1.0 mean line but are left unadjusted because only one mean line of each series is represented and because no measured pressure distributions can be offered.

Table 3.3.3.1-11 and Figures 3.3.3.1-2 and -3 may be summarized by:

$$c_{m_{ac}} = - c_{\ell_{i_{eff}}} (c.p._c - a.c.) + \sigma \qquad 3.3.3.1\text{-}2$$

where: $c_{\ell_{i_{eff}}}$ is from Equation 3.3.1.4-7

a.c. is from Figure 3.3.2.1-10

$c.p._c$ is the thin airfoil potential theory value except for a $\geqslant .94$ mean lines for which it is .485

σ = 0 to .012 for 4 digit sections

= .006 to .020 for 5 digit sections

= ± .006 for all other sections

LIMITATIONS

The standard deviation of Equation 3.3.3.1-2 is only 10% of the typical hydrofoil moment coefficient, but the sample is scarcely adequate for any of the mean line families represented. The heavy empirical content of the equation is a measure of the inability to define adequately the distribution of the camber lift, particularly at the trailing edge. A consequence in the prediction of the residual flap hinge moment is to be expected.

The 230 mean line result of Figure 3.3.3.1-2 is of particular interest. In theory this mean line would substantially reduce incidence lift control moments and the figure indicates that the actual reduction might be significantly better than theory. The mechanism by which the 24% section produces lift without moment about the a.c. could have practical significance.'

REFERENCES

1. Abbott, Ira H. and vonDoenhoff, Albert E.: Theory of Wing Sections, Dover, 1959.

In summary, the flap lift flap hinge moment can be defined by:

$$c_{h_{c_{\ell\delta}}} = (1 - \zeta)\, c_{h_{c_{\ell\alpha}}} + \zeta\, c_{h_{c_{\ell b\delta}}} + \Delta\, c_{h_{c_{\ell\delta}}} \qquad 3.3.4.3\text{-}10$$

where: ζ is from Equation 3.3.2.4-1

$c_{h_{c_{\ell\alpha}}}$ is from Equation 3.3.4.2-11

$$c_{h_{c_{\ell b\delta}}} = c_{h_{c_{\ell b\delta 0}}} + .1557\,\frac{t/c}{c_f/c}$$

$c_{h_{c_{\ell b\delta 0}}}$ is from Table 3.3.4.2-I or Figure 3.3.4.3-1

$\Delta\, c_{h_{c_{\ell\delta}}} = .0055\, \Delta\phi^{\circ}$

$\Delta\phi$ = trailing edge bevel angle - $\phi_{5\%}$

Nominal accuracy is ± .02 for the true contour flap and ± .04 for the beveled trailing edge flap.

LIMITATIONS

As for $c_{h_{c_{\ell\alpha}}}$, neglect of the thickness distribution in the derivation of $c_{h_{c_{\ell\delta}}}$ is questionable, particularly for the 16-series section. The thick airfoil potential aerodynamic center is available only for the 66-series section of the 6-series family. No data for any typical hydrofoil section can be offered.

REFERENCES

1. Theodorsen, T.: General Theory of Aerodynamic Instability and the Mechanism of Flutter. NACA Report 496, 1935. Currently available in AIAA Selected Reprints, "Aerodynamic Flutter", I.E., Garrick, Editor, March 1969.

2. Toll, Thomas, A.: Summary of Lateral-Control Research. NACA Report No. 868, 1947.

3. Allen, H. Julian: Calculation of the Chordwise Load Distribution Over Airfoil Sections with Plain, Split, or Serially Hinged Trailing-Edge Flaps. NACA Report No. 634, 1938.

TABLE 3.3.3.1-II $c_{m_{a_c}}$ STATISTICAL ANALYSIS

SECTION	MEAN LINE	NUMBER IN SAMPLE N	MEAN $\Delta c_{m_{a_c}}$ (1)	$\Delta c_{m_{a_c}}$ STD DEVIATION
16-SERIES	a = 1.0	SEE NOTE 2		
63-SERIES	a = 1.0	13	-0.0003	0.0031
64-SERIES	a = 1.0	16	-0.0003	0.0052
65-SERIES	a = 1.0	13	-0.0002	0.0044
66-SERIES	a = 1.0	06	-0.0003	0.0046
4 DIGIT	64	13	0.0059	0.0059
5 DIGIT	230	05	0.0129	0.0068
a = 1.0		48	-0.0003	0.0042
4 & 5 DIGIT		18	0.0078	0.0068
STANDARD SECTIONS		66	0.0019	0.0062
6 X A SERIES				
63A SERIES	a = 1.0	01	0.0038	—
64A SERIES	a = 1.0	04	-0.0010	0.0022
6 x A SERIES		05	0	0.0028
a < 1.0				
65-SERIES	a = 0.5(4), 0.6	05	-0.0029	0.0019
TOTAL EXPERIENCE				
ALL EXCEPT 5 DIGIT SECTIONS		71	0.0007	0.0050
ALL SECTIONS		76	0.0015	0.0059

NOTES: 1. $\Delta c_{m_{a_c}}$ = MEASURED $c_{m_{a_c}}$ − PREDICTED $c_{m_{a_c}}$

2. NO APPROPRIATE DATA SAMPLE AVAILABLE

1892-098B

ESDU/DATCOM

The ESDU/DATCOM procedure is numerical and contained in ESDU controls 01.01.03, 04.01.01, and 04.01.02. The ESDU procedure is modified here to the extent that the $c_{\ell_\alpha}/c_{\ell_{\alpha_{pot}}}$ of Equation 3.3.1.2-9 and the $\phi_{5\%}$ of Table 6.1.1.2-I were employed. The ESDU/DATCOM hinge moment derivative is compared with Equation 3.3.4.3-7 on Figure 3.3.4.3-3. The comparison is poor; the two procedures differ by twice the ESDU nominal c_{h_δ} accuracy.

TOLL

As for c_{h_α}, Toll's Reference 2 offers the only experimental c_{h_δ} data which can be offered here. Toll's data is presented here in Tables 3.3.4.3-II and -III which are from Figure 13 and Table II of Reference 3. Toll's correlation of Figure 13 of Reference 3 may be written:

$$c_{h_\delta}{}^\circ = -.0105 - .02\frac{c_f}{c} + .0004\,\phi^\circ \qquad 3.3.4.3\text{-}8$$

which is compared with the data on Figure 3.3.4.3-4. The standard deviation for that correlation is twice the nominal accuracy of ESDU and DATCOM. It will be noted that Toll's correlation is almost entirely determined by beveled trailing edge data.

The form of Equation 3.3.4.3-8 and Figure 3.3.4.3-4 is convenient to the comparison of predictions of different form which can only be compared for particular cases. Figure 3.3.4.3-5 relates the ESDU/ DATCOM prediction to Equation 3.3.4.3-7 and to Toll's data by reference to Toll's correlation. Equation 3.3.4.3-7 is better suited to Toll's data than is the ESDU/DATCOM procedure.

ALLEN

Equation (15) of Reference 3 includes Equation 3.3.4.3-7 in a different nomenclature. Allen's η_{a_δ} of his Table X and η_{b_δ} of his Table VIII are the viscous $c_{h_{c\ell\alpha}}$ and $c_{h_{c\ell b\delta}}$, respectively, of this note. It is of interest then to compare them individually with the values of Equation 3.3.4.3-7.

Allen's $c_{h_{c\ell\alpha}}$ is compared with that of Equation 3.3.4.2-11 on Figure 3.3.4.3-6 where it will be noted that Allen has no provision for thickness ratio, neglecting this variable in whatever data sample he had. The very distinctive nature of the 16-series $c_{h_{c\ell\alpha}}$, caused by the extreme viscous aerodynamic center shift for this section, should be noted. Unfortunately, no flap hinge moment test of this characteristic can be offered.

Figure 3.3.4.3-7 compares Allen's $c_{h_{c\ell b\delta}}$ with that of Equation 3.3.4.3-6. The comparison indicates that, as assumed by Equation 3.3.4.3-7, Allen finds no significant viscous effect on this derivative for $\delta \leqslant 15^\circ$.

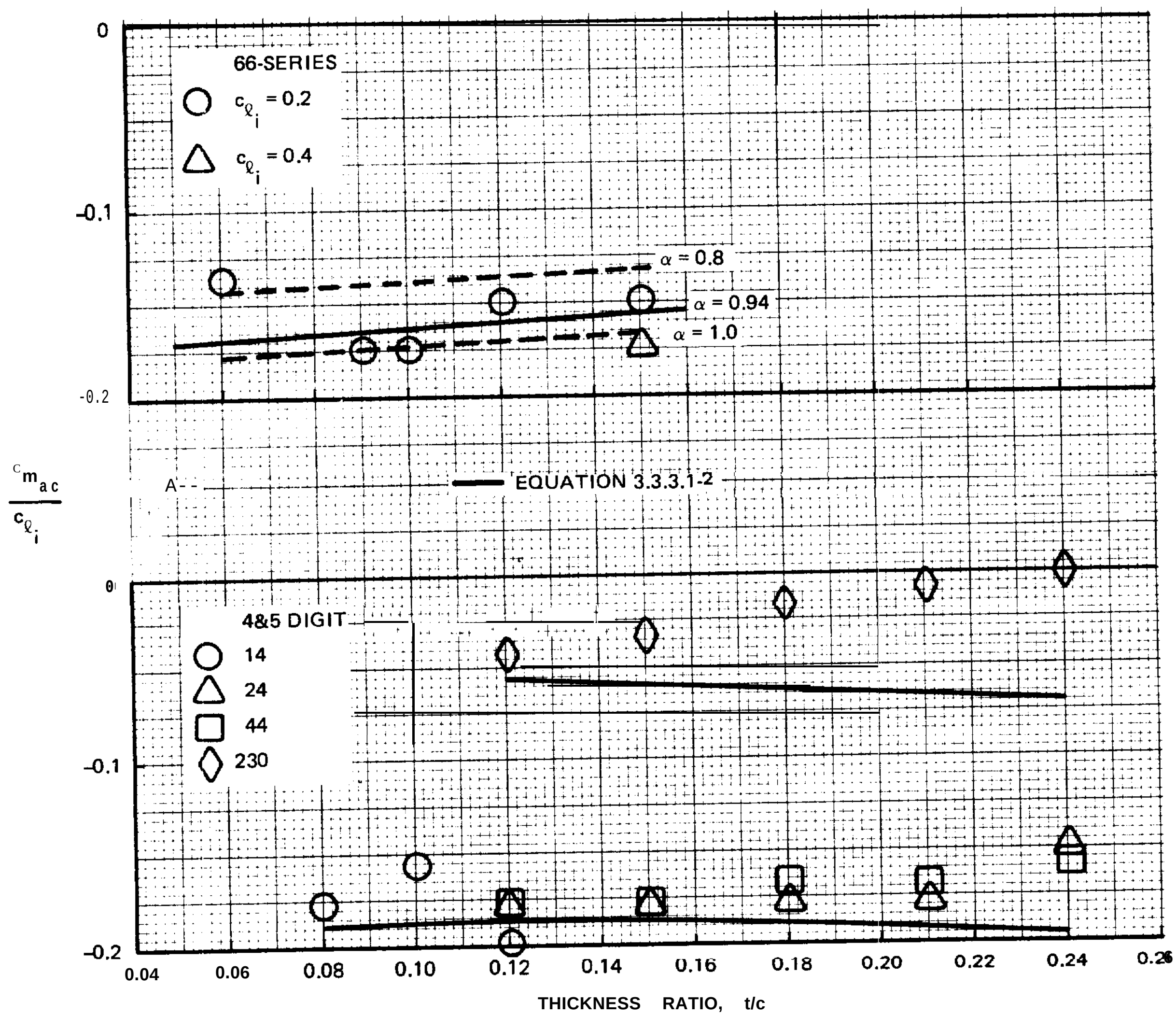

Fig. 3.3.3.1-2 $c_{m_{ac}}$ Correlation, 4&5 Digit and 66-Series Sections

3.3.4.3 Flap Hinge Moment Due to Flap Deflection.

THIN AIRFOIL THEORY

$c_{h_{c_{\ell\delta}}}$ is the centroid for that portion of the lift due to flap deflection which is carried on the flap, normalized by the product of the flap chord and the total lift due to flap deflection and expressed as a fraction of the flap chord. Because a portion of the lift due to flap deflection is of additional lift distribution type, the flap lift flap hinge moment contains a pitch lift flap hinge moment component.

The flap hinge moment coefficient due to flap deflection is given by:

$$(c_h)_\delta = -\left(\frac{c}{c_f}\right)^2 \int_{h/c}^{1} \left(\frac{x}{c} - \frac{h}{c}\right) (c_{\ell_x})_\delta \, d\frac{x}{c} \qquad 3.3.4.3\text{-}1$$

From Section 3.3.2.4 this equation may be written:

$$c_{h_{c_{\ell\delta}}} = (1 - \zeta)\left(\frac{c}{c_f}\right)^2 \int_{h/c}^{1} \left(\frac{h}{c} - \frac{x}{c}\right)\left(\frac{c_{\ell_x}}{c_\ell}\right)_a d\frac{x}{c} + \zeta\left(\frac{c}{c_f}\right)^2 \int_{h/c}^{1} \left(\frac{h}{c} - \frac{x}{c}\right)\left(\frac{c_{\ell_x}}{c_\ell}\right)_{b\delta} d\frac{x}{c} \qquad 3.3.4.3\text{-}2$$

and from Equation 3.3.4.2-1:

$$c_{h_{c_{\ell\delta}}} = (1 - \zeta)\, c_{h_{c_{\ell\alpha}}} + \zeta\left(\frac{c}{c_f}\right)^2 \int_{h/c}^{1} \left(\frac{h}{c} - \frac{x}{c}\right)\left(\frac{c_{\ell_x}}{c_\ell}\right)_{b\delta} d\frac{x}{c} \qquad 3.3.4.3\text{-}3$$

$$= (1 - \zeta)\, c_{h_{c_{\ell\alpha}}} + \delta\, c_{h_{c_{\ell b\delta}}}$$

The basic flap lift distribution, $(c_{\ell_x}/c_\ell)_{b\delta}$, is given by Equation 3.3.2.4-2. No direct solution for the integral of Equation 3.3.4.3-3 can be offered here. However Theodorsen offers an evaluation for the total $c_{h_{c_{\ell\delta}}}$ in Reference 1:

$$c_{h_{c_{\ell\delta}}} = \frac{1}{4\pi}\left(\frac{c}{c_f}\right)^2 \left(T_4 - T_{12} - \frac{T_5}{T_{10}}\right) \qquad 3.3.4.3\text{-}4$$

Equations 3.3.2.4-1, 3.3.4.2-4, and 3.3.4.3-3 and -4 provide the evaluation for $c_{h_{c_{\ell b\delta}}}$ given in Table 3.3.4.3-I and on Figure 3.3.4.3-1.

3.3.3.2 Flap Lift Pitching Moment Slope. All of the flap lift pitching moment about the section aerodynamic center is produced by the basic component of the flap lift. The center of pressure for the basic flap lift is given by the integral of Equation 3.3.2.4-2 over the section chord. No direct evaluation of the integral can be offered here but an indirect evaluation through the pitching moment characteristics of Theodorsen in Reference 1 locates the center of pressure at:

$$c.p._{\delta} = \frac{1}{4} + \frac{1}{2}\,\frac{h}{c} \qquad 3.3.3.2\text{-}1$$

Allen gives full scale (aircraft) viscous locations for this center of pressure in Table IV of Reference 2 where Allen's "G" is the negative of the distance between the quarter-chord station and the flap basic lift center of pressure. Allen's viscous values for the center of pressure are compared with thin airfoil theory on Figure 3.3.3.2-l which reflects the slight, untestable modification which Allen makes to the flap basic lift distribution, shown on Figure 3.3.2.4-6.

Equation 3.3.3.2-l defines the flap contribution to the section pitching moment:

$$\Delta c_{m_{ac_\delta}} = -\zeta\,(c.p._{\delta} - a.c.)\,(c_{\ell})_{\delta} \qquad 3.3.3.2\text{-}2$$

and the flap lift and flap angle pitching moment slopes:

$$\boxed{d\,c_{m_{ac}}/d\,(c_{\ell})_{\delta} = -\zeta\,(c.p._{\delta} - a.c.) \qquad 3.3.3.2\text{-}3}$$

$$\boxed{d\,c_{m_{ac}}/d\,\delta = -\zeta\,(c.p._{\delta} - a.c.)\,c_{\ell_\delta} \qquad 3.3.3.2\text{-}4}$$

LIMITATIONS

Except for Allen, no experimental tests of Equation 3.3.3.2-l can be offered here and no confidence level can be assigned. Examination of the DeHavilland data of Reference 3 would be particularly interesting but would require analysis of the scale effect in that data. Reference to typical aircraft flap data at large flap angles, 20° or more, should be avoided for hydrodynamic applications.

REFERENCES

1. Theodorsen, 'I'.: General Theory of Aerodynamic Instability and the Mechanism of Flutter. NACA Report 496, 1935. Currently available in AIAA Selected Reprints, "Aerodynamic Flutter", I.E. Garrick, Editor, March 1969.

2. Allen, H. Julian: Calculation of the Chordwise Load Distribution Over Airfoil Sections with Plain, Split, or Serially Hinged Trailing-Edge Flaps. NACA Report No. 634, 1938.

3. Teeling, P.: Low Speed Wind Tunnel Tests of a NACA 16-309 Airfoil with Trailing-Edge Flap, DeHavilland Aircraft of Canada, Limited Report No. ECS 76-3, October 1976.

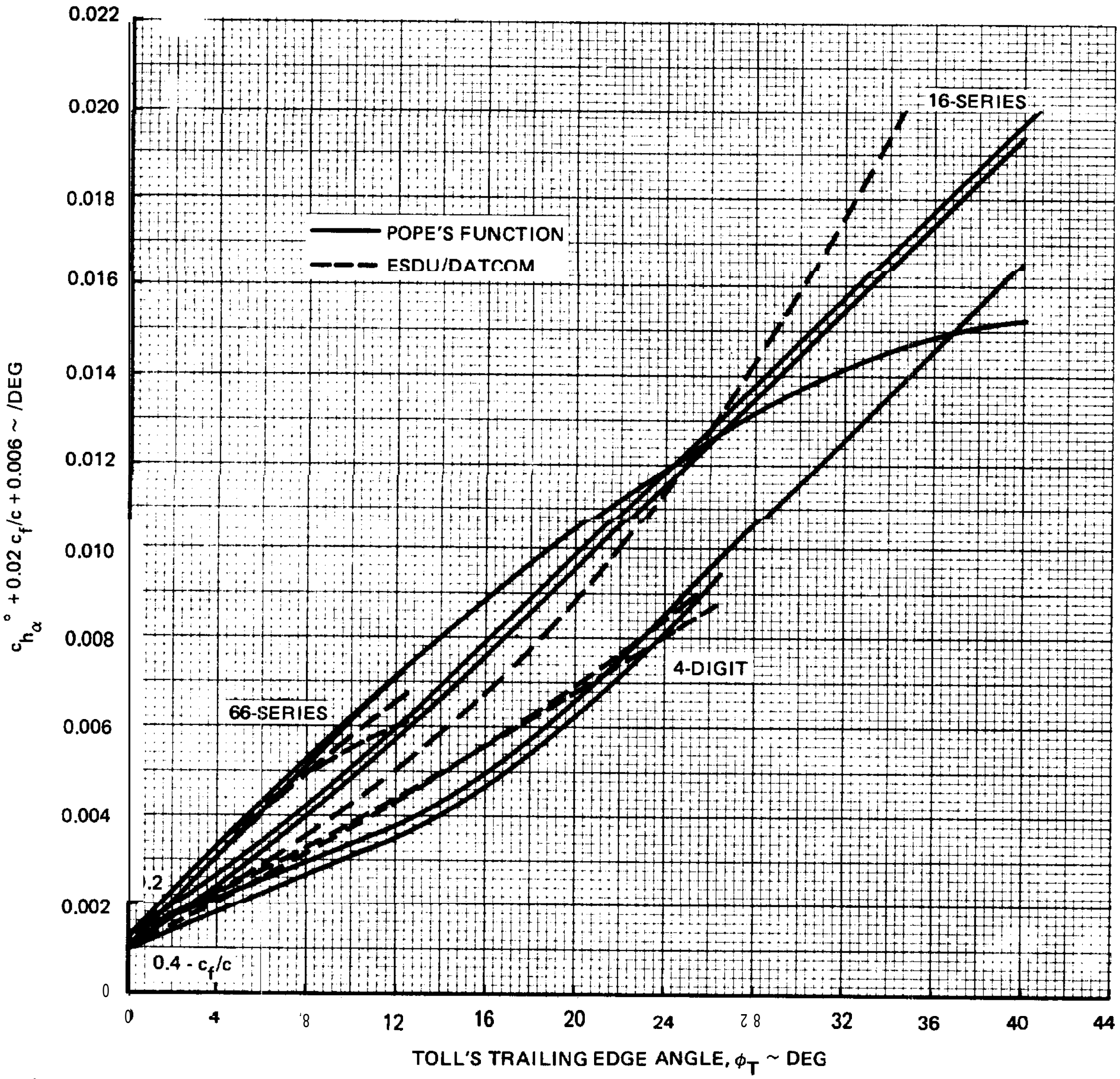

1892-113B

Fig. 3.3.4.2-6 Application of Pope's Function, c_f/c = 0.2 and 0.4

3.3.3.3 Section Moment Curve. It is convenient to design and to the analysis of measured data to express the section moment curve in the form:

$$c_{m_{a.c.\ total}} = c_{m_{ac}} + (c_\ell)_\delta \, d\, c_{m_{ac}} / d\, (c_\ell)_\delta \qquad 3.3.3.3\text{-}1$$

which is the slope-intercept form of the section moment equation.

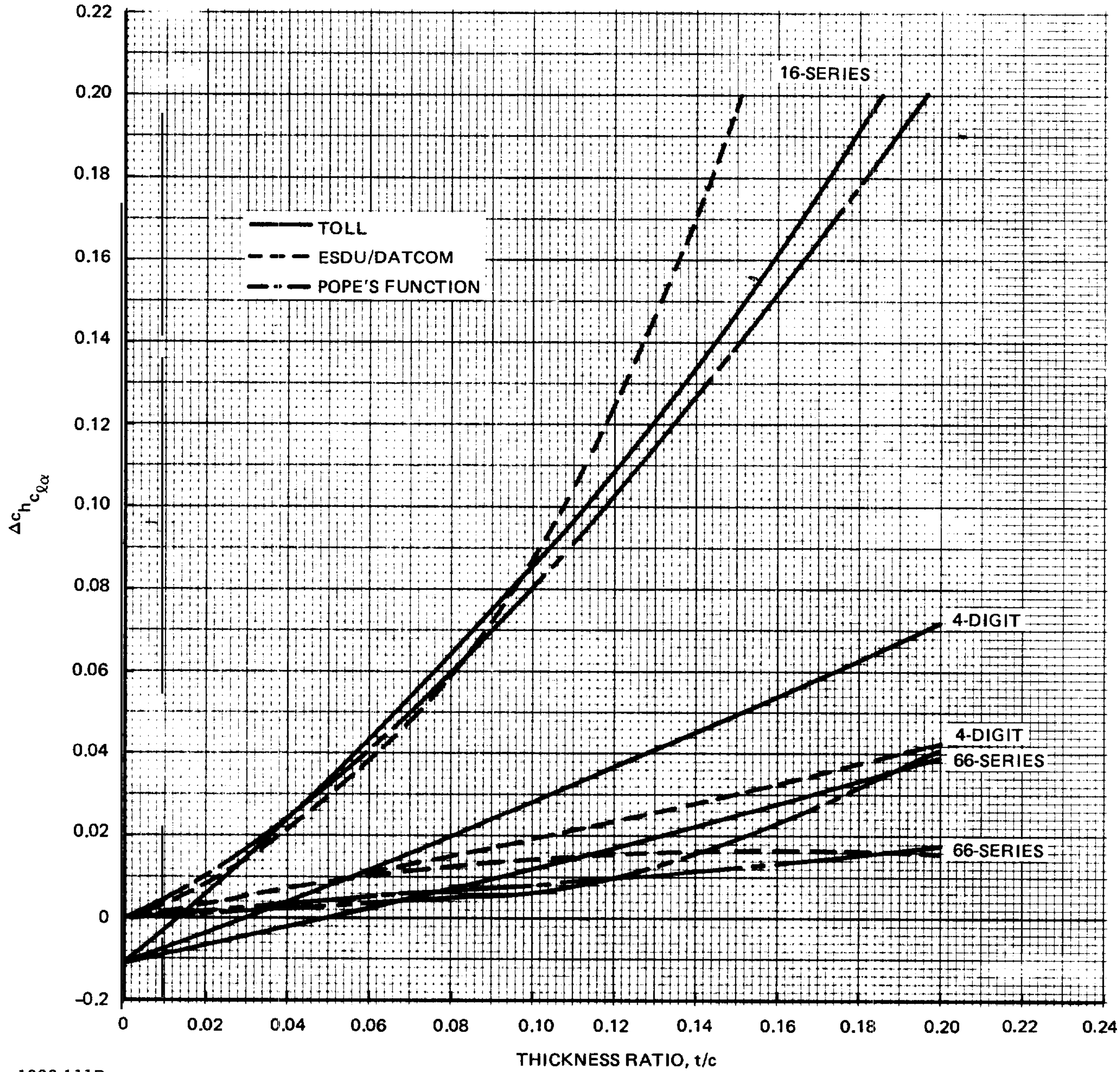

1892-111B

Fig. 3.3.4.2-4 Viscous Incremental $c_{h_{c_{\ell\alpha}}}$, $c_f/c = 0.2$

3.3.4 Section Flap Hinge Moment.

3.3.4.1 Residual Flap Hinge Moment. The residual, $\alpha = \delta = 0$, flap hinge moment is neglected in the literature. No reference to the subject was found in DATCOM and the ESDU controls section presents a zero residual moment.

In thick airfoil potential theory the residual flap hinge moment is given by:

$$c_{h_0} = -\left(\frac{c}{c_f}\right)^2 \int_{h/c}^{1} \left(\frac{x}{c} - \frac{h}{c}\right) c_{\ell_{cx}} \, d\frac{x}{c} \qquad 3.3.4.1\text{-}1$$

$$\frac{c_{h_0}}{c_{\ell_{i_{eff}}}} = -\left(\frac{c}{c_f}\right)^2 \int_{h/c}^{1} \left(\frac{x}{c} - \frac{h}{c}\right)\left(\frac{v}{V}\right)_{x/c} \frac{c_{\ell_x}}{c_{\ell_{i_{eff}}}} \, d\frac{x}{c}$$

The thickness velocity ratio, $(v/V)_{x/c}$, is a refinement of some 5% significance typically and insignificant to the viscous problem presented.

Figure 3.3.2.3-2 illustrates the viscous problem associated with the prediction of this coefficient. That problem extends to the measurement of the coefficient because model scale effects not evident in the lift and pitching moment curves might persist in the flap region and because the significance of model measurements to the prototype Reynolds number have not been established for this characteristic.

In the absence of guidance, Equation 3.3.4.1-1 is specified for this coefficient but without the thickness refinement:

$$\frac{c_{h_0}}{c_{\ell_{i_{eff}}}} = -\left(\frac{c}{c_f}\right)^2 \int_{h/c}^{1} \left(\frac{x}{c} - \frac{h}{c}\right) \frac{c_{\ell_x}}{c_{\ell_{i_{eff}}}} \, d\frac{x}{c} \qquad 3.3.4.1\text{-}2$$

where: $c_{h_0} = h_0/q\, c_f^2\, b_f$

$c_{\ell_{i_{eff}}}$ is from Equation 3.3.1.4-1

$c_{\ell_x}/c_{\ell_{i_{eff}}}$ is the thin airfoil potential theory camber lift distribution except for $a > .94$ mean lines for which the $a = .94$ lift distribution is employed.

$c_{h_0}/c_{\ell_{i_{eff}}}$ is the center of pressure for that portion of the camber lift carried on the flap, referenced to the flap hinge and expressed as a fraction of the flap chord. The values of $c_{h_0}/c_{\ell_{i_{eff}}}$ for six particular configurations of interest are presented in Table 3.3.4.1-I.

LIMITATIONS

No experience can be offered for the residual flap hinge moment. No procedure exists for insuring that model measurements represent the prototype.

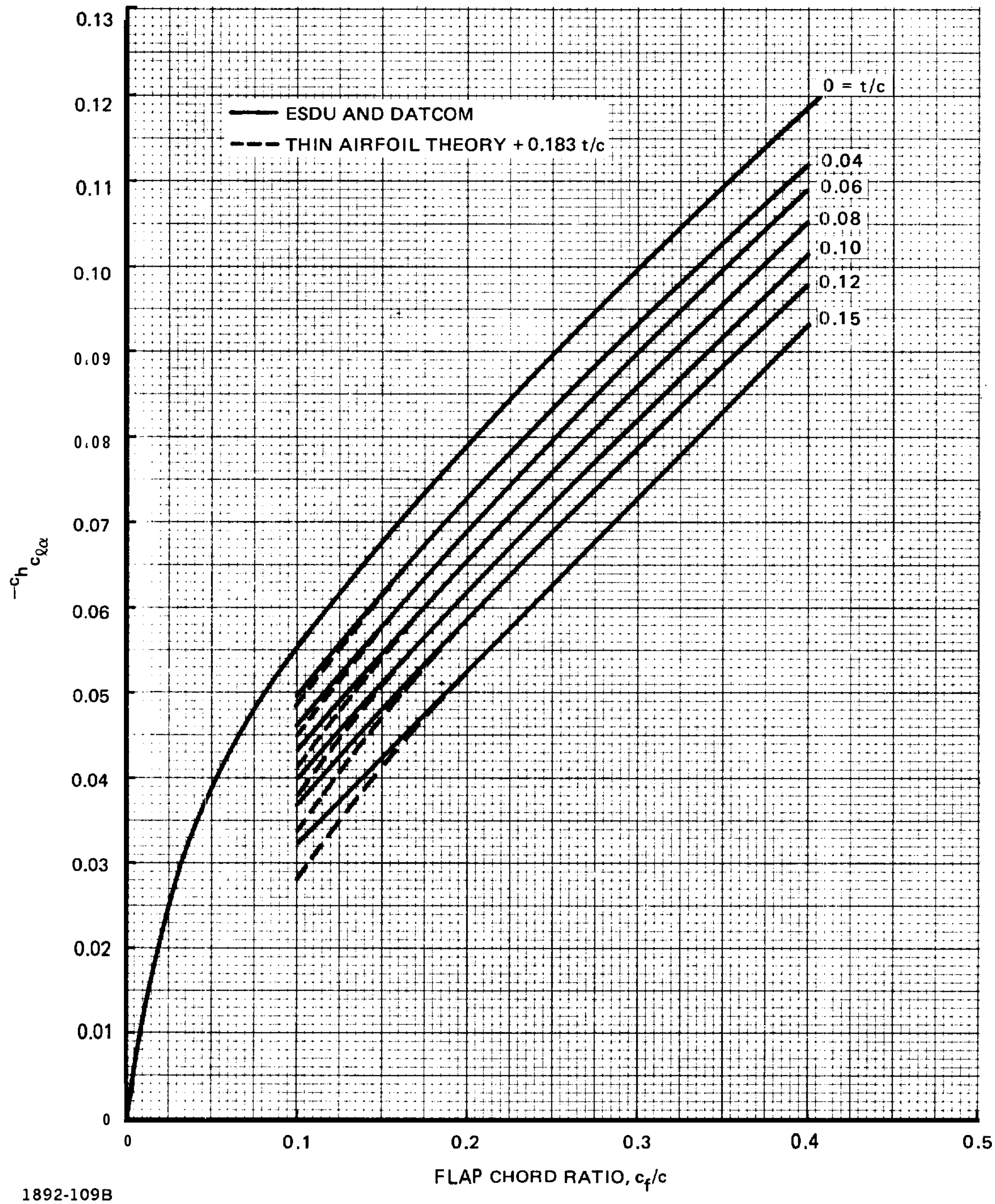

1892-109B

Fig. 3.3.4.2-2 Flap Hinge Moment Derivative, $c_{h_{c_{\ell\alpha}}}$, Thick Airfoil Potential Theory

3.3.4.2 Flap Hinge Moment Due to Angle of Attack.

THIN AIRFOIL THEORY

The flap hinge moment coefficient due to pitch lift is given by:

$$(c_h)_\alpha = -\left(\frac{c}{c_f}\right)^2 \int_{h/c}^{1} \left(\frac{x}{c} - \frac{h}{c}\right)(c_{\ell_x})_\alpha \, d\frac{x}{c} \qquad 3.3.4.2\text{-}1$$

$$c_{h_{c\ell\alpha}} \equiv (c_h)_\alpha/(c_\ell)_\alpha = -\left(\frac{c}{c_f}\right)^2 \int_{h/c}^{1} \left(\frac{x}{c} - \frac{h}{c}\right)\left(\frac{c_{\ell_x}}{c_\ell}\right)_\alpha d\frac{x}{c}$$

This coefficient is the centroid for that portion of the lift due to angle of attack which is carried on the flap, normalized by the product of the flap chord and the total lift due to angle of attack and expressed as a fraction of the flap chord. It is subject to all the uncertainties associated **with** the lift distribution in the vicinity of the trailing edge.

This hinge moment coefficient is traditionally presented in terms of a derived quantity:

$$c_{h_\alpha} \equiv d\,c_h/d\alpha = (c_h)_\alpha/\alpha = c_{h_{c\ell\alpha}}\, c_{\ell_\alpha} \qquad 3.3.4.2\text{-}2$$

The traditional practice is unfortunate because it includes the uncertainties associated with lift curve slope with those associated with the distribution of the pitch lift. In particular, Equation 3.3.4.2-2 introduces the lift curve slope trailing edge angle dependency into the flap hinge moment coefficient, making it difficult to distinguish the lift slope and lift distribution contributions to the **flap** moment trailing edge angle dependency.

In thin airfoil potential theory the lift distribution of Equation 3.3.4.2-1 is given by Equation 3.3.2.1-1 and the equation may be written:

$$c_{h_{c\ell\alpha}} = -\frac{2}{\pi}\left(\frac{c}{c_f}\right)^2 \int_{h/c}^{1} \left(\frac{x}{c} - \frac{h}{c}\right)\sqrt{\frac{1-\frac{x}{c}}{x/c}}\, d\frac{x}{c} \qquad 3.3.4.2\text{-}3$$

$$= \frac{2}{\pi}\left(\frac{c}{c_f}\right)^2 \int_{h/c}^{1} \left[\frac{h}{c}\sqrt{\frac{1-\frac{x}{c}}{x/c}} - \sqrt{\frac{x}{c} - \left(\frac{x}{c}\right)^2}\right] d\frac{x}{c}$$

TABLE 3.3.4.2-II

TOLL'S c_{h_α} DATA, 66-SERIES SECTIONS

SYMBOL	PRIMARY REFERENCE	SECTION	c_f/c	RN $\times 10^{-6}$	TOLL TRUE CONTOUR $\phi°$, DEG	T.E. ANGLE $\phi°$ DEG	c_{h_α} /DEG	$c_{h_\alpha}° + 0.02\, c_f/c + 0.006$
■	1	66-009	0.3	1.43	5.6	7	-0.0070	0.0050
▲	5	66(215)-216	0.2	2.8	10	9	-0.0058	0.0042
○	6	66(215)-216	0.15	3.8		6	-0.0061	0.0029
		a = 0.6		9.5		8	-0.0051	0.0039
							-0.0054	0.0036
						13	-0.0023	0.0067
						21	0.0006	0.0096
							0.0018	0.0108
△			0.2			6	-0.0072	0.0028
						8	-0.0056	0.0044
							-0.0066	0.0034
						17	-0.0005	0.0095
							-0.0024	0.0076
						22	0.0013	0.0087
						23	0.0031	0.0131
							0.0038	0.0138
						26	0.0051	0.0151
						31	0.0049	0.0149
							0.0059	0.0159
■		66(215)-014	.03	1.43	8.75	8	-0.0072	0.0048

1892-107B

NOTE: SEE TABLE 3.3.4.2-II FOR PRIMARY REFERENCES.

Toll's correlation of Figure 13 of Reference 3 may be written:

$$c_{h_\alpha}^{\circ} = -.006 - .02\, c_f/c + .0005\, \phi^\circ \qquad 3.3.4.2\text{-}6$$

which is compared with the data on Figure 3.3.4.2-3. The standard deviation for that correlation is twice the nominal accuracy of ESDU and DATCOM. The slope of Toll's correlation on Figure 3.3.4.2-3 is entirely determined by the beveled trailing edge angle data which Toll identifies with the true contour trailing edge angle. It should be noted that Hoerner places an entirely different interpretation on almost the same data sample of Figure 14 (D) of Chapter 9 of Reference 4.

Equation 3.3.4.2-6 defines a viscous incremental $c_{h_{c_{\ell\alpha}}}$ which may be written:

$$\Delta c_{h_{c_{\ell\alpha}}} = \frac{c_{h_\alpha}^{\circ}}{c_{\ell_\alpha}^{\circ}} - c_{h_{c_{\ell\alpha pot}}} \qquad 3.3.4.2\text{-}7$$

where : c_{h_α} is Toll's c_{h_α} of Equation 3.3.4.2-6

$= -.006 - .02\, c_f/c + .0005\, \phi^\circ$

$\phi^\circ = c_\phi^\circ\ t/c$

c_ϕ° is from Table 6.1.1.2-I

$c_{\ell_\alpha}^{\circ} = .10965\, [1 + c_{1_\kappa}\, t/c + c_{2_\kappa}\, (t/c)^2]$

c_{1_κ} and c_{2_κ} are from Table 3.3.1.2-XI

$c_{h_{c_{\ell\alpha pot}}}$ is from Equation 3.3.4.2-4

Equation 3.3.4.2-7 has been evaluated for a 20% flap chord ratio for three sections with the result shown on Figure 3.3.4.2-4. Since the form of $c_{h_{c_{\ell\alpha}}}$ makes it independent of the viscous additional lift effect, the increment of Equation 3.3.4.2-7 and Figure 3.3.4.2-4 is entirely due to the viscous basic lift effect of Section 3.3.2.2.

ESDU AND DATCOM

The pitch lift flap hinge moment derivative is identically given in c_{h_α} form on ESDU controls 04.01.01, which is the source, and DATCOM Figure 6.1.3.1-11. The **thick airfoil** potential $c_{h_{\alpha pot}}$ is that of Equation 3.3.4.2-5 which must then be corrected for viscosity by the ratio $c_{h_{\alpha std}}/c_{h_{\alpha pot}}$ which is graphically presented. The result is said to be valid only for a "standard" section which is symmetric and over the last 10% of t'he chord has straight upper and lower surfaces including the angle $\phi = 2 \tan^{-1} t/c$. An analytic increment is then provided for general sections so that the final result may be written:

TABLE 3.3.4.2-II

TOLL'S c_{h_α} DATA, 4- AND 5-DIGIT SECTIONS

SYMBOL	PRIMARY REFERENCE	SECTION	c_f/c	RN X 10^{-6}	TOLL TRUE CONTOUR ϕ'', DEG	T.E. ANGLE $\phi°$ DEG	c_{h_α} /DEG	c_{h_α} + 0.02 c_f/c + 0.006
●	1	0009	0.15	1.43	11.9	11.5	-0.00350	0.00550
▲	Z		0.2			11.5	-0.00450	0.00550
△						20	0	0.01000
						30	0.00375	0.01375
							0.00330	0.01330
						40	0.00325	0.01325
O	1		0.3			18	-0.00400	0.00800
						25	-0.00200	0.01000
						29	0.00150	0.01350
						30	0.00550	0.01750
						43	0.00300	0.01500
■	Z					11.5	-0.00700	0.00500
□						ZO	-0.00280	0.00920
						30	0.00140	0.01340
						40	0.00600	0.01700
◆			0.4			11.5	-0.00950	0.00450
◇						20	-0.00400	0.01000
						30	0.00100	0.01500
						40	0.00475	0.01875
	1	0016	0.3		19.8	17	-0.00235	0.00966
◆						19	-0.00200	0.01000
●	3	23012	0.2	2.19	15.8	16	-0.00400	0.00600
●	4	0009	0.3	3	11.9	11.9	-0.00882	0.00318
◠						(1)	-0.00808	0.00392
						(2)	-0.00300	0.00900
1892-106B						(3)	-0.00099	0.01101

APPLYING POPE'S FUNCTION

For the basic lift distribution viscous effect of Equation 3.3.2.2-5, Equation 3.3.4.2-l becomes:

$$\Delta c_{h_{c_{\ell\alpha}}} = -\left(\frac{c}{c_f}\right)^2 \int_{h/c}^{1} \left(\frac{x}{c} - \frac{h}{c}\right) \frac{\Delta c_{\ell_{xb}}}{c_\ell}\, d\frac{x}{c} \qquad 3.3.4.2\text{-}9$$

$$= -\Delta\, a.c. \left(\frac{c}{c_f}\right)^2 \int_{h/c}^{1} \left(\frac{x}{c} - \frac{h}{c}\right) P_{ac}\, d\frac{x}{c}$$

where: A a.c. = $a.c._{pot}$ - a.c

which is the integral of Equation 3.3.2.2-4, Table 3.3.2.2-1, and Figure 3.3.2.2-6.

For the ESDU/DATCOM thick airfoil potential $ch_{c_{\ell\alpha}}$ of Equation 3.3.4.2-5, Equation 3.3.4.2-9 produces for $c_{h_{c_{\ell\alpha}}}$:

$$c_{h_{c_{\ell\alpha}}} = c_{h_{c_{\ell\alpha 0}}} + .183\ t/c + \Delta\, a.c.\left(\frac{c}{c_f}\right)^2 \int_{h/c}^{1} \left(\frac{h}{c} - \frac{x}{c}\right) P_{ac}\, d\frac{x}{c} \qquad 3.3.4.2\text{-}10$$

Equation 3.3.4.2-10 is compared with the ESDU/DATCOM prediction for some particular cases on Figure 3.3.4.2-6. The ESDU/DATCOM nominal accuracy is ± .001/deg so the two predictions are practically the same in the geometry range where the ESDU data sample would be expected to be found. Presumably the ESDU $c_{h_\alpha}/c_{h_{\alpha_{pot}}}$ is smoothed across a variety of sections and would therefore compare differently with an analytic procedure for particular sections.

Equation 3.3.4.2-10 is compared with Toll's data on Figure 3.3.4.2-7 in the form of prediction error vs the difference between Toll's nominal trailing edge angle and the true contour $\phi_{5\%}$. The form of this presentation helps to distinguish the true contour cases from those which have been beveled or wedged. The figure emphasizes the small size of the sample for true contour **cases.** The ESDU nominal ch_α accuracy corresponds to about ±.008 for $ch_{c_{\ell\alpha}}$ and the true contour cases of Figure 3.3.4.2-7, $\Delta\phi \approx 0$, span this range with one point lying well outside the range.

Figures 3.3.4.2-3 and -5 indicate that neither Toll nor ESDU/DATCOM predicts the Toll beveled flap data impressively and, in fact, the "◻" symbols of Figure 3.3.4.2-5 indicate that ch_α is quite sensitive to the flap geometry though ESDU notes particularly that c_{ℓ_α} is not sensitive to trailing edge angle. There being no analytic explanation for the ch_α sensitivity to flap trailing edge angle, it can be empirically fitted to measured $ch_{c_{\ell\alpha}}$'s as well as to measured ch_α's and Figure 3.3.4.2-7 suggests such an empirical fit to Toll's data, displaying the accuracy to be expected.

2. Theodorsen, T.: General Theory of Aerodynamic Instability and the Mechanism of Flutter. NACA Report 496, 1935. Currently available in AIAA Selected Reprints, "Aerodynamic Flutter", I.E. Garrick, Editor, March 1969.

3. Toll. Thomas A.: Summary of Lateral Control Research. NACA Report No. 868, 1947.

4. Hoerner, S.F. and Borst, H.V.: Fluid-Dynamic Lift. Published by Mrs. Liselotte A. Hoerner, 1975.

2. Theodorsen, T.: General Theory of Aerodynamic Instability and the Mechanism of Flutter. NACA Report 496, 1935. Currently available in AIAA Selected Reprints, "Aerodynamic Flutter", I.E. Garrick, Editor, March 1969.

3. Toll. Thomas A.: Summary of Lateral Control Research. NACA Report No. 868, 1947.

4. Hoerner, S.F. and Borst, H.V.: Fluid-Dynamic Lift. Published by Mrs. Liselotte A. Hoerner, 1975.

For the basic lift distribution viscous effect of Equation 3.3.2.2-5, Equation 3.3.4.2-1 becomes:

$$\Delta c_{h_{c_{\ell\alpha}}} = -\left(\frac{c}{c_f}\right)^2 \int_{h/c}^{1} \left(\frac{x}{c} - \frac{h}{c}\right) \frac{\Delta c_{\ell_{xb}}}{c_\ell} d\frac{x}{c} \qquad 3.3.4.2\text{-}9$$

$$= -\Delta \text{a.c.} \left(\frac{c}{c_f}\right)^2 \int_{h/c}^{1} \left(\frac{x}{c} - \frac{h}{c}\right) P_{ac}\, d\frac{x}{c}$$

where: Δ 8,ε, = 8,ε.$_{pot}$ - a.c

which is the integral of Equation 3.3.2.2-4, Table 3.3.2.2-I, and Figure 3.3.2.2-6.

For the ESDU/DATCOM thick airfoil potential $c_{h_{c_{\ell\alpha}}}$ of Equation 3.3.4.2-5, Equation 3.3.4.2-9 produces for $c_{h_{c_{\ell\alpha}}}$:

$$c_{h_{c_{\ell\alpha}}} = c_{h_{c_{\ell\alpha 0}}} + .183\, t/c + \Delta \text{a.c.}\left(\frac{c}{c_f}\right)^2 \int_{h/c}^{1} \left(\frac{h}{c} - \frac{x}{c}\right) P_{ac}\, d\frac{x}{c} \qquad 3.3.4.2\text{-}10$$

Equation 3.3.4.2-10 is compared with the ESDU/DATCOM prediction for some particular cases on Figure 3.3.4.2-6. The ESDU/DATCOM nominal accuracy is ± .001/deg so the two predictions are practically the same in the geometry range where the ESDU data sample would be expected to be found. Presumably the ESDU $c_{h_\alpha}/c_{h_{\alpha_{pot}}}$ is smoothed across a variety of sections and would therefore compare differently with an analytic procedure for particular sections.

Equation 3.3.4.2-10 is compared with Toll's data on Figure 3.3.4.2-7 in the form of prediction error vs the difference between Toll's nominal trailing edge angle and the true contour $\phi_{5\%}$. The form of this presentation helps to distinguish the true contour cases from those which have been beveled or wedged. The figure emphasizes the small size of the sample for true contour cases. The ESDU nominal c_{h_α} accuracy corresponds to about ± .008 for $c_{h_{c_{\ell\alpha}}}$ and the true contour cases of Figure 3.3.4.2-7, $\Delta\phi \approx 0$, span this range with one point lying well outside the range.

Figures 3.3.4.2-3 and -5 indicate that neither Toll nor ESDU/DATCOM predicts the Toll beveled flap data impressively and, in fact, the "◠" symbols of Figure 3.3.4.2-5 indicate that c_{h_α} is quite sensitive to the flap geometry though ESDU notes particularly that c_{ℓ_α} is not sensitive to trailing edge angle. There being no analytic explanation for the c_{h_α} sensitivity to flap trailing edge angle, it can be empirically fitted to measured $c_{h_{c_{\ell\alpha}}}$'s as well as to measured c_{h_α}'s and Figure 3.3.4.2-7 suggests such an empirical fit to Toll's data, displaying the accuracy to be expected.

TABLE 3.3.4.2-11

TOLL'S c_{h_α} DATA, 4- AND 5-DIGIT SECTIONS

SYMBOL	PRIMARY REFERENCE	SECTION	c_f/c	RN x 10^{-6}	TOLL TRUE CONTOUR $\phi°$, DEG	T.E. ANGLE $\phi°$ DEG	c_{h_α} /DEG	c_{h_α} + 0.02 c /c + 0.00%
●	1	0009	0.15	1.43	11.9	11.5	-0.00350	0.00550
▲	2		0.2			30	-0.00450	0.00550
△							0	0.01000
						40	3040 0.00375 0.00330 0.00325	0.01330 0.01325 0.01375
□	1		0.3			18	-0.00400	0.00800
						25	-0.00200	0.01000
						29	0.00150	0.01350
						30	0.00550	0.01750
						43	0.00300	0.01500
■	2 -					20 11.5	-0.00700 0.00280	0.00920 0.00500
0								
						30	0.00140	0.01340
						40	0.00500	0.01700
◆			0.4			11.5	-0.00950	0.00450
◇						20	-0.00400	0.01000
						30	0.00100	0.01500
						40	0.00475	0.01875
	1	0015	0.3		19.8	17	-0.00235	0.00965
◆						19	-0.00200	0.01000
●	3	23012	0.2	2.19	15.8	16	6.00400	0.00600
●	4	0009	0.3	3	11.9	11.9	-0.00882	0.00318
○						(1)	-0.00808	0.00392
					-0.00300	(2)		0.00900
					-0.00099	(3)		0.01101

1892-106B

Toll's correlation of Figure 13 of Reference 3 may be written:

$$c_{h_\alpha}^{\circ} = -.006 - .02\, c_f/c + .0005\, \phi^{\circ} \qquad 3.3.4.2\text{-}6$$

which is compared with the data on Figure 3.3.4.2-3. The standard deviation for that correlation is twice the nominal accuracy of ESDU and DATCOM. The slope of Toll's correlation on Figure 3.3.4.2-3 is entirely determined by the beveled trailing edge angle data which Toll identifies with the true contour trailing edge angle. It should be noted that Hoerner places an entirely different interpretation on almost the same data sample of Figure 14 (D) of Chapter 9 of Reference 4.

Equation 3.3.4.2-6 defines a viscous incremental $c_{h_{c_{\ell\alpha}}}$ which may be written:

$$\Delta c_{h_{c_{\ell\alpha}}} = \frac{c_{h_\alpha}^{\circ}}{c_{\ell_\alpha}^{\circ}} - c_{h_{c_{\ell\alpha pot}}} \qquad 3.3.4.2\text{-}7$$

where: c_{h_α} is Toll's c_{h_α} of Equation 3.3.4.2-6

$= -.006 - .02\, c_f/c + .0005\, \phi^{\circ}$

$\phi^{\circ} = c_\phi^{\circ}\, t/c$

c_ϕ° is from Table 6.1.1.2-I

$c_{\ell_\alpha}^{\circ} = .10965\, [1 + c_{1_\kappa}\, t/c + c_{2_\kappa}\, (t/c)^2]$

c_{1_κ} and c_{2_κ} are from Table 3.3.1.2-XI

$c_{h_{c_{\ell\alpha pot}}}$ is from Equation 3.3.4.2-4

Equation 3.3.4.2-7 has been evaluated for a 20% flap chord ratio for three sections with the result shown on Figure 3.3.4.2-4. Since the form of $c_{h_{c_{\ell\alpha}}}$ makes it independent of the viscous additional lift effect, the increment of Equation 3.3.4.2-7 and Figure 3.3.4.2-4 is entirely due to the viscous basic lift effect of Section 3.3.2.2.

ESDU AND DATCOM

The pitch lift flap hinge moment derivative is identically given in c_{h_α} form on ESDU controls 04.01.01, which is the source, and DATCOM Figure 6.1.3.1-11. The thick airfoil potential $c_{h_{\alpha_{pot}}}$ is that of Equation 3.3.4.2-5 which must then be corrected for viscosity by the ratio $c_{h_{\alpha_{std}}}/c_{h_{\alpha_{pot}}}$ which is graphically presented. The result is said to be valid only for a "standard" section which is symmetric and over the last 10% of the chord has straight upper and lower surfaces including the angle $\phi = 2 \tan^{-1} t/c$. An analytic increment is then provided for general sections so that the final result may be written:

TABLE 3.3.4.2-III

TOLL'S c_{h_α} DATA, 66-SERIES SECTIONS

SYMBOL	PRIMARY REFERENCE	SECTION	c_f/c	RN x 10^{-6}	TOLL TRUE CONTOUR $\phi°$, DEG	T.E. ANGLE $\phi°$ DEG	c_{h_α} /DEG	$c_{h_\alpha}° + 0.02\ c_f/c + 0.006$
■	1	66-009	0.3	1.43	5.6	7	-0.0070	0.0050
▲	5	66(215)-216	0.2	2.8	10	9	-0.0058	0.0042
○	6	66(215)-216	6.15	3.8		6	6.0061	0.0029
		a = 0.6		9.5		8	-0.0051	0.0039
							-0.0054	0.0036
						13	6.0023	0.0067
						21	0.0006	0.0096
							0.0018	0.0108
△			0.2			6	-0.0072	0.0028
						8	-0.0056	0.0044
							-0.0066	0.0034
						17	-0.0005	0.0095
							-0.0024	0.0076
						22	0.0013	0.0087
						23	0.0031	0.0131
							0.0038	0.0138
						26	0.0051	0.0151
						31	0.0049	0.0149
							0.0059	0.0159
■	7	66(215)-014	.03	1.43	a.75	8	-0.0072	0.0048

1892-107B

NOTE: SEE TABLE 3.3.4.2-II FOR PRIMARY REFERENCES.

3.3.4.2 Flap Hinge Moment Due to Angle of Attack.

THIN AIRFOIL THEORY

The flap hinge moment coefficient due to pitch lift is given by:

$$(c_h)_\alpha = -\left(\frac{c}{c_f}\right)^2 \int_{h/c}^{1} \left(\frac{x}{c} - \frac{h}{c}\right)(c_{\ell_x})_\alpha \, d\frac{x}{c} \qquad 3.3.4.2\text{-}1$$

$$c_{h_{c\ell\alpha}} \equiv (c_h)_\alpha/(c_\ell)_\alpha = -\left(\frac{c}{c_f}\right)^2 \int_{h/c}^{1} \left(\frac{x}{c} - \frac{h}{c}\right)\left(\frac{c_{\ell_x}}{c_\ell}\right)_\alpha d\frac{x}{c}$$

This coefficient is the centroid for that portion of the lift due to angle of attack which is carried on the flap, normalized by the product of the flap chord and the total lift due to angle of attack and expressed as a fraction of the flap chord. It is subject to all the uncertainties associated with the lift distribution in the vicinity of the trailing edge.

This hinge moment coefficient is traditionally presented in terms of a derived quantity:

$$c_{h_\alpha} \equiv d\, c_h/d\alpha = (c_h)_\alpha/\alpha = c_{h_{c\ell\alpha}}\, c_{\ell_\alpha} \qquad 3.3.4.2\text{-}2$$

The traditional practice is unfortunate because it includes the uncertainties associated with lift curve slope with those associated with the distribution of the pitch lift. In particular, Equation 3.3.4.2-2 introduces the lift curve slope trailing edge angle dependency into the flap hinge moment coefficient, making it difficult to distinguish the lift slope and lift distribution contributions to the flap moment trailing edge angle dependency.

In thin airfoil potential theory the lift distribution of Equation 3.3.4.2-1 is given by Equation 3.3.2.1-1 and the equation may be written:

$$c_{h_{c\ell\alpha}} = -\frac{2}{\pi}\left(\frac{c}{c_f}\right)^2 \int_{h/c}^{1} \left(\frac{x}{c} - \frac{h}{c}\right)\sqrt{\frac{1-\frac{x}{c}}{x/c}}\, d\frac{x}{c} \qquad 3.3.4.2\text{-}3$$

$$= \frac{2}{\pi}\left(\frac{c}{c_f}\right)^2 \int_{h/c}^{1} \left[\frac{h}{c}\sqrt{\frac{1-\frac{x}{c}}{x/c}} - \sqrt{\frac{x}{c} - \left(\frac{x}{c}\right)^2}\right] d\frac{x}{c}$$

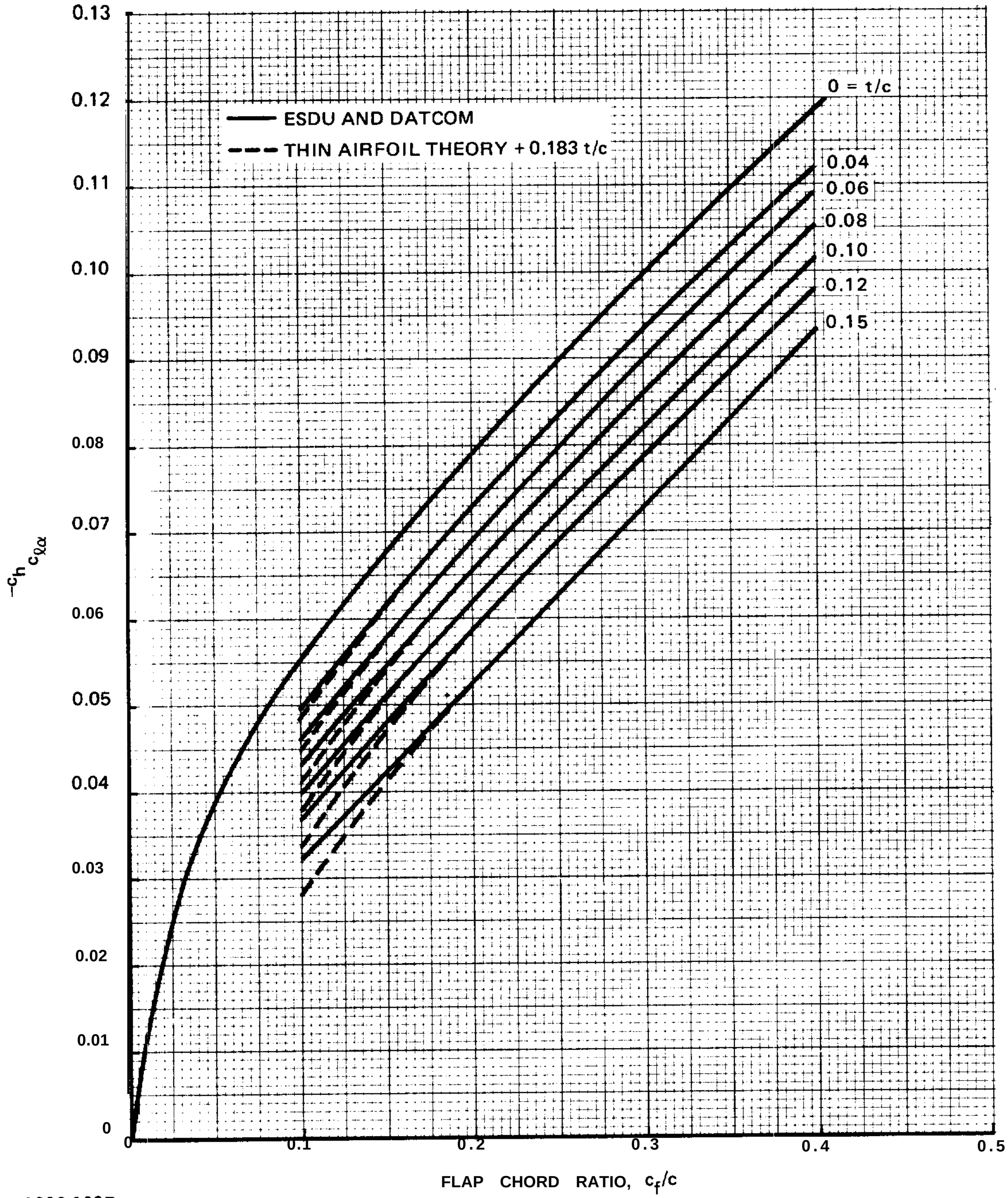

1892-109B

Fig. 3.3.4.2-2 Flap Hinge Moment Derivative, $c_{h_{c_{\ell\alpha}}}$, Thick Airfoil Potential Theory

3.3.4 Section Flap Hinge Moment.

3.3.4.1 Residual Flap Hinge Moment. The residual, $\alpha = \delta = 0$, flap hinge moment is neglected in the literature. No reference to the subject was found in DATCOM and the ESDU controls section presents a zero residual moment.

In thick airfoil potential theory the residual flap hinge moment is given by:

$$c_{h_0} = -\left(\frac{c}{c_f}\right)^2 \int_{h/c}^{1} \left(\frac{x}{c} - \frac{h}{c}\right) c_{\ell_{cx}} \, d\frac{x}{c} \qquad 3.3.4.1\text{-}1$$

$$\frac{c_{h_0}}{c_{\ell_{i_{eff}}}} = -\left(\frac{c}{c_f}\right)^2 \int_{h/c}^{1} \left(\frac{x}{c} - \frac{h}{c}\right)\left(\frac{v}{V}\right)_{x/c} \frac{c_{\ell_x}}{c_{\ell_{i_{eff}}}} \, d\frac{x}{c}$$

The thickness velocity ratio, $(v/V)_{x/c}$, is a refinement of some 5% significance typically and insignificant to the viscious problem presented.

Figure 3.3.2.3-2 illustrates the viscous problem associated with the prediction of this coefficient. That problem extends to the measurement of the coefficient because model scale effects not evident in the lift and pitching moment curves might persist in the flap region and because the significance of model measurements to the prototype Reynolds number have not been established for this characteristic.

In the absence of guidance, Equation 3.3.4.1-1 is specified for this coefficient but without the thickness refinement:

$$\frac{c_{h_0}}{c_{\ell_{i_{eff}}}} = -\left(\frac{c}{c_f}\right)^2 \int_{h/c}^{1} \left(\frac{x}{c} - \frac{h}{c}\right) \frac{c_{\ell_x}}{c_{\ell_{i_{eff}}}} \, d\frac{x}{c} \qquad 3.3.4.1\text{-}2$$

where: $c_{h_0} = h_0/q\, c_f^2\, b_f$

$c_{\ell_{i_{eff}}}$ is from Equation 3.3.1.4-1

$c_{\ell_x}/c_{\ell_{i_{eff}}}$ is the thin airfoil potential theory camber lift distribution except for a > .94 mean lines for which the a = .94 lift distribution is employed.

$c_{h_o}/c_{\ell_{i_{eff}}}$ is the center of pressure for that portion of the camber lift carried on the flap, referenced to the flap hinge and expressed as a fraction of the flap chord. The values of $c_{h_o}/c_{\ell_{i_{eff}}}$ for six particular configurations of interest are presented in Table 3.3.4.1-I.

LIMITATIONS

NO experience can be offered for the residual flap hinge moment. NO procedure exists for insuring that model measurements represent the prototype.

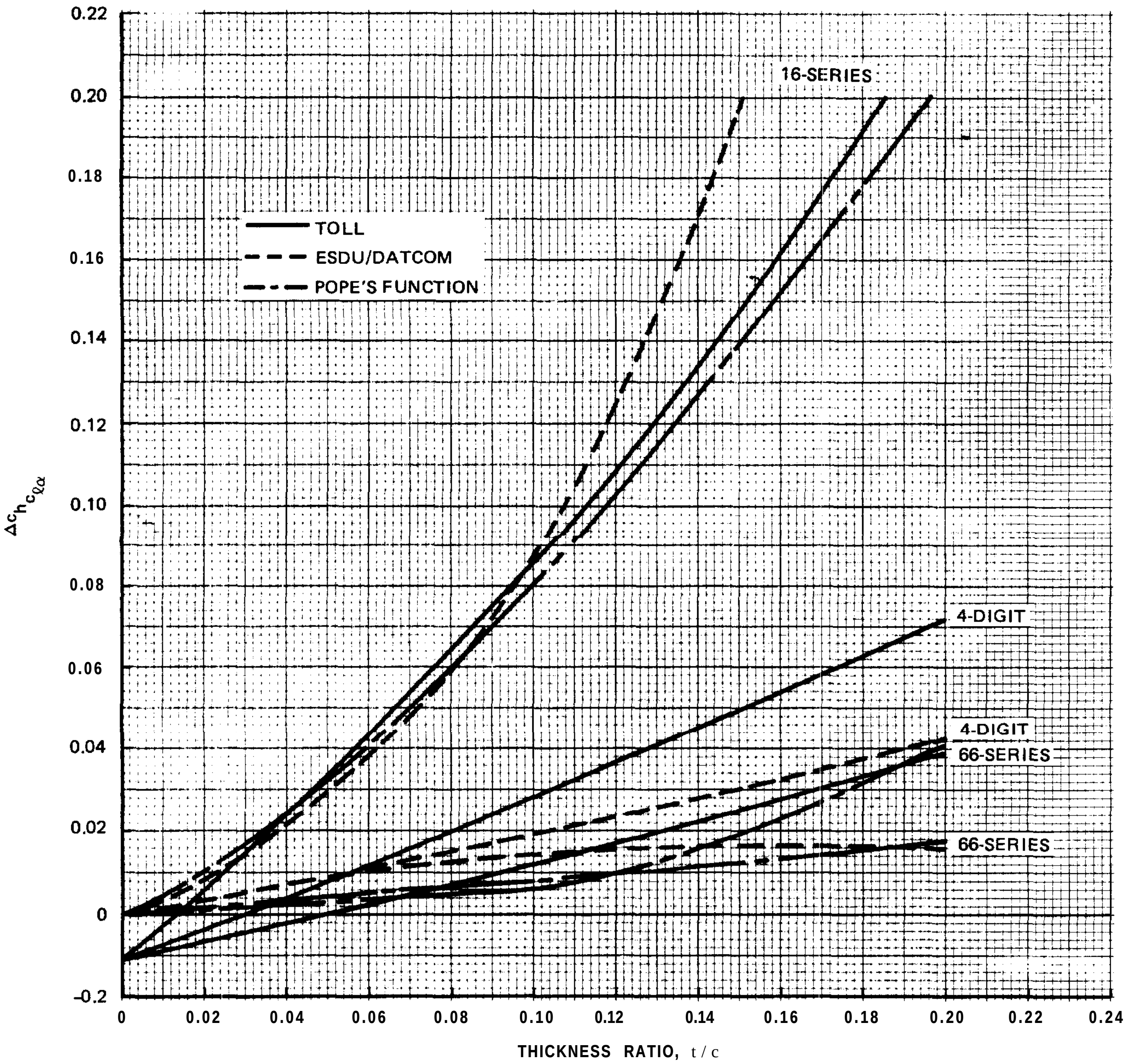

1892-111B

Fig. 3.3.4.2-4 Viscous Incremental $c_{h_{c_{\ell\alpha}}}$, $c_f/c = 0.2$

Z

3.3.3.3 Section Moment Curve. It is convenient to design and to the analysis of measured data to express the section moment curve in the form:

$$c_{m_{a.c.\ total}} = c_{m_{ac}} + (c_\ell)_\delta \, d\, c_{m_{ac}} / d\, (c_\ell)_\delta \qquad 3.3.3.3\text{-}1$$

which is the slope-intercept form of the section moment equation.

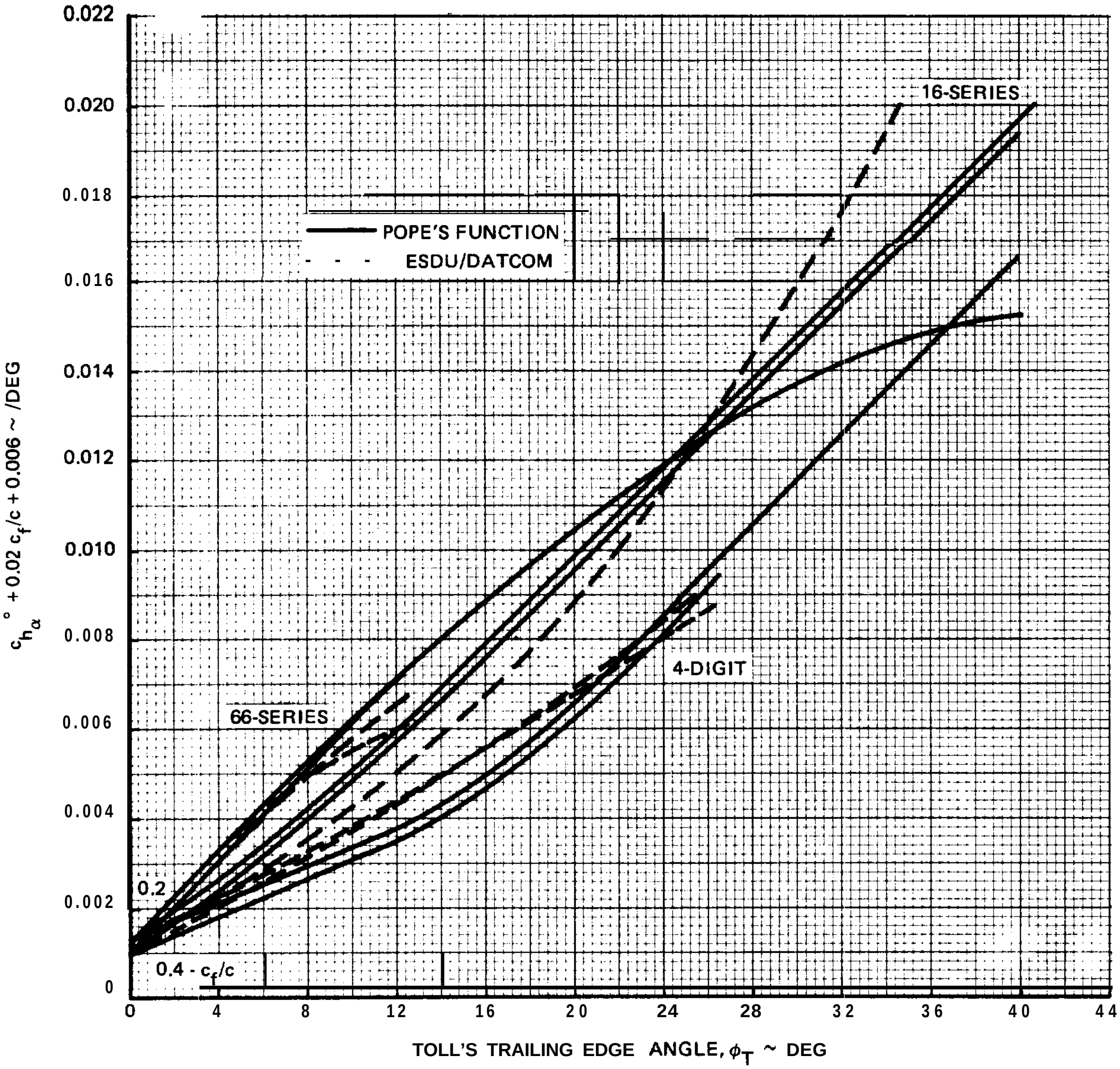

1892-113B

Fig. 3.3.4.2-6 Application of Pope's Function, $c_f/c = 0.2$ and 0.4

3.3.3.2 Flap Lift Pitching Moment Slope. All of the flap lift pitching moment about the section aerodynamic center is produced by the basic component of the flap lift. The center of pressure for the basic flap lift is given by the integral of Equation 3.3.2.4-2 over the section chord. No direct evaluation of the integral can be offered here but an indirect evaluation through the pitching moment characteristics of Theodorsen in Reference 1 locates the center of pressure at:

$$c.p._\delta = \frac{1}{4} + \frac{1}{2}\,\frac{h}{c} \qquad 3.3.3.2\text{-}1$$

Allen gives full scale (aircraft) viscous locations for this center of pressure in Table IV of Reference 2 where Allen's "G" is the negative of the distance between the quarter-chord station and the flap basic lift center of pressure. Allen's viscous values for the center of pressure are compared with thin airfoil theory on Figure 3.3.3.2-1 which reflects the slight, untestable modification which Allen makes to the flap basic lift distribution, shown on Figure 3.3.2.4-6.

Equation 3.3.3.2-1 defines the flap contribution to the section pitching moment:

$$\Delta\, c_{m_{ac_\delta}} = -\,\zeta\,(c.p._\delta - a.c.)\,(c_\ell)_\delta \qquad 3.3.3.2\text{-}2$$

and the flap lift and flap angle pitching moment slopes:

$$\boxed{d\, c_{m_{ac}} / d\,(c_\ell)_\delta = -\,\zeta\,(c.p._\delta - a.c.) \qquad 3.3.3.2\text{-}3}$$

$$\boxed{d\, c_{m_{ac}} / d\,\delta = -\,\zeta\,(c.p._\delta - a.c.)\, c_{\ell_\delta} \qquad 3.3.3.2\text{-}4}$$

LIMITATIONS

Except for Allen, no experimental tests of Equation 3.3.3.2-1 can be offered here and no confidence level can be assigned. Examination of the DeHavilland data of Reference 3 would be particularly interesting but would require analysis of the scale effect in that data. Reference to typical aircraft flap data at large flap angles, 20° or more, should be avoided for hydrodynamic applications.

REFERENCES

1. Theodorsen, T.: General Theory of Aerodynamic Instability and the Mechanism of Flutter. NACA Report 496, 1935. Currently available in AIAA Selected Reprints, "Aerodynamic Flutter", I.E. Garrick, Editor, March 1969.

2. Allen, H. Julian: Calculation of the Chordwise Load Distribution Over Airfoil Sections with Plain, Split, or Serially Hinged Trailing-Edge Flaps. NACA Report No. 634, 1938.

3. Teeling, P.: Low Speed Wind Tunnel Tests of a NACA 16-309 Airfoil with Trailing-Edge Flap, DeHavilland Aircraft of Canada, Limited Report No. ECS 76-3, October 1976.

3.3.4.3 Flap Hinge Moment Due to Flap Deflection.

THIN AIRFOIL THEORY

$c_{h_{c_{\ell\delta}}}$ is the centroid for that portion of the lift due to flap deflection which is carried on the flap, normalized by the product of the flap chord and the total lift due to flap deflection and expressed as a fraction of the flap chord. Because a portion of the lift due to flap deflection is of additional lift distribution type, the flap lift flap hinge moment contains a pitch lift flap hinge moment component.

The flap hinge moment coefficient due to flap deflection is given by:

$$(c_h)_\delta = -\left(\frac{c}{c_f}\right)^2 \int_{h/c}^{1} \left(\frac{x}{c} - \frac{h}{c}\right) (c_{\ell_x})_\delta \, d\frac{x}{c} \qquad 3.3.4.3\text{-1}$$

From Section 3.3.2.4 this equation may be written:

$$c_{h_{c_{\ell\delta}}} = (1-\zeta)\left(\frac{c}{c_f}\right)^2 \int_{h/c}^{1} \left(\frac{h}{c} - \frac{x}{c}\right)\left(\frac{c_{\ell_x}}{c_\ell}\right)_a d\frac{x}{c} + \zeta\left(\frac{c}{c_f}\right)^2 \int_{h/c}^{1} \left(\frac{h}{c} - \frac{x}{c}\right)\left(\frac{c_{\ell_x}}{c_\ell}\right)_{b\delta} d\frac{x}{c}$$

3.3.4.3-2

and from Equation 3.3.4.2-1:

$$c_{h_{c_{\ell\delta}}} = (1-\zeta)\, c_{h_{c_{\ell\alpha}}} + \zeta\left(\frac{c}{c_f}\right)^2 \int_{h/c}^{1} \left(\frac{h}{c} - \frac{x}{c}\right)\left(\frac{c_{\ell_x}}{c_\ell}\right)_{b\delta} d\frac{x}{c} \qquad 3.3.4.3\text{-3}$$

$$= (1-\zeta)\, c_{h_{c_{\ell\alpha}}} + \delta\, c_{h_{c_{\ell b\delta}}}$$

The basic flap lift distribution, $(c_{\ell_x}/c_\ell)_{b\delta}$, is given by Equation 3.3.2.4-2. No direct solution for the integral of Equation 3.3.4.3-3 can be offered here. However Theodorsen offers an evaluation for the total $c_{h_{c_{\ell\delta}}}$ in Reference 1:

$$c_{h_{c_{\ell\delta}}} = \frac{1}{4\pi}\left(\frac{c}{c_f}\right)^2 \left(T_4 - T_{12} - \frac{T_5}{T_{10}}\right) \qquad 3.3.4.3\text{-4}$$

Equations 3.3.2.4-1, 3.3.4.2-4, and 3.3.4.3-3 and -4 provide the evaluation for $c_{h_{c_{\ell b\delta}}}$ given in Table 3.3.4.3-I and on Figure 3.3.4.3-1.

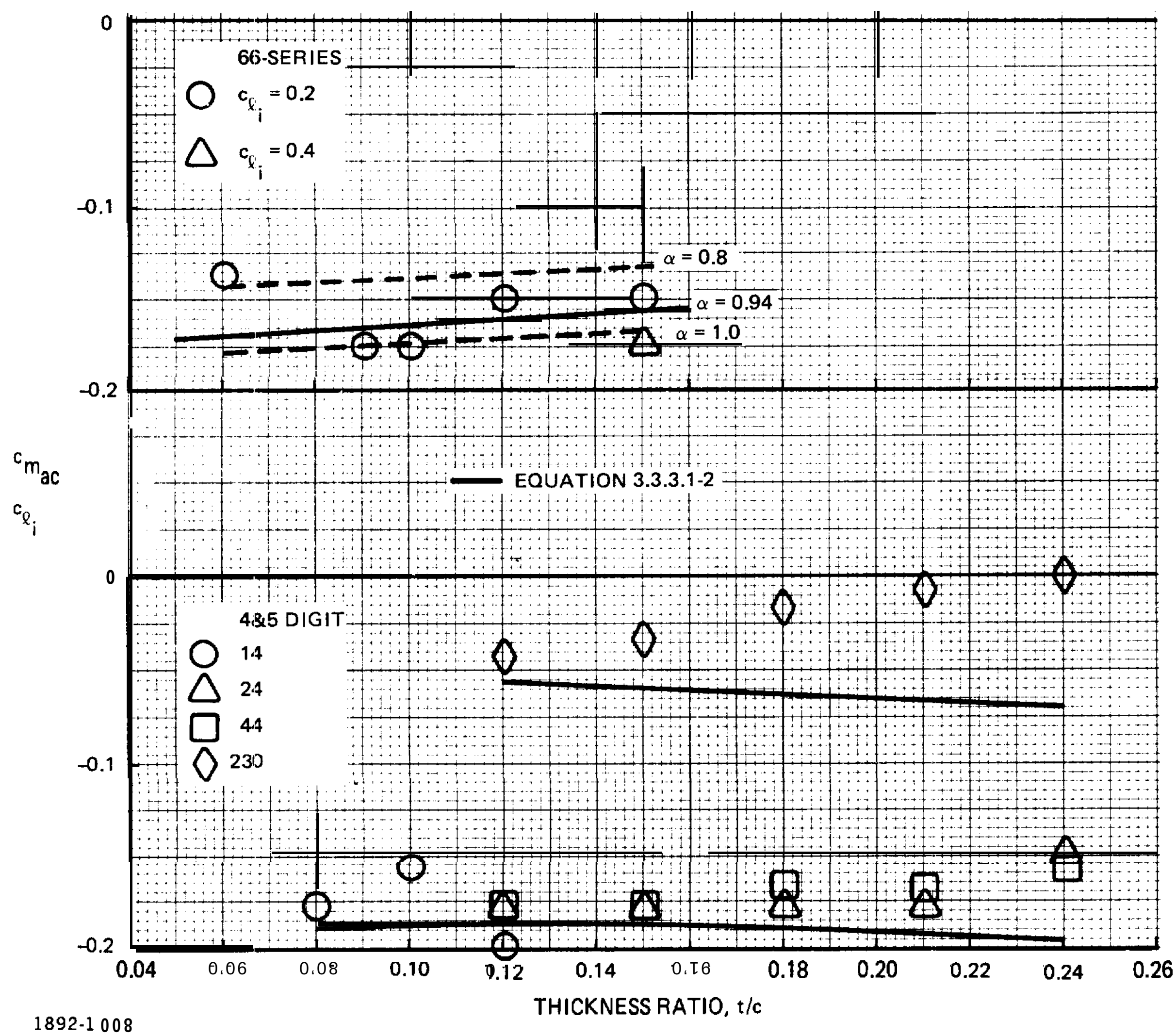

Fig. 3.3.3.1-2 $c_{m_{ac}}$ Correlation, 4&5 Digit and 66-Series Sections

ESDU/DATCOM

The ESDU/DATCOM procedure is numerical and contained in ESDU controls 01.01.03, 04.01.01, and 04.01.02. The ESDU procedure is modified here to the extent that the $c_{\ell_\alpha}/c_{\ell_{\alpha_{pot}}}$ of Equation 3.3.1.2-9 and the $\phi_{5\%}$ of Table 6.1.1.2-I were employed. The ESDU/DATCOM hinge moment derivative is compared with Equation 3.3.4.3-7 on Figure 3.3.4.3-3. The comparison is poor; the two procedures differ by twice the ESDU nominal c_{h_δ} accuracy.

TOLL

As for c_{h_α}, Toll's Reference 2 offers the only experimental c_{h_δ} data which can be offered here. Toll's data is presented here in Tables 3.3.4.3-R and -III which are from Figure 13 and Table II of Reference 3. Toll's correlation of Figure 13 of Reference 3 may be written:

$$c_{h_\delta}{}^\circ = -.0105 - .02\frac{c_f}{c} + .0004\,\phi^\circ \qquad 3.3.4.3\text{-}8$$

which is compared with the data on Figure 3.3.4.3-4. The standard deviation for that correlation is twice the nominal accuracy of ESDU and DATCOM. It will be noted that Toll's correlation is almost entirely determined by beveled trailing edge data.

The form of Equation 3.3.4.3-8 and Figure 3.3.4.3-4 is convenient to the comparison of predictions of different form which can only be compared for particular cases. Figure 3.3.4.3-5 relates the ESDU/DATCOM prediction to Equation 3.3.4.3-7 and to Toll's data by reference to Toll's correlation. Equation 3.3.4.3-7 is better suited to Toll's data than is the ESDU/DATCOM procedure.

ALLEN

Equation (15) of Reference 3 includes Equation 3.3.4.3-7 in a different nomenclature. Allen's η_{a_δ} of his Table X and η_{b_δ} of his Table VIII are the viscous $c_{h_{c_{\ell\alpha}}}$ and $c_{h_{c_{\ell b\delta}}}$, respectively, of this note. It is of interest then to compare them individually with the values of Equation 3.3.4.3-7.

Allen's $c_{h_{c_{\ell\alpha}}}$ is compared with that of Equation 3.3.4.2-11 on Figure 3.3.4.3-6 where it will be noted that Allen has no provision for thickness ratio, neglecting this variable in whatever data sample he had. The very distinctive nature of the l&series $c_{h_{c_{\ell\alpha}}}$, caused by the extreme viscous aerodynamic center shift for this section, should be noted. Unfortunately, no flap hinge moment test of this characteristic can be offered.

Figure 3.3.4.3-7 compares Allen's $c_{h_{c_{\ell b\delta}}}$ with that of Equation 3.3.4.3-6. The comparison indicates that, as assumed by Equation 3.3.4.3-7, Allen finds no significant viscous effect on this derivative for $\delta \leqslant 15$".

TABLE 3.3.3.1-II $c_{m_{a_c}}$ STATISTICAL ANALYSIS

SECTION	MEAN LINE	NUMBER IN SAMPLE N	MEAN $\Delta c_{m_{a_c}}$ (1)	$\Delta c_{m_{a_c}}$ STD DEVIATION
16-SERIES	a = 1.0	SEE NOTE Z		
63-SERIES		13	-0.0003	0.0031
64-SERIES		16	-0.0003	0.0052
65-SERIES		13	-0.0002	0.0044
66-SERIES		06	-0.0003	0.0046
4 DIGIT	64	13	0-0069	0.0059
5 DIGIT	230	06	0.0129	0-0068
a = 1.0		48	-0.0003	0.0042
4 & 5 DIGIT		18	0.0078	0.0068
STANDARD SECTIONS		66	0.0019	0.0062
6 x A SERIES				
63A SERIES	a = 1.0	10	0.0038	–
64A SERIES		04	-0.0010	0.0022
6 x A SERIES		05	0	0.0028
a < 1.0				
65-SERIES	a = 0.5(4), 0.6	06	-0.0029	0.0019
TOTAL EXPERIENCE				
ALL EXCEPT 6 DIGIT SECTIONS		71	0.0007	0.0050
ALL SECTIONS		76	0.0015	0.0059

NOTES: 1. $\Delta c_{m_{a_c}}$ = MEASURED $c_{m_{a_c}}$ – PREDICTED $c_{m_{a_c}}$

2. NO APPROPRIATE DATA SAMPLE AVAILABLE

1892-098B

In summary, the! flap lift flap hinge moment can be defined by:

$$c_{h_{c_{\ell\delta}}} = (1 - \zeta)\, c_{h_{c_{\ell\alpha}}} + \zeta\, c_{h_{c_{\ell b\delta}}} + \Delta\, c_{h_{c_{\ell\delta}}} \qquad 3.3.4.3\text{-}10$$

where: ζ is from Equation 3.3.2.4-l

$c_{h_{c_{\ell\alpha}}}$ is from Equation 3.3.4.2-11

$$c_{h_{c_{\ell b\delta}}} = c_{h_{c_{\ell b\delta 0}}} + .1557\,\frac{t/c}{c_f/c}$$

$c_{h_{c_{\ell b\delta 0}}}$ is from Table 3.3.4.2-I or Figure 3.3.4.3-l

$$\Delta\, c_{h_{c_{\ell\delta}}} = .0055\,\Delta\phi^\circ$$

$\Delta\phi$ = trailing edge bevel angle $- \phi_{5\%}$

Nominal accuracy is $\pm$ .02 for the true contour flap and $\pm$ .04 for the beveled trailing edge flap.

LIMITATIONS

As for $c_{h_{c_{\ell\alpha}}}$, neglect of the thickness distribution in the derivation of $c_{h_{c_{\ell\delta}}}$ is questionable, particularly for the 16-series section. The thick airfoil potential aerodynamic center is available only for the 66-series section of the 6-series family. No data for any typical hydrofoil section can'be offered.

REFERENCES

1. Theodorsen, T.: General Theory of Aerodynamic Instability and the Mechanism of Flutter. NACA Report 496, 1935. Currently available in AIAA Selected Reprints, "Aerodynamic Flutter", I.E., Garrick, Editor, March 1969.
2. Toll, Thomas, A.: Summary of Lateral-Control Research. NACA Report No. 868, 1947.
3. Allen, H. Julian: Calculation of the Chordwise Load Distribution Over Airfoil Sections with Plain, Split, or Serially Hinged Trailing-Edge Flaps. NACA Report No. 634, 1938.

Table 3.3.3.1-II and Figures 3.3.3.1-2 and -3 may be summarized by:

$$c_{m_{ac}} = -c_{\ell_{i_{eff}}} (c.p._c - a.c.) + \sigma \qquad 3.3.3.1\text{-}2$$

where: $c_{\ell_{i_{eff}}}$ is from Equation 3.3.1.4-7

a.c. is from Figure 3.3.2.1-10

$c.p._c$ is the thin airfoil potential theory value except for a $\geqslant$ .94 mean lines for which it is .48[illegible]

σ = 0 to .012 for 4 digit sections

= .006 to .020 for 5 digit sections

= ± .006 for all other sections

LIMITATIONS

The standard deviation of Equation 3.3.3.1-2 is only 10% of the typical hydrofoil moment coefficient, but the sample is scarcely adequate for any of the mean line families represented. The heavy empirical content of the equation is a measure of the inability to define adequately the distribution of the camber lift, particularly at the trailing edge. A consequence in the prediction of the residual flap hinge moment is to be expected.

The 230 mean line result of Figure 3.3.3.1-2 is of particular interest. In theory this mean line would substantially reduce incidence lift control moments and the figure indicates that the actual reduction might be significantly better than theory. The mechanism by which the 24% section produces lift without moment about the a.c. could have practical significance.

REFERENCES

1. Abbott, Ira H. and vonDoenhoff, Albert E.: Theory of Wing Sections, Dover, 1959.

TABLE 3.3.4.3-II TOLL'S c_{h_δ} DATA, 4- AND 5-DIGIT SECTIONS

SYMBOL	PRIMARY REFERENCE	SECTION	c_f/c	RN X 10^{-6}	TOLL TRUE CONTOUR $\phi°$ DEG	T.E. ANGLE $\phi°$ DEG	c_{h_δ} /DEG	$c_{h_\delta}°$ + 0.02 c_f/c + 0.0105
●	1	0009	0.15	1.43	11.9	11.5	-0.0101	0.0034
▲	2		0.2			11.5	-0.0112	0.0033
△						20	-0.0077	0.0068
						30	-0.0003	0.0142
						40	-0.0043	0.0102
□	1		0.3			18	-0.0097	0.0068
						25	-0.0068	0.0097
						29	-0.0049	0.0116
						30	-0.0041	0.0124
						43	-0.0029	0.0136
■	2					11.5	-0.0127	0.0038
□						20	-0.0098	0.0067
						30	-0.0021	0.0144
						40	-0.0026	0.0139
◆			0.4			11.5	-0.0140	0.0045
◇						20	-0.0106	0.0079
						30	-0.0046	0.0139
						40	-0.0026	0.0159
	1	0015	0.3		19.8	17	-0.0085	0.0080
●						19	-0.0078	0.0087
◆	3	23012	0.2	2.19	15.8	16	0.0088	0.0057
	4	0009	0.3	3	11.9	11.9	-0.01353	0.00297
						(1)	-0.01163	0.00482
						(2)	-0.00600	0.01050
						(3)	-0.003034	0.01347

NOTES: 1. THICKENED FLAP SECTION
2. ELLIPSOIDAL FLAP SECTION
3. BEVELED T.E.
4. SEE TABLE 3.3.4.2-II FOR PRIMARY REFERENCES.

1892-116B

TABLE 3.3.4.3-III TOLL'S c_{h_δ} DATA, 66SERIES SECTIONS

SYMBOL	PRIMARY REFERENCE	SECTION	c_f/c	RN x 10^{-6}	TOLL TRUE CONTOUR $\phi°$ DEG	T.E. ANGLE $\phi°$ DEG	c_{h_δ} /DEG	$c_{h_\delta}° + 0.02\ c_f/c$ + 0.0105
■	1	66-009	).3	1.43	5.6	7	-0.0117	0.0048
▲	5	66(215)-216	3.2	2.8	10	9	-0.0101	0.0044
○	6	66(215)-216 a = 0.6	).15	3.8 & 9.5		6	-0.0090	0.0045
						8	-0.0089 -0.0086	0.0049 0.0046
						13	a.0074	0.0061
						21	-0.0056	0.0079
							-0.0062	0.0073
△			0.2			6	-0.0110	0.0035
						8	-0.0097	0.0048
							-0.0099	0.0046
						17	-0.0071	0.0074
							-0.0079	0.0066
						2:		
						23	-0.0050 -0.0049	0.0095 0.0096
							-0.0053	0.0092
						26	-0.0033	0.0112
						31	-0.0005	0.0140
							-0.0037	0.0108
■	7	66 (215)-014	0.3	1.43	8.75	8	-0.0129	0.0036

NOTE: SEE TABLE 3.3.4.2-II FOR PRIMARY REFERENCES

1892-117B

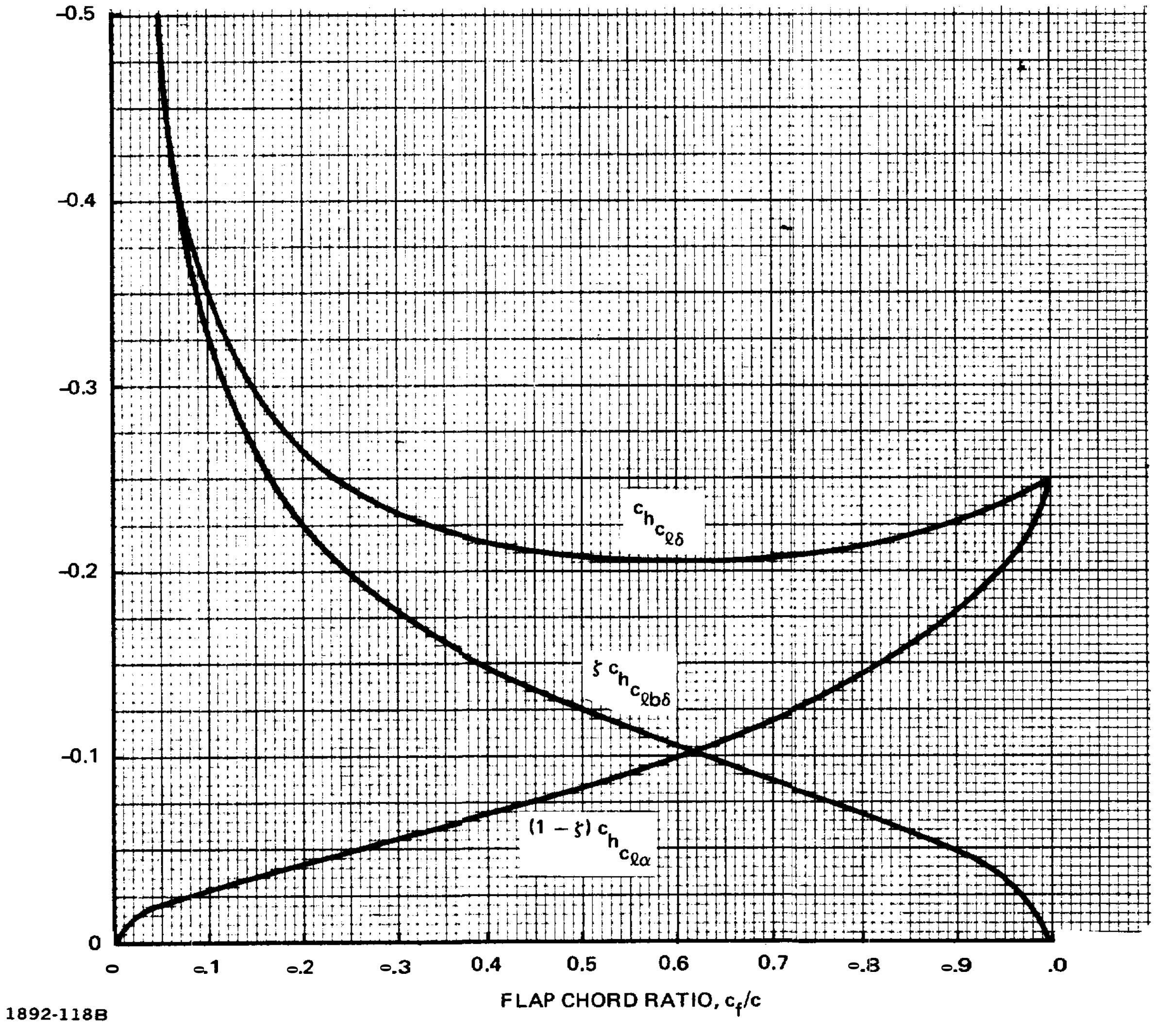

Fig. 3.3.4.3-1 Flap Hinge Moment Derivative, $c_{h_{c_{\ell\delta}}}$, Thin Airfoil Potential Theory

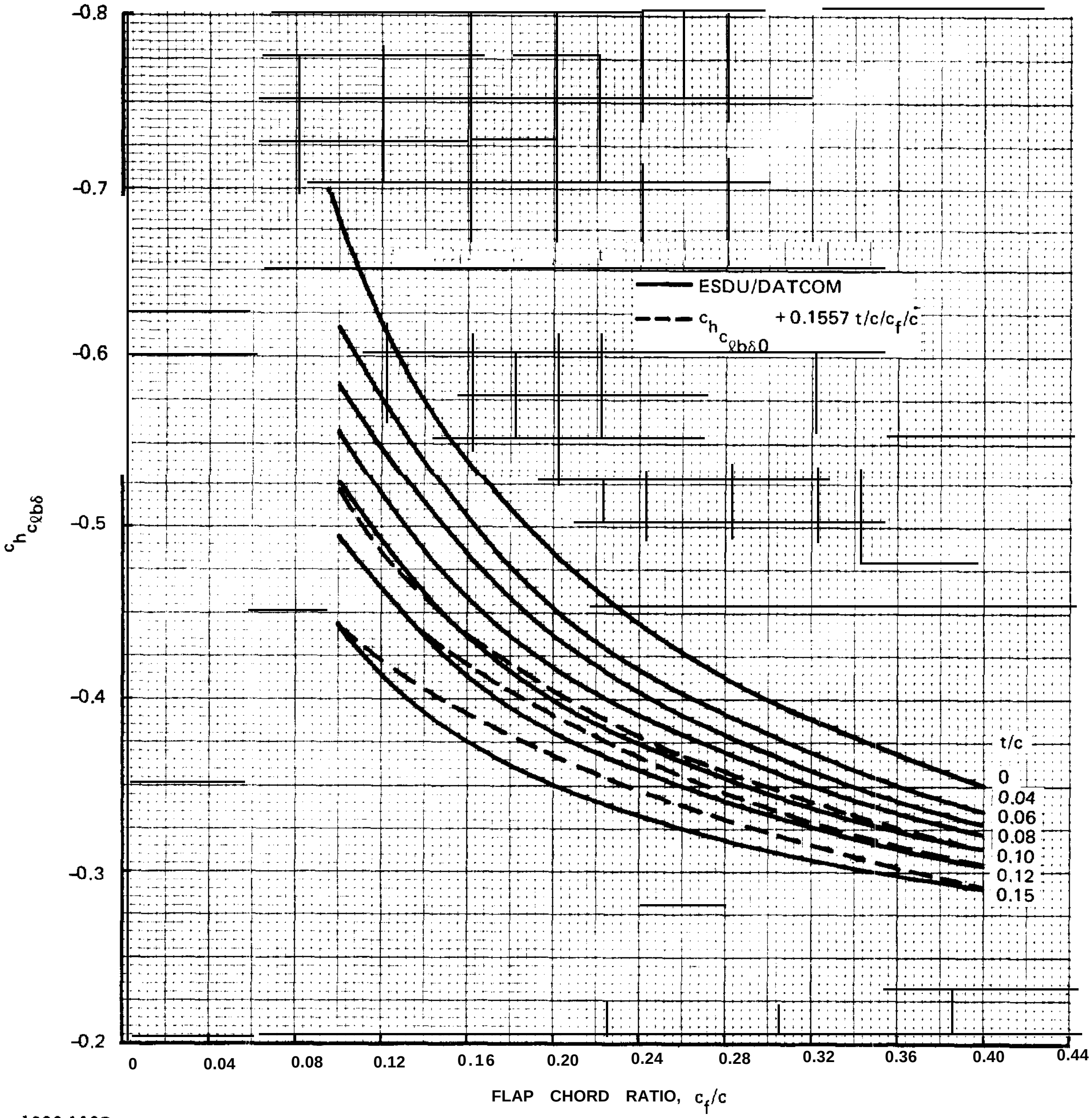

1892-119B

Fig. 3.3.4.3-2 Flap Hinge Moment Parameter, $c_{h_{c_{\ell b \delta}}}$, Thick Airfoil Potential Theory

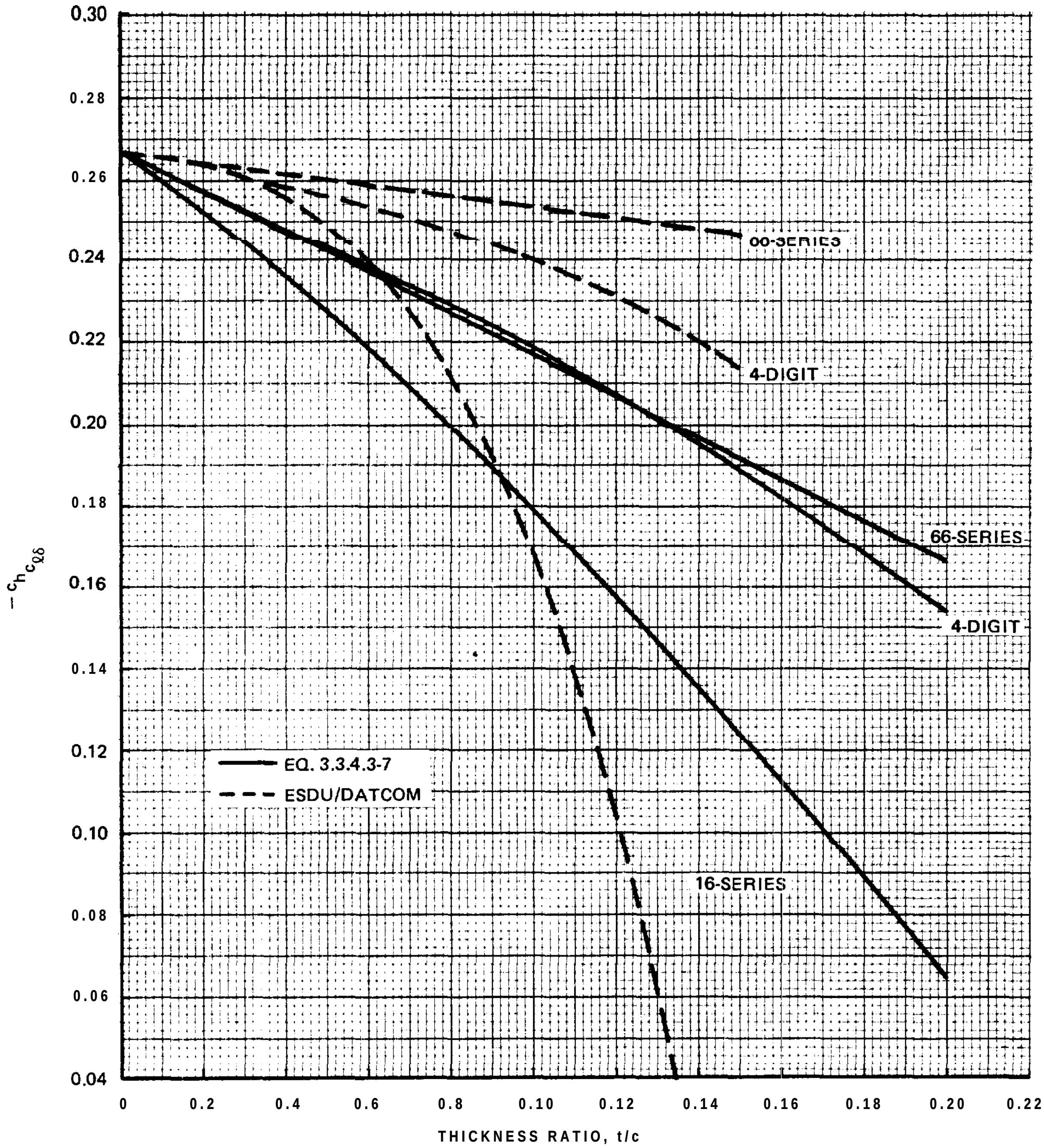

1892-120B

Fig. 3.3.4.3-3 Flap Hinge Moment Derivative, $c_{h_{c_{\ell\delta}}}$, $c_f/c = 0.2$

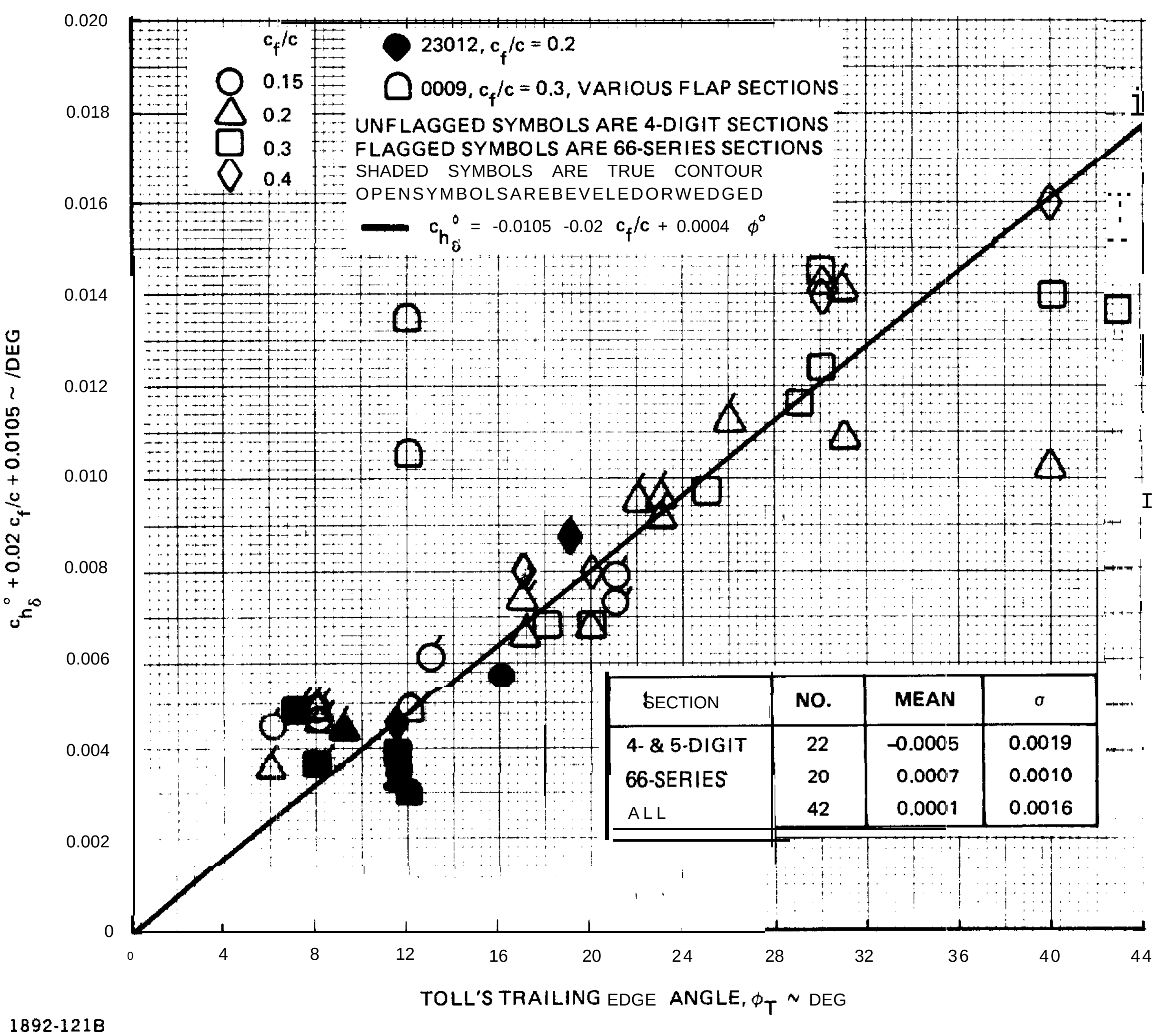

Fig. 3.3.4.3-4 Toll's c_{h_δ} Correlation

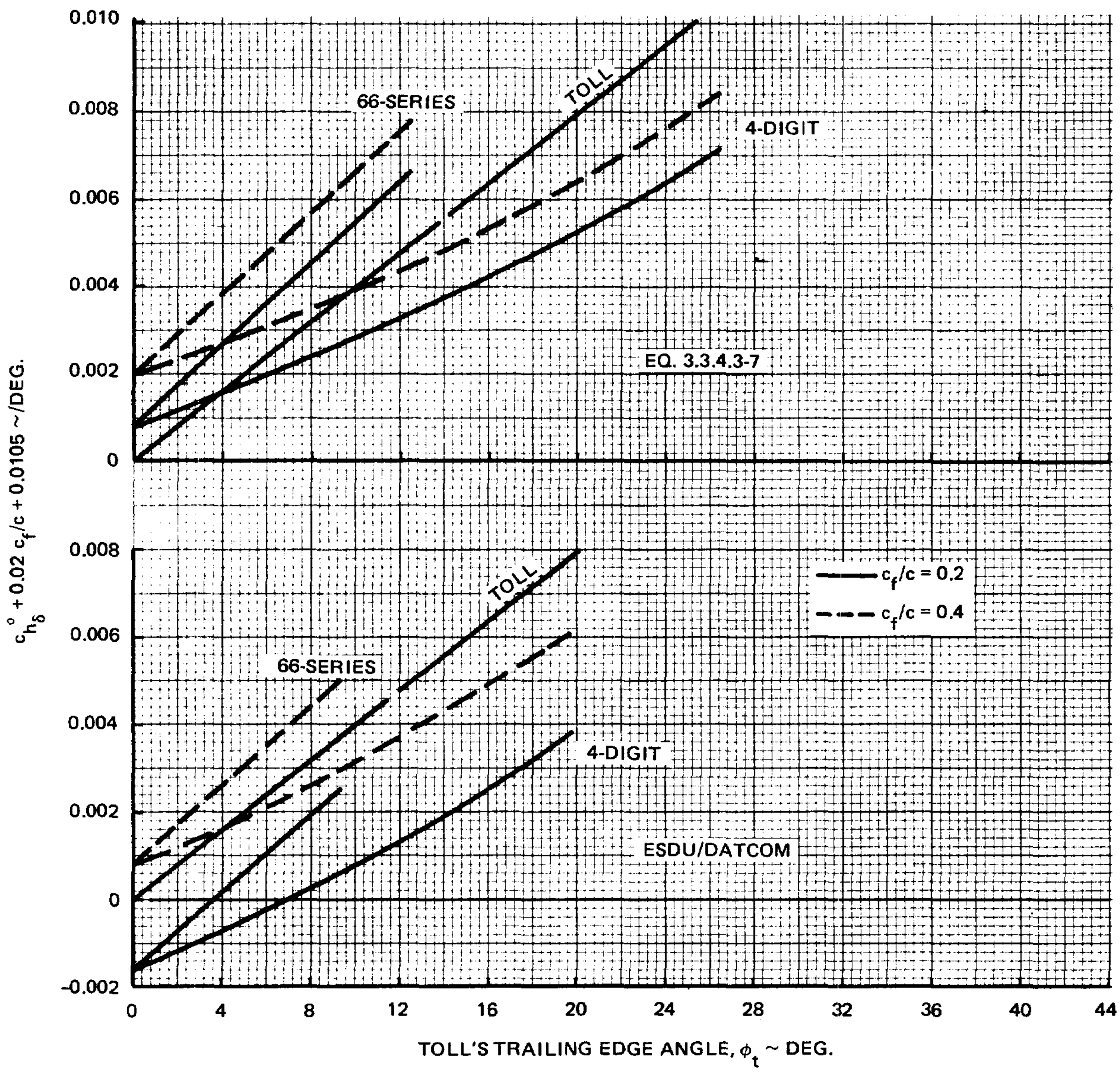

Fig. 3.3.4.3-5 c_{h_δ} Prediction Comparison

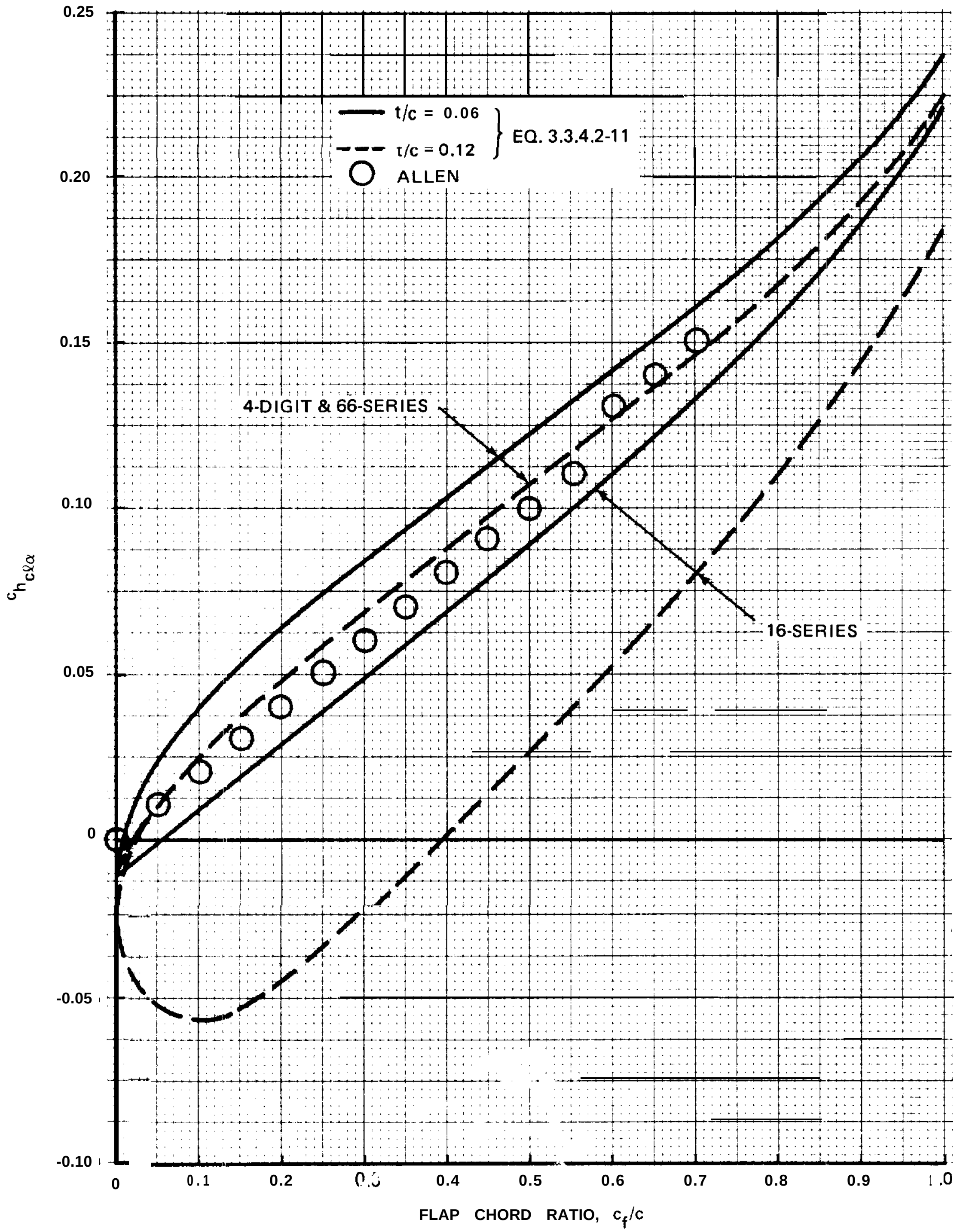

Fig. 3.3.4.3-6 Allen's $c_{h_{c_{\ell\alpha}}}$

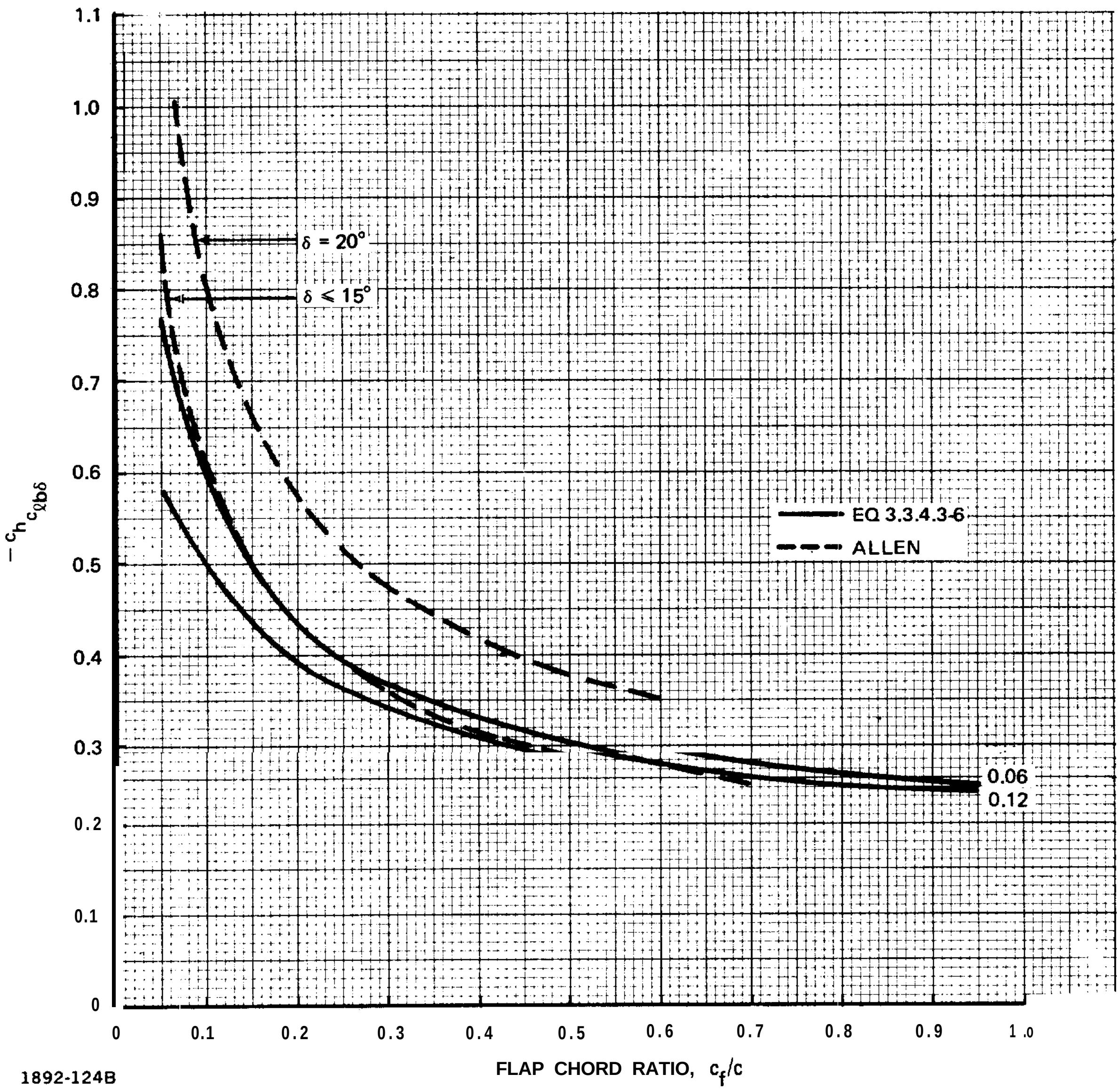

Fig. 3.3.4.3-7 Allen's $c_{h_{c_{\ell b \delta}}}$

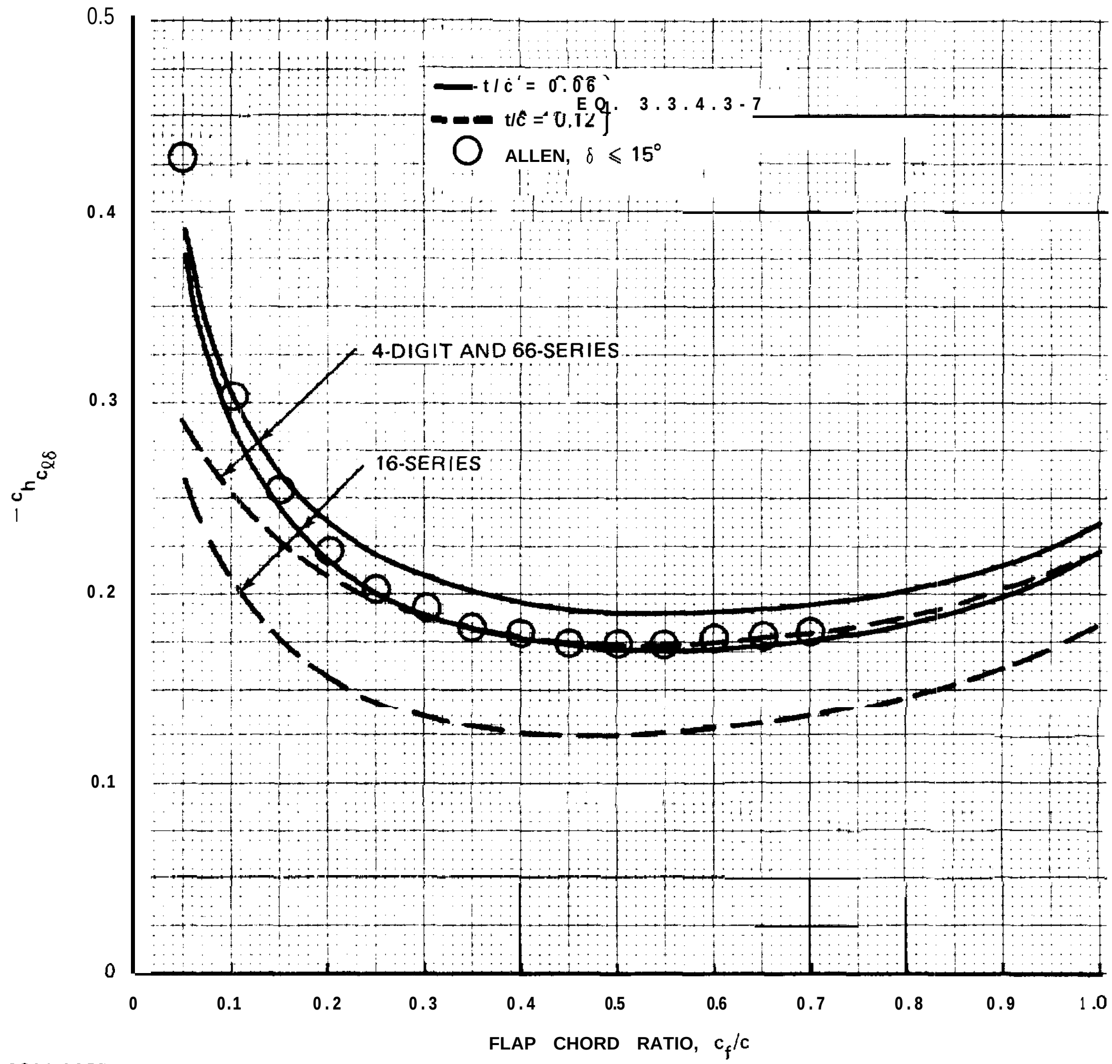

1892-125B

Fig. 3.3.4.3-8 Allen's $c_{h_{c_{\ell\delta}}}$

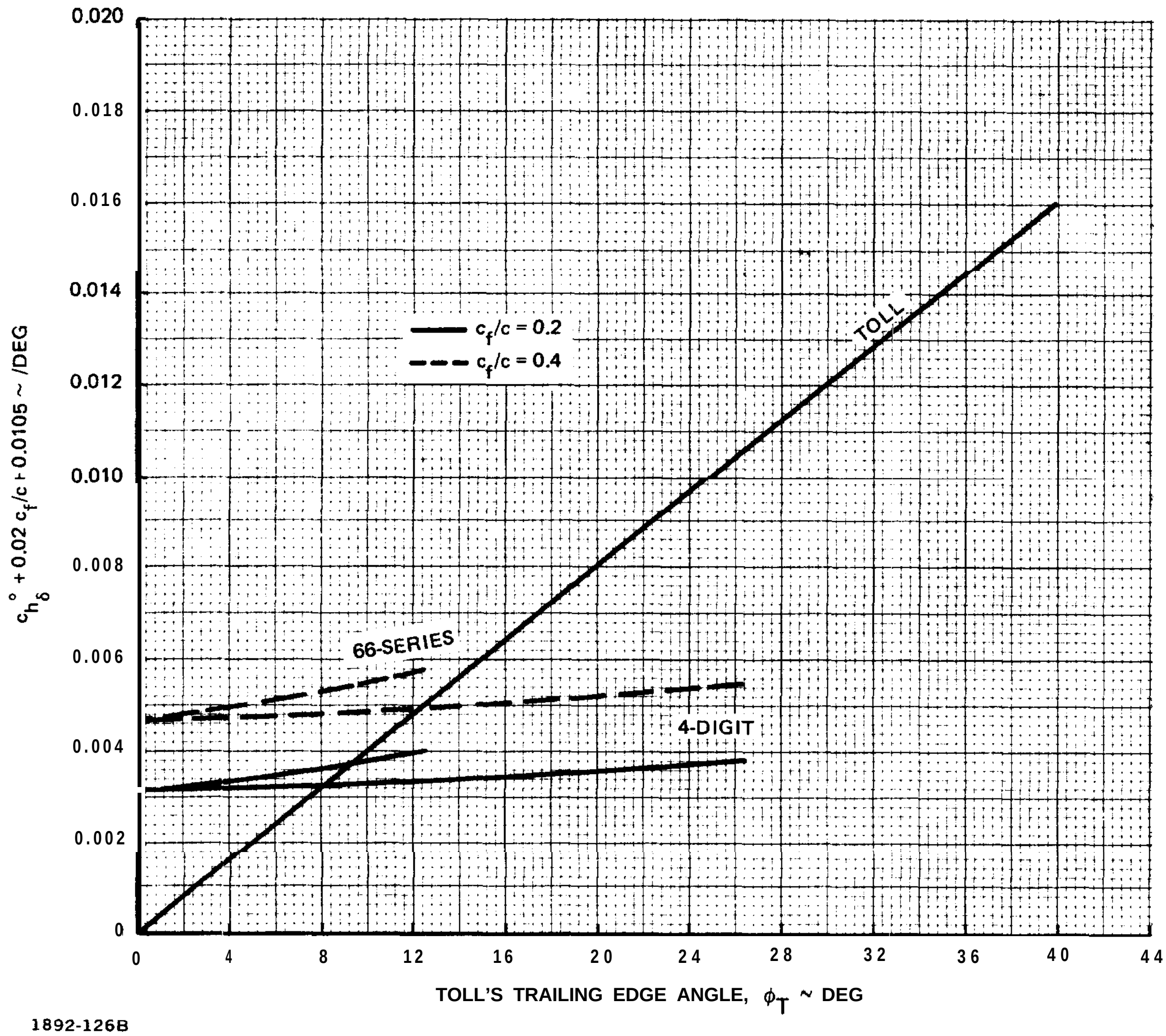

Fig. 3.3.4.3-9 Allen's c_{h_δ}

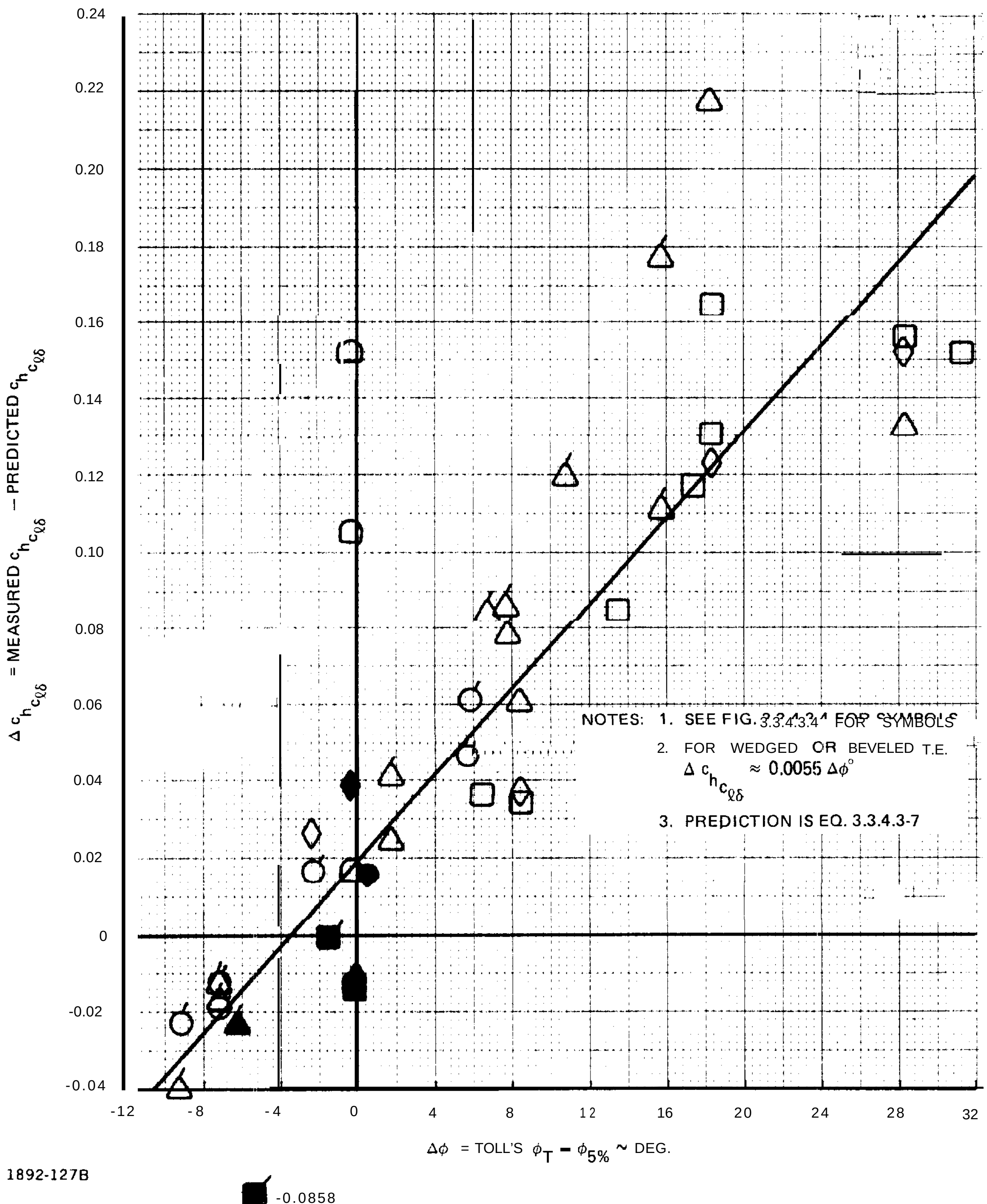

Fig, 3.3.4.3-10 Bevel Effect

3.3.4.4 Section Flap Hinge Moment. The total section flap hinge moment is given by:

$$c_h = c_{h_0} + c_{h_{c_{\ell_\alpha}}} (c_\ell)_\alpha + c_{h_{c_{\ell_\delta}}} (c_\ell)_\delta \qquad 3.3.4.4\text{-}1$$

where: c_{h_0} is from Equation 3.3.4.1-2

$c_{h_{c_{\ell_\alpha}}}$ is from Equation 3.3.4.2-11

$c_{h_{c_{\ell_\delta}}}$ is from Equation 3.3.4.3-10

For the purpose of analyzing flap hinge moment data it is convenient to consider this equation in the form:

$$c_h = c_{h_0} + c_{h_{c_{\ell_\alpha}}} c_{\ell_\alpha} \left(\alpha + \frac{c_{h_{c_{\ell_\delta}}}}{c_{h_{c_{\ell_\alpha}}}} \frac{d\alpha}{d\delta}\, \delta \right) \qquad 3.3.4.4\text{-}2$$

where: c_{ℓ_α} is from Equation 3.3.1.2-10

$\frac{d\alpha}{d\delta}$ is from Table 3.3.1.5-I or Figure 3.3.1.5-3

Equation 3.3.4.4-2 presents the flap hinge moment coefficient as a linear function of the parenthetical parametric angle.

3.3.5 Linear Lift Range.

3.3.5.1 Section Linear Lift Range. Figure 3.3.5-1, taken from Reference 1, presents the only measured section hydrodynamic lift curve which can be offered for review here. Reference 2 would be of more immediate significance but is not yet available for review. The hydrodynamic section lift curve is, therefore, best known as hypothesized from model and prototype measurements on three dimensional foils of 16-Series section,

At relatively low cavitation number and lift coefficient, cavitation produces an abrupt and substantial reduction in lift coefficient. At relatively high cavitation number and lift coefficient cavitation was expected to produce a more gradual increase in lift coefficient, perhaps indicated by a single point at 4° angle of attack on Figure 3.3.5-1, leading to a well rounded maximum lift coefficient. Figure 3.3.5-l is not inconsistent with this characterization though it does not provide a conclusive confirmation.

The initial effect of cavitation upon the lift curve slope does not, in general, correspond with the incipient cavitation boundary and is not predictable. Therefore Section 3.8 defines the lift effect cavitation boundary as an experimentally determined boundary. It is assumed that any cavitation induced lift increases are of negligible practical significance and the effective lift boundary definition is limited to reductions in the lift curve slope.

3.3.5.2 Flap Linear Lift Range. Figure 3.3.5-2 presents the zero pitch flap lift curve provided by Reference 1. A pure curve fit to this data provides a flap effectiveness which lies just within the nominal accuracy of Section 3.3.1.5.1. At the same time the nominal flap effectiveness of Section 3.3.1.5.1 fits the -6°, 0, and 2” data with half the standard deviation and displays an expected high cavitation number effect. More experience is required for a proper judgement and analysis of Reference 2 would be particularly significant.

As for the section lift curve, the significant effect of cavitation on the flap lift curve is the abrupt and substantial reduction of lift coefficient which occurs on an unpredictable boundary which is emperically defined in Section 3.8. Between the upper and lower surface lift effect boundaries the flap lift curve is assumed to be linear.

REFERENCES

1. Baloga, Paul: Water Tunnel Tests Of The NACA 64A-309 Foil Section Fitted With An Adjustable Flap In Fully-Wetted And Cavitating Flows. Graduate Aeronautical Laboratories, California Institute Of Technology Report HSWT 1131, August, 1979.

2. Jones, E.A. and MacKay, M.: Water Tunnel Tests on a NACA 16-309 Section Equipped with a Simple, Sealed Flap. Defense Research Establishment Technical Memorandum. In preparation.

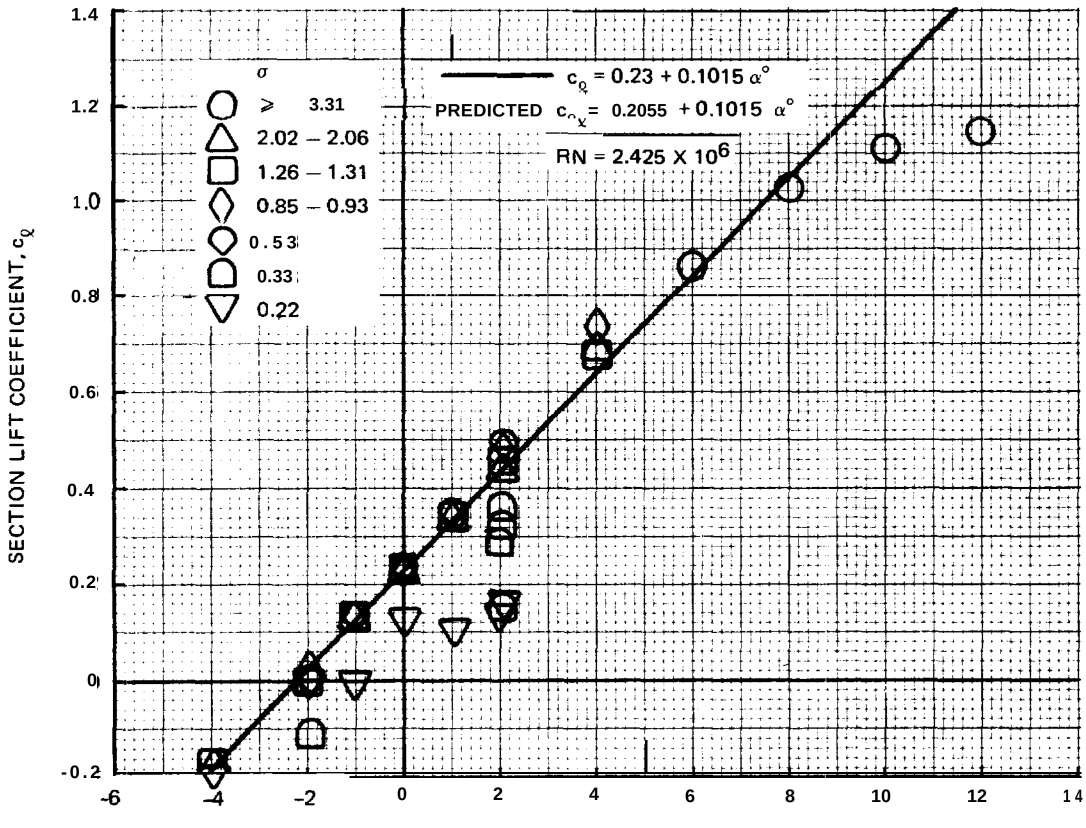

1892-128B

Fig. 3.3.5-l Hydrodynamic Lift Curve, 64A309 Section, RN = 2.425 X 10^6

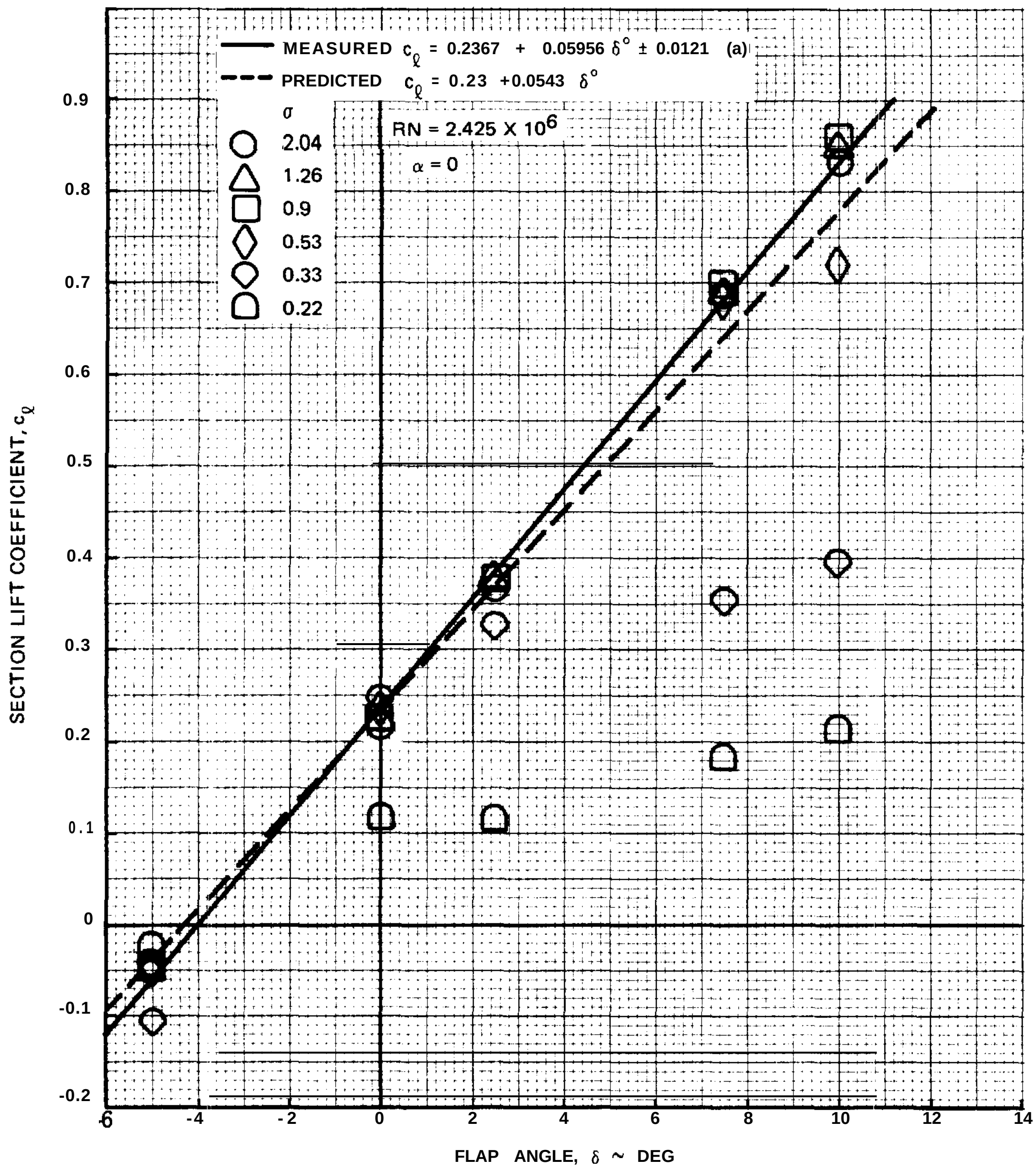

1892-129B

Fig. 3.3.5-2 Hydrodynamic Flap Lift Curve, 64A309 Section, 25% Chord Flap

3.3.6 Section Maximum Lift, For typical hydrofoil sections, and particularly for the 16-Series section, it is possible in hydrodynamic model scale for the separation, or stall, lift coefficient to fall within the incipient cavitation bucket. The ten and twelve degree angle of attack points of Figure 3.3.5-l are likely examples. For such cases the significance of the hydrodynamic model data to the prototype is not yet known. It is not likely that this model test condition can always be avoided but its existence should be identified as an aid to data interpretation by reference to ESDU Wings 01.01.06, DATCOM 4.1.1.4 (which is identical), or equivalent.

The aerodynamic maximum lift coefficient for the flapped section is equally significant to the interpretation of hydrodynamic model test data but no estimate for this characteristic can be offered here. ESDU does not include this characteristic. DATCOM Section 6.1.1.3 presents a $\Delta c_{\ell_{max}}$ for flaps but it is not clear that this is to be identified in any way with the maximum lift coefficient for the flapped section, it has no Reynolds number dependency, and it is derived out of a data sample including few potential hydrofoil sections.

3.3.7 Free Surface Effect.

3.3.7.1 Lift Curve Slope.

CLASSIC POTENTIAL SOLUTIONS

Hough and Moran, Reference 1, present a relatively well systematized and advanced example of the results of a potential attack upon the section lift curve slope beneath a free surface. All such results, particularly if left general in Froude number and section geometry, can be evaluated numerically for particular cases but with a difficulty which discourages illustration. Such attacks are frequently limited to the infinite Froude number case but as craft grow larger this practice becomes increasingly questionable. Zero lift angle and pressure distribution are implicit in these results but are rarely systematized or illustrated. Hough and Moran are particularly notable for their systemization of the general Froude number case for angle of attack, camber, and flap angle, all being illustrated in Reference 1.

Plotkin employs Hough and Moran as a standard forcomparison with the Keldysh and Lavrentiev results for angle of attack and camber in Reference 2.

That lift curve slope comparison is repeated here on Figure 3.3.7.1-1 and a camber comparison is included in Reference 2. Most of these potential theory results are expressed. in chord Froude number but the depth Froude number presents a better systemization of the results with a minimum lift curve slope in the vicinity of $\sqrt{2}$ for all foil depths.

Pattison, Reference 3, employed the Giesing and Smith modification of the Douglas Neumann program, Reference 4, for the theoretical lift curve slope for comparison with theoretical results. Those theoretical and experimental results are compared with Hough and Moran on Figure 3.3.7.1-2 where Pattison's measured results have been adjusted to a Reynolds number of three million by Equation 3.3.1.1-1. Only the measured slopes at the deepest and shallowest depths are shown on Figure 3.3.7.1-2 because the data does not provide a test for the theory. This is the only section data which can be offered.

References 2 and 3 present the best systematized presentation of the general case for the section which has been reviewed. Panchenkov's Reference 5 is very detailed, but contains no illustrative results. Reference 6 contains a digest of the Reference 5 infinite Froude number results, though written earlier.

THE INFINITE FROUDE NUMBER CASE

Infinite Froude number presents a degenerate special case of the general problem which provides a practical approximation for cruise for many craft designs; it is the take off of relatively large craft still in the conceptual stage which has generated interest in the general case.

Panchenkov has reduced the infinite Froude number case to a desk top calculation by the use of two hypergeometric series. One of the series is required only for three-dimensional foils but both are defined here for convenience.

Panchenkov's hypergeometric series have the form:

$$F_1 = F\left(\frac{1}{4}, \frac{3}{4}, 1; x\right) \qquad 3.3.7.1\text{-}1$$

$$F_2 = F\left(\frac{3}{4}, \frac{5}{4}, 2; x\right)$$

where: $$F(a,b,c;x) = 1 + \frac{ab}{c} x + \frac{ab}{c} x \frac{(a+1)(b+1)}{(1+1)(c+1)} x + \frac{ab}{c} x \frac{(a+1)(b+1)}{(1+1)(c+1)} x \frac{(a+2)(b+2)}{(1+2)(c+2)} x + \ldots$$

$$= 1 + \frac{ab}{c} x + \sum_{n=1}^{\infty} \Pi_{n-1} \frac{(a+n)(b+n)}{(1+n)(c+n)} x$$

$$\Pi_0 = \frac{ab}{c} x$$

Each of these series can be evaluated explicitly for an argument of 1/2:

$$F_1 \left(\frac{1}{2}\right) = \sqrt{\pi} \frac{\Gamma(1)}{\Gamma\left(\frac{5}{8}\right)\Gamma\left(\frac{7}{8}\right)} = 1.13391 \qquad 3.3.7.1\text{-}2$$

and:

$$F_2\left(\frac{1}{2}\right) = -4\sqrt{\pi}\,\Gamma(2)\left[\frac{1}{\Gamma\left(\frac{3}{8}\right)\Gamma\left(\frac{9}{8}\right)} - \frac{1}{\Gamma\left(\frac{7}{8}\right)\Gamma\left(\frac{5}{8}\right)}\right] = 1.3597 \qquad 3.3.7.1\text{-}3$$

Each of these results can be obtained with a twenty term series which is therefore adequate for any larger argument. The two functions have thus been evaluated over the range of interest with the results shown in Table 3.3.7.1-I where the identification of Panchenkov's x with h/c is::

$$x = \frac{1}{8\left(\frac{h}{c}\right)^2 + 1} \qquad 3.3.7.1\text{-}4$$

For the flat plate section, neglecting non-linearities, Panchenkov's infinite Froude number lift curve slope is:

$$\frac{c_{\ell_\alpha}}{c_{\ell_{\alpha_\infty}}} = \frac{1}{2} + \frac{h/c}{\sqrt{4\left(\frac{h}{c}\right)^2 + \frac{1}{2}}} F_1 \qquad 3.3.7.1\text{-}5$$

which is shown on Figure 3.3.7.1-3 where it is compared with Hough and Moran and with two approximations considered later. Figure 3 of Reference 5 compares this curve with an experimental result which differs from it by no more than 0.03 and with a Keldysh and Lavrentiev curve which is substantially below any of those shown on Figure 3.3.7.1-3.

For the thin cambered section, again neglecting non-linearities, Panchenkov's section lift curve slope is:

$$\frac{c_\ell}{c_{\ell_\infty}} = 1 - \frac{1}{2\cos 2\alpha_{0\ell}}\left[1 - \frac{2\,h/c}{\sqrt{4\left(\frac{h}{c}\right)^2 + \frac{1}{2}}} F_1\right] \qquad 3.3.7.1\text{-}6$$

The cosine term introduces about a one-half percent effect and makes the angle of attack and camber effects practically identical, inferring zero lift angle independence of depth. This contrasts with Hough and Moran's results which present distinct angle of attack and camber effects and, therefore, a zero lift angle depth dependency. The Hough and Moran camber effect is also shown on Figure 3.3.7.1-3 where it corresponds precisely with Panchenkov's flat plate curve. It will be noted in Section 3.3.7.2 that Panchenkov does have a three dimensional zero lift angle depth effect, not present in his section equation.

For the thick cambered section, and again neglecting his sin $(\alpha - \alpha_{0\ell})$ term which introduces a lift curve non-linearity, Panchenkov adds an additional term and an additional factor to Equation 3.3.7.1-6:

$$\frac{c_\ell}{c_{\ell_\infty}} = 1 - \frac{(1+\mu)^2}{2\cos 2\alpha_{0\ell}}\left[1 - \frac{2\,h/c}{\sqrt{4\left(\frac{h}{c}\right)^2 + \frac{1}{2}}} F_1\right] \qquad 3.3.7.1\text{-}7$$

$$+ \frac{\frac{y_c}{c}(1+\mu)^4 F_2}{4\sqrt{2}\left[8\left(\frac{h}{c}\right)^2 + 1\right]^{3/2} \alpha_{0\ell}\cos 3\,\alpha_{0\ell}}$$

where: yc = camber = $.05515\ c_{\ell_i}$ for a = 1.0 mean line

$$\mu = \frac{.77\ t/c}{1 - .6\ t/c}$$

$\alpha_{0\ell}$ = zero lift angle

$= -c_{\ell_i}/2\pi$ for a = 1.0 mean line.

For the a = 1.0 camber line this equation reduces to:

$$\frac{c_\ell}{c_{\ell_\infty}} = 1 - \frac{(1+\mu)^2}{2\cos\left(c_{\ell_i}/\pi\right)}\left[1 - \frac{2\,h/c}{\sqrt{4\left(\frac{h}{c}\right)^2 + \frac{1}{2}}}\ F_1\right] \qquad 3.3.7.1\text{-}8$$

$$- \frac{.05515\pi\,(1+\mu)^4\,F_2}{2\sqrt{2}\left[8\left(\frac{h}{c}\right)^2 + 1\right]^{3/2}\cos\left(3\,c_{\ell_i}/2\,\pi\right)}$$

This thickness effect is significant as illustrated on Figure 3.3.7.1-3 for an extreme and for a practical case.

THE GIBBS AND COX HANDBOOK

The Gibbs and Cox hydrodynamic section lift curve slope of Reference 7 lacks the rigor of the analyses previously considered but presents the general case with desk top analytic simplicity and with a result remarkably similar to Hough and Moran numerically.

Equation (8.19.24) of Reference 8 gives the lift for a vortex line moving beneath the free surface as:

$$\frac{L}{b} = \rho V \Gamma - \frac{\rho \Gamma^2}{4\pi h}\left[1 - \frac{4gh}{V^2}\ e^{-2gh/V^2}\ \mathrm{Ei}\left(\frac{2gh}{V^2}\right)\right] \qquad 3.3.7.1\text{-}9$$

The bracketed term is the Gibbs and Cox Ω function which may be written:

$$\Omega = 1 - 2 \times \frac{2}{F_h^2}\ e^{-2/F_h^2}\ E_i\left(\frac{2}{F_h^2}\right) \qquad 3.3.7.1\text{-}10$$

$$= 1 - 8\,f(F_h)\ \mathrm{Ei}\left(\frac{2}{F_h^2}\right)$$

where: $f(F_h) = e^{-2/F_h^2}/2\,F_h^2$

The exponential integral is now readily available in tabular form, e.g. Reference 9, or on desk or pocket computers. The first form of Equation 3.3.7.1-10 is better suited to some tabulations. The variation of this function with Froude number is shown on Figure 3.3.7.1-4 and tabulated values are given in Table 3.3.7.1-11.

In terms of the Ω function Equation 3.3.7.1-9 may be written:

$$\frac{L}{b} = \rho V \Gamma - \frac{\rho \Gamma^2 \Omega}{4nh} \qquad 3.3.7.1\text{-}11$$

$$= \rho V \Gamma \left(1 - \frac{\Gamma \Omega}{4\pi h V}\right)$$

presenting the effect of an image vortex line located 2h above the lift line. Such an image introduces a non-linearity in the lift curve slope which can be displayed as:

$$c_\ell = c_{\ell_{\alpha_\infty}} \alpha \left(1 - \frac{c_{\ell_{\alpha_\infty}} \alpha \Omega}{8\pi\, h/c}\right) \qquad 3.3.7.1\text{-}12$$

$$= 2\pi\alpha - \frac{\pi}{2} \frac{\Omega}{h/c} \alpha^2$$

Some towing tank data, e.g. Appendix D of Reference 10, may display this slope reduction with increasing, relatively high, lift coefficient though the effect would be difficult to distinguish from early cavitation or even aerodynamic stall in model scale. This non-linearity is incorporated into the Gibbs and Cox lift and drag equations but is not significant to the prototype and is not considered further here.

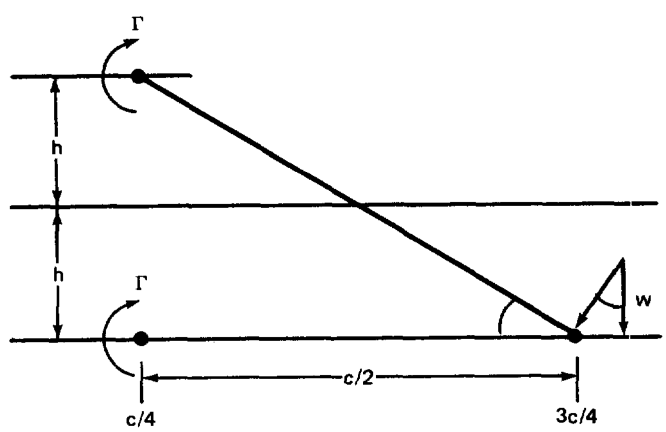

1892-130B

The image vortex produces a flow through the finite chord which the Gibbs and Cox handbook minimizes by modifying the angle of attack by the induced **downwash** angle, α_c, at the 3/4 chord station. That **downwash** is given by:

$$w = \frac{\Omega\Gamma}{2\pi\sqrt{4h^2 + c^2/4}} \times \frac{c/2}{\sqrt{4h^2 + c^2/4}} \qquad 3.3.7.1\text{-}13$$

$$= \frac{\Omega\, c_\ell\, V}{2\pi\left[(4h/c)^2 + 1\right]}$$

The corresponding incremental angle, which is a "curvature correction" rather than an induced angle (i.e. it does not tilt the lift vector), is given by:

$$\alpha_c / c_\ell = w/Vc_\ell = \frac{\Omega}{2\pi\left[(4h/c)^2 + 1\right]} \qquad 3.3.7.1\text{-}14$$

Equation (319.24) of Reference 8 also gives the (wave) drag for a vortex line moving beneath the free surface as:

$$\frac{D}{b} = \frac{\rho g \Gamma^2}{V2} e^{-2/F_h^2} \qquad 3.3.7.1\text{-}15$$

$$\approx \frac{gh}{V^2} \frac{c}{h} \frac{c_\ell^2}{2} e^{-2/F_h^2}$$

which Gibbs & Cox identifies with the induced angle:

$$\alpha_i / c_\ell = c_{d_w} / c_\ell^2 = \frac{f(F_h)}{h/c} \qquad 3.3.7.1\text{-}16$$

From Equations 3.3.7.1-14 and -16, then, the total inverse lift curve slope 'becomes:

$$\alpha_{c_\ell} = \frac{\alpha}{c_\ell} = \alpha_\infty / c_\ell + \alpha_c / c_\ell + \alpha_i / c_\ell \qquad 3.3.7.1\text{-}17$$

$$= \frac{1}{2\pi} + \frac{\Omega}{2\pi\left[(4h/c)^2 + 1\right]} + \frac{f(F_h)}{h/c}$$

where: $f(F_h) = e^{-2/F_h^2} / 2\, F_h^2$

The influence of the individual components on the lift curve slope is illustrated on Figure 3.3.7.1-5 for a one chord depth. The lift curve slope variation with Froude number is compared with Hough and Moran and with the **Pattison** data on Figure 3.3.7.1-6. The agreement with Hough and Moran is quite remarkable for such a simple expression. The persistence of Equation 3.3.7.1-17 with depth, particularly at Froude numbers in the vicinity of 1.5, is to be noted and is further illustrated on Figure 3.3.7.1-7.

At infinite Froude number Equation 3.3.7.1-17 reduces to:

$$c_{\ell_\alpha} = 2\pi \frac{(4h/c)^2 + 1}{(4h/c)^2 + 2} \qquad 3.3.7.1\text{-}18$$

$$\frac{c_{\ell_\alpha}}{c_{\ell_{\alpha_\infty}}} = \frac{(4h/c)^2 + 1}{(4h/c)^2 + 2} \qquad \text{for flat plate}$$

This is the result given by Wadlin, et. al., in Reference 11 where the curvature incremental angle was derived from a biplane image, $\Omega = 1$, of the lift line. Equation 3.3.7.1-18 is compared with Panchenkov and with Hough and Moran on Figure 3.3.7.1-3 where there are substantial differences at shallow depth.

SUMMARY

The Gibbs and Cox hydrodynamic lift curve slope accounts for depth and Froude number in an explicit, convenient equation and is therefore a desirable standard for this characteristic. In the absence of a data base the Gibbs and Cox equation was compared with those classical potential theory results which were immediately available with conflicting results which could only be resolved by definitive data. Pending the acquisition of such data the Gibbs and Cox equation is to be preferred for its convenience.

The hydrodynamic lift curve slope is therefore defined by:

$$c_{\ell_\alpha} = c_{\ell_{\alpha_\infty}} \Big/ \left[1 + \frac{\Omega}{(4h/c)^2 + 1} + 2\pi \frac{f(F_h)}{h/c}\right] \qquad 3.3.7.1\text{-}19$$

where: $c_{\ell_{\alpha_\infty}}$ is the aerodynamic section lift curve slope of Equation **3.3.1.2-10**

$$\Omega = 1 - 8\, f(F_h)\, Ei\,(2/F_h^2)$$

$$f(F_h) = e^{-2/F_h^2} / 2F_h^2$$

$$F_h = V/\sqrt{gh}$$

No accuracy can be assigned to this equation which produces an infinite Froude number lift curve slope 20% less than that of Panchenkov at quarter-chord depth and 10% less than Panchenkov and 2% less than Hough and Moran at half-chord depth.

HANDE

The HANDE foil lift curve slope is a curve fit to three dimensional data, of a form which precludes identification of the section lift curve slope.

REFERENCES

1. Hough, G. R. and Moran, J. P.: Froude Number Effects on Two-Dimensional Hydrofoils. SNAME Journal of Ship Research, Vol. 13, No. 1, March 1969.

2. Plotkin, Allen: A Note on the Thin-Hydrofoil Theory of Keldysh and Lavrentiev. SNAME Journal of Ship Research, Vol. 20, No. 2, June 1976.

3. Pattison, John H.,: Unsteady Hydrodynamic Loads On A Two-Dimensional Hydrofoil. Naval Ship Research and Development Center Report 3245, November 1970.

4. Giesing, J. P. and Smith, A. M. 0.: Potential Flow about Two-Dimensional Hydrofoils. Douglas Aircraft Division Paper 3541, October 1965.

5. Panchenkov, A. N.: The Hydrodynamics of the Hydrofoil. Institute of Hydromechanics, Ukr.S.S.R., Academy of Sciences, 1965. Available as Naval Intelligence Support Center Translation No. 3867, October 1976.

6. Panchenkov, A. N.: Approximate Analysis of Lifting Forces On A Wing Near A Free Surface. Zh. Prikl, Mekh. Fix. (PMTF) no. 4 (Nov./Dec. 1960). Available as Bureau of Ships Translation No. 825, August 1963.

7. Michel, W. H.; Hoemer, S. F.; Ward, L. W.; and Buermann, T. M.: Hydrofoil Handbook Vol. II, Hydrodynamic Characteristics of Components. Bath Iron Works Corp. by Gibbs and Cox, Inc., 1954.

8. Kochin, N. E.; Kibel, I. A.; and Roze, N. V.: Theoretical Hydromechanics. Interscience Publishers Div., John Wiley & Sons, 1964.

9. Abramowitz, Milton and Stegun, Irene A.; Editors: Handbook of Mathematical Functions. National Bureau of Standards Applied Mathematics Series -55, December 1965.

10. Layne, Douglas E.: Lift and Drag Characteristics of NACA 16-309 and NACA 64A309 Hydrofoils. DTNSRDC Report SPD-326-07, October 1976.

11. Wadlin, Kenneth L.; Shuford, Charles L., Jr.; and McGehee, John R.: A Theoretical and Experimental Investigation Of The Lift And Drag Characteristics Of Hydrofoils At Subcritical And Supercritical Speeds. NACA Report 1232, 1955.

TABLE 3.3.7.1-I PANCHENKOV'S HYPERGEOMETRIC FUNCTIONS

h/c	x	F_1	F_2
0.22754	1/2	1.1339	1.3597
0.25	0.44444	1.1131	1.3006
0.30	0.33802	1.0788	1.2058
0.35	0.25508	1.0560	1.1444
0.40	0.19237	1.0405	1.1035
0.45	0.14568	1.0297	1.0756
0.50	0.11111	1.0222	1.0562
0.60	0.066426	1.0129	1.0326
0.70	0.041311	1.0079	1.0199
0.80	0.026699	1.0051	1.0127
0.90	0.017873	1.0034	1.0085
1.00	0.012346	1.0023	1.0058
1.50	2.7701E-3	1.0005	1.0013
2.00	9.1827E-4	1.0002	1.0004
2.50	3.8447E-4	1.0001	1.0002
3.00	1.8765E-4	1	1.0001
3.50	1.0203E-4	1	1
4.00	6.0090E-5	1	1

1892-131B

TABLE 3.3.7.1-II THE Ω FUNCTION

F_h	F_h^2	Ω	F_h^2	F_h	Ω
0		-1		0	-1
0.1	200	-1.0101	200	0.1	-1.0101
0.2	50	-1.0570	50	0.2	-1.0570
0.4	12.5	-1.1955	22.222	0.3	-1.0995
0.5	8	-1.3637	12.5	0.4	-1.1955
0.6	5.5556	-1.6201	10	0.4472 1	-1.2629
0.7	4.0816	-1.8632	8	0.5	-1.3637
0.75	3.5556	-1.9377	5.5	0.60302	-1.6283
0.8	3.125	-1.9677	4	0.70711	-1.8764
0.85	2.7782	-1.9523	3.5	0.75593	-1.9436
0.9	2.46910	-1.8949	3	0.81650	-1.9675
1	2	-1.6819	2.5	0.89443	-1.9032
1.2	1.3889	-1.0607	2	1	-1.6819
1.4	1.0204	-0.4349	1.4	1.1953	-1.0764
1.57	0.81139	0.0059	1	1.4142	-0.3944
1.6	0.78125	0.0735	0.81	1.5713	0.0089
1.8	0.61728	0.4526	0.8	1.5811	0.0313
2	0.5	0.7245	0.6	1.8257	0.4930
2.25	0.39506	0.9541	0.5	2	0.7245
2.5	0.32	1.0998	0.4	2.2361	0.9438
2.75	0.26446	1.1908	0.32	2.5	1.0998
3	0.22222	1.2462	0.26	2.7735	1.1972
4	0.125	1.3030	0.22	3.0151	1.2487
5	0.08	1.2757	0.12	4.0825	1.3021
6	0.055556	1.2372	0.08	5	1.2757
7	0.040816	1.2022	0.05	6.3246	1.2252
8	0.03125	1.1731	0.04	7.0711	1.1999
9	0.024691	1.1493	0.03	8.1650	1.1688
10	0.02	1.1300	0.02	10	1.1300
	0	1	0.01	14.1421	1.0796
			0		1

1892-132B

,80768	3.06585	-1.96816
1.56747	.814012	0
3.89685	.131705	1.30336

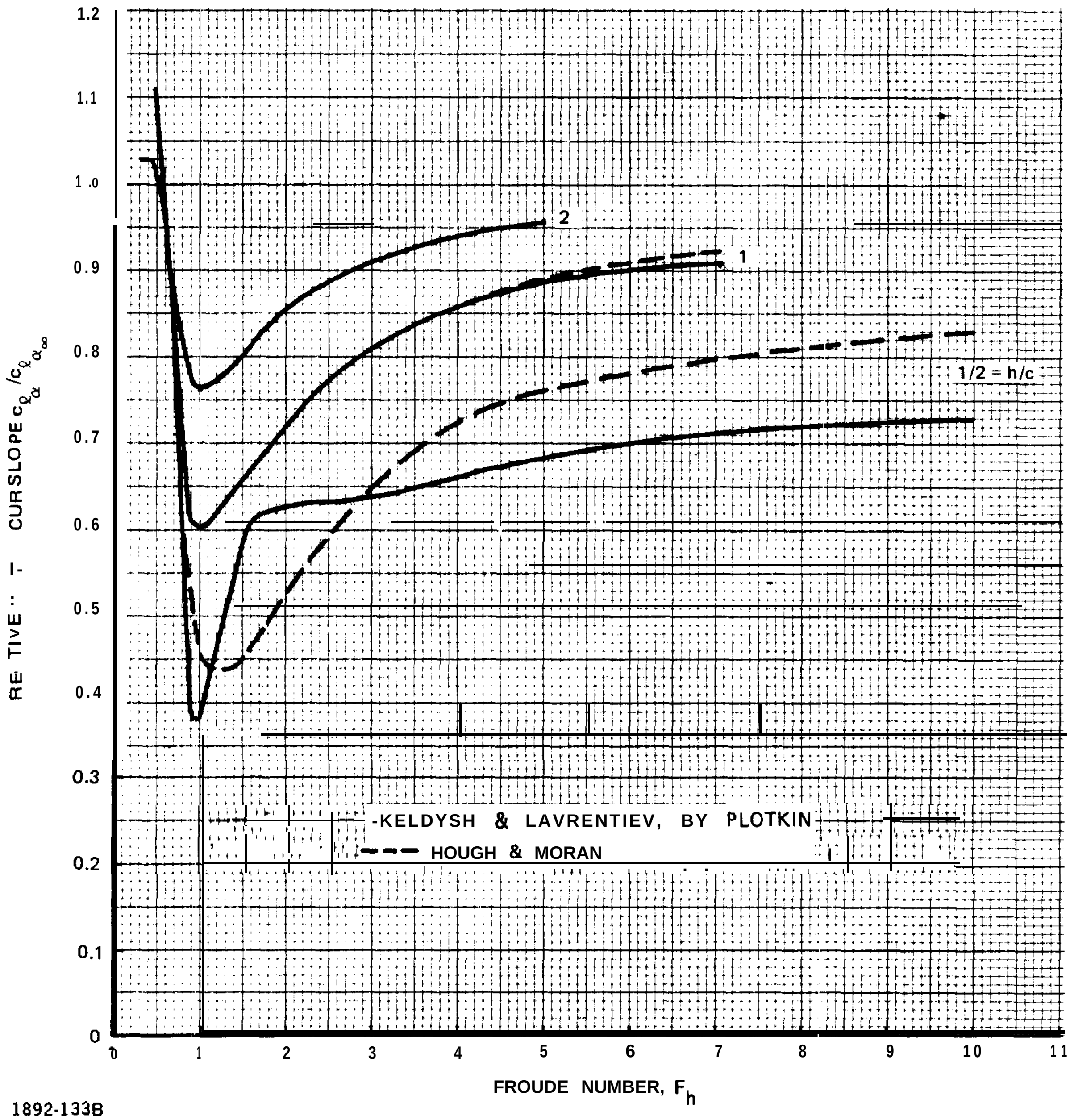

Fig. 3.3.7.1-1 Section Lift Curve Slope, Hough & Moran, Keldysh & Lavrentiev

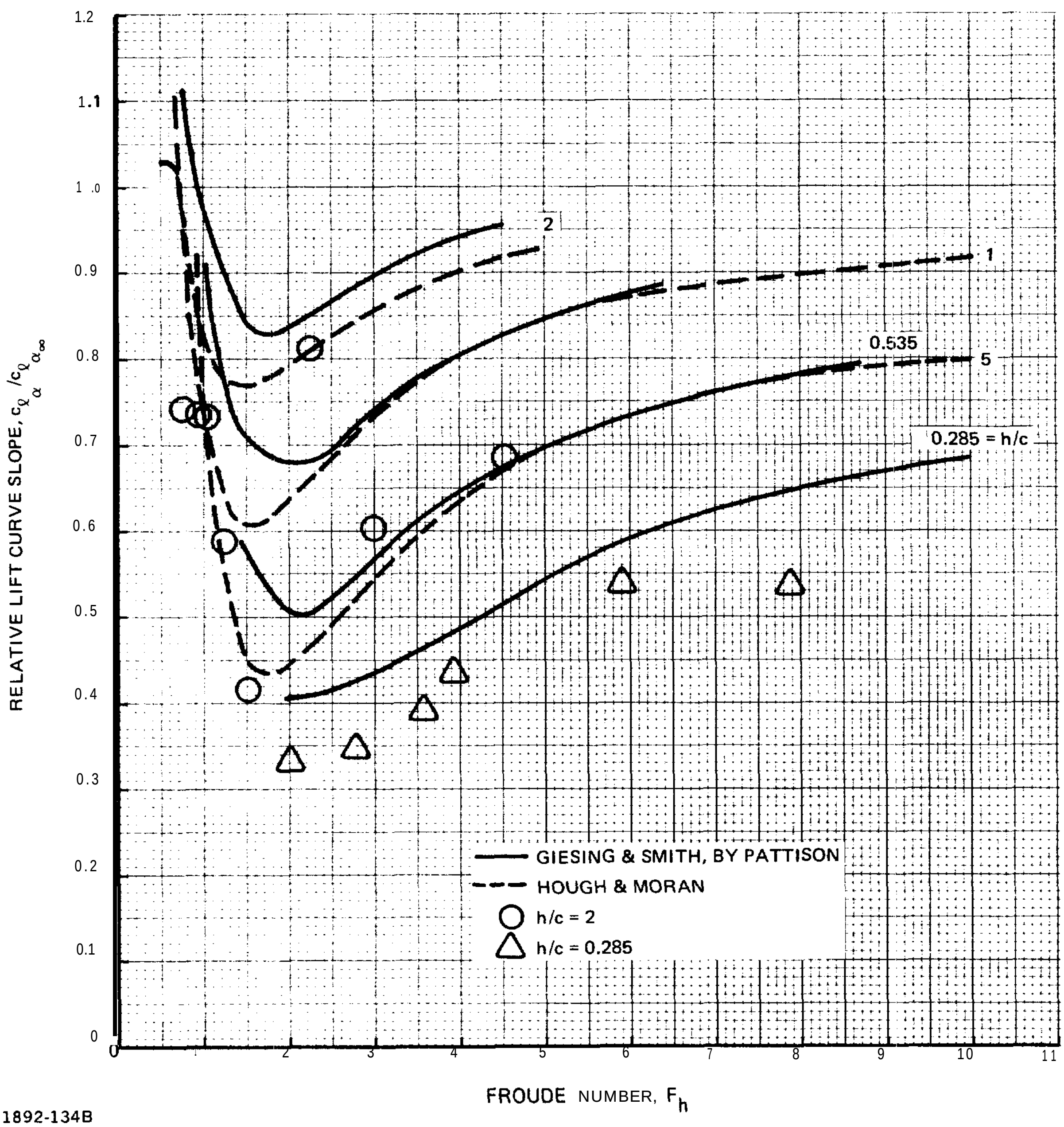

1892-134B

Fig. 3.3.7.1-2 Pattison Section Lift Curve Slope

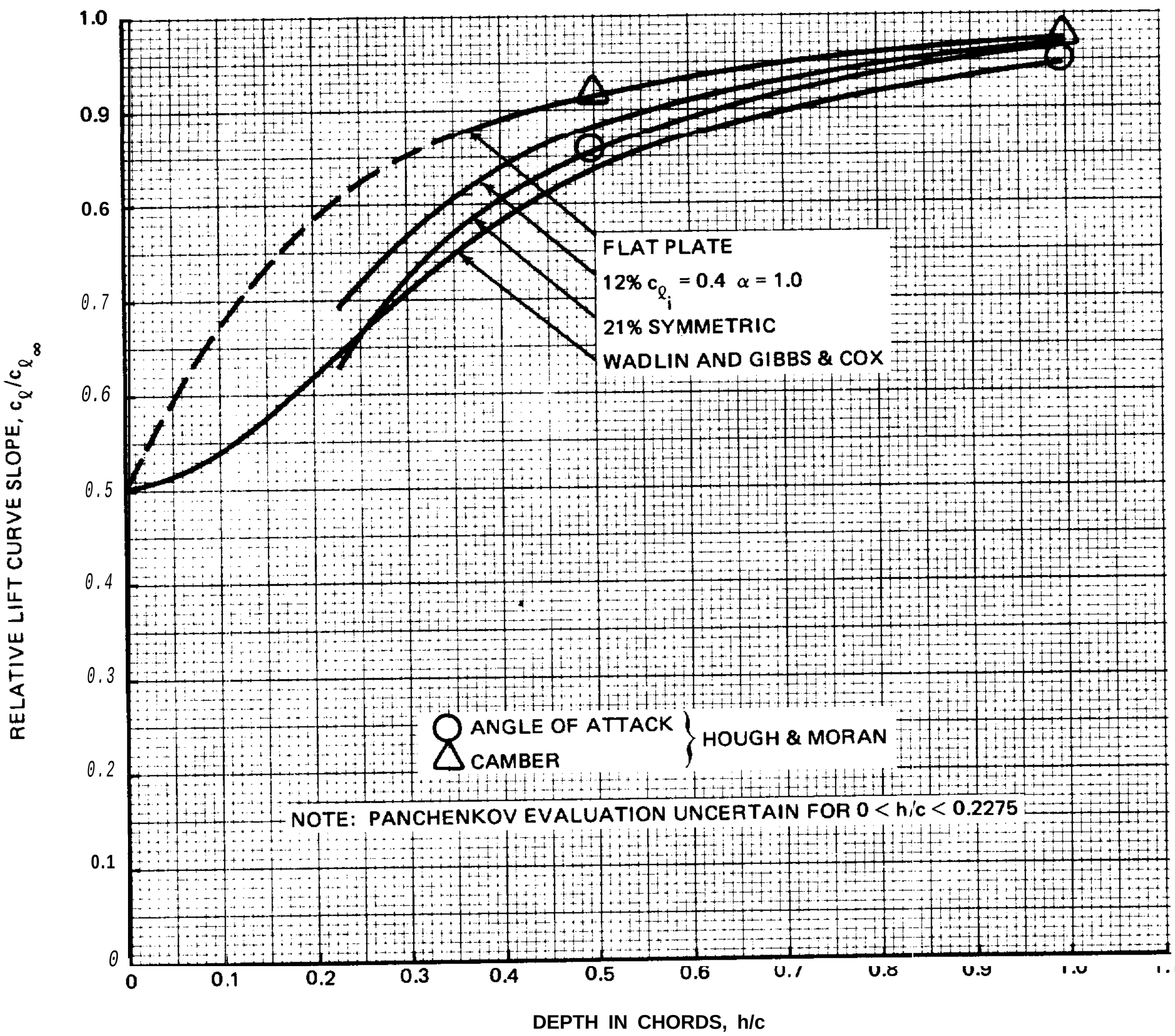

1892-135B

Fig. 3.3.7.1-3 Panchenkov Section Lift Curve Slope, $F_h = \infty$

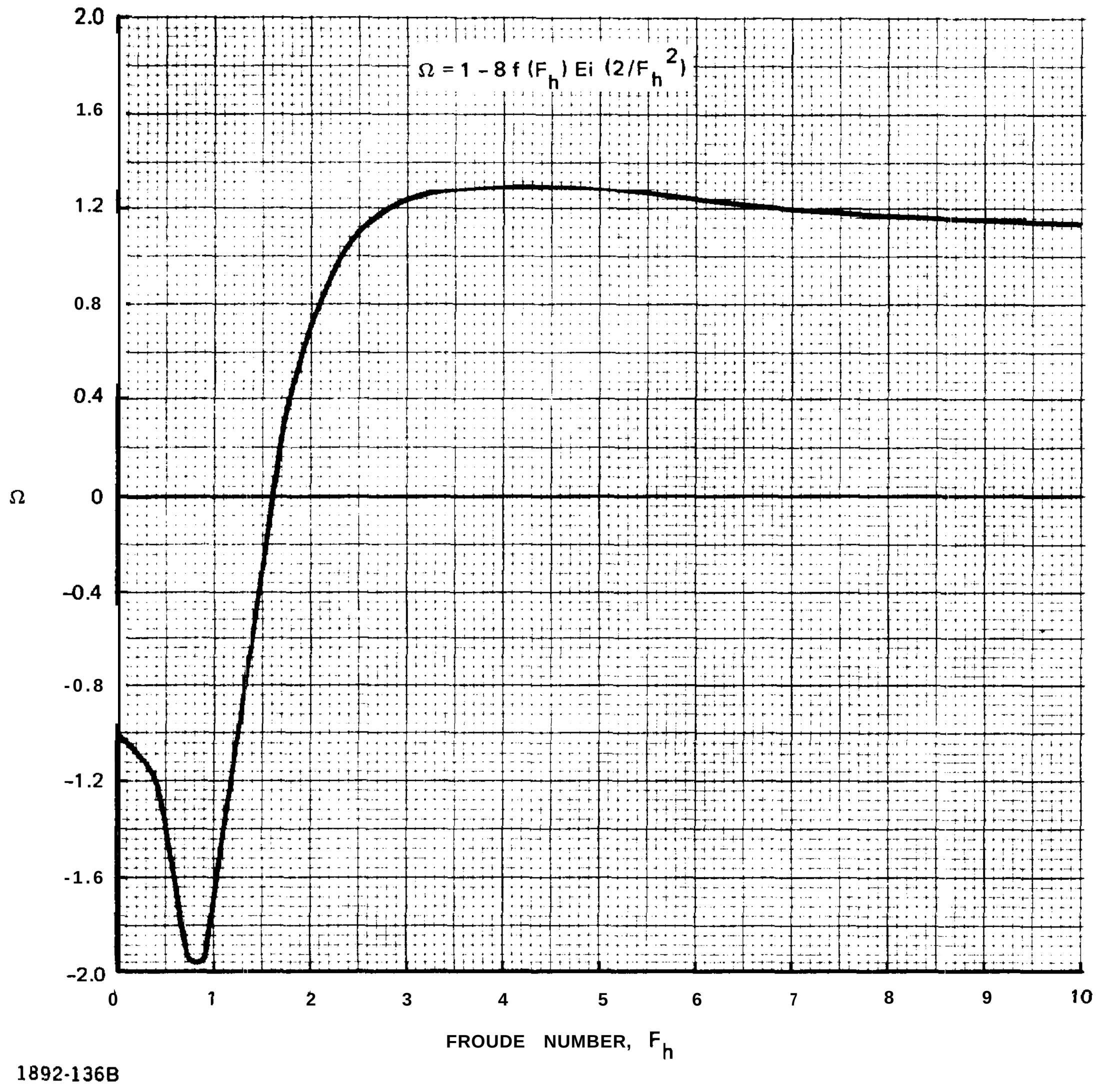

Fig. 3.3.7.1-4 The Gibbs & Cox Ω Function

h/c = 1
0 2 f(F_H)
× 1 f(F_H)

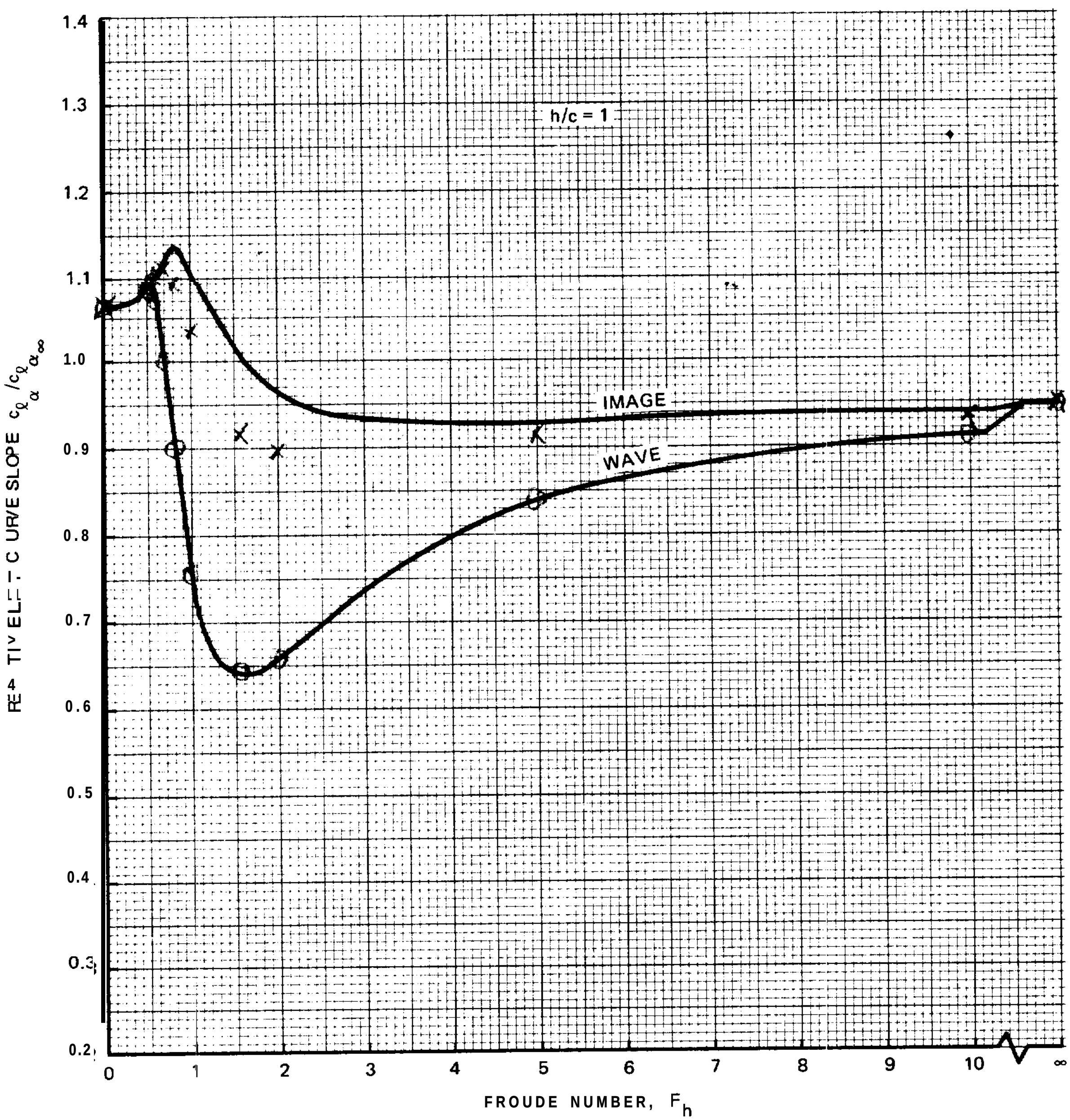

1892-137B

Fig. 3.3.7.1-5 Section Induced Angle Components, Gibbs and Cox

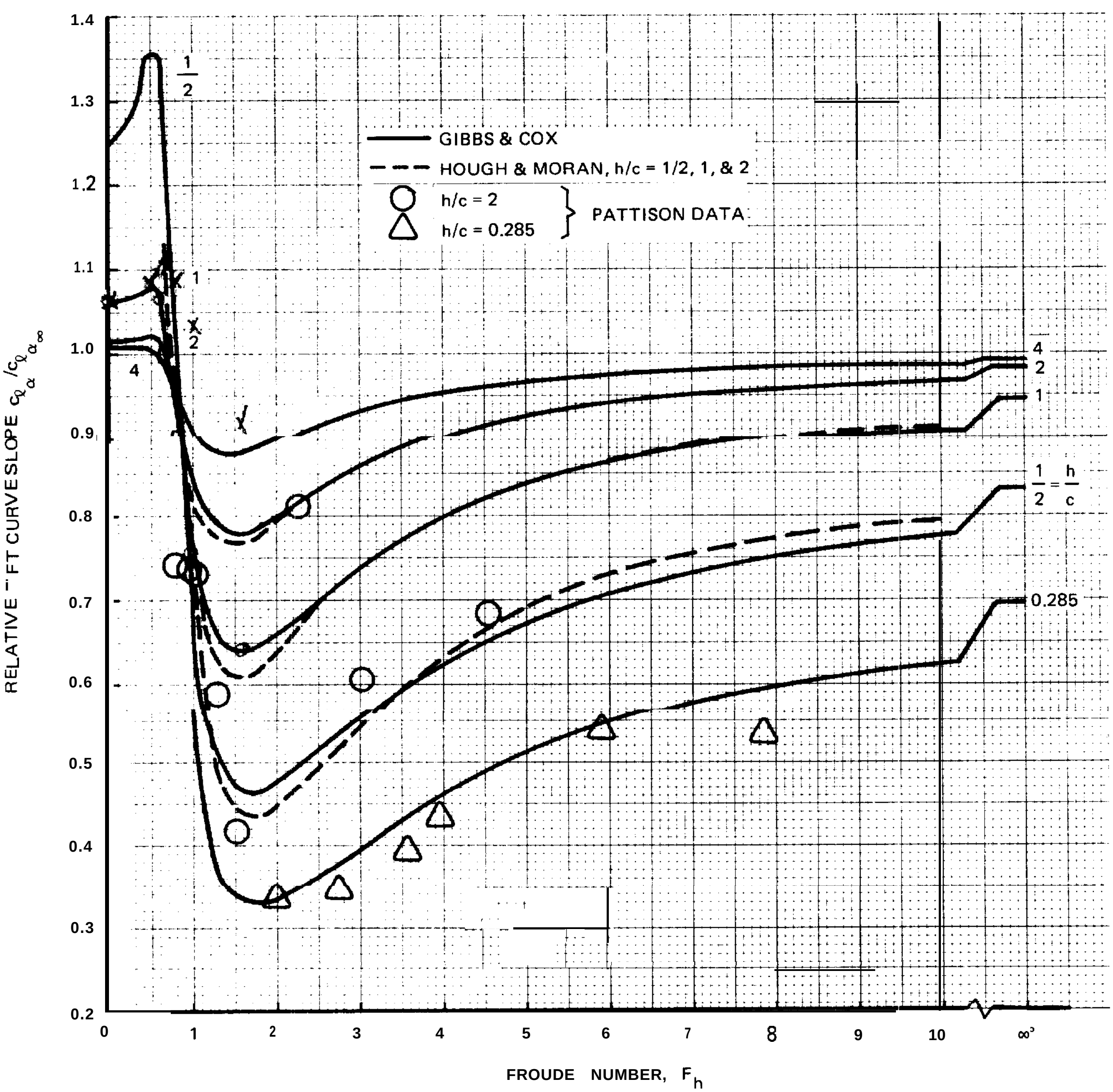

1892-138B

Fig, 3.3.7.1-6 Section Lift Curve Slope vs Froude Number

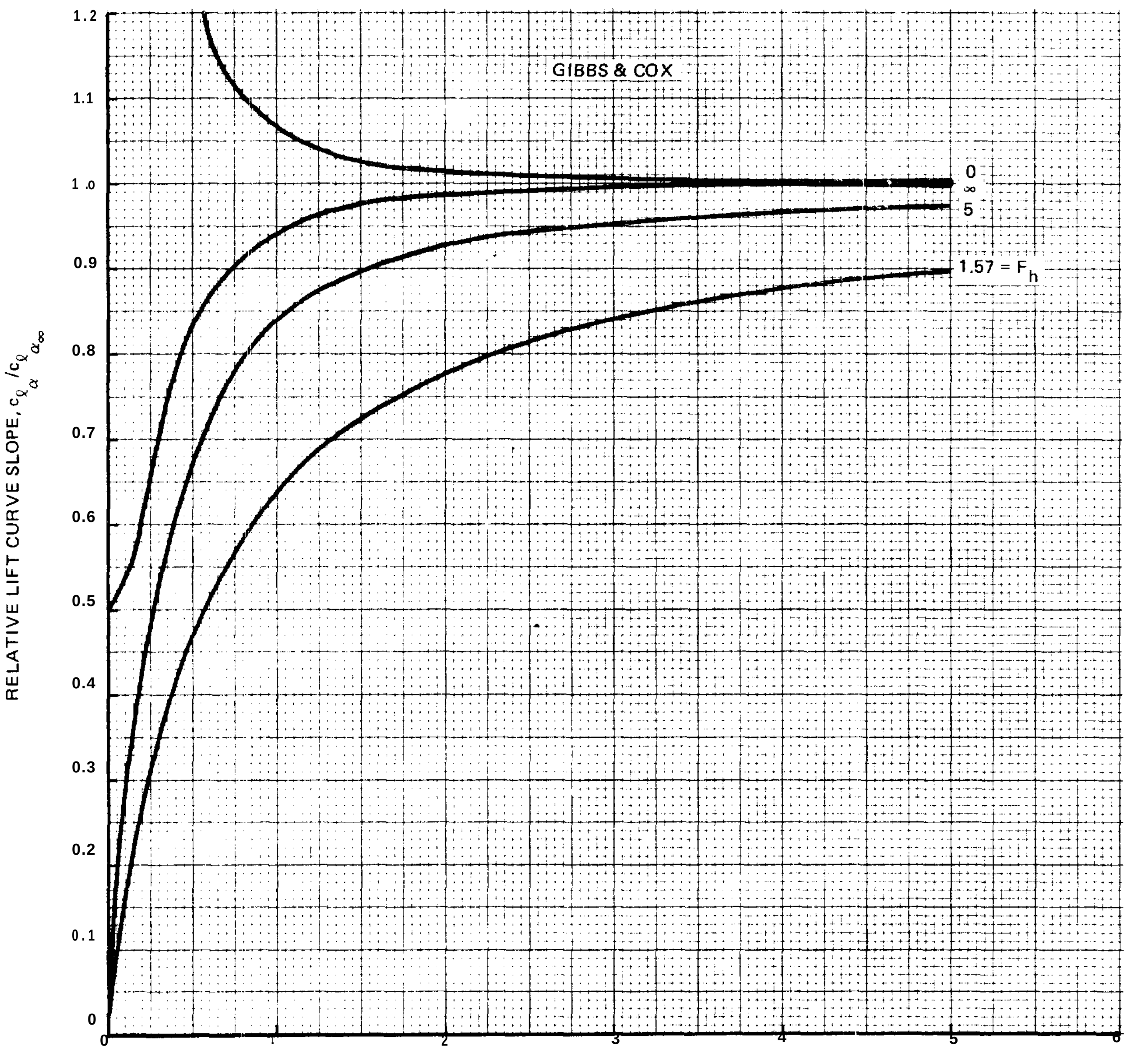

1892-139B

Fig. 3.3.7.1-7 Section Lift Curve Slope vs Depth

3.3.7.2 Zero Lift Angle.

HOUGH & MORAN

Restricting discussion to sections of zero ideal angle of attack, e.g. the a = 1.0 mean line, the zero lift angle may be written in the Hough and Moran notation of Reference 1 where the ideal lift coefficient is called the camber lift coefficient:

$$\alpha_{0\ell} = -\frac{c_{\ell_C}}{c_{\ell_\alpha}} = -\frac{c_{\ell_{c\infty}}\left(c_{\ell_C}/c_{\ell_{c\infty}}\right)}{c_{\ell_{\alpha\infty}}\left(c_{\ell_\alpha}/c_{\ell_{\alpha\infty}}\right)} \qquad 3.3.7.2\text{-}1$$

$$= \alpha_{0\ell_\infty}\frac{\left(c_\ell/c_{\ell_\infty}\right)_c}{\left(c_\ell/c_{\ell_\infty}\right)_\alpha}$$

$$\frac{\alpha_{0\ell}}{\alpha_{0\ell_\infty}} = \frac{\left(c_\ell/c_{\ell_\infty}\right)_c}{\left(c_\ell/c_{\ell_\infty}\right)_\alpha}$$

Of the classical potential theory results examined in Section 3.3.7.1 only Hough and Moran drew the distinction between camber and angle of attack free surface effects. The resultant zero lift angle effect is shown on Figure 3.3.7.2-l.

PANCHENKOV

In Reference 2, which is limited to the infinite Froude number case, Panchenkov implies in some rather obscure angular nomenclature a zero lift angle shift for the three dimensional foil which is not present for the section. That zero lift angle shift is defined by:

$$\Delta\alpha_{0\ell} - \frac{c_{\ell_{\alpha\infty}}}{c_{\ell_\alpha}} - \frac{\frac{y_c}{y}(1+\mu)^4 F_2}{4\sqrt{2}\left[8\left(\frac{h}{c}\right)^2+1\right]^{3/2}\cos 3\,\alpha_{0\ell_\infty}} \qquad 3.3.7.2\text{-}2$$

and for the a = 1.0 mean line:

$$\Delta\alpha_{0\ell} - \frac{c_{\ell_{\alpha\infty}}}{c_{\ell_\alpha}} - \frac{.05515\, c_{\ell_i}(1+\mu)^4\ F2}{4\sqrt{2}\left[8\left(\frac{h}{c}\right)^2+1\right]^{3/2}\cos\left(3\,c_{\ell_i}/2\pi\right)} \qquad 3.3.7.2\text{-}3$$

For any mean line presenting a zero ideal angle of attack this shift can be expressed as a ratio:

$$\frac{\alpha_{0\ell}}{\alpha_{0\ell_\infty}} = \frac{\alpha_{0\ell_\infty} + \Delta\ \alpha_{0\ell}}{\alpha_{0\ell_\infty}} = \frac{-\frac{c_{\ell_i}}{2\pi} + \Delta\ \alpha_{0\ell}}{-\frac{c_{\ell_i}}{2\pi}} \tag{3.3.7.2-4}$$

$$= 1 - \frac{\frac{y_c/c}{c_{\ell_i}}\pi\ (1+\mu)^4\ F_2}{2\sqrt{2}\ \frac{c_{\ell_\alpha}}{c_{\ell_{\alpha_\infty}}}\ \left[8\,(h/c)^2 + 1\right]^{3/2} \cos 3\ \alpha_{0\ell_\infty}}$$

and for the a = 1.0 mean line

$$\frac{\alpha_{0\ell}}{\alpha_{0\ell_\infty}} = 1 - \frac{.05515\ \pi\ (1+\mu)^4\ F_2}{2\sqrt{2}\ \frac{c_{\ell_\alpha}}{c_{\ell_{\alpha_\infty}}}\left[8\,(h/c)^2 + 1\right]^{3/2} \cos\left(3\ c_{\ell_i}/2\pi\right)} \tag{3.3.7.2-5}$$

This variation witb depth is compared with Hough and Moran on Figure 3.3.7.2-2.

EXPERIMENTAL DATA

No section measurements and only one set of three dimensional measurements, Wadlin of Reference 3, of the hydrodynamic zero lift angle can be offered. Wadlin's measurements would have had increased significance if the aerodynamic lift curve had also been measured of if the section employed had been one of those included in Appendix IV of Reference 4.

For the plain, untwisted foil of constant section the section and three-dimensional zero lift angles should be identical Wadlin's aspect ratio 4 data considered here was measured with the foil sting mounted and should approach this ideal. The aspect ratio 10 data has the foil mounted on a 66_1 - 012 strut of equal chord and without fillets and some zero lift angle three dimensional effect can be expected; more so than for the typical hydrofoil case which houses such an intersection with a prismatic pod.

The theoretical zero lift angles of Figures 3.3.7.2-2 and -3 are expressed in terms of the 64_1A412 section zero lift angle of Equation 3.3.1.3-2 for comparison with the Wadlin data.

The deepest depth, highest Froude number measured zero lift angle was 1/2 degree less negative than expected for the aspect ratio 4 foil which was expected to represent the aerodynamic case. The difference exceeds the nominal zero lift angle accuracy and in the opposite direction from the shift associated with Reynold's number effects. The aspect ratio 10 measured zero lift angle differs from that expected by only 1/10 degree and in a direction, relative to the aspect ratio 4 measurement, expected to result from the strut influence. It is assumed here that the aspect ratio 4 foil presents the zero lift angle for the test section and that the aspect ratio 10 foil presents the strut influence.

Figure 3.3.7.2-2 indicates that at high Froude number, greater than 4 or 5, no depth effect on zero lift angle was measured and none was expected for any practical depth.

Figure 3.3.7.2-3 is quite inconclusive only because of the shallow depth aspect ratio 10 result. It is to be noted that the lowest practical Froude number currently in the conceptual stage is $\sqrt{2}$. Partly because of the Hough & Moran prediction but also largely for convenience it is assumed here that the shallow aspect ratio 10 result of Figure 3.3.7.2-3 is a three dimensional result and that the figure indicates that no Froude number effect on section zero lift angle was measured or expected for any practical Froude number.

SUMMARY

No significant free surface effect upon the zero lift angle of thin trailing edge sections has been conclusively demonstrated by theory or measurement for practical depths or depth Froude numbers; i. e. for depths greater than 1/2 chord or depth Froude numbers greater than $\sqrt{2}$.

HANDE

HANDE employs the following hydrodynamic incremental zero lift angle:

$$\Delta \alpha^{\circ}_{0\ell} = 1.9912 / \left(\frac{h}{c} + \frac{3}{4}\right)^2 + 5.2480 \exp\left[-\sqrt{\frac{h}{c}}\left(.6555\sqrt{\frac{h}{c}} + .8645\,F_h\right)\right] \qquad 3.3.7.2\text{-}5$$

The equation is said to be developed by utilizing potential theory and model test data. The data base is unspecified except for the inclusion of PCH, PGH-2, and PHM data. The increment is referred to as being for the section but there appears to be no distinct increment for the three dimensional foil.

Comparison of Equation 3.3.7.2-5 with the measurements of Figures 3.3.7.2-2 and -3 indicates that it does not present a two dimensional section increment.

REFERENCES

1. Hough, G. R. and Moran, J. P.: Froude Number Effects on Two-Dimensional Hydrofoils. SNAME Journal of Ship Research, Vol. 13, No. 1, March 1969.

2. Panchenkov, A. N.: Approximate Analysis of Lifting Forces On A Wing Near A Free Surface. Zh. Prkl, Mekh. Fix. (PMTF) no. 4 (Nov./Dec. 1960.) Available as Bureau of Ships Translation No. 825, August 1963.

3. Wadlin, Kenneth L.; Shuford, Charles L., Jr.; and McGehee, John R.: A Theoretical And Experimental Investigation Of The Lift And Drag Characteristics Of Hydrofoils At Subcritical And Supercritical Speeds. NACA Report 1232, 1955.

4. Abbott, Ira H. and VonDoenhoff, Albert E.; Theory Of Wing Sections. Dover Publications, 1959.

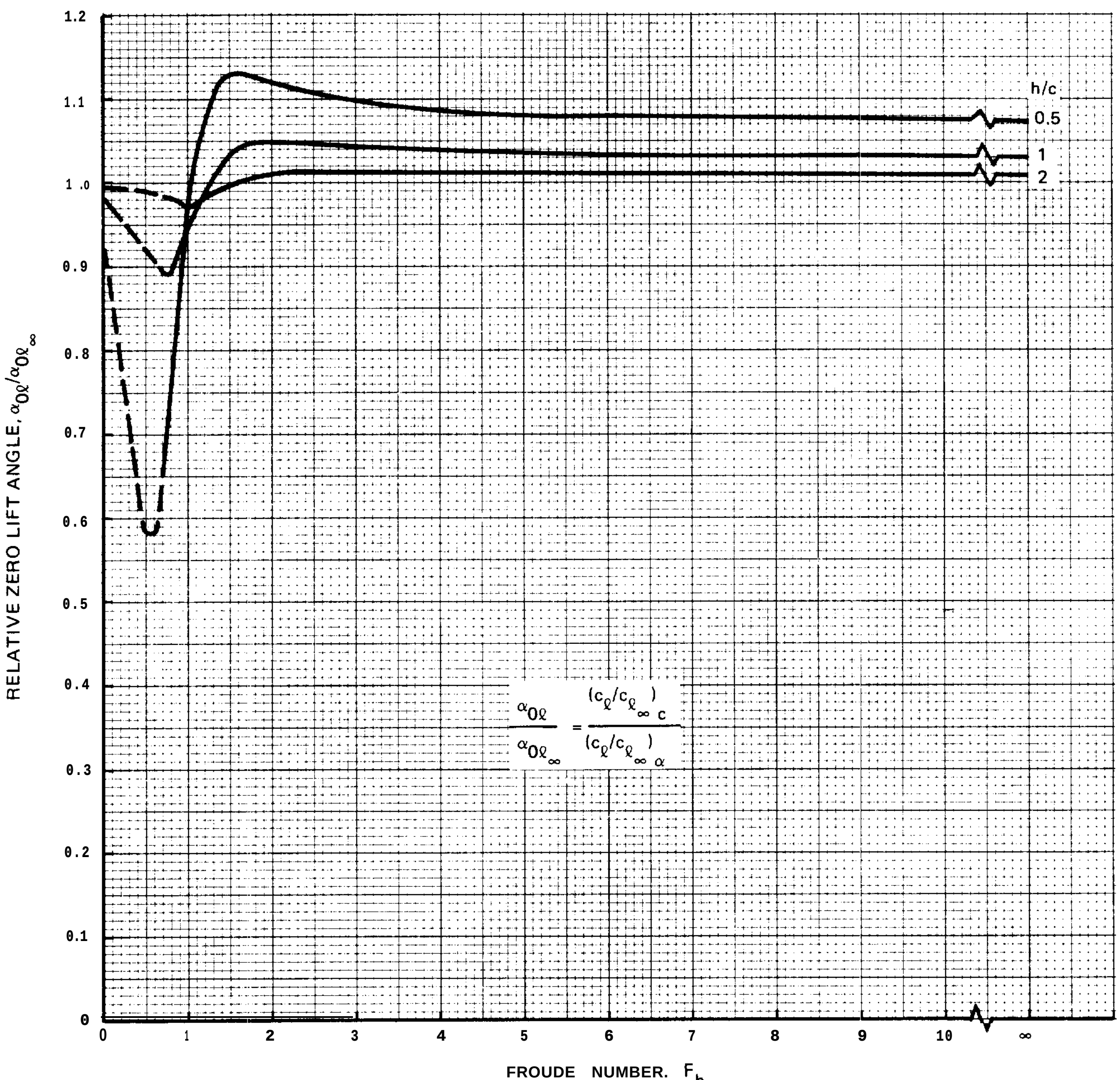

1892-140B

Fig. 3.3.7.2-l Section Zero Lift Angle, Hough & Moran

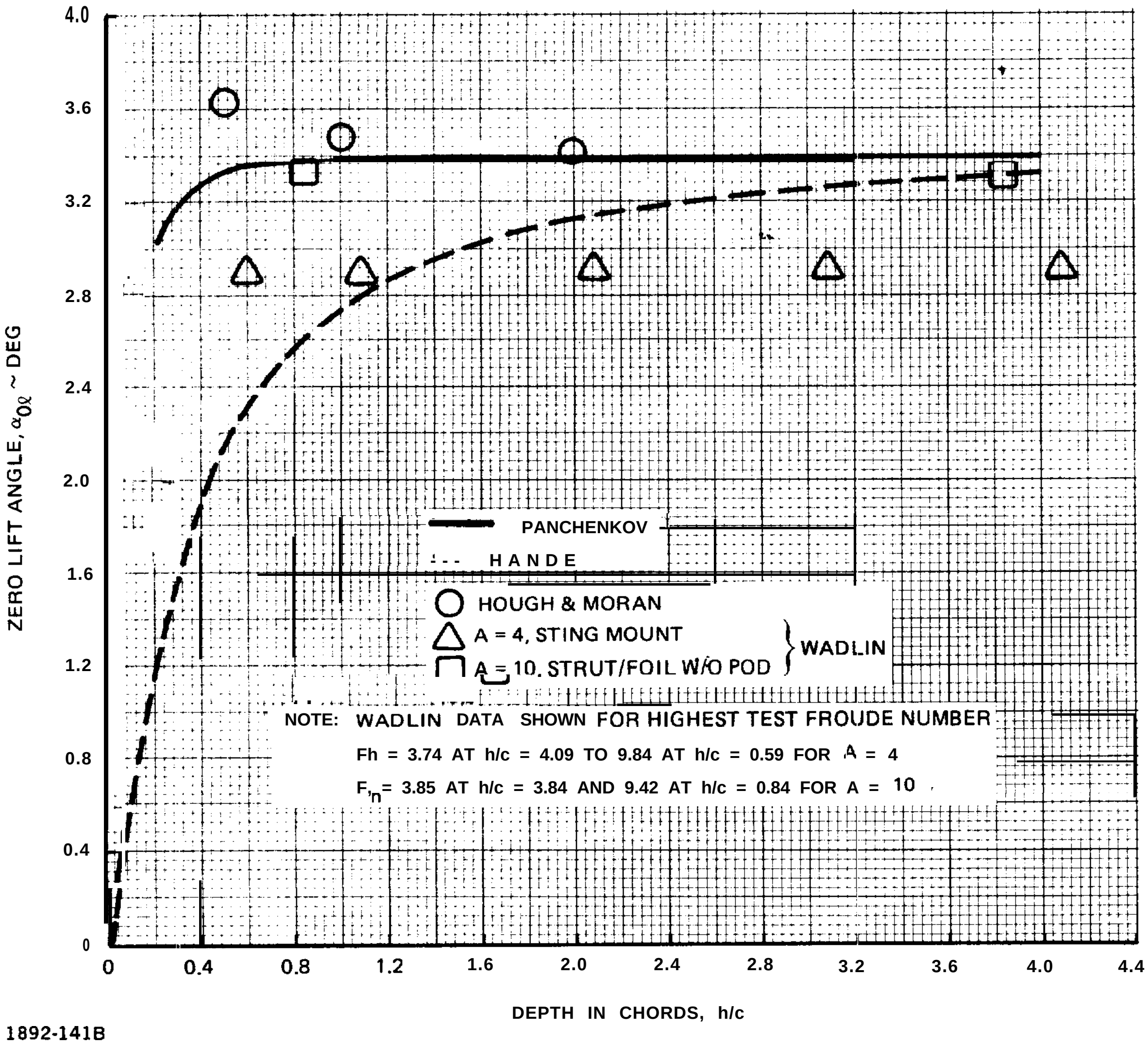

Fig. 3.3.7.2-2 Infinite Froude Number Zero Lift Angle, 641 A412 Section

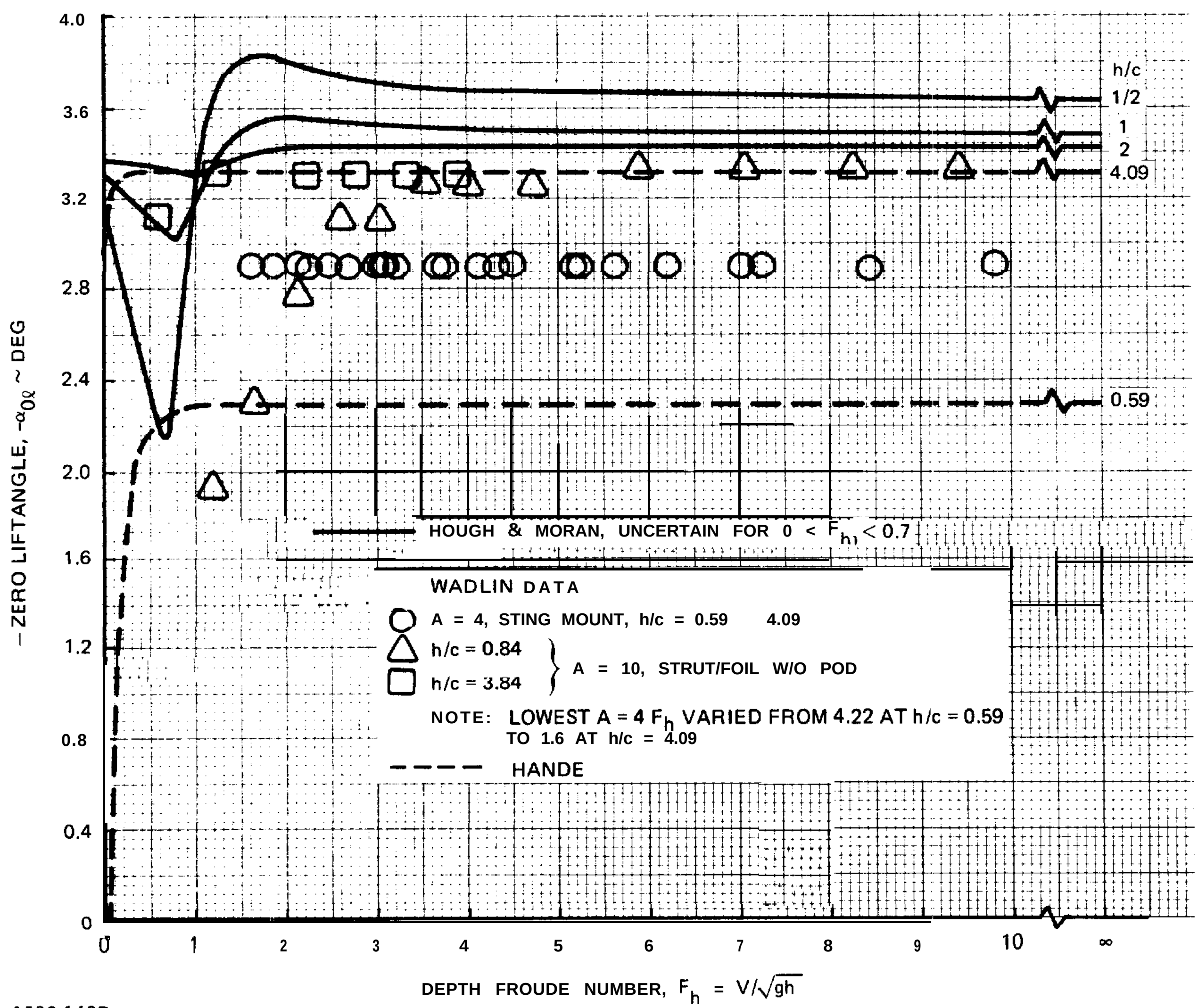

1892-142B

Fig. 3.3.7.2-3 Section Zero Lift Angle Comparisons

3.3.7.3 **Free** Surface Effect.

Section 3.3.7.2 has concluded that the free surface effect upon the basic lift component is of the same or lower order than current experimental precision. Since lift distribution presents still more difficulty for which no theoretical or experimental evidence can be offered here, it is here assumed pending evidence to the contrary that the hydrodynamic and aerodynamic lift distributions are identical and that the only effect of the free surface is a reduction of the lift curve slope.

The aerodynamic lift curve of Equation 3.3.1.6-1 may be written:

$$c_{\ell_\infty} = c_{\ell_{\alpha_\infty}} \left(\alpha + \frac{d\alpha}{d\delta}\ \delta - \alpha_{0\ell}\right) \qquad 3.3.7.3\text{-}1$$

from which it follows that:

$$c_\ell = \frac{c_{\ell_\alpha}}{c_{\ell_{\alpha_\infty}}}\ c_{\ell_\infty} \qquad 3.3.7.3\text{-}2$$

where: c_{ℓ_∞} is the aerodynamic lift coefficient of Equation 3.3.1.6-1

$c_{\ell_\alpha}/c_{\ell_{\alpha_\infty}}$ is from Equation 3.3.7.1-19

3.3.8 Section Cavitation Characteristics.

3.3.8.1 Significance of the Section Velocity Distribution.

LIFT, MOMENT, AND THE CAVITATION BUCKET

Sections 3.3.2, 3.3.3, and 3.3.4 of this volume employed the section velocity distribution to insure that the section moments were consistent with the lift characteristics of Section 3.3.1. This section considers the cavitation implications of the section velocity distribution.

Of the hydrodynamic section characteristics, experience is most limited for cavitation. It is a difficult and expensive characteristic to measure and it is distinctively hydrodynamic, receiving no benefit from aerodynamic resources, It is therefore important to note the intimate relationship between the section force and cavitation characteristics because the force characteristics are more firmly established and do provide the benefit of aerodynamic resources. Lift and moment characteristics can make a substantial contribution to interpretation of uncertain cavitation data and, conversely, interpretation of such data must not do violence to established lift and moment theory.

BASIC ASSUMPTIONS

Two basic assumptions in the cavitation theory of this volume must be noted.

The superposition of velocities, particularly in the manner of Abbott and von Doenhoff, is assumed. Abbott and von Doenhoff note in Section 4.5 of Reference 1 that neglect of the effect of thickness upon the thin airfoil basic and additional velocity distributions produced certain limitations upon the superposition of those distributions. Because velocity distribution has added significance and fewer resources in hydrodynamics, accountability for that thickness effect has been provided to the fullest possible extent in the preceeding sections and, indeed, that accountability constitutes much o:f the material in those sections.

Prandtl's hypothesis, that each section of the wing acts as though it is an isolated section, is assumed. Pope's assumption of this hypothesis is found in Section 9.2 of Reference 2. Pope's reservations with regard to highly loaded wings, particularly if highly swept, concerns conditions for which the hydrofoil is partially cavitated and not yet amenable to theoretical analysis; i.e. those conditions are equally difficult for the hydrodynamicist but for different reasons. Prandtl's hypothesis identifies the foil upper surface incipient cavitation boundary with that for the most highly loaded section on the span and the foil lower surface boundary with that for the most lightly loaded section on the span; i.e. it makes the foil cavitation bucket a trivial application of the section bucket. The application of Prandtl's hypothesis and limitations on that application are considered further in Sections 3.4 and 3.8.

Note that the effects of cavitation are not the same in two and three dimensions. The appearance of cavitation on the foil produces uncertain section and **spanwise** loading effects. This section considers two-dimensional cavitation effects and Section 3.8 considers three-dimensional cavitation effects.

DISCRETE AND CONTINUOUS CAVITATION BUCKET DEFINITIONS

From the superposition of velocities as systematized in Reference 1, Equation 3.3.8.3-3 gives the total velocity at any particular chord station on the upper or lower surface of the section as a linear function of the section lift coefficient:

$$\sqrt{S} = \text{local velocity/free stream velocity} \qquad 3.3.8.1\text{-}1$$

$$= c \pm mc_{\ell}$$

The potential velocity distributions of Appendices I and II of Reference 1 therefore define the cavitation bucket for any thickness/camber combination included there in the form of an included envelope of straight lines:

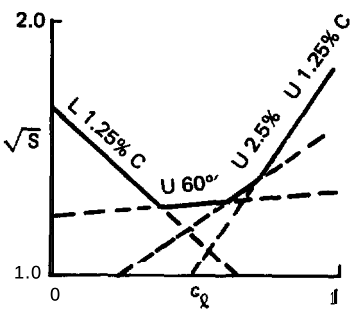

R80-0941-001B

The systemization of Abbott and von Doenhoff was essential to practical section studies at the time of original publication :in Reference 3. Increased availability of the computer has brought computer programs to serve the purpose of the systemization of Reference 1, that of Brockett's Reference 4 being of particular interest to the cavitation bucket. Such programs do not obsolete tlhe methods of Reference 1 and it is important to note the distinctive and complimentary characteristics of the two procedures. Unfortunately, introduction of the computer has brought neglect of the methods of Reference 1 and no direct comparison of the results of the two procedures can be offered.

Not being limited to a discrete set of chord stations, the numerical program produces a non-linear cavitation bucket although the difference should be of practical significance only when the station for maximum local velocity moves forward of the most forward discrete station considered. The stations provided in Reference 1 afford good definition for the upper surface bucket boundary and significant discrepancies between the two procedures in this region are indicative of a procedural or numerical error which should be resolved.

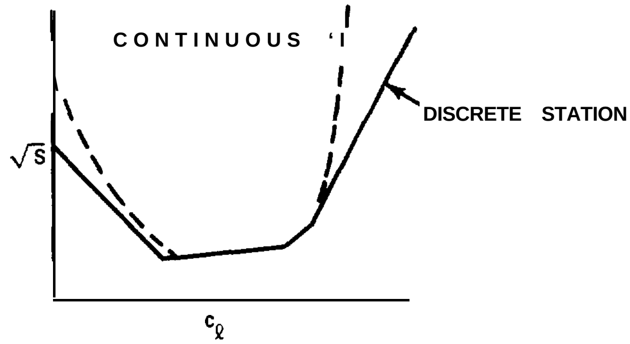

R80-0941-002B

For high lift coefficients for which the chord station for maximum velocity moves within 1% of the leading edge, numerical analysis will produce a substantially more restricted cavitation boundary than that for, say, the 1.25% chord station. This is the case of the leading edge pressure coefficient "spike" for which the aerodynamic and hydrodynamic significance is considered further in! Sections 3.3.8.3 and 3.3.8.5. Those sections also consider the lower surface cavitation boundary for which Reference 1 and aerodynamic and hydrodynamic experience are all in apparent disagreement.

Numerical programs offer a capacity for higher-order effects which are not available using the method of Abbott and von Doenhoff except in highly systematized form as, e.g., Pope's systemization of Pinkerton's function. That capacity should be employed to evaluate the method of Reference 1, and of this volume, and to develop it further as required. Note, however, that neither procedure has any more significance than the experimental measurement.

The most significant advantage of the numerical analysis is that it is not limited by geometry. The specification volume anticipates utilization of this advantage to expand the data base of Appendices I and II of Reference 1 by requiring the inviscid velocity distributions for any thickness and/or camber distributions employed which are not already included in that reference. That data will also provide a check on the numerically-predicted viscous characteristics for the section.

Numerical analyses, however, present solutions for particular cases and require inductive approaches to optimization. The simplicity of Equation 3.3.8.1-1 lends itself to deductive and explicit identification of optimums. That simplicity also reduces the derivation of the section cavitation bucket to a trivial effort, requiring only a pocket computer.

It must be emphasized that neither the methods of numerical analysis nor of Reference 1 have yet been adequately related to the hydrodynamic section characteristics and that rudimentary analyses and rudimentary configurations will be most productive of understanding at this rudimentary level of the state of the art.

FORMS OF THE CAVITATION BUCKET

Angle of attack is an initial condition for the numerically-derived cavitation bucket and numerical analysts therefore generally present the cavitation bucket as a function of angle of attack. It is this propensity of the numerical analyst for angle of attack variation which has delayed comparisons of the numerical results with those provided by the methods of Reference 1. In fact the numerical analysis is not defined until the lift and moment curves, produced by the same analysis, are displayed for examination. Presumably, these would be the lift and moment curves of Sections 3.3.1 through 3.3.4 although the specification volume specifically requires only that the cavitation bucket be presented as a function of lift coefficient.

The requirement that the unflapped section cavitation bucket be presented as a function of lift coefficient is an accomodation to the design process. The hydrofoil must be designed to produce a cavitation-free lift coefficient range. The design of the control system to suit the lift curve, i.e. reference to the angle of attack, is a distinct design problem which follows the design of the hydrofoil.

The added freedom provided by the flapped section presents an awkward graphical problem for which no wholly satisfactory solution has yet appeared. The formats of Sections 3.3.8.4 and 3.3.8.5 are suited to specific questions but can be expected to undergo some evolutionary development with added experience.

"Cavitation", or "incipient" or "theoretical" cavitation, usually refers to the equality:

$$S = 1 + \sigma_C = 1 - C_P \qquad 3.3.8.1\text{-}2$$

where: S is the pressure coefficient of Reference 1 and of Equation 3.3.8.1-1

σ_C is the cavitation number for incipient cavitation

CP is the traditional pressure coefficient, $(P_\ell - P_S)/q$.

Several authors, e.g. Brockett in Reference 4, have challenged Equation 3.3.8.1-2 on theoretical grounds but there are equally important practical limitations upon its significance. Nothing has been found in the literature on the extent of cavitation necessary for observation, and the question is important to the significance of the leading edge pressure coefficient spikes. More important, cavitation tests must be extended until the cavitation is sufficiently well advanced to insure that cavities behind surface imperfections have not been identified as a cavitation boundary.

Cavitation has no significance unless it acts upon the section forces or produces erosion. Thus, prototype experience has indicated that there are distinct upper surface leading edge cavitation boundaries for incipient cavitation, force effects (possibly distinct for lift, drag, and moment) and erosion. Very little is yet known about the relationship between these boundaries for the three-dimensional foil or, especially, for the section. This volume must provide a context for that experience as it is obtained. The reference for that context is the incipient boundary of Equation 3.3.8.1-2.

Further, the specification volume must anticipate the indications of the experience to be obtained; that is, a "working" hypothetical effective cavitation bucket must be adopted for the present. Because lower surface cavities close in a high pressure region and because propeller experience confirms that the lower surface erosion boundary is closely associated with the incipient boundary, the two boundaries are assumed to be identical here. Because upper surface mid-chord cavitation is associated with a relatively flat pressure distribution and because propeller experience also associates this boundary with destructive potential, the upper surface mid-chord incipient, force effective, and erosion boundaries are all assumed identical here. Two- and three-dimensional measures of the upper surface leading edge force-effective cavitation boundary so far obtained are difficult to reconcile. For the present, the force effect boundary is assumed to require experimental definition and the erosion boundary is assumed to lie outside the force effect boundary. That is, the effective section cavitation bucket is assumed to consist of the lower surface leading edge and upper surface mid-chord incipient cavitation boundaries and an experimentally-defined upper surface leading edge force effect cavitation boundary. The specification consequences of this assumption are considered in Section 3.3.8.7 and 3.8 but its validation and comprehension are sought in Sections 3.3.8.5 and 3.3.8.6.

CAVITY CLOSURE

Because cavitation effectively alters the section geometry, generally producing a thicker section of modified camber, the "incipient" cavitation boundary can be expected to be more restrictive of cavitation number and/or lift coefficient approached from the cavitated case than from the wetted case; i.e., vapor pressure cavitation is associated with a hysteresis band. It must be noted that this volume is limited to consideration of vapor pressure cavities on foils and, therefore, does not consider the cavitation/Froude number source for cavitation hysteresis for foils, which is predominate in the characteristics of ventilated foils and struts.

Vapor pressure cavitation hysteresis is noted in References 4, 5 (where cavity closure is "suppression"), and 6 (where cavity closure is "desinence") among other references. The significance of the hysteresis, however, is generally neglected in the literature. In fact if significant force or erosion effects are found in the hysteresis region, and none can be identified here, the foil cavitation bucket would require a new definition and the prediction of incipient cavitation would become an academic exercise.

STRUCTURE OF THE CAVITATION PROBLEM

Consideration of the foil cavitation characteristics presents two objectives:

- Provision of a prediction for the effective cavitation bucket, presumably employing the incipient cavitation bucket as a frame of reference

- Provision of an effective model test procedure for the validation of the predicted effective cavitation bucket by means of appropriate test and/or interpretive procedures.

These objectives are framed for the three dimensional foil, of course, but their satisfaction requires first a mastery of the degenerate case provided by the section.

Considerations of the two objectives fall into two distinct classes:

- Aerodynamic Considerations

  1. Validity of the estimates for thickness, camber, angle of attack, and flap velocity distributions and of their superposition
  2. Significance of spiked velocity distributions; i.e. existence and effect of leading edge and hingeline vortices
  3. Identification of model conditions not representative of the prototype, and interpretation of their significance to the prototype
  4. Model test techniques for reproduction of prototype aerodynamic characteristics.

- Hydrodynamic! Considerations

  1. Significance of the aerodynamic "cavitation" bucket to the observed incipient cavitation bucket, particularly with regard to spiked velocity distributions
  2. Relationship between the theoretical (aerodynamic), observed incipient, and effective cavitation buckets
  3. Interpretation of model cavitation characteristics in terms of the prototype, and test techniques for the elimination of such interpretive requirements
  4. Significance of the cavitation hysteresis.

The following subsections approach these considerations by proceeding from the most degenerate to the most general aerodynamic case, and then to the hydrodynamic experience:

Section 3.3.8.2 Symmetric Section
3.3.8.3 Cambered Section
3.3.8.4 Flapped Section
3.3.8.5 16-309 Hydrodynamic Experience
3.3.8.6 64A309 Hydrodynamic Experience

Section 3.3.8.7 summarizes the experience of Sections 3.3.8.5 and 3.3.8.6.

REFERENCES

1. Abbott, Ira H. and von Doenhoff, Albert E.: Theory of Wing Sections. Dover Publications, 1959.
2. Pope, Alan: Basic Wing and Airfoil Theory. McGraw-Hill Book Company, 1951.
3. Abbott, Ira H.; von Doenhoff, Albert E.; and Stivers, Louis S., Jr.: Summary of Airfoil Data. NACA Report No. 824, 1945.
4. Brockett, Terry: Steady Two-Dimensional Pressure Distributions on Arbitrary Profiles. DTNSRDC Report 1821, October 1965.
5. Baloga, Paul: Water Tunnel Tests of the NACA 64A-309 Foil Section Fitted with an Adjustable Flap in Fully-Wetted and Cavitating Flows. Graduate Aeronautical Laboratories California Institute of Technology Report HSWT 1131, August 1979.
6. Jones, E.A.: Model Scale Effects on a 16-Series Flapped Hydrofoil Section. Defense Research Establishment Atlantic, informal communication, February 1978.

3.3.8.2 Symmetric Section.

Appendix I of Reference 1 provides thickness and additional velocity distributions for a wide range of thickness distributions. Ratios of v/V for the more significant chord stations for certain of those thickness distributions are presented graphically on Figures 3.3.8.2-l through 3.3.8.2-S as a convenience for interpolation. Linear and parabolic regressions for v/V and $\Delta v_a/V$ for leading edge and mid-chord stations for the **16-Series** section are presented in Tables 3.3.8.1-I and -11. The velocity distribution viscous accountability as defined by Pope is given by Equation 3.3.2.2-6.

The total velocity at any chord station on the symmetric section is the sum of the velocity due to thickness and the velocity increments due to lift and viscosity:

$$\sqrt{S} = \text{total local v/free stream V} \qquad \text{3.3.8.2-I}$$

$$= \frac{v}{V} \pm \frac{\Delta v_a}{V} c_\ell \pm \frac{\Delta v_P}{V} c_\ell$$

$$= \frac{v}{V} \pm \left(\frac{\Delta v_a}{V} + \frac{P_{ac}\ \text{Aa.c.}}{4\ v/v} \right) c_\ell$$

$$= \frac{v}{v} + \frac{\Delta v_a'}{v} \cdot c_\ell$$

where the primed incremental velocity is simply a convenience parameter.

Equation 3.3.8.2-l presents a potential confusion in terminology which exists also in Sections 3.3.2.1 and 3.3.2.2. The tabulated $\Delta v_a/V$ of Reference 1 is for a unit lift coefficient and must be multiplied by the actual lift coefficient for application, as in Equation 3.3.8.2-l. The left side of Equation 3.3.2.2-6, similarly, omits a lift coefficient denominator to put $\Delta v_P/V$ in the same form as $\Delta v_a/V$.

No experimental tests of Equation 3.3.8.2-l can be offered.

REFERENCES

1. Abbott, Ira H. and von Doenhoff, Albert, E.; Theory of Wing Sections. Dover Publications, 1959.

TABLE 3.3.8.2-I THICKNESS VELOCITY DISTRIBUTION, v/V, 16-SERIES SECTION, 6% ⩽ t/c ⩽ 21%

CHORD STATION x/c, %	PARABOLIC REGRESSION	LINEAR REGRESSION
1.25	1.0278 + 0.2592 t/c − 3.9087 $(t/c)^2$ ± 0.002	−
2.5	1.0101 + 0.7211 t/c − 2.9563 $(t/c)^2$ ± 0.002	−
5	0.9929 + 1.0440 t/c − 2.4206 $(t/c)^2$ ± 0.001	−
10	1.0007 + 0.9096 t/c − 0.7341 $(t/c)^2$ ± 0.001	1.0121 + 0.7114 t/c ± 0.003
15	1.0038 + 0.8701 t/c − 0.1786 $(t/c)^2$ ± 0.001	1.0065 + 0.8219 t/c ± 0.001
20	1.0000 + 0.9674 t/c − 0.2778 $(t/c)^2$ ± 0.000	1.0044 + 0.6924 t/c ± 0.001
50	1.0007 + 1.0755 t/c + 0.2778 $(t/c)^2$ ± 0.000	0.9964 + 1.1505 t/c ± 0.001
-60	0.9982 + 1.1948 t/c − 0.2381 $(t/c)^2$ ± 0.002	1.0019 + 1.1306 t/c ± 0.002
8		
R8	70 0.9[illegible] + 0.7692 1.1390 t/c − 0.3176 0.0198 $(t/c)^2$ ± 0.002 0.001	1.0025 1.0056 + + 0.7636 1.0533 t/c t/c ± ± 0.002 0.001

R80-0941-003B

TABLE 3.3.8.2-II ADDITIONAL VELOCITY DISTRIBUTION, $\Delta v_a/V$, 16-SERIES SECTION, 6% ⩽ t/c ⩽ 21%

CHORD STATION x/c, %	PARABOLIC REGRESSION	LINEAR REGRESSION	CONSTANT
1.25	1.4629 − 1.2413 t/c − 3.0357 $(t/c)^2$ ± 0.003	−	−
2.5			−
5		−	−
10	0.4749 + 0.0449 t/c − 0.4762 $(t/c)^2$ ± 0.000 0.6682 ± 0.3804 t/c − 1.5029 $(t/c)^2$ ± 0.0015	0.4823 − 0.0838 t/c ± 0.002	−
15	0.3783 + 0.0177 t/c − 0.1786 $(t/c)^2$ ± 0.000	0.3811 − 0.0305 t/c ± 0.001	−
20	0.3186 + 0.0135 t/c − 0.0992 $(t/c)^2$ ± 0.000	0.3201 − 0.0133 t/c ± 0.000	.318 ± 0.001
50	0.1589 + 0.0152 t/c ± 0.000	0.1589 + 0.0152 t/c ± 0.000	.161 ± 0.001
60	0.1286 + 0.0315 t/c − 0.0992 $(t/c)^2$ ± 0.000	0.1302 + 0.0048 t/c ± 0.000	.131 ± 0.001
70	0.1070 − 0.0606 t/c + 0.1786 $(t/c)^2$ ± 0.000	0.1042 − 0.0124 t/c ± 0.001	.103 ± 0.001
80	0.0790 − 0.0333 t/c ± 0.000	0.0790 − 0.0333 t/c ± 0.000	−

R80-0941-004B

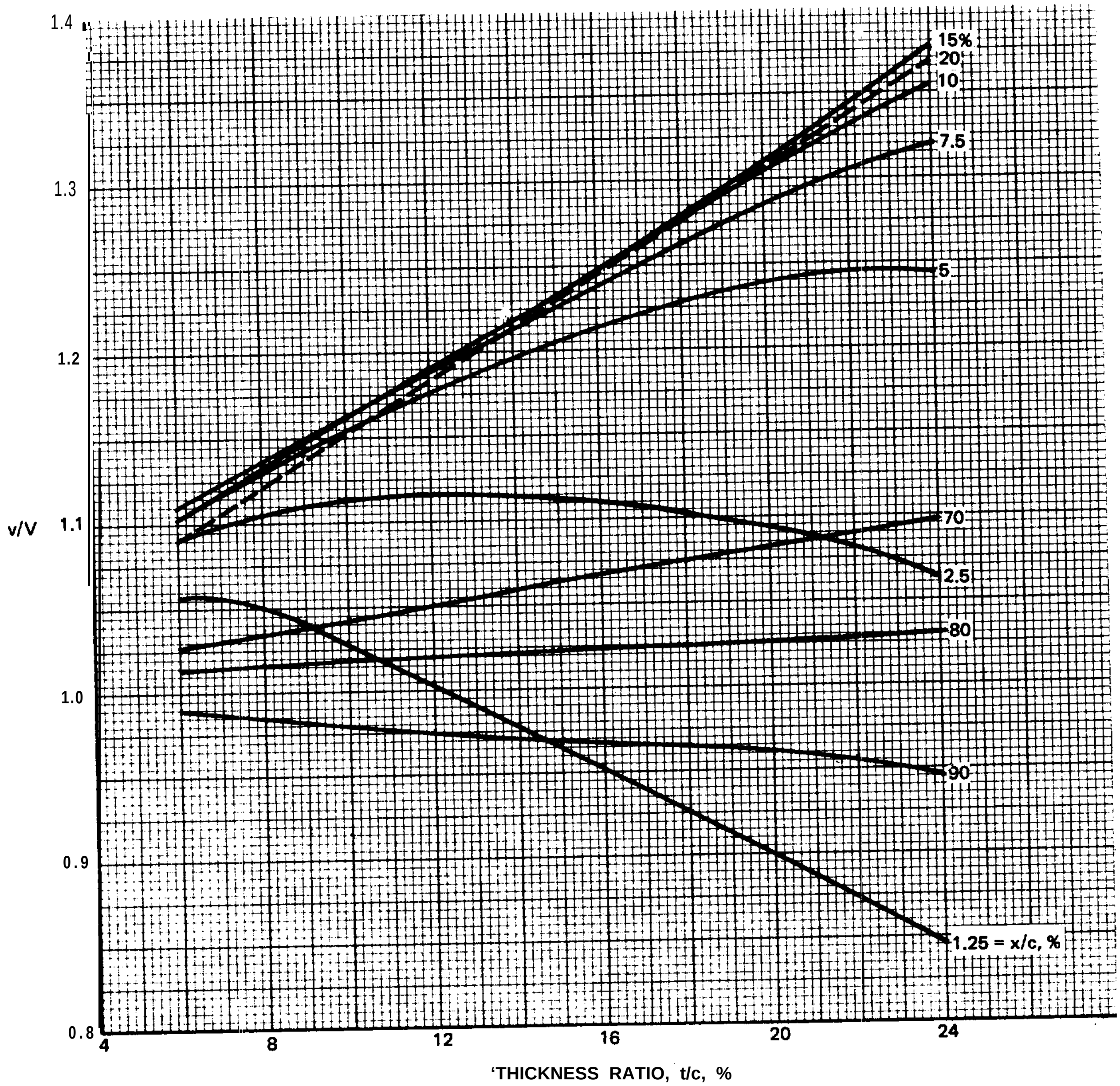

R80-0941-005B

Fig. 3.3.8.2-I Thickness Velocity Distribution, **v/V, 4- and 5-Digit Sections**

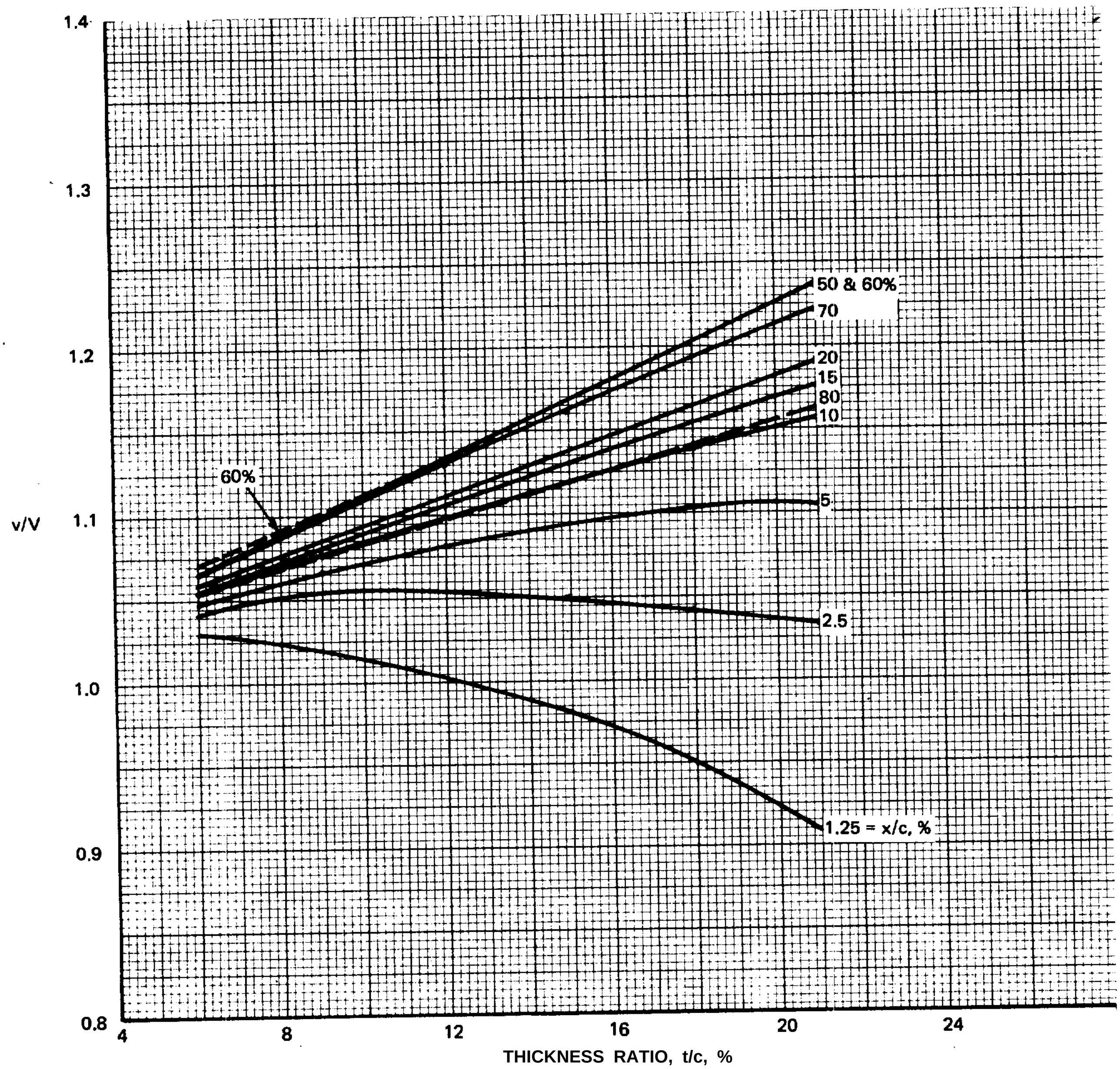

R80-0941-006B

Fig. 3.3.8.2-2 Thickness Velocity Distribution, v/V, 16-Series Section

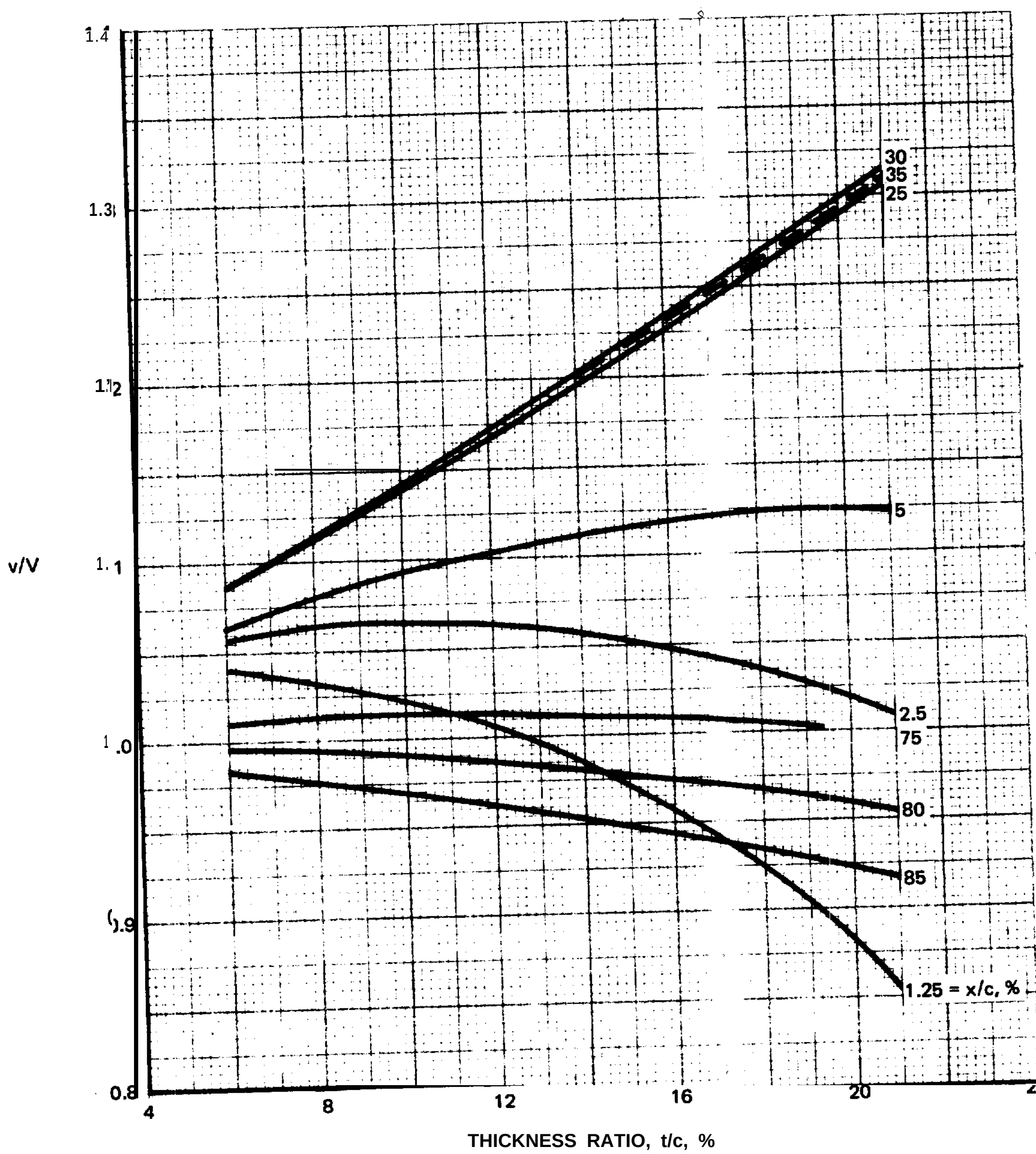

R80-0941-007B

Fig. 3.3.8.2-3 Thickness Velocity Distribution, v/V, 63-Series Sections

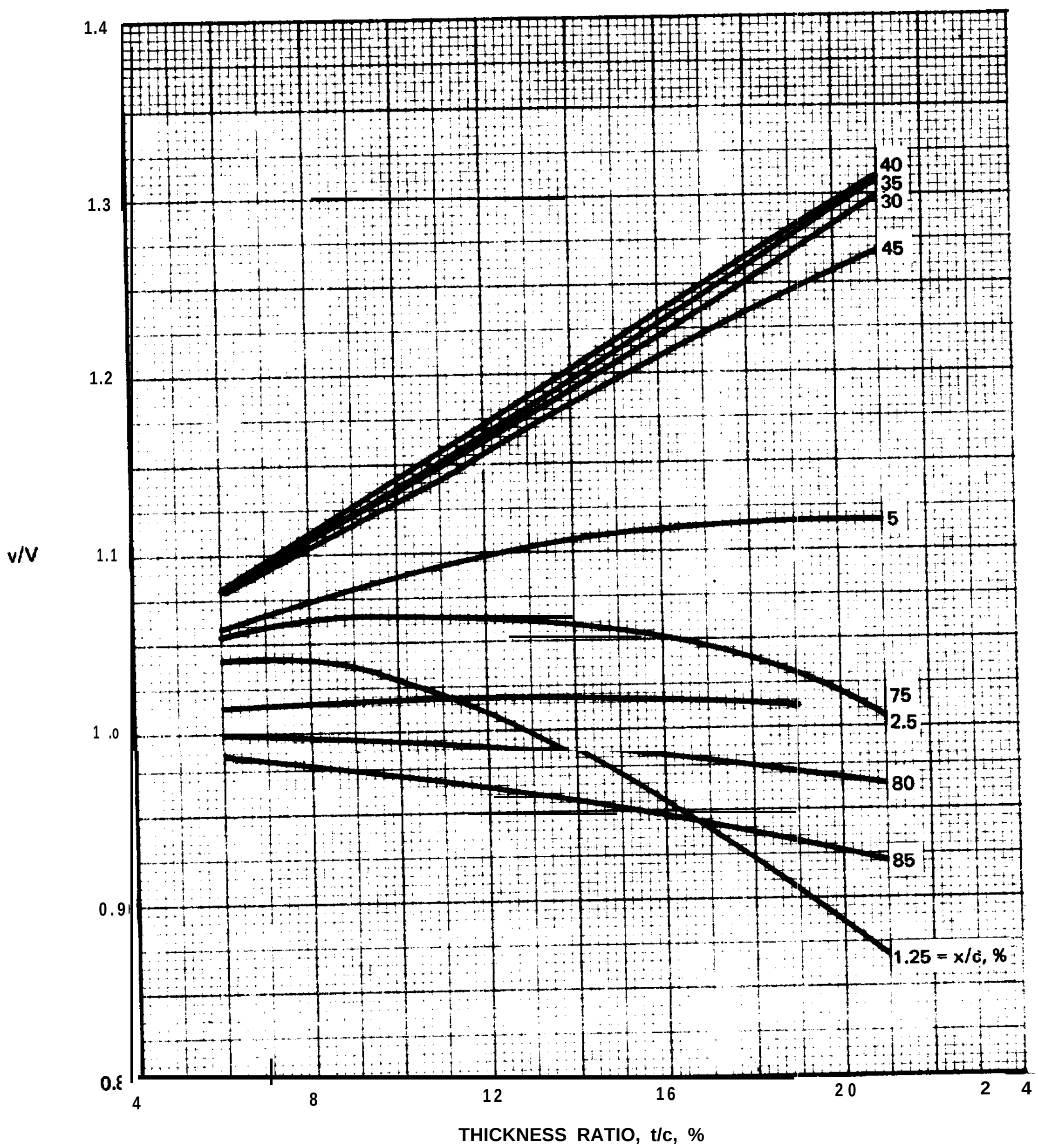

R80-0941-008B

Fig. 3.3.8.2-4 Thickness Velocity Distribution, v/V, 64-Series Sections

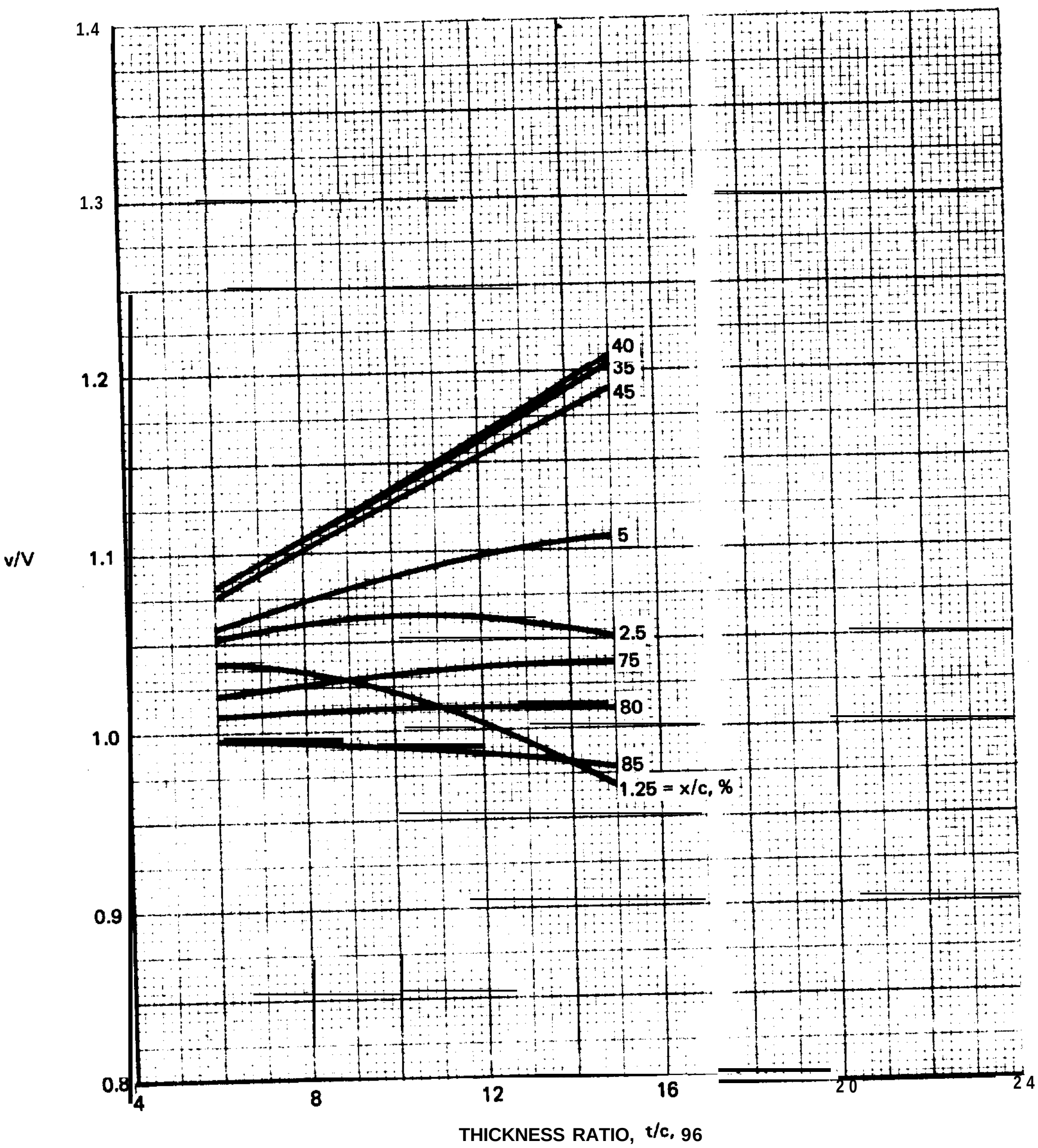

R80-0941-009B

Fig. 3.3.8.2-5 Thickness Velocity Distribution, v/V, 64 A-Series Sections

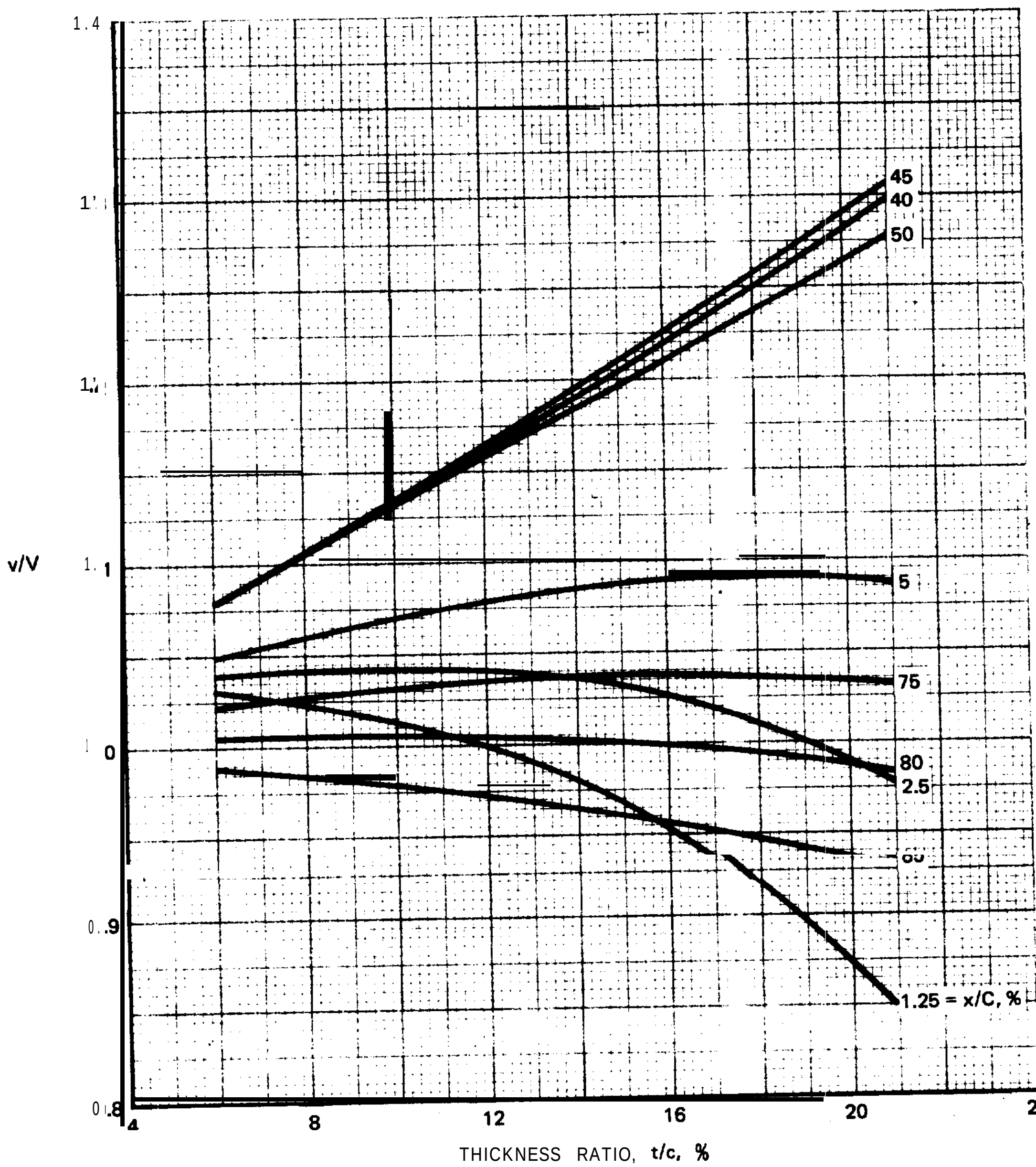

R80-0941-010B

Fig. 3.3.8.2-6 Thickness Velocity Distribution, v/V, 65-Series Sections

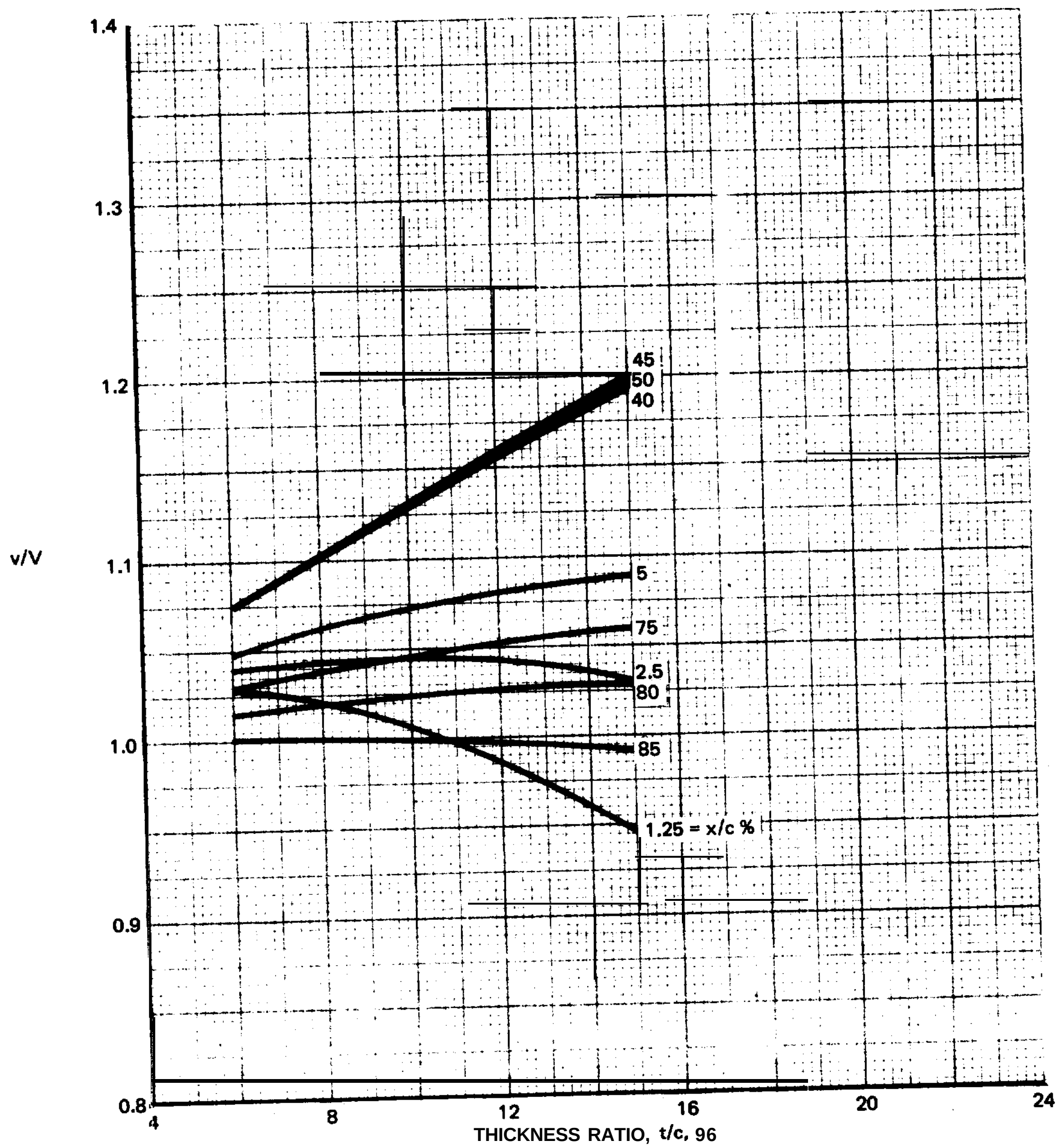

R80-0941-011B

Fig. 3.3.8.2-7 Thickness Velocity Distribution, v/V, 65 A-Series Sections

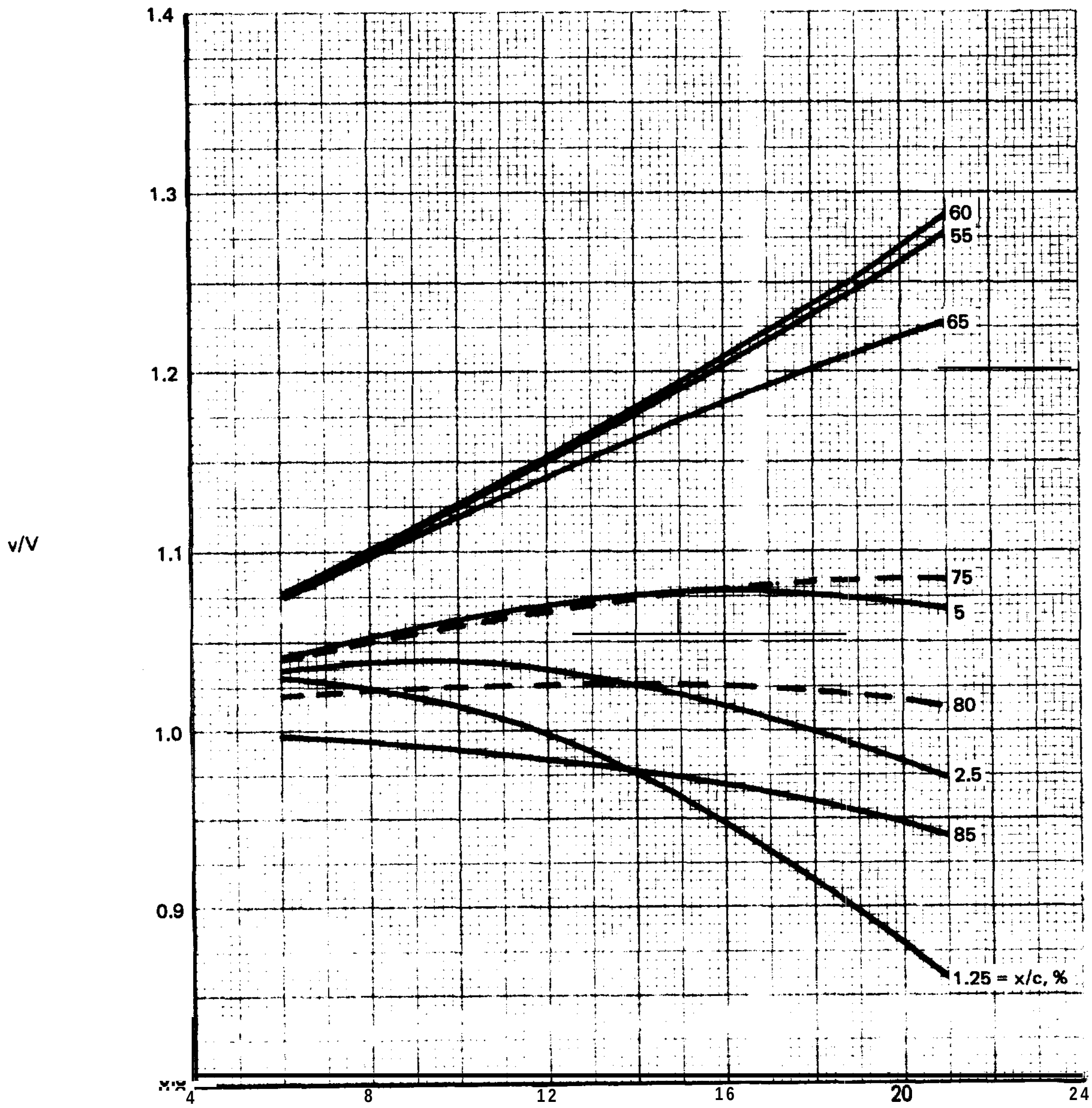

R80-0941-012B

Fig. 3.3.8.2-8 Thickness Velocity Distribution, v/V, 66-Series Sections

3.3.8.3 Cambered Section.

Appendix II of Reference 1 gives the velocity distributions for a wide **range** of mean lines. It is noted in Section 3.3.3.1 that the a = 1.0 velocity distribution of Reference 1 is **impractically** idealized and is better represented by the velocity distribution for the a = .94 mean line which is uniform over 94% of the chord with a velocity given by:

$$\Delta v/V = 1/2(a + 1) \qquad 3.3.8.3\text{-}1$$

$$= .258 \text{ for } a = .94 \text{ mean line.}$$

It is to be noted that the camber velocity distributions of Reference 1 are given for the **inviscid** ideal lift coefficient which is identified as c_{ℓ_i} in the heading of each table, as $c_{\ell_{i\,\text{Table}}}$ in other references, and as $c_{\ell_{i_{ref}}}$ here. For application, the tabulated velocity ratios must be multiplied by **the** ratio of the section effective c_{ℓ_i}/reference c_{ℓ_i}.

In adding the camber incremental velocity to the symmetric section velocity of Equation 3.3.8.2-1, the lift coefficient of that equation must be identified as that for the "additional" lift component, c_{ℓ_a}, where:

$$c_{\ell_a} = c_\ell - c_{\ell_{i_{eff}}} \qquad 3.3.8.3\text{-}2$$

Thus the velocity distribution for the cambered section is given by:

$$\sqrt{S} = \frac{v}{V} \pm \frac{\Delta v_a{}'}{V}\left(c_\ell - c_{\ell_{i_{eff}}}\right) \pm \frac{\Delta v/V}{c_{\ell_{i_{ref}}}}\, c_{\ell_{i_{eff}}} \qquad 3.3.8.3\text{-}3$$

$$= \frac{v}{V} \pm \left(\frac{\Delta v/V}{c_{\ell_{i_{ref}}}} - \frac{\Delta v_a{}'}{V}\right) c_{\ell_{i_{eff}}} \pm \frac{\Delta v_a{}'}{V}\, c_\ell$$

$$= \psi \pm \frac{\Delta v_a{}'}{V}\, c_\ell$$

where: $$\psi = \frac{v}{V} \pm \left(\frac{\Delta v/V}{c_{\ell_{i_{ref}}}} - \frac{\Delta v_a{}'}{V}\right) c_{\ell_{i_{eff}}}$$

Derivation of the slope and intercept of Equation 3.3.8.3-3 from the tabulated velocity distributions of Reference 1 is illustrated in Table 3.3.8.3-I for the 16-309 section, with the result presented graphically on Figure 3.3.8.3-l.

The cavitation bucket of Figure 3.3.8.3-l is easily constructed with a straightedge by calculating one point, in addition to the intercept, for each chord station. It is only necessary to examine enough stations to insure the identification of the most restrictive stations.

The significance of the effective design lift coefficient to the aerodynamic measurement of section velocity distribution has been noted in Section 3.3.1.4. An abnormal extent of laminar flow, relative to the prototype, will increase the effective c_{ℓ_i} to something approaching the inviscid value. Typically, the model effective c_{ℓ_i} is a function of the lift coefficient, with the scale effect being most persistent at the lift coefficients of greatest interest to the cavitation bucket. The effect on the cavitation bucket is shown on Figure 3.3.8.3-2 where the 0.21 $c_{\ell_{i_{eff}}}$ bucket would be expected to represent the prototype while the model might be expected to range from the 0.28 $c_{\ell_{i_{eff}}}$ bucket at low lift coefficient to the prototype bucket at high lift coefficient.

The illustration of the effect of Pope's function, also included on Figure 3.3.8.3-2, is of particular significance. It indicates first that the effect represented, the lift redistribution which shifts the aerodynamic center, is not likely to be measured by the precision of current experimental equipment, even for the 16-Series section where that effect is extraordinarily large. More significantly, it indicates that viscous effect is practically limited to lift curve slope; i.e. numerically derived cavitation buckets presented as a function of lift coefficient with and without Pinkerton's function should be very nearly the same. Conversely, if such buckets differ Pinkerton's function and/or Pope's function do not adequately present the viscous effect upon the aerodynamic center. This line of investigation deserves pursuit.

Reference 2 presents a wealth of velocity distribution data significant to hydrofoil theory, experiment and design, which can only be sampled in the time available. An examination of the 16-309 camber velocity distribution measured in Reference 2 is shown in Figure 3.3.2.3-3.

Figures 3.3.8.3-3 and 3.3.8.3-4 compare measured and predicted velocity distributions for two chord stations and graphically illustrate the difficulty in testing the theory and in insuring a valid test of prototype characteristics. The value of Reference 2 would be substantially enhanced if similar data were available for the 16-009 section. Without that basic data, a substantial amount of quantitative significance could still be derived from the pressure measurements of Reference 2 by means of three identities:

$$(\sqrt{S_u} + \sqrt{S_\ell})/2 = \frac{v}{V} \qquad 3.3.8.3\text{-}4$$

$$(\sqrt{S_u} - \sqrt{S_\ell})/4 + (S_u - S_\ell)/8\frac{v}{V} = \frac{\Delta v}{V} \qquad 3.3.8.3\text{-}5$$

$$(S_u - S_\ell)/8\frac{v}{V} - (\sqrt{S_u} - \sqrt{S_\ell})/4 = \frac{\Delta v_a}{V} \quad c_{\ell_{i_{eff}}} + \frac{\Delta v_a}{V} \quad c_\ell \qquad 3.3.8.3\text{-}6$$

where: $\frac{\Delta v_a}{V}$ = slope

$c_{\ell_{i_{eff}}}$ = intercept/slope

and $S = 1 - C_p$.

Figures 3.3.8.3-3 and 3.3.8.3-4 are concerned with the confidence level associated with the prediction of the velocity distribution on the chord. Figure 3.3.8.3-5 addresses the additional question of the identification of that chord station which presents the peak pressure coefficient. The wind tunnel cavitation buckets of this figure are taken from Jones, Reference 3, which presents valuable insight into the hydrodynamic significance of Reference 2. Figure 3.3.8.3-5 illustrates the cavitation bucket constraints produced by the pressure peaks which occur forward of the 1.25% chord station. The significance of these peaks is considered in Sections 3.3.8.5 and 3.3.8.6. The significance at the lower surface comer of the bucket should be noted.

No conclusions are to be drawn from this brief review, which can serve only as an introduction to an adequate study of the significance of Reference 2.

REFERENCES

1. Abbott, Ira H. and von Doenhoff, Albert E.: Theory of Wing Sections. Dover Publications, 1959.
2. Teeling, P.: Low Speed Wind Tunnel Tests of a NACA 16-309 Airfoil with Trailing Edge Flap. DeHavilland Aircraft of Canada Report ECS 76-3, October 1976.
3. Jones, E. A.: Model Scale Effects on a 16-Series Flapped Hydrofoil Section. Defense Research Establishment Atlantic, Dartmouth, N.S., February 1978 informal communication.

TABLE 3.3.8.3-I VELOCITY DISTRIBUTION, 16-309 SECTION, $c_{\ell_{i_{eff}}}$ = 0.21, Δ a.c. = 0.0315

STATION,%	1.25	2.5	5	10	20	30	40	45*	50	60	70	75*	80
v/V	1.021	1.053	1.067	1.076	1.085	1.091	1.096	1.098	1.100	1.106	1.099	1.087	1.075
$(\Delta v/V)/c_{\ell_{i_{ref}}}$	0.258												
$\Delta v_a/V$	1.330	0.964	0.684	0.475	0.319	0.246	0.197	0.178	0.160	0.131	0.103	0.090	0.076
P_{ac}	3.0762	4.3256	5.2869	5.4794	4.1095	2.7397	1.3699	0.6500	0	-1.3699	-2.7397	-3.4500	-4.1095
$\Delta v_p/V$	0.024	0.032	0.039	0.040	0.030	0.020	0.010	0.005	0	-0.010	-0.020	-0.025	-0.030
$\Delta v_a'/V$	1.354	0.996	0.723	0.515	0.349	0.265	0.207	0.183	0.160	0.121	0.083	0.065	0.046
ψ_u	0.791	0.898	0.967	1.022	1.066	1.090	1.107	1.114	1.121	1.135	1.136	1.128	1.120
ψ_ℓ	1.251	1.208	1.167	1.130	1.104	1.092	1.085	1.082	1.079	1.077	1.062	1.046	1.030

'INTERPOLATED

$\Delta v_p/V = 0.0315\ P_{ac}/4\ v/V = 0.007875\ P_{ac}/v/V$

$\Delta v_a'/V = \Delta v_a/V + \Delta v_p/V$

$$\psi = v/V \pm \left(\frac{\Delta v/V}{c_{\ell_{i_{ref}}}} - \frac{\Delta v_a'}{V} \right) c_{\ell_{i_{eff}}}$$

R80-0941-013B

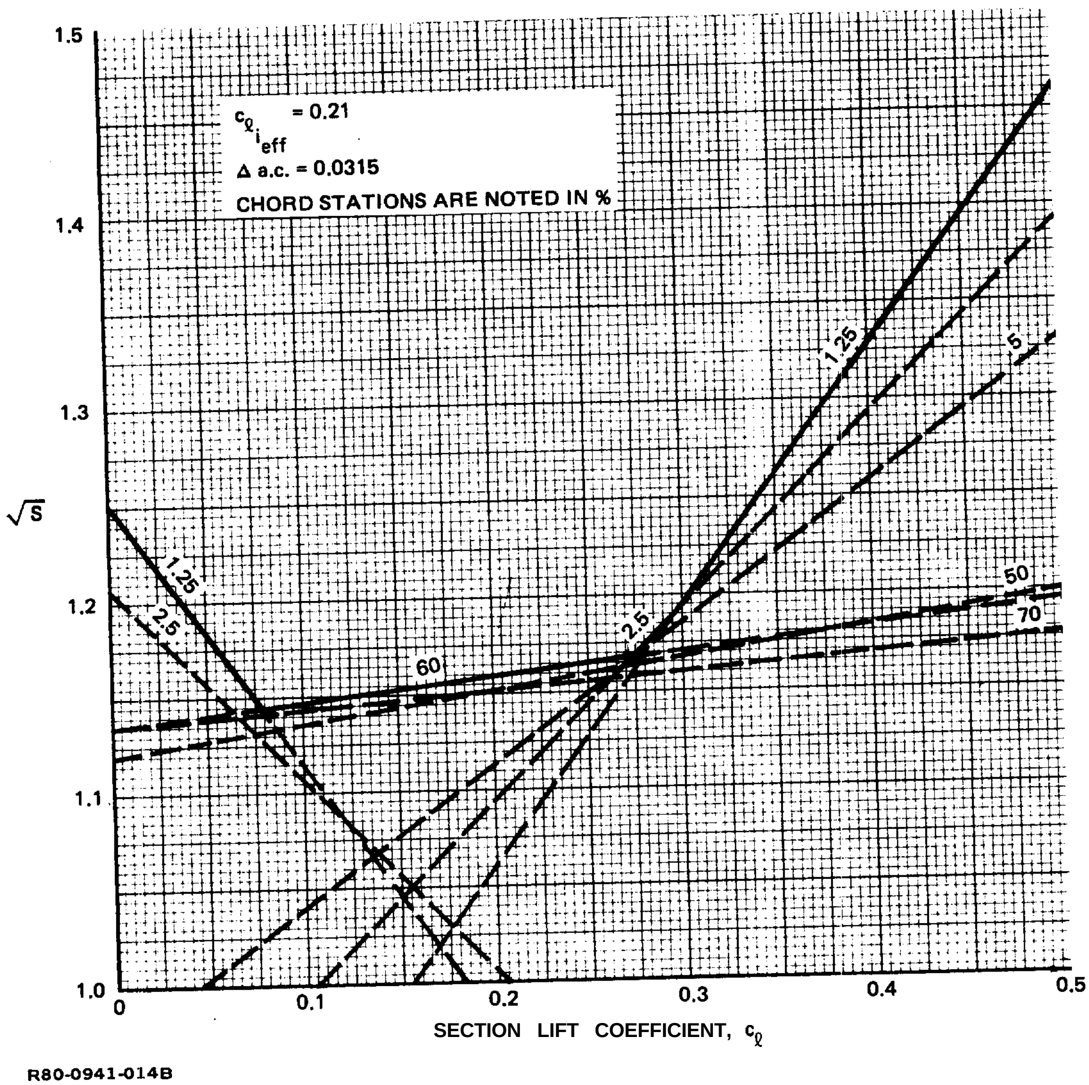

Fig. 3.3.8.3-I Cavitation Bucket, 16-309 Section

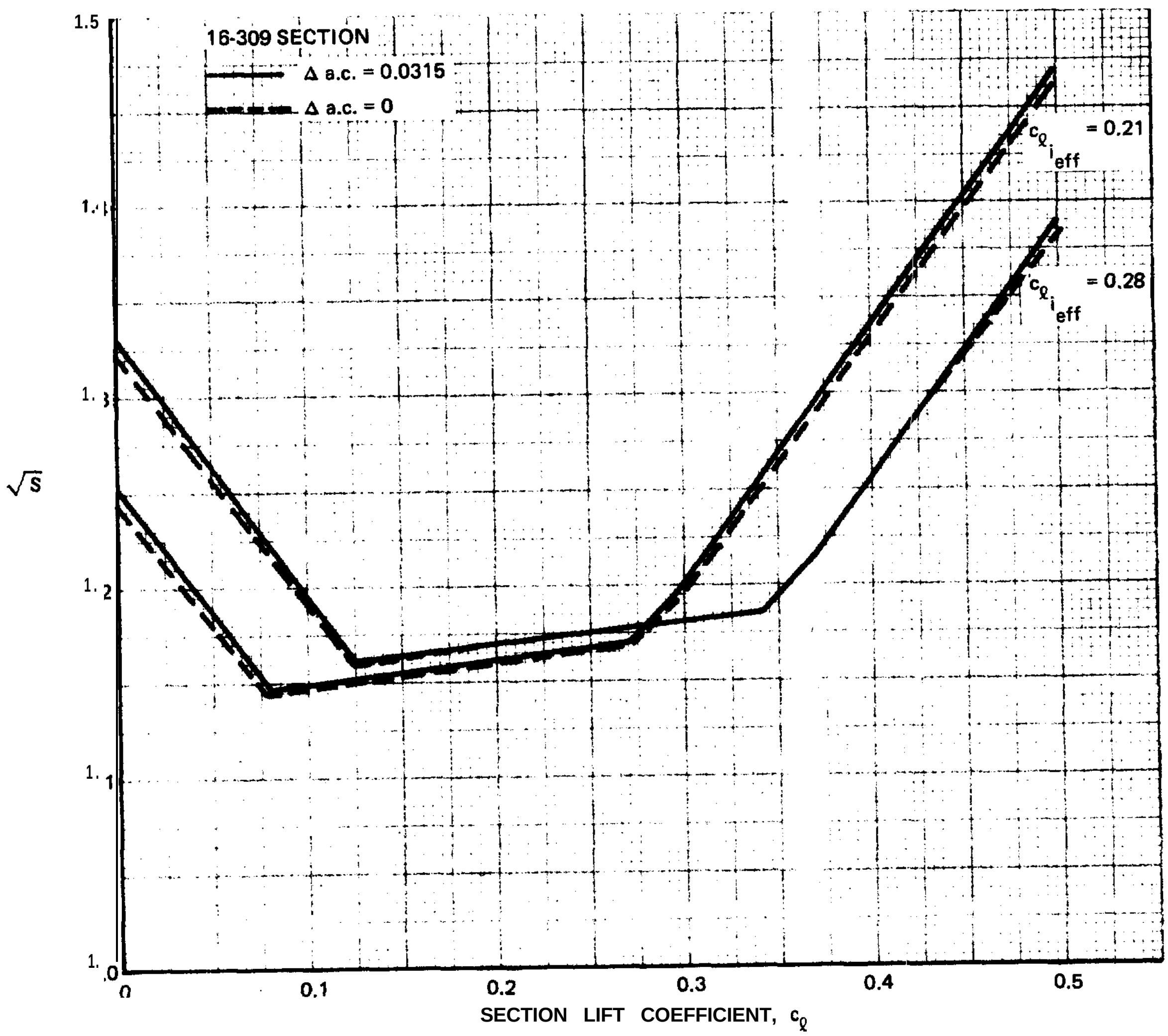

R80-0941-015B

Fig. 3.3.8.3-2 Cavitation Bucket Scale Effect

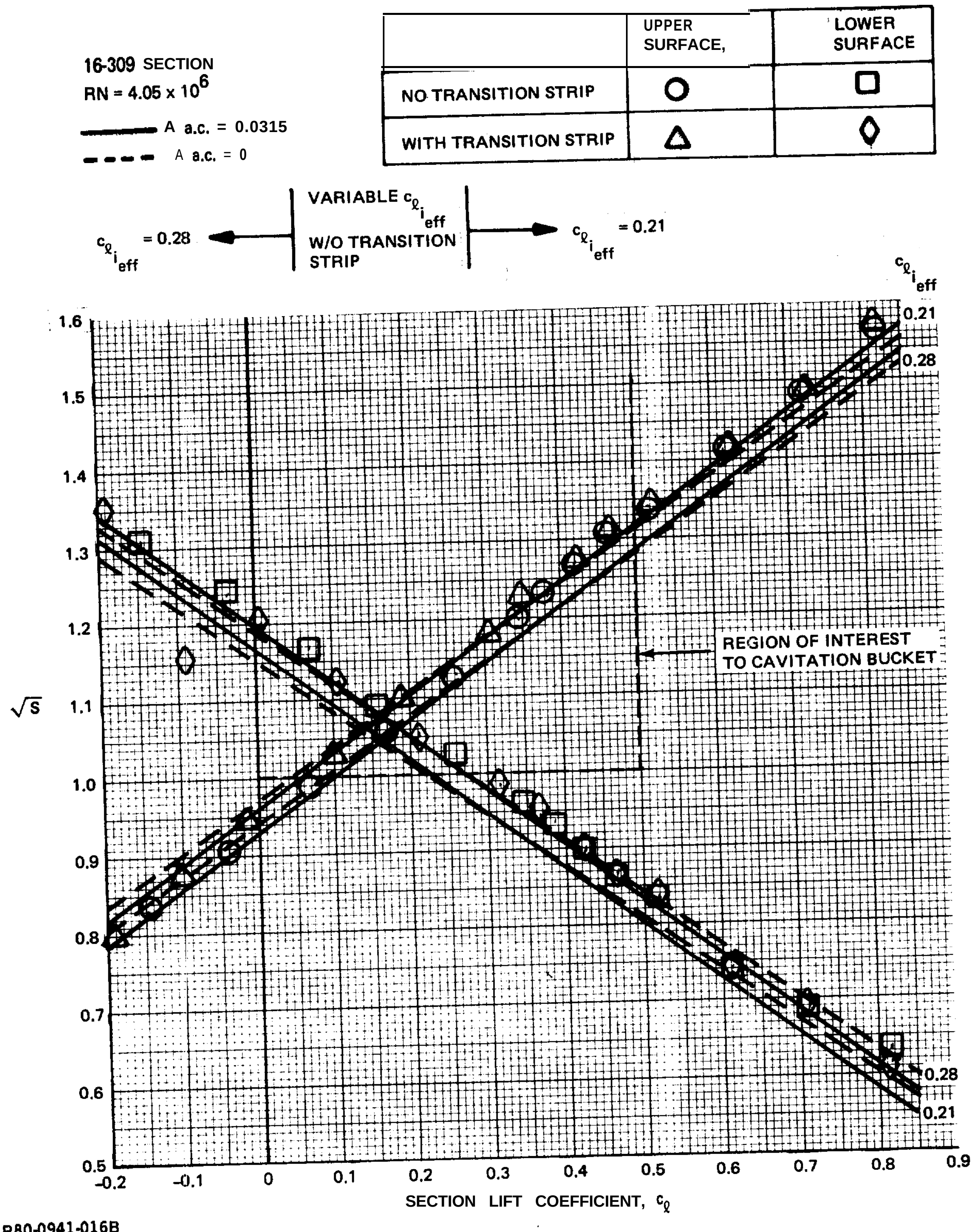

Fig. 3.3.8.3-3 Measured Velocity Distribution, 5% Chord Station

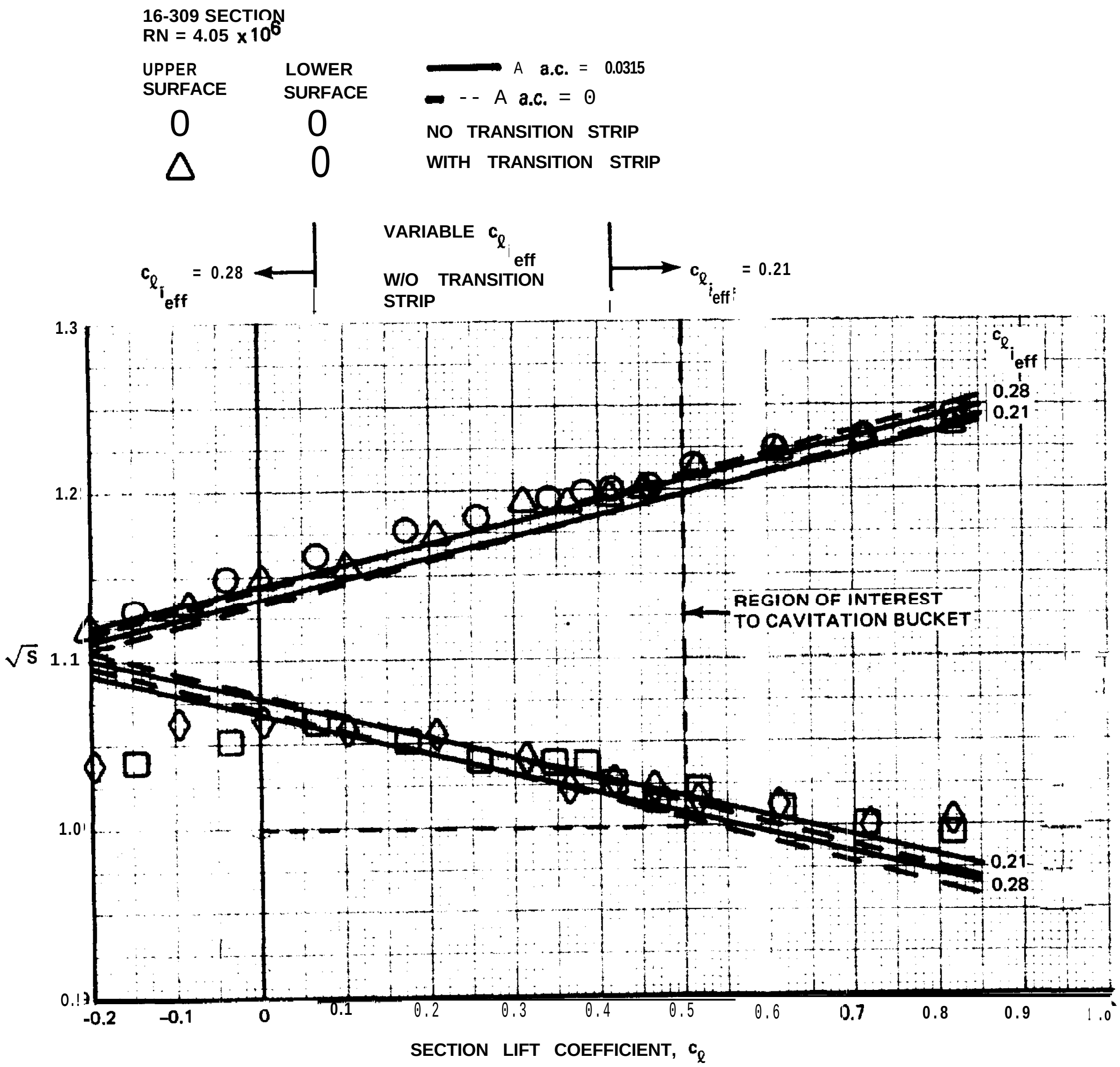

R80-0941-017B

Fig. 3.3.8.34 Measured Velocity Distribution, 60% Chord Station

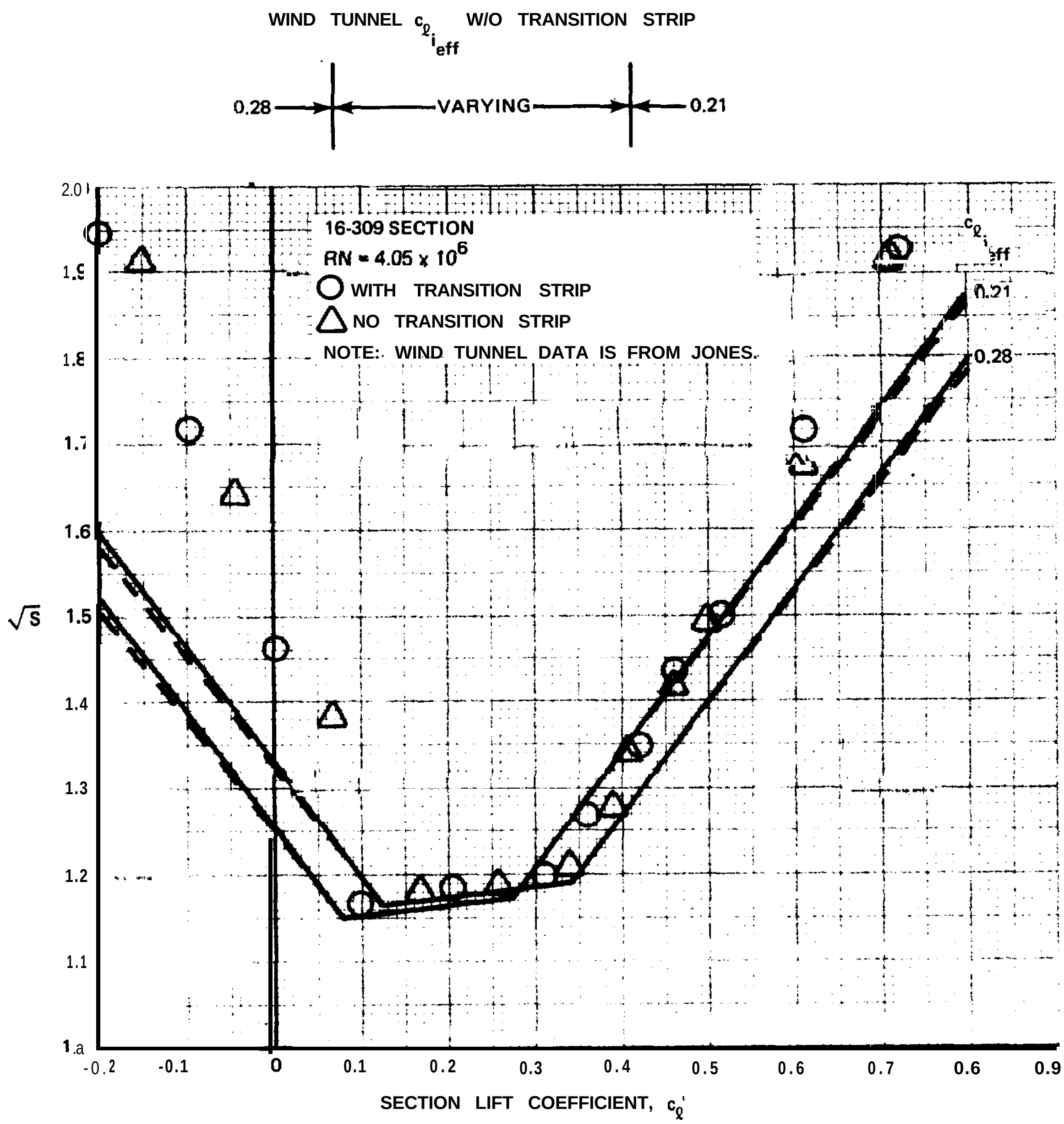

R80-0941-018B

Fig. 3.3.8.3-5 Aerodynamic Cavitation Bucket

3.3.8.4 Flapped Section.

VELOCITY DISTRIBUTION

Equations 3.3.2.4-2 and 3.3.2.4-4 identify the incremental velocity distribution due to the basic component of the flap lift as:

$$\left(\frac{\Delta v}{V}\right)_F \Big/ c_{\ell_{b\delta}} = \frac{1}{4}\left(\frac{c_{\ell_{xb}}}{c_{\ell_b}}\right)_\delta \qquad 3.3.8.4\text{-}l$$

$$= \frac{1}{4\pi\sqrt{\frac{h}{c}}\left(1-\frac{h}{c}\right)} \ln \frac{\left(\sqrt{\frac{h}{c}}\sqrt{1-\frac{x}{c}}+\sqrt{1-\frac{h}{c}}\sqrt{\frac{x}{c}}\right)^2}{\left|\frac{h}{c}-\frac{x}{c}\right|}$$

where it is concluded in Section 3.3.2.4 that Allen's viscous redistribution of the velocity over the flap is not testable.

Equation 3.3.8.4-l does not provide the hinge line velocity which is therefore taken from Table III of Reference 1. To avoid the necessity of referring to a table for these velocities, they are approximated by the equation:

$$\left(\frac{\Delta v}{V}\right)_{F_h} \Big/ c_{\ell_{b\delta}} = \frac{1}{2} + 0.175\ (c_f/c)^{-3/4} \quad \text{for } \delta \leqslant 15^\circ \qquad 3.3.8.4\text{-}2$$

$$= 0.415 + 0.1034\ (c_f/c)^{-3/4} \text{ for } \delta = 20^\circ$$

The incremental velocity distribution of Equation 3.3.8.4-l is illustrated. in Table 3.3.8.4-I and in Figure 3.3.8.4-l for flap chord ratios of 20% and 25%. The table and figure also present comparisons of Equation 3.3.8.4-2 with Allen's values.

The total incremental velocity for the flap lift is given by:

$$\left(\frac{\Delta v}{V}\right)_\delta = \left(\frac{\Delta v}{V}\right)_{a\delta} + \left(\frac{\Delta v}{v}\right)_{b\delta} \qquad 3.3.8.4\text{-}3$$

$$= \left(\frac{\Delta v_a{}'}{V}\right) c_{\ell_{a\delta}} + \frac{\left(\frac{\Delta v}{V}\right)_F}{c_{\ell_{b\delta}}}\ c_{\ell_{b\delta}}$$

$$= \left(\frac{\Delta v_a{}'}{V}\right)(1-\zeta)(c_\ell)_\delta + \frac{\left(\frac{\Delta v}{V}\right)_F}{c_{\ell_{b\delta}}}\ \zeta\ (c_\ell)_\delta$$

$$= \left\{\frac{\Delta v_a{}'}{V} + \zeta\left[\frac{\left(\frac{\Delta v}{V}\right)_F}{c_{\ell_{b\delta}}} - \frac{\Delta v_a{}'}{V}\right]\right\}(c_\ell)_\delta$$

The parameter Ω is defined for convenience:

$$\Omega = \frac{\left(\frac{\Delta v}{V}\right)_F}{c_{\ell_{b\delta}}} - \frac{\Delta v_a'}{V} \qquad 3.3.8.4\text{-}4$$

to reduce Equation 3.3.8.4-3 to:

$$\left(\frac{\Delta v}{V}\right)_\delta = \left(\frac{\Delta v_a'}{V} + \zeta\,\Omega\right)(c_\ell)_\delta \qquad 3.3.8.4\text{-}5$$

Reference 2 contains many tests of Equation 3.3.8.4-5 of which time permitted only those on Figures 3.3.2.4-7, 3.3.2.4-8, and 3.3.2.4-9.

For the flapped section, the incremental velocity of Equation 3.3.8.4-5 is added to the summation of Equation 3.3.8.3-3:

$$\boxed{\sqrt{S} = \frac{v}{V} \pm \frac{\Delta v/V}{c_{\ell_{i_{ref}}}}\, c_{\ell_{i_{eff}}} \pm \frac{\Delta v_a'}{V}(c_\ell)_\alpha \pm \left(\frac{\Delta v_a'}{V} + \zeta\,\Omega\right)(c_\ell)_\delta \qquad \mathbf{3.3.8.4\text{-}6}}$$

Equation 3.3.8.4-6 presents the most general form of the flapped section cavitation bucket, The added variable presented by the flap adds very substantially to the analytic, **experimental,** and intuitive complexity of the cavitation characteristics.

FORMS OF THE FLAPPED SECTION CAVITATION BUCKET

Traditionally, the flapped section cavitation characteristics are presented graphically as a family of pitch lift cavitation buckets for a range of fixed flap angles. Analytically, that presentation replaces the pitch lift of Equation 3.3.8.4-6 by its equivalent in terms of total, flap, and camber lift from the relationship:

$$c_\ell = (c_\ell)_\alpha + (c_\ell)_\delta + c_{\ell_{i_{eff}}} , \qquad 3.3.8.4\text{-}7$$

to obtain:

$$\begin{aligned}
\sqrt{S} &= \frac{v}{V} \pm \frac{\Delta v_a'}{V}\left[c_\ell - (c_\ell)_\delta - c_{\ell_{i_{eff}}}\right] \pm \frac{\frac{\Delta v}{V}}{c_{\ell_{i_{ref}}}}\, c_{\ell_{i_{eff}}} \pm \left(\frac{\Delta v_a'}{V} + \zeta\,\Omega\right)(c_\ell)_\delta \qquad 3.3.8.4\text{-}8 \\
&= \frac{v}{V} \pm \left(\frac{\frac{\Delta v}{V}}{c_{\ell_{i_{ref}}}} - \frac{\Delta v_a'}{V}\right) c_{\ell_{i_{eff}}} \pm \zeta\,\Omega\,(c_\ell)_\delta \pm \frac{\Delta v_a'}{V}\, c_\ell \\
&= \psi \pm \zeta\,\Omega\,(c_\ell)_\delta \pm \frac{\Delta v_a'}{V}\, c_\ell
\end{aligned}$$

For any given flap lift coefficient or flap angle, and section chord station, Equation 3.3.8.4-8 still presents the incipient cavitation boundary as a linear function of the section lift coefficient and the cavitation bucket as an included envelope of such boundaries. The derivation of the pitch lift cavitation bucket for a particular flap lift is illustrated in Table **3.3.8.4-II** and on Figure **3.3.8.4-2.** A family of such cavitation buckets is shown on Figure 3.3.8.4-3. Such cavitation buckets are traditionally identified by flap angle but identification by incremental flap lift coefficient distinguishes lift and lift distribution uncertainties.

The format of Figure 3.3.8.4-3 is ill-suited to study of the flap lift control system, being subject to misinterpretation. The format is an incidence lift control format, presenting the cavitation advantage obtained when such a system is fitted with a flap which can be scheduled with speed. The optimum cavitation bucket for such a system has the envelope of the upper surface **bucket** corners of Figure 3.3.8.4-3 for a boundary. That is, the flap can be employed to produce equal pressures at the leading edge and flap hinge throughout the speed range, thus tending to maintain a uniform chordwise lift distribution throughout that speed range.

The locus of the upper surface bucket comers of Figure 3.3.8.4-3 is the simultaneous solution of Equation 3.3.8.4-S written for the leading edge and hingeline stations:

$$\sqrt{S} = \frac{\Omega_h \psi_{LE} - \Omega_{LE} \psi_h}{\Omega_h - \Omega_{LE}} + \frac{\Omega_h \left(\frac{\Delta v_a'}{V}\right)_{LE} - \Omega_{LE} \left(\frac{\Delta v_a'}{V}\right)_h}{\Omega_h - \Omega_{LE}} c_\ell \qquad 3.3.8.4\text{-}9$$

The required flap schedule with speed is obtained by solving Equation 3.3.8.4-9 for c_ℓ and substituting the result into the boundary equation for the leading edge or hinge station:

$$(c_\ell)_\delta = c_{\ell_\delta} \delta = \frac{\left(\frac{\Delta v_a'}{V}\right)_{LE} - \left(\frac{\Delta v_a'}{H}\right)_h}{\Omega_h \left(\frac{\Delta v_a'}{V}\right)_{LE} - \Omega_{LE} \left(\frac{\Delta v_a'}{V}\right)_h} \frac{\sqrt{S}}{\zeta} - \qquad 3.3.8.4\text{-}10$$

$$\frac{\left(\frac{\Delta v_a'}{V}\right)_{LE} \psi_h - \left(\frac{\Delta v_a'}{V}\right)_h \psi_{LE}}{\Omega_h \left(\frac{\Delta v_a'}{V}\right)_{LE} - \Omega_{LE} \left(\frac{\Delta v_a'}{V}\right)_h} \frac{1}{\zeta}$$

where: $S = 1 + \sigma$

The same flap schedule reduces the incidence hinge moment although it is not the optimum schedule for that purpose.

The appropriate analytical form of Equation 3.3.8.4-6 for flap lift control is obtained by eliminating the flap lift term by reference to Equation 3.3.8.4-7:

$$\sqrt{S} = \psi \mp \zeta \Omega c_{\ell_{i_{eff}}} \mp \zeta \Omega (c_\ell)_\alpha \pm \left(\frac{\Delta v_a'}{V} + \zeta \Omega\right) c_\ell \qquad 3.3.8.4\text{-}11$$

The derivation of the flap lift cavitation bucket is illustrated in Table **3.3.8.4-III** and on Figure 3.3.8.4-4 for zero pitch lift, i.e. for straight and level flight in smooth water. Again, it must be emphasized that the lift control system design problem is one of providing effectively cavitation-free lift coefficient ranges and is therefore most conveniently considered in speed $(\sqrt{S})$ — lift coefficient form. The corresponding flap angles are a mechanical design problem, of interest only for the final configuration and available from Equation 3.3.8.4-7.

The flap lift control cavitation characteristics are the product of the distinctive chordwise lift distributions for pitch lift, Section 3.3.2.1, and flap lift, Section 3.3.2.4. These two distributions are compared on Figure 3.3.8.4-5 for the section of Figure 3.3.8.4-4. Because flap lift does not load the leading edge as heavily as pitch lift, flap lift control effectively expands the smooth water (zero pitch lift) pitch lift cavitation bucket as shown on Figure 3.3.8.4-4.

The flap lift control system works at a disadvantage when the foil is not at the design pitch angle. The incidence lift control system cancels such induced angles; the flap lift control system cancels the induced lifts by applying opposite lift of another chord distribution. Thus, the flap lift cannot fully relieve the leading edge load produced by a positive pitch angle and exposes the hingeline to cavitation to restore the lift lost at a negative pitch angle. The effect is accounted for by the $(c_\ell)_\alpha$ term of Equation 3.3.8.4-11.

Coordinated turns produce such steady state induced angles which might range to two degrees, negative on forward foils and positive on aft foils. The corresponding section angle of attack is subject to many influences but 1.52 degrees, $(c_\ell)_\alpha = .15$, is assumed here for illustration. The pitched flap lift cavitation bucket is derived in Table **3.3.8.4-IV** and compared with the zero pitch flap lift bucket and with the pitch lift bucket on Figure 3.3.8.4-6.

The $\sqrt{S} - c_\ell$ section cavitation bucket format is well suited to analysis but is intuitively obscure. The boundaries of Figure 3.3.8.4-6 can be transformed to the V — L/S format by the definition of Equation 3.3.8.1-2 in the form:

$$V = \left[(P_s - P_v)/\frac{\rho}{2}(S-1)\right]^{1/2} \qquad 3.3.8.4\text{-}12$$

where: Ps = static pressure at section depth

Pv = vapor pressure

$$L/S = q\,c_\ell = \frac{\rho}{2} V^2\,c_\ell$$

The V – L/S format is valid only for a particular depth, and angular relationships for the section are a complex function of the foil planform. Therefore the format is not suited to analysis although well suited to the intuition. Figure 3.3.8.4-6 is therefore repeated in the V – L/S format on Figure 3.3.8.4-7 only to provide a qualitative appreciation for its significance.

Every flapped section has some chord station for which the incipient cavitation boundary is independent of the lift mode, i.e. it is identical for pitch and flap lift. That chord station is marked by the intersection of the two lift distributions of Figure 3.3.8.4-5. Its location is a weak function of the flap chord ratio and a very weak function of camber and thickness for characteristic hydrofoil sections. It is therefore characteristically found in the vicinity of the 45% chord station for such sections. The mid-chord position for this station means that it provides a close measure of the section speed capability under all lift requirements and therefore becomes a significant station for preliminary optimization studies.

The significance of the 45% station is illustrated in Figure 3.3.8.4-7 which shows the insensitivity of this station to pitch. The station has a similar insensitivity to flap angle; for optimization applications it is the pitch lift boundary of the unflapped section which would be employed. The significance of the 45% station boundary lies in its relationship to the top of the cavitation bucket and particularly, to the upper surface comer of that bucket.

Orbital velocity presents a pitch lift case where the induced angle is inversely proportional to speed. The case is well-defined only for the three-dimensional foil, but is illustrated here to show its relationship to the fixed pitch case. For the orbital velocity case, Equation 3.3.8.4-11 may be written:

$$\sqrt{S} = \psi \mp \zeta\,\Omega\,c_{\ell_{i_{eff}}} \mp \zeta\,\Omega\,c_{\ell_\alpha}\,\frac{v_w}{V} \pm \left(\frac{\Delta v_a{}'}{V} + \zeta\,\Omega\right) c_\ell \qquad 3.3.8.4\text{-}13$$

$\sqrt{S}$ is not a linear function of c_ℓ for this case and studies of the orbital velocity effect on the section are not productive for the current state of the art, so the case is presented here only in the V – L/S format where Equation 3.3.8.4-13 may be written:

$$\frac{L}{S} = q\left(\pm\sqrt{S} \mp \psi + \zeta\,\Omega\,c_{\ell_{i_{eff}}} + \zeta\,\Omega\,c_{\ell_\alpha}\,\frac{v_w}{V}\right)\Bigg/\left(\frac{\Delta v_a{}'}{V} + \zeta\,\Omega\right) \qquad 3.3.8.4\text{-}14$$

where: q ranges over the speed range of interest.

The 2.43 ft/sec orbital velocity for a 9 ft mean depth in a 6 ft x 120 ft wave **might** be considered a typical value, but 1.85 **ft/sec** is employed here for the section to account for the finite span induced angle. This orbital velocity produces the 1.52 pitch angle of Figure 3.3.8.4-7 at 41.3 knots, The orbital velocity cavitation buckets, shown on Figure 3.3.8.4-8, differ quantitatively but not qualitatively from the fixed pitch angle buckets of Figure 3.3.8.4-7.

The pressure coefficient, S, can be written as a function of the section lift coefficient:

$$S = 1 + \frac{P_s - P_v}{q} = 1 + \frac{P_s - P_v}{L/S}\,\frac{L/S}{q} = 1 + \frac{P_s - P_v}{L/S}\,c_\ell \qquad 3.3.8.4\text{-}15$$

$$= 1 + \frac{P_s - P_v}{L/S}\,c_{\ell_{i_{eff}}} + \frac{P_s - P_v}{L/S}\,(c_\ell)_\alpha + \frac{P_s - P_v}{L/S}\,(c_\ell)_\delta$$

With this identification for S, the general form of the flapped section cavitation boundary of Equation 3.3.8.4-6 may be written:

$$\left(\frac{\Delta v_a'}{V} + \zeta\,\Omega\right)^2 (c_\ell)_\delta^{\;2} + \left\{2\left[\pm\frac{v}{V} + \frac{\Delta v/V}{c_{\ell_{i_{ref}}}}\,c_{\ell_{i_{eff}}} + \frac{\Delta v_a'}{V}\,(c_\ell)_\alpha\right]\left(\frac{\Delta v_a'}{V} + \zeta\,\Omega\right) - \qquad 3.3.8.4\text{-}16$$

$$\left.\frac{P_s - P_v}{L/S}\right\}(c_\ell)_\delta \pm \left[\pm\frac{v}{V} + \frac{\Delta v/V}{c_{\ell_{i_{ref}}}}\,c_{\ell_{i_{eff}}} + \frac{\Delta v_a'}{V}\,(c_\ell)_\alpha\right]^2 - \left[1 + \frac{P_s - P_v}{L/S}\,c_{\ell_{i_{eff}}} + \frac{P_s - P_v}{L/S}\,(c_\ell)_\alpha\right] = 0$$

which is forbidding algebraically but not numerically. For example, for the 16-309 section, for a $(P_s - P_v)/(L/S)$ of 1.7627, Equation 3.3.8.4-16 becomes:

$$\left(\frac{\Delta v_a'}{V} + \zeta\,\Omega\right)^2 (c_\ell)_\delta^{\;2} + \left\{2\left[\frac{v}{V} + 0.054 + \frac{\Delta v_a'}{V}\,(c_\ell)_\alpha\right]\left(\frac{\Delta v_a'}{V} + \zeta\,\Omega\right) - 1.7627\right\}(c_\ell)_\delta +$$

$$+\left[\frac{v}{V} + 0.054 + \frac{\Delta v_a'}{V}(c_\ell)_\alpha\right]^2 - 1.3702 - 1.7627\,(c_\ell)_\alpha = 0 \qquad 3.3.8.4\text{-}17$$

where the station parameters required are presented in Table 3.3.8.4-V.

Equations 3.3.8.4-16 and 3.3.8.4-17 present the incipient cavitation flap lift coefficient for any chord station, for a particular $(P_s - P_v)/(L/S)$ as a quadratic function of the pitch lift coefficient. The angular relationships are obtained simply by substituting the product of the lift curve slopes and angles for the two lift coefficients. **This** form of the cavitation bucket is illustrated in Figure 3.3.8.4-9, where the cavitation-free area is the included “corridor” between the leading edge and hingeline boundaries. The bottom of the corridor is marked by mid-chord cavitation, where the relationship with the 45% station boundary should be noted, and the top of the corridor is marked by theoretical uncertainties associated with the flap effectiveness at large flap angles. The alternative hingeline boundary is discussed later in this subsection.

For a particular foil loading, the lift curve may be written:

$$\delta = \left(\frac{L/S}{q} - c_{\ell_{i_{eff}}} - c_{\ell_\alpha}\alpha\right) \Big/ c_{\ell_\delta} \qquad 3.3.8.4\text{-}18$$

which provides the speed grid within the corridor of Figure 3.3.8.4-9. At some effective leading edge and hingeline boundary, these speed lines take a different form where form and effective boundary are still uncertain.

The restriction of the $\alpha - \delta$ corridor to a particular foil loading and depth limits its usefulness but it is ideally suited to prototype testsconducted under this restriction. Only elementary measurements are required, and the angular measurements display the effect of cavitation; in fact such cavitated angular measurements should define the cavitated form of the lift equation, Equation 3.3.8.4-18.

Note that Figure 3.3.8.4-9 could be viewed from the δ scale or plotted as a flap angle corridor on a speed scale or, alternatively, it could be viewed from the α scale or plotted as a pitch corridor on a speed scale. Neither practice can be recommended because all three dimensions, flap angle, pitch, and speed, are required to identify a cavitation-affected point. Prototype observations on such forms of the $\alpha - \delta$ corridor can be particularly misleading because the lift effect of the cavitation makes flap angle observations optimistic and pitch angle observations pessimistic.

Again, it must be emphasized that all of the prevalent forms of the flapped section cavitation bucket have been shown here for the purpose of comparison. Some of these forms are not suited to section study, particularly in angular dimensions, but are employed effectively in Section 3.8. Experience with the flapped section cavitation characteristics is still so limited that no preferred format for their display is yet evident.

AERODYNAMIC TESTS OF THE FLAPPED SECTION CAVITATION BUCKET

Aerodynamic pressure distribution data for the flapped section is quite limited and time permits only an indication of the precautions which must be observed in interpreting that data.

Jones offers a cavitation bucket interpretation of the 4.05 x 10^6 Reynolds Number zero- and six-degree flap angle pressure distribution data of Reference 2 on Figure 15 of Reference 3. The zero-flap bucket has already been examined in Figure 3.3.8.3-5. The six-degree flap angle bucket is examined here.

The lift curves for this case are shown in Section 7.2.1, Page 5 of Reference 2, which is repeated as Figure 3.3.8.4-10. The flap lift coefficients, with and without the transition strip, are obtained by comparing the measurements, using the appropriate unflapped lift curves of Tables 3.3.1.2-VIII and 3.3.1.2-IX, with the results shown on Figure 3.3.8.4-10.

The moment curves for zero- and six-degree flap are found on Pages 4 and 5 of Section 7.2.4 of Reference 2 and are combined here for reference in Figure 3.3.8.4-11. These curves are more difficult to correlate than the lift curves, but more significant to the cavitation bucket because they are sensitive to the distribution of the lift.

The intercept for the moment curves of Figure 3.3.8.4-11 is the $c_{m_{ac}}$ which, for the unflapped section, is given by Equation 3.3.3.1-2 as:

$$c_{m_{ac}} = - c_{\ell_{i_{eff}}} (c.p._c - a.c.) \qquad 3.3.8.4\text{-}19$$

where: $c_{\ell_{i_{eff}}}$ = 0.2086 from Table 3.3.1.2-1X for this particular case with fixed transition

$c.p._c =$ 0.485 from Equation 3.3.3.1-2

a.c. = 0.2325 from Figure 3.3.2.1-10 for this particular case with fixed **transition**

The fixed-transition, zero-flap intercept of Figure 3.3.8.4-11, then, is given by::

$$c_{m_{ac}} = - 0.2086 (0.485 - 0.2325) = -0.0527 \qquad 3.3.8.4\text{-}20$$

Since the lift is defined as acting through the aerodynamic center, the moment about the quarter chord point is given by:

$$c_{m_{c/4}} = c_{m_{ac}} - c_\ell (a.c. - 0.25) \qquad 3.3.8.4\text{-}21$$

$$= -0.0527 - c_\ell (0.2325 - 0.25)$$

$$= -0.0527 + 0.0175\, c_\ell$$

which is the equation for the fixed transition, zero flap line of Figure 3.3.8.4-11.

The $c_{m_{ac}}$ increment due to flap is given by Equation 3.3.3.2-3 as:

$$\Delta c_{m_{ac\delta}} = - \zeta (c.p._\delta - a.c.) (c_\ell)_\delta \qquad 3.3.8.4\text{-}22$$

where: ζ = 0.4527 from Figure 3.3.2.4-l

$c.p._\delta = \frac{1}{4} + \frac{1}{2} \times 0.75 = 0.626$ from Equation 3.3.3.2-l

$(c_\ell)_\delta$ = 0.2936 for this particular case from Figure 3.3.8.4-10.

For this particular case, then, the flap incremental $c_{m_{ac}}$ is:

$$\Delta c_{m_{ac_\delta}} = -0.4527 (0.625 - 0.2325) \times 0.2936 \qquad 3.3.8.4\text{-}23$$

$$= -0.0522$$

and, with Equation 3.3.8.4-21, the quarter-chord moment for the fixed transition, 6 degree flap case becomes:

$$c_{m_{c/4}} = -0.0527 - 0.0522 + 0.0175\, c_\ell \qquad 3.3.8.4\text{-}24$$
$$= -0.1049 + 0.0175\, c_\ell$$

as shown in Figure 3.3.8.4-11.

For low lift coefficients without fixed transition, Table 3.3.1.2-VIII gives the c_{ℓ_i} as 0.2798, nearly the inviscid value, for this particular case. The inviscid center of pressure for the a = 1.0 camber line is 0.5 and the inviscid aerodynamic center for the 9% 16-Series thickness distribution is 0.2639 from Figure 3.3.2.1-4. If the case without fixed transition approximates the inviscid case, then Equation 3.3.8.4-19 becomes:

$$c_{m_{ac}} = -0.2798\,(0.5 - 0.2639) = -0.0661 \qquad 3.3.8.4\text{-}25$$

and Equation 3.3.8.4-21 becomes:

$$c_{m_{c/4}} = -0.0661 - c_\ell\,(0.2639 - 0.25) \qquad 3.3.8.4\text{-}26$$
$$= -0.0661 - 0.0139\, c_\ell$$

This is shown in Figure 3.3.8.4-11 for the unflapped case without fixed transition.

The ζ and $c.p._\delta$ of Equation 3.3.8.4-22 are the inviscid values and, with the inviscid aerodynamic center and the flap lift of Figure 3.3.8.4-10, that equation becomes:

$$\Delta c_{m_{ac\delta}} = -0.4527\,(0.625 - 0.2639) \times 0.3406 \qquad 3.3.8.4\text{-}27$$
$$= -0.0557$$

This, with Equation 3.3.8.4-26, provides:

$$c_{m_{c/4}} = -0.0661 - 0.0557 - 0.0139\, c_\ell \qquad 3.3.8.4\text{-}28$$
$$= -.1218 - 0.0139\, c_\ell$$

which is shown on Figure 3.3.8.4-11 for the 6degree flap case without fixed transition.

The fixed-transition correlations of Figure 3.3.8.4-11 are quite good, though subject to systematic error at the high lift coefficients where the lift begins to fall off on Figure 3.3.8.4-10. The fixed-transition case is the case of interest to the prototype. The case without fixed transition, of interest to model tests, promises difficulty in the interpretation of model tests. Note that the zero-moment slope of Figure 3.3.8.4-11 without fixed transition might be indicative of a quarter-chord aerodynamic center position, the inviscid flat plate value. It is more likely, however, that the zero slope is apparent only, and results from qualitative boundary layer changes at low lift coefficients.

The six-degree flap lift and moment curves of Figures 3.3.8.4-10 and 3.3.8.4-11 describe two cases.

With fixed transition: Without fiied transition: 3.3.8.4-29

With fixed transition	Without fiied transition
$c_{\ell_{i_{eff}}} = 0.2086 \approx 0.21$	$c_{\ell_{i_{eff}}} = 0.2798 \approx 0.28$
$\Delta a.c. = 0.2639 - 0.2325 = 0.0314 \approx 0.0315$	$\Delta a.c. = 0$
$(c_\ell)_\delta = 0.2936$	$(c_\ell)_\delta = 0.3406$

The case with fixed transition, the prototype case, is well defined. It must be emphasized, however, that transition strip effects are subject to the configuration of the transition strip. It is shown in Section 3.3.9 that the transition strip of Reference 2 produced prototype drag characteristics while that of Reference 4 did not, The two transition strip configurations are compared in Section 6.1.1.1. The case without fixed transition is ill-defined, with an abrupt pressure distribution transition between the 0.5 and 0.7 lift coefficients and with some indication of a smaller transition throughout the lower lift coefficient range. It is unfortunate that this data was not continued to the stable negative lift coefficient range in order to aid understanding of the transition range. It is still more unfortunate that comparable data is not available for the symmetric section.

The cavitation buckets for the two cases of Equation 3.3.8.4-29 are shown in Figure 3.3.8.4-12; the boundary derivations are similar to those of Table 3.3.8.4-U and are not shown. A companion wind tunnel test for zero flap is shown in Figure 3.3.8.3-5.

Figure 3.3.8.4-12 shows a surprising similarity between the measured results with and without the transition strip. The high lift coefficient measurement/theory comparison shows the effect of pressure peaks forward of the 1-1/4% station and/or separation and is not very significant since this area of the bucket does not guide design. The lower surface, similarly, does not guide current design practice but could become significant to larger craft of large fuel/weight ratios. The lower surface measurement/theory comparison needs further investigation. The discrepancy is probably, though not certainly, due to pressure peaks forward of the 1-1/4% station. That possibility could be evaluated easily if the 16-Series thickness distribution velocity distributions of Reference 4 were extended further forward. Note that measurement density and precision complicate interpretations of this type of data.

The most significant indication of Figure 3.3.8.4-12 is the hingeline theoretical optimism, which is given added intuitive significance by the dimensional comparison of Figure 3.3.8.4-1.3. Note that the bucket of Figure 3.3.8.4-13 is only one of the continuum of buckets which define the flap lift control system, each dominated by the hingeline boundary and, together, constraining the operational flap/pitch range as shown in Figure 3.3.8.4-9. That hingeline pressure is not available to theory, presenting an analytic singularity and practical local configuration problems.

The only general definition for hingeline pressure which can be offered here is Allen's empirical definition of Reference 1, shown in Table 3.3.8.4-I and on Figure 3.3.8.4-1. Allen's hingeline pressure coefficient was derived from aerodynamic section data obtained at a Reynold's number of 1×10^6. From comparison of this data with unspecified data obtained at a Reynolds number of 3.7×10^6, Allen concludes that the scale effect is unimportant (to aerodynamic application) although a delay in separation is noted.

Sections 7.5.8 and 7.5.15 of Reference 2 provide measurements of the hingeline pressure coefficients for the two cases of Figure 3.3.8.4-13. Assuming that every other coefficient of Equation 3.3.8.4-8 is correct, the $(\Delta v/V)_{F_I} c_{\ell_{b\delta}}$ can be derived from those measurements as

$$\frac{(\Delta v/V)_F}{c_{\ell_{b\delta}}} = \left[\sqrt{S} - \psi_u + (c_\ell)_\delta \zeta \frac{\Delta v_a' - \Delta v_a'}{V} - c_{\ell_I} (c_\ell)_\delta \zeta \right. \qquad 3.3.8.4\text{-}30$$

where: $S = 1 - C_P$.

The result is shown in Figure 3.3.8.4-14. Figure 3.3.8.4-14, then, displays those values of $(\Delta v/V)_F / c_{\ell_{b\delta}}$ which would provide perfect experimental correlation for the bottoms of the buckets of Figure 3.3.8.4-12. The effect of the transition strip on the correlations of Figure 3.3.8.4-14 could, therefore, be of substantial significance because a contradiction to Allen's scale effect conclusion is indicated. The effect of the fixed-transition 1.5 coefficient is shown in Figure 3.3.8.4-9 where it profoundly affects the $\alpha - \delta$ corridor. The effect of Figure 3.3.8.4-9, however, differs rather significantly from the unknown prototype effect of Section 3.8 although both constrain the theoretical corridor.

It will be recognized that no single test result can redefine the hingeline pressure. The characteristics of Figure 3.3.8.4-14 may be functions of thickness, thickness distribution, camber, flap chord ratio and/or flap angle. A great deal more experience is required for a confident general definition for $(\Delta v/V)_F / c_{\ell_{b\delta}}$.

REFERENCES

1. Allen, H. Julian: Calculation of the Chordwise Load Distribution Over Airfoil Sections with Plain, Split, or Serially Hinged Trailing-Edge Flaps. NACA Report No. 634, 1938.

2. Teeling, P.: Low Speed Wind Tunnel Tests of a NACA 16-309 Airfoil with Trailing Edge Flap. DeHavilland Aircraft of Canada Limited Report No. ECS 76-3, October 1976.

3. Jones, E.A.: Model Scale Effects on a 16-Series Flapped Hydrofoil Section. Defence Research Establishment Atlantic informal communication, February 1978.

4. Abbott, Ira H. and Von Doenhoff, Albert E.: Theory of Wing Sections. Dover Publications, 1959.

TABLE 3.3.8.4-I FLAP BASIC LIFT VELOCITY DISTRIBUTION

h/c = 80%	
x/c %	$\frac{(\Delta v/V)_F}{c_{\ell_{b\delta}}}$
0	0
2.5	0.032
5.0	0.046
7.5	0.057
10	0.067
15	0.085
20	0.102
25	0.118
30	0.135
35	0.153
40	0.172
45	0.194
50	0.219
55	0.248
60	0.284
65	0.331
70	0.400
72.5	0.451
75.0	0.524
77.5	0.654
80.0	1.085
82.5	0.635
85.0	0.486
87.5	0.393
90	0.320
95	0.197
100	0

h/c = 75%	
x/c %	$\frac{(\Delta v/V)_F}{c_{\ell_{b\delta}}}$
0	0
2.5	0.034
5.0	0.049
7.5	0.061
10	0.072
15	0.091
20	0.109
25	0.127
30	0.146
35	0.166
40	0.188
45	0.213
50	0.242
55	0.278
60	0.324
65	0.391
67.5	0.439
70.0	0.509
72.5	0.631
75.0	0.995
77.5	0.619
80.0	0.484
82.5	0.401
85	0.339
90	0.242
95	0.155
100	0

	HINGE LINE $(\Delta v/V)_F/c_{\ell_{h\delta}}$			
c_f/c	$\delta < 15°$		$\delta = 20°$	
%	EQUATION	ALLEN	EQUATION	ALLEN
5	2.155	2.185	1.393	1.468
10	1.484	1.510	0.996	1.013
15	1.226	1.223	0.844	0.845
20	1.085	1.100	0.761	0.755
25	0.995	1.003	0.707	0.708
30	0.932	0.928	0.670	0.675
35	0.885	0.875	0.642	0.658
40	0.848	0.838	0.621	0.645
45	0.819	0.808	0.603	0.640
50	0.794	0.788	0.589	0.640
55	0.774	0.778	0.577	0.645
60	0.757	0.765	0.567	0.655
65	0.742	0.760		
70	0.729	0.755		

$$(\Delta v/V)_F/c_{\ell_{b\delta}} = \frac{1}{4\pi\sqrt{h/c\,(1-h/c)}} \ln \frac{\left(\sqrt{h/c}\sqrt{1-x/c}+\sqrt{1-h/c}\sqrt{x/c}\right)^2}{|h/c - x/c|}$$

AT FLAP HINGE: $(\Delta v/V)_F/c_{\ell_{b\delta}} = 1/2 + 0.176\ (c_f/c)^{-3/4}$ FOR $\delta < 15°$

$= 0.415 + 0.1034\ (c_f/c)^{-3/4}$ FOR $\delta = 20°$

R80-0941-019B

TABLE 3.3.8.4-11 FLAPPED SECTION CAVITATION BUCKET, $(c_\ell)_\delta$ = 0.5276

NOTE:	16-309 SECTION	c_f/c = 0.25
	A a.c. = 0.0315	$c_{\ell_{I_{eff}}}$ = 0.21

ROW NO.	STATION, %	1.25	25	5	10	20	30	40	45	60	60	70	75	80
1	$\Delta v_a'/V$	1.354	0.996	0.723	0.515	0.349	0.265	0.207	0.183	0.160	0.121	0.083	0.065	0.046
	ψ_u	0.791	0.898	0.967	1.022	1.066	1.090	1.107	1.114	1.121	1.135	1.136	1.128	1.120
	ψ_l	1.251	1.208	1.167	1.130	1.104	1.092	1.085	1.082	1.079	1.077	1.062	1.046	1.030
2	$(\Delta v/V)_F/c_{\ell_{b\delta}}$	0.024	0.034	0.049	0.072	0.109	0.146	0.188	0.213	0.242	0.324	0.509	0.995 1.5	0.484
3	Ω	-1.330	-0.962	-0.674	-0.443	-0.240	-0.119	-0.019	0.030	0.082	0.203	0.426	0.930 1.435	0.438
4	$\zeta\Omega$	-0.602	-0.435	-0.305	-0.201	-0.109	-0.054	-0.009	0.014	0.037	0.092	0.193	0.421 65	0.198
5	$\psi + \zeta\Omega(c_\ell)_\delta$	0.473	0.668	0.806	0916	1.008	1.062	1.102	1.121	1.141	1.184	1.238	1.350	1.224
	$\psi_\ell - \zeta\Omega(c_\ell)_\delta$	1.569	1 A38	1.328	1.236	1.162	1.120	1.090	1.075	1.059	1.028	0.960	0.824	0.926

ROW NO. 1. FROM TABLE 3.3.8.3-I

2. FROM TABLE 3.3.8.4-I

3. $(\Delta v/V)_F/c_{\ell_{b\delta}} - \Delta v_a'/V$

4. ζ = 0.4527 FROM FIGURE 3.3.2.4-I

5. c_ℓ= 0 INTERCEPT FOR INCIPIENT CAVITATION BOUNDARY. SLOPE IS ± A v_a'/V.

R80-0941-020B

TABLE 3.3.8.4-III FLAP LIFT CAVITATION BUCKET, $(c_\ell)_\alpha = 0$

NOTE: 16-309 SECTION — $c_{\ell_{i_{eff}}} = 0.21$

A a.c. = 0.0315 — $c_f/c = 0.25$

ROW NO.	STATION, %	125	25	5	10	20	30	40	45	50	60	70	75	80
1	$\Delta v_a'/V$	1.354	0996	0.723	0.515	0.349	0.265	0.207	0.183	0.160	0.121	0.083	0.065	0.046
	ψ_u	0.791	0898	0.967	1.022	1.066	1.090	1.107	1.114	1.121	1.135	1.136	1.128	1.120
	ψ_l	1.251	1.208	1.167	1.130	1.104	1.092	1.085	1.082	1.079	1.077	1.062	1.046	1.030
	$\zeta\,\Omega$	-0.602	-0.435	-0.305	-0.201	-0.109	-0.054	-0.009	0.014	0.037	0.092	0.193	0.421 .145	0.198
2	$\Delta v_a'/V + \zeta\,\Omega$	0.752	0.561	0.418	0.314	0 240	0.211	0.198	0.197	0.197	0.213	0.276	0.487 .715	0.244
3	$\psi_u - \zeta\,\Omega\, c_{\ell_{i_{eff}}}$	0.917	0.989	1.031	1.064	1.089	1.101	1.109	1.111	1.113	1.116	1.095	1.040	1.078
	$\psi_l + \zeta\,\Omega\, c_{\ell_{i_{eff}}}$	1.125	1.117	1.103	1.088	1.081	1.081	1.083	1.085	1.087	1.096	1.103	1.134	1.072

ROW NO. 1. FROM TABLE 3.3.8.4-II

2. SLOPE FOR INCIPIENT CAVITATION BOUNDARY

3. $c_\ell = 0$ INTERCEPTS FOR INCIPIENT CAVITATION BOUNDARY

R80-0941-021B

TABLE 3.3.8.4-W PITCHED FLAP LIFT CAVITATION BUCKETS

NOTE: 16-309 SECTION $\quad c_{\ell_{i_{eff}}} = 0.21$

Δ a.c. = 0.0315 $\quad c_f/c = 0.25$

ROW NO.	STATION, %	1.25	2.5	5	10	20	30	40	45	50	60	70	75	80
1	$\Delta v_a'/V + \zeta\Omega$	0.752	0.561	0.418	0.314	0.240	0.211	0.198	0.197	0.197	0.213	0.276	0.487	0.244
	$\psi_u - \zeta\Omega c_{\ell_{i_{eff}}}$	0.917	0.989	1.031	1.064	1.089	1.101	1.109	1.111	1.113	1.116	1.095	1.040	1.078
	$\psi_\ell + \zeta\Omega c_{\ell_{i_{eff}}}$	1.125	1.117	1.103	1.088	1.081	1.081	1.083	1.085	1.087	1.096	1.103	1.134	1.072
	$\zeta\Omega$	-0.602	-0.435	-0.305	-0.201	-0.109	-0.054	-0.009	0.014	0.037	0.092	0.193	0.421	0.198
~	$0.15\,\zeta\Omega$	-0.090	-0.065	-0.046	-0.030	-0.016	-0.008	-0.001	0.002	0.006	0.014	0.029	0.063	0.030
2	$(c_\ell)_\alpha = 0.15$													
	I_u	1.007	1.054	1.077	1.094	1.105	1.109	1.110	1.109	1.107	1.102	1.066	0.977	1.048
	I_ℓ	1.035	1.052	1.057	1.058	1.065	1.073	1.082	1.087	1.093	1.110	1.132	1.197	1.102
3	$(c_\ell)_\alpha = -0.15$													
	I_u	0.827	0.924	0.985	1.034	1.073	1.093	1.108	1.113	1.119	1.130	1.124	1.103	1.108
	I_ℓ	1.215	1.182	1.149	1.118	1.097	1.089	1.084	1.083	1.081	1.082	1.074	1.071	1.042

ROW NO. 1. FROM TABLE 3.3.8.4-III

2 & 3. $I = c_\ell = 0$ INTERCEPT $= \psi \mp \zeta\Omega c_{\ell_{i_{eff}}} \mp \zeta\Omega (c_\ell)_\alpha$. SLOPE IS $\Delta v_a'/V + \zeta\Omega$

R80-0941-022B

TABLE 3.3.8.4-V FLAPPED SECTION $\alpha - \delta$ PARAMETERS

NOTE: 16-309 SECTION $\quad c_{\ell_{i_{eff}}} = 0.21$

Δ a.c. = 0.0315 $\quad$ UPPER SURFACE $\quad c_f/c = 0.25$

ROW NO.	STATION, %	1.25	2.5	5	10	20	30	40	45	50	60	70	75	80
1	v/V	1.021	1.053	1.067	1.076	1.085	1.091	1.096	1.098	1.100	1.106	1.099	1.087	1.075
2	$\Delta v_a'/V$	1.354	0.996	0.723	0.515	0.349	0.265	0.207	0.183	0.160	0.121	0.083	0.065	0.046
	$\Delta v_a'/V + \zeta\Omega$	0.752	0.561	0.418	0.314	0.240	0.211	0.198	0.197	0.197	0.213	0.276	0.487 .715	0.244

ROW NO. 1. FROM TABLE 3.38.3-I

2. FROM TABLE 3.3.8.4-III

R80-0941-023B

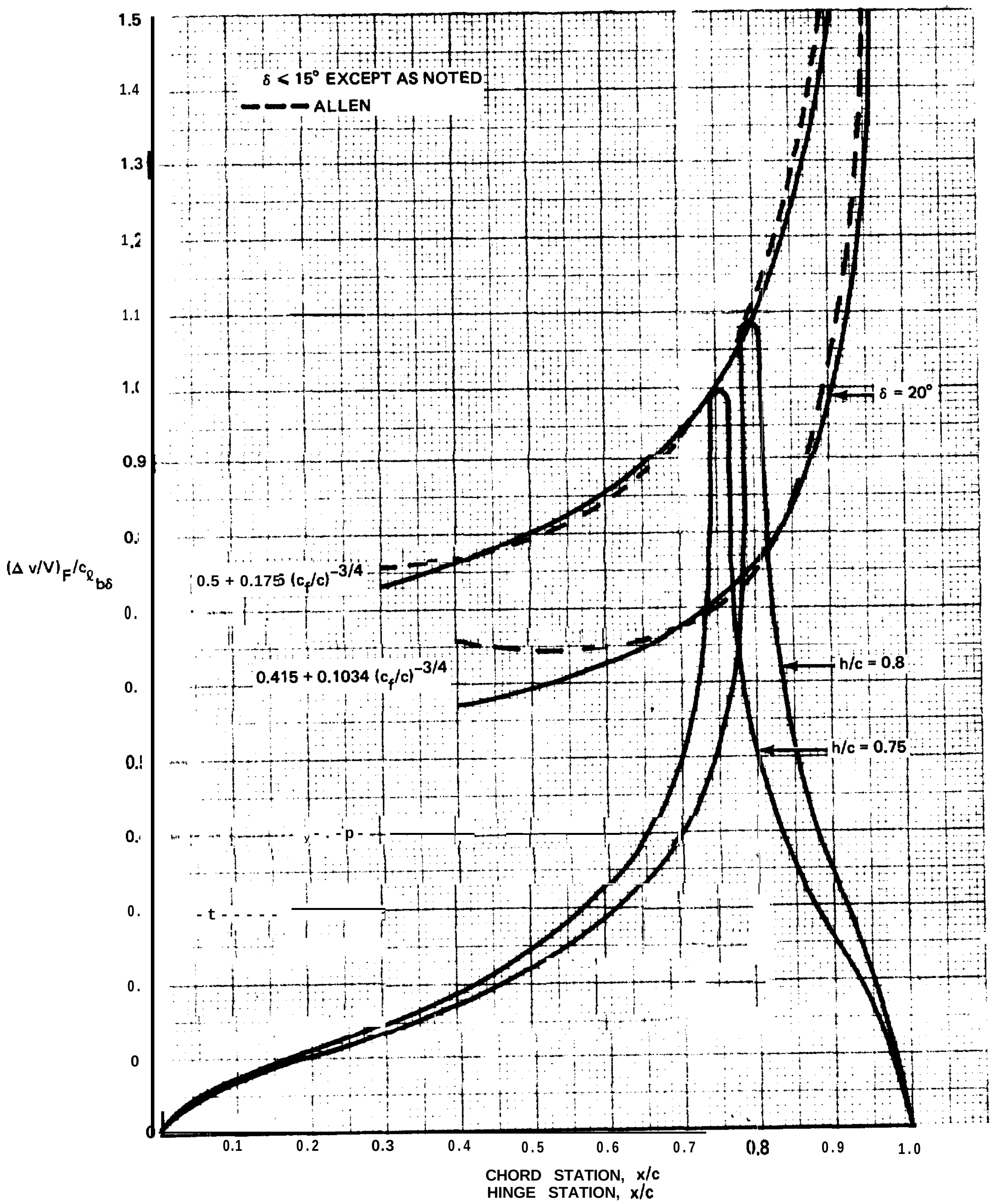

R80-0941-024B

Fig. 3.3.8.4-l Flap Basic Lift Velocity Distribution

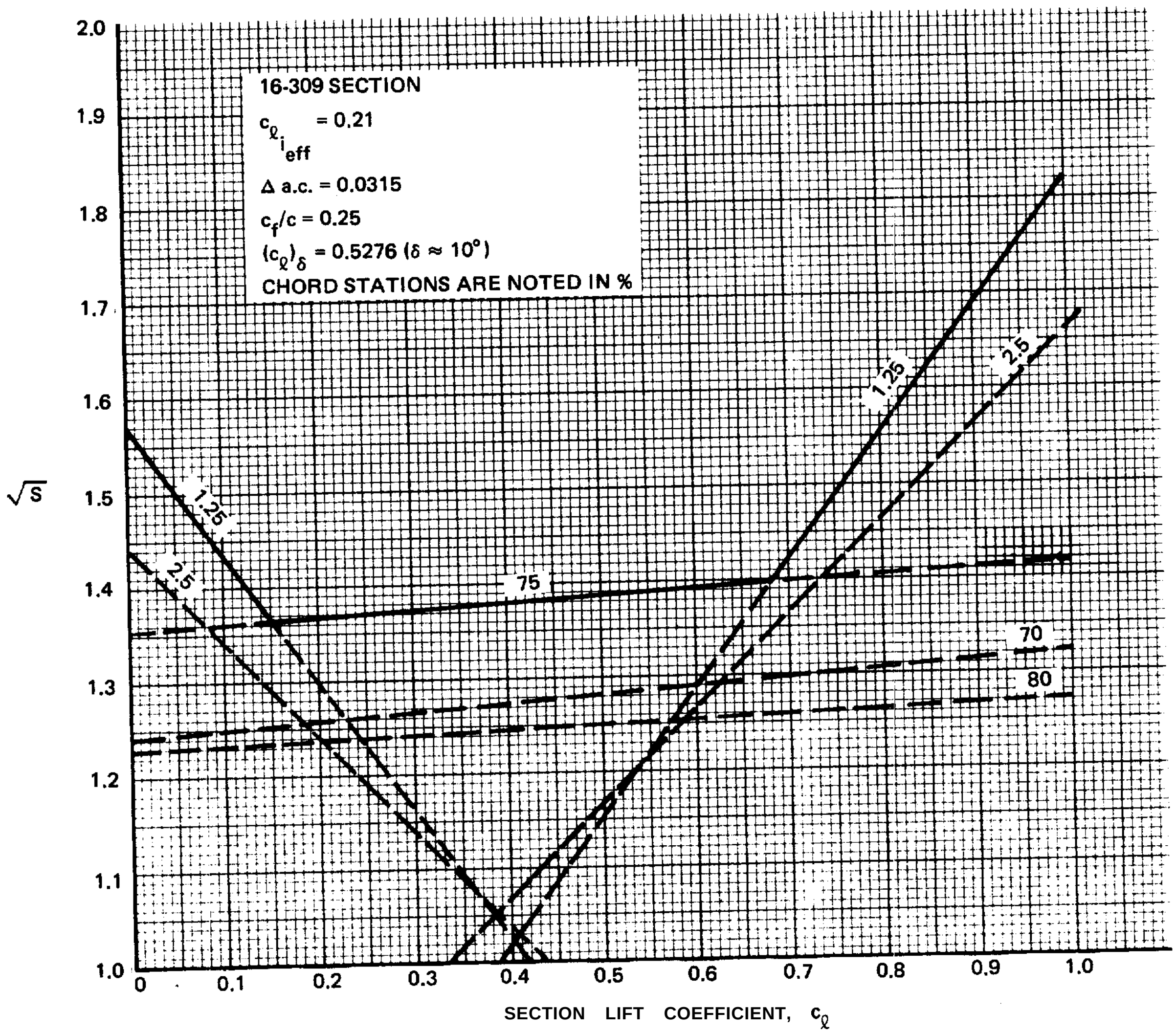

R80-0941-025B

Fig. 3.3.8.4-2 Flapped Section Cavitation Bucket

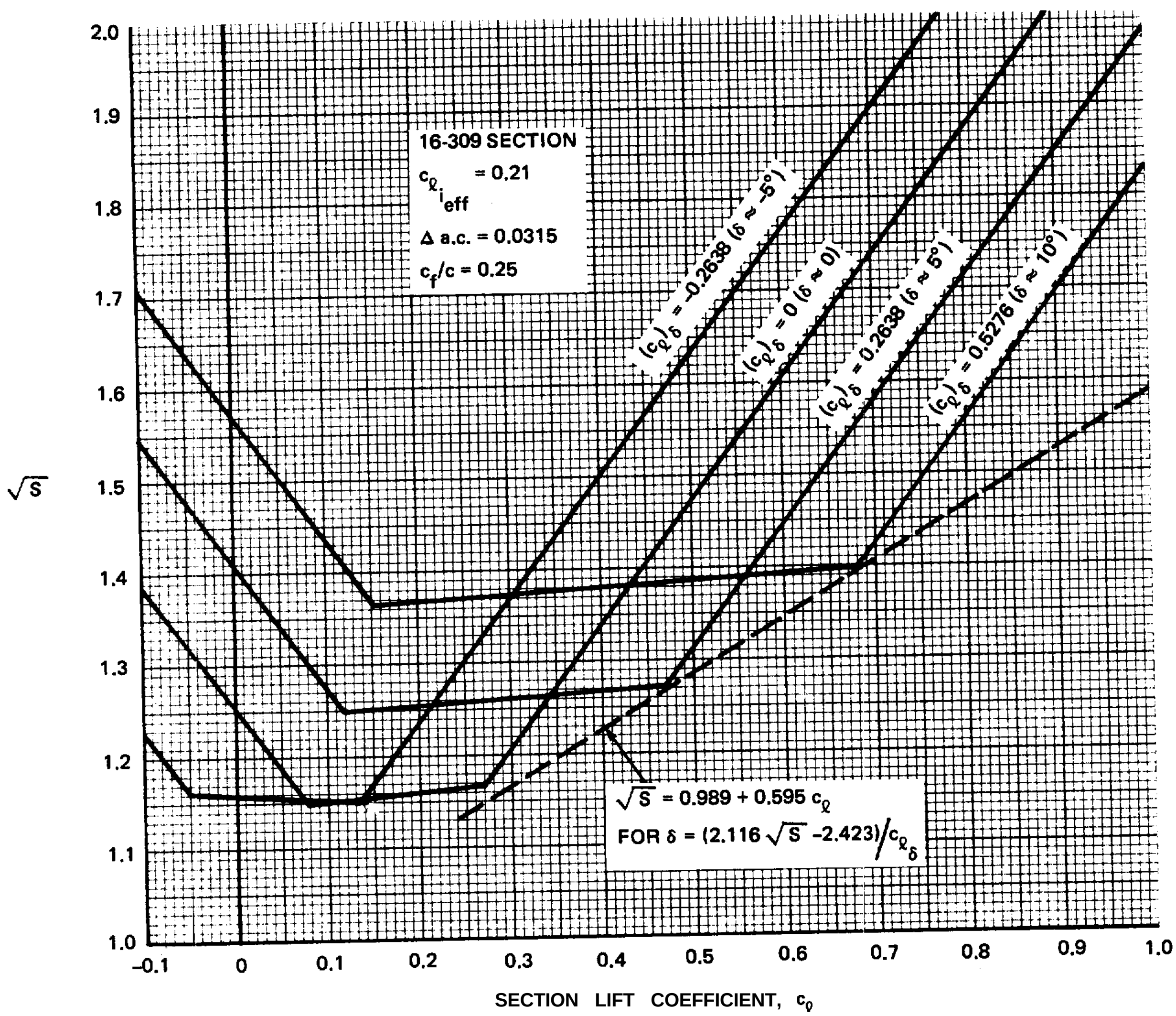

R80-0941-026B

Fig. 3.3.8.4-3 Flapped Section Cavitation

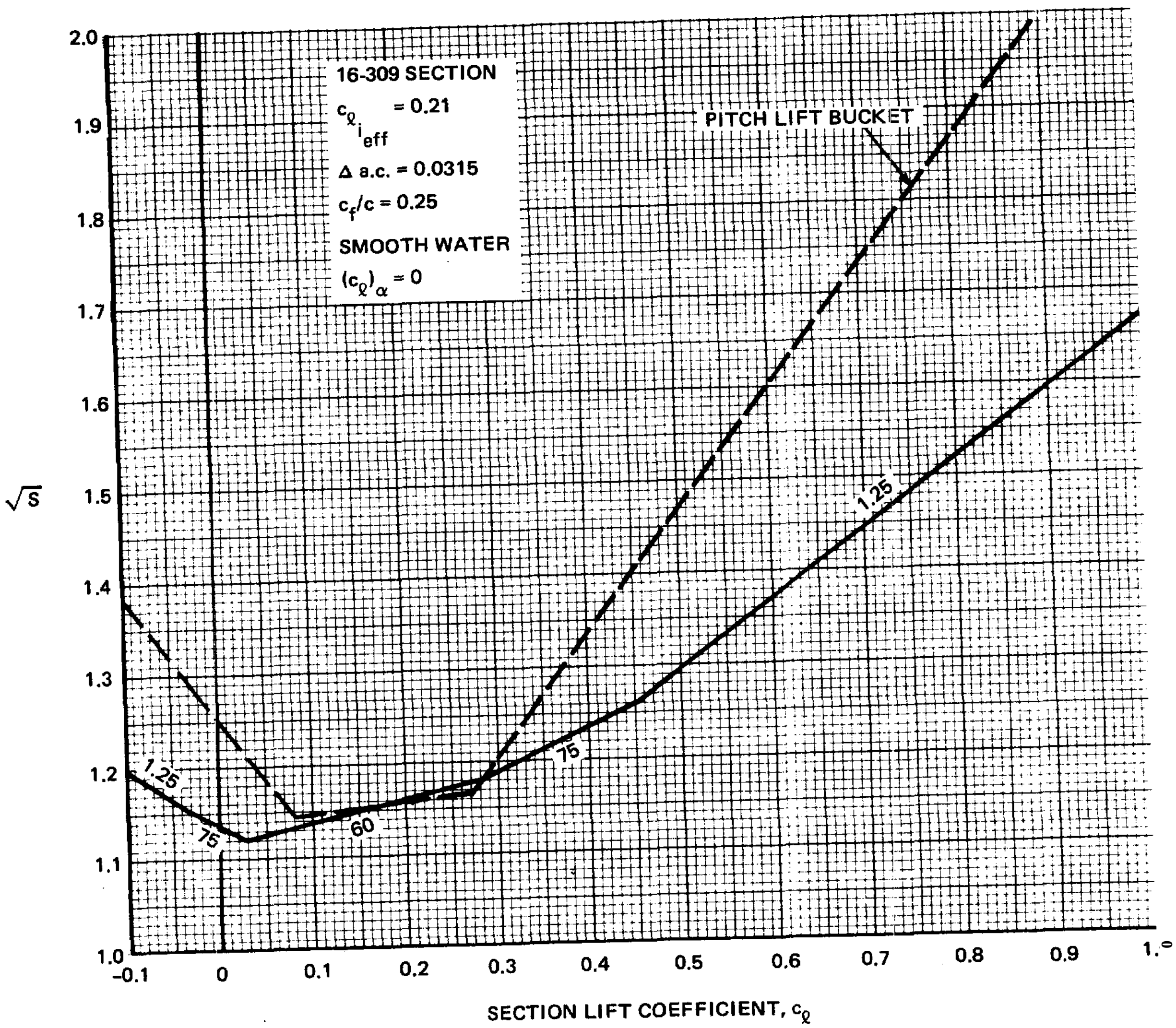

Fig. 3.3.8.4-4 Flap Lift Cavitation Bucket

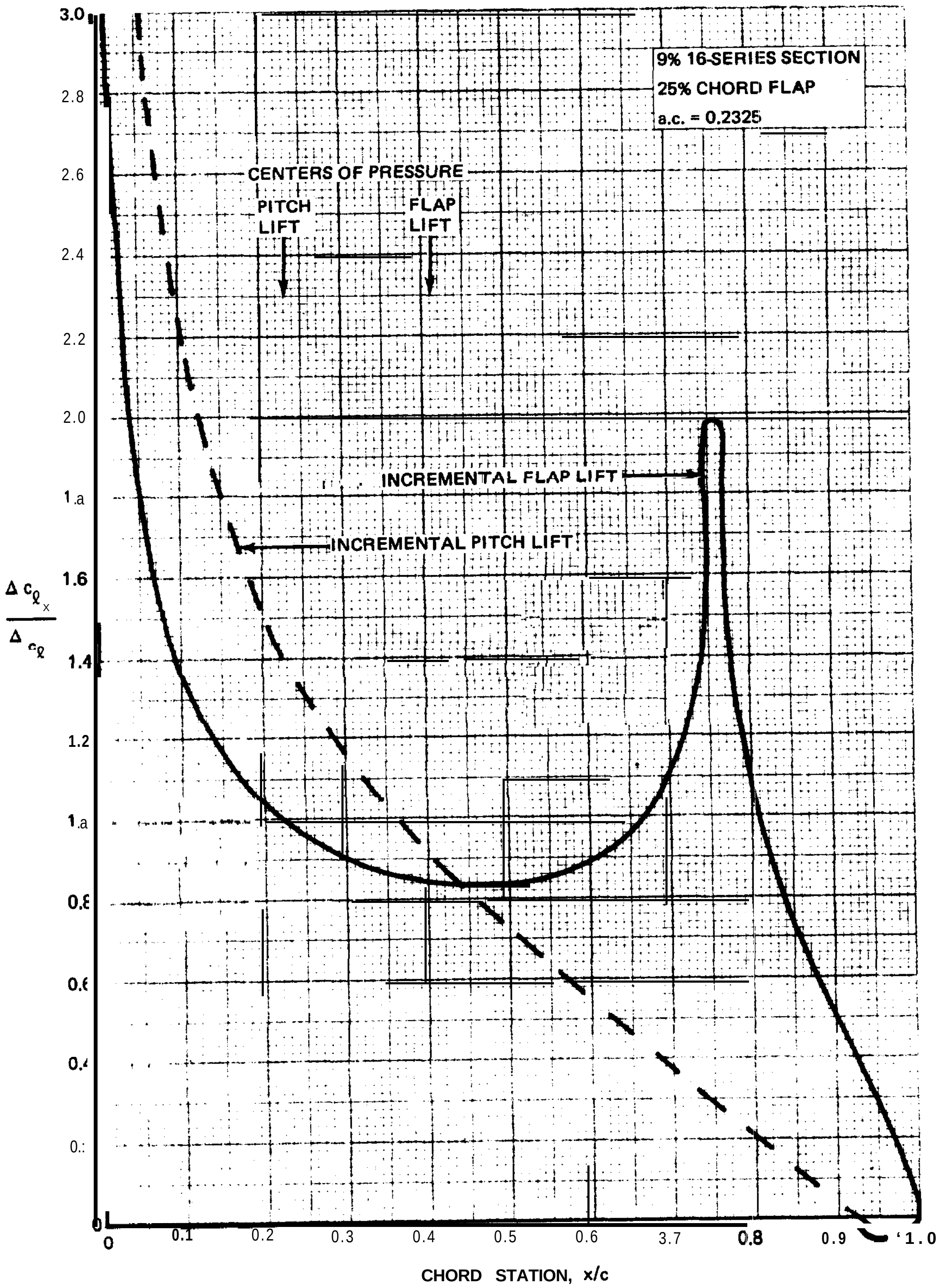

R80-0941-028B

Fig. 3.3.8.4-5 Pitch and Flap Lift Distribution

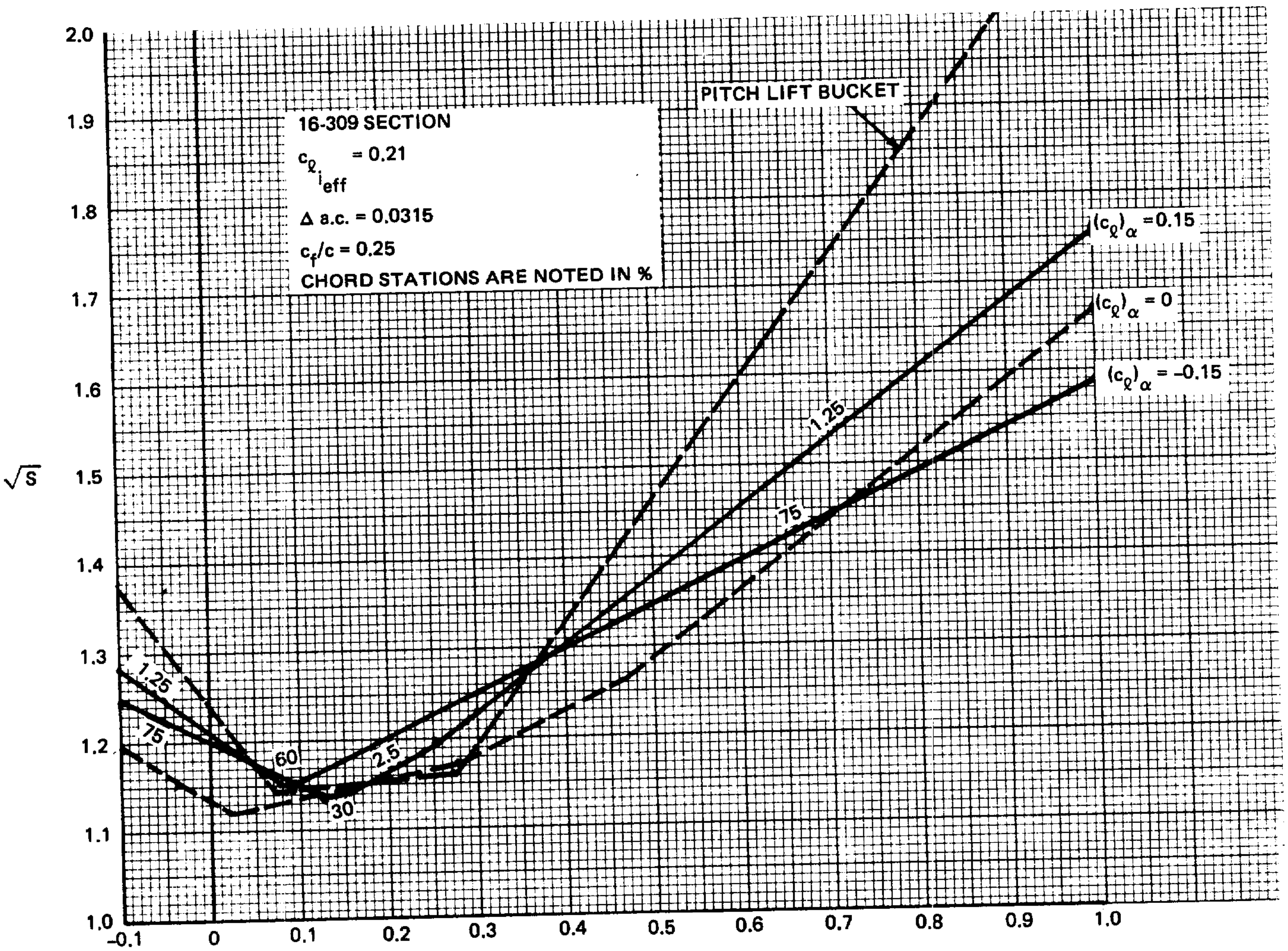

R80-0941-029B

Fig. 3.3.8.4-8 Pitched Flap Lift Cavitation Buckets

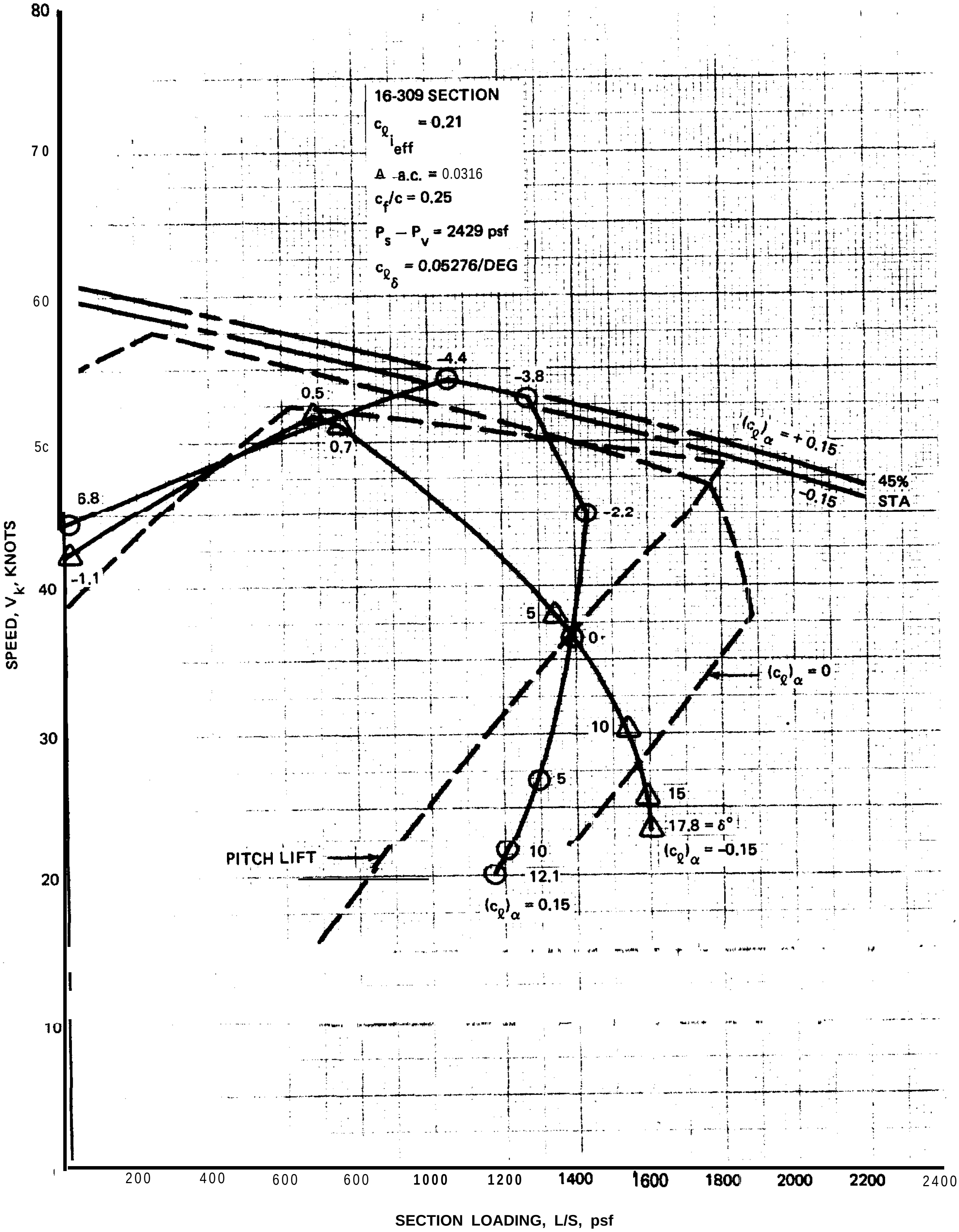

R80-0941-030B

Fig. 3.3.8.4-7 Section Speed vs Foil Loading Cavitation Buckets

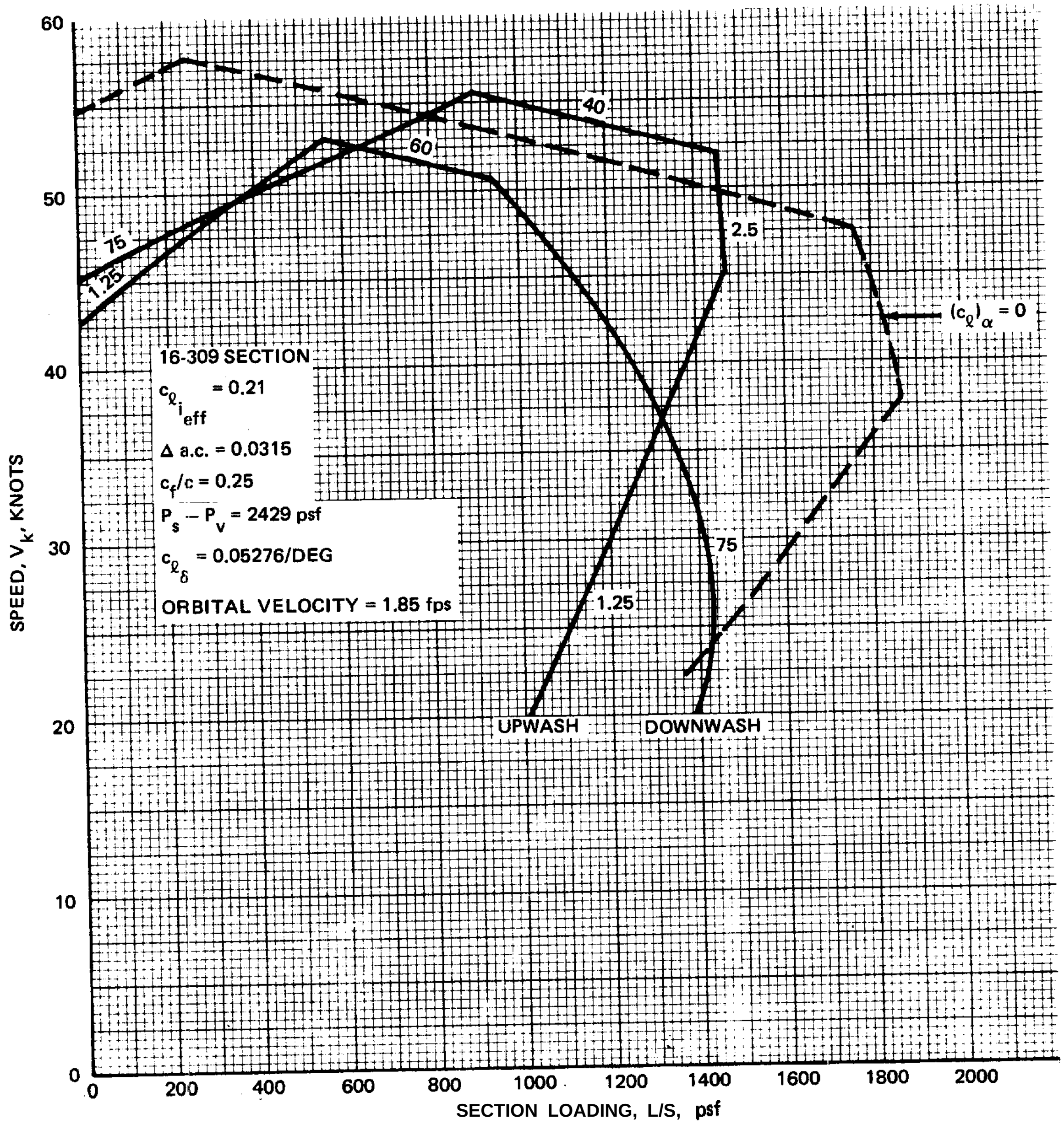

R80-0941-031B

Fig. 3.3.8.4-8 Flap Lift Orbital Velocity Effect

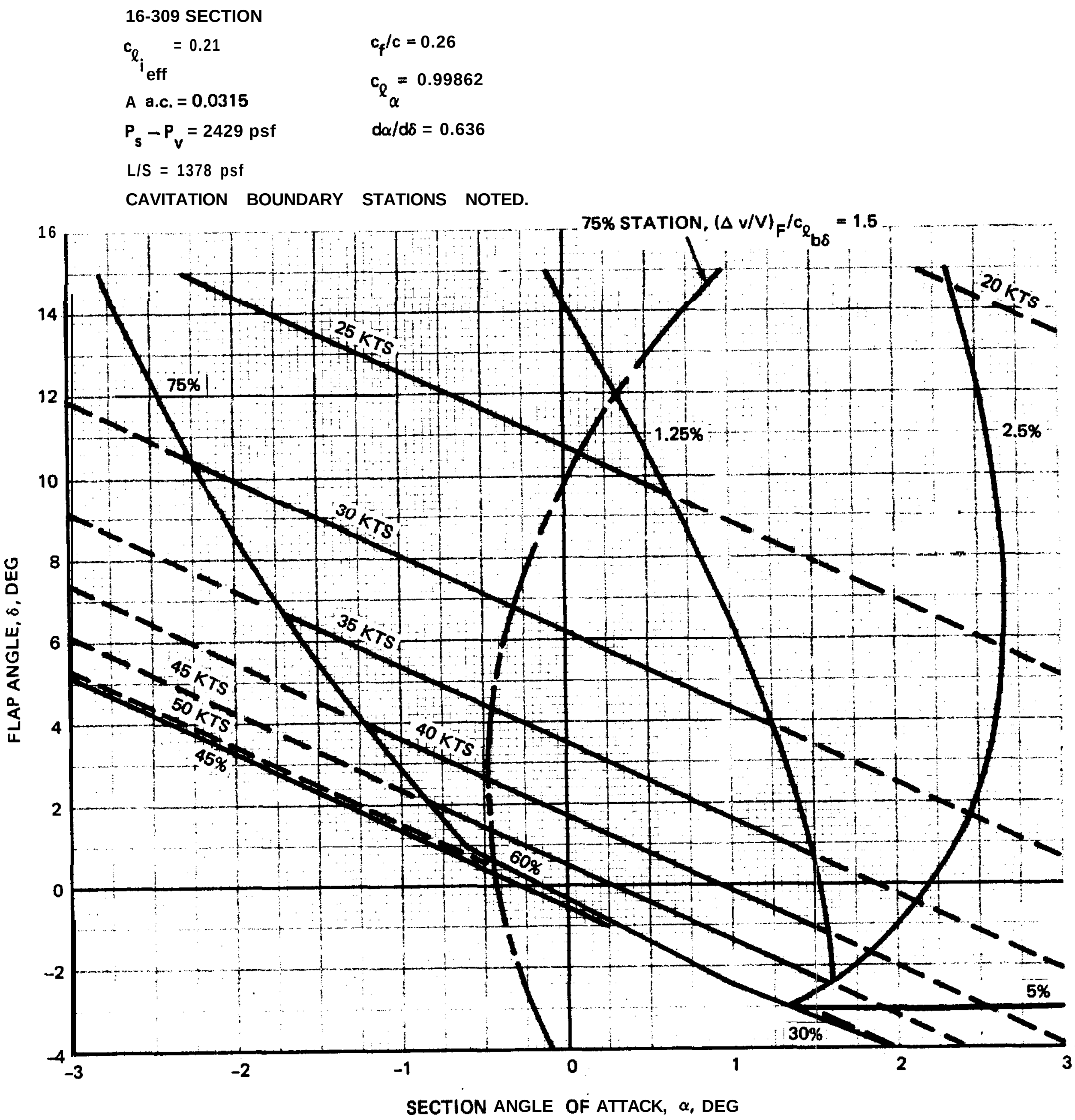

R80-0941-032B

Fig. 3.3.8.4-9 Flapped Section $\alpha - \delta$ Plane

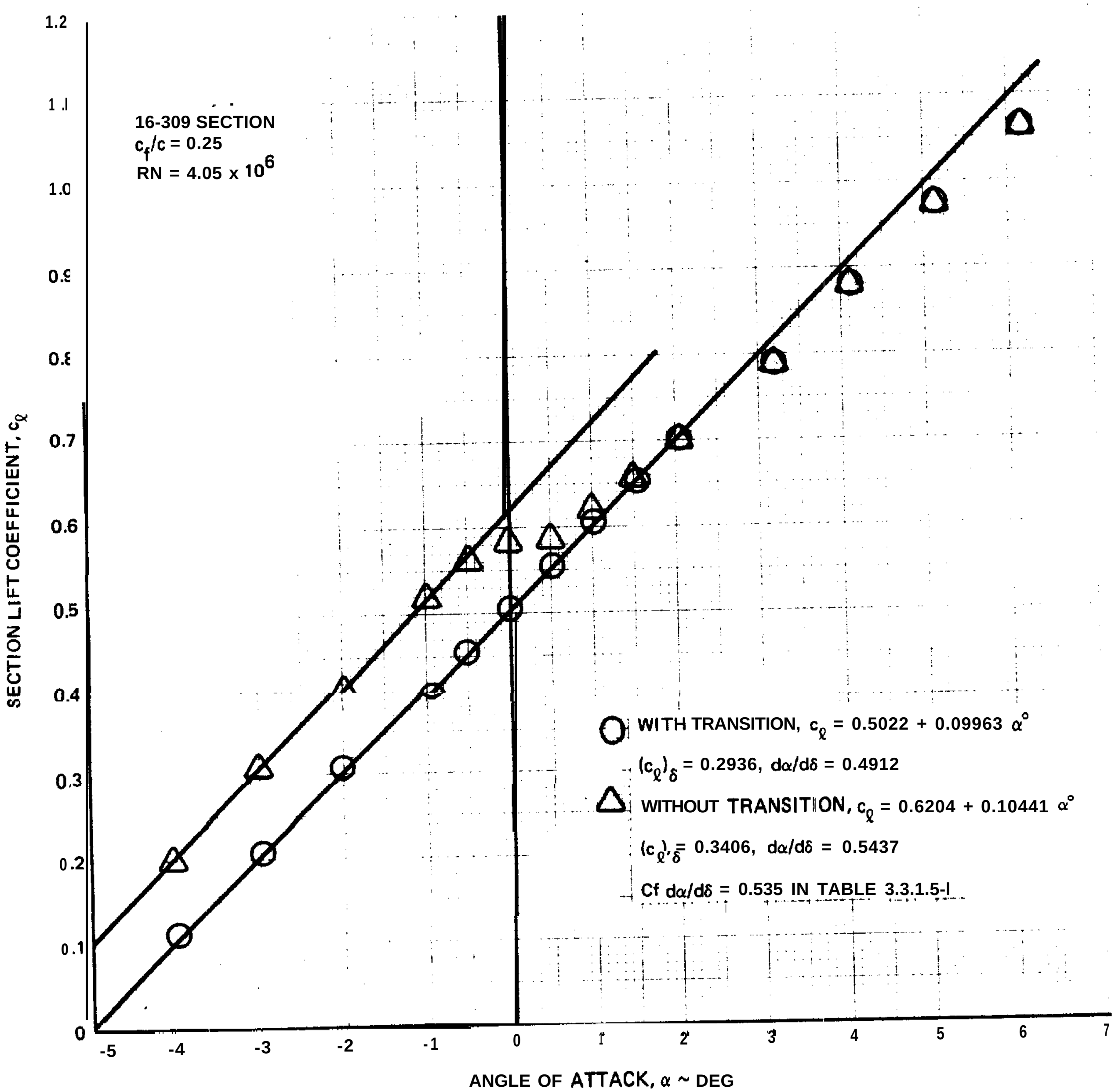

R80-0941-033B

Fig. 3.3.8.4-10 Section Lift Curves, $\delta = 6°$

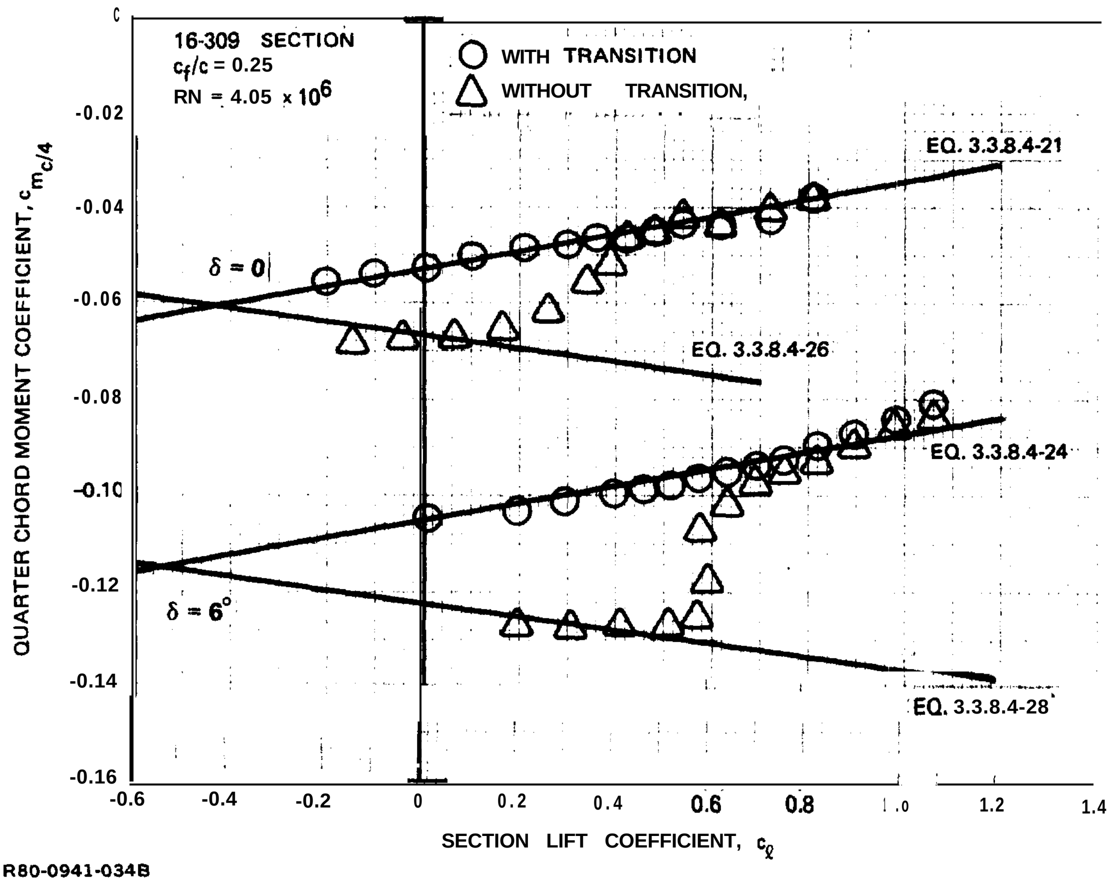

Fig. 3.3.8.4-l 1 Section Moment Curves, δ = 0” and 6°

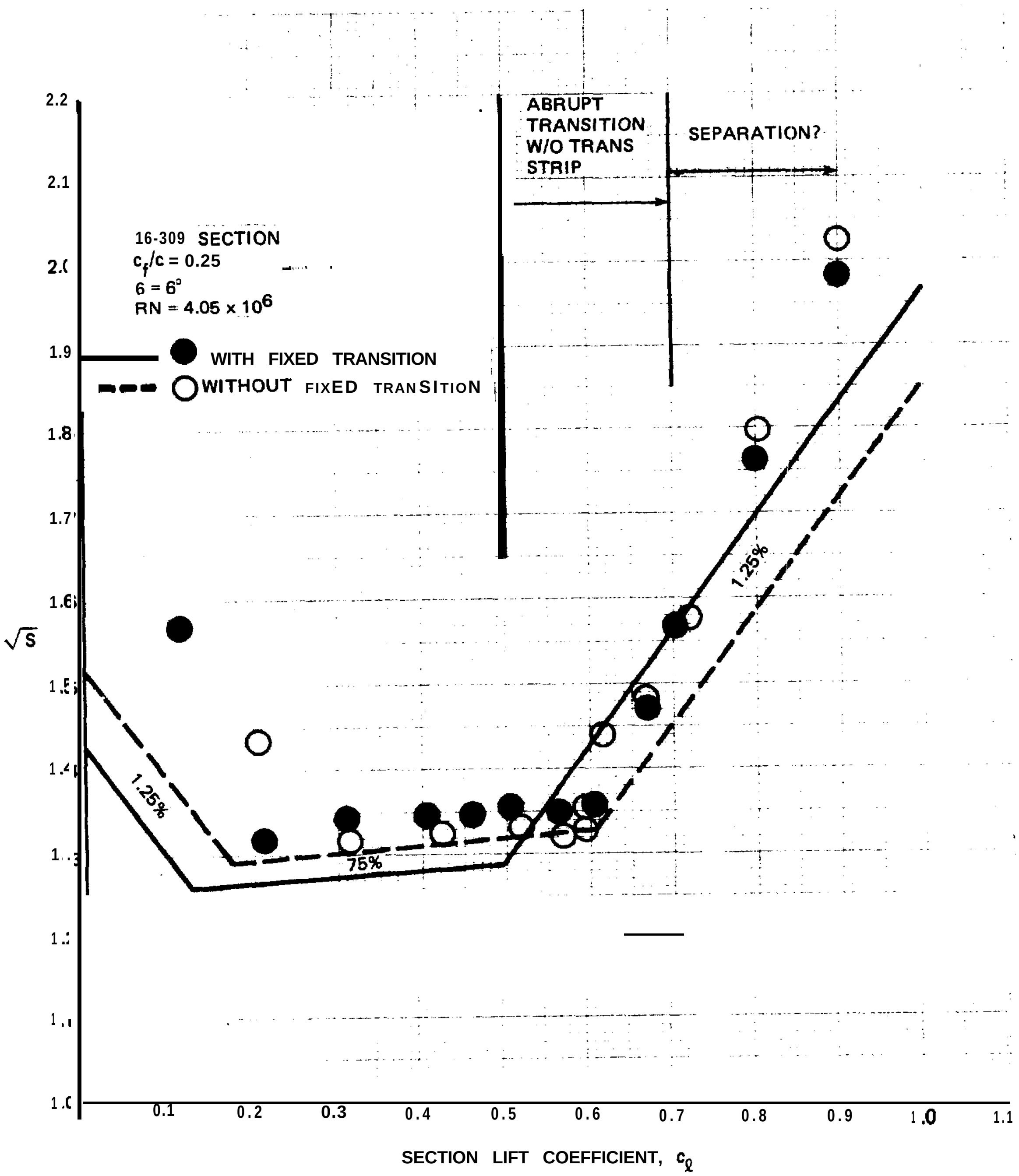

R80-0941-035B

Fig. 3.3.8.4-12 Flapped Pitch Cavitation Bucket, Wind Tunnel Test

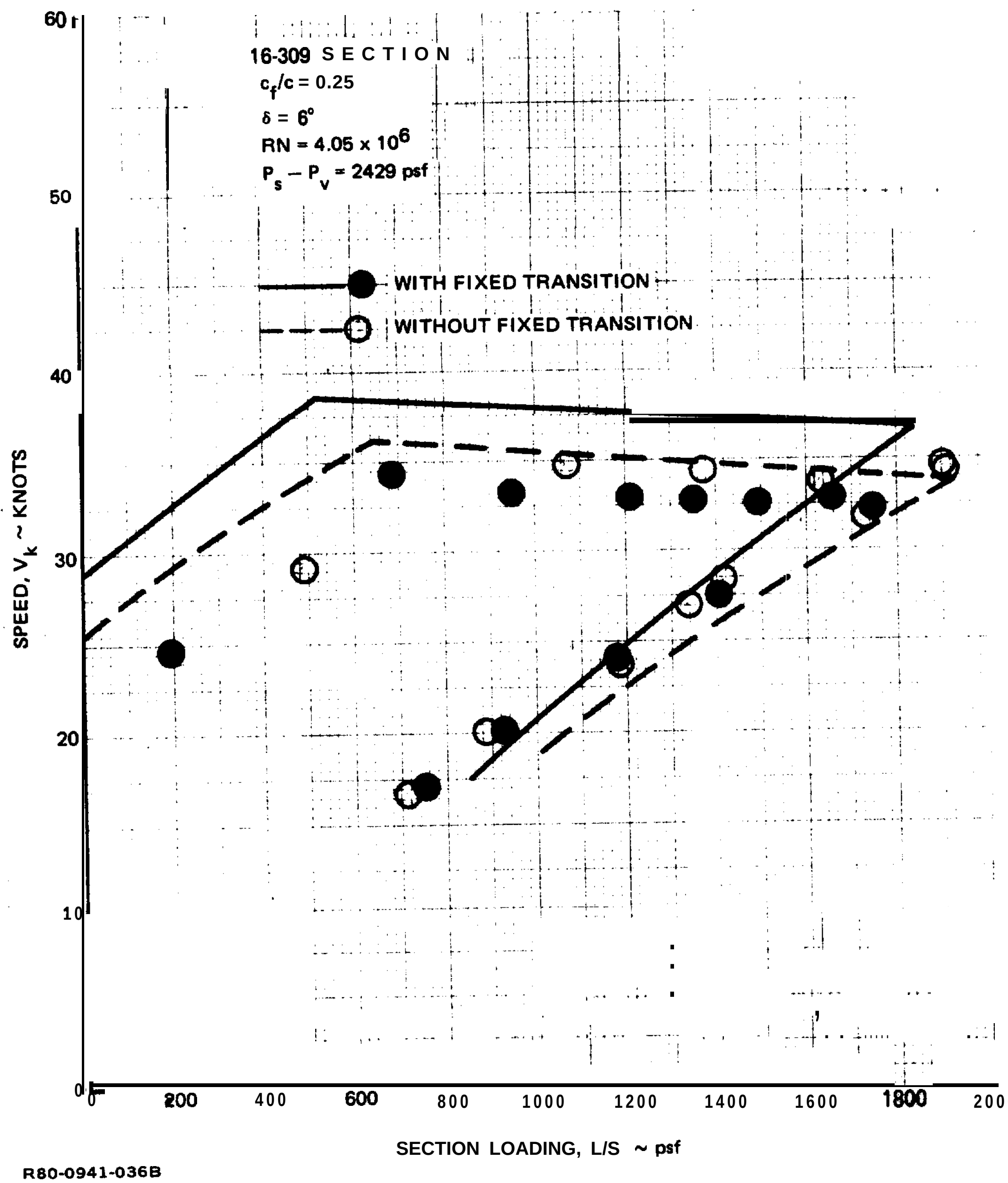

Fig. 3.3.8.4-13 Flapped Pitch Cavitation Bucket, Wind Tunnel Test
Dimensional Interpretation

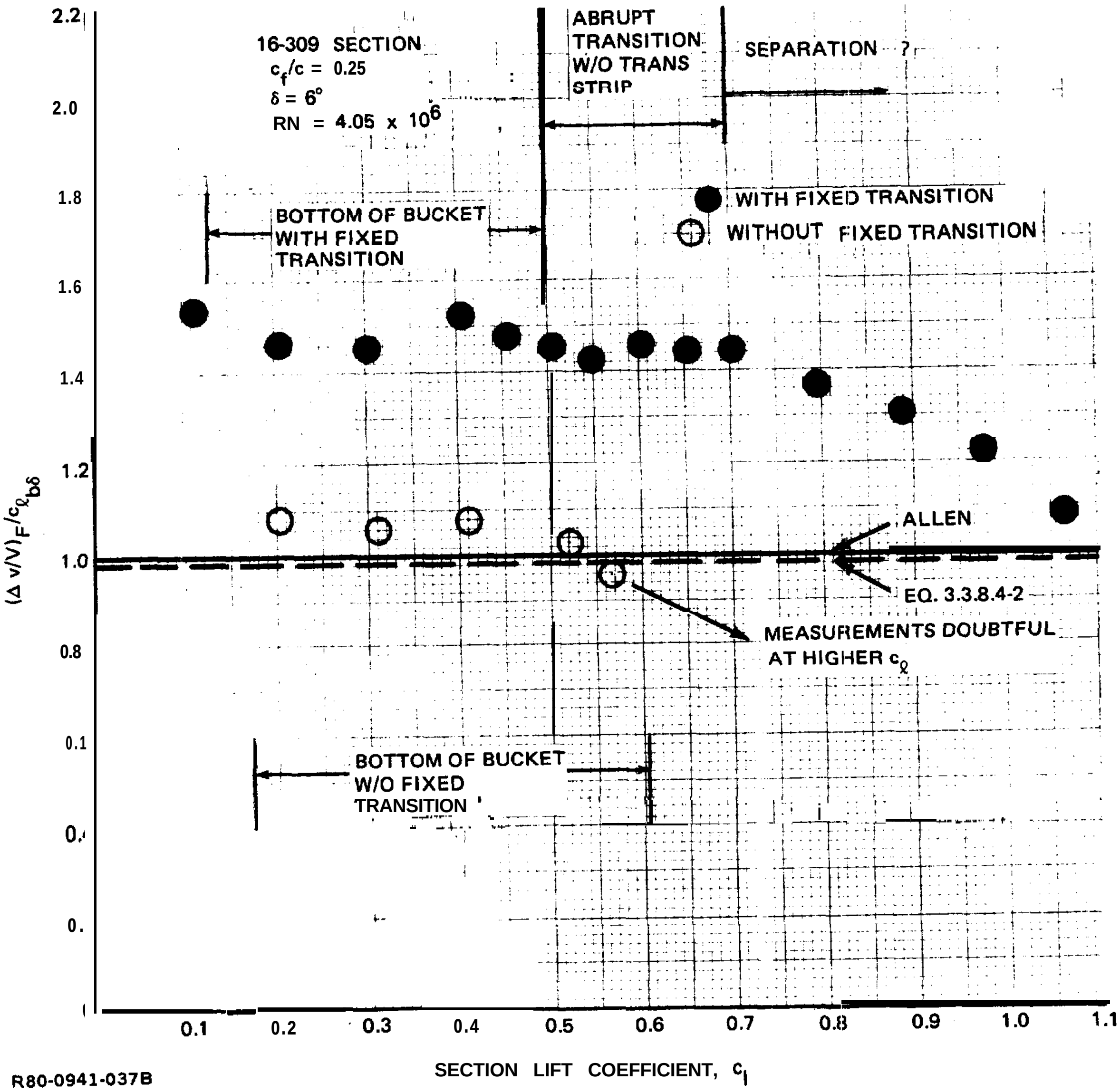

Fig. 3.3.8.4-14 Measured Hingeline Velocities

3.3.8.5 16-309 Hydrodynamic Experience.

LIFT CURVES

The data most significant to current hydrofoil state of the art is that of Reference 1 which is known here only as summarized in Reference 2. The measured lift curves shown in Reference 2 are presented here as Figure 3.3.8.5-1. The expected lift curve slope for this data is:

$$c_{\ell_\alpha} = 2\pi \frac{c_{\ell_{\alpha RN}}}{c_{\ell_\alpha}} \kappa = 2\pi \text{ X } 0.9786 \text{ X } 0.8993 \qquad 3.3.8.5\text{-}1$$

$$= 5.530 = 0.09650/\text{deg}$$

where: $c_{\ell_{\alpha RN}} / c_{\ell_\alpha}$ is from Equation 3.3.1.1-1

κ is from Table 3.3.1.2-XI

The expected zero lift angle is:

$$\alpha_{0\ell} = -\kappa_0 \frac{c_{\ell_i}}{2\pi} = -0.74 \text{ X } \frac{0.3}{2\pi} \qquad 3.3.8.5\text{-}2$$

$$= -0.03533 = -2.024°$$

where: κ_0 is from Equation 3.3.1.3-2

The expected effective design lift coefficient for leading edge transition is:

$$c_{\ell_{i_{eff}}} = -c_{\ell_\alpha} \alpha_{0\ell} = 0.0965 \text{ X } 2.024 = 0.1953 \qquad 3.3.8.5\text{-}3$$

but Table 3.3.1.2-VIII, for example, indicates that this effective design lift coefficient can approach its 0.3 potential value in model scale.

The expected flap lift curve slope is:

$$c_{\ell_\delta} = \frac{d\alpha}{d\delta} c_{\ell_\alpha} = 0.535 \text{ X } 0.0965 = 0.05163 \qquad 3.3.8.5\text{-}4$$

where: $d\alpha/d\delta$ is from Table 3.3.1.5-I

The expected values for the data of Figure 3.3.8.5-1 are therefore bounded by:

$$c_\ell = c_{\ell_{i_{eff}}} + c_{\ell_\delta} \delta + c_{\ell_\alpha} \alpha \qquad 3.3.8.5\text{-}5$$

$$= 0.1953 + 0.05163\ \delta° + 0.0965\ \alpha°$$

$$\text{to } 0.3 + 0.05163\ \delta° + 0.0965\ \alpha°$$

These boundaries are compared with the data in Figure 3.3.8.5-1. Within the limits imposed by the effective design lift coefficient uncertainty, the data really provides no measure of the lift curve slope or flap effectiveness. It is of interest to note that the 0-degree flap data has a slope 1% higher than expected and a zero lift angle 0.13 degrees lower than expected, neither discrepancy being significant.

Figure 3.3.8.5-1 examines the data in the manner of Figure 5 of Reference 2, but a more compact correlation is obtained by plotting the data in the parametric angle form of Equation 3.3.1.6-1 as done in Figure 3.3.8.5-2. Here the data is seen to be consistent with the expected values, with an allowance for an abnormal laminar flow extent, except for some apparent separation at about 0.7 c_ℓ for the large flap angle.

Figure 3.3.1.5-5 presents the aerodynamic version of Figure 3.3.8.5-2, except that the aerodynamic data was interpreted in terms of an emperical lift curve and flap effectiveness derived from a three-term linear regression analysis of the data. The aerodynamic data is repeated in Figure 3.3.8.5-3 in terms of the expected characteristics for the test Reynolds Number, with a result almost identical to the hydrodynamic case although the extent of the laminar flow appears to have been greater in the wind tunnel.

MOMENT CURVES

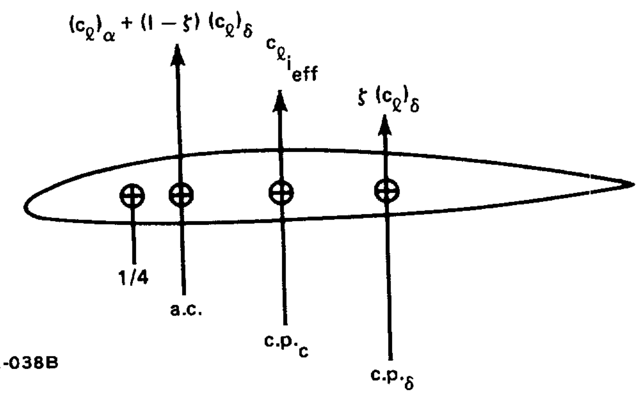

R80-0941-038B

It is not yet clear what the most convenient format for the consideration of hydrodynamic moments will be. The formats, however, can be varied more easily if the lift components are located on the chord, as shown in the sketch above. For the quarter chord reference, the usual experimental reference, the moment components can be assembled as:

$$c_{m_{c/4}} = -\left(\text{a.c.} - \frac{1}{4}\right)\left[(c_\ell)_\alpha + (1-\zeta)(c_\ell)_\delta\right] - \left(\text{c.p.}_c - \frac{1}{4}\right) c_{\ell_{i_{eff}}} - \left(\text{c.p.}_\delta - \frac{1}{4}\right)\zeta\,(c_\ell)_\delta \qquad 3.3.8.5\text{-}6$$

$$= -\left(\text{c.p.}_c - \frac{1}{4}\right) c_{\ell_{i_{eff}}} - \left(\text{a.c.} - \frac{1}{4}\right)(c_\ell)_\alpha - \left[\left(\text{a.c.} - \frac{1}{4}\right)(1-\zeta) + \left(\text{c.p.}_\delta - \frac{1}{4}\right)\zeta\right](c_\ell)_\delta$$

There are, of course, an infinite number of ways to compare this expression with measurements. The moment equivalent of Figure 3.3.8.5-1 is obtained by substituting for the pitch lift coefficient its equivalent in terms of the camber and flap lift to obtain:

$$c_{m_{c/4}} = -(\text{c.p.}_c - \text{a.c.})\, c_{\ell_{i_{eff}}} - (\text{c.p.}_\delta - \text{a.c.})\,\zeta\, c_{\ell_\alpha}\frac{d\alpha}{d\delta}\,\delta - \left(\text{a.c.} - \frac{1}{4}\right) c_\ell \qquad 3.3.8.5\text{-}7$$

The result expected from this equation for the moment data of Figure 7 of Reference 2 is:

$$c_{m_{c/4}} = -(0.485 - 0.2325) \text{ X } 0.1953 \qquad 3.3.8.5\text{-}8$$

$$-(0.625 - 0.2325) \text{ X } 0.4527 \text{ X } 0.0965 \text{ X } 0.535\ \delta^\circ - (0.2325 - 0.25)\, c_\ell$$

$$= -0.04931 - 0.009173\ \delta^\circ + 0.0175\, c_\ell$$

The potential result for that data is:

$$c_{m_{c/4}} = -(0.5 - 0.2639) \times 0.3 - (0.625 - 0.2639) \times 0.4527 \times 0.0965 \times 0.535\ \delta^\circ - (0.2639 - 0.25)\ c_\ell = -\ 0.07083 - 0.008440\ \delta^\circ - 0.0139\ c_\ell \quad 3.3.8.5\text{-}9$$

Equations 3.3.8.5-8 and 3.3.8.5-9 are compared with the data in Figure 3.3.8.5-4. The lift coefficient abscissa is preferred here, as in Section 7.2.4 of Reference 3, to the angular abscissa of Figure 7 of Reference 2. This is because the intercept here is the moment coefficient about the aerodynamic center and the slope locates the aerodynamic center.

The sensitivity of the moment to flow conditions gives it value as an indicator for those conditions but also complicates interpretation. The 0-degree flap case of Figure 3.3.8.5-4 presents excellent correlation, as does the lift correlation of Figure 3.3.8.5-2. On the other hand, the ten-degree flap lift correlation is excellent to 0.7 lift coefficient but the moment correlation indicates either an abnormal laminar flow extent or a deficient theoretical accountability for the flap moment. The ten-degree flap case does provide a characteristic moment effect for separation.

A parametric form of the moment correlation, the equivalent of Figure 3.3.8.5-2, is obtained simply by expressing the lift coefficients of Equation 3.3.8.5-6 as angles:

$$c_{m_{c/4}} = -\left(\text{c.p.}_c - \frac{1}{4}\right) c_{\ell_{i_{eff}}} - \left(\text{a.c.} - \frac{1}{4}\right) c_{\ell_\alpha}\alpha - \left[\left(\text{a.c.} - \frac{1}{4}\right)(1 - \zeta) + \left(\text{c.p.}_\delta - \frac{1}{4}\right)\zeta\right] c_{\ell_\alpha} \frac{d\alpha}{d\delta}\ \delta \quad 3.3.8.5\text{-}10$$

The expected results for the Reference 2 moments is:

$$c_{m_{c/4}} = -\left(0.495 - \frac{1}{4}\right) \times 0.1953 - \left(0.2355 - \frac{1}{4}\right) \times 0.0965\ \alpha^\circ - \left[\left(0.2325 - \frac{1}{4}\right) \times 0.5473 + \left(0.625 - \frac{1}{4}\right) \times 0.4527\right] \times 0.0965 \times 0.535\ \delta^\circ = -0.0459 - 0.00827\ (\delta^\circ - 0.2042\ \alpha^\circ) \quad 3.3.8.5\text{-}11$$

The potential result is:

$$c_{m_{c/4}} = -\left(\frac{1}{2} - \frac{1}{4}\right) \times 0.3 - \left(0.2639 - \frac{1}{4}\right) \times 0.0965\ \alpha^\circ - \left[\left(0.2639 - \frac{1}{4}\right) \times 0.5473 + \left(0.625 - \frac{1}{4}\right) \times 0.4527\right] \times 0.0965 \times 0.535\ \delta^\circ = -0.075 - 0.009157\ (\delta^\circ + 0.1464\ \alpha^\circ) \quad 3.3.8.5\text{-}12$$

The form at once loses the convenience it has for lift because the expected and potential parametric angles are not the same for moment. Equation 3.3.8.5-12, however, can be written as:

$$c_{m_{c/4}} = -0.075 - 0.01572\ \delta^\circ + 0.006565\ (\delta^\circ - 0.2042\ \alpha^\circ) \quad 3.3.8.5\text{-}13$$

for comparison with the data as shown in Figure 3.3.8.5-5. The result has no obvious advantage over Figure 3.3.8.5-4.

DRAG

Drag provides a still more sensitive measure of the section flow conditions but the model drag has such a complex pattern that extremely dense, extremely precise data is required for interpretation. The drag data of Figure 6 of Reference 2 is presented here as Figure 3.3.8.5-6. The expected drag curves of Figure 3.3.8.5-6 anticipate the conclusions of Section 3.3.9 and reflect the aerodynamic drag data of Reference 3 for the same section.

The zero flap data of Figure 3.3.8.5-6 seems to present a drag bucket although there is no evidence of an abnormal extent of laminar flow in the lift and moment curves of Figures 3.3.8.5-2 and 3.3.8.5-4 and the minimum drag coefficient is very high for a drag bucket. There is no indication in this data of a flap incremental minimum drag coefficient; on the contrary, the zero- and 10-degree flap drag curves are remarkably similar.

Figure 3.3.8.5-6 is repeated in an analytic form as Figure 3.3.8.5-7, where the slope for the data is the wake factor, K_{wake}. The slope of this data is practically identical with that of Reference 4 and is five to ten times the normal, prototype Reynolds Number, wake factor; such wake factors are considered here to be characteristic of a moving transition point. Such an interpretation would be credible for the ten-degree data of Figure 3.3.8.5-6 but carries the zero flap data to an incredible turbulent friction drag coefficient. In short, as noted by Jones, the drag data of Reference 2 must be discounted.

CAVITATION HYSTERESIS

For convenience, water tunnel cavitation tests are conducted by reducing tunnel pressure and cavitation number for a fixed geometry. Traditionally the pressure and cavitation number are then increased, without force measurements, to record the cavitation number at which the cavitation disappears — "closure". Several analytical difficulties result.

Effective cavitation is defined by the lift, drag, and moment curves. It requires several points on each of those curves for the wetted performance, and for each of the cavitated modes, for good definition. Where those curves are of cross-plot construction, the test program must be very dense in cavitation number. The Reference 2 performance characteristics are limited to wetted performance, although hinge cavitation is within the flap lift control operating envelope and leading edge cavitation is within the operating envelope for flap and incidence lift control systems.

In Reference 2 Jones presents hydrodynamic pitch cavitation buckets which are a mean of the observed incipient and closure cavitation numbers. This is the type of data required to give significance to the theoretical boundaries except that, where there is a distinction, that data must be for incipient cavitation and/or closure. If there are no force effects in the hysteresis region, closure is inconsequential. If there are force effects in the hysteresis region, incipient cavitation and the theoretical boundaries are inconsequential.

Jones presents a few individual incipient and closure cavitation numbers which indicate that the difference is small for mid-chord cavitation, where the precision requirement is greatest. All of his cavitation boundaries are therefore employed here as comparable with theory; i.e., indicative of incipient cavitation.

The mid-chord observations are shown in Figures 3.3.8.5-8 and 3.3.8.5-9, where they are compared with the theoretical boundaries of Section 3.3.8.4. The leading edge cavitation observations are shown in Figures 3.3.8.5-10 and 3.3.8.5-11, of which the 3.3.8.5-10 figure is particularly significant. Jones attributes the scatter at 2.49 X 10^6 Reynolds Number to scale effect. Note that there is a lift disturbance for this case on Figure 3.3.8.5-2. For this particular case Jones' mean was based upon the shaded points of Figure 3.3.8.5-10.

The 2.49 X 10^6 Reynolds Number observations of Figures 3.3.8.5-8 through 3.3.8.5-11 are carried throughout the following analyses, where significant, as an indication of the analytical precision.

HINGELINE BOUNDARY

Figures 3.3.8.5-12 and 3.3.8.5-13 compare two of Jones' cavitation buckets with the theoretical buckets of Section 3.3.8.4. These figures should be compared with the lift and moment characteristics of Figures 3.3.8.5-2 and 3.3.8.5-4, and with the wind tunnel buckets of Figures 3.3.8.3-5 and 3.3.8.4-12.

Figures 3.3.8.5-12 and 3.3.8.5-13 are repeated in V vs L/S form in Figures 3.3.8.5-14 and 3.3.8.5-15. The zero-degree flap case is strikingly similar to three-dimensional model experience, while the five-degree flap case lacks the leading edge theoretical conservatism in the vicinity of the bucket corner. The hingeline and leading edge boundaries will be considered separately in systemizations which allow simultaneous consideration of the seven buckets provided by Jones. Figure 3.3.8.5-14 presents the only mid-chord test provided by Jones, and indicates correlation within the limits of the experimental precision.

Figure 3.3.8.5-15 is typical of theoretical hingeline optimism throughout the data. The hydrodynamic hingeline boundaries were therefore treated by deriving the $(\Delta v/V)_F/c_{\ell_{b\delta}}$ coefficient indicated by the measured boundary if every other term of the boundary equation were correct. The result, presented in Figure 3.3.8.5-16, provides a direct comparison with the aerodynamic data by way of Figure 3.3.8.4-14 and confirms the aerodynamic data within the limits of the experimental data precision. Figures 3.3.8.4-14 and 3.3.8.5-16 thus lend added confidence to the theory of Section 3.3.8.4 while indicating, with Figures 3.3.8.5-2 and 3.3.8.5-4, that the water tunnel provided near-prototype characteristics. Of course, Figure 3.3.8.5-16 would have substantially more significance presenting incipient and closure observations, rather than smoothed means.

Figure 3.3.8.5-17 compares the measured hingeline boundaries with theory in a parametric form where the 1.5 $(\Delta v/V)_F/c_{\ell_{b\delta}}$ has been incorporated into the theory and Figure 3.3.8.5-18 makes the same comparison in the V vs L/S format.

UPPER SURFACE LEADING EDGE BOUNDARY

Equation 3.3.8.4-6 may be written:

$$\sqrt{S} = \frac{v}{V} \pm \frac{\Delta v/V}{c_{\ell_{i_{ref}}}} c_{\ell_{i_{eff}}} \pm \frac{\Delta v_a{}'}{V} c_{\ell_\alpha} \left\{ \alpha + \left[1 + \zeta \left(\frac{(\Delta v/V)_F / c_{\ell_{b\delta}}}{\Delta v_a{}'/V} - 1 \right) \right] \frac{d\alpha}{d\delta} \delta \right\} \qquad 3.3.8.5\text{-}14$$

$$= \frac{v}{V} \pm \frac{\Delta v/V}{c_{\ell_{i_{ref}}}} c_{\ell_{i_{eff}}} \pm \frac{\Delta v_a{}'}{V} c_{\ell_\alpha} \left\{ \alpha + \frac{d\alpha}{d\delta} \left[1 - \zeta + \zeta \, \frac{(\Delta v/V)_F / c_{\ell_{b\delta}}}{\Delta v_a{}'/V} \right] \delta \right\}$$

The flap basic component of this velocity, $(\Delta v/V)_F / c_{\ell_{b\delta}}$, vanishes at the leading edge so that in the vicinity of the leading edge, this equation may be approximated by:

$$\sqrt{S} = \frac{v}{V} \pm \frac{\Delta v/V}{c_{\ell_{i_{ref}}}} c_{\ell_{i_{eff}}} \pm \frac{\Delta v_a{}'}{V} c_{\ell_\alpha} \left[\alpha + \frac{d\alpha}{d\delta} (1 - \zeta)\, \delta \right]. \qquad 3.3.8.5\text{-}15$$

For the model of References 1 and 2 and Figure 3.3.8.5-2:

$$\sqrt{S} \approx \frac{v}{V} \pm 0.258\, c_{\ell_{i_{eff}}} \pm \frac{\Delta v_a{}'}{V} \times 0.0965 \, [\alpha^\circ + 0.535\, (1 - 0.4527)\, \delta^\circ] \qquad 3.3.8.5\text{-}16$$

$$\sqrt{S} \mp 0.258\, c_{\ell_{i_{eff}}} \approx \frac{v}{V} \pm 0.0965 \frac{\Delta v_a{}'}{V} (\alpha^\circ + 0.2928\, \delta^\circ)$$

The five upper surface leading edge boundaries of Figure 15 of Reference 2 are presented in terms of this parametric angle in Figure 3.3.8.5-19, where the correlation is remarkably good for the type of data presented. Figures 13 and 14 of Reference 2, for example, illustrate the judgements Jones had to make in drawing the cavitation buckets of his Figure 15. Figure 3.3.8.5-19 should, however, be revised to display the characteristics of the incipient and closure boundaries separately, as time permits.

By reference to Equation 3.3.8.5-16, the slope and intercept of the correlation line of Figure 3.3.8.5-19 identify the characteristics of the leading edge cavitation station as:

3.3.8.5-17

$$(\Delta v/V)_F / c_{\ell_{b\delta}} \approx 0$$

$$v/V = 0.569$$

$$\Delta v_a{}'/V = 2.914$$

It would be of great interest to extend the 16-Series velocity distributions of Reference 5 forward for comparison with this result. Comparison with the other sections indicates that this station must be in the vicinity of 1/2% chord. Figure 3.3.8.5-19, then, indicates that pressure spikes produce visible cavitation; their force significance remains to be examined.

The lower results of Figure 3.3.8.5-19 are of substantial interest to the understanding of previous three-dimensional experience reviewed in Section 3.8. Note that the parametric angle of Figure 3.3.8.5-19 transforms the flapped cavitation bucket in a manner which provides a common leading edge boundary for all flap angles. The boundaries for any other chord station then become a function of flap angle. For example, for the hingeline, Equation 3.3.8.5-16 becomes:

$$\begin{aligned} \sqrt{S} - 0.258\, c_{\ell_{i_{eff}}} &= 1.087 + 0.0965 \text{ X } 0.065 \left\{ \alpha^\circ + 0.535 \left[0.5473 + 0.4527 \text{ X } \frac{1.5}{0.065} \right] \delta^\circ \right\} \\ &= 1.087 + 0.006273\,(\alpha^\circ + 5.8819\,\delta^\circ) \qquad 3.3.8.5\text{-}18 \\ &= 1.087 + 0.03506\,\delta^\circ + 0.006273\,(\alpha^\circ + 0.2928\,\delta^\circ) \end{aligned}$$

Several stations of interest have been added to Figure 3.3.8.5-19 in this manner. The expected bucket for the ten-degree flap angle consists of the 75% station and leading edge boundaries. The expected bucket for the zero flap consists of the 60% and 1.25% stations and the leading edge; a short 2.5% station segment has been omitted for clarity.

For the zero flap case, cavitation-free operation was observed well outside the bucket — to about the 20% station boundary. This is the case shown in Figure 3.3.8.5-14, which closely resembles three-dimensional effective boundary experience where it was presumed to be an incipient-effective distinction or a three-dimensional effect. A substantial region of pressures less than vapor pressure, certainly not a spike, is indicated, with no visible cavitation and no explanation can be offered here. The effect is evident to a lesser extent on Figures 3.3.8.5-15 and 3.3.8.5-19 for 2.5-degree flap, but the flap hinge boundary limits the extent to which the flapped cases can penetrate the leading edge boundaries; cavitation at any point on the section effectively changes the section geometry and invalidates the theoretical boundaries.

Precisely what path the observed incipient boundary takes outside the theoretical bucket is not clear. For the zero- 7-1/2-degree, and 10-degree flap cases, this "effective incipient" cavitation bucket seems to consist only of the hinge and the unidentified leading edge boundaries; intermediate stations seem to play a part for the 2-1/2-degree and 5-degree observations. The question deserves a more detailed examination of the data.

Figure 3.3.8.5-20 and 3.3.8.5-21 compare the aerodynamic upper surface leading edge "cavitation" boundaries of Figures 3.3.8.5-5 and 3.3.8.4-12 with the hydrodynamic boundary of Figure 3.3.8.5-19. The figures add little to the definition, largely because of the shifting boundary layer conditions in the aerodynamic data. The aerodynamic pressure measurements were at 0, 1/3, 1, and 2 percent at the leading edge, and the shifts from mid-chord to 1% and from 1% to 1/3% occurred as indicated by the theoretical boundaries. Peak $-C_p$ occurred at the zero station only, for lift coefficients well into separation, which are not shown. Note the hydrodynamic penetration of the aerodynamic boundary on Figure 3.3.8.5-20, obscured by the hinge boundary and effective lift coefficient uncertainty in Figure 3.3.8.5-21.

LOWER SURFACE LEADING EDGE BOUNDARY

For the lower surface, Equation 3.3.8.5-16 can be written:

$$\sqrt{S} + 0.258\, c_{\ell_{i_{eff}}} \approx \frac{v}{V} + 0.0965 \frac{\Delta v_a{}'}{V} \left[-(\alpha^\circ + 0.2928\, \delta^\circ) \right] \qquad 3.3.8.5\text{-}19$$

If, then, the characteristics of Equation 3.3.8.5-17 are the characteristics for a real chord station and not just emperical coefficients describing a pressure spike movement in the vicinity of the leading edge, the observed lower surface leading edge boundary should plot on top of the upper surface boundary of Figure 3.3.8.5-19 and aid the definition of that boundary.

In fact, the lower surface boundaries of Reference 2 are in substantial contradiction to the upper surface characteristics of Figure 3.3.8.5-19, as shown in Figure 3.3.8.5-22. The aerodynamic data for the lower surface leading edge boundary introduces further analytic difficulty, shown in Figure 3.3.8.5-23, which requires the tabulated data volume of Reference 3 for study.

The lower surface leading edge cavitation boundary cannot, then, be defined in general at this time. This boundary is not significant to the flap lift control system and is significant to the incidence lift control system only for extreme designs currently in the conceptual stage. Nevertheless, the inability to reconcile theory and experiment on the lower surface leading edge boundary reflects upon the confidence with which the upper surface leading edge boundary is predicted.

SUMMARY

References 2 and 3 provide a remarkably definitive view of the theory/model/prototype relationship for the flapped 16-Series section. With fixed transition, Reference 3 provides what are expected to be nominal lift, drag, and pitching moment for the prototype. Without fixed transition, Reference 3 provides scale effect symptoms for all three characteristics.

Reference 1, as summarized by Jones in Reference 2, produced nominal lift and pitching moment at high lift coefficients but with questionable drag. The drag appears to be subject to some difficulty other than the classic drag bucket associated with low Reynolds Numbers. The lift and moment shift toward the potential characteristics at the lower lift coefficients, although not to the extent displayed by the wind tunnel data.

All of the cavitation conclusions drawn from Reference 2 are somewhat tentative for the following reasons:

- As the first definitive study of cavitation boundaries, References 2 and 3 present a relatively unfamiliar data analysis problem

- Abnormal laminar boundary layer extent, for the prototype, produced rather uncertain characteristics for the hydrodynamic model at the lower lift coefficients
- The analysis employed the hydrodynamic cavitation buckets provided by Jones in Reference 2 and these are judgemental means between the incipient cavitation and closure boundaries.

Reference 3 provides a rather conclusive demonstration that the hingeline pressure coefficient is sensitive to Reynolds Number, in contradiction of Allen, and that Allen's values are typical of the model rather than the prototype (Section 3.3.8.4). The hydrodynamic hingeline cavitation boundary agrees with the aerodynamic fixed transition boundary, the prototype case, within the limits of the data precision.

The hydrodynamic model provides reasonably good definition for the thickness and additional velocity ratios for some station in the vicinity of the leading edge. This characterizes the upper surface leading edge boundary. That station could not be identified because the velocity ratios of Reference 5 do not proceed forward of the 1-1/4% station for the 16-Series section. Without that identification, this result cannot safely be generalized over sections even within the 16-Series family but should be considered an emperical characteristic of the flapped 16-309 section.

The aerodynamic peak pressure coefficient agrees with the upper surface leading edge cavitation boundary within the limits of data precision, clearly indicating a hydrodynamic significance for the aerodynamic pressure spikes.

The zero-degree flap hydrodynamic data indicates equally clearly, for the mean incipient/closure boundary, that the stations between the leading edge and, say, 10% are not significant to the cavitation boundary; i.e. the hydrodynamic upper surface bucket corner was at the intersection of the leading edge and 60% stations. Thus, the cavitation bucket penetrated the theoretical bucket deeply in the vicinity of the upper surface corner, just as has been noted previously for the effective bucket for three-dimensional foils. The significance of Pope's function to this observation was not adequately explored in this analysis.

Aerodynamic and hydrodynamic measurement and theory were all found in substantial contradiction for the lower surface cavitation boundary and could not be reconciled in the time available. Reynolds Number effects are most troublesome in this region of the bucket, and it is assumed for the present that the leading edge station characteristics provided by the model for the upper surface will apply also to the lower surface for the prototype.

This analysis should be revised to distinguish incipient and closure boundaries as time permits. The more important question of the significance of the hysteresis region to the foil forces does not appear to be addressed by the test program of Reference 1.

The effect of References 2 and 3, considered together, upon the cavitation boundaries of Section 3.3.8.4, is illustrated in three formats on Figures 3.3.8.5-24, 3.3.8.5-25, and 3.3.8.5-26. Figure 3.3.8.5-26 is particularly significant to PCH-1 forward foil observations.

REFERENCES

1. Jones, E. A. and MacKay, M.: Water Tunnel Tests on a NACA 16-309 Section Equipped with a Simple, Sealed Flap. Defence Research Establishment Technical Memorandum in preparation.

2. Jones, E. A.: Model Scale Effects on a 16-Series Flapped Hydrofoil Section. Defence Research Establishment informal communication.

3. Teeling, P.: Low Speed Wind Tunnel Tests of a NACA 16-309 Airfoil with Trailing Edge Flap. DeHavilland Aircraft of Canada Report No. ECS 76-3, October 1976.

4. Lindsey, W. F.; Stevenson, D. B.; and Daley, Bernard N.: Aerodynamic Characteristics of 24 NACA 16-Series Airfoils at Mach Numbers Between 0.3 and 0.8. NACA TN 1546, September 1948.

5. Abbott, Ira H. and Von Doenhoff, Albert E.: Theory of Wing Sections, Dover Publications, 1959.

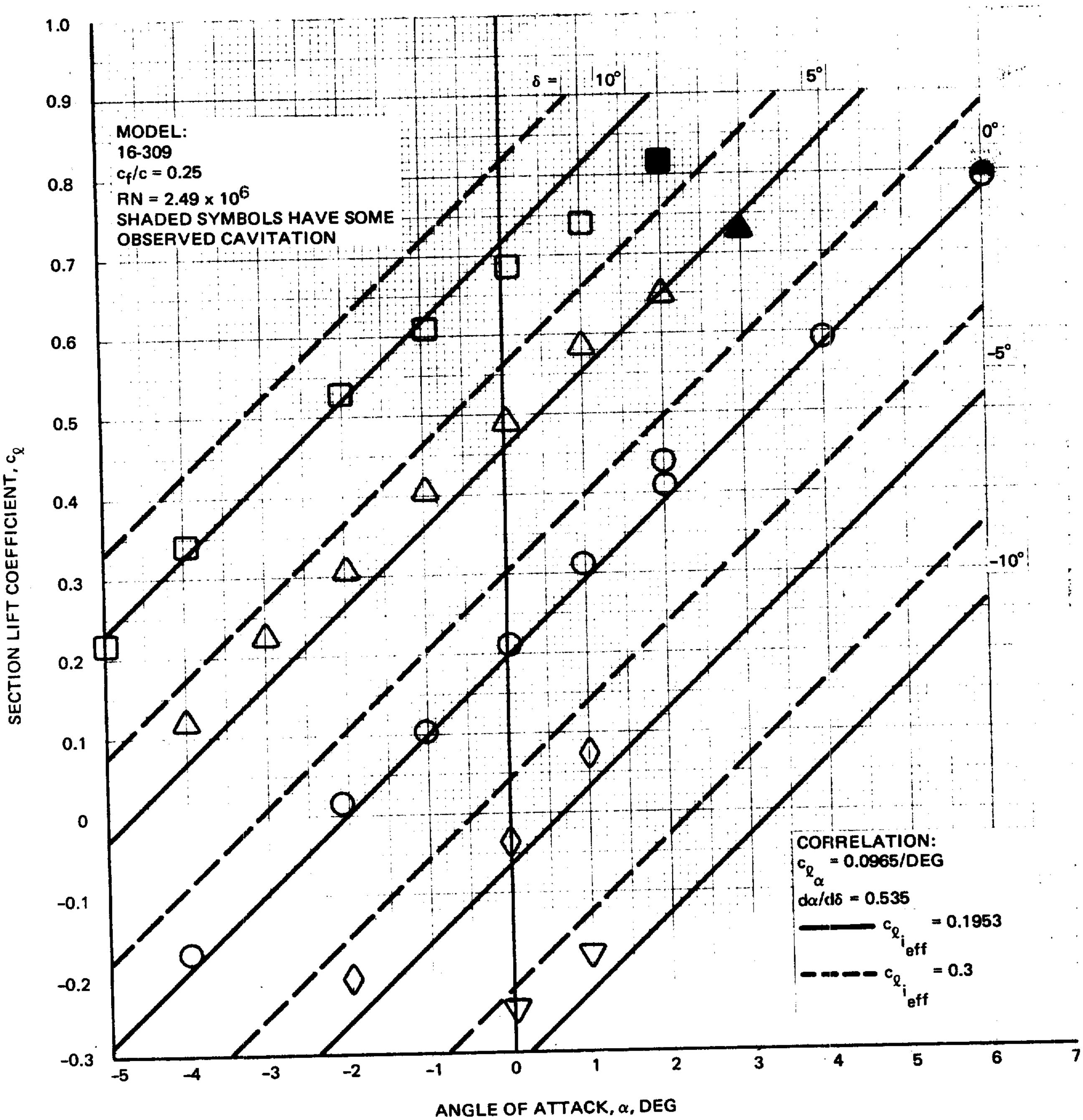

R80-0941-039B

Fig. 3.3.8.5-1 Hydrodynamic Lift Curves

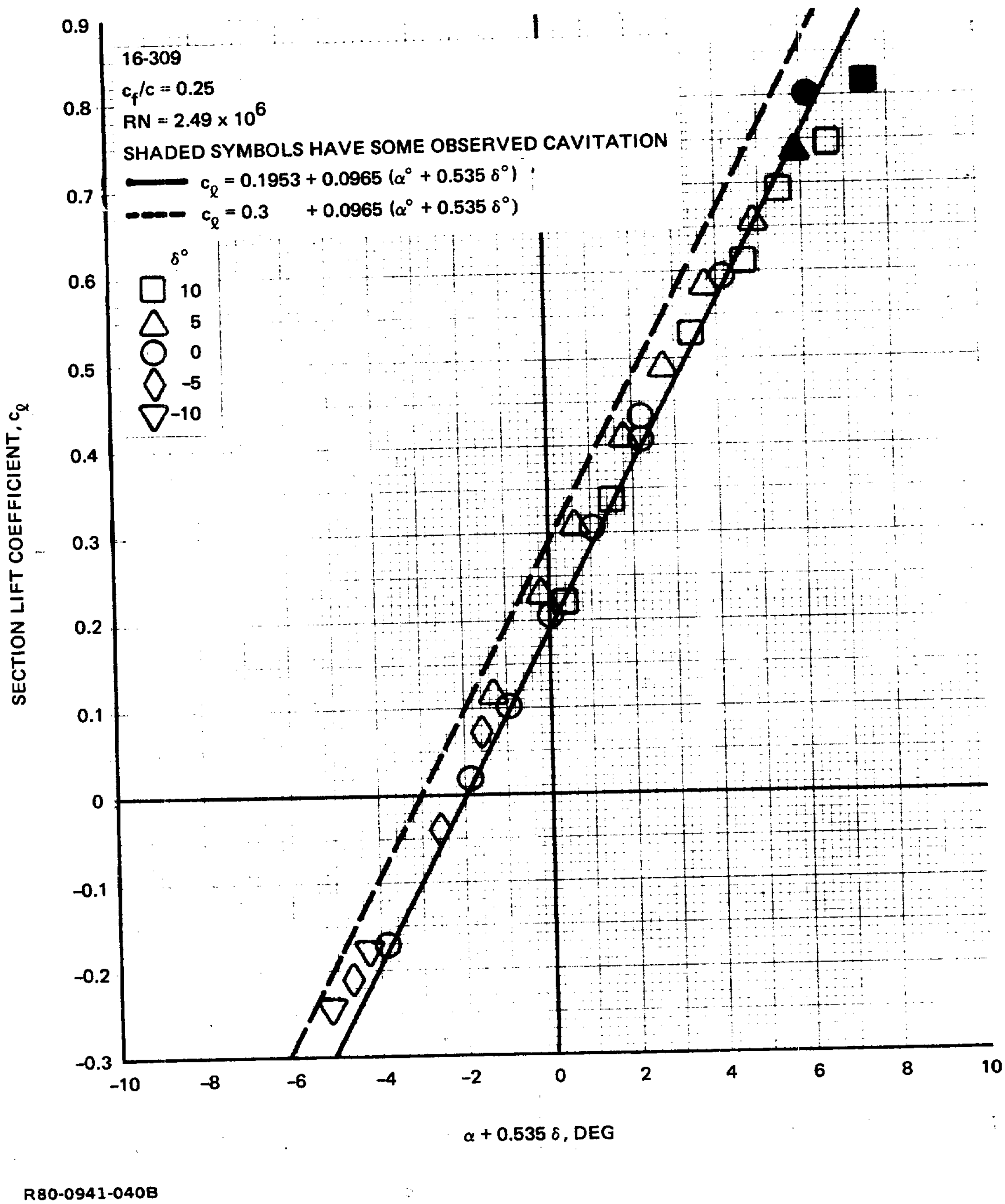

Fig. 3.8.5-2 Lift Data Correlation

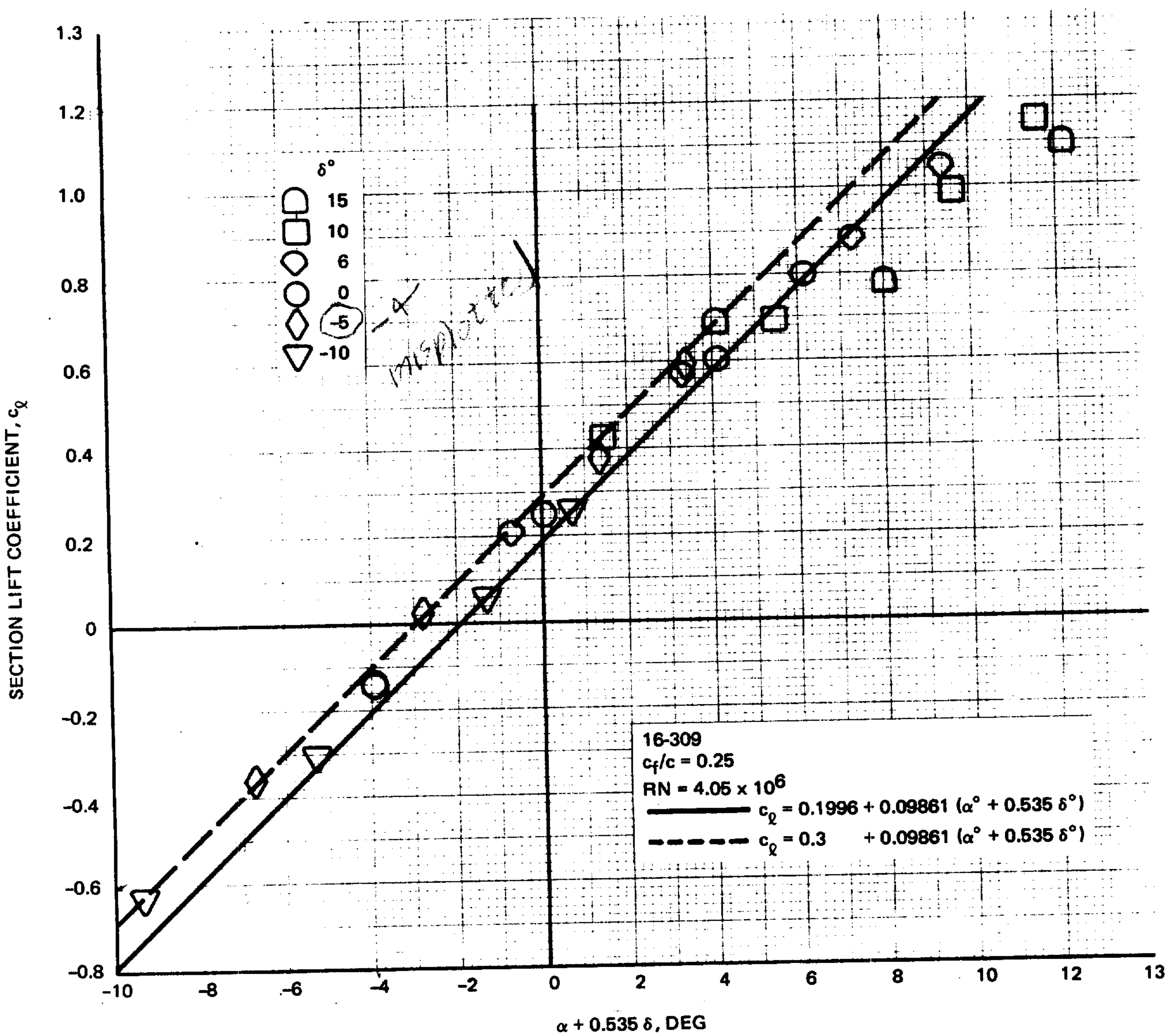

R80-0941-041B

Fig. 3.3.8.5-3 Aerodynamic Lift Data Correlation

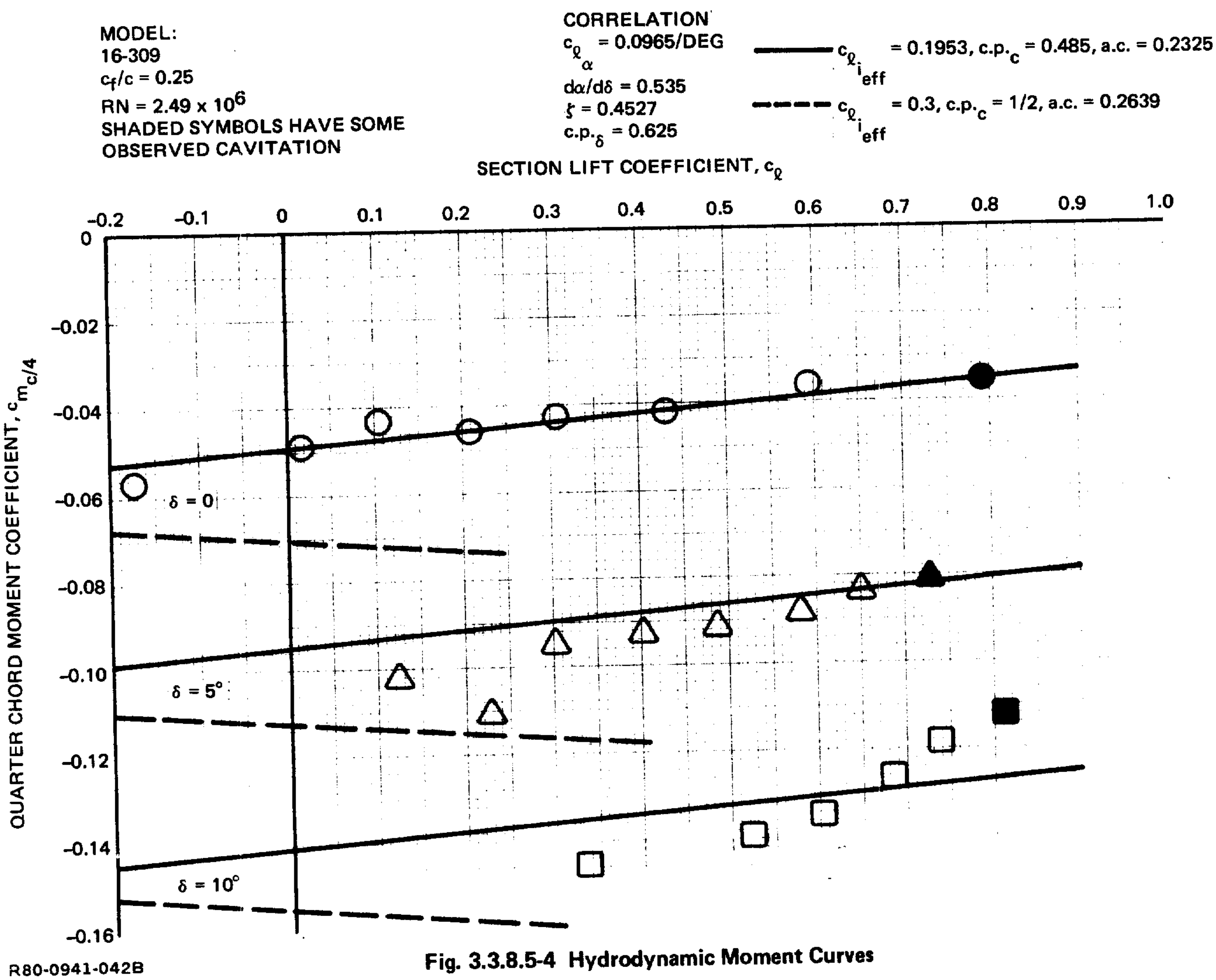

Fig. 3.3.8.5-4 Hydrodynamic Moment Curves

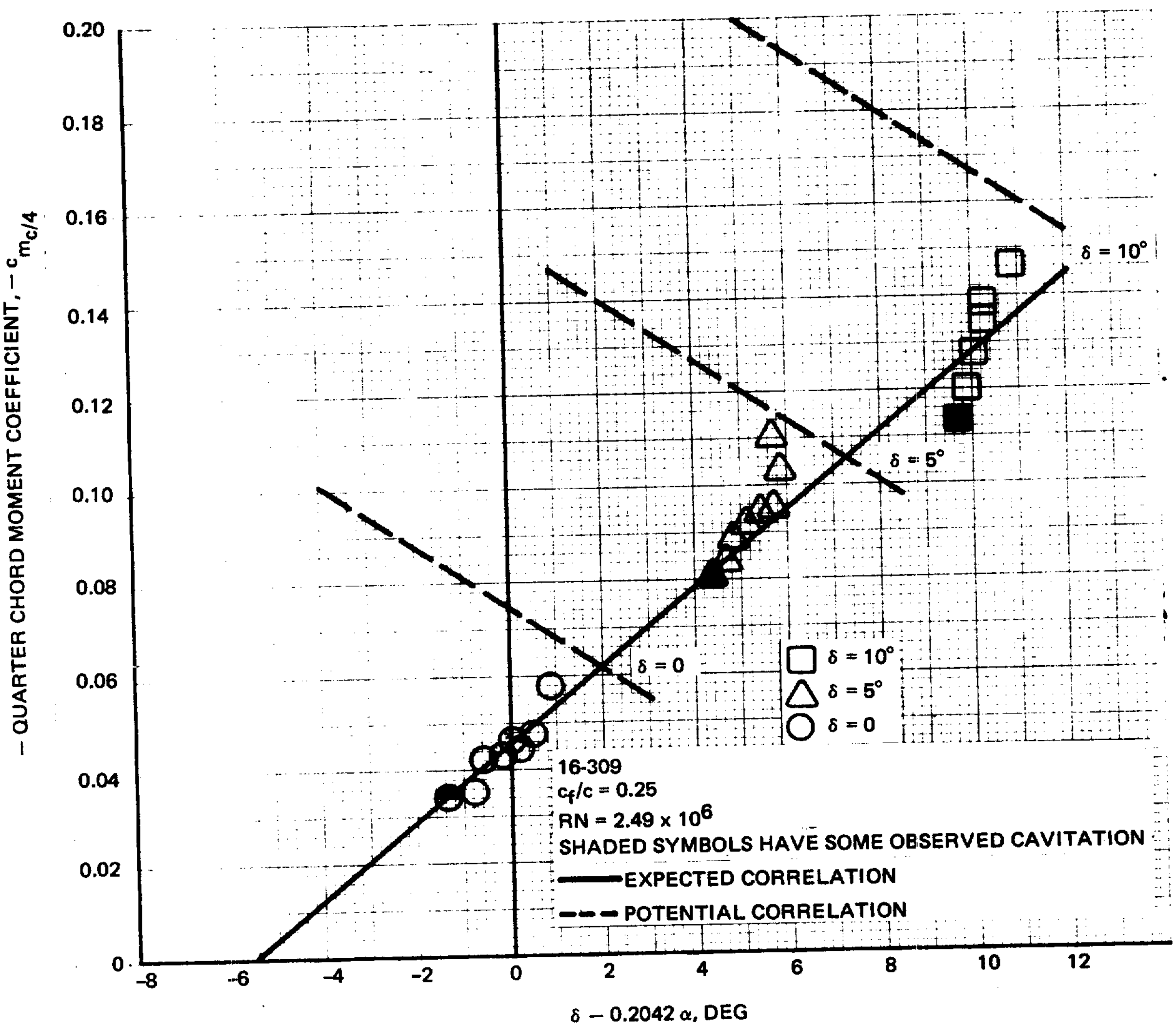

R80-0941-043B

Fig. 3.3.8.5-5 Hydrodynamic Moment Correlation

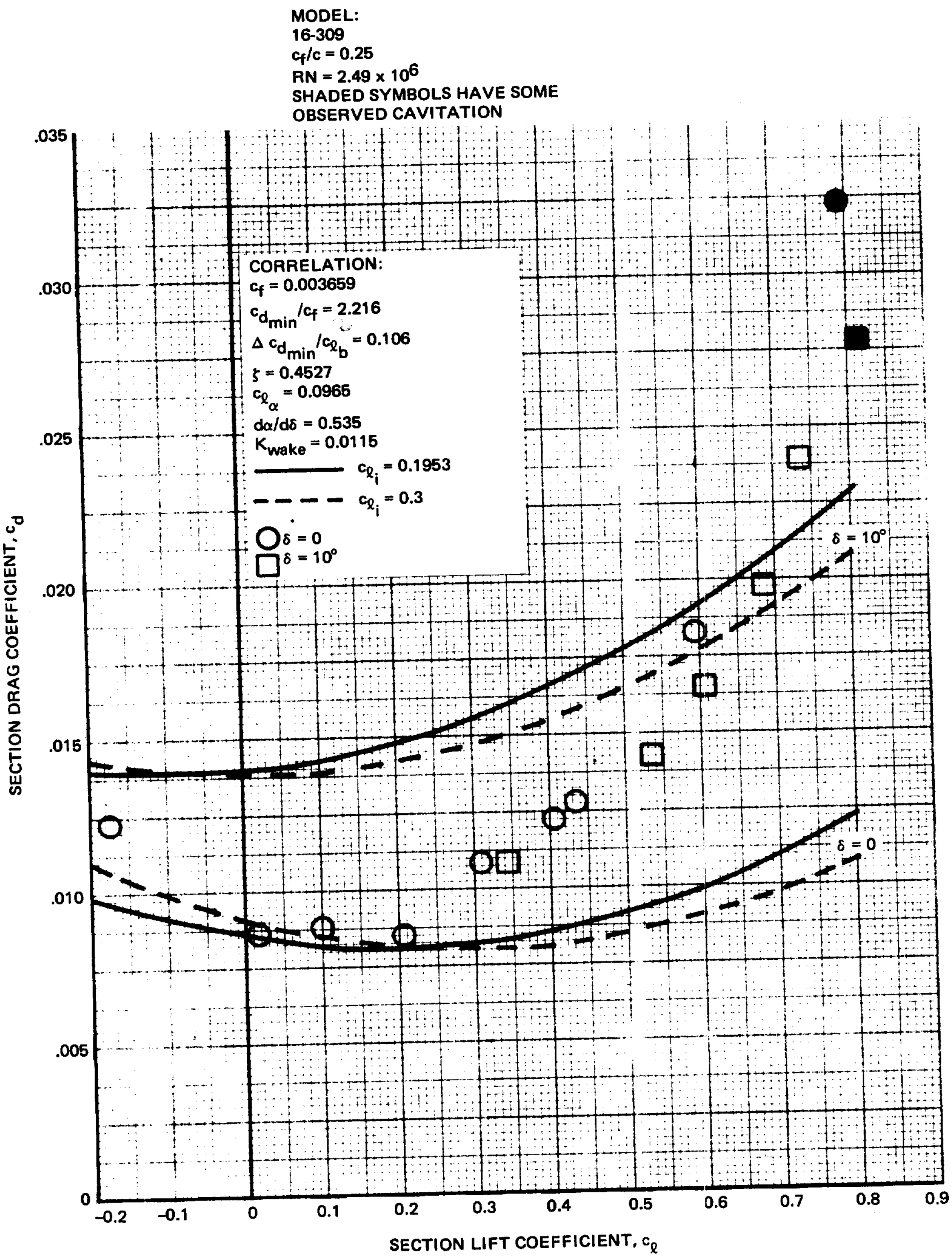

R80-0941-044B

Fig. 3.3.8.5-6 Hydrodynamic Drag Curves

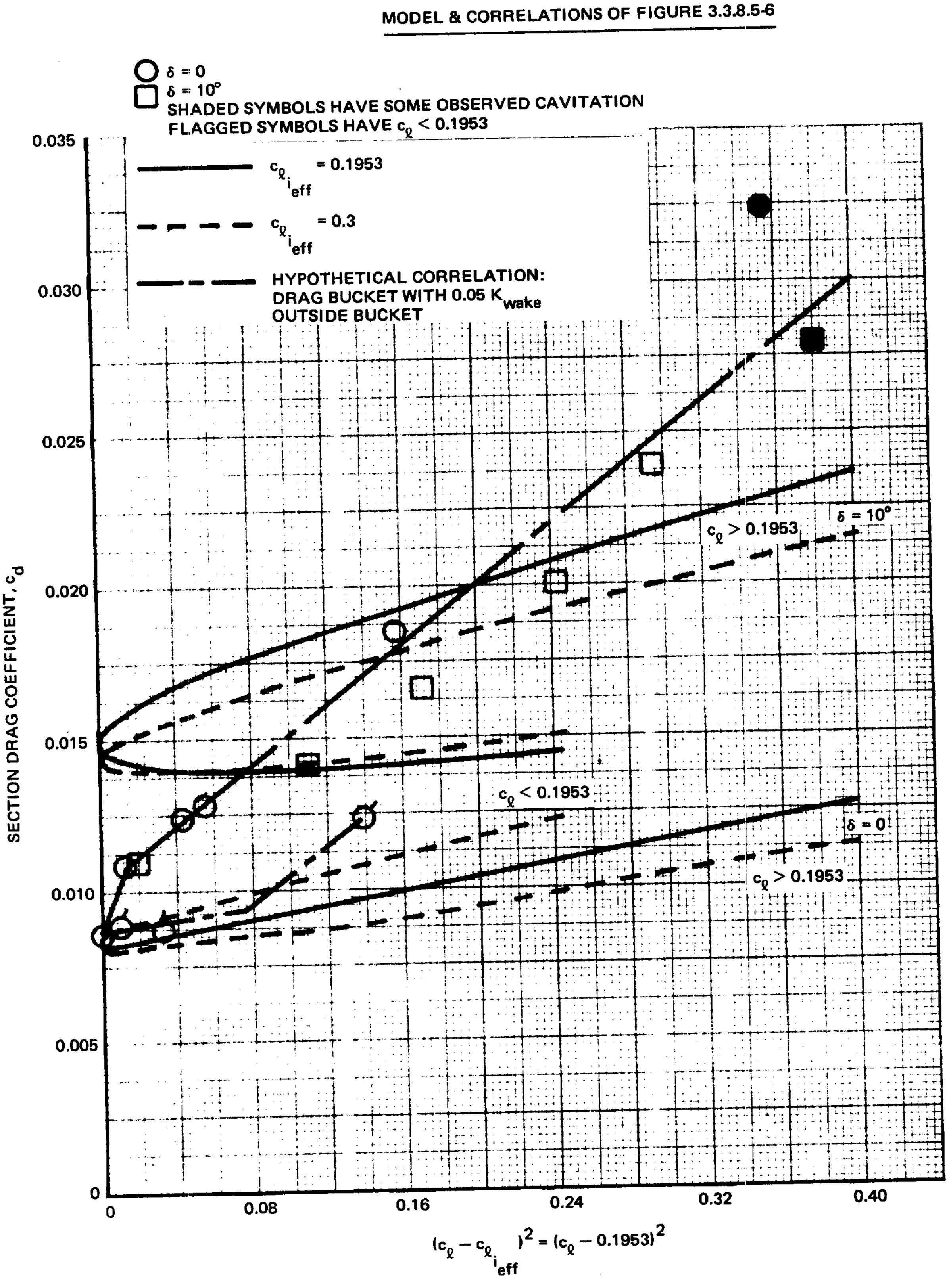

Fig. 3.3.8.5-7 Drag Data Correlation

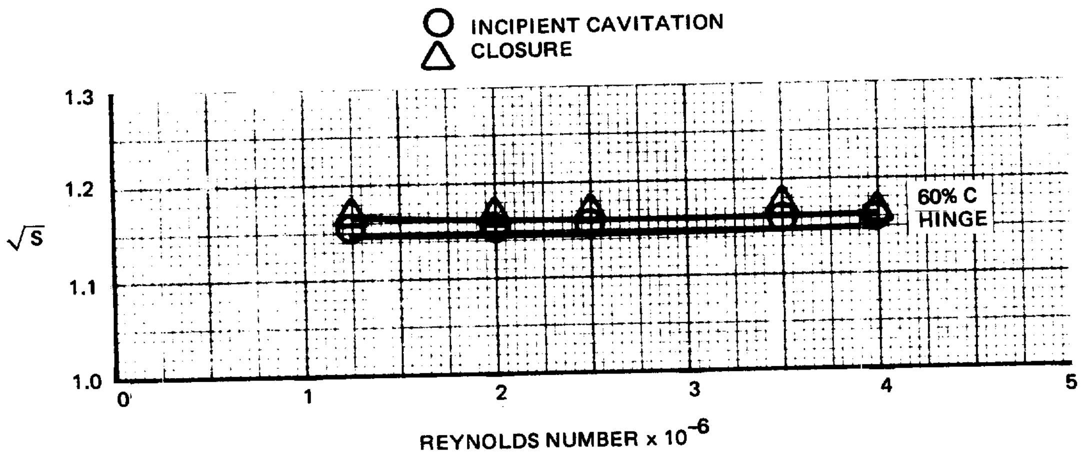

Fig. 3.3.8.5-8 Cavitation Hysteresis, Hinge and Mid-Chord, $\alpha = \delta = 0$

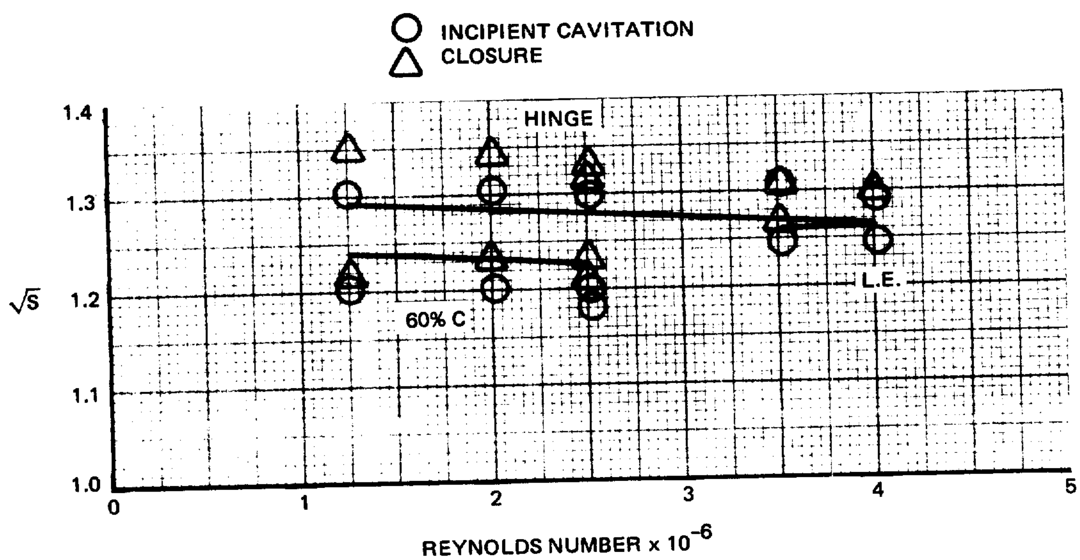

R80-0941-046B

Fig. 3.3.8.5-9 Cavitation Hysteresis, $\alpha = 0$, $\delta = 5°$

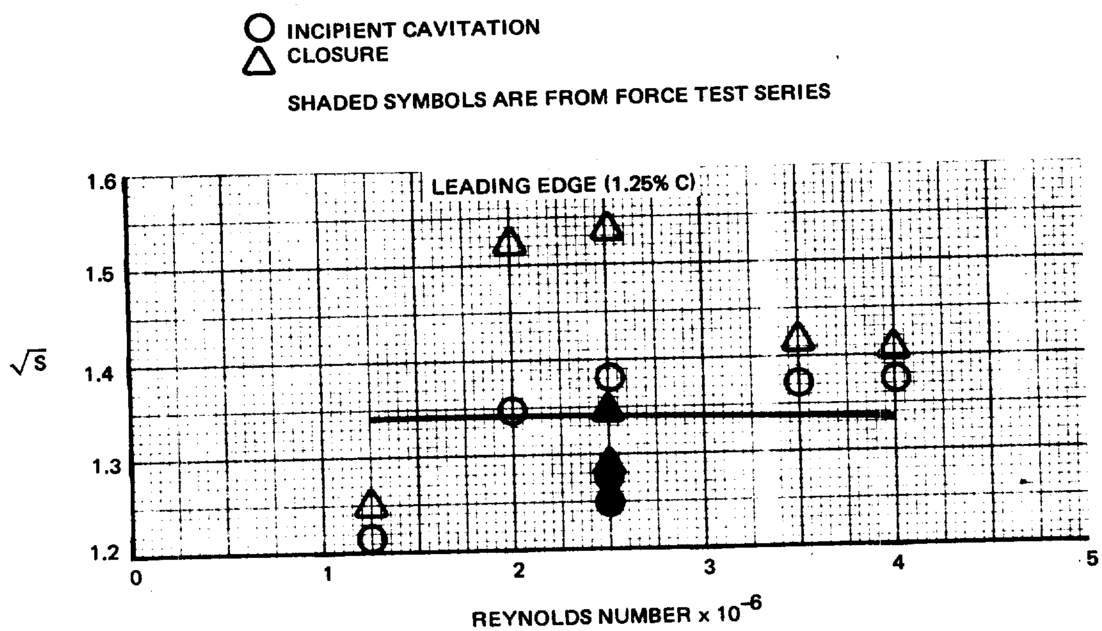

Fig. 3.3.8.5-10 Cavitation Hysteresis, $\alpha = 2^{\circ}, \delta = 0$

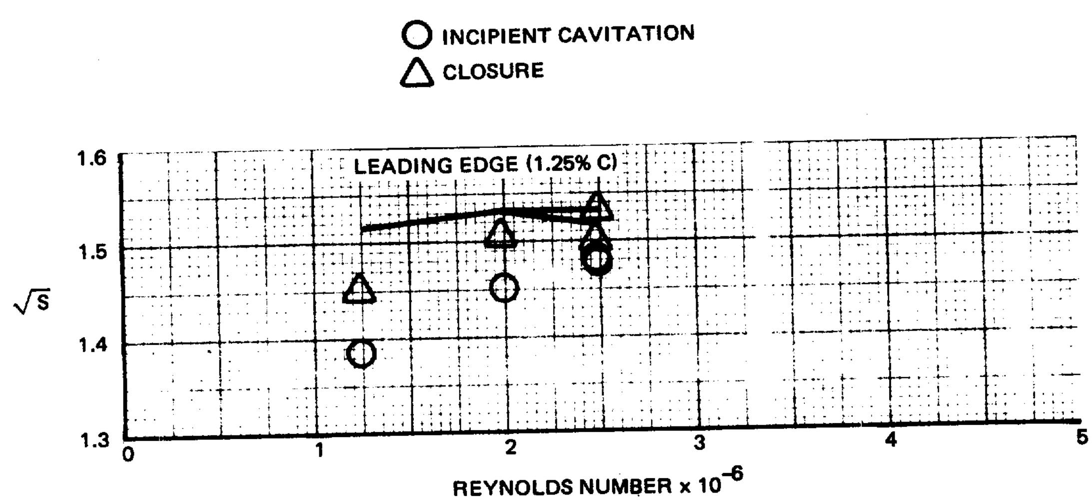

Fig. 3.3.8.5-11 Cavitation Hysteresis, $\alpha = 2^{\circ}, \delta = 5^{\circ}$

R80-0941-047B

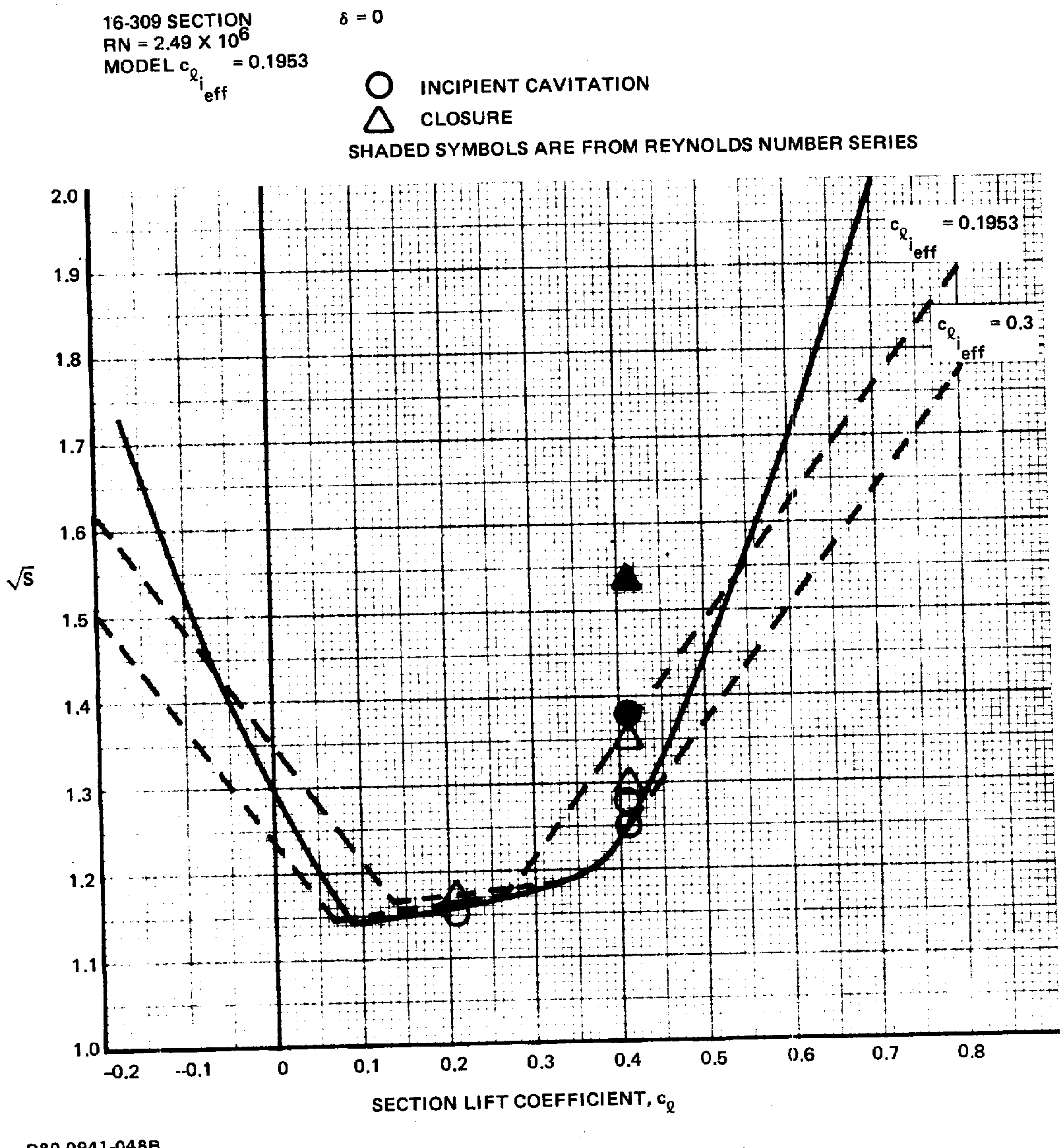

Fig. 3.3.8.5-12 Hydrodynamic Cavitation Bucket

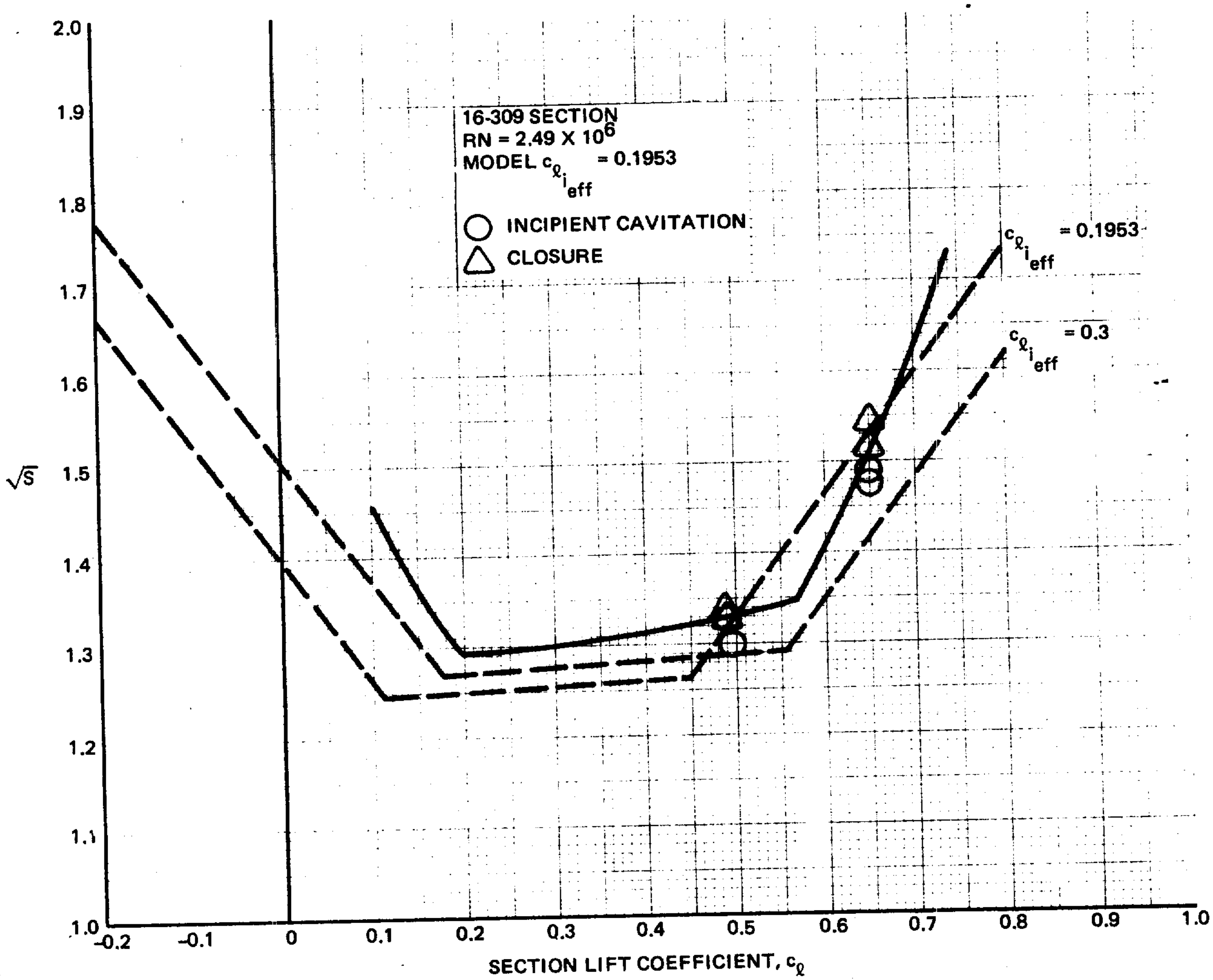

R80-0941-049B

Fig. 3.3.8.5-13 Hydrodynamic Cavitation Bucket, $\delta = 5°$

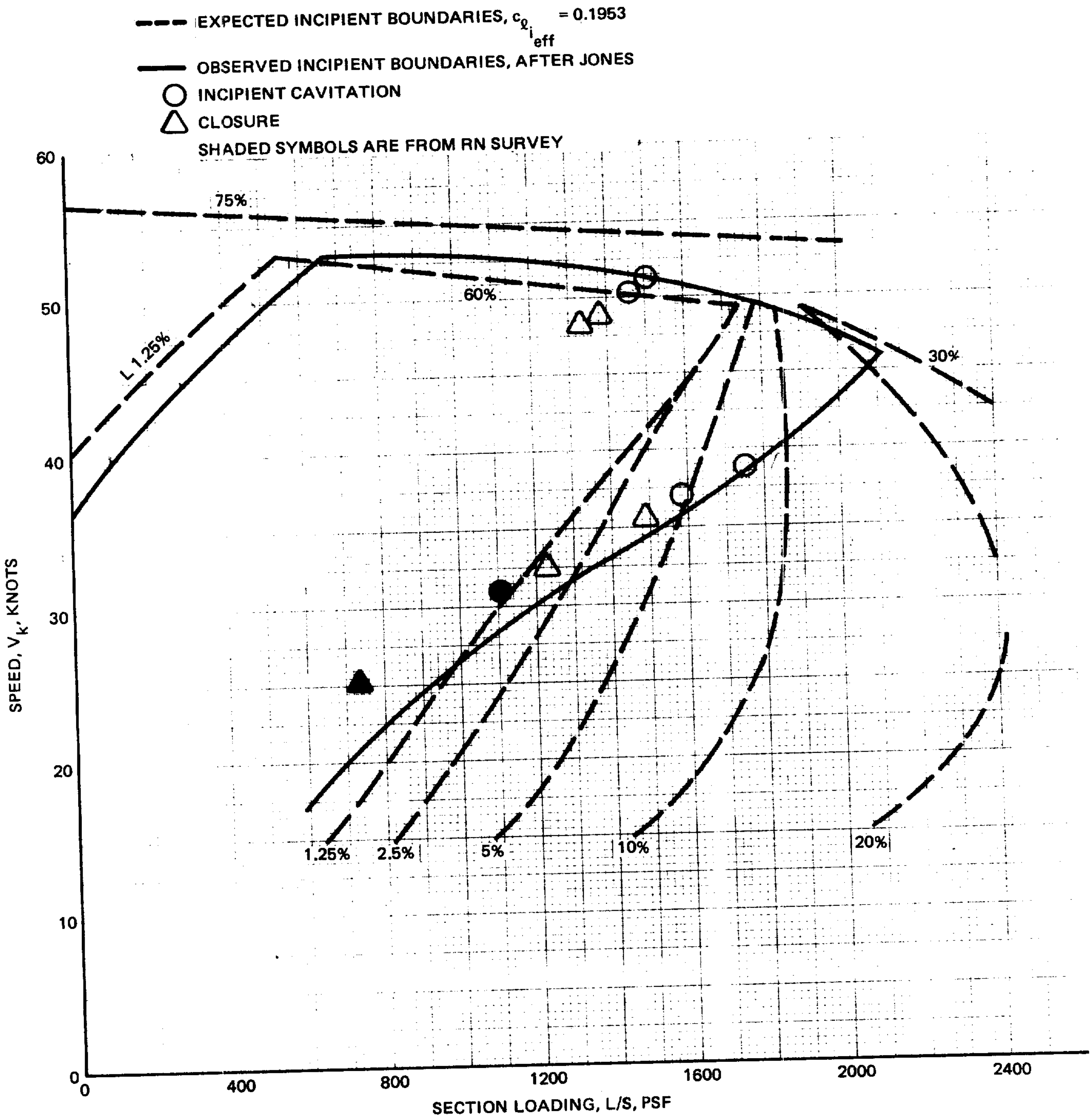

R80-0941-050B

Fig. 3.3.8.5-14 Hydrodynamic V_k – L/S Cavitation Bucket, $\delta = 0$

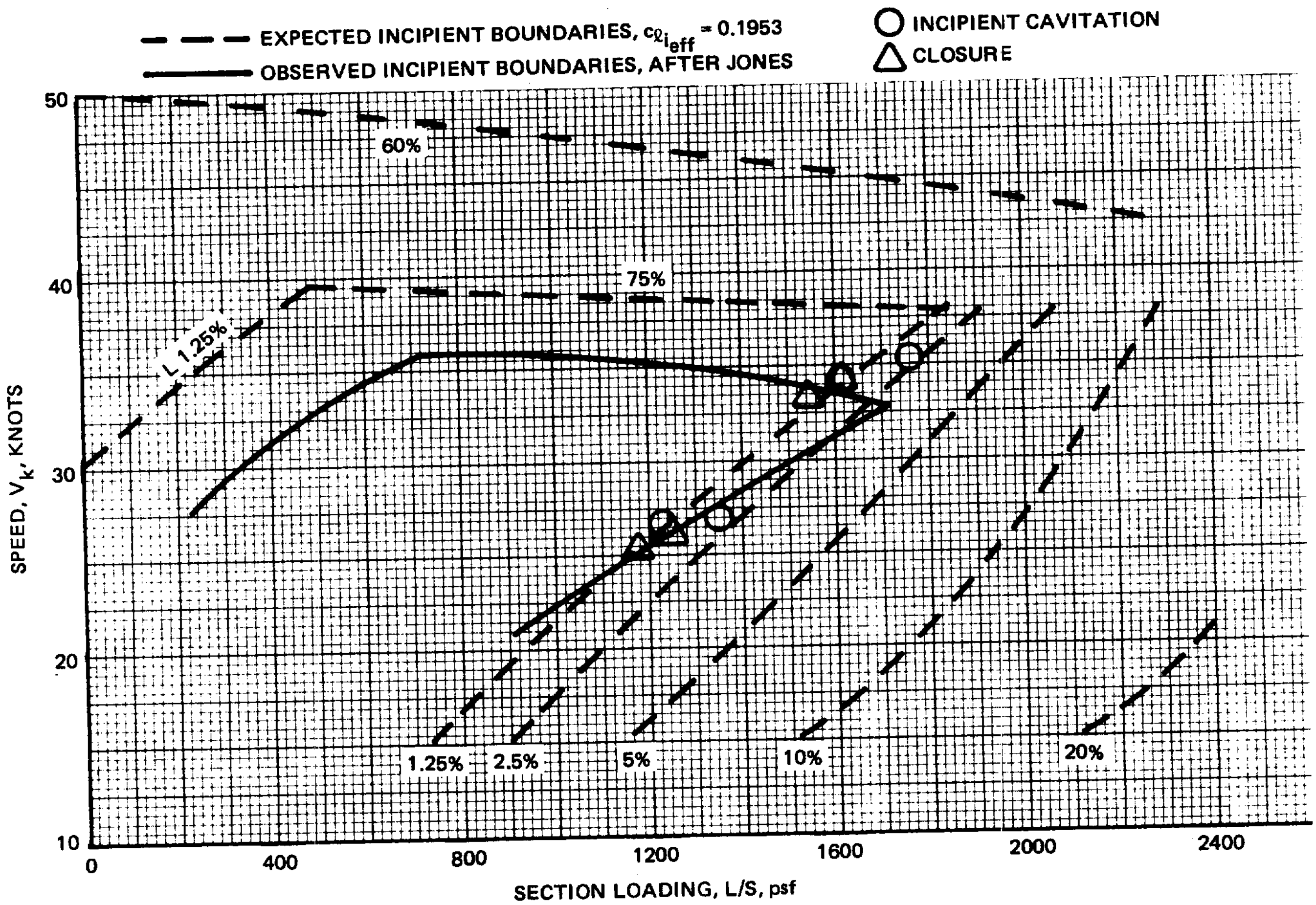

Fig. 3.3.8.5-15 Hydrodynamic V_k – L/S Bucket, $\delta = 5°$

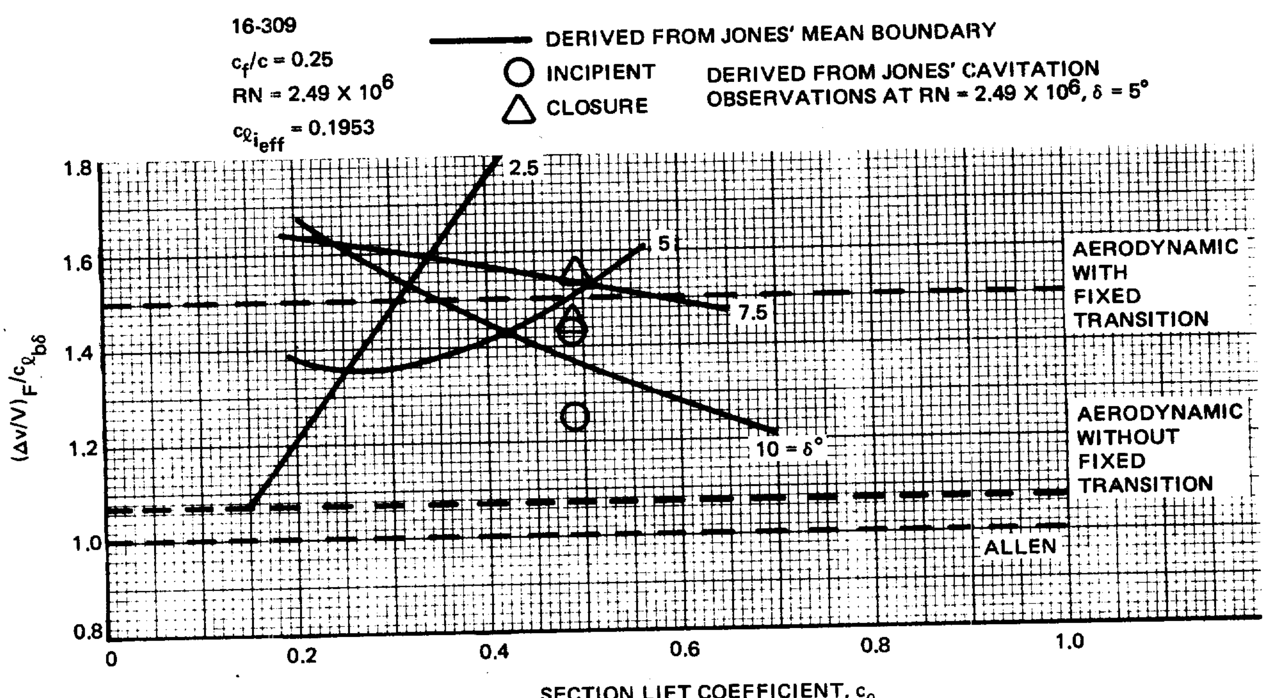

R80-0941-051B

Fig. 3.3.8.5-16 Hydrodynamic Hingeline Velocity Measurements

CORRELATION:

$\zeta = 0.4527$
$c_{\ell_\alpha} = 0.0965$
$d\alpha/d\delta = 0.535$
$v/V = 1.087$
$(\Delta v/V)/c_{\ell_{ref}} = 0.258$
$(\Delta v/V)_F/c_{\ell_{b_\delta}} = 1.5$
$c_{\ell_{i_{eff}}} = 0.1953$ OR $c_{\ell_{i_{eff}}} = 0.3$
$\Delta v_a'/V = 0.065$ $\quad \Delta v_a'/V = 0.090$
(POTENTIAL CASE)

MODEL:

16-309
$c_f/c = 0.25$
$RN = 2.49 \times 10^6$
JONES' OBSERVED BOUNDARY
JONES' OBSERVED CAVITATION
JONES' OBSERVED CLOSURE

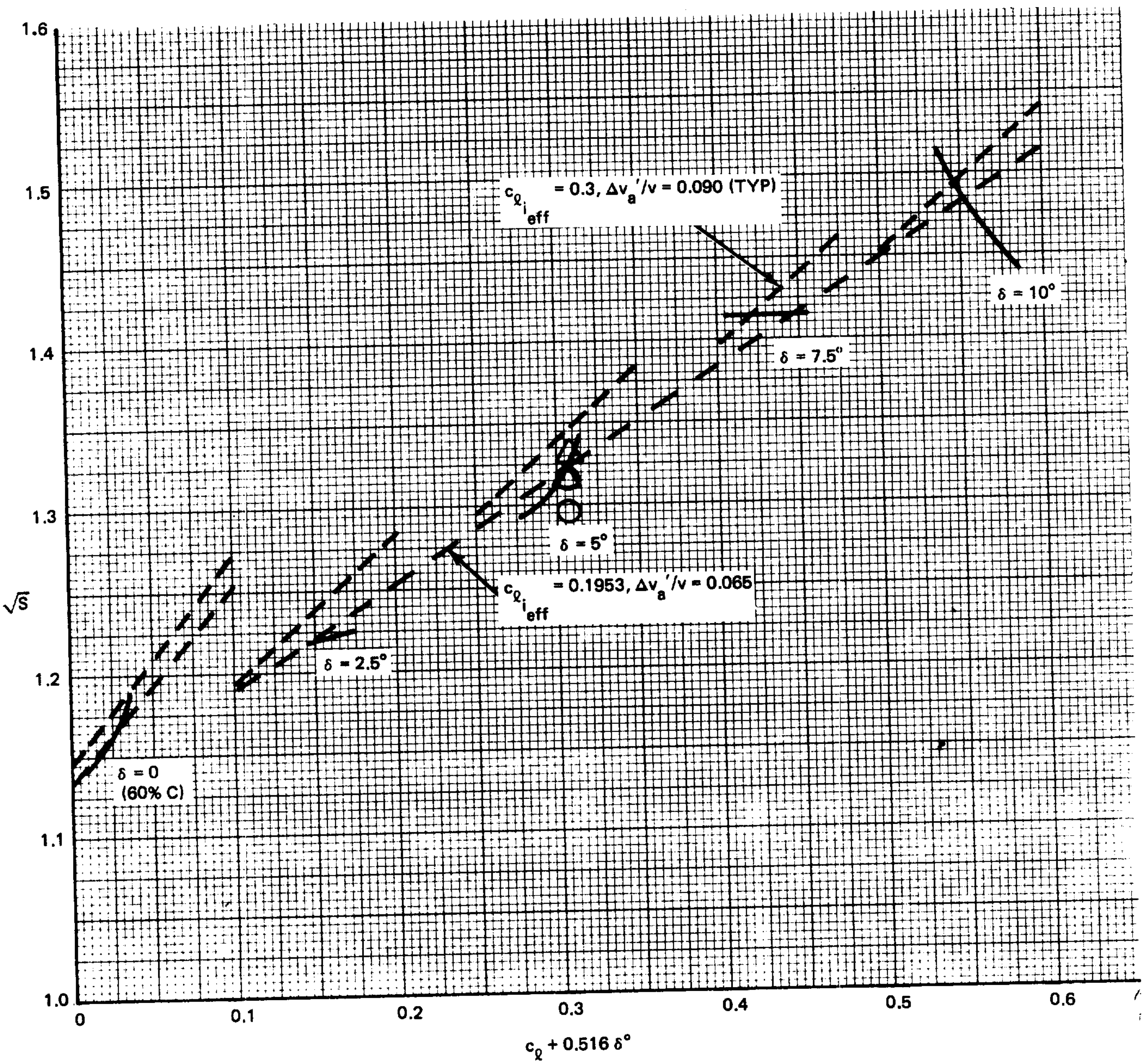

R80-0941-052B

Fig. 3.3.8.5-17 Hingeline Cavitation Correlation

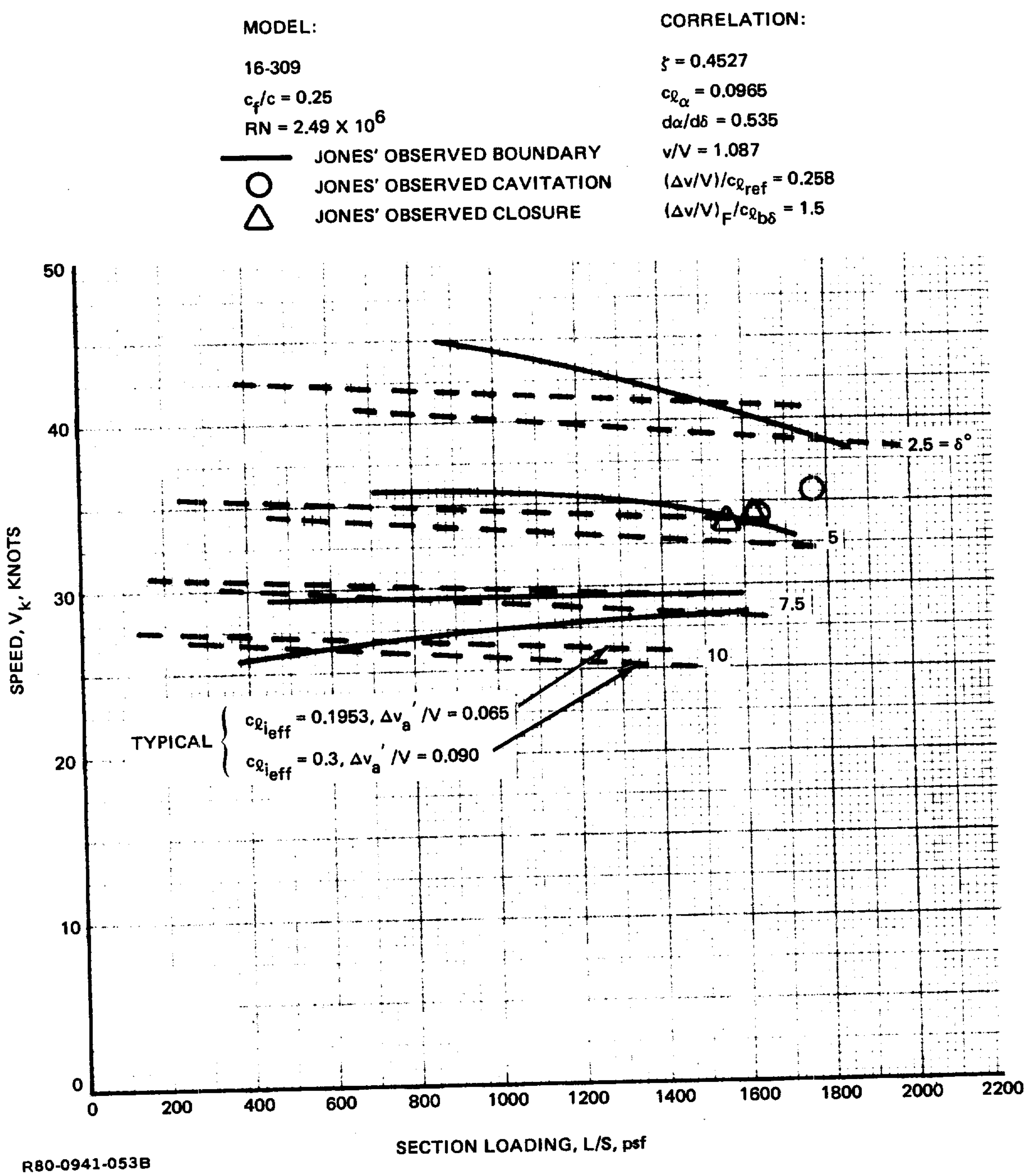

Fig. 3.3.8.5-18 Hingeline Cavitation Correlation – Dimensional Interpretation

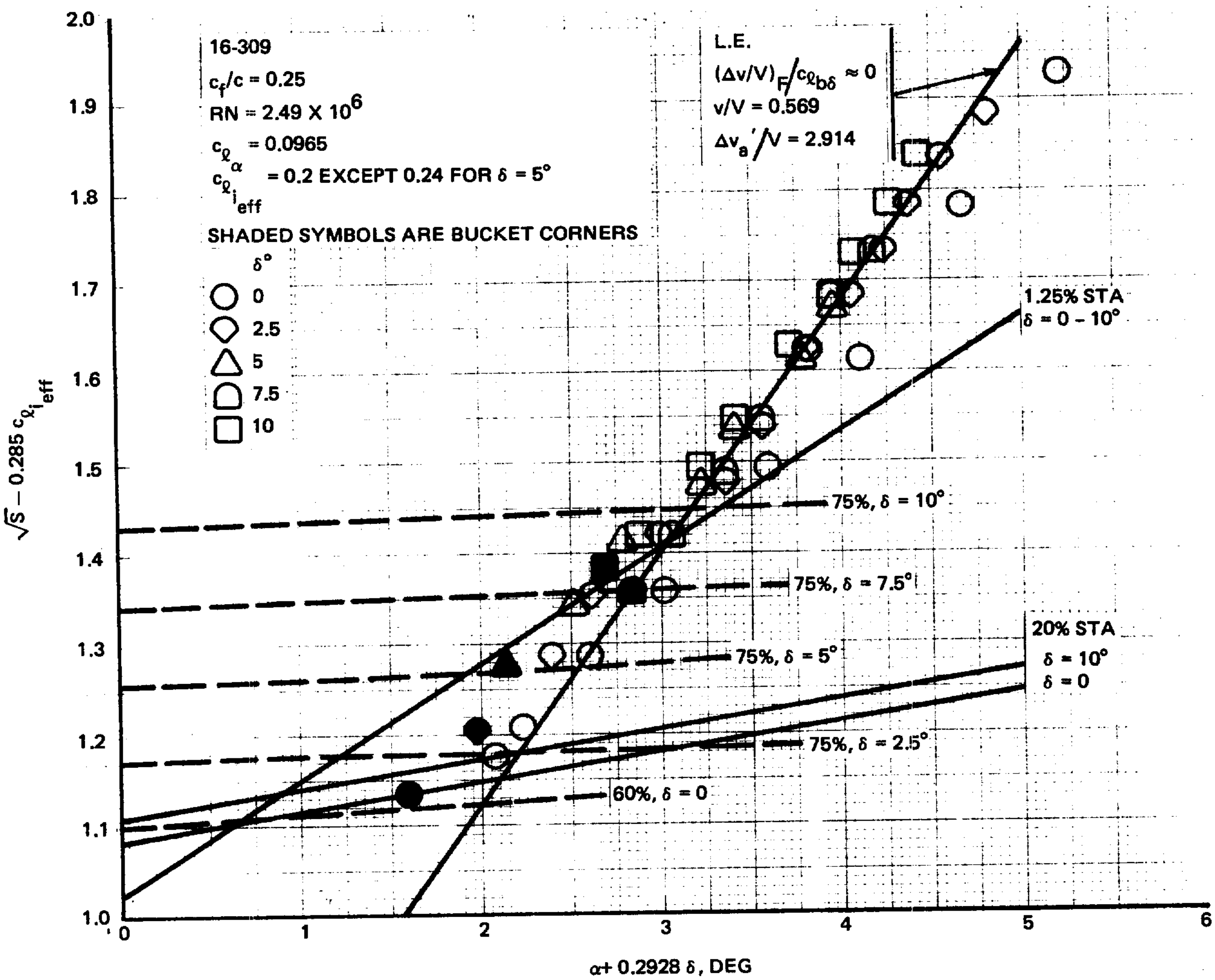

R80-0941-054B

Fig. 3.3.8.5-19 Observed Leading Edge Cavitation Boundary

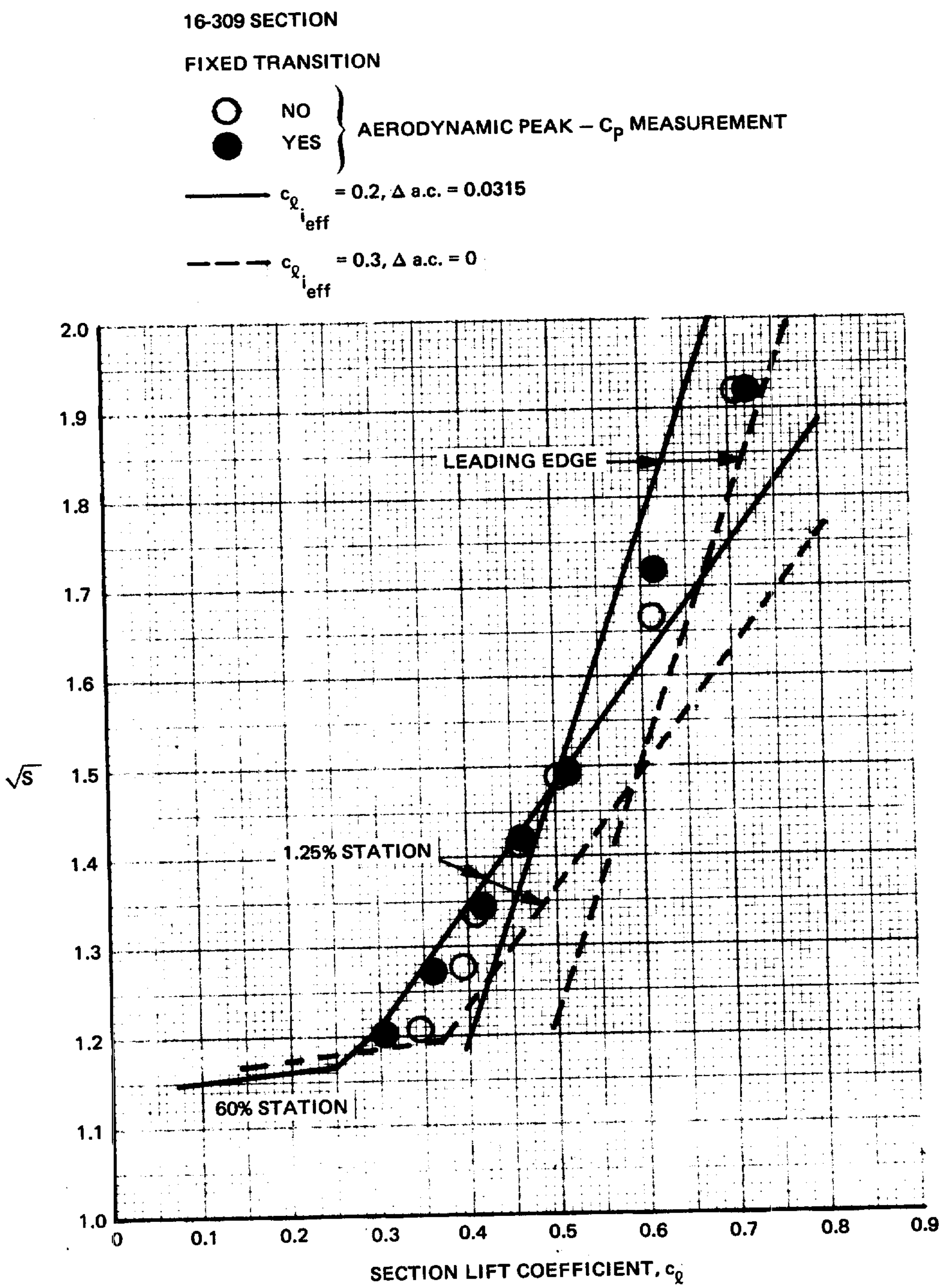

R80-0941-055B

Fig. 3.3.8.5-20 Pressure Spike Significance, $\delta = 0°$

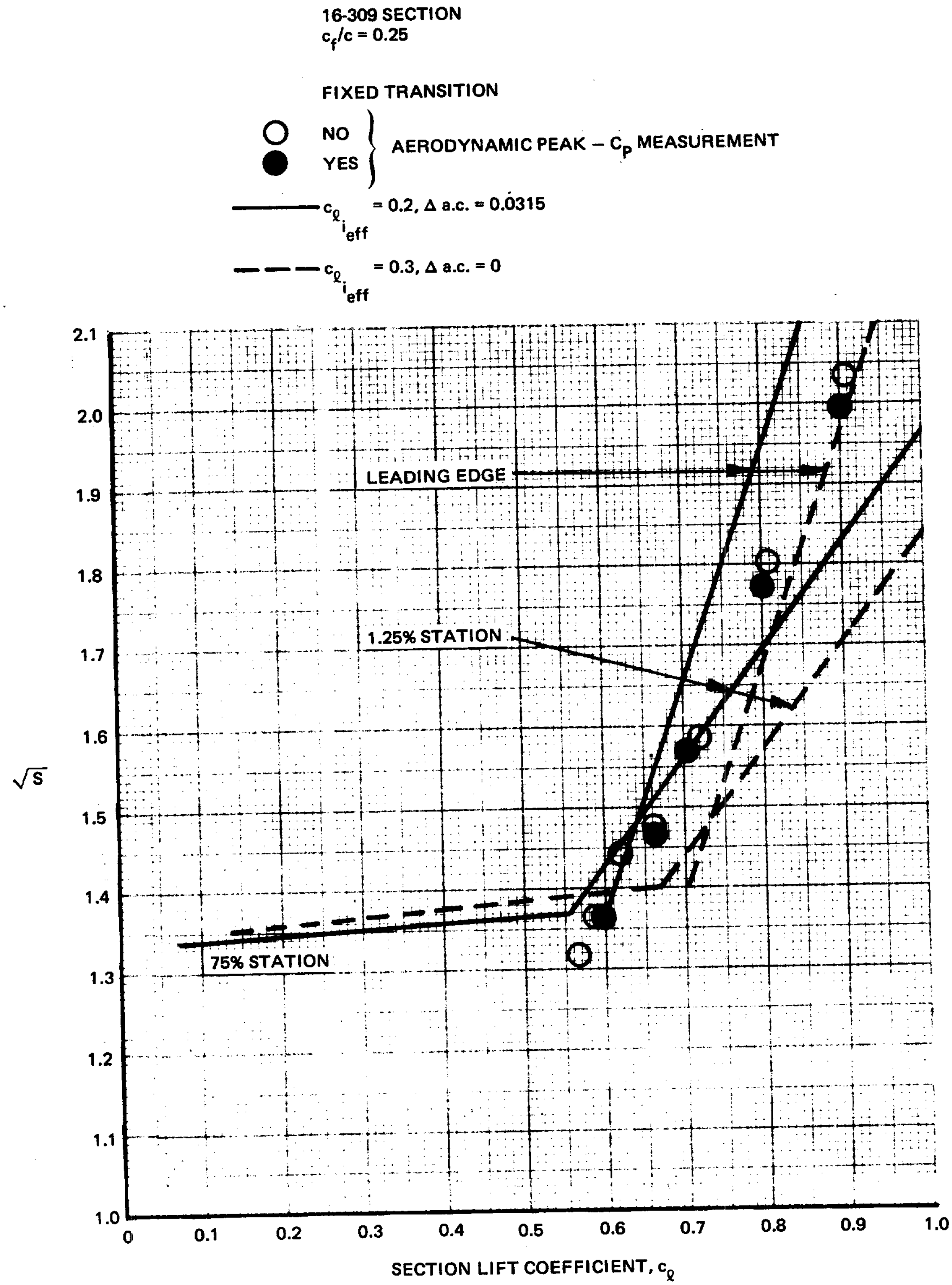

R80-0941-056B

Fig. 3.3.8.5-21 Pressure Spike Significance, $\delta = 6°$

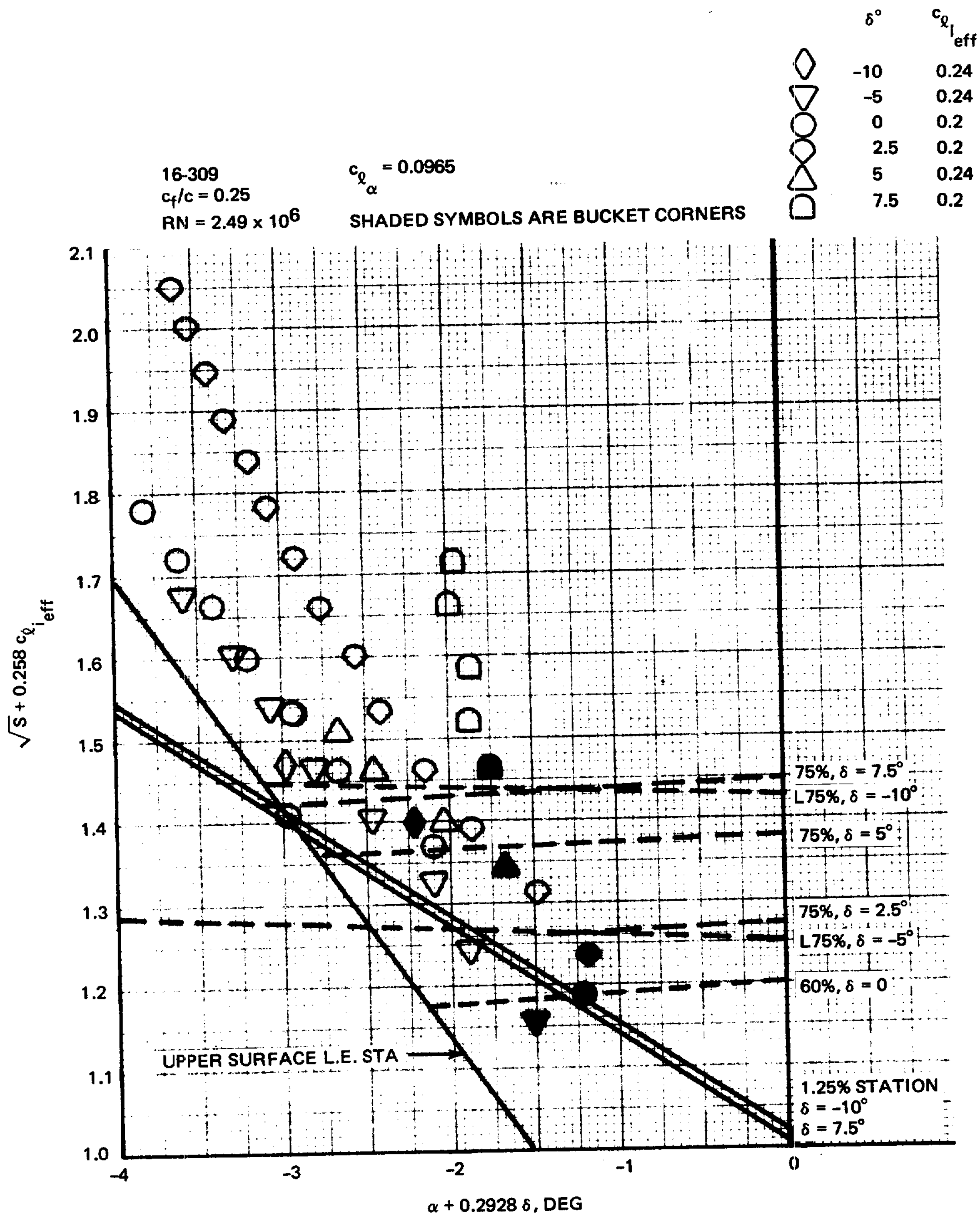

R80-0941-057B

Fig. 3.3.8.5-22 Lower Surface Leading Edge Boundary

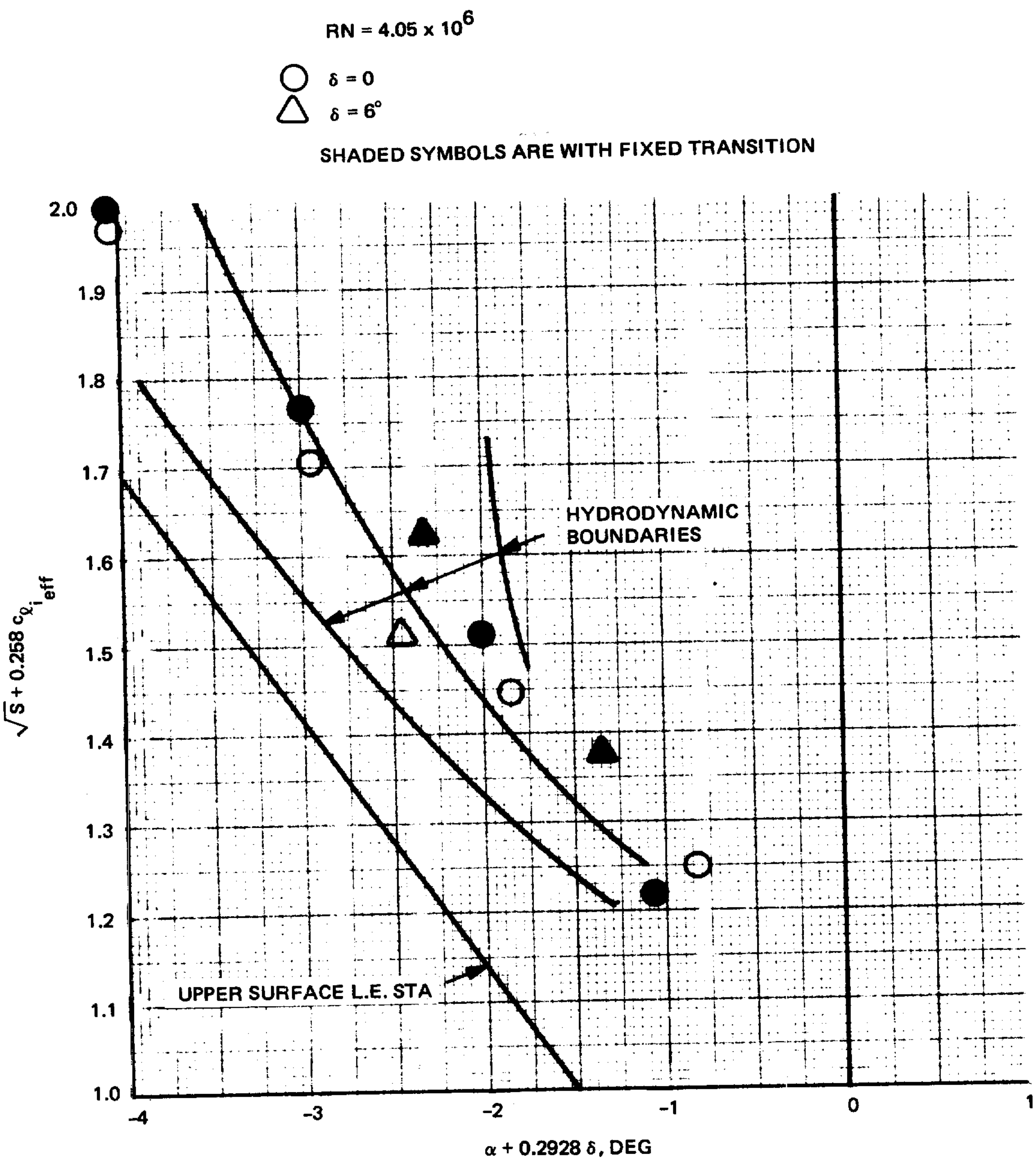

R80-0941-058B

Fig. 3.3.8.5-23 Lower Surface Leading Edge Boundary — Wind Tunnel

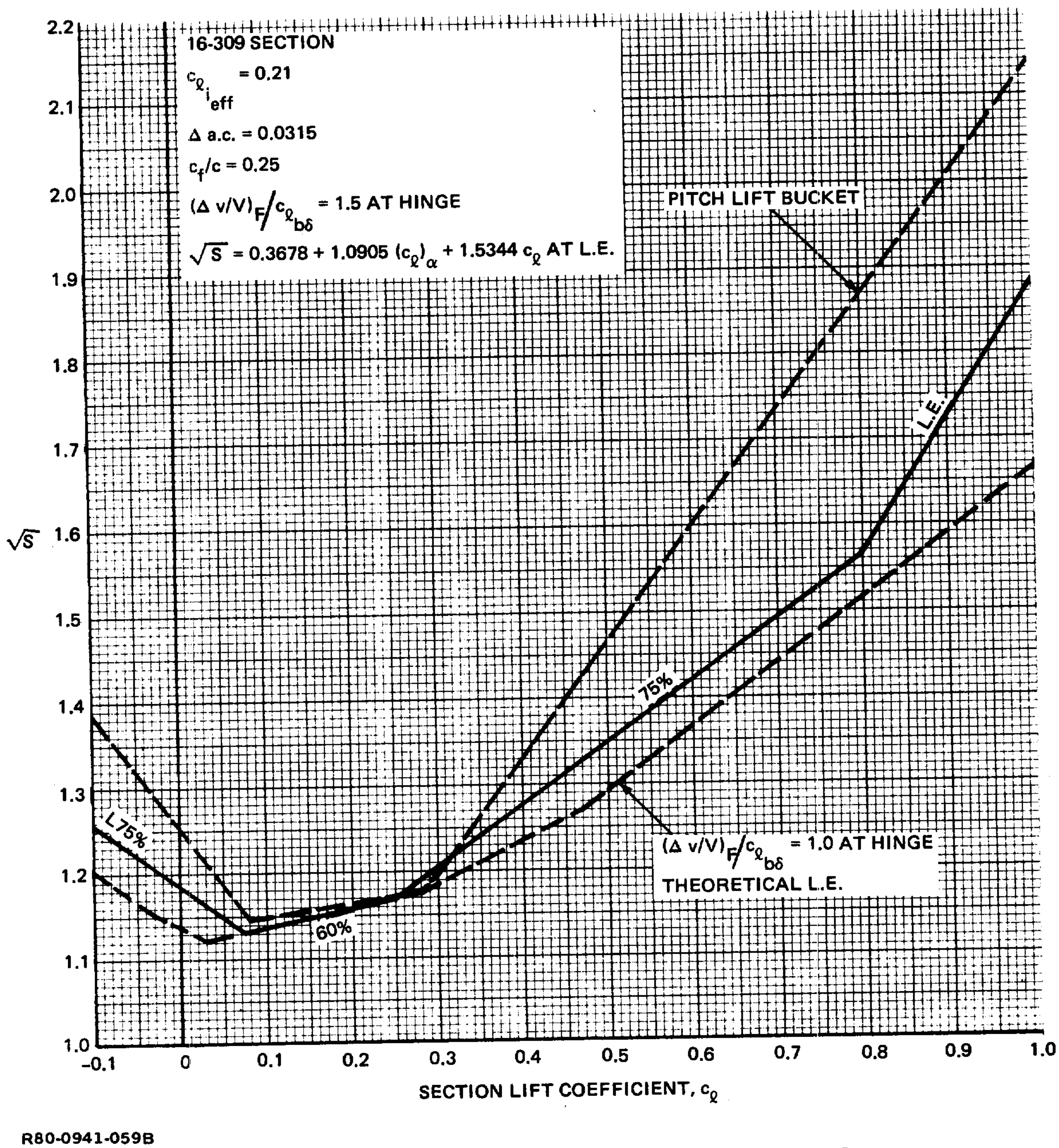

Fig. 3.3.8.5-24 Revised Flap Lift Cavitation Bucket, $\alpha = 0$

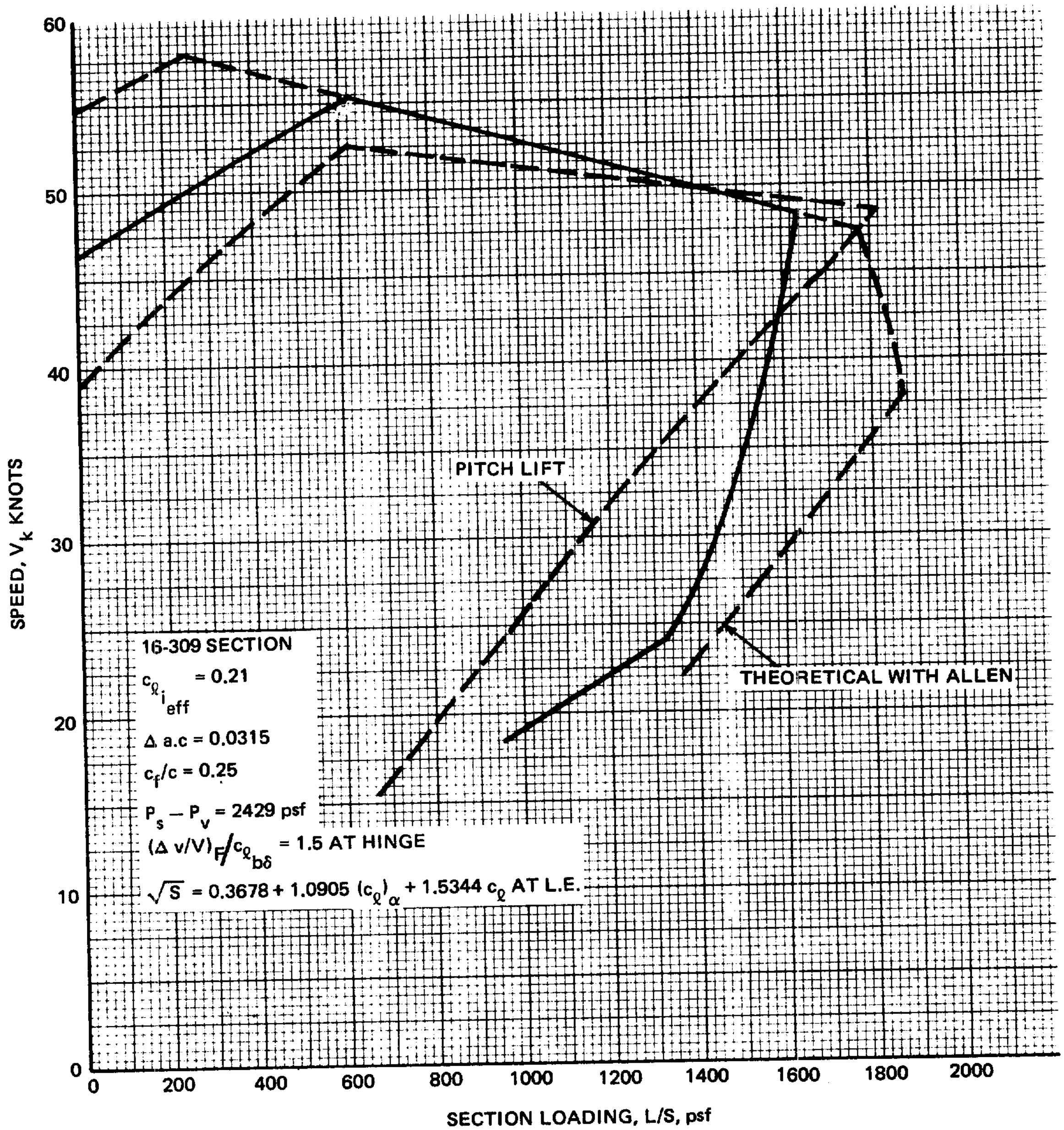

R80-0941-060B

Fig. 3.3.8.5-25 Revised Flap Lift V-L/S Bucket, $\alpha = 0$

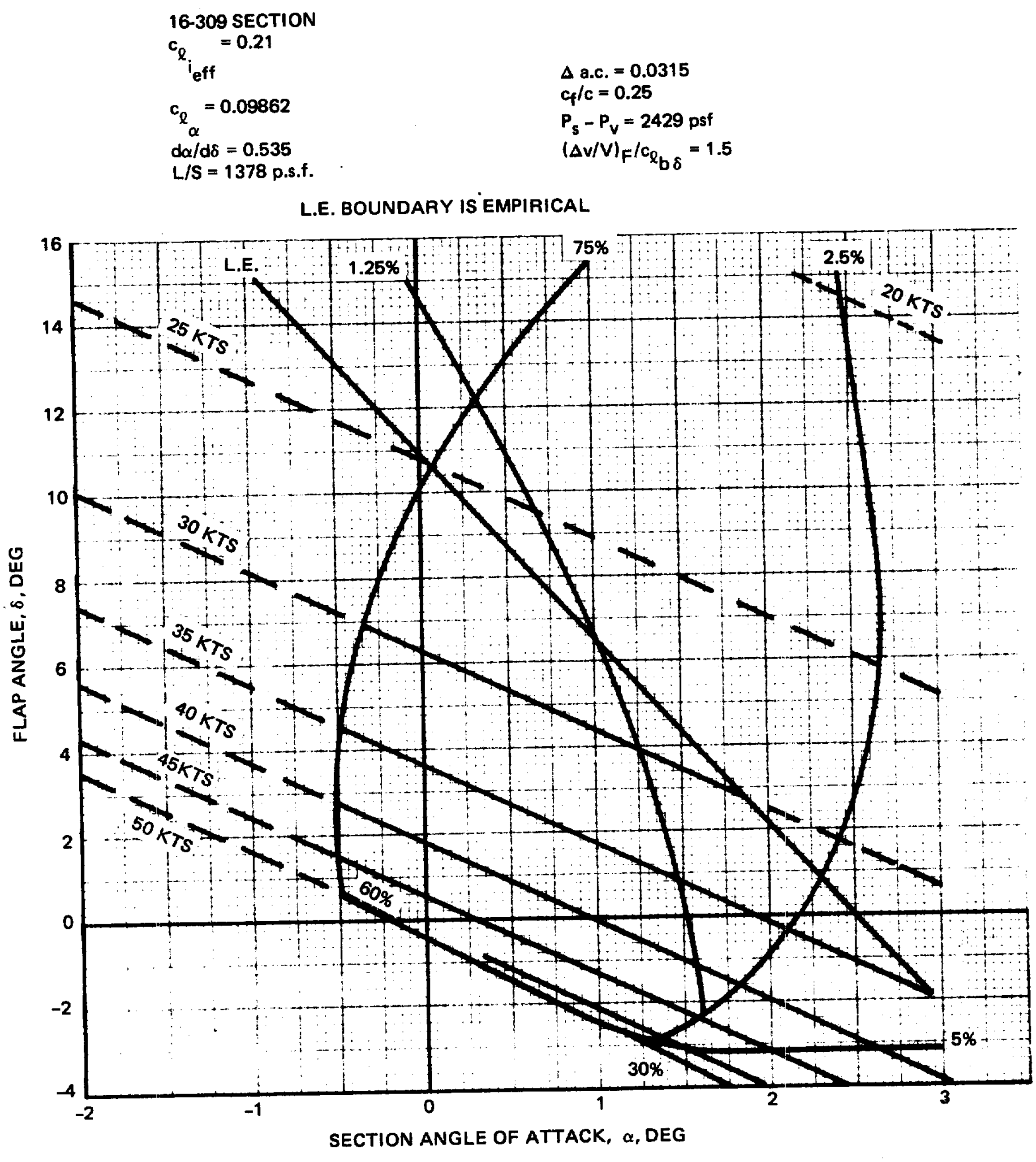

R80-0941-061B

Fig. 3.3.8.5-26 Revised Flapped Section, α-δ Plane